NEXT EVOLUTIONS IN CHARGED PARTICLE THERAPY

EDITED BY: Thomas Tessonnier, Giuseppe Magro and Stewart Mac Mein
PUBLISHED IN: Frontiers in Oncology

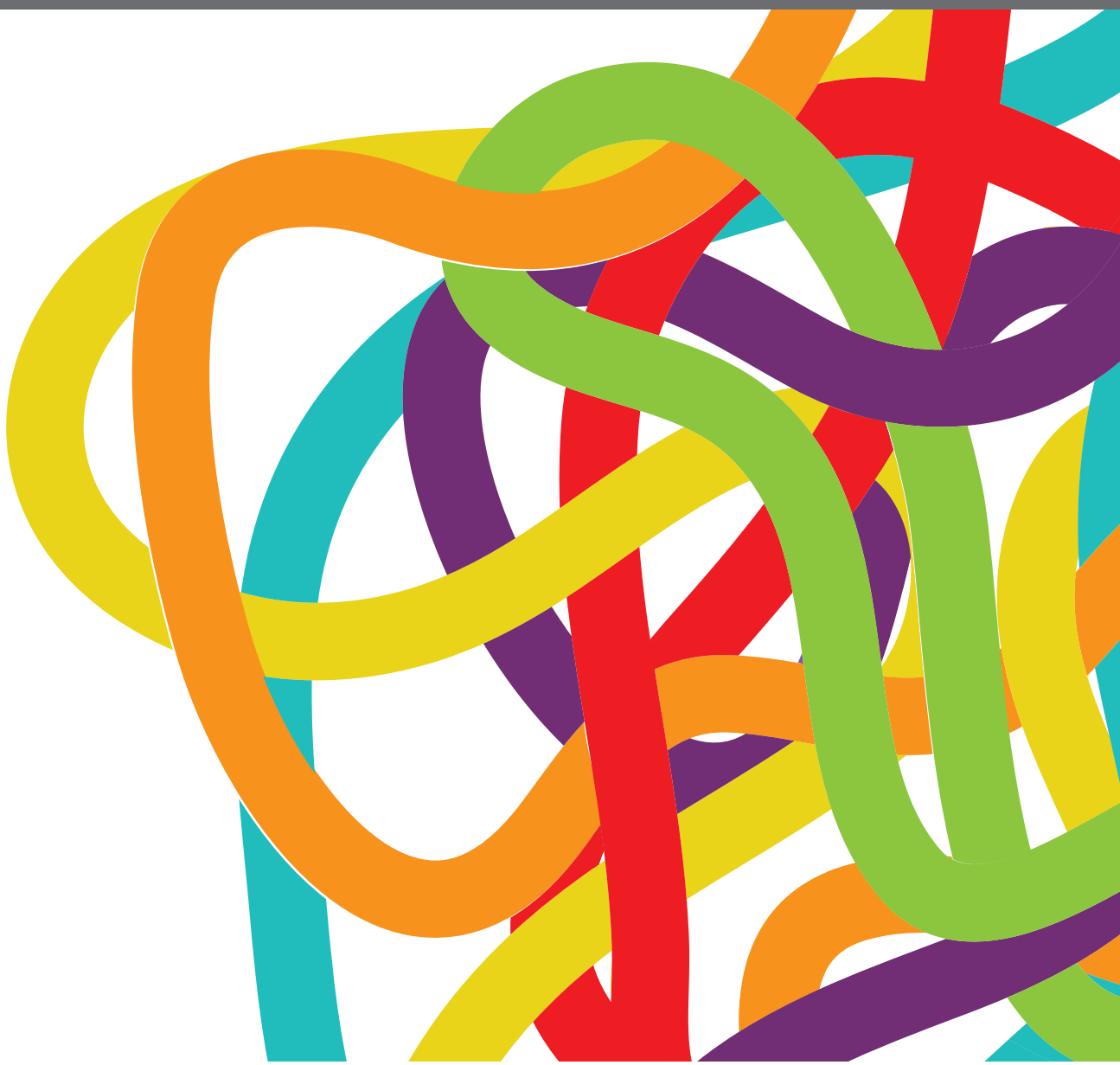

frontiers Research Topics

frontiers

ISSN 1664-8714
ISBN 978-2-88976-694-9
DOI 10.3389/978-2-88976-694-9

About Frontiers

Frontiers is more than just an open-access publisher of scholarly articles: it is a pioneering approach to the world of academia, radically improving the way scholarly research is managed. The grand vision of Frontiers is a world where all people have an equal opportunity to seek, share and generate knowledge. Frontiers provides immediate and permanent online open access to all its publications, but this alone is not enough to realize our grand goals.

Frontiers Journal Series

The Frontiers Journal Series is a multi-tier and interdisciplinary set of open-access, online journals, promising a paradigm shift from the current review, selection and dissemination processes in academic publishing. All Frontiers journals are driven by researchers for researchers; therefore, they constitute a service to the scholarly community. At the same time, the Frontiers Journal Series operates on a revolutionary invention, the tiered publishing system, initially addressing specific communities of scholars, and gradually climbing up to broader public understanding, thus serving the interests of the lay society, too.

Dedication to Quality

Each Frontiers article is a landmark of the highest quality, thanks to genuinely collaborative interactions between authors and review editors, who include some of the world's best academicians. Research must be certified by peers before entering a stream of knowledge that may eventually reach the public - and shape society; therefore, Frontiers only applies the most rigorous and unbiased reviews.
Frontiers revolutionizes research publishing by freely delivering the most outstanding research, evaluated with no bias from both the academic and social point of view. By applying the most advanced information technologies, Frontiers is catapulting scholarly publishing into a new generation.

What are Frontiers Research Topics?

Frontiers Research Topics are very popular trademarks of the Frontiers Journals Series: they are collections of at least ten articles, all centered on a particular subject. With their unique mix of varied contributions from Original Research to Review Articles, Frontiers Research Topics unify the most influential researchers, the latest key findings and historical advances in a hot research area! Find out more on how to host your own Frontiers Research Topic or contribute to one as an author by contacting the Frontiers Editorial Office: frontiersin.org/about/contact

NEXT EVOLUTIONS IN CHARGED PARTICLE THERAPY

Topic Editors:
Thomas Tessonnier, Heidelberg University Hospital, Germany
Giuseppe Magro, National Center of Oncological Hadrontherapy, Italy
Stewart Mac Mein, German Cancer Research Center (DKFZ), Germany

Citation: Tessonnier, T., Magro, G., Mein, S. M., eds. (2022). Next Evolutions in Charged Particle Therapy. Lausanne: Frontiers Media SA. doi: 10.3389/978-2-88976-694-9

Table of Contents

frontiers in Oncology

ORIGINAL RESEARCH
published: 23 June 2021
doi: 10.3389/fonc.2021.694749

Clinical Implementation of a 6D Treatment Chair for Fixed Ion Beam Lines

Jiayao Sun[1,2,3], *Lin Kong*[2,3,4], *Zhi Chen*[1,2,3], *Dan You*[2,3,5], *Jingfang Mao*[2,3,4], *Xiyin Guan*[2,3,6], *Xiaodong Wu*[1,2,3*†] *and Yinxiangzi Sheng*[1,2,3*†]

[1] *Department of Medical Physics, Shanghai Proton and Heavy Ion Center, Shanghai, China,* [2] *Shanghai Key Laboratory of Radiation Oncology (20dz2261000), Shanghai, China,* [3] *Shanghai Engineering Research Center of Proton and Heavy Ion Radiation Therapy, Shanghai, China,* [4] *Department of Radiation Oncology, Shanghai Proton and Heavy Ion Center, Fudan University Cancer Hospital, Shanghai, China,* [5] *Department of Medical Physics, Shanghai Proton and Heavy Ion Center, Fudan University Cancer Hospital, Shanghai, China,* [6] *Department of Radiation Oncology, Shanghai Proton and Heavy Ion Center, Shanghai, China*

OPEN ACCESS

Edited by:
Thomas Tessonnier, Heidelberg University Hospital, Germany

Reviewed by:
Davide Maestri, National Center of Oncological Hadrontherapy, Italy
Niek Schreuder, Leo Cancer Care, Ltd, United Kingdom

***Correspondence:**
Xiaodong Wu
xiaodong.wu@sphic.org.cn
Yinxiangzi Sheng
yinxiangzi.sheng@sphic.org.cn

†These authors have contributed equally to this work and share senior authorship

Specialty section:
This article was submitted to Radiation Oncology, a section of the journal Frontiers in Oncology

Received: *13 April 2021*
Accepted: *31 May 2021*
Published: *23 June 2021*

Citation:
Sun J, Kong L, Chen Z, You D, Mao J, Guan X, Wu X and Sheng Y (2021) Clinical Implementation of a 6D Treatment Chair for Fixed Ion Beam Lines. Front. Oncol. 11:694749. doi: 10.3389/fonc.2021.694749

Purpose: To verify the practicality and safety of a treatment chair with six degrees of freedom (6DTC) through demonstrating the efficacy of the workflow in clinical settings and analyzing the obtained technical data, including intra-fraction patient movement during the use of the 6DTC.

Materials and Methods: A clinical study was designed and conducted to test the clinical treatment workflow and the safety of the 6DTC. Based on the demonstrated dosimetric advantages, fifteen patients with head and neck tumors were selected and treated with the 6DTC. The positional error at the first beam position (PE-B1) and the second beam position (PE-B2) were analyzed and compared with the results from daily quality assurance (QA) procedures of the 6DTC and imaging system performed each day before clinical treatment. The intra-fraction patient movement was derived from the total patient alignment positional error and the QA data based on a Gaussian distribution formulism.

Results: The QA results showed sub-millimeter mechanical accuracy of the 6DTC over the course of the clinical study. For 150 patient treatment fractions, the mean deviations between PE-B1 and PE-B2 were 0.13mm (SD 0.88mm), 0.25mm (SD 1.17mm), -0.57mm (SD 0.85mm), 0.02° (SD 0.35°), 0.00° (SD 0.37°), and -0.02° (SD 0.37°) in the x, y, z (translational), and u, v, w (rotational) directions, respectively. The calculated intra-fraction patient movement was -0.08mm (SD 0.56mm), 0.71mm (SD 1.12mm), -0.52mm (SD 0.84mm), 0.10° (SD 0.32°), 0.09° (SD 0.36°), and -0.04° (SD 0.36°) in the x, y, z, u, v, w directions, respectively.

Conclusions: The performance stability of the 6DTC was satisfactory. The position accuracy and intra-fraction patient movement in an upright posture with the 6DTC were verified and found adequate for clinical implementation.

Keywords: carbon-ion radiotherapy (C-ion RT), treatment chair, upright posture, intra-fraction movement, setup error

INTRODUCTION

Radiation therapy with proton or carbon-ion beams offers physical and biological advantages over x ray beams for many clinical indications (1, 2). An optimal ion beam plan can often be achieved with only two to four beam entry angles; either by rotating the beam delivery gantry, rotating the patient positioning table, or both. Selection of the angles is crucial for achieving the desired target dose coverage while minimizing the dose to the organs at risk (OARs). Most operating proton centers are equipped with one or more rotating gantries. Due to the high cost of carbon-ion beam gantries, however, carbon ion centers typically only have fixed direction beam lines (3). The flexibility of beam orientation for achieving optimal plans and treatments is naturally compromised when using fixed beam lines compared to rotating gantries. To overcome this disadvantage, a treatment chair with six degrees-of-freedom (6DTC) was designed, manufactured, and installed in Shanghai Proton and Heavy Ion Center (SPHIC) for use with a fixed beam line. The 6DTC consists of a 360°-rotating platform, a six-degree-of-freedom (6DOF) hexapod platform, an XYZ-translation platform, and a seat with an adjustable height carbon fiber head and shoulder fixation interface plate (4). Before the clinical study with patients commenced, a series of measurements to test the performance of the 6DTC showed that it had met the requirements for clinical applications (5).

Due to the high geometrical and physical definition of ion beams, patient localization and position correction are essential. This is especially so for the treatment of head and neck cancers given the complexity of the anatomy and the proximity of tumors to critical organs (6, 7). In most modern ion beam therapy facilities, image-guided radiotherapy (IGRT) systems with orthogonal kV images or cone beam CT (CBCT) are used to obtain position correction vectors for patient alignment. Treatments with patients in a lying posture are most commonly used in radiation therapy and there have been many reports of that clinical experience including setup accuracy and intra-fraction patient movement (8–13). On the other hand, there have been only a few studies that reported on the experience of radiation treatments using an upright posture, either with x ray or ion beams (14–21). To the best of our knowledge, beside a preliminary study of intra-faction movement in seated posture by films in 1980s (22), neither the clinical workflow nor the intra-fraction patient movement of the treatment with patients in an upright posture on a chair has been reported after the advent of image guidance.

A clinical trial to verify the practicality and safety of the 6DTC was designed and conducted at SPHIC. The results presented herein demonstrate the efficacy of the workflow for the clinical implementation of the 6DTC. Furthermore, the obtained technical data, including the intra-fraction patient movement, have not only confirmed the adequate accuracy of the 6DTC for clinical applications, but also provided the direction for future improvements of the 6DTC.

MATERIALS AND METHODS

For the clinical implementation of the 6DTC, two sets of policies and procedures were developed: first for technical quality assurance (QA) to assure the accuracy and mechanical performance of the chair, and second for the clinical workflow from simulation through planning, patient alignment, and treatment delivery.

Daily QA of the 6DTC With Rigid Phantom

An anthropomorphic head phantom (PBU-60, KYOTO KAGAKU, Japan) was used for performing the daily QA of the 6DTC before clinical treatment every day. The daily QA procedure was described in detail previously (5). In brief, a random setup error was manually introduced when positioning the head phantom on the chair at the pre-treatment position which was also the setup position. The positional error at the pre-treatment position (PE-P) was obtained by comparing a first pair of orthogonal kV x-ray images with digitally reconstructed radiographs (DRRs) generated from the planning CT images. The 6DTC was subsequently rotated to the treatment position as provided in the treatment plan without applying the correction vector of PE-P, followed by a second pair of KV images to obtain the positional error at the treatment position (PE-T). The correction vector of PE-T was applied, and a third pair of orthogonal kV x-ray images were acquired to obtain the residual positional error at the treatment position (RPE-T).

In essence, the daily QA executes a setup simulation with a head phantom. The purpose of the third pair of orthogonal kV x-ray images is to confirm the final alignment accuracy after the corrections have been applied. The residual positional errors determine whether the performance integrity of the chair is acceptable to proceed with its clinical usage each day.

In this paper, the daily QA data was acquired on each of the 91 treatment days over a period of nine months were recorded. The deviations between PE-P and PE-T and between PE-T and RPE-T were analyzed to assess the performance stability of the chair.

Clinical Implementation

A clinical study was designed to evaluate the feasibility of the clinical implementation of the 6DTC. The structure of the study followed the 6DTC clinical treatment workflow as shown in **Figure 1**. The implementation of the 6DTC involves three basic steps described in the following subsections.

Immobilization and CT Simulation

Due to the design of the fixation equipment, the patient immobilization procedure was the same regardless of whether the posture during treatment would be lying or sitting. All patients were scanned in the lying position (23, 24). A low-density foam cradle attached to a head and shoulder fixation interface plate was used to immobilize each patient's head, neck, and shoulders with a nine-pin commercial thermoplastic face mask. Planning CTs were acquired using a 1.5 mm slice thickness

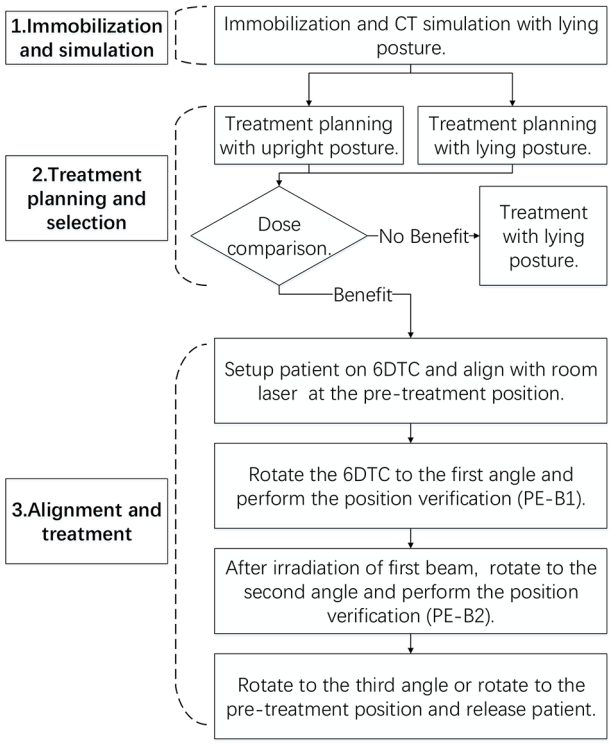

FIGURE 1 | The clinical treatment workflow for this clinical trial.

in helical mode and then transferred to the Syngo® treatment planning system (TPS) (V13B, Siemens, Germany). When the positioner type of "chair" was selected, the CT image set was re-orientated automatically by the TPS to change the patient posture from lying to sitting. The patient's internal anatomy was assumed to remain rigid during the re-orientation.

Treatment Planning and Selection of Treatment Technique

Two types of treatment plans were generated for each patient; one using the treatment table and one using the chair. The planning objectives were to cover at least 95% of clinical target volume (CTV) with 95% of the prescription dose and to minimize the dose to the OARs using two to three beam entry angles. Since the lack of robust planning technique in Syngo, planning target volume (PTV) was added depending on individual factor such as beam angle chosen and was ranged from 3-5mm (23, 25). CTV coverage and OARs dose were compared for the two types of plans. Patients were selected for the treatment with 6DTC only if the chair plan fulfilled three eligibility criteria: superiority in sparing the OARs, comparable target coverage, and without increasing the penetration uncertainty. Patients with CTV lower than the head were excluded.

Alignment and Treatment

For each fraction of treatment, the patient alignment was carried out as follows:

A Vac-lok cushion (CIVCO Radiotherapy, USA) was used to register the patient's thigh and butt and a back cushion was used to support the back when setting up the patient on the chair (**Figure 2**). The patient's head was immobilized with the customized thermoplastic mask and foam cradle. The patient was initially aligned with the room lasers at the pre-treatment position (with the 6DTC facing the nozzle), then rotated to the planned chair iso rotation angle of the first beam. A pair of orthogonal kV x-ray images were acquired and the registration of the kV images with the DRRs was performed with respect to the bony anatomy. The positional errors at the first beam position (PE-B1) (three translational shifts lateral x_{B1}, longitudinal y_{B1}, vertical z_{B1}, and three rotational shift iso u_{B1}, pitch v_{B1}, roll w_{B1}) were then recorded. The coordinate system follows the International Electrotechnical Commission (IEC) convention and was well illustrated by Sheng et al. (5) The patient position was then corrected by applying the PE-B1 to the 6DTC after which the planned beam was delivered. After finishing the irradiation of the first beam, the 6DTC was rotated to the planned chair iso rotation angle for the second beam. The second pair of orthogonal KV x-ray images were acquired and registered with the DRRs to obtain the positional errors for the second beam position (PE-B2) (three translational shifts x_{B2}, y_{B2}, z_{B2}, and three rotational shift u_{B2}, v_{B2}, w_{B2}). The 6DTC was then repositioned and the second beam delivered. The last procedure was repeated if there were more than two beams for the fraction of treatment. The treating physician was required to be present to review and approve the alignment procedures for each fraction of the treatment.

Analysis of Position Accuracy

In a previous report, it was shown that under x-ray-based image guidance, the 6DTC could provide positional alignment with sub-millimeter accuracy with a rigid phantom in an upright posture (5). The sources of errors came from different components of the chair and the imaging system. When applied to clinical settings, however, an additional source of positioning error is present due to patient motion. This source should also be assessed and addressed.

In this clinical study, the chair and imaging related mechanical errors and the patient-specific intra-fraction position error were derived and evaluated. The measurements representing the composite effects from both sources of errors were identified, collected and analyzed. Specifically, the deviation between PE-T and PE-P representing the positional errors introduced by both the chair and the IGRT system (5) can be considered as a Gaussian distribution denoted as $N_1(\mu_1, \sigma_1^2)$. In this study, $N_1(\mu_1, \sigma_1^2)$ was calculated from the daily QA data with the rigid phantom. In this study, the intra-fraction movement from patients was not directly assessed; rather, the net excursion from the final setup position of the first beam to the final setup position of the second beam was used as a presentation of patient-specific intra-fraction movement; this excursion can be considered as another independent Gaussian distribution, denoted as $N_2(\mu_2, \sigma_2^2)$. In the afore-described alignment procedure, the deviation between PE-B1 and PE-B2 was the

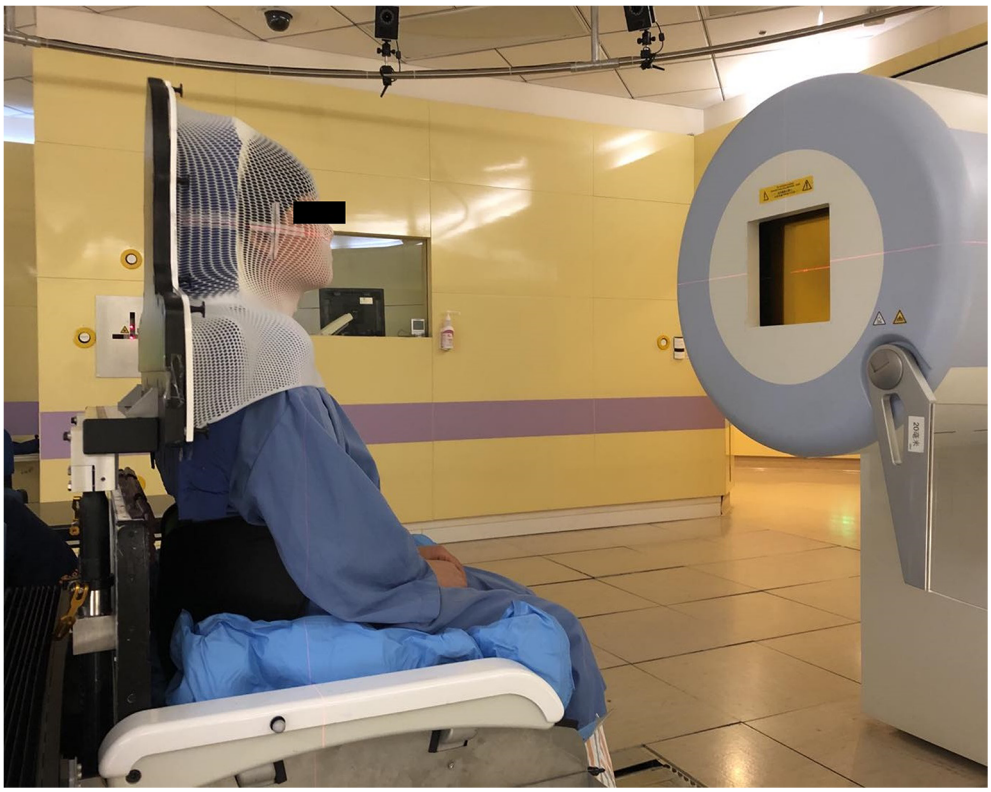

FIGURE 2 | The patient setup on the 6DTC.

composite or total positional errors introduced by the chair/IGRT system and the patient's intra-fraction movement was denoted as $N_3(\mu_3, \sigma_3^2)$. It naturally follows that

$$N_3\left(\mu_3, \sigma_3^2\right) = N_1\left(\mu_1, \sigma_1^2\right) + N_2\left(\mu_2, \sigma_2^2\right) \quad (1)$$

$$\mu_3 = \mu_1 + \mu_2 \quad (2)$$

$$\sigma_3^2 = \sigma_1^2 + \sigma_2^2 \quad (3)$$

where μ_i is the expectation of Gaussian distribution, and σ_i is the standard deviation.

The study was reviewed and approved by the Institutional Review Board (Approval No: 1812-29-04).

RESULTS

Patient Accrual

15 patients were selected to receive treatments with the 6DTC based on the criteria mentioned above. The characteristics of these 15 patients are listed in **Table 1**.

Treatment Planning, Dosimetric Comparison and Selection of Treatment Technique

For each of the fifteen patients, the target received comparable coverages with the chair and table plans. The volumes of the CTV that received ≥95% of the prescription dose (V95) were 98.81% ± 1.45% (mean ± standard deviation) and 98.48% ± 2.14% for the chair plans and table plans respectively, i.e., no significant difference (p=0.334).

For the OARs, in the eight NPC patients, chair plans achieved a lower mean dose in both the bilateral parotids and cochleae. Specifically, the mean doses to the right parotid, left parotid, right cochlea and left cochlea were 28.5% ± 18.3%, 28.0 ± 21.0%, 26.6% ± 22.7%, and 32.9% ± 25.0% lower with the chair plans comparing with the table plans, respectively. (p=0.006, 0.002, 0.017, and 0.016, respectively.) Furthermore, chair plans could also decrease the mean dose to temporal lobes by 49% ± 27%, compared with table plans. (p=0.007)

In the two patients with tumors around the orbits, chair plans showed 50% to 100% lower mean dose to the contralateral eye globe. For the other five patients, the chair plans reduced the mean dose of the parotid and the cochlea by 4% to 26%.

TABLE 1 | Characteristics of patients.

Characteristics	No. of patients
Age	
Median (Range)	48 (21-83)
Weight (kg)	
Median (Range)	61 (49-105)
Height (cm)	
Median (Range)	168 (146-177)
Gender	
Male	9
Female	6
KPS	
100	7
90	8
Disease (Tumor Site)	
Nasopharyngeal carcinoma (NPC) (Nasopharyngeal)	8
Meningioma (Cerebellopontine Angle)	1
Adenoid cystic carcinoma (Maxillary sinus)	1
Squamous cell carcinoma (External auditory canal)	1
Adipose-derived tumor (Orbit)	1
Osteosarcoma (Orbit)	1
Atypical carcinoid tumor (Slope)	1
Chordoma (Skull base)	1
No. of fractions treated with 6DTC	
5*	9
8	1
10	1
20	3
27	1
No. of beams per plan	
2	14
3	1

**For these nine patients, the prescriptions were 56 Gy(RBE) delivered by either protons or x rays in 28 fractions using a lying posture plus 17.5Gy(RBE) by carbon ions in five fractions using a sitting posture.*

Treatment Delivery

Daily QA of 6DTC With Rigid Phantom

On each day when at least one fraction of a chair treatment was scheduled, the daily QA of the 6DTC with a rigid phantom was performed.

The mean deviations between PE-T and PE-P were 0.21mm (SD 0.70mm), -0.49mm (SD 0.36mm), -0.02mm (SD 0.11mm), -0.08 (SD 0.13°), -0.09(SD 0.09°), and 0.02 (SD 0.08°) in the x, y, z, u, v, w directions, respectively.

The mean deviations between RPE-T and PE-T were 0.18mm (SD 0.23mm), -0.18mm (SD 0.18mm), 0.06mm (SD 0.12mm), 0.09° (SD 0.13°), 0.02°(SD 0.14°), and 0.01° (SD 0.09°) in the x, y, z, u, v, w directions, respectively.

The acceptance criteria for the deviation between PE-T and PE-P and between RPE-T and PE-T is within 1.5mm and 1.5°. If the deviation is out of tolerance, the daily QA must be repeated, and if the result still fails, the chair would need to be re-calibrated, especially for the rotation center of the 360°-rotating platform. Having performed the daily QA for the 91 fractions of treatments, only two of them failed, which were promptly restored after re-calibrating the rotation center.

Patient Alignment

For the fifteen patients selected for chair-treatment, a total of 150 fractions of treatments were delivered, with fourteen patients having two beam angles and one patient having three beam angles in each treatment fraction. The average treatment time from the patient sitting down on the chair to leaving the chair was 30 minutes (SD 7 minutes). The PE-B1 and PE-B2 were recorded and their deviations, defined as the total positional error were calculated. **Figure 3** shows the mean deviations in all six degrees of freedom for each patient.

The mean deviations between PE-B1 and PE-B2 for all patients were 0.13mm (SD 0.88mm), 0.25mm (SD 1.17mm), -0.57mm (SD 0.85mm), 0.02° (SD 0.35°), 0.00° (SD 0.37°), and -0.02° (SD 0.37°) in the x, y, z, u, v, w directions, respectively. Of the mean translational deviations between beams, 91.1% were within ±1.5mm, while all the mean deviations were within ±2mm except for the vertical value of one patient (No. 13). For rotational deviations, only one value exceeded 0.5°.

For each fraction, as shown in **Table 2**, the frequencies of deviation greater than 1 mm in the x, y, z, directions were 27.3%, 33.3%, and 26.7%, respectively. The frequencies of deviation greater than 1° in the u, v, w directions were 1.3%, 2.7%, and 2.0%, respectively. There were no deviations >4mm in the x and z translational directions and only 2 in the y direction. There were no deviations > 2° in any of the rotational directions. Note that these deviations were those present before the position correction was applied to the alignment for the second angle.

Intra-Fraction Movement

Based on the formula 1-3, the mean intra-fraction patient movements were calculated, which were -0.08mm (SD 0.56mm), 0.71mm (SD 1.12mm), -0.52mm (SD 0.84mm), 0.10° (SD 0.32°), 0.09° (SD 0.36°), and -0.04° (SD 0.36°) in the x, y, z, u, v, w directions, respectively (**Figure 4**).

DISCUSSION

We have introduced a clinical treatment workflow for using the 6DTC to deliver particle treatment in an upright seated posture and presented our experience in a feasibility clinical study. During the course of this clinical study, a total of 320 head and neck patients received particle radiotherapy with the table and the 6DTC. Of these patients, 15 patients were selected to receive the treatment of the 6DTC. For other patients, due to no obvious benefit from the 6DTC, lying posture was chosen. Using our designed workflow, the immobilization procedures for upright treatment were designed to be the same as the lying treatment. If the advantage of the chair plan was observed, treatment in the upright posture can be easily achieved by transferring the alpha-cradle (with the bottom cut off) to the chair head/shoulder fixation interface plate. On the other hand, if no benefit was indicated, patients can go on to receive the treatment in lying posture without changing the immobilization device or undergoing planning CT simulation again.

The rotating gantries of particle therapy provide a wide range of beam entry orientations, and are therefore desirable for obtaining optimal plans and treatments. Notwithstanding, there are challenging issues, including inaccuracy of the iso-center due

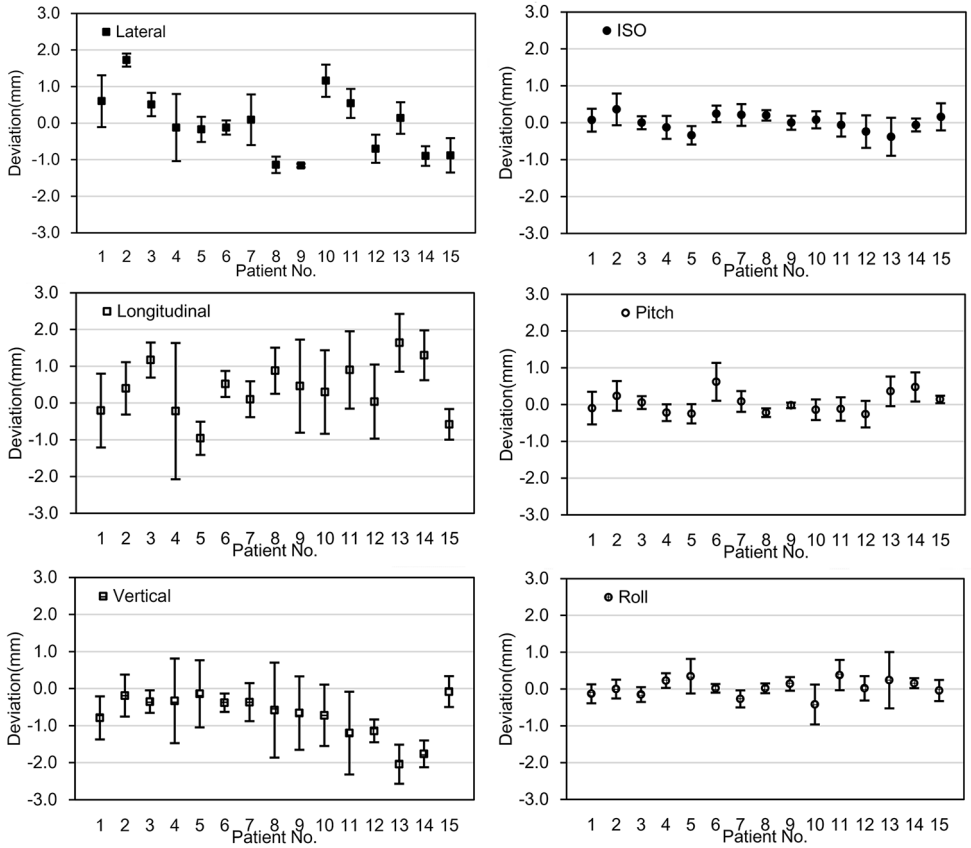

FIGURE 3 | The deviation between PE-B1 and PE-B2. The x-axis represents the fifteen individual patients; the y-axis represents the mean value of the deviation of the specific patient in 6 degrees of freedom. Error bars represent for the standard deviation.

TABLE 2 | Frequency of deviation [%] between PE-B1 and PE-B2 by thresholds.

	Translational				Rotational		
	x	y	z		u	v	w
>1mm	41(27.3)*	50(33.3)	40(26.7)	>1°	2(1.3)	4(2.7)	3(2.0)
>2mm	1(0.7)	10(6.7)	8(5.3)	>2°	0(0.0)	0(0.0)	0(0.0)
>3mm	0(0.0)	2(1.3)	1(0.7)	>3°	0(0.0)	0(0.0)	0(0.0)
>4mm	0(0.0)	2(1.3)	0(0.0)	>4°	0(0.0)	0(0.0)	0(0.0)
>5mm	0(0.0)	0(0.0)	0(0.0)	>5°	0(0.0)	0(0.0)	0(0.0)

**Data in parentheses are percentages.*

to its excessive weight and the instability of beam qualities when the beam nozzle rotates. Moyers et al. (26) reported the maximum iso-center shifts of 1.17 mm along the clockwise path and 1.26 mm along the counterclockwise path for proton rotating gantries. Kato et al. (27) also reported up to 1mm of deviation at iso-center in proton rotating gantries. With a markedly more massive carbon-ion gantry, one could only expect the worse, although no data have been reported. The initial intent of developing the 6DTC was to compensate for the lack of beam rotation with a fixed beam line. Our studies have shown that the mechanical accuracy of the 6DTC is comparable to the rotating gantries. Given its simplicity over the

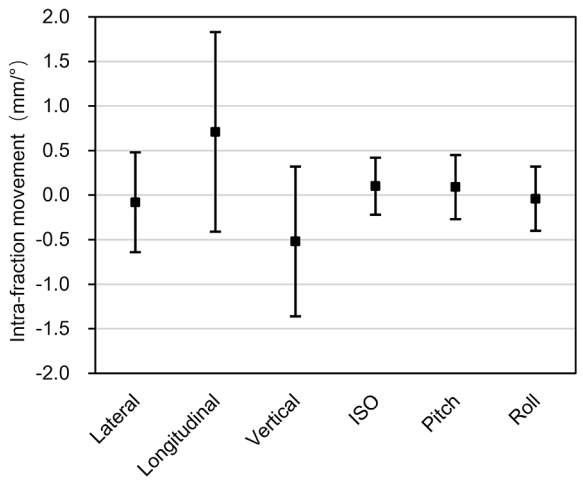

FIGURE 4 | Intra-fraction patient movements. The x-axis represents the three translational directions and three rotational directions, while the y-axis represents the amplitude of the intra-fraction patient movements. The error bars represent the standard deviation.

gantry, the improvement to further reduce errors will be logically easier to achieve with the chair. With the development of vertical CT (28), when equipped with a 6DTC, the fixed beam nozzle may become the preferred configuration for modern carbon-ion radiotherapy facilities.

Positional shifts of patients related totable rotation during treatments have been reported in several studies. Rosenfelder et al. (29) reported up to -0.8 ± 0.7 mm positional shifts in the longitudinal direction for noncoplanar beams in external beam radiotherapy. Sarkar et al. (30) reported an average shift of 0.6 ± 0.9mm in the lateral direction for noncoplanar beams in stereotactic radiotherapy (SRT) and stereotactic radiosurgery (SRS) using frameless setup. Lewis et al. (31) reported an average shift of 0.55 ± 0.43 mm in the lateral direction for noncoplanar beams in SRS. Overall, the shifts observed in this study are comparable to those found in these other studies. The position deviation between PE-B1 and PE-B2 is attributed to the positional errors introduced by both the chair and the patients' intra-fraction patient movement. The maximum mean deviation in our study was -0.57 ± 0.85mm (z-direction). The maximum combined translational and rotational shifts reported by Sarkar et al. (30) were -3.1mm and 4.2°, while we found 4.6mm and 1.6° in our study. By analyzing the CBCT performed before and after IMRT treatment Den et al. (32) reported the residual error frequencies ranging from 23.0% to 34.0% and 3.0% to 5.4% for >1mm and >3mm thresholds, while Lu et al. (33) reported frequencies from 17.5% to 30.8% and from 0.0% to 4.5% for 1mm and 2mm thresholds using similar methods. In our study, the frequencies of the deviations between PE-B1 and PE-B2 with thresholds >1mm, >2mm and >3mm ranged from 26.7% to 33.3%, 0.7% to 6.7%, and 0.0% to 1.3%, respectively, again, comparable to the published data. For the frequencies of the rotational deviation, 1.3% to 2.7% exceeded 1° threshold, while none exceeded 2°.

Even with an immobilizing thermoplastic mask, the considerable patient movement had been reported for treatments with lying posture (13). For patients treated in sitting posture for about 30 minutes (including setup, position correction procedures, and treatment delivery), the potential impact of intra-fraction patient movement should call for the same if not more attention. The results of the sub-millimeter magnitude of intra-fraction patient movement in this study were similar to the findings given in other published studies. Linthout et al. (13) evaluated the mean intra-fraction patient movement for head and neck patient in lying posture and reported 0.0mm, 0.3mm, -0.5mm, -0.1°, 0.1° and -0.2° in the x, y, z, u, v, w directions, respectively. Pang et al. (11) showed that the mean translational intra-fraction patient movement in all directions ranged from -1.8 to 1.1 mm and that the calculated mean overall intra-fraction patient movement was 0.3mm for head and neck patients in lying posture. For treatments in the upright posture, McCarroll et al. (16) reported a range of the order of several millimeters for intra-fraction patient movements. Balakin et al. (17) reported up to a 3 to 4mm shift in the thermoplastic mask during proton beam radiation therapy while in the sitting posture. In our study, the mean intra-fraction patient movements were -0.08mm, 0.71mm, -0.52mm, 0.10°, 0.09°, and -0.04° in the x, y, z, u, v, w directions, respectively, and only the intra-fraction patient movements in the y and z direction exceeded 0.5mm. The aforementioned intra-fraction patient movement was based on 30-minute (SD 7 minutes) treatment time. Although 6DTC could offer wide range of beam entry angles, its true advantage is in the selection optimal beam entry angles rather than adding more beams to a plan. Two to three beam entry angles can often achieve an optimal plan in particle radiotherapy. Adding more beam entry angles will prolong the treatment time and cause a larger intra-fraction patient movement with minimal gain in improving the dose distribution.

There are several factors that contribute to intra-fraction patient movement. Strategies devised to mitigate each specific cause could potentially reduce the associated errors. From our experience, when patients sit in a chair for a long time, they tend to sag their heads from fatigue, although being immobilized in the thermoplastic head mask. Tilting the chair slightly backward might overcome this movement. A few patients complained about the mask being too tight for the jaw, making them uncomfortable. Pitching the chair five to ten degrees backwards during the planning stage would make the patient lean against the head/shoulder fixation interface plate and could reduce the discomfort. Pitching the chair, however, requires a significant translation of the chair rotating platform between beam applications to perform isocentric treatments which could induce additional errors. In general, finding a comfortable yet secure position should relieve stress and reduce the intra-fraction patient movement.

CONCLUSIONS

In this study, the feasibility for ion beam radiotherapy using the 6DTC in upright seated posture and the performance stability of the 6DTC were demonstrated. Over the span of 150 fractions of treatment (nine months), our results indicated that the position accuracy and intra-fraction patient movement in upright seated posture were similar to published data for lying posture, which is considered acceptable by the state of the art of current clinical practice. Due to the inevitably increased physical demand on patients in sitting posture, however, an improved immobilization method to further reduce intra-fraction patient movement is desirable.

DATA AVAILABILITY STATEMENT

The raw data supporting the conclusions of this article will be made available by the authors, without undue reservation.

ETHICS STATEMENT

The studies involving human participants were reviewed and approved by the Institutional Review Board of Shanghai Proton

and Heavy Ion Center. The patients/participants provided their written informed consent to participate in this study. Written informed consent was obtained from the individual(s) for the publication of any potentially identifiable images or data included in this article.

AUTHOR CONTRIBUTIONS

JS, XW and YS contributed conception and design of this study. JS and YS organized the database. JS and ZC performed the statistical analysis. JS wrote the first draft of the manuscript. LK, DY, JM, XG, XW and YS wrote sections of the manuscript. All authors contributed to the article and approved the submitted version.

FUNDING

This project was sponsored by Science and Technology Development Fund of Shanghai Pudong New Area (Project No. PKJ2019-Y08), Shanghai Academic/Technology Research Leader (Project No. 18XD1423000) and Science and Technology Commission of Shanghai Municipality No. 15411950100.

ACKNOWLEDGMENTS

The authors would like to thank Michael F. Moyers at Shanghai Proton and Heavy Ion Center for his review of this manuscript and Wenchien Hsi at University of Florida Health Proton Therapy Institute for his help with designing the 6DTC.

REFERENCES

1. Schulz-Ertner D, Tsujii H. Particle Radiation Therapy Using Proton and Heavier Ion Beams. *J Clin Oncol* (2007) 25(8):953–64. doi: 10.1200/JCO.2006.09.7816
2. Okada T, Kamada T, Tsuji H, Mizoe JE, Baba M, Kato S, et al. Carbon Ion Radiotherapy: Clinical Experiences at National Institute of Radiological Science (Nirs). *J Radiat Res* (2010) 51(4):355–64. doi: 10.1269/jrr.10016
3. Yan S, Lu HM, Flanz J, Adams J, Trofimov A, Bortfeld T. Reassessment of the Necessity of the Proton Gantry: Analysis of Beam Orientations From 4332 Treatments at the Massachusetts General Hospital Proton Center Over the Past 10 Years. *Int J Radiat Oncol Biol Phys* (2016) 95(1):224–33. doi: 10.1016/j.ijrobp.2015.09.033
4. Zhang X, Hsi WC, Yang F, Wang Z, Sheng Y, Sun J, et al. Development of an Isocentric Rotating Chair Positioner to Treat Patients of Head and Neck Cancer at Upright Seated Position With Multiple Nonplanar Fields in a Fixed Carbon-Ion Beamline. *Med Phys* (2020) 47(6):2450–60. doi: 10.1002/mp.14115
5. Sheng Y, Sun J, Wang W, Stuart B, Kong L, Gao J, et al. Performance of a 6D Treatment Chair for Patient Positioning in an Upright Posture for Fixed Ion Beam Lines. *Front Oncol* (2020) 10:122. doi: 10.3389/fonc.2020.00122
6. Mori S, Shibayama K, Tanimoto K, Kumagai M, Matsuzaki Y, Furukawa T, et al. First Clinical Experience in Carbon Ion Scanning Beam Therapy: Retrospective Analysis of Patient Positional Accuracy. *J Radiat Res* (2012) 53(5):760–8. doi: 10.1093/jrr/rrs017
7. Li H, Zhu XR, Zhang L, Dong L, Tung S, Ahamad A, et al. Comparison of 2D Radiographic Images and 3D Cone Beam Computed Tomography for Positioning Head-and-Neck Radiotherapy Patients. *Int J Radiat Oncol Biol Phys* (2008) 71(3):916–25. doi: 10.1016/j.ijrobp.2008.01.008
8. van Kranen S, van Beek S, Rasch C, van Herk M, Sonke JJ. Setup Uncertainties of Anatomical Sub-Regions in Head-and-Neck Cancer Patients After Offline CBCT Guidance. *Int J Radiat Oncol Biol Phys* (2009) 73(5):1566–73. doi: 10.1016/j.ijrobp.2008.11.035
9. Meyer J, Wilbert J, Baier K, Guckenberger M, Richter A, Sauer O, et al. Positioning Accuracy of Cone-Beam Computed Tomography in Combination With a HexaPOD Robot Treatment Table. *Int J Radiat Oncol Biol Phys* (2007) 67(4):1220–8. doi: 10.1016/j.ijrobp.2006.11.010
10. Suzuki M, Nishimura Y, Nakamatsu K, Okumura M, Hashiba H, Koike R, et al. Analysis of Interfractional Set-Up Errors and Intrafractional Organ Motions During IMRT for Head and Neck Tumors to Define an Appropriate Planning Target Volume (PTV)- and Planning Organs at Risk Volume (PRV)-Margins. *Radiother Oncol* (2006) 78(3):283–90. doi: 10.1016/j.radonc.2006.03.006
11. Pang PPE, Hendry J, Cheah SL, Soong YL, Fong KW, Wee TSJ, et al. An Assessment of the Magnitude of Intra-Fraction Movement of Head-and-Neck IMRT Cases and Its Implication on the Action-Level of the Imaging Protocol. *Radiother Oncol* (2014) 112(3):437–41. doi: 10.1016/j.radonc.2014.09.008
12. Drabik DM, MacKenzie MA, Fallone GB. Quantifying Appropriate PTV Setup Margins: Analysis of Patient Setup Fidelity and Intrafraction Motion Using Post-Treatment Megavoltage Computed Tomography Scans. *Int J Radiat Oncol Biol Phys* (2007) 68(4):1222–8. doi: 10.1016/j.ijrobp.2007.04.007
13. Linthout N, Verellen D, Tournel K, Storme G. Six Dimensional Analysis With Daily Stereoscopic X-Ray Imaging of Intrafraction Patient Motion in Head and Neck Treatments Using Five Points Fixation Masks. *Med Phys* (2006) 33(2):504–13. doi: 10.1118/1.2165417
14. Wiernik G. A New Radiotherapy Treatment Chair. *Br J Radiol* (1961) 34:676–8. doi: 10.1259/0007-1285-34-406-676
15. Marcus KC, Svensson G, Rhodes LP, Mauch PM. Mantle Irradiation in the Upright Position: A Technique to Reduce the Volume of Lung Irradiated in Patients With Bulky Mediastinal Hodgkin's Disease. *Int J Radiat Oncol Biol Phys* (1992) 23(2):443–7. doi: 10.1016/0360-3016(92)90766-b
16. McCarroll RE, Beadle BM, Fullen D, Balter PA, Followill DS, Stingo FC, et al. Reproducibility of Patient Setup in the Seated Treatment Position: A Novel Treatment Chair Design. *J Appl Clin Med Phys* (2017) 18(1):223–9. doi: 10.1002/acm2.12024
17. Balakin VE, Belikhin MA, Pryanichnikov AA, Shemyakov AE, Strelnikova NS. Clinical Application of New Immobilization System in Seated Position for Proton Therapy. *KnE Energy* (2018) 3(2):45–51. doi: 10.18502/ken.v3i2.1790
18. Boag JW, Hodt HJ. Adjustable Chair for Radiotherapy of Head and Neck Cancer. *Br J Radiol* (1971) 44(520):316–7. doi: 10.1259/0007-1285-44-520-316
19. Miller RW, Raubitschek AA, Harrington FS, van de Geijn J, Ovadia J, Glatstein E. An Isocentric Chair for the Simulation and Treatment of Radiation Therapy Patients. *Int J Radiat Oncol Biol Phys* (1991) 21(2):469–73. doi: 10.1016/0360-3016(91)90798-9
20. Maes D, Janson M, Regmi R, Egan A, Rosenfeld A, Bloch C, et al. Validation and Practical Implementation of Seated Position Radiotherapy in a Commercial TPS for Proton Therapy. *Phys Med* (2020) 80:175–85. doi: 10.1016/j.ejmp.2020.10.027
21. Ciocca M, Magro G, Mastella E, Mairani A, Mirandola A, Molinelli S, et al. Design and Commissioning of the Non-Dedicated Scanning Proton Beamline for Ocular Treatment at the Synchrotron-Based CNAO Facility. *Med Phys* (2019) 46(4):1852–62. doi: 10.1002/mp.13389
22. Verhey LJ, Goitein M, McNulty P, Munzenrider JE, Suit HD. Precise Positioning of Patients for Radiation Therapy. *Int J Radiat Oncol Biol Phys* (1982) 8(2):289–94. doi: 10.1016/0360-3016(82)90530-2
23. Kong L, Hu J, Guan X, Gao J, Lu R, Lu JJ. Phase I/II Trial Evaluating Carbon Ion Radiotherapy for Salvaging Treatment of Locally Recurrent Nasopharyngeal Carcinoma. *J Cancer* (2016) 7(7):774–83. doi: 10.7150/jca.14399
24. Yang J, Gao J, Wu X, Hu J, Hu W, Kong L, et al. Salvage Carbon Ion Radiation Therapy for Locally Recurrent or Radiation-Induced Second Primary Sarcoma of the Head and Neck. *J Cancer* (2018) 9(12):2215–23. doi: 10.7150/jca.24313
25. Guan X, Gao J, Hu J, Hu W, Yang J, Qiu X, et al. The Preliminary Results of Proton and Carbon Ion Therapy for Chordoma and Chondrosarcoma of the

Skull Base and Cervical Spine. *Radiat Oncol* (2019) 14(1):206. doi: 10.1186/s13014-019-1407-9
26. Moyers MF, Lesyna W. Isocenter Characteristics of an External Ring Proton Gantry. *Int J Radiat Oncol Biol Phys* (2004) 60(5):1622–30. doi: 10.1016/j.ijrobp.2004.08.052
27. Kato T, Yamazaki Y, Kato R, Komori S, Endo H, Oyama S, et al. End-to-End Test to Evaluate the Comprehensive Geometric Accuracy of a Proton Rotating Gantry Using a Cone-Shaped Scintillator Screen Detector. *Radiol Phys Technol* (2020) 13(2):144–51. doi: 10.1007/s12194-020-00562-7
28. Shah AP, Strauss JB, Kirk MC, Chen SS, Kroc TK, Zusag TW. Upright 3D Treatment Planning Using a Vertical CT. *Med Dosim* (2009) 34(1):82–6. doi: 10.1016/j.meddos.2008.05.004
29. Rosenfelder NA, Corsini L, McNair H, Pennert K, Aitken A, Lamb CM, et al. Comparison of Setup Accuracy and Intrafraction Motion Using Stereotactic Frame Versus 3-Point Thermoplastic Mask-Based Immobilization for Fractionated Cranial Image Guided Radiation Therapy. *Pract Radiat Oncol* (2013) 3(3):171–9. doi: 10.1016/j.prro.2012.06.004
30. Sarkar B, Munshi A, Ganesh T, Manikandan A, Krishnankutty S, Chitral L, et al. Technical Note: Rotational Positional Error Corrected Intrafraction Set-Up Margins in Stereotactic Radiotherapy: A Spatial Assessment for Coplanar and Noncoplanar Geometry. *Med Phys* (2019) 46(11):4749–54. doi: 10.1002/mp.13810
31. Lewis BC, Snyder WJ, Kim S, Kim T. Monitoring Frequency of Intra-Fraction Patient Motion Using the ExacTrac System for LINAC-Based SRS Treatments. *J Appl Clin Med Phys* (2018) 19(3):58–63. doi: 10.1002/acm2.12279
32. Den RB, Doemer A, Kubicek G, Bednarz G, Galvin JM, Keane WM, et al. Daily Image Guidance With Cone-Beam Computed Tomography for Head-and-Neck Cancer Intensity-Modulated Radiotherapy: A Prospective Study. *Int J Radiat Oncol Biol Phys* (2010) 76(5):1353–9. doi: 10.1016/j.ijrobp.2009.03.059
33. Lu H, Lin H, Feng G, Chen J, Shu L, Pang Q, et al. Interfractional and Intrafractional Errors Assessed by Daily Cone-Beam Computed Tomography in Nasopharyngeal Carcinoma Treated With Intensity-Modulated Radiation Therapy: A Prospective Study. *J Radiat Res* (2012) 53(6):954–60. doi: 10.1093/jrr/rrs041

Conflict of Interest: The authors declare that the research was conducted in the absence of any commercial or financial relationships that could be construed as a potential conflict of interest.

frontiers in Oncology

ORIGINAL RESEARCH
published: 14 July 2021
doi: 10.3389/fonc.2021.708884

Effectiveness of Carbon Ion Radiation in Locally Advanced Pancreatic Cancer

Jakob Liermann[1,2,3,4,5*], *Patrick Naumann*[1,2,3], *Fabian Weykamp*[1,2,3], *Philipp Hoegen*[1,2,3,4], *Juergen Debus*[1,2,3,4,5,6] *and Klaus Herfarth*[1,2,3,4,5,6]

[1] Department of Radiation Oncology, Heidelberg University Hospital, Heidelberg, Germany, [2] Heidelberg Institute for Radiation Oncology (HIRO), Heidelberg, Germany, [3] National Center for Tumor Diseases (NCT), Heidelberg, Germany, [4] Clinical Cooperation Unit Radiation Oncology, German Cancer Research Center (DKFZ), Heidelberg, Germany, [5] Heidelberg Ion Beam Therapy Center, Heidelberg, Germany, [6] German Cancer Consortium (DKTK), partner site Heidelberg, German Cancer Research Center (DKFZ), Heidelberg, Germany

Purpose: Effective treatment strategies for unresectable locally advanced pancreatic cancer (LAPC) patients are eagerly warranted. Recently, convincing oncological outcomes were demonstrated by carbon ion radiotherapy. Nevertheless, there is a lack of evidence for this modern radiation technique due to the limited number of carbon ion facilities worldwide. Here, we analyze feasibility and efficacy of carbon ion radiotherapy in the management of LAPC at Heidelberg Ion Beam Therapy Center (HIT).

Methods: Between 2015 and 2020, 21 LAPC patients were irradiated with carbon ions with a total dose of 48 Gy (RBE) in single doses of 4 Gy (RBE). Three patients (14%) were treated with concomitant chemotherapy with gemcitabine 300 mg/m^2 body surface weekly. Toxicity rates were extracted from the charts. Overall survival, progression free survival, local control, and locoregional control were evaluated using Kaplan–Meier estimates.

Results: One patient developed ascites CTCAE grade III during radiotherapy, which was related to a later histologically confirmed metachronous peritoneal carcinomatosis. No further higher-graded toxicity could be observed. The most common symptoms were nausea and abdominal pain. After a median estimated follow-up time of 19.1 months, the median progression free survival was 3.7 months, and the median overall survival was 11.9 months. The estimated 1-year local control and locoregional control rates were 89 and 84%, respectively.

Conclusion: Carbon ion radiotherapy of LAPC patients is safely feasible. Local tumor control rates were high. Nevertheless, compared to historical data, an overall survival improvement could not be observed. This could be explained by the poor prognosis of the selected underlying patients that mostly did not respond to prior chemotherapy as well as the early and frequent emergence of distant metastases that demonstrate the necessity of additional chemotherapy in further studies.

Keywords: pancreatic cancer, carbon ion radiotherapy, particle therapy, locally advanced pancreatic cancer, irradiation, heavy ion

OPEN ACCESS

Edited by:
Giuseppe Magro, National Center of Oncological Hadrontherapy, Italy

Reviewed by:
Silvia Molinelli, National Center of Oncological Hadrontherapy, Italy
Amelia Barcellini, National Center of Oncological Hadrontherapy, Italy

***Correspondence:**
Jakob Liermann
jakob.liermann@med.uni-heidelberg.de

Specialty section:
This article was submitted to Radiation Oncology, a section of the journal Frontiers in Oncology

Received: *12 May 2021*
Accepted: *24 June 2021*
Published: *14 July 2021*

Citation:
Liermann J, Naumann P, Weykamp F, Hoegen P, Debus J and Herfarth K (2021) Effectiveness of Carbon Ion Radiation in Locally Advanced Pancreatic Cancer. Front. Oncol. 11:708884. doi: 10.3389/fonc.2021.708884

INTRODUCTION

In pancreatic cancer, there is a lack of effective therapy options. Over the last decades, the limited five-year overall survival rate of 5–10% (1) could only be marginally challenged by modern treatment strategies. So far, surgical resection is the only curative therapy (2). However, in the majority of the patients, the tumor is deemed unresectable due to distant metastases or due to vessel involvement. Recently, Iacobuzio-Donahue et al. demonstrated local disease burden to be the cause of approximately one third of all pancreatic cancer related deaths (3). These findings demonstrate the urgent need for effective local treatment strategies.

In the last decades, several approaches tried to improve the oncological outcome of patients suffering from locally advanced pancreatic cancer (LAPC). One important goal in LAPC therapy is downstaging to gain secondary resectability. Because of the promising local effects of radiotherapy, multiple trials tested a potential benefit of chemoradiation over chemotherapy alone (4–6), but the data remain inconclusive. The Eastern Cooperative Oncology Group (ECOG) trial E4201 (6) and the Gastrointestinal Tumor Study Group (GITISG) trial 9283 (7) showed a slight beneficial effect of chemoradiation over chemotherapy. However, the LAP07 trial (4) revealed no difference in the median overall survival, although local tumor progression was significantly lower after chemoradiation compared to chemotherapy alone (32% *vs.* 46%). The efficacy of chemotherapy could also be improved, recently. The most effective chemotherapy regime consisting of folinic acid, fluorouracil, irinotecan, and oxaliplatin (FOLFIRINOX) as part of LAPC therapy is correlated with a median overall survival of 24.2 months (8). However, many patients do not tolerate this aggressive chemotherapy regime due to comorbidity. As the results of chemoradiotherapy remain controversial, there is an ongoing discussion on the role of chemoradiation in the management of LAPC.

The observed limited effect of conventional radiotherapy in pancreatic cancer could partially be explained by the relatively low radiation doses applicable. This is due to the gastrointestinal tract which is highly sensitive to radiotherapy and which is situated adjacent to the pancreas (9, 10). To improve radiotherapy in LAPC, radiation doses should be increased. This could be reached by modern radiation techniques, such as stereotactic body radiotherapy, magnetic resonance (MR)-guided radiotherapy or particle therapy (11–14). Using these techniques, higher doses can be applied to the tumor while respecting the dose limits for the adjacent organs at risk (OARs). Recently, Shinoto et al. presented convincing results of carbon ion radiotherapy in LAPC (15). In a dose-escalating trial, the observed median overall survival was 19.6 months after chemoradiation with 43.2–55.2 Gy (RBE) carbon ions applied in 12 fractions and combined with gemcitabine.

Carbon ion radiotherapy is known for two major advantages over conventional photon radiotherapy. First, there are physical characteristics making carbon ion radiotherapy highly conformal and precise. Energy deposition of particle therapy in irradiated tissue is different to the one of photon radiotherapy. Within a particle beam, there is a relatively low energy deposition in the entrance channel. The particles slow down and finally stop in a calculable depth, depending on their speed, represented by an increase of energy deposition and resulting in a maximum of energy deposition at a certain depth, the so-called Bragg Peak (16). There is almost no energy deposition behind this Bragg Peak. The resulting dose gradients in particle therapy are therefore very steep which makes the dose application highly precise. Second, carbon ions are known for a higher linear energy transfer (LET) and a higher relative biological effectiveness (RBE) compared to photons and even compared to protons (17). This is a biological advantage over photon radiotherapy as carbon ions are *e.g.* not as oxygen-dependent as photons. The biological characteristics of carbon ions could translate in improved therapy outcomes in so-far deemed radioresistant tumors (18).

In carbon ion radiotherapy planning, one of the most crucial aspects is the multifactorial dependency of the RBE resulting in different RBE values within the beam (19). Different carbon ion facilities use different RBE-models for carbon ion radiotherapy planning. Therefore, dose and therapy concepts cannot simply be transferred from one facility to another (20).

The advantages of carbon ion radiotherapy over conventional photon radiotherapy could improve oncological outcomes of LAPC patients as demonstrated by Shinoto et al. (15) In the present study, we analyze the feasibility and the efficacy of this promising radiation technique in the treatment of LAPC patients at Heidelberg Ion Beam Therapy Center (HIT).

METHODS

Patients

All patients presented with histologically confirmed pancreatic ductal adenocarcinoma or suspicious pancreatic tumor in imaging with correlating elevated tumor markers. To be included in the study, patients needed to suffer from inoperable LAPC without any sign of distant metastases (American Joint Committee on Cancer stage III). Two exceptions were made. One patient presented with a radiological suspicion of a distant lymph node metastasis, but the metastasis was not histologically confirmed at the time of radiotherapy. Another patient was included in the study, although he presented with hepatic metastases due to the fact that the hepatic metastases responded excellently to initial chemotherapy. A certain distance between the gastrointestinal tract and the tumor was not required. Any type and duration of prior chemotherapy was allowed. Recurrent cancer cases and patients participating in the ongoing PACK-trial (21) were excluded from the analysis. The inclusion criteria were chosen widely, as the institutional LAPC patient cohort treated with carbon ion radiotherapy is too small to define more specific subgroups.

Target Volume Definition

Planning imaging for radiotherapy was performed using four-dimensional native CT scans with a slice thickness of 3 mm to consider respiratory movement. Contrast-enhanced images were generated for differentiation of tumor and healthy tissue in

delineation. Additionally, in six cases (29%), fibroblast activation protein inhibitor-positron emission tomography (FAPI-PET) was performed prior to radiotherapy to improve target definition as recently demonstrated for locally recurrent pancreatic cancer (22). Contouring and radiotherapy planning were performed with the treatment planning system Syngo PT Planning (Siemens, Erlangen, Germany).

For delineation of the gross tumor volume (GTV), all applicable imaging was used to define the macroscopic tumor. Assumed microscopic tumor invasion was defined as clinical target volume (CTV). Therefore, the GTV was isometrically expanded by 6 mm and corrected considering anatomic boundaries such as non-infiltrated bone. Locoregional lymph nodes and the neuro-plexus were only part of the CTV when infiltrated. Considering respiratory movement, an internal target volume (ITV) was generated. The planning target volume (PTV) consisted of the ITV, enlarged by 5 mm in all directions (7 mm in beam direction).

Dose Prescription and Dose Constraints

Patients were irradiated with a total dose of 48 Gy (RBE) applied in 12 fractions. The corresponding equivalent dose at 2 Gy (EQD2) is 61.7 Gy, assuming an α/β-ratio of 5 Gy. A dose maximum in the upper gastrointestinal tract of 43.2 Gy (RBE) should be respected. Underdosage of the planning target volume (PTV) to respect gastrointestinal constraints in challenging cases was decided upon individually case by case. A representative underdosage within the target volume is demonstrated in **Figure 1**. The dosage of the spinal cord was restricted to a maximum of 36 Gy (RBE), and the kidney volume receiving more than 24 Gy (RBE) was not allowed to exceed 20% of the whole organ.

Treatment Delivery

Carbon ion radiotherapy was applied with an intensity-controlled raster scanning system for beam application at a rotating gantry. The first six patients (29%) were situated in prone position to avoid a beam entry through the couch. After commissioning irradiation through the treatment table, the remaining 15 patients (71%) could be treated in supine position. Accordingly, patients were predominantly situated on their back with the arms over the head (in Wing-Step mount) and with support in the back of the knee (knee cushion or Pro-Step mount). The laser-marked reference spots were defined by three small ink marks (Beekley spots). In all but one cases, two dorsal oblique radiation beams were used. Four-dimensional CT data of each patient were analyzed to evaluate the respiratory movement. In cases with large cranio-caudal target movement, gating was considered. In cases with an acceptable movement of the target, an ITV of all respiration phases was generated instead. In the presented patient cohort, finally, none of the patients was irradiated in a gating technique. Abdominal compression was not used to avoid a forced proximity of the gastrointestinal to the target volume. Image-guidance was performed through daily orthogonal X-rays and regular CT scans (at least once per week). If available, operation clips or stents were used for alignment. Otherwise, the spine was used to match X-rays and planning CT images. To consider organ movement and anatomical changes, a planning risk volume of the gastrointestinal was generated based on the four-dimensional CT data and patients needed to fast for at least 3 h prior to irradiation. If necessary, a new plan was generated based on the performed control CT. In the presented analysis, this was the case in two patients.

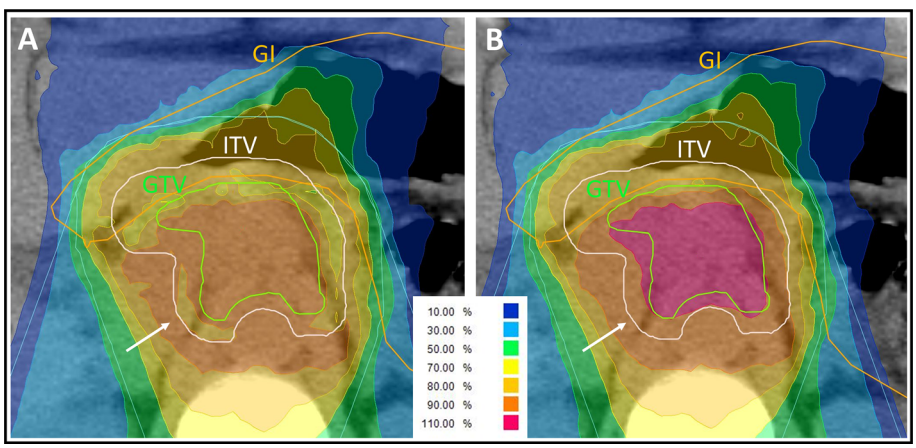

FIGURE 1 | Representative carbon ion radiation plan of a locally advanced pancreatic cancer patient using a clinical α/β-ratio of 5 Gy for the internal target volume (ITV) and 2 Gy for the surrounding tissue in the treatment planning software's integrated relative biological effectiveness (RBE) model. The isodose lines are demonstrated in different colors. The percentages of the isodose lines shown in the legend correspond to the prescribed dose of 48 Gy (RBE) in 12 fractions. Underdosage of the ITV and of the gross tumor volume (GTV) needed to be accepted to respect the gastrointestinal (GI) constraints. **(A)** Due to the α/β-ratio shift at the edge of the ITV, the peripheral ITV is irradiated with a lower biological dose than the surrounding tissue (white arrow), whereas the physically applied dose is increasing towards the center of the ITV. **(B)** Forward calculation using an α/β-ratio of 2 Gy for all volumes in the RBE model. The dose distribution at the edge of the ITV is more homogenous (white arrow) but in this plan presentation, the GTV seems to be overdosed. This forward calculation helps in analyzing the plan but is not assumed to be correct, because of the missing biological assumption of the higher α/β-ratio for the ITV.

Treatment Planning

For biological plan optimization in carbon ion radiotherapy, different RBE values within the beam need to be considered. Therefore, the local effect model (LEM) I is integrated in the used treatment planning system (TPS). In LEM I, different α/β-ratios for the ITV (first three patients: α/β = 2 Gy, remaining 18 patients: α/β = 5 Gy) and for the surrounding tissues (α/β = 2 Gy) were used.

The implementation of two different α/β-ratios in the RBE model results in a complex dose distribution. In the ITV (α/β = 5 Gy), the physically applied dose needs to be higher than in the surrounding tissue (α/β = 2 Gy) to achieve the same biological dose. Thus, in the biological dose distribution prediction, there is a shift from the α/β-ratio of 2 Gy (within the surrounding tissue) to the α/β-ratio of 5 Gy (within the ITV). The biological dose in the peripheral margin of the ITV is deemed lower than the one of the surrounding tissue adjacent to the ITV edge (**Figure 1A**). This uncommon presentation of dose distribution seems inappropriate from the point of view of a conventional radiation oncologist. To facilitate plan evaluation, a forward calculation is performed using an α/β-ratio of 2 Gy in LEM I for all structures including the ITV and the surrounding tissue (**Figure 1B**). As a consequence, the biological dose within the ITV is much higher in this forward calculation and should not be taken for granted. On the other hand, dose distribution seems more appropriate at the edge of the ITV. For adequate plan evaluation, both the actual plan and the forward calculation should be analyzed.

Follow-up and Response Evaluation

Follow-up was defined from the start of radiotherapy and was calculated using the reverse Kaplan–Meier method (23). Three-monthly contrast-enhanced CT scans and clinical visits were evaluated, whenever available. RECIST 1.1.-criteria were used in CT-based response evaluation. In-field tumor progression was denominated as "local tumor recurrence". "Regional tumor recurrence" was defined as out-field (<90% of the prescribed dose) tumor progression of lymph nodes, soft tissue nearby or within the pancreas. "Distant tumor recurrence" was defined as any other tumor progression.

Overall survival (OS) was defined as time from the start of radiotherapy until death. Local control (LC) was defined from the start of radiotherapy until local tumor recurrence or last imaging available. Locoregional control (LRC) was defined from the start of radiotherapy until local or regional tumor recurrence or last imaging available. Progression free survival (PFS) was defined from the start of radiotherapy until any tumor progression or death or last imaging available.

Toxicity

Symptoms and complaints were graded according to the International Common Terminology Criteria for Adverse Events of the National Cancer Institute (NCI CTC AE), Version 5. Toxicity rates were extracted from the charts before the start of radiotherapy, during radiotherapy and at all available time points after the end of radiotherapy.

Statistics

OS, LC, LRC, and PFS were analyzed using the Kaplan–Meier method. Statistics and figures were performed with SPSS Statistics, version 27 (International Business Machines Corporation: IBM, New York, USA).

Ethics

The study was approved by the Ethics Committee of the University of Heidelberg, Germany (S-688/2020).

RESULTS

Patient and Treatment Characteristics

A total of 21 patients could be included in the analysis. Fourteen patients were treated with chemotherapy and one patient underwent partial tumor resection by whipple procedure prior to radiation. Prior chemotherapy regimen was heterogenous with a median of five cycles of FOLFIRINOX chemotherapy (range 1–10). Initial chemotherapy was predominantly performed as treatment of choice in LAPC patients or as neoadjuvant therapy to gain secondary operability. The majority of the patients presented in our institution due to missing tumor remission under chemotherapy or to avoid further chemotherapy. Radiotherapy with carbon ions was performed between January 2015 and July 2020. A total dose of 48 Gy (RBE) was delivered in 12 fractions in all cases. In three cases, concomitant chemotherapy with gemcitabine 300 mg/m^2 body surface was administered weekly (2–3 cycles). Patients that were known non-responder to gemcitabine and patients that could not receive chemotherapy due to their general condition were not treated with concomitant chemotherapy. Additionally, the combination of gemcitabine chemotherapy and carbon ion radiotherapy was not tested to be safely applicable in 2015 which resulted in restrictive concomitant chemotherapy prescription at our institution. After radiotherapy, two initially inoperable patients were operated. One patient underwent total pancreatectomy (R1) after having developed local tumor recurrence after radiotherapy. In the second case, the tumor was deemed unresectable during operation and the procedure was completed without resection. During both operations, slight fibrosis was seen without leading to any interventional complications. Accordingly, the overall secondary resection rate was 5%. In case of tumor progression during follow-up, patients were treated with different chemotherapy and immunotherapy regimen. Four patients were treated with gemcitabine and nab-paclitaxel, two patients with FOLFIRINOX, and further two patients with a combination of ipilimumab, nivolumab, and maraviroc. Detailed patient and treatment characteristics are summarized in **Tables 1** and **2**. A representative radiation plan is shown in **Figure 2**.

Survival and Tumor Control

After a median follow-up time of 19.1 months, the estimated 1-year OS rate was 40.0% (**Figure 3A**). Two years after the start of radiotherapy, two of the observed patients were still alive and

TABLE 1 | Patient characteristics.

	n	(%)
Number of patients	**21**	**(100)**
Sex		
Male	16	(76)
Female	5	(24)
Age at radiotherapy (median in years, range)	70 (48–83)	
Localization of initial pancreatic cancer		
Pancreatic head	13	(62)
Pancreatic body	7	(33)
Pancreatic tail	1	(5)
Initial AJCC* stage		
IIB	1	(5)
III	17	(81)
IV	3	(14)
Prior chemotherapy		
FOLFIRINOX°	10	(48)
FOLFIRINOX°, followed by gemcitabine + nab-paclitaxel	4	(19)
None	7	(33)
Time in months: prior chemotherapy (median, range)	5 (1–10)	
Prior surgery		
Whipple procedure (R2 resection)	1	(5)
None (apart from biopsy)	20	(95)
Histology		
Ductal adenocarcinoma	18	(86)
unknown	3	(14)
Secondary resection	1	(5)

AJCC, American Joint Committee on Cancer.
°FOLFIRINOX, chemotherapy regimen consisting of folinic acid, fluorouracil, irinotecan, and oxaliplatin.

TABLE 2 | Treatment characteristics.

	n	(%)
Radiotherapy	**21**	**(100)**
Time in months: diagnosis to radiotherapy (median, range)	8 (2–13)	
Pre-radiotherapy AJCC* stage		
III	19	(91)
IV	2	(9)
Radiation technique		
Carbon ions, active raster-scanning	21	(100)
Prescribed dose		
48 Gy (RBE) in 12 fractions	21	(100)
Concurrent chemotherapy		
Gemcitabine 300 mg/m^2 body surface weekly	3	(14)
None	18	(86)
Patient position		
Supine	15	(71)
Prone	6	(29)
Volume in ccm (median, range)		
GTV (Gross tumor volume)	43.6 (13.0–129.7)	
CTV (Clinical target volume)	128.4 (26.1–323.3)	
ITV (Internal target volume)	183.4 (48.3–583.5)	
PTV (Planning target volume)	303.2 (96.7–812.0)	
Number of radiation beams		
2	21	(100)
α/β-ratio used in local effect model (LEM) I		
2 Gy	3	(14)
5 Gy	18	(86)

AJCC, American Joint Committee on Cancer.

three patients were lost to follow-up. The observed median overall survival was 11.9 months. The corresponding 95% confidence interval (CI) was 6.0–17.8 months. The estimated 1-year PFS rate was 10% (**Figure 3B**), and the median PFS was 3.7 months (95% CI 0.0–9.2).

Local progression could be observed in one patient 10 months after the start of radiotherapy (**Figure 3C**). The corresponding tumor could be resected but two months later distant metastases occurred. Regional and distant tumor recurrences were simultaneously observed in another patient that was treated with chemotherapy thereafter. No further locoregional tumor recurrence could be observed. One-year local control and one-year locoregional control rates were 89 and 84%, respectively.

Toxicity

During radiotherapy, there was an increase of reported nausea (13% before radiotherapy *vs.* 48% during radiotherapy) and diarrhea. Nevertheless, these symptoms decreased after radiotherapy. One patient developed ascites CTCAE grade III during radiotherapy. Histopathological examination revealed underlying metachronous peritoneal carcinomatosis. No further higher-graded toxicity could be observed. After radiotherapy, 14% of the patients reported on fatigue. Toxicity rates are shown in **Table 3**.

DISCUSSION

To the best of our knowledge, we present the first European data on carbon ion radiotherapy in LAPC. The observed results demonstrate that carbon ion radiotherapy in pancreatic cancer is both feasible and well tolerable. Whereas convincing local tumor control rates could be achieved, OS rates were low due to a very short PFS of 3.7 months since distant metastases occurred early in most patients.

In all cases, radiation was completed as intended, and no radiation-induced higher graded toxicity was seen. Observed nausea and diarrhea could adequately be explained by radiation-induced mucositis of the gastrointestinal tract. Accordingly, these two symptoms decreased after the end of radiotherapy. Those findings are in line with the current literature. There are two retrospective analyses regarding carbon ion radiotherapy in LAPC (24, 25). Furthermore, Shinoto et al. published results of a prospective phase II dose-escalating trial of 76 patients (15). In the mentioned studies, the most common toxicities included anorexia and gastrointestinal ulcer or bleeding. The latter could be observed in <3% of the patients. In the present analysis, only one grade II bleeding of the lower gastrointestinal could be observed during follow-up. The patient was treated with anticoagulant therapy at the time of the event so that a correlation with the performed radiation seems to be less probable.

In the only prospective trial published so far, Shinoto et al. demonstrated a 1- and 2-year local tumor control rate of 92 and 83%, based on CT imaging (15). We could confirm the local

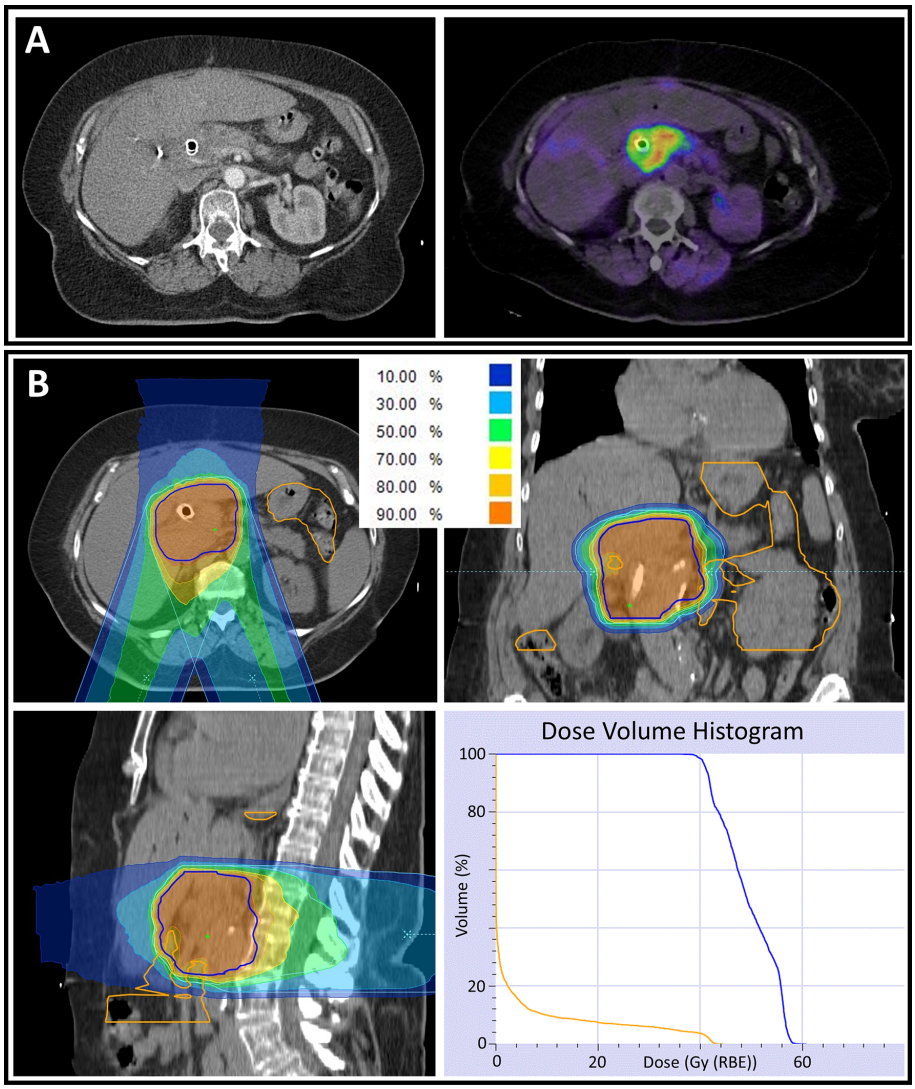

FIGURE 2 | **(A)** Computed tomography (CT) scan of a locally advanced pancreatic cancer patient demonstrating a pancreatic tumor mass with an implanted biliary metal stent (left). To improve target volume definition in radiation planning, a fibroblast activation protein inhibitor-positron emission tomography (FAPI-PET) with a high tumor to background contrast was performed and matched with CT data (right). **(B)** Radiation plan of the same patient in axial (upper left), coronal (upper right) and sagittal (lower left) CT slices. The percentages of the different-colored isodose lines correspond to the prescribed dose of 48 Gy (RBE) in 12 fractions. For all volumes, an α/β-ratio of 2 Gy was used in the underlying relative biological effectiveness model. Partially, underdosage of the planning target volume (PTV, delineated in blue) needed to be accepted to respect the gastrointestinal (GI, delineated in orange) constraints. The dose volume histogram (lower right) demonstrates a 'stereotactic-radiotherapy-like' dose escalation within the PTV while respecting the GI constraints.

effectiveness of carbon ion radiotherapy with an observed 1-year local control rate of 87%.

Nevertheless, OS results differed considerably. Shinoto et al. observed a median OS of 19.6 months (15). Kawashiro et al. presented an even higher median OS of 21.5 months after carbon ion radiotherapy in LAPC patients (25). This is almost twice as high as the observed 11.9 months of the present study. In the LAP 07 trial which compared photon radiotherapy-based chemoradiation with chemotherapy after induction therapy, the observed median overall was 12.8 months (4). Compared to these historical findings, we did not observe an OS improvement by carbon ion radiotherapy over photon radiotherapy in the present study.

One difference between the Japanese data and the present analysis is the underlying radiation dose concept. Kawashiro et al. irradiated with total doses of up to 55.2 Gy (RBE) delivered in 12 fractions. Furthermore, they described a correlation of higher-dosed radiotherapy and OS improvement (25). In the present analysis, we irradiated with a total dose of 48 Gy (RBE) in 12 fractions. However, dose concepts of different carbon ion facilities cannot be compared directly, which aggravates the interpretation of these findings. To be able to compare the

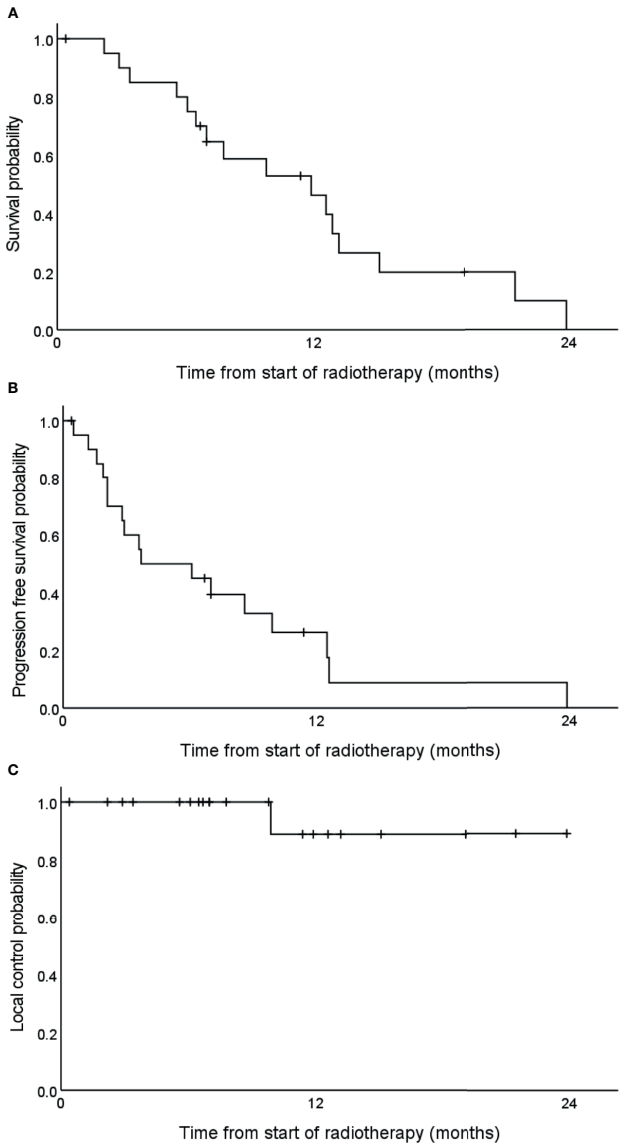

FIGURE 3 | Estimated overall survival **(A)**, progression free survival **(B)** and local tumor control **(C)** rates of 21 locally advanced pancreatic cancer patients after carbon ion radiotherapy with 48 Gy (RBE) in 12 fractions.

approach at the Heavy-Ion Medical Accelerator (HIMAC) at the National Institute of Radiological Science (NIRS) in Japan with the LEM I-based approach at our institution, Steinstrater et al. published conversion tables (20). According to these assumptions, the irradiated maximum single doses of 4.6 Gy (RBE) by Kawashiro et al. should correlate with single doses of 4.4–5.0 Gy (RBE) at our institution. Altogether, the radiation dose concept at our institution [single dose: 4.0 Gy (RBE)] is supposed to be lower than the maximum one used in Japan. Nevertheless, considering the comparable local tumor progression rates of the different analyses, it seems rather unlikely that the diverse radiation dose concepts satisfactorily explain the OS differences.

TABLE 3 | Toxicity rates.

Symptoms (NCI CTCAE grades)	Before RT* n (%)	During RT* n (%)	After RT* n (%)
Abdominal pain			
I	5 (24)	5 (24)	3 (14)
II	5 (24)	4 (19)	2 (9)
Gastric hemorrhage			
II	0	0	1 (5)
Diarrhea			
I	2 (9)	3 (14)	1 (8)
Ascites			
II	0	0	1 (5)
III	0	1 (5)	1 (5)
Nausea			
I	2 (9)	6 (29)	1 (5)
II	1 (5)	4 (19)	3 (14)
Dermatitis			
I	0	2 (9)	0
Fatigue			
I	0	2 (9)	1 (5)
II	0	0	2 (9)
No complaints	10 (48)	7 (33)	6 (29)

RT, radiotherapy.

Shinoto et al. and Kawashiro et al. performed elective nodal irradiation and included the neuro-plexus region in the CTV (15, 25). At our institution, carbon ion radiotherapy volumes were kept as small as possible without elective nodal irradiation. The latter could lead to a higher rate of tumor recurrences. However, we did not observe high rates of locoregional tumor progression which partially contradicts this hypothesis.

Another significant difference between the Japanese trials and our study is the administration of chemotherapy. Shinoto et al. and Kawashiro et al. combined carbon ion radiotherapy with gemcitabine-based chemotherapy using doses of up to 1,000 mg/m^2. In the present study, only 14% of the patients were treated with simultaneous chemotherapy and administered gemcitabine doses were lower (300 mg/m^2). The missing chemotherapy in the present treatment concept could explain the observed high rate of distant tumor progression and the relatively low OS rate.

Finally, there is a selection bias in the presented patient cohort. Since the final publication of the LAP 07 trial results, LAPC patients in Europe are predominantly treated with chemotherapy. Patients that are capable of being treated with intense chemotherapy regimen such as FOLFIRINOX will typically not be assigned to radiotherapy unless they did not respond to chemotherapy pretreatment. Sixty-seven percent of the irradiated patients of the present analysis were pre-treated with intense chemotherapy regimen and did not or did only poorly respond to pre-treatment. The median time from initial diagnosis to irradiation was 8 months. Altogether, the irradiated patient cohort consisted mostly of non-responding patients to pre-treatment with chemotherapy.

This selection bias could possibly explain the observed limited OS of the present study. The low secondary resection rate of 5% supports this hypothesis. In a large meta-analysis of LAPC patients being treated with different modalities, the secondary resection rate was approximately 25% (8). Furthermore, the median gross tumor size of 43.6 ccm in the present analysis is

almost three times larger than the observed tumor size of the prospective trial of Shinoto et al. (14.8 ccm) (15) indicating a negative selection bias of the present patient cohort, too.

The present study has several limitations. First, the quality of data acquisition is limited because of the retrospective character of the analysis. Several patients did not regularly perform follow-up examinations, and no standardized quality of life questionnaires were used. Second, a sample size of 21 patients is small, which is due to the limited number of carbon ion facilities making carbon ion radiotherapy a rare treatment option. Third, the observed high local tumor control rate could be biased by the high rate of distant tumor progression during follow-up examination. It is possible that patients did not reach the criteria of local tumor progression because they deceased early after the end of radiotherapy.

On the other hand, a strength of the analysis is the reliability of the estimated overall survival due to the high number of reported deaths. Furthermore, the observed local tumor control rate and the toxicity rates seem to confirm the radiation dose concept as only one patient developed local tumor progression and no higher-graded radiation-induced toxicity was seen.

In conclusion, carbon ion radiotherapy in pancreatic cancer is well tolerable and locally effective. In the present analysis, an expected OS benefit over historical photon radiotherapy data could not be observed. This seems to be due to a negative selection bias of the described patient cohort. Considering the high rate of distant tumor progression, carbon ion radiotherapy should be combined with chemotherapy in future studies.

DATA AVAILABILITY STATEMENT

The raw data supporting the conclusions of this article will be made available by the authors, without undue reservation.

ETHICS STATEMENT

The study was approved by the Ethics Committee of the University of Heidelberg, Germany (S-688/2020). Written informed consent for participation was not required for this study in accordance with the national legislation and the institutional requirements.

AUTHOR CONTRIBUTIONS

JL and KH designed and directed the project. JL gathered the data. JL analyzed the data and wrote the manuscript. PN, FW, PH, JD, and KH helped in finalizing the manuscript. JD and KH supervised the project. All authors contributed to the article and approved the submitted version.

FUNDING

JL is funded by the Physician-Scientist Program of Heidelberg University, Faculty of Medicine. We acknowledge financial support by the Open Access Publishing Fund of Heidelberg University.

REFERENCES

1. Rawla P, Sunkara T, Gaduputi V. Epidemiology of Pancreatic Cancer: Global Trends, Etiology and Risk Factors. *World J Oncol* (2019) 10(1):10–27. doi: 10.14740/wjon1166
2. Doi R, Imamura M, Hosotani R, Imaizumi T, Hatori T, Takasaki K, et al. Surgery Versus Radiochemotherapy for Resectable Locally Invasive Pancreatic Cancer: Final Results of a Randomized Multi-Institutional Trial. *Surg Today* (2008) 38(11):1021–8. doi: 10.1007/s00595-007-3745-8
3. Iacobuzio-Donahue CA, Fu B, Yachida S, Luo M, Abe H, Henderson CM, et al. DPC4 Gene Status of the Primary Carcinoma Correlates With Patterns of Failure in Patients With Pancreatic Cancer. *J Clin Oncol* (2009) 27 (11):1806–13. doi: 10.1200/JCO.2008.17.7188
4. Hammel P, Huguet F, Laethem JL, Goldstein D, Glimelius B, Artru P, et al. Effect of Chemoradiotherapy vs Chemotherapy on Survival in Patients With Locally Advanced Pancreatic Cancer Controlled After 4 Months of Gemcitabine With or Without Erlotinib: the LAP07 Randomized Clinical Trial. *JAMA* (2016) 315(17):1844–53. doi: 10.1001/jama.2016.4324
5. Huguet F, Andre T, Hammel P, Artru P, Balosso J, Selle F, et al. Impact of Chemoradiotherapy After Disease Control With Chemotherapy in Locally Advanced Pancreatic Adenocarcinoma in GERCOR Phase II and III Studies. *J Clin Oncol* (2007) 25(3):326–31. doi: 10.1200/JCO.2006.07.5663
6. Loehrer PJSr., Feng Y, Cardenes H, Wagner L, Brell JM, Cella D, et al. Gemcitabine Alone Versus Gemcitabine Plus Radiotherapy in Patients With Locally Advanced Pancreatic Cancer: an Eastern Cooperative Oncology Group Trial. *J Clin Oncol* (2011) 29(31):4105–12. doi: 10.1200/JCO.2011.34.8904
7. Treatment of Locally Unresectable Carcinoma of the Pancreas: Comparison of Combined-Modality Therapy (Chemotherapy Plus Radiotherapy) to Chemotherapy Alone. Gastrointestinal Tumor Study Group. *J Natl Cancer Inst* (1988) 80(10):751–5. doi: 10.1093/jnci/80.10.751
8. Suker M, Beumer BR, Sadot E, Marthey L, Faris JE, Mellon EA, et al. FOLFIRINOX for Locally Advanced Pancreatic Cancer: a Systematic Review and Patient-Level Meta-Analysis. *Lancet Oncol* (2016) 17(6):801–10. doi: 10.1016/S1470-2045(16)00172-8
9. Kavanagh BD, Pan CC, Dawson LA, Das SK, Li XA, Haken RKT, et al. Radiation Dose-Volume Effects in the Stomach and Small Bowel. *Int J Radiat Oncol Biol Phys* (2010) 76(3 Suppl):S101–107. doi: 10.1016/j.ijrobp.2009.05.071
10. Marks LB, Yorke ED, Jackson A, Haken RKT, Constine LS, Eisbruch A, et al. Use of Normal Tissue Complication Probability Models in the Clinic. *Int J Radiat Oncol Biol Phys* (2010) 76(3 Suppl):S10–19. doi: 10.1016/j.ijrobp.2009.07.1754
11. Koong AC, Christofferson E, Le QT, Goodman KA, Ho A, Kuo T, et al. Phase II Study to Assess the Efficacy of Conventionally Fractionated Radiotherapy Followed by a Stereotactic Radiosurgery Boost in Patients With Locally Advanced Pancreatic Cancer. *Int J Radiat Oncol Biol Phys* (2005) 63 (2):320–3. doi: 10.1016/j.ijrobp.2005.07.002
12. Liermann J, Shinoto M, Syed M, Debus J, Herfarth K, Naumann P. Carbon Ion Radiotherapy in Pancreatic Cancer: A Review of Clinical Data. *Radiother Oncol* (2020) 147:145–50. doi: 10.1016/j.radonc.2020.05.012
13. Rutenberg MS, Nichols RC. Proton Beam Radiotherapy for Pancreas Cancer. *J Gastrointest Oncol* (2020) 11(1):166–75. doi: 10.21037/jgo.2019.03.02
14. van Sornsen de Koste JR, Palacios MA, Bruynzeel AME, Slotman BJ, Senan S, Lagerwaard FJ. MR-Guided Gated Stereotactic Radiation Therapy Delivery for Lung, Adrenal, and Pancreatic Tumors: a Geometric Analysis. *Int J Radiat Oncol Biol Phys* (2018) 102(4):858–66. doi: 10.1016/j.ijrobp.2018.05.048
15. Shinoto M, Yamada S, Terashima K, Yasuda S, Shioyama Y, Honda H, et al. Carbon Ion Radiation Therapy With Concurrent Gemcitabine for Patients With Locally Advanced Pancreatic Cancer. *Int J Radiat Oncol Biol Phys* (2016) 95(1):498–504. doi: 10.1016/j.ijrobp.2015.12.362
16. Brown A, Suit H. The Centenary of the Discovery of the Bragg Peak. *Radiother Oncol* (2004) 73(3):265–8. doi: 10.1016/j.radonc.2004.09.008

17. Suit H, DeLaney T, Goldberg S, Paganetti H, Clasie B, Gerweck L, et al. Proton vs Carbon Ion Beams in the Definitive Radiation Treatment of Cancer Patients. *Radiother Oncol* (2010) 95(1):3–22. doi: 10.1016/j.radonc.2010.01.015
18. Schlaff CD, Krauze A, Belard A, O'Connell JJ, Camphausen KA. Bringing the Heavy: Carbon Ion Therapy in the Radiobiological and Clinical Context. *Radiat Oncol* (2014) 9(1):88. doi: 10.1186/1748-717X-9-88
19. Karger CP, Peschke P. RBE and Related Modeling in Carbon-Ion Therapy. *Phys Med Biol* (2017) 63(1):01TR02. doi: 10.1088/1361-6560/aa9102
20. Steinstrater O, Grun R, Scholz U, Friedrich T, Durante M, Scholz M. Mapping of RBE-Weighted Doses Between HIMAC- and LEM-Based Treatment Planning Systems for Carbon Ion Therapy. *Int J Radiat Oncol Biol Phys* (2012) 84(3):854–60. doi: 10.1016/j.ijrobp.2012.01.038
21. Liermann J, Naumann P, Hommertgen A, Pohl M, Kieser M, Debus J, et al. Carbon Ion Radiotherapy as Definitive Treatment in non-Metastasized Pancreatic Cancer: Study Protocol of the Prospective Phase II PACK-Study. *BMC Cancer* (2020) 20(1):947. doi: 10.1186/s12885-020-07434-8
22. Liermann J, Syed M, Ben-Josef E, Schubert K, Schlampp I, Sprengel SD, et al. Impact of FAPI-PET/CT on Target Volume Definition in Radiation Therapy of Locally Recurrent Pancreatic Cancer. *Cancers (Basel)* (2021) 13(4):796. doi: 10.3390/cancers13040796
23. Shuster JJ. Median Follow-Up in Clinical Trials. *J Clin Oncol* (1991) 9(1):191–2. doi: 10.1200/JCO.1991.9.1.191
24. Shinoto M, Terashima K, Suefuji H, Matsunobu A, Toyama S, Fukunishi K, et al. A Single Institutional Experience of Combined Carbon-Ion Radiotherapy and Chemotherapy for Unresectable Locally Advanced Pancreatic Cancer. *Radiother Oncol* (2018) 129(2):333–9. doi: 10.1016/j.radonc.2018.08.026
25. Kawashiro S, Yamada S, Okamoto M, Ohno T, Nakano T, Shinoto M, et al. Multi-Institutional Study of Carbon-Ion Radiotherapy for Locally Advanced Pancreatic Cancer: Japan Carbon-Ion Radiation Oncology Study Group (J-CROS) Study 1403 Pancreas. *Int J Radiat Oncol Biol Phys* (2018) 101(5):1212–21. doi: 10.1016/j.ijrobp.2018.04.057

Conflict of Interest: JD received grants from Viewray Incorporated, The Clinical Research Institute GmbH (CRI), Accuray International Sarl, RaySearch Laboratories AB, Vision RT Limited, Merck Seono GmbH, Astellas Pharma GmbH, Astra Zeneca GmbH, Siemens Healthcare GmbH, Solution Akademie GmbH, Egomed PLC Surrey Research Park, Quintiles GmbH, Pharmaceutical Research Associates GmbH, Boehringer Ingelheim Pharma GmbH&CoKG, PTW-Freiburg Dr. Pychlau GmbH, Nanobiotix SA, Accuray Incorporated, Bristol-Myer Squibb GmbH&CoKG aA and Merck KHG aA. As chairman of HIRO (Heidelberg Institute of Radiation Oncology, Heidelberg, Germany) and a managing director of the NCT (National Center for Tumor Diseases) Heidelberg, Germany, Juergen Debus is responsible for collaborations with a multitude of companies and institutions. Juergen Debus is CEO of the HIT Betriebs-GmbH and a member of the board of trustees of the Physikalisch-Technische Bundesanstalt (PTB). He attended advisory board meetings of MERCK KGaA (Darmstadt).

The remaining authors declare that the research was conducted in the absence of any commercial or financial relationships that could be construed as a potential conflict of interest.

frontiers in Oncology

ORIGINAL RESEARCH
published: 08 September 2021
doi: 10.3389/fonc.2021.712126

Dosimetric Validation of a System to Treat Moving Tumors Using Scanned Ion Beams That Are Synchronized With Anatomical Motion

Michelle Lis[1,2], *Wayne Newhauser*[2,3], *Marco Donetti*[4], *Moritz Wolf*[1], *Timo Steinsberger*[1,5], *Athena Paz*[1] *and Christian Graeff*[1]*

[1] Biophysics, GSI Helmholtzzentrum für Schwerionenforschung GmbH, Darmstadt, Germany, [2] Department of Physics and Astronomy, Louisiana State University, Baton Rouge, LA, United States, [3] Department of Radiation Physics, Mary Bird Perkins Cancer Center, Baton Rouge, LA, United States, [4] Research and Development Department, CNAO National Center for Oncological Hadrontherapy, Pavia, Italy, [5] Institute of Condensed Matter Physics, Technical University of Darmstadt, Darmstadt, Germany

OPEN ACCESS

Edited by:
Stewart Mac Mein,
German Cancer Research Center (DKFZ), Germany

Reviewed by:
Jörg Wulff,
West German Proton Therapy Centre Essen (WPE), Germany
Christian Bäumer,
West German Proton Therapy Centre Essen (WPE), Germany

***Correspondence:**
Christian Graeff
c.graeff@gsi.de

Specialty section:
This article was submitted to Radiation Oncology, a section of the journal Frontiers in Oncology

Received: 19 May 2021
Accepted: 16 August 2021
Published: 08 September 2021

Citation:
Lis M, Newhauser W, Donetti M, Wolf M, Steinsberger T, Paz A and Graeff C (2021) Dosimetric Validation of a System to Treat Moving Tumors Using Scanned Ion Beams That Are Synchronized With Anatomical Motion. Front. Oncol. 11:712126. doi: 10.3389/fonc.2021.712126

Purpose: The purpose of this study was to validate the dosimetric performance of scanned ion beam deliveries with motion-synchronization to heterogenous targets.

Methods: A 4D library of treatment plans, comprised of up to 10 3D sub-plans, was created with robust and conventional 4D optimization methods. Each sub-plan corresponded to one phase of periodic target motion. The plan libraries were delivered to a test phantom, comprising plastic slabs, dosimeters, and heterogenous phantoms. This phantom emulated range changes that occur when treating moving tumors. Similar treatment plans, but without motion synchronization, were also delivered to a test phantom with a stationary target and to a moving target; these were used to assess how the target motion degrades the quality of dose distributions and the extent to which motion synchronization can improve dosimetric quality. The accuracy of calculated dose distributions was verified by comparison with corresponding measurements. Comparisons utilized the gamma index analysis method. Plan quality was assessed based on conformity, dose coverage, overdose, and homogeneity values, each extracted from calculated dose distributions.

Results: High pass rates for the gamma index analysis confirmed that the methods used to calculate and reconstruct dose distributions were sufficiently accurate for the purposes of this study. Calculated and reconstructed dose distributions revealed that the motion-synchronized and static deliveries exhibited similar quality in terms of dose coverage, overdose, and homogeneity for all deliveries considered. Motion-synchronization substantially improved conformity in deliveries with moving targets. Importantly, measurements at multiple locations within the target also confirmed that the motion-synchronized delivery system satisfactorily compensated for changes in beam range caused by the phantom motion. Specifically, the overall planning and delivery approach achieved the desired dose distribution by avoiding range undershoots and overshoots caused by tumor motion.

Conclusions: We validated a dose delivery system that synchronizes the movement of the ion beam to that of a moving target in a test phantom. Measured and calculated dose distributions revealed that this system satisfactorily compensated for target motion in the presence of beam range changes due to target motion. The implication of this finding is that the prototype system is suitable for additional preclinical research studies, such as irregular anatomic motion.

Keywords: motion-synchronized dose delivery, carbon ion therapy, range compensation, motion mitigation, multi-phase 4D delivery, scanned ion beams

INTRODUCTION

Proton and ion therapy provide conformal dose distributions for static targets, and in the past few decades, have emerged as a formidable alternative to photon therapy. Ion therapies have mainly been used to treat static tumors, including several in the regions of the head and neck region, cranium, retina, and the spine, with high conformity (1, 2), resulting in reduced toxicities and tumor recurrence (3). Conformal treatments have been shown to be partially effective in reducing complications associated with radiotherapy of moving tumors, such as non-small cell lung cancer, including pneumonitis and cardiac complications (4, 5). However, contemporary ion beam therapies for thoracic tumors still have high complication rates and low survival rates (6). Additional unmet clinical needs include shorter treatment times and streamlined patient-specific quality assurance procedures. Thus, it is imperative to develop treatment methods that can meet these clinical needs.

Currently, about two thirds of proton and ion therapy centers use relatively simple motion mitigation strategies to treat moving tumors, including various combinations of techniques such as breath hold, beam gating, and internal target volumes (ITV), used with or without rescanning (7). These motion mitigation strategies for scanned ion therapy have been used to successfully treat some, but not all, moving tumors, yet treatment complication rates remain a serious problem (8, 9). The local failures are largely believed to be caused by insufficient dose to the tumor and complications are believed to be caused by excessive dose to surrounding healthy tissues (10). An obvious approach to overcome these limitations is to amend treatment planning and dose delivery methods to increase tumor coverage and reduce dose to normal tissues. To achieve these, improvements are needed to mitigate against range variations that are induced by moving heterogenous anatomy, including cases where the movements of the tumor and surrounding healthy tissue differ from one another. The most advanced motion mitigation approach currently in clinical use, namely the phase-controlled rescanning method at the National Institute of Radiological Sciences (NIRS), combines rapid beam delivery with fluoroscopy-guided beam gating. This requires minimal changes to the target position during the time where the treatment unit actively delivers beam to the tumor. With this approach, treatments must be halted if tumor motion changes substantially from the expected tumor location (11). The advantage of the gating approach is that it avoids the technical complexity of motion mitigation, but increases the compliance requirements of patients, and some patients cannot comply with respiratory requirements. The most technologically advanced approach, commonly called 4D-optimized tracking, allows the patient to breath freely and requires the treatment system to modify the trajectories of the delivered ion beams to follow the moving tumor, using real-time monitoring of the tumor position. This approach, developed at GSI for more than a decade (12), revealed promising dosimetric qualities and technical feasibility, but the vast technological complexity required to compensate anatomical motion has thus far been a major obstacle to its translation to clinical practice. To overcome these obstacles, Lis et al. (13) developed a technologically straightforward approach, called multi-phase 4D beam delivery (MP4D), which provides comparable dosimetric quality to that of beam tracking without the associated complications. It takes anatomical and tumor motion into account during treatment planning and subsequently synchronizes the beam delivery in real-time so that it follows the moving tumor. The MP4D approach was previously characterized for moving targets with promising preliminary results, but the tests did not attempt to compensate for range changes that occur in a heterogeneous phantom. To our knowledge, no system with such capabilities has yet been validated or clinically commissioned.

The objective of this study was to validate, by measurement and calculation, the performance of a recently created motion-synchronized dose delivery system (M-DDS) (13), used to deliver MP4D treatments. In particular, we validated, for the first time, the ability of the M-DDS to compensate for tumor motion in the presence of anatomical, motion-induced range changes. Libraries of 4D-optimized carbon-ion treatment plans were delivered to phantoms and absorbed dose distributions were measured. The dosimetric quality was assessed by examination of the dose coverage, conformity, overdose and uniformity. These quantities were compared for deliveries with a variety of test cases, including those with stationary and moving tumors, with and without the application of motion synchronization.

MATERIALS AND METHODS

We validated a prototype system to treat moving targets with scanned ion beams. The overall approach was to synchronize the delivery of the beam to the periodic motion of the target, to allow

for almost continuous delivery of the beam to the moving target. This approach inherently includes compensating for motion in heterogenous anatomy, which would otherwise cause range over- and under-shoots due to the anatomical, motion-induced range changes. For the convenience of the reader, we briefly review here the previously reported methods for motion mitigation with MP4D deliveries (13, 14), the treatment planning system (TPS) (11), and the experimental apparatus (13). We then describe the analysis methods for assessing the impact of managing heterogenous anatomical motion with the multi-phase 4D approach.

Treatment Planning System and Treatment Delivery System

Treatment plans were created with the research TPS developed at GSI Helmholtzzentrum für Schwerionenforschung GmbH (GSI), called TRiP4D (15). This is an extension of TRiP98 (16, 17), which takes into account changes in patient anatomy caused by respiratory motion. Several previously established planning strategies were used, including conventional- and robust 4D optimization and conventional- and robust 3D optimization (these are each explained below). To create a 4D treatment plan, a 3D sub-plan is created on each of the respiratory motion phases found in a 4DCT image set. The library of sub-plans is utilized together as a complete, or composite, treatment plan. In this study, we used two simple phantoms to represent the human thorax and a moving tumor. We purposefully selected simple phantoms to facilitate direct comparisons of calculated and measured dose distributions. These comparisons were essential for validating the dosimetric performance in test scenarios where the target depth or range varied in time. More specifically, two types of variations were considered, including constant range variations (created with a moving, homogenous wedge), and discrete range variations (created by a moving slab containing heterogeneities).

4D treatment plans were created for each phantom. First, 4DCT image sets were created by shifting a $4/3\pi\ 3 \times 3 \times 2\ cm^3$ ellipsoid target or a $6 \times 6 \times 4\ cm^3$ cuboid target contour within a simulated water box phantom. The targets followed a 20 mm, Lujan2-type motion trajectory (18) that was lateral to the beam axis. To explore the impact of the number of motion phases on delivery quality, we created 4D plans containing 3, 6 and 10 motion phases. Sub-plans were optimized to cover the clinical target volume (CTV) in each motion phase with a fraction of the prescription dose, such that the sum of the sub-plan doses results in the target receiving the prescription dose. For 3D optimization, 3DCT image sets of the ellipsoid and cuboid targets were created and used during treatment planning.

Analogous treatment plans were created using conventional and robust optimization planning techniques. For conventional optimization, treatment plans were created for CTVs which had 3 mm isotropic margins, while for robust optimization, margins were calculated from nine uncertainty scenarios, including range uncertainties and target position shifts, to minimize their dosimetric impact. Robust optimization was described by Wolf et al. (19). Robustly and conventionally optimized plan libraries were created for both target volumes, on all 4DCT images and to a homogeneous absorbed dose of 3 Gy.

The plan libraries were delivered with the motion-synchronized dose delivery system (M-DDS) (13), which was created to accelerate research and translation of motion mitigation strategies in ion therapy. This system was implemented in a research version of the dose delivery system (DDS) that is used clinically at the National Center for Oncological Hadrontherapy (CNAO) (20). It was similarly implemented in the radiotherapy research facility (Cave M) at GSI (21).

The general approach considers motion of the entire anatomy during treatment planning. This allows for compensating for the motion of heterogeneous tissue and variable target depths without the need for real-time modifications to the beam spot delivery positions during delivery. Instead, the real-time target position is monitored to redirect delivery from sub-plan to sub-plan, as the target moves to another motion phase. As such, the sub-plans are delivered as a series of discrete stationary plans. This continues until the entire prescription dose is delivered. For this study, up to 10 motion phases were considered, corresponding to the number of phases typically found in a 4DCT for lung cancer patients; however, additional motion phases can be trivially added if needed. Though the number of motion phases is discrete, the tumor motion is continuously monitored, and a variety of motion monitoring devices can be selected.

In this study, we used continuous monitoring of target motion to adapt the delivery sequence of sub-plans. The 1D target motion was monitored with an optical distance sensor (OD100—35P840, SICK, Waldkirch, Germany). The signal amplitude was digitized and analyzed to yield a discrete motion phase. The sub-plan found in the plan library, corresponding to the detected phase, was then accessed. During beam delivery, the beam spots in the sub-plan that corresponded to the detected motion phase were delivered in sequence until complete, or until another motion phase was detected. When another phase was detected, the delivery was then redirected to the nearest beam spot within the corresponding sub-plan and delivery continued as before. Once all of the spots in an iso-energy slice (IES) were delivered for the given sub-plan, the beam was suspended until delivery was directed to a sub-plan containing yet undelivered spots of the same energy. This process continued until all beam spots for that IES were delivered, then delivery progressed to the next IES. For deliveries to static targets (plan libraries with one motion phase), all the beam spots are delivered in sequence for each IES until all beam spots were delivered.

At the time of this study, the refurbished accelerator system at GSI was only capable of single-energy deliveries and the beam range was modulated with a range shifter to deliver beams to entire target volumes. Subsequent work will implement fast and automated switching between accelerated beam energies to efficiently deliver multiple beam energies. Therefore, all plans were delivered with a nominal beam energy of 280 MeV/u. As a provisional means to produce multiple beam energies and ranges

within a single delivery, we used a binary range shifter comprising polyethylene (PE) plastic slabs (21, 22). The treatment plans contained beam energy codes, that specified the needed beam energy for each slice of the treatment plan. These codes were converted to range shifter settings, where the range shifter settings specified the insertion of a combination of range shifting absorber slabs to modulate the beam range. Each of the selected binary codes corresponds to a combination of plastic slabs that allowed for shifting the beam spots longitudinally by as little as 0.1 mm increments. During beam delivery, the switching of range shifter settings was synchronized with the spill cycles of the synchrotron. The range shifter was further described elsewhere (22).

This motion-synchronized dose delivery system was previously implemented into the M-DDS and preliminary tests were reported (13).

Experimental Setup

Plan libraries were delivered to two setups, containing a heterogenous phantom, and moving slabs and dosimeters (**Figure 1**). Treatment deliveries were repeated twice for each setup: once to irradiate a 2D ionization chamber (IC) array detector (Octavius 1500XDR; PTW, Freiburg, Germany) and again to a stack of six radiochromic films (EBT3 Gafchromic; International Specialty Products, Wayne, NJ). The 2D IC array detector was placed within a 5 mm thick PMMA holder, and 6 films, were slotted into the films stack, between 10 mm slabs of PMMA (21). The 2D IC array detector, containing ICs filled with air at ambient pressure, was set to integral mode to measure total delivered dose. Both holders were mounted on top of a motorized linear stage (M-414.2PD; Physik Instrumente (PI) GmbH, Karlsruhe, Germany), aligned perpendicularly to the beamline. Slabs of water equivalent plastic, corresponding to 56.7 mm water-equivalent thickness (WET) were placed in front of these holders, on the linear stage. The linear stage was programmed to move with a 20 mm, uni-axial Lujan2-type respiratory motion-like pattern (18), and the motion was monitored in real time with an optical distance laser sensor (13, 23).

Both setups contained a range modifying phantom. These included a wedge-shaped piece of PMMA ('wedge phantom') and a rectangular shaped piece of PMMA ('density phantom') with three air cavities (**Figure 1**). These were used to test uniform, gradual changes to the thickness proximal to the target, and discrete gradients from air gaps, respectively. The wedge phantom was $100 \times 70 \times 128$ mm^3, with a lateral slope of 0.3 mm/mm. The density phantom was a $160 \times 109.9 \times 30$ mm^3 block of PMMA with 15.8-, 12.0-, and 8.1-mm diameter cylindrical air gaps. In both cases, the wedge and density phantoms remained stationary and were placed in front of the detector and water-equivalent plastic slabs, which were placed on top of the moving linear stage. The density phantom induced range changes of 5.5 to 18.4 mm and the wedge phantom induced a maximum range gradient of 8.8 mm/mm. In addition to the MP4D deliveries, 3D optimized plans were delivered to moving targets, without motion mitigation, to assess the dosimetric impact of motion interplay effects. Similarly, 3D-optimized plans were delivered to static targets to determine the reference dosimetric performance of the treatment delivery system.

Data Analysis

The dosimetric quality of deliveries through the multiple range phantoms was analyzed by reconstructing beam monitoring data from treatment delivery log files of the M-DDS. The dose delivery data log files were reconstructed on the 4DCT images containing a simulated water-box phantom. The dose delivery data log files and motion monitoring data log files, from the motion monitoring system (13), were parsed and reformatted into the TRiP4D treatment plan format. TRiP4D was then used to calculate (reconstruct) the delivered dose distributions from the reformatted files. The dose distributions were calculated on the same target volumes as used during treatment planning. We then compared the reconstructed, planned and measured dose

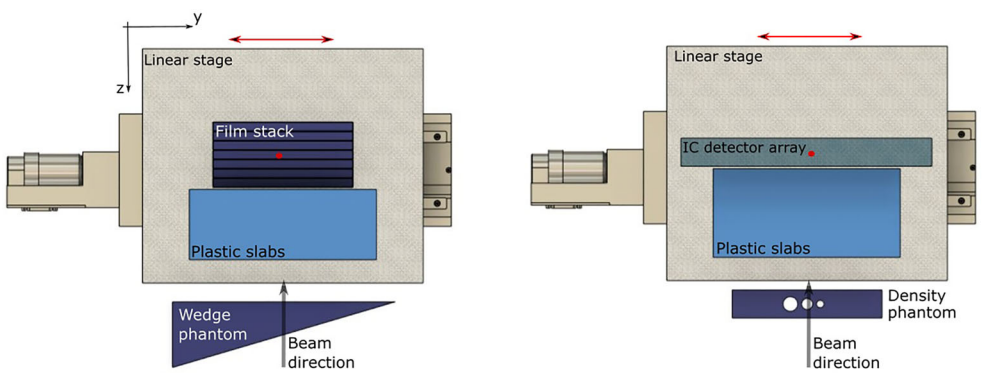

FIGURE 1 | Setups for testing motion compensation through heterogenous targets. A combination of four setups were used with either the wedge or density phantom and where measurements were made with either an IC array detector or film stack. A top view of the wedge-shaped phantom (left) and slab phantom with density heterogeneities (right) are shown, placed in front of a periodically moving linear stage. For all setups, the dosimeter was placed behind a set of plastic slabs. Isocenter is marked with a red circle and the linear stage movement is indicated with a red arrow.

distributions. The dosimetric quality metrics we selected to assess motion management included uniformity, conformity, dose coverage and overdose. Each of these metrics were calculated from dose volume histogram (DVH) data from planned and delivered dose reconstructions. Conformity number is

$$CN = \frac{V_{T,p}}{V_T} \times \frac{V_{T,p}}{V_p} \quad (1)$$

where $V_{T,p}$ is the portion of the CTV that receives a dose that is greater than or equal to the prescribed dose, D_p, V_T is the CTV, and V_p is the volume that receives a dose that is greater than or equal to D_p (24). A CN value of 100% is ideal and, while there is no threshold for an acceptable CN, we considered > 60% to be acceptable. Homogeneity (HI), which is a measure of delivery uniformity, is

$$HI = D_5 - D_{95} \quad (2)$$

where D_5 and D_{95} are the percentages of the prescription dose, D_p = 3 Gy, which are delivered to 5 % and 95 % of the tumor volume, respectively (25). An HI of 0 % is ideal and < 5 % was considered acceptable (26). Tumor dose coverage, which is the percentage volume of the CTV that received at least 95% of the D_p, is represented by V_{95}. A V_{95} of 95% was considered clinically acceptable. Overdose, denoted by V_{107}, is the percentage of the CTV that receives over 107 % of the prescription dose. Zero overdose is ideal. The acceptable ranges for these metrics were selected for the purposes of this study.

Each measured dose distribution was compared to the corresponding planned dose distribution and reconstructed dose distribution. The 3D generalized gamma index analysis (27), was used to quantify the degree of agreement between each pair of dose distributions. With the generalized gamma index analysis, we were able to objectively select magnitudes for the distance to agreement and dose difference criteria for our data set. This allowed for more accurate characterization of the dosimetric agreement in the low-dose region. Pass criteria of 3 % dose difference and 3 mm distance to agreement were applied in all cases. Pass rates of > 90 % were considered acceptable. The purpose of comparing measured and reconstructed dose distributions was to validate the accuracy of the dose reconstruction method. The purpose of comparing measured and planned dose distributions was to determine the amount of unintended delivered dose during beam gating and spill pauses.

Quality Assurance

We performed limited quality assurance (QA) on the beam output prior to dosimetry measurements. The QA comprised relative dosimetry, using the methods described by Luoni et al. (28). Specifically, the constancy of the beam output (relative absorbed dose) was measured with a farmer-type ionization chamber (PTW 30010 Farmer Chamber; PTW, Freiburg, Germany), placed at isocenter. The farmer chamber was inserted into a 30 × 30 × 1 cm^3 water-equivalent plastic holder slab, with a water-equivalent point of measurement at 5 mm depth. A 5 × 5 cm^2 square field of 2 Gy absorbed dose was delivered with 280 MeV/u carbon ion beams without range modulation. Each measurement was repeated three times. The same field was delivered to a film at 5 mm depth to measure field homogeneity. This QA approach was selected because it is well established, fast and because beamtime for QA procedures was severely limited at the time of this study.

We defined reference conditions to facilitate calibrations of two dosimeters (a 2D IC array detector and radiochromic films). The reference conditions comprise three major elements, namely, a reference radiation field, a reference phantom, and a reference measurement location. The reference radiation field comprised a 280 MeV/u carbon ion beam without range modulation and with an incident beam spot size of 6.7 mm full-width half maximum, delivered to a measurement depth of 5 mm, at isocenter.

We calibrated the 2D IC array detector and film to absorbed dose under reference conditions. The calibrations of these dosimeters were based on measurements of their responses to irradiations of known absorbed dose. The known absorbed dose was determined from dose reconstructions, which were previously calibrated and are described elsewhere (11). We simultaneously calibrated the IC array detector and films. The detector was positioned at isocenter, inside of a 31 × 40 × 4 cm^3 box-like holder with 5 mm water-equivalent thick walls. A film was taped directly in front of the 2D IC array detector, inside the holder. A calibration plan was delivered that comprised eight 30 × 30 mm^2 square fields, ranging in fluences from 5 × 10^4 to 1 × 10^7 particles/mm^2, corresponding to absorbed doses of 0.1 to 9.9 Gy at 1 cm depth, in the plateau region. The initial beam energy was 280 MeV/u, and no additional range modulation was introduced. This interval of absorbed dose values was selected to encompass the dynamic range anticipated for the clinical deliveries and to remain within the dynamic range of optical densities for radiochromic films.

We used an established formalism to calibrate the IC array detector (13, 21, 29). These are briefly reviewed here for the convenience of the reader. The IC array detector was calibrated to absorbed dose to water under reference conditions. Measured absorbed dose is given by

$$D_{IC} = M \times C \times k_Q \quad (3)$$

where M is the measured response (corrected for leakage, temperature, and pressure) and C is the calibration coefficient under reference conditions, k_Q corrects for the effects of the difference between the reference conditions and the non-reference conditions. We confirmed the stability of the previously determined value of C = 1.2 Gy per unit of measured response, following methods similar to those described by Stelljes et al. (30). The effects of non-reference conditions were negligible and k_Q was approximated as unit value. The absolute absorbed dose values, at the same locations as the ICs and under reference conditions, were also reconstructed from delivery log files, which allowed us to calculate dosimetric outcomes from the reconstructions.

We used radiochromic films to simultaneously measure relative 2D absorbed dose distributions under reference and

non-reference conditions. Films allowed for faster data acquisition at multiple depths during the limited beamtime available. They also provided the high spatial resolution needed to measure dose distributions distal to the wedge and density phantoms.

We used methods similar to those of Yonai et al. (31) for calibrating the film response to relative absorbed dose, which are briefly reviewed here for the convenience of the reader. First, the TPS was used to create a calibration plan under reference conditions, described above. The calibration plan was delivered to the radiochromic film, in the geometry described above. The exposed films aged for one day, then were digitized (DosimetryPro Advantage Red; VIDAR Systems Corporation, Herndon, VA, USA) using a 16-bit sampling and 300 dots per inch resolution. The net optical density of the scanned film was determined by

$$OD_{net} = OD_m - OD_{bkg} \quad (4)$$

where OD_m is the measured (scanned) optical density, and OD_{bkg} is the background optical density scanned in an unirradiated area on each film. The OD_{net} was determined in the central region of each square field in the calibration film. The known absorbed dose values at the center of each square field, D_{film}, were fit to eight measured OD_{net} values according to

$$D_{film} = D_{film,uncorr} \times k_{Q,film} \quad (5)$$

where $D_{film,uncorr}$ is the uncorrected, measured absorbed dose from films, and $k_{Q,film}$ is a correction factor for changes in the film response due to changes in beam quality at non-reference conditions, including other depths. The value $k_{Q,film}$ corresponds to a factor that is called relative efficiency elsewhere (31, 32). By definition, $k_{Q,film}$ took a value of 1 at the reference condition used for the calibration. Under non-reference conditions, the value of the correction factor $k_{Q,film}$ corrected for changes in the film response due to quenching, which depends on beam quality, as specified by the beam's linear energy transfer. Both $D_{film,uncorr}$ and $k_{Q,film}$ were calculated using methods modified from Yonai et al. (31). The calibration procedure above was performed separately for each batch of film used.

RESULTS

Figure 2 reveals that the reconstructed dose distributions agree well with the corresponding dose distributions obtained from measurements with film. This result confirms the suitability of the method for reconstructing dose distribution for the main purpose of this study, which is to assess the quality of dose distributions delivered by various techniques. We defer discussion of the results on confirming of the reconstruction methods until later in this section.

Dosimetric Validation

Relative dosimetry was performed prior to experiments by delivering a uniform square profile to a farmer-type IC and a radiochromic film. Output constancy was verified, and beam output ranged from 2.57 to 2.59 Gy at isocenter. Field homogeneity was also measured with the homogeneity index, and was 4.8%.

We assessed the dosimetric quality of deliveries through the wedge and the density phantoms. Measured absorbed dose distributions were compared to the corresponding dose distributions from reconstructions and treatment plans. **Figure 3** plots the absorbed dose distributions for these deliveries, including those with a static target, moving target without motion compensation (revealing the extent of interplay), and moving target with the multi-phase 4D approach (revealing the effectiveness of motion mitigation).

Specifically, dosimetric quality was assessed with four metrics: conformity, homogeneity, coverage, and overdose (**Figure 4**). The major qualitative finding from these results is that 10-phase MP4D deliveries provided the best overall dosimetric quality. The major qualitative finding is that 10-phase and 6-phase MP4D deliveries had acceptable dosimetric quality, while quality metrics for 3-phase MP4D were mixed. **Figures 2**, **3** reveals that the reconstructed dose distributions agree well with measurements. Acceptable conformity ($CN > 60$ %) was obtained in all MP4D deliveries with 6 and 10 phases. However, at least 10 motion phases were required to achieve acceptable homogeneity ($HI < 5$ %) of the absorbed dose in the CTV. Fewer motion phases produced unacceptably large heterogeneities, due to interplay effects within each motion phase (so-called "residual motion").

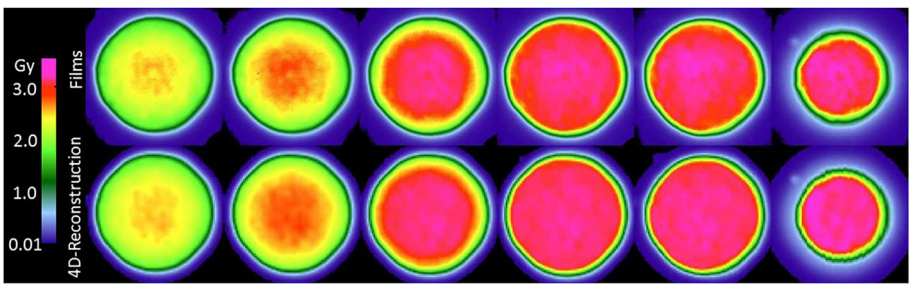

FIGURE 2 | Comparison of film measurements (top row) to dose reconstructions (middle row). The top row shows the films from a film stack for a multi-phase 4D delivery using 10 motion phases to the wedge phantom with 20 mm uniaxial motion. Films are ordered left to right with increasing depth in the wedge phantom. The depth increment between films is approximately 11 mm water-equivalent thickness. The corresponding dose reconstructions for the same delivery are shown in the middle row.

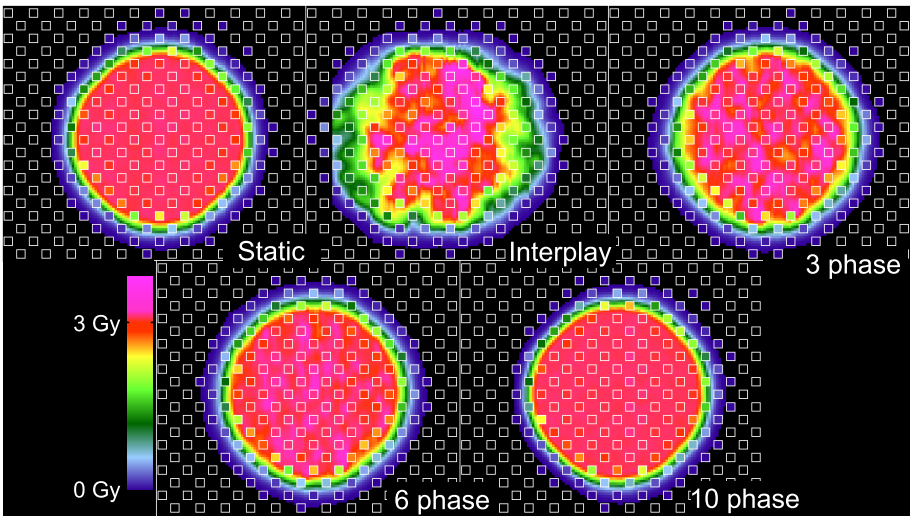

FIGURE 3 | Comparison of 2D ionization chamber array detector measurements to dose reconstructions. The bottom row shows measured absorbed dose values (values inside of small white squares) overlaid on reconstructed absorbed dose distributions (values outside of the small white squares). The dose distributions are distal to the density phantom (see **Figure 1**). Distributions are from four delivery techniques: static target, moving target without motion compensation (interplay), and moving target with multi-phase 4D motion compensation. Multi-phase 4D deliveries are shown using 3, 6, and 10 motion phases in the treatment plan libraries.

The average *HI* value for all of the 10-phase MP4D deliveries (both phantom types and CTV shapes) was 8 %, approaching the criteria of < 5 %, which was achieved for static deliveries and is considered acceptable for other deliveries. Target coverage was 100 % for 10-phase MP4D deliveries and was > 98 % for 6-phase MP4D deliveries, also approaching the ideal results of 100%, which were obtained from deliveries to a static target. These findings on coverage and heterogeneity are qualitatively supported by dose distributions plotted in **Figure 3**, which shows that the MP4D approach produces similar results for the static and 10-phase MP4D deliveries. It was expected that the deliveries using 10 motion phases would have superior results, since the residual motion was less than that with 6 or 3 motion phases. The increasing homogeneity is also seen in **Figure 5**, where the range of average measured absorbed dose values narrow with increasing number of motion phases. Here, the average absorbed dose was within ± 1.5 % of the prescription dose for MP4D deliveries. Finally, the 10-phase MP4D approach produced hotspots in the CTV that were < 103% of the prescribed absorbed dose. Together, these findings suggest that the 10-phase MP4D approach provides good dosimetric quality that closely approaches the quality that was achieved for static-target deliveries.

Effectiveness of Multi-Phase 4D Delivery

The results of MP4D deliveries also yielded important findings regarding over- and undershoot of the beam range and regarding the inverse interplay effect. Regarding range effects, absorbed dose distributions from treatment plans and dose reconstructions are shown in **Figure 6** (SlicerRT, Kingston CA), which illustrates that static robust optimization created dose distributions with range over- and undershoots. These are a consequence of taking the large range uncertainties in low density material of the phantom into account. These range effects manifest distal to the cavities of the density phantom, near the end of range. The MP4D approach reduced these range defects as, the dose delivered to these regions were "blurred out" by delivering multiple sub-plans to the target volumes. Regarding the inverse interplay effect, the MP4D approach exhibited no dose defects from this (**Figures 6B, D**). The inverse interplay effect is a serious concern that is associated with the beam tracking delivery approach (15). With beam tracking, the beam spot positions are modified from their planned positions to compensate for detected real-time motion. This can deliver uniform doses to the target but introduces hotspots and cold spots in the beam path, proximal to the target in healthy tissue. With the MP4D approach, there were no hotspots in the proximal healthy tissue. Instead, the lateral extent of the irradiated healthy tissue was broadened by the amplitude of the target motion. These findings on range defects and inverse interplay further suggest that MP4D approach can provide high quality deliveries.

Figure 2 reveals that the dose reconstruction methods were confirmed by measurements. In particular, high gamma-index pass rates confirmed the accuracy of the treatment planning and dose reconstructions in this study. Specifically, we compared dose distributions from measurements with the IC detector array to those from the corresponding log file reconstructions (**Figure 7C**) and treatment plans (**Figure 7B**) obtained with moving targets. Average pass rates increased with the number of motion phases, due to the decreasing residual motion within each motion phase. In all cases, reconstructed dose distributions agreed well with measured dose distributions (**Figure 7C**), with pass rates > 90 %, confirming the validity of the dose reconstruction strategy. Gamma index analysis pass rates were

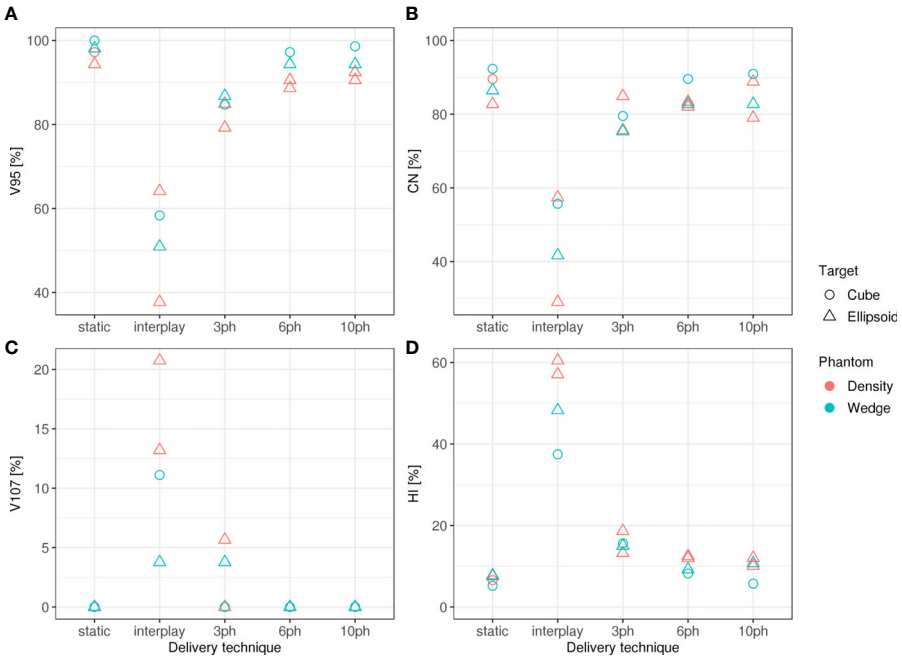

FIGURE 4 | **(A)** Dose coverage (V_{95}), **(B)** conformity (CN), **(C)** overdose (V_{107}), and **(D)** homogeneity (HI) for static deliveries to stationary targets (static), static deliveries to moving targets (interplay), and 3-phase, 6-phase and 10-phase multi-phase 4D deliveries to cube and ellipsoid target volumes through the wedge and density phantom.

lower for comparisons between planned and measured dose distributions and only static deliveries and 10-phase MP4D deliveries had pass rates > 90 %.

Similarly, we compared all dose distributions from measurements to reconstructions of static deliveries (**Figure 7A**). This comparison provided important contextual information on the magnitude of dose degradations that were caused by target motion occurring within a motion phase and without motion compensation. Pass rates were < 90 % for comparisons between static reconstructions and 3 phase MP4D measurements and were < 60 % for comparisons between static reconstructions and interplay deliveries. For planning studies, 10 or more motion phases should be selected.

The total delivery time was calculated from treatment log files. Average total delivery time for static ellipsoid deliveries was 7.4 min. The relative increase in delivery time for 3-phase, 6-phase and 10-phase MP4D deliveries, compared to static deliveries, was 7%, 17%, and 21%, respectively. This suggests that the MP4D method provides motion-mitigated deliveries with increases to delivery time that would be well-tolerated by most radiotherapy patients and compatible to existing patient caseloads.

DISCUSSION

In this study, we validated the dosimetric performance of a novel multi-phase 4D treatment approach with deliveries to heterogenous phantoms. Specifically, we measured dosimetric quality of absorbed dose distributions from plan libraries delivered through two phantoms. The major findings of this study are that the multi-phase 4D (MP4D) dose delivery approach has acceptable dosimetric quality without introducing inverse interplay effects.

The implication of this study is that MP4D delivery offers a promising new alternative approach to motion mitigation that provides good dosimetric quality with moderate technical complexity. The magnitude of technical complexity is an important characteristic because it can be a barrier on the path of translation of new technologies to clinical practice. One such technology, ion beam tracking, entails rapidly modifying planned beam spot positions to the real-time detected target motion (12, 33). Consequently, the dose distributions delivered to a patient cannot be fully confirmed by pre-treatment quality assurance testing. One type of beam tracking, called 4D-optimized tracking, that pre-computes tracking vectors to take anatomical motion from 4DCTs into account during planning, still exhibited inverse interplay effects and other dose degradations (10). The process of adjusting planned beam spot positions with tracking vectors results in cold- and hotspots in the proximal normal tissues. Our results suggest that, in the absence of respiratory-motion-related uncertainties (baseline drifts and changes to the tumor trajectory), clinically acceptable projected therapeutic outcomes could be achieved with the MP4D approach without inducing significant hotspots

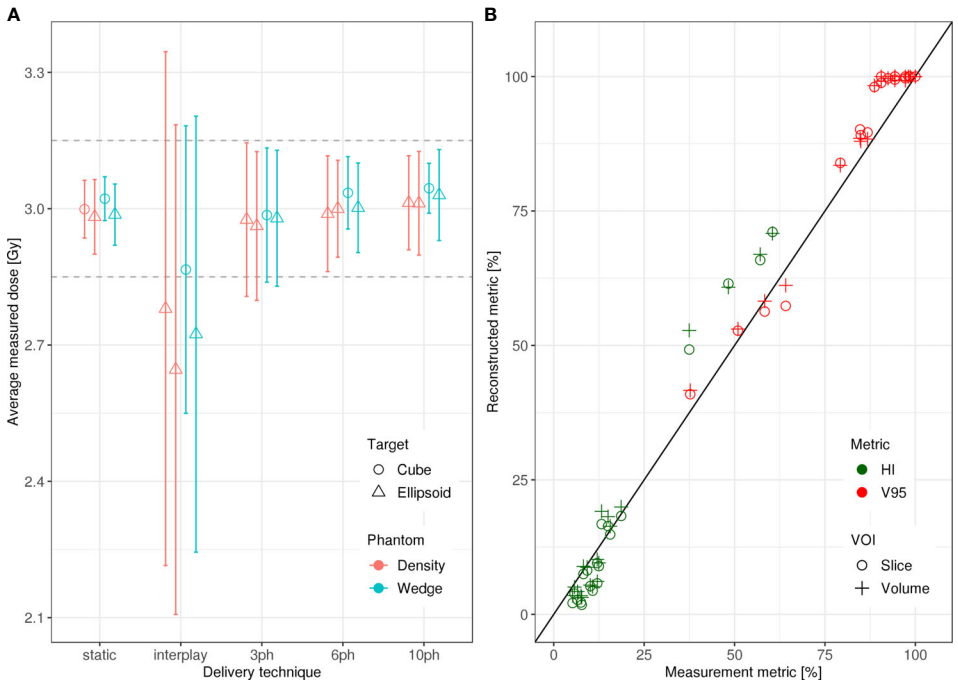

FIGURE 5 | **(A)** Average measured absorbed dose *versus* delivery technique evaluated using the density and wedge phantoms. The dashed grey lines delineate the ± 5 % tolerance interval centered about the prescription absorbed dose of 3 Gy and the bars indicate the spread measured dose values from each ionization chamber (IC) of the 2D IC array detector in the clinical target volume (CTV) **(B)** Homogeneity (HI) and coverage (V_{95}) for measured *versus* reconstructed absorbed dose distributions in the target volume. Dosimetric quality was calculated in a single iso-energy slice within the CTV and in the entire CTV for each delivery. All delivery techniques for both phantom types and for both VOIs are plotted. Data points that fall on the line indicate full agreement of measured and reconstructed HI and V_{95} values.

in normal tissues (due to inverse interplay effects) and the target volume (due to interplay effects). This study provides new evidence that, when considered with other recent studies (13, 29), suggest it may be feasible to translate the MP4D approach to clinical practice for both carbon ion and proton beam treatments. It must be emphasized that the MP4D approach is still in the early stages of preclinical development and testing; further work is needed to understand how dosimetric quality is impacted by irregular motion (*e.g.*, baseline drifts and changes to target trajectories caused by coughs and sneezes). Furthermore, additional research is needed to implement and evaluate MP4D deliveries with real-time corrective tracking and to compare the MP4D approach to the 4D-optimized tracking approach.

This work is broadly coherent with previous literature on motion mitigation approaches for proton and ion therapies. Our findings extend previous preliminary studies that suggested feasibility of a novel dose delivery system (M-DDS) with integrated motion-synchronization strategies (13, 29). The MP4D delivery approach poses a straightforward solution to solve the limitations of 3D tracking and 4D-optimized tracking. Previous research at GSI focused on 3D tracking, which required utilizing a fast wedge system to modulate beam spot delivery depth and compensate for motion-induced target depth changes in real-time, during treatment delivery (33, 34). Experiments confirmed the range compensation capabilities of this system. The 3D tracking method was reported by Saito et al. (33), and compensated for translational target motion (only), but beam spot delivery accuracy was still within 5 mm in the lateral and longitudinal directions. Importantly, this work revealed several complications with potentially important clinical implications for certain situations. First, the so-called "inverse interplay" effect was observed, due to differences in motions of the target and the tissue of the entrance channel (35). Second, complex motion, such as tumor rotations or deformations could not be fully compensated for (36). Finally, for tissues with large heterogeneities, no solution was found to compensate for motion-induced range changes. 4D-optimized tracking (12), or online adaptive tracking (37) partially solved the latter problem. However, that 4D tracking implementation encountered several obstacles, including limitations on the available hardware speed and memory, and difficulties with synchronizing the system timing. These issues rendered the system obsolete; it was dismantled and replaced with the motion-synchronized dose delivery system described here and elsewhere (13).

In consideration of the above, the MP4D delivery strategy is generally less complex, and allows for integrating a variety of treatment planning strategies, such as 4D optimization (38). It also accommodates the pre-treatment quality assurance methods similar to those currently used clinically (29). Our findings on dosimetric quality are comparable to those of the system at NIRS.

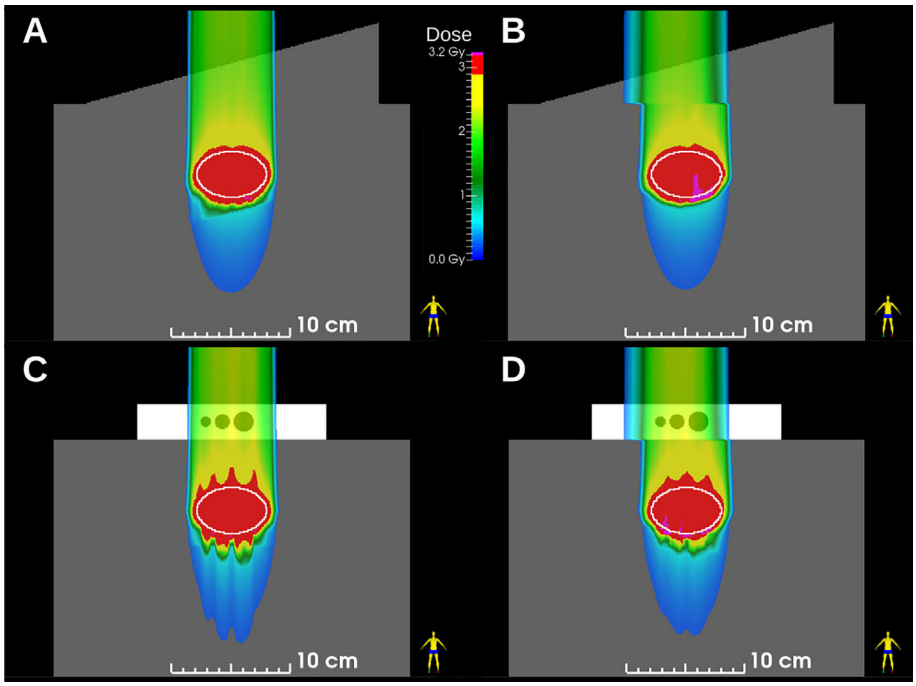

FIGURE 6 | Dose distributions in ellipsoid targets (white ovals) for **(A)** static and **(B)** 10-phase multi-phase dose deliveries through the wedge phantom and for **(C)** static and **(D)** 10-phase multi-phase 4D deliveries through the density phantom. Plans were robustly optimized and deliveries were reconstructed from beam delivery log files and motion monitoring log files.

At NIRS, phase-controlled rescanning is used to deliver a full set of rescans during each gating window (39). X-ray fluoroscopy detects when the tumor is within a pre-defined gating window, resulting in accurate treatment to the tumor volume. Typical results for phase-controlled rescanning were a D_{95} of over 95 %. Further, clinical outcome data revealed 2-year survival rates were as high as 82 % for stage 3 lung cancers treated with passive ion beams (40). This method relies on the fast-scanning magnets of the HIMAC accelerator at NIRS, and slower beam deliveries may not be able to achieve the same results. In contrast, our approach allows for continuously adapting the delivery sequence to detected motion, with minimal delivery pauses (a maximum 21% observed increase to total delivery time with regular motion), and with minimal residual motion during active beam delivery. For these reasons, it appears that the MP4D approach may find broader applicability than is possible with other approaches.

Our study has several strengths. First, we performed all of our measurements with a modular and portable dose delivery system (13), with integrated solutions for motion-synchronized dose delivery. This is potentially broadly applicable and the M-DDS has already been demonstrated at multiple centers, including CNAO and GSI. Additionally, as the motion mitigation portion of the M-DDS is an optional module, the M-DDS requires no modifications to run either with or without the motion mitigation module. This allows for implementing the M-DDS in a stepwise manner into existing facilities. We also selected methods for assessing dosimetric quality that are standard techniques within ion therapy centers (26, 41). Further, the range changes were measured by delivering beams to simple phantoms rather than anthropomorphic phantoms (42–44), eliminating additional variables, such as range uncertainties associated with variations in tissue density, irregular breathing patterns, and generally more complex range changes that are found in a human anatomy. As a result, the delivery quality more directly reflects the capabilities of the MP4D deliver approach. Nevertheless, geometries that are more complex could further confirm that our motion-synchronized dose delivery strategy can compensate for range changes and represent scenarios that are closer to clinical conditions. Further, in later stages, pre-clinical tests will be performed with anthropomorphic phantoms to characterize the full capabilities of the M-DDS.

Our study had several limitations. At the time of these experiments at GSI, our beam gating system (based on radiofrequency knockout extraction) could not yet fully gate the beam (21), and the accelerator system could not yet provide beams of multiple energies in any one delivery. We discuss both of these limitations in detail here. The inability to completely gate the beam results in an insignificant but observable amount of undesired radiation that only slightly degraded the dose distributions. Specifically, a trend was apparent (**Figure 7**) that, as the number of motion phases increased, the average absorbed dose in the CTV increased as well. The increase was under 0.4% undesired, additional dose. To overcome the limitation of having only single energies available, a passive range shifter system was utilized to modulated beam energy and range. Due to the

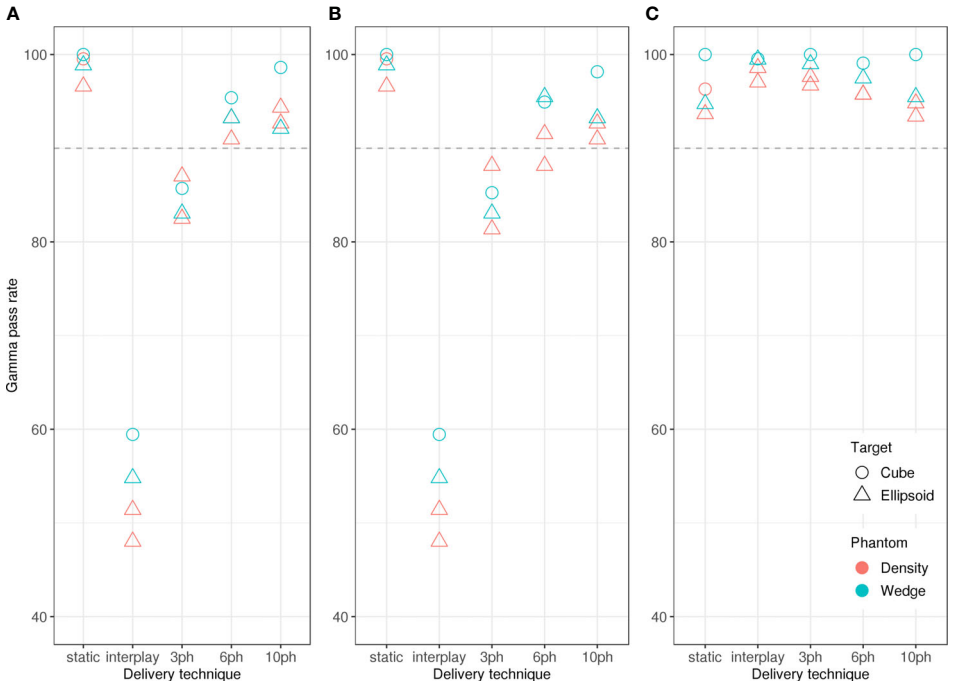

FIGURE 7 | Gamma index analysis pass rates *versus* beam delivery technique. The pass rates indicate good agreement between measured absorbed dose distributions and **(A)** reconstructed absorbed dose distributions for the static delivery, **(B)** planned absorbed dose distributions and **(C)** reconstructed absorbed dose distributions. Comparisons were made for static deliveries to stationary targets (static), static deliveries to moving targets (interplay), and multi-phase deliveries to moving targets with 3 phases, 6 phases, and 10 phases of motion compensation. Pass rates showed only a weak dependence on phantom type (wedge or density types) and target shape (cube or ellipsoid types).

additional material and air gaps between the range shifter plates, the beam spot size was strongly dependent on the amount of range shifter material (29). This was not a serious limitation, as the range compensation capabilities could still be demonstrated, and the TRiP4D TPS was updated to take the correct spot sizes into account in the dose calculation algorithm. In the next stage, the experiments reported here will be reproduced at CNAO, where the gating system is tuned for therapy and beam energies of 120 – 400 MeV/u are available for carbon ions (20). Another limitation of our study is that we have not tested the MP4D delivery strategy under more complex respiratory scenarios, including baseline drifts, changes to breathing amplitude and changes to breathing speed, as well as more extreme respiratory irregularities, including coughing. Some of these irregular motion scenarios could result in cold and hotspots in the target volume and dose to surrounding tissue. These capabilities will be implemented in later stages, along with improved beam gating, which will be used for handling unforeseen motion, including coughing. Finally, we did not compare the MP4D delivery strategy to other motion handling methods currently used in clinics [including the gating methods, and ITV-based deliveries with rescanning (45)] or study the results of combining motion mitigation strategies. These strategies are studied in detail elsewhere (45, 46), and delivery degradations in the complete absence of motion mitigation are shown in this study.

The results presented in this work are part of an ongoing effort to develop motion-synchronized dose delivery strategies at GSI. The motion-synchronized dose delivery system was previously assessed for safety (29), and the strategy has been validated against other approaches, including ITV-based deliveries with rescanning (45). In the future, dose degradation due to irregular motion and differences between motion during imaging and during delivery will be quantified, and corrective motion tracking will be implemented to correct for irregular target motion. The long-term goal is to translate the multi-phase 4D delivery approach and motion-synchronized dose delivery system into clinical use at CNAO.

CONCLUSIONS

We validated the dosimetric performance of multi-phase 4D treatment delivery with scanned ion beams in the presence of multiple beam ranges. The results of this work demonstrate that it is possible to deliver motion compensated dose distributions in the presence of anatomical heterogeneities. Notably, the dosimetric performance was achieved without high technological demands or specialized equipment for mitigating target motion.

DATA AVAILABILITY STATEMENT

The raw data supporting the conclusions of this article will be made available by the authors, without undue reservation.

AUTHOR CONTRIBUTIONS

ML, CG, and WN wrote the manuscript. CG and MD devised the project. ML and MD developed the M-DDS that is the device validated in this work. WN and CG supervised this work. ML, MW, TS, AP, and CG performed experiments and gathered data. ML, MW, CG, and TS contributed to analyzing the data of this study, including log file reconstructions and data post-processing procedures. All authors contributed to the article and approved the submitted version.

FUNDING

This project has received funding from the European Union's Horizon 2020 research and innovation program under the Marie Skłodowska-Curie grant agreement No 675265, OMA – Optimization of Medical Accelerators, from the Charles E. Coates travel award (LSU), and from the August Family Professorship (LSU).

ACKNOWLEDGMENTS

We would like to thank U Weber and C Schuy for providing our group with the detectors and phantoms used in this study. The research presented here is a result of a R&D project experiment SBIO at the beam line SIS-18 in the frame of FAIR Phase-0 supported by the GSI Helmholtzzentrum für Schwerionenforschung in Darmstadt (Germany).

REFERENCES

1. Malouff TD, Mahajan A, Krishnan S, Beltran C, Seneviratne DS, Trifiletti DM. Carbon Ion Therapy: A Modern Review of an Emerging Technology. *Front Oncol* (2020) 10(82). doi: 10.3389/fonc.2020.00082
2. Kamada T, Tsujii H, Blakely EA, Debus J, De NW, Durante M, et al. Carbon Ion Radiotherapy in Japan: An Assessment of 20 Years of Clinical Experience. *Lancet Oncol* (2015) 16(2):e93–e100. doi: 10.1016/S1470-2045(14)70412-7
3. Tsujii H, Kamada T. A Review of Update Clinical Results of Carbon Ion Radiotherapy. *Jpn J Clin Oncol* (2012) 42(8):670–85. doi: 10.1093/jjco/hys104
4. Chun SG, Hu C, Choy H, Komaki RU, Timmerman RD, Schild SE, et al. Impact of Intensity-Modulated Radiation Therapy Technique for Locally Advanced Non-Small-Cell Lung Cancer: A Secondary Analysis of the NRG Oncology RTOG 0617 Randomized Clinical Trial. *J Clin Oncol* (2017) 35(1):56–62. doi: 10.1200/JCO.2016.69.1378
5. Rios J, Gosain R, Goulart BH, Huang B, Oechsli MN, McDowell JK, et al. Treatment and Outcomes of non-Small-Cell Lung Cancer Patients With High Comorbidity. *Cancer Manag Res* (2018) 10:167–75. doi: 10.2147/CMAR.S151935
6. Wang Y, Bao Y, Zhang L, Fan W, He H, Sun Z-W, et al. Assessment of Respiration-Induced Motion and Its Impact on Treatment Outcome for Lung Cancer. *BioMed Res Int* (2013) 2013:872739–. doi: 10.1155/2013/872739
7. Mori S, Knopf A-C, Umegaki K. Motion Management in Particle Therapy. *Med Phys* (2018) 45(11):e994–e1010. doi: 10.1002/mp.12679
8. Bradley JD, Paulus R, Komaki R, Masters G, Blumenschein G, Schild S, et al. Standard-Dose *Versus* High-Dose Conformal Radiotherapy With Concurrent and Consolidation Carboplatin Plus Paclitaxel With or Without Cetuximab for Patients With Stage IIIA or IIIB non-Small-Cell Lung Cancer (RTOG 0617): A Randomised, Two-by-Two Factorial Phase 3 Study. *Lancet Oncol* (2015) 16(2):187–99. doi: 10.1016/S1470-2045(14)71207-0
9. Trnkova P, Knausl B, Actis O, Bert C, Biegun AK, Boehlen TT, et al. Clinical Implementations of 4D Pencil Beam Scanned Particle Therapy: Report on the 4D Treatment Planning Workshop 2016 and 2017. *Phys Med* (2018) 54:121–30. doi: 10.1016/j.ejmp.2018.10.002
10. Eley JG, Newhauser WD, Richter D, Lüchtenborg R, Saito N, Bert C. Robustness of Target Dose Coverage to Motion Uncertainties for Scanned Carbon Ion Beam Tracking Therapy of Moving Tumors. *Phys Med Biol* (2015) 60(4):1717–40. doi: 10.1088/0031-9155/60/4/1717
11. Richter D, Saito N, Chaudhri N, Hartig M, Ellerbrock M, Jakel O, et al. Four-Dimensional Patient Dose Reconstruction for Scanned Ion Beam Therapy of Moving Liver Tumors. *Int J Radiat Oncol Biol Phys* (2014) 89(1):175–81. doi: 10.1016/j.ijrobp.2014.01.043
12. Eley JG, Newhauser WD, Luchtenborg R, Graeff C, Bert C. 4D Optimization of Scanned Ion Beam Tracking Therapy for Moving Tumors. *Phys Med Biol* (2014) 59(13):3431–52. doi: 10.1088/0031-9155/59/13/3431
13. Lis M, Donetti M, Newhauser W, Durante M, Dey J, Weber U, et al. A Modular Dose Delivery System for Treating Moving Targets With Scanned Ion Beams: Performance and Safety Characteristics, and Preliminary Tests. *Physica Med* (2020) 76:307–16. doi: 10.1016/j.ejmp.2020.07.029
14. Graeff C. Motion Mitigation in Scanned Ion Beam Therapy Through 4D-Optimization. *Phys Med* (2014) 30(5):570–7. doi: 10.1016/j.ejmp.2014.03.011
15. Richter D. Treatment Planning for Tumors With Residual Motion in Scanned Ion Beam Therapy [Dissertation]. Darmstadt, Germany: Technical University Darmstadt. (2012).
16. Krämer M, Jäkel O, Haberer T, Kraft G, Schardt D, Weber U. Treatment Planning for Heavy-Ion Radiotherapy: Physical Beam Model and Dose Optimization. *Phys Med Biol* (2000) 45(11):3299–317. doi: 10.1088/0031-9155/45/11/313
17. Krämer M, Scholz M. Treatment Planning for Heavy-Ion Radiotherapy: Calculation and Optimization of Biologically Effective Dose. *Phys Med Biol* (2000) 45(11):3319–30. doi: 10.1088/0031-9155/45/11/314
18. Lujan AE, Balter JM, Ten Haken RK. A Method for Incorporating Organ Motion Due to Breathing Into 3D Dose Calculations in the Liver: Sensitivity to Variations in Motion. *Med Phys* (2003) 30(10):2643–9. doi: 10.1118/1.1609057
19. Wolf ME, Anderle K, Durante M, Graeff C. Robust Treatment Planning With 4D Intensity Modulated Carbon Ion Therapy for Multiple Targets in Stage IV Non-Small Cell Lung Cancer. *Phys Med Biol* (2020) 65:215012. doi: 10.1088/1361-6560/aba1a3
20. Giordanengo S, Garella MA, Marchetto F, Bourhaleb F, Ciocca M, Mirandola A, et al. The CNAO Dose Delivery System for Modulated Scanning Ion Beam Radiotherapy. *Med Phys* (2015) 42(1):263–75. doi: 10.1118/1.4903276
21. Lis M, Newhauser W, Donetti M, Durante M, Weber U, Zipfel B, et al. A Facility for the Research, Development, and Translation of Advanced Technologies for Ion-Beam Therapies. *J Instrumentation* (2021) 16(03):T03004. doi: 10.1088/1748-0221/16/03/t03004
22. Simeonov Y, Weber U, Penchev P, Ringbæk TP, Schuy C, Brons S, et al. 3D Range-Modulator for Scanned Particle Therapy: Development, Monte Carlo Simulations and Experimental Evaluation. *Phys Med Biol* (2017) 62(17):7075–96. doi: 10.1088/1361-6560/aa81f4
23. Saito N, Bert C, Chaudhri N, Gemmel A, Schardt D, Kraft G, et al. *Technical Accuracy of a Beam Tracking System for Scanned Particle Therapy of Intra-Fractionally Moving Targets. World Congress on Medical Physics; 2009 9/7/2009; Munich*. Germany. Heidelberg: Springer (2009).
24. van't Riet A, Mak AC, Moerland MA, Elders LH, van der Zee W. A Conformation Number to Quantify the Degree of Conformality in Brachytherapy and External Beam Irradiation: Application to the Prostate. *Int J Radiat Oncol Biol Phys* (1997) 37(3):731–6. doi: 10.1016/S0360-3016(96)00601-3
25. Lauve A, Morris M, Schmidt-Ullrich R, Wu Q, Mohan R, Abayomi O, et al. Simultaneous Integrated Boost Intensity-Modulated Radiotherapy for Locally

Advanced Head-and-Neck Squamous Cell Carcinomas: II—Clinical Results. *Int J Radiat OncologyBiologyPhysics* (2004) 60(2):374–87. doi: 10.1016/j.ijrobp.2004.03.010
26. Mirandola A, Molinelli S, Vilches Freixas G, Mairani A, Gallio E, Panizza D, et al. Dosimetric Commissioning and Quality Assurance of Scanned Ion Beams at the Italian National Center for Oncological Hadrontherapy. *Med Phys* (2015) 42(9):5287–300. doi: 10.1118/1.4928397
27. Wilson LJ, Newhauser WD, Schneider CW. An Objective Method to Evaluate Radiation Dose Distributions Varying by Three Orders of Magnitude. *Med Phys* (2019) 46(4):1888–95. doi: 10.1002/mp.13420
28. Luoni F, Weber U, Boscolo D, Durante M, Reidel C-A, Schuy C, et al. Beam Monitor Calibration for Radiobiological Experiments With Scanned High Energy Heavy Ion Beams at FAIR. *Front Phys* (2020) 8(397). doi: 10.3389/fphy.2020.568145
29. Lis M, Newhauser W, Donetti M, Wolf M, Steinsberger T, Paz A, et al. A Modular System for Treating Moving Anatomical Targets With Scanned Ion Beams at Multiple Facilities: Pre-Clinical Testing for Quality and Safety of Beam Delivery. *Front Oncol* (2021) 11(323). doi: 10.3389/fonc.2021.620388
30. Stelljes TS, Harmeyer A, Reuter J, Looe HK, Chofor N, Harder D, et al. Dosimetric Characteristics of the Novel 2D Ionization Chamber Array OCTAVIUS Detector 1500. *Med Phys* (2015) 42(4):1528–37. doi: 10.1118/1.4914151
31. Yonai S, Arai C, Shimoyama K, Fournier-Bidoz N. Experimental Evaluation of Dosimetric Characterization of Gafchromic EBT3 and EBT-XD Films for Clinical Carbon Ion Beams. *Radiat Prot Dosimetry* (2018) 180(1-4):314–8. doi: 10.1093/rpd/ncy006
32. Reinhardt S, Würl M, Greubel C, Humble N, Wilkens JJ, Hillbrand M, et al. Investigation of EBT2 and EBT3 Films for Proton Dosimetry in the 4–20 MeV Energy Range. *Radiat Environ Biophysics* (2015) 54(1):71–9. doi: 10.1007/s00411-014-0581-2
33. Saito N, Bert C, Chaudhri N, Gemmel A, Schardt D, Rietzel E. Speed and Accuracy of a Beam Tracking System for Treatment of Moving Targets With Scanned Ion Beams. *Phys Med Biol* (2009) 54(16):4849–62. doi: 10.1088/0031-9155/54/16/001
34. Grözinger SO, Bert C, Haberer T, Kraft G, Rietzel E. Motion Compensation With a Scanned Ion Beam: A Technical Feasibility Study. *Radiat Oncol* (2008) 3(1):34. doi: 10.1186/1748-717X-3-34
35. Bert C, Grözinger SO, Rietzel E. Quantification of Interplay Effects of Scanned Particle Beams and Moving Targets. *Phys Med Biol* (2008) 53(9):2253–65. doi: 10.1088/0031-9155/53/9/003
36. Lüchtenborg R. Real-Time Dose Compensation Methods for Scanned Ion Beam Therapy of Moving Tumors [Dissertation], Darmstadt, Germany: Technical University Darmstadt (2012). Available at: http://tuprints.ulb.tu-darmstadt.de/2876/.
37. Lüchtenborg R, Saito N, Chaudhri N, Durante M, Bert C. On-Line Compensation of Dose Changes Caused by Intrafractional Tumor Motion. *Radiother Oncol* (2010) 96(S1):S539.
38. Wolf ME. Robust Optimization in 4D Treatment Planning for Carbon Ion Therapy of Lung Tumors [Dissertation]. Darmstadt, Germany: Technical University of Darmstadt (2018).
39. Furukawa T, Inaniwa T, Sato S, Shirai T, Mori S, Takeshita E, et al. Moving Target Irradiation With Fast Rescanning and Gating in Particle Therapy. *Med Phys* (2010) 37(9):4874–9. doi: 10.1118/1.3481512
40. Karube M, Mori S, Tsuji H, Yamamoto N, Nakajima M, Nakagawa K, et al. Carbon-Ion Pencil Beam Scanning for Thoracic Treatment - Initiation Report and Dose Metrics Evaluation. *J Radiat Res* (2016) 57(5):576–81. doi: 10.1093/jrr/rrw057
41. Hara Y, Furukawa T, Mizushima K, Takeshita E, Shirai T, Noda K. Application of Radiochromic Film for Quality Assurance in the Heavy-Ion Beam Scanning Irradiation System at HIMAC. *Nucl Instruments Methods Phys Res Section B: Beam Interact Mater Atoms* (2014) 331:253–6. doi: 10.1016/j.nimb.2013.11.030
42. Bolwin K, Czekalla B, Frohwein LJ, Büther F, Schäfers KP. Anthropomorphic Thorax Phantom for Cardio-Respiratory Motion Simulation in Tomographic Imaging. *Phys Med Biol* (2018) 63(3):035009. doi: 10.1088/1361-6560/aaa201
43. Perrin RL, Zakova M, Peroni M, Bernatowicz K, Bikis C, Knopf AK, et al. An Anthropomorphic Breathing Phantom of the Thorax for Testing New Motion Mitigation Techniques for Pencil Beam Scanning Proton Therapy. *Phys Med Biol* (2017) 62(6):2486–504. doi: 10.1088/1361-6560/62/6/2486
44. Colvill E, Krieger M, Bosshard P, Steinacher P, Rohrer Schnidrig BA, Parkel T, et al. Anthropomorphic Phantom for Deformable Lung and Liver CT and MR Imaging for Radiotherapy. *Phys Med Biol* (2020) 65(7):07NT2. doi: 10.1088/1361-6560/ab7508
45. Shih HA, Jiang SB, Aljarrah KM, Doppke KP, Choi NC. Internal Target Volume Determined With Expansion Margins Beyond Composite Gross Tumor Volume in Three-Dimensional Conformal Radiotherapy for Lung Cancer. *Int J Radiat OncologyBiologyPhysics* (2004) 60(2):613–22. doi: 10.1016/j.ijrobp.2004.05.031
46. Giraud P, Houle A. Respiratory Gating for Radiotherapy: Main Technical Aspects and Clinical Benefits. *ISRN Pulmonol* (2013) 2013:519602. doi: 10.1155/2013/519602

Conflict of Interest: The authors declare that the research was conducted in the absence of any commercial or financial relationships that could be construed as a potential conflict of interest.

Publisher's Note: All claims expressed in this article are solely those of the authors and do not necessarily represent those of their affiliated organizations, or those of the publisher, the editors and the reviewers. Any product that may be evaluated in this article, or claim that may be made by its manufacturer, is not guaranteed or endorsed by the publisher.

frontiers in Oncology

ORIGINAL RESEARCH
published: 28 September 2021
doi: 10.3389/fonc.2021.740661

Dosimetric Impact of Inter-Fraction Anatomical Changes in Carbon Ion Boost Treatment for High-Risk Prostate Cancer (AIRC IG 14300)

Stefania Russo[1†], Rosalinda Ricotti[2*†], Silvia Molinelli[1], Filippo Patti[3,4], Amelia Barcellini[3], Edoardo Mastella[1], Andrea Pella[2], Chiara Paganelli[5], Giulia Marvaso[4,6], Matteo Pepa[4], Stefania Comi[7], Mattia Zaffaroni[4], Barbara Avuzzi[8], Tommaso Giandini[9], Emanuele Pignoli[9], Riccardo Valdagni[6,7], Guido Baroni[2,5], Federica Cattani[7], Mario Ciocca[1], Barbara Alicja Jereczek-Fossa[4,6], Ester Orlandi[3], Roberto Orecchia[10‡] and Barbara Vischioni[3*‡]*

[1] Medical Physics Unit, Clinical Department, National Center for Oncological Hadrontherapy (CNAO), Pavia, Italy, [2] Bioengineering Unit, Clinical Department, National Center for Oncological Hadrontherapy (CNAO), Pavia, Italy, [3] Radiotherapy Unit, Clinical Department, National Center for Oncological Hadrontherapy (CNAO), Pavia, Italy, [4] Division of Radiotherapy, IEO, European Institute of Oncology Istituto di Ricovero e Cura a Carattere Scientifico (IRCCS), Milan, Italy, [5] Department of Electronics, Information and Bioengineering, Politecnico di Milano, Milan, Italy, [6] Department of Oncology and Hemato-oncology, University of Milan, Milan, Italy, [7] Medical Physics Unit, IEO, European Institute of Oncology Istituto di Ricovero e Cura a Carattere Scientifico (IRCCS), Milan, Italy, [8] Department of Radiation Oncology, Fondazione Istituto di Ricovero e Cura a Carattere Scientifico (IRCCS) Istituto Nazionale dei Tumori, Milan, Italy, [9] Medical Physics Unit, Fondazione Istituto di Ricovero e Cura a Carattere Scientifico (IRCCS) Istituto Nazionale dei Tumori, Milan, Italy, [10] Scientific Directorate, IEO, European Institute of Oncology Istituto di Ricovero e Cura a Carattere Scientifico (IRCCS), Milan, Italy

Rectum and bladder volumes play an important role in the dose distribution reproducibility in prostate cancer adenocarcinoma (PCa) radiotherapy, especially for particle therapy, where density variation can strongly affect the dose distribution. We investigated the reliability and reproducibility of our image-guided radiotherapy (IGRT) and treatment planning protocol for carbon ion radiotherapy (CIRT) within the phase II mixed beam study (AIRC IG 14300) for the treatment of high-risk PCa. In order to calculate the daily dose distribution, a set of synthetic computed tomography (sCT) images was generated from the cone beam computed tomography (CBCT) images acquired in each treatment session. Planning target volume (PTV) together with rectum and bladder volume variation was evaluated with sCT dose-volume histogram (DVH) metric deviations from the planning values. The correlations between the bladder and rectum volumes, and the corresponding DVH metrics, were also assessed. No significant difference in the bladder, rectum, and PTV median volumes between the planning computed tomography (pCT) and the sCT was found. In addition, no significant difference was assessed when comparing the average DVHs and median DVH metrics between pCT and sCT. Dose deviations determined by bladder and rectum filling variations demonstrated that dose distributions were reproducible in terms of both target coverage and organs at risk (OARs) sparing.

Keywords: carbon ion radiotherapy (CIRT), high-risk prostate cancer, image-guided radiotherapy (IGRT), inter-fraction anatomical changes, dose-of-the-day calculation, deformable image registration (DIR)

OPEN ACCESS

Edited by:
Thomas Tessonnier, Heidelberg University Hospital, Germany

Reviewed by:
Stefan Koerber, Heidelberg University Hospital, Germany
Hirokazu Makishima, University of Tsukuba, Japan

***Correspondence:**
Stefania Russo
stefania.russo@cnao.it
Rosalinda Ricotti
rosalinda.ricotti@cnao.it
Barbara Vischioni
barbara.vischioni@cnao.it

†*These authors have contributed equally to this work and share first authorship*

‡*These authors have contributed equally to this work and share last authorship*

Specialty section:
This article was submitted to Radiation Oncology, a section of the journal Frontiers in Oncology

Received: *13 July 2021*
Accepted: *06 September 2021*
Published: *28 September 2021*

Citation:
Russo S, Ricotti R, Molinelli S, Patti F, Barcellini A, Mastella E, Pella A, Paganelli C, Marvaso G, Pepa M, Comi S, Zaffaroni M, Avuzzi B, Giandini T, Pignoli E, Valdagni R, Baroni G, Cattani F, Ciocca M, Jereczek-Fossa BA, Orlandi E, Orecchia R and Vischioni B (2021) Dosimetric Impact of Inter-Fraction Anatomical Changes in Carbon Ion Boost Treatment for High-Risk Prostate Cancer (AIRC IG 14300). Front. Oncol. 11:740661. doi: 10.3389/fonc.2021.740661

INTRODUCTION

Essential issues in prostate cancer adenocarcinoma (PCa) irradiation are prostate motion and shape variations due to rectum and/or bladder filling modifications (1), which may strongly affect the target dose distribution and Organs at Risk (OAR) sparing (2). In order to maintain consistent rectum and bladder volume throughout the treatment, preparation instructions about food and fluid intake are usually given to each patient before treatment simulation and delivery. Despite this, inter-fractional unpredictable OAR volume variation might occur, and the reproducibility of dose distribution remains essential to providing an adequate and safe treatment of patients.

In this context, image-guided radiation therapy (IGRT) is essential to ensuring treatment efficacy and safety. In recent years, the introduction of new advanced techniques of IGRT using online cone beam computed tomography (CBCT) allows the tracking of daily positioning and anatomical changes of patients in treatment position. It also has the potential to be used to evaluate the dose-of-the-day distributions in comparison to the dose distribution calculated on the planning computed tomography (pCT) (3).

Since 2016 at the Centro Nazionale di Adroterapia Oncologica (CNAO, Pavia, Italy), we have enrolled patients in the phase II clinical trial with a mixed-beam approach for prostate irradiation, in collaboration with Istituto Europeo di Oncologia IRCCS (IEO) and Fondazione IRCCS Istituto Nazionale dei Tumori (INT) in Milan, Italy. The irradiation scheme consisted of a hypo-fractionated carbon ion radiotherapy (CIRT) anticipated boost to the prostate, followed by photon intensity modulated radiation therapy (IMRT) to the prostate and pelvic lymph nodes (grant AIRC IG 14300) (4).

The rationale of the hypo-fractionated CIRT boost is to escalate the biological dose to the target by exploiting carbon ion favorable physical and biological properties. The higher radiobiological effectiveness (RBE) of carbon ions on cancer radioresistant clones and more hypoxic tumor components (5) should enhance the efficacy of the subsequent photon phase of the scheme, delivered with conventional fractionation. Safety and effectiveness data on CIRT are derived from Japanese experience, where CIRT has been employed for unresected PCa since 1995 at the National Institute of Radiological Sciences (NIRS, Chiba, Japan), with excellent clinical toxicity and efficacy outcomes (6, 7).

Our study aimed to evaluate the impact of bladder and rectum filling variations in the CIRT dose-of-the-day distribution of target and OARs in the context of our phase II mixed beam study for high-risk PCa. Additionally, our IGRT and patient preparation protocol reliability was assessed, evaluating the dose distribution reproducibility during the treatment course using CBCT data.

Dose evaluation on daily CBCTs for particle therapy is challenging due to increased scatter, beam hardening, Hounsfield unit (HU) inaccuracy and often small field-of-view (FOV) sizes (3). In this study, we proposed a method for dose-of-the-day calculation. Synthetic computed tomography (sCT) images were obtained by deforming pCT images into the daily CBCT frame of reference. Subsequently, the pCT Hounsfield units (HUs) were transferred to sCT to obtain the corresponding stopping power maps for CIRT dose calculation.

Abbreviations: PCa, prostate cancer adenocarcinoma; OARs, organs at risk; CNAO, Centro Nazionale di Adroterapia Oncologica; IEO, Istituto Europeo di Oncologia; IRCCS, INT Fondazione IRCCS Istituto Nazionale dei Tumori; CIRT, carbon ion radiotherapy; IMRT, intensity modulated radiation therapy; RBE, radiobiological effectiveness; IGRT, image-guided radiation therapy; CT computed tomography; CBCT, cone beam computed tomography; FOV, field of view; sCT, synthetic computed tomography; pCT, planning computed tomography; CTV, clinical target volume; PTV planning target volume; MR, magnetic resonance; LEM, local effect model; DRR, digitally reconstructed radiograph; RO, radiation oncologist; ROI, region of interest; DVH, dose volume histogram; CV, coefficient of variation.

MATERIAL AND METHODS

Patient Cohort

We retrospectively analyzed treatment and imaging data of 16 consecutive patients, enrolled from 2016 to 2020 in a phase II study for CIRT boost treatment at CNAO, diagnosed with high-risk PCa according to the inclusion criteria previously described in Marvaso et al. (4). Patients' enrollment started after trial approval from all treating centers' Ethical Committees (8). The selected patients underwent carbon-ion boost at CNAO, followed by photon intensity-modulated radiotherapy (IMRT) at IEO or INT, and signed informed consents at the coordinating center prior to treatment. Daily imaging data sets of two patients were incomplete and excluded from the study.

Target Definition and Treatment Planning

The simulation CT acquired at CNAO was registered with the magnetic resonance (MR) image set for clinical target volume (CTV) delineation. The CTV included the prostate and the proximal third of the seminal vesicles. According to the protocol, planning target volume (PTV) was created by adding safety margins to the CTV, 5 mm in all directions. Rectum, bladder, bowel, and femoral heads were contoured as OARs for plan optimization with the following constraints for the boost phase: rectum $D_{0.03cm3} \leq 100\%$, $V_{16Gy(RBE)} \leq 5\%$, $V_{15Gy(RBE)} \leq 20\%$, bladder $D_{0.03cm3} \leq 102\%$, $V_{15Gy(RBE)} \leq 35\%$, femoral head $V_{10Gy(RBE)} \leq 15\%$, and bowel $V_{16.6Gy(RBE)} = 0\%$. Target coverage objectives were PTV $D_{98\%} \geq 95\%$, $D_{0.03cm3} \leq 107\%$, and median dose $\leq 102\%$. Priority was given to OAR dose constraints over PTV coverage for boost plans. More details on the cumulative plan acceptance criteria can be found in Gugliandolo et al. (8).

A total dose of 16.6 Gy (RBE) in four fractions (4.15 Gy (RBE)/fraction, over 1 week) was delivered for the CIRT anticipated boost at CNAO. Afterward, patients received a whole-pelvis IMRT of 50 Gy in 25 fractions at IEO or INT. In this study, only the CIRT treatment phase was considered.

Since no gantry was available, two opposed lateral beams were delivered using a fixed horizontal line and rotating the couch. This beam orientation was chosen to avoid placing the rectum and bladder distally from the beam (9), where range uncertainties can strongly degrade the dose distribution (10).

The planned dose was delivered with pencil beam scanning technique with lateral spot spacing and energy layer spacing of 2 mm.

Treatment plans were optimized with RayStation v8.1 Treatment Planning System (TPS, RaySearch Laboratories Stockholm, Sweden). In order to mitigate range and setup uncertainties, a robust planning strategy was used based on minimax optimization, with setup and range uncertainties of 2 mm in all directions and 3%, respectively (11). The RBE-weighted dose was determined according to the local effect model LEM I (12) with an ideal α/β ratio of 2 Gy.

Patient Positioning

For each treated patient, a pCT was acquired on a SOMATOM Sensation Open CT scanner (Siemens Medical Systems, Germany) using a slice thickness of 2 mm with a pixel spacing of 0.98 × 0.98 mm with machine parameters varying in the interval of 190–300 mAs at 120–140 kV.

During the pCT acquisition and the whole treatment course, all patients were immobilized in supine position with a pelvic personalized solid thermoplastic mask (Renfu Medical Equipment, Guangzhou, China) fixed on an indexed base plate. In addition, customized large cushions (TOTIM® Patient Cushions Immobilization System, Essebi Medical SRL, Faetano, San Marino) were used in combination with knee and foot holders. An MR scan (Siemens Medical Systems, Germany) in the same setup condition was acquired after the pCT.

Patients were asked to empty the rectum with two micro enemas and drink 500 ml of water after bladder voiding, 30 minutes before starting the CT examination and before each treatment fraction, in order to maintain consistency in rectum and bladder filling and have a comfortable position with the rigid mask.

Before treatment delivery, patient setup optimization was image-guided by acquiring double planar orthogonal kV images in the anteroposterior and right–left directions. The acquired images were aligned automatically (after a preliminary manual alignment when necessary) to the corresponding digitally reconstructed radiographs (DRRs). Subsequently, the six degrees of freedom robotic couch (13) compensated for the estimated translations and rotations. After patient setup adjustment (14) and before treatment delivery, a daily CBCT was acquired for soft tissue anatomical change inspection purposes. Each CBCT image was evaluated by a radiation oncologist (RO), and if rectum or bladder filling was considered inadequate for treatment, the patient was asked to repeat the preparation.

CBCT images were acquired with a non-isocentric, custom-designed robotic imaging system (15). About 600 projective images were acquired during 220° gantry rotation around the patient. CBCT acquisition parameters were set to 120 kVp and 31 mAs. According to this clinical workflow, the bony anatomy imaged in the CBCTs is intrinsically co-registered to the pCT. The validity of this assumption was assessed by computing the 3D–3D registration between CBCTs and pCT, which resulted in sub-millimeter/degree of setup residuals.

CBCT volumetric images were reconstructed with a spatial resolution of 1 × 1 × 1 mm and stored in Meta Image file format (text-based tagged file format ".mha"). For this study, the axial field of view (FOV) of the CBCT was reduced to a diameter of 200 mm in order to mitigate the truncation artifacts. In addition, CBCTs were converted in DICOM format with the same frame of reference of the planning CT, for loading into the RayStation TPS.

Synthetic CT of the Day and Dose Recalculation

The sCTs were created by deforming the initial pCT (*target image set*) on each daily CBCT (*reference image set*) by using the ANAtomically CONstrained Deformation Algorithm (ANACONDA) implemented in RayStation TPS (16). We mainly exploited the structure-based approach of the algorithm discarding the image intensity information during algorithm computation and focusing the deformation on the CBCT FOV. At first, femur heads and other pelvic bones, including sacrum and coccyx, contoured as landmarks on the pCT, were cropped according to the CBCT FOV. Subsequently, these contours were rigidly transferred on each CBCT. CTV, PTV, rectum, bladder, and bowel were manually re-contoured on each CBCT for each patient by an in-training RO and verified by an experienced RO. PTV, rectum, bladder, and the FOV-cropped bony structures were used as controlling regions of interest (ROIs) to drive the deformation. The deformation vector field was estimated with a resolution comparable to pCT of 1 × 2 × 1 mm/voxel in right–left, inferior–superior, and posterior–anterior directions, respectively. Each resulting deformation vector field was exported from RayStation and applied to the pCT using Plastimatch (version 1.9.0), yielding a sCT. The resulting sCT mimicked the original pCT outside the CBCT FOV, where the deformation vector field was zero, while inside the FOV the pCT was deformed according to the soft tissue geometry as detected in the CBCT. The planned dose distribution was recalculated on each sCT to have a reasonable estimation of the patient delivered dose on the anatomy of each treatment session. The resulting sCTs were evaluated in terms of quality of the deformation, analyzing the correspondence of bladder, rectum, prostate, and bones position between sCTs and CBCTs and confirming the absence of the deformation field outside the CBCT FOV. A schematic representation of the method described here to generate a sCT for dose-of-the-day recalculation is depicted in **Figure 1**.

Data Analysis

Inter-fractional changes in patient anatomy were estimated computing bladder, rectum, and PTV volume variations between planning and treatment fractions. The coefficient of variation (CV) of the structure volumes was investigated for the whole patient cohort and each patient separately.

Average DVHs were obtained for the PTV, rectum, and bladder for pCT and sCT dose distributions, and the standard deviation of the population was computed at each dose level.

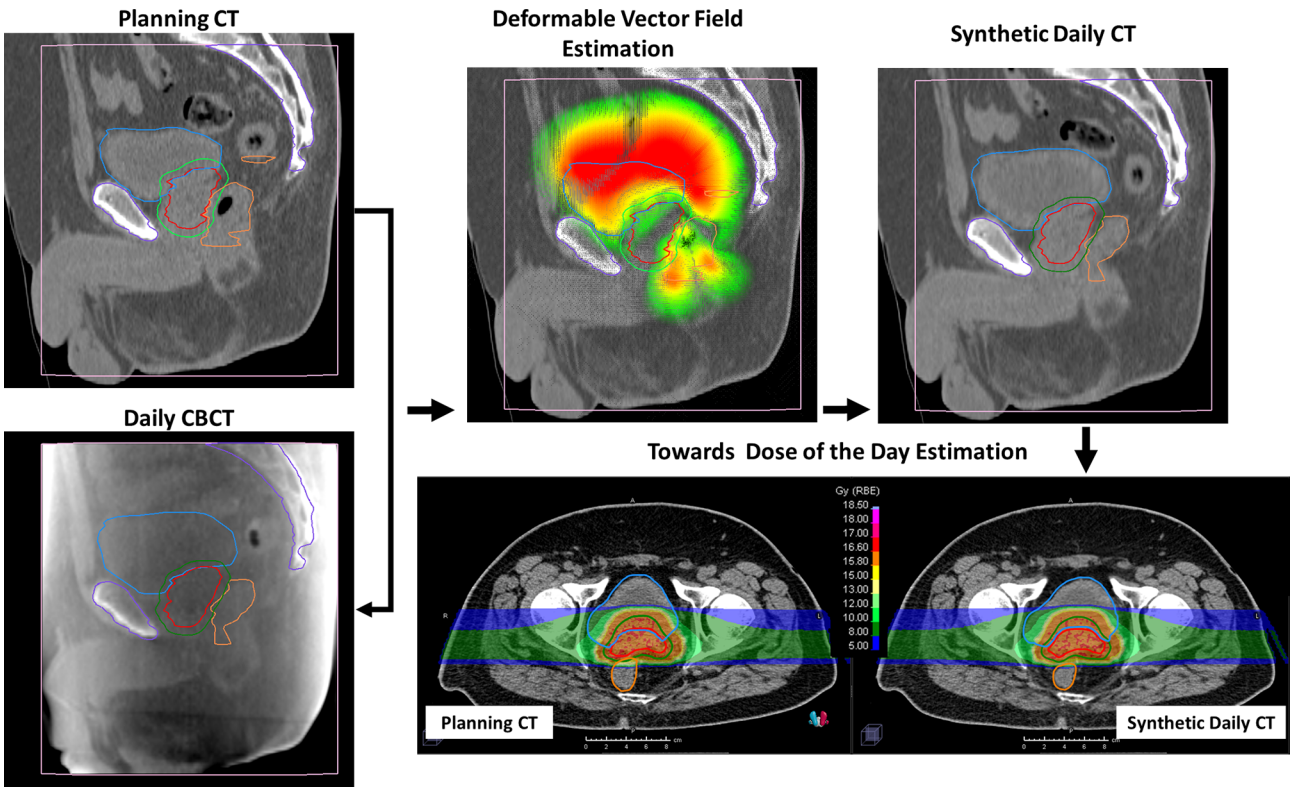

FIGURE 1 | Representative example of the study workflow. Bladder (blue), rectum (orange), clinical target volume (CTV) (red), and planning target volume (PTV) (green) were contoured both on planning computed tomography (pCT) and on cone beam computed tomography (CBCT). Bony anatomy (violet) was delineated in pCT and rigidly propagated on CBCTs. The deformation vector field was estimated considering the delineated structures as "controlling ROIs," focusing on the CBCT field of view. The planned dose distribution was then recalculated on the resulting synthetic CT (sCT).

Treatment plan dose constraints for the bladder and rectum, together with PTV coverage objectives, were verified on each recalculation plan. The following DVH-based metrics were extracted for the pCT and each sCT: $V_{5Gy(RBE)}$, $V_{10Gy(RBE)}$, $V_{15Gy(RBE)}$, and $V_{16Gy(RBE)}$ for rectum and bladder, and $D_{95\%}$, $D_{98\%}$ $D_{50\%}$, $D_{2\%}$, and $D_{0.03cm3}$ for PTV. sCT metric deviations from the planning values were evaluated with the Wilcoxon signed-rank test.

Finally, correlations between the bladder and rectum volumes, and the corresponding DVH metrics, were evaluated with the Spearman correlation test.

RESULTS

A total of 56 CBCTs were evaluated: 4 daily CBCTs for each of the 14 enrolled patients.

Volumes of bladder and rectum varied across patients and fractions. **Figure 2A** shows the bladder, rectum, and PTV simulation contours on the planning CT, with the contours derived from the daily CBCTs superimposed, for P7, as an example. For bladder, a higher-volume variability across patients and treatment fractions was found (ranging from 44 to 455.5 cm^3, CV: 54.2%), as compared to rectum (ranging from 22.9 to 65.3 cm^3, CV: 25.4%) and PTV (ranging from 60.2 to 146.5 cm^3, CV: 21.0%). **Figure 2B** shows the distribution of organ volumes at pCT and during the treatment course, considering the whole patient cohort. According to the Wilcoxon test, there was no significant difference in the bladder, rectum, and PTV median volumes between the pCT and the CBCTs acquired during the treatment course (**Table 1**).

Considering each patient separately, the volumes of bladder and rectum on the CBCTs were different compared to the volume on the pCT. Volume variations during the CIRT course were mostly patient-dependent: CV of bladder volume ranged from 8% for P13 to 70% for P6. Similarly, CV for rectum varied between 2% for patient P11 to 35% for P6 (**Figure 3**).

In addition, no significant difference was found when comparing planned and treatment average DVHs as in **Figure 4**, and median DVH metrics between pCT and CBCTs for rectum, bladder, and PTV (**Table 1**).

Distributions of DVH parameters for bladder, rectum, and PTV are presented separately for each patient in **Figures 5**–**7**, respectively. pCT treatment plans always satisfied all OAR constraints. Bladder $V_{15Gy(RBE)} \leq 35\%$ was always met except for P11 for three out of four fractions. Rectum $V_{16Gy(RBE)} \leq 5\%$

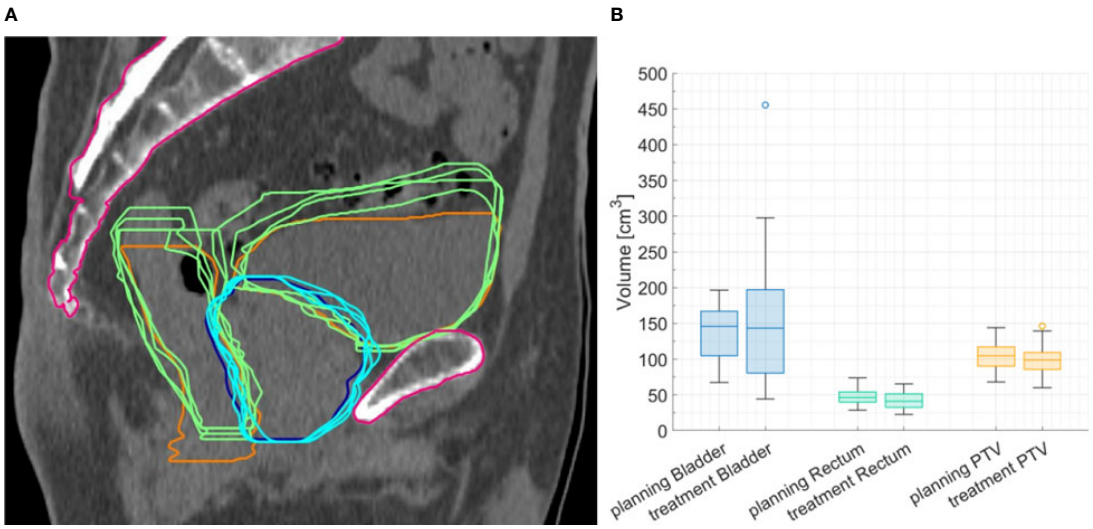

FIGURE 2 | **(A)** Representative planning image with planning computed tomography (CT) contours of planning target volume (PTV) (blue line) and rectum and bladder (orange lines), with contours delineated on cone beam CTs (CBCTs) superimposed (light-blue and green lines). **(B)** Boxplots for bladder, rectum, and PTV volume at planning CT and CBCT for the whole cohort.

TABLE 1 | Comparison of volumes and dose–volume histogram (DVH) indices of bladder, rectum, and planning target volume (PTV) at planning CT (pCT) and at synthetic CTs (sCTs) for all the patients.

		Bladder			Rectum		
		Planning median (IQR)	Treatment median (IQR)	Wilcoxon test p-value	Planning median (IQR)	Treatment median (IQR)	Wilcoxon test p-value
Volume	**$cm^{(3)}$ apex**	146.3 (62.3)	143.5 (116.6)	0.924	46.5 (14.6)	40.8 (18.8)	0.125
DVH metrics	**V16 Gy(RBE) [%]**	14.1 (6.5)	12.6 (10.0)	0.659	4 (1.1)	2.8 (2.8)	0.165
	V15 Gy(RBE) [%]	17.5 (9.0	16.1 (11.8)	0.654	11.9 (7.4)	9.8 (9.1)	0.336
	V10 Gy(RBE) [%]	26.8 (10.9)	27.1 (16.0	0.724	28.7 (11.5)	26.5 (14.2)	0.463
	V5 Gy(RBE) [%]	35.2 (13.8)	33.9 (20.8)	0.774	36.2 (11.4)	35.2 (19.1)	0.592
			PTV				
		Planning median (IQR)	**Treatment median (IQR)**	**Wilcoxon test p-value**			
Volume	**$cm^{(3)}$ apex**	104.8 (26.7)	98.5 (23.9)	0.45			
DVH metrics	**D98% [%]**	96.5 (1.9)	95.6 (3.0)	0.148			
	D95% [%]	98.6 (0.9)	98.2 (2.4)	0.354			
	D50% [%]	99.8 (0.3)	99.8 (0.3)	0.595			
	D2% [%]	100.6 (0.3)	100.6 (0.3)	0.699			

and $V_{15Gy(RBE)} \leq 20\%$ dose constraints were met in 47 (84%) and 50 (80%) recalculation plans, respectively. In only one case (P3), rectum dose constraints were not met in all the recalculation plans. When considering high doses, no hot spots were found either in the rectum or in the bladder, with $D_{0.03cm3}$ below 100% and 102% of the prescribed dose, respectively.

Median PTV $D_{98\%}$ and $D_{95\%}$ for treatment planning were not significantly higher compared to the sCT-recalculated plans (**Table 1**). The PTV coverage objective ($D_{98\%} \geq 95\%$) was achieved in 12 of the 14 pCT optimized plans (85.7%), while this dose criterion was met in 34 of 56 (60.7%) cases in the recalculation plans (**Figure 7**). Concerning the hot spots, $D_{0.03cm3}$ was lower than 107% of the prescription dose in all the cases.

In order to assess how bladder and rectum filling might affect OAR dose distribution, we considered these OARs' overlap volumes with the 16-Gy (RBE) and 15-Gy (RBE) isodoses for each patient treatment plan. No correlation was found between the variation in rectum and bladder volume as compared to the pCT and the variation in the OAR overlap volume. In particular, rectum correlation coefficients were 0.19 (*p-value: 0.156*) and 0.34 (*p-value: 0.011*), respectively, whereas for bladder, correlation coefficients were 0.10 (*p-value: 0.444*) and 0.11 (*p-value: 0.425*).

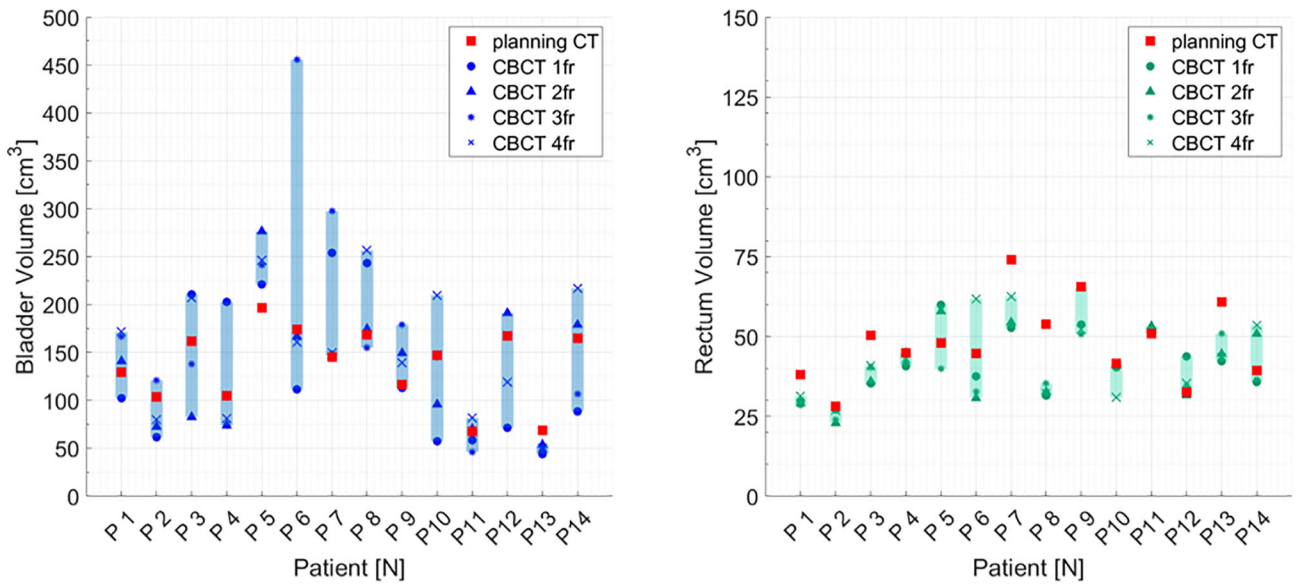

FIGURE 3 | Bladder and rectum volume at planning CT (red squares) and at each cone beam CT (dark symbols) for all the patients separately. Graphical shades indicate the extent of volume variability.

On the contrary, the correlation between the absolute volumes of rectum and bladder with the respective absolute volumes receiving 16 Gy (RBE), 15 Gy (RBE), 10 Gy (RBE), and 5 Gy (RBE) increased as the considered dose decreases. For rectum, in particular, the correlation coefficient increased from 0.40 to 0.55 (*p-value <<0.001*), while for bladder the coefficient increased from 0.34 (*p-value: 0.0038*) to 0.61 (*p-value<<0.001*). The greater the OAR absolute volume, the greater the absolute volume receiving low doses.

A statistically significant correlation was found between the bladder absolute volume variation at pCT and CBCTs and the DVH metric variation at pCT and CBCTs expressed as a percentage of the corresponding volumes when considering the entire patient cohort. If bladder volume decreased during treatment, the percentage of bladder volume receiving 16 Gy (RBE), 15 Gy (RBE), 10 Gy (RBE), and 5 Gy (RBE) increased (correlation coefficient >0.5, *p-value <<0.001*).

DISCUSSION

The impact of inter-fractional variation in urinary bladder volume and rectum filling on daily dose distribution during CIRT for high-risk pCA was investigated in 14 patients enrolled in the AIRC IG 14300 grant frame (4).

For dose calculation on daily CBCT, we generate a sCT to overcome various CBCT limitations that forbid CIRT dose calculation. So far, sCT has been reported for proton dose calculations (17). This approach, based on Deformable Image Registration (DIR), has the advantage of not introducing HU inaccuracies in sCT images since the deformation does not modify the original pCT numbers. The distribution of HU between pCT and sCT was consistent for each contoured structure (bladder, rectum, PTV). Nonetheless, we are aware that this method has several issues that have to be addressed. Firstly, the air pockets eventually found in the CBCT images were propagated in the sCT, or conversely, when air pockets were found in the pCT they were not propagated in the sCT (18). However, considering the beam irradiation geometry, such areas were not included in the beam path. Secondly, the limited CBCT FOV resulted in incomplete patient external contour. Assuming that simulation CT was a reasonable estimation of the patient anatomy not included in the CBCT, pCT data were used to compensate for this missing information (19). Moreover, DIR could deform bones when large deformation occurs close to bony structures (20). To overcome any unrealistic bone deformations, we included bone ROI as a shape constraint during DIR computation.

One of the main goals of this study was to evaluate the validity of our IGRT approach consisting in bone-matching followed by CBCT acquisition. At present, the primary IGRT approach for moving targets, including pCA treatment positioning verification in particle therapy, consists in DRR bone-matching or target (prostate)-matching using implanted fiducials. Using orthogonal X-ray images for patient positioning verification is the standard procedure for CIRT in most centers (21). In our investigation, we found only very slight displacements of the PTV center of mass as determined by the contours on the sCT obtained from CBCT, with median (IQR) of 0.1(0.3)mm, -0.3(1.3)mm, and -0.3(0.5) mm toward the right, anterior, and inferior directions, respectively. These values were smaller than the prostate displacement found with IGRT techniques for photon IMRT prostate treatment (22). One possible explanation could be patient mask immobilization for CIRT, which might strongly reduce bowel and pelvic anatomy changes and thus prostate

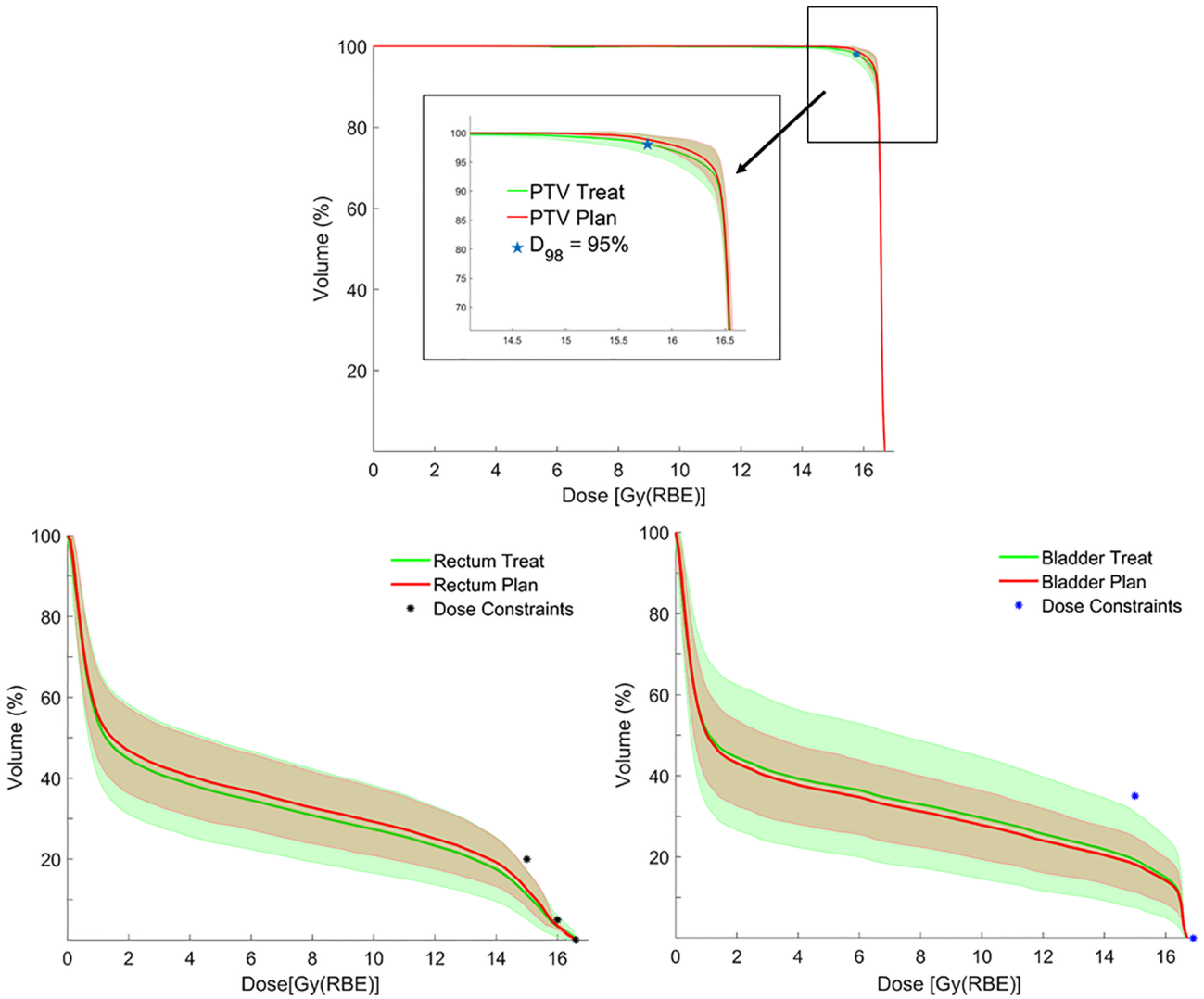

FIGURE 4 | Average dose–volume histograms (DVHs) for planning target volume (PTV), rectum and bladder calculated on planning CTs (pCTs) (red lines), and synthetic CTs (sCTs) (green lines), with corresponding error bands (± 1 standard deviation) together with bladder/rectum dose constraints and PTV coverage objective.

displacement (2). Looking at our results in terms of target displacement, our PTV margins (5 mm in all directions) appear suitable for the considered patient population.

Maeda et al. (23) reported that prostate-matching was more reliable than the bone-matching approach regarding rectum dose constraint adherence and target coverage in prostate proton therapy delivered with geometry of two opposed beams. At CNAO, thin golden filaments called Gold Anchor™ were investigated to assess the improvement in prostate position verification (24). Their visibility on both CT and radiographic images and the possible perturbation of the carbon ion beams were investigated through tests in an anthropomorphic phantom and turned out to be acceptable. In the future, we aim to implant the Gold Anchor™ seeds in some patients to perform further validation of our IGRT protocol, comparing prostate-matching versus bone-matching approach for patient positioning before CBCT acquisition.

Another essential purpose of the presented study was the validation of our patient preparation protocol. Bladder filling or rectal gas movement may influence the prostate position and therefore affect the target coverage. In parallel, the rectum and bladder could eventually receive unwanted hot spots if such OARs move in the high-dose treatment area resulting from the two-lateral opposed beam irradiation geometry.

At present, optimal rectum and bladder filling conditions for prostate external beam photon RT are still debated. In our study, patient preparation aimed at achieving a comfortable bladder filling compatible with pelvic mask compression and treatment duration while preventing major rectum and bladder volume variation compared to simulation conditions. Despite that precise fluid intake instructions were given to the patients, bladder volume varied considerably during the CIRT course in the analyzed patient cohort—as for P7, a patient with important

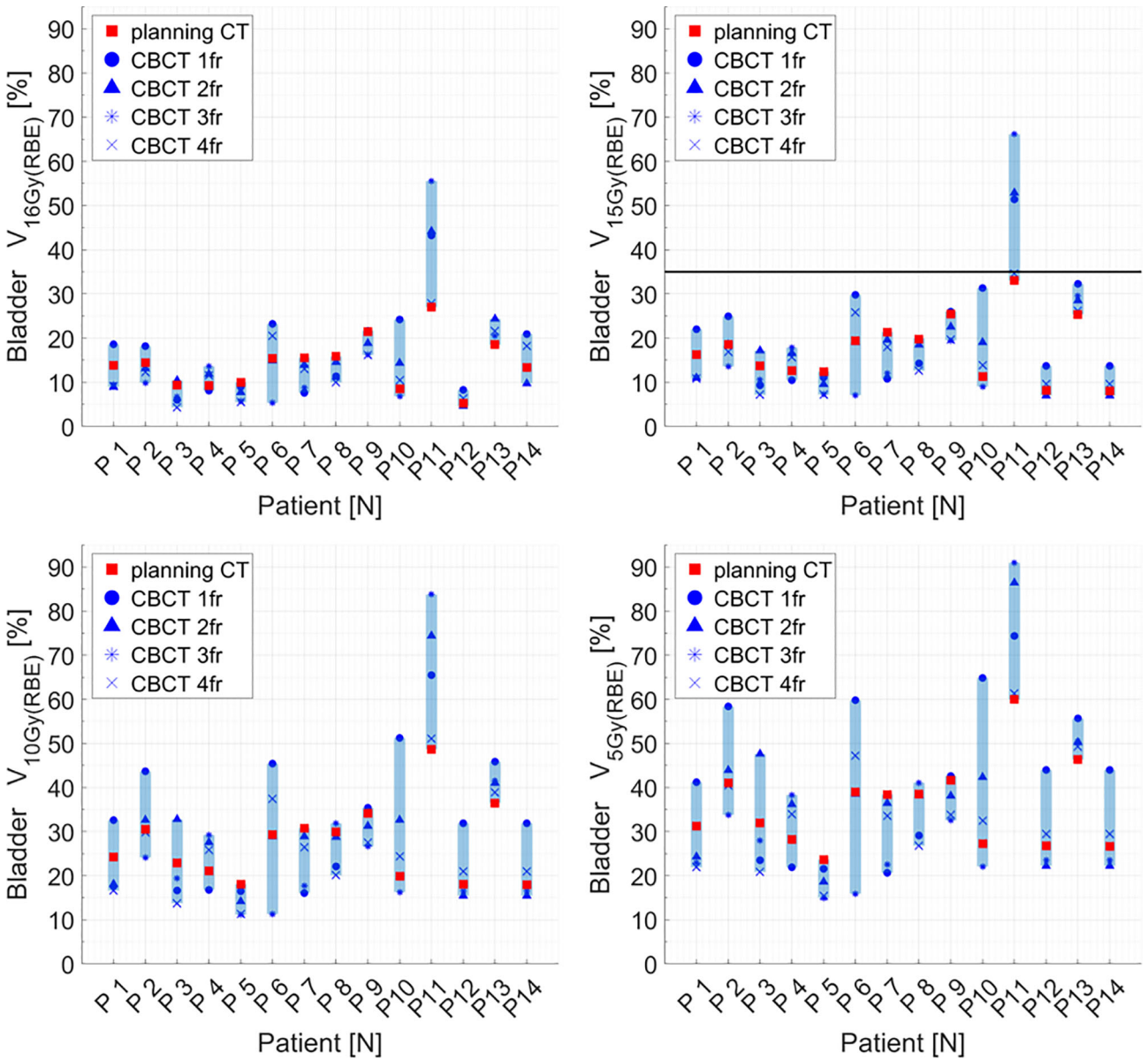

FIGURE 5 | Distribution of bladder dose–volume histogram (DVH) metrics ($V_{16Gy(RBE)}$, $V_{15Gy(RBE)}$, $V_{10Gy(RBE)}$, $V_{5Gy(RBE)}$) for each patient at planning CT (red squares) and at each synthetic CT (sCT) (dark markers). Colored range bars indicate the maximum variation extent within a single patient. The bladder constraint $V_{15Gy(RBE)}$ ≤35% is indicated as a black line. CBCT, cone beam computed tomography; fr, fraction.

obstructive urine retention. To a lesser extent, also the volume of the rectum varied among the fractions during the CIRT course. However, no statistically significant increase of the dose to OARs at treatment was observed.

Similarly, no major dose degradation in terms of PTV dose was observed. Even if the PTV D98% ≥ 95% goal failed in 40.7% of the recalculated plans, only slight deviations were found in D95% for the pCT optimized plans, with a mean relative difference of 0.1%, considering all the treatment fractions in the series of patients.

At CNAO, patients with high-risk localized prostate cancer are currently being treated either with a photon-CIRT mixed beam approach or with a full course of CIRT of 66.4 Gy (RBE) delivered in 16 fractions (4 days/week) to the prostate and seminal vesicles (25), according to Japanese experience (26, 27). Our findings showed that the setup and IGRT protocols described here appeared to be suitable also for patients treated with a full course of CIRT.

In our investigation, we focused exclusively on the residual inter-fraction anatomical variations after bony alignment and did not consider intra-fraction motion. However, several recent studies on cine-MR imaging extensively reported that prostate intra-fraction motion could affect the target dose distribution (28, 29).

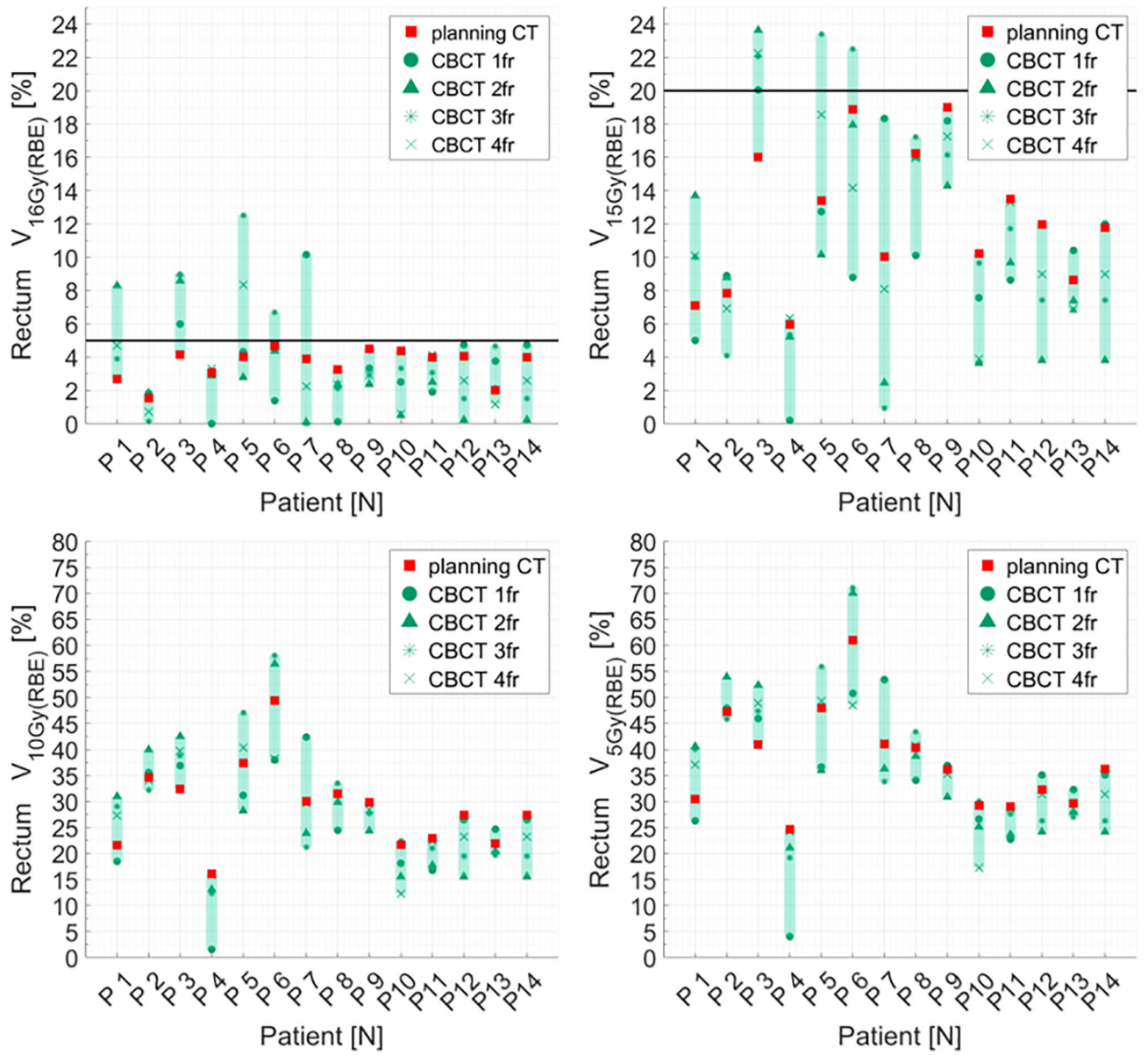

FIGURE 6 | Distribution of rectum dose–volume histogram (DVH) metrics ($V_{16Gy(RBE)}$, $V_{15Gy(RBE)}$, $V_{10Gy(RBE)}$, $V_{5GY(RBE)}$) for each patient at planning CT (red squares) and at each synthetic CT (sCTs) (dark markers). Colored range bars indicate the maximum variation extent within a single patient. The rectum constraints $V_{16Gy(RBE)}$ ≤5% $V_{15Gy(RBE)}$ ≤20% are indicated as a black line. CBCT, cone beam computed tomography; fr, fraction.

These studies concluded that 5-mm PTV margins were adequate to guarantee target coverage even during long-lasting treatments (>10 min). Since the presented CIRT prostate treatment time was approximately 2 min per beam and a rigid thermoplastic mask was used for patient immobilization, we do not expect the intra-fraction prostate motion to impact the dose distribution significantly.

We are aware that one of the limitations of the current analysis is the small patient cohort. However, the enrolment of patients in the phase II protocol described here is ongoing, and we aim to validate the current data in a larger patient series as soon as more patients are treated.

CONCLUSION

The dosimetric impact of anatomical changes on CIRT was assessed in the context of our phase II mixed beam study for high-risk pCa patients. Dose deviations as determined by bladder and rectum filling variations demonstrated that the preparation

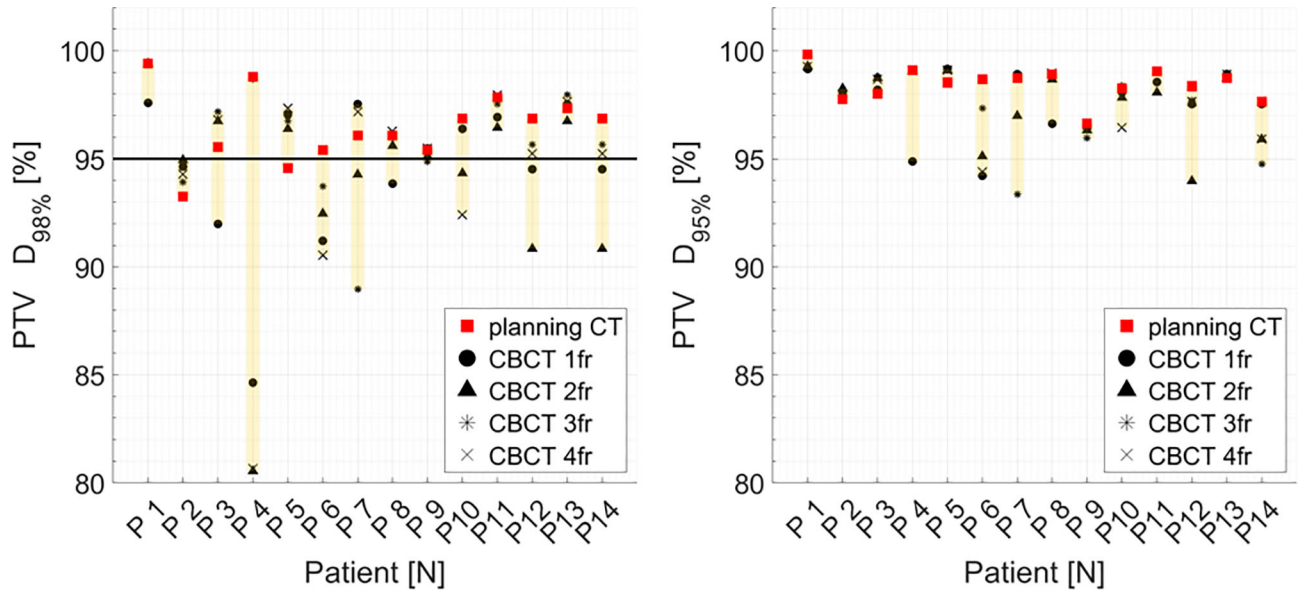

FIGURE 7 | Distribution of PTV DVH metrics ($D_{98\%}$, $D_{95\%}$) for each patient at planning CT (red squares) and at each synthetic CT (sCTs) (dark markers). Colored range bars indicate the maximum variation extent within a single patient. Target coverage objective PTV $D_{98\%}$ ≥95% is indicated as a black line. CBCT, cone beam computed tomography; fr, fraction.

protocol and the IGRT approach described here could generate reproducible dose distributions in terms of target coverage and OARs sparing.

The generation of sCTs from daily CBCTs for dose-of-the-day calculation in CIRT for high-risk pCA is clinically feasible. The proposed method is suitable for an adaptive treatment strategy providing a daily treatment plan based on the actual anatomy.

DATA AVAILABILITY STATEMENT

The raw data supporting the conclusions of this article will be made available by the authors, without undue reservation.

ETHICS STATEMENT

The studies involving human participants were reviewed and approved by Comitato Etico Pavia, Fondazione IRCCS Policlinico San Matteo, Pavia, Italy, notification no. 20140025096. The patients/participants provided their written informed consent to participate in this study.

AUTHOR CONTRIBUTIONS

Conceptualization, SR, RR, and BV. Methodology, SR, RR BV, SM, and AP. Software, SR and RR. Validation, SR, RR, BV, SM, AP, FP, and MC. Formal analysis, SR, RR, SM, BV, AP, GB, and MC. Data curation, SR, RR, BV, SM, and AP. Investigation, SR, RR, SM, FP, AB, EM, AP, CP, GM, MP, MZ, SC, BA, TG, EP, RV, GB, FC, MC, BAJF, EO, and RO. Writing—original draft preparation, SR, RR, and BV. Writing—review and editing, SR, RR, SM, FP, AB, EM, AP, CP, GM, MP, MZ, SC, BA, TG, EP, RV, GB, FC, MC, BJ, EO, and RO. All authors contributed to the article and approved the submitted version.

FUNDING

This study was partially supported by a research grant from Associazione Italiana per la Ricerca sul Cancro (AIRC IG 14300): "Carbon ion boost followed by pelvic photon radiotherapy for high risk prostate cancer", registered at ClinicalTrials.gov (NCT02672449).

REFERENCES

1. Ten Haken RK, Forman JD, Heimburger DK, Gerhardsson A, McShan DL, Perez-Tamayo C, et al. Treatment Planning Issues Related to Prostate Movement in Response to Differential Filling of the Rectum and Bladder. *Int J Radiat Oncol Biol Phys* (1991) 20(6):1317–24. doi: 10.1016/0360-3016(91)90244-x
2. Yokoyama A, Kubota Y, Kawamura H, Miyasaka Y, Kubo N, Sato H, et al. Impact of Inter-Fractional Anatomical Changes on Dose Distributions in Passive Carbon-Ion Radiotherapy for Prostate Cancer: Comparison of Vertical and Horizontal Fields. *Front Oncol* (2020) 10:1264. doi: 10.3389/fonc.2020.01264
3. Giacometti V, Hounsell AR, McGarry CK. A Review of Dose Calculation Approaches With Cone Beam CT in Photon and Proton Therapy. *Phys Med* (2020) 76:243–76. doi: 10.1016/j.ejmp.2020.06.017
4. Marvaso G, Jereczek-Fossa BA, Vischioni B, Ciardo D, Giandini T, Hasegawa A, et al. Phase II Multi-Institutional Clinical Trial on a New Mixed Beam RT Scheme of IMRT on Pelvis Combined With a Carbon Ion Boost for

High-Risk Prostate Cancer Patients. *Tumori* (2017) 103(3):314–8. doi: 10.5301/tj.5000587
5. Nomiya T, Tsuji H, Kawamura H, Ohno T, Toyama S, Shioyama Y, et al. A Multi-Institutional Analysis of Prospective Studies of Carbon Ion Radiotherapy for Prostate Cancer: A Report From the Japan Carbon Ion Radiation Oncology Study Group (J-Cros). *Radiother Oncol* (2016) 121:288–93. doi: 10.1016/j.radonc.2016.10.009
6. Akakura K, Tsujii H, Morita S, Tsuji H, Yagishita T, Isaka S, et al. Phase I/II Clinical Trials Of Carbon Ion Therapy for Prostate Cancer. *Prostate* (2004) 58 (3):252–8. doi: 10.1002/pros.10328
7. Ishikawa H, Tsuji H, Kamada T, Yanagi T, Mizoe JE, Kanai T, et al. Working Group for Genitourinary Tumors. Carbon Ion Radiation Therapy for Prostate Cancer: Results of a Prospective Phase II Study. *Radiother Oncol* (2006) 81 (1):57–64. doi: 10.1016/j.radonc.2006.08.015
8. Gugliandolo SG, Marvaso G, Comi S, Pepa M, Romanò C, Zerini D, et al. Mixed-Beam Approach for High-Risk Prostate Cancer: Carbon-Ion Boost Followed by Photon Intensity-Modulated Radiotherapy. Dosimetric and Geometric Evaluations (AIRC IG-14300). *Phys Med* (2020) 76:327–36. doi: 10.1016/j.ejmp.2020.07.012
9. Schwarz M, Molinelli S. What can Particle Therapy Add to the Treatment of Prostate Cancer? *Phys Med* (2016) 32(3):485–91. doi: 10.1016/j.ejmp.2016.03.017
10. Sakai M, Kubota Y, Saitoh JI, Irie D, Shirai K, Okada R, et al. Robustness of Patient Positioning for Interfractional Error in Carbon Ion Radiotherapy for Stage I Lung Cancer: Bone Matching *Versus* Tumor Matching. *Radiother Oncol* (2018) 129(1):95–100. doi: 10.1016/j.radonc.2017.10.003
11. Fredriksson A, Forsgren A, Hårdemark B. Minimax Optimization for Handling Range and Setup Uncertainties in Proton Therapy. *Med Phys* (2011) 38(3):1672–84. doi: 10.1118/1.3556559
12. Krämer M, Scholz M. Treatment Planning for Heavy-Ion Radiotherapy: Calculation and Optimization of Biologically Effective Dose. *Phys Med Biol* (2000) 45(11):3319–30. doi: 10.1088/0031-9155/45/11/314
13. Pella A, Riboldi M, Tagaste B, Bianculli D, Desplanques M, Fontana G, et al. Commissioning and Quality Assurance of an Integrated System for Patient Positioning and Setup Verification in Particle Therapy. *Technol Cancer Res Treat* (2014) 13(4):303–14. doi: 10.7785/tcrt.2012.500386
14. Ricotti R, Pella A, Tagaste B, Elisei G, Fontana G, Bonora M, et al. Long-Time Clinical Experience in Patient Setup for Several Particle Therapy Clinical Indications: Management of Patient Positioning and Evaluation of Setup Reproducibility and Stability. *Br J Radiol* (2020) 93(1107):20190595. doi: 10.1259/bjr.20190595
15. Fattori G, Riboldi M, Pella A, Peroni M, Cerveri P, Desplanques M, et al. Image Guided Particle Therapy in CNAO Room 2: Implementation and Clinical Validation. *Phys Med* (2015) 31(1):9–15. doi: 10.1016/j.ejmp.2014.10.075
16. Kadoya N, Nakajima Y, Saito M, Miyabe Y, Kurooka M, Kito S, et al. Multi-Institutional Validation Study of Commercially Available Deformable Image Registration Software for Thoracic Images. *Int J Radiat Oncol Biol Phys* (2016) 96(2):422–31. doi: 10.1016/j.ijrobp.2016.05.012
17. Landry G, Nijhuis R, Dedes G, Handrack J, Thieke C, Janssens G, et al. Investigating CT to CBCT Image Registration for Head and Neck Proton Therapy as a Tool for Daily Dose Recalculation. *Med Phys* (2015) 42(3):1354–66. doi: 10.1118/1.4908223
18. Ziegler M, Nakamura M, Hirashima H, Ashida R, Yoshimura M, Bert C, et al. Accumulation of the Delivered Treatment Dose in Volumetric Modulated Arc Therapy With Breath-Hold for Pancreatic Cancer Patients Based on Daily Cone Beam Computed Tomography Images With Limited Field-of-View. *Med Phys* (2019) 46(7):2969–77. doi: 10.1002/mp.13566
19. de Smet M, Schuring D, Nijsten S, Verhaegen F. Accuracy of Dose Calculations on kV Cone Beam CT Images of Lung Cancer Patients. *Med Phys* (2016) 43(11):5934. doi: 10.1118/1.4964455
20. Motegi K, Tachibana H, Motegi A, Hotta K, Baba H, Akimoto T. Usefulness of Hybrid Deformable Image Registration Algorithms in Prostate Radiation Therapy. *J Appl Clin Med Phys* (2019) 20(1):229–36. doi: 10.1002/acm2.12515
21. Li Y, Kubota Y, Tashiro M, Ohno T. Value of Three-Dimensional Imaging Systems for Image-Guided Carbon Ion Radiotherapy. *Cancers (Basel)* (2019) 11(3):297. doi: 10.3390/cancers11030297
22. Li M, Ballhausen H, Hegemann NS, Ganswindt U, Manapov F, Tritschler S, et al. A Comparative Assessment of Prostate Positioning Guided by Three-Dimensional Ultrasound and Cone Beam CT. *Radiat Oncol* (2015) 10:82. doi: 10.1186/s13014-015-0380-1
23. Maeda Y, Sato Y, Minami H, Yasukawa Y, Yamamoto K, Tamamura H, et al. Positioning Accuracy and Daily Dose Assessment for Prostate Cancer Treatment Using in-Room CT Image Guidance at a Proton Therapy Facility. *Med Phys* (2018) 45(5):1832–43. doi: 10.1002/mp.12858
24. Panizza D, Ciocca M, Mirandola A, Molinelli S, Mairani A, Gallio E, et al. P087: Are Fiducial Markers for IGRT Suitable for Use in Particle Beam Radiotherapy? In: *Proceedings to the 53rd Annual Meeting for the Particle Therapy Cooperative Group (PTCOG) 8-14 June 2014: Hosted by the Shanghai Proton and Heavy Ion Center and the Fudan University Shanghai Cancer Center. Int J Part Ther* (2014) 1(2):408–670. doi: 10.14338/IJPT.14-PTCOG.1
25. Choi K, Molinelli S, Russo S, Mirandola A, Fiore MR, Vischioni B, et al. Rectum Dose Constraints for Carbon Ion Therapy: Relative Biological Effectiveness Model Dependence in Relation to Clinical Outcomes. *Cancers (Basel)* (2019) 12(1):46. doi: 10.3390/cancers12010046
26. Okada T, Tsuji H, Kamada T, Akakura K, Suzuki H, Shimazaki J, et al. Carbon Ion Radiotherapy in Advanced Hypofractionated Regimens for Prostate Cancer: From 20 to 16 Fractions. *Int J Radiat Oncol Biol Phys* (2012) 84 (4):968–72. doi: 10.1016/j.ijrobp.2012.01.072
27. Nomiya T, Tsuji H, Maruyama K, Toyama S, Suzuki H, Akakura K, et al. Phase I/II Trial of Definitive Carbon Ion Radiotherapy for Prostate Cancer: Evaluation of Shortening of Treatment Period to 3 Weeks. *Br J Cancer* (2014) 110(10):2389–95. doi: 10.1038/bjc.2014.191
28. de Muinck Keizer DM, Kerkmeijer LGW, Willigenburg T, van Lier ALHMW, Hartogh MDD, van der Voort van Zyp JRN, et al. Prostate Intrafraction Motion During the Preparation and Delivery of MR-Guided Radiotherapy Sessions on a 1.5T MR-Linac. *Radiother Oncol* (2020) 151:88–94. doi: 10.1016/j.radonc.2020.06.044
29. De Muinck Keizer DM, Willigenburg T, der Voort van Zyp JRN, Raaymakers BW, Lagendijk JJW, Boer JCJ. Seminal Vesicle Intrafraction Motion During the Delivery of Radiotherapy Sessions on a 1.5 T MR-Linac. *Radiother Oncol* (2021) 162:162–9. doi: 10.1016/j.radonc.2021.07.014

Conflict of Interest: The authors declare that the research was conducted in the absence of any commercial or financial relationships that could be construed as a potential conflict of interest.

Publisher's Note: All claims expressed in this article are solely those of the authors and do not necessarily represent those of their affiliated organizations, or those of the publisher, the editors and the reviewers. Any product that may be evaluated in this article, or claim that may be made by its manufacturer, is not guaranteed or endorsed by the publisher.

frontiers in Oncology

ORIGINAL RESEARCH
published: 29 November 2021
doi: 10.3389/fonc.2021.780221

Investigation of Suitable Detection Angles for Carbon-Ion Radiotherapy Monitoring in Depth by Means of Secondary-Ion Tracking

Laura Ghesquière-Diérickx[1,2,3†], Annika Schlechter[1,2,4†], Renato Félix-Bautista[1,2,4], Tim Gehrke[1,2], Gernot Echner[1,2], Laurent Kelleter[1,2‡] and Mária Martišíková[1,2‡]*

[1] Department of Medical Physics in Radiation Oncology, German Cancer Research Center (DKFZ), Heidelberg, Germany, [2] National Center for Radiation Research in Oncology (NCRO), Heidelberg Institute for Radiation Oncology (HIRO), Heidelberg, Germany, [3] Heidelberg Medical Faculty, University of Heidelberg, Heidelberg, Germany, [4] Faculty of Physics and Astronomy, Heidelberg University, Heidelberg, Germany

OPEN ACCESS

Edited by:
Giuseppe Magro,
National Center of Oncological Hadrontherapy, Italy

Reviewed by:
Silvia Muraro,
National Institute of Nuclear Physics of Milan, Italy
Giuseppe Battistoni,
Ministry of Education, Universities and Research, Italy

***Correspondence:**
Mária Martišíková
m.martisikova@dkfz-heidelberg.de

†These authors share first authorship

‡These authors share last authorship

Specialty section:
This article was submitted to Radiation Oncology, a section of the journal Frontiers in Oncology

Received: 20 September 2021
Accepted: 10 November 2021
Published: 29 November 2021

Citation:
Ghesquière-Diérickx L, Schlechter A, Félix-Bautista R, Gehrke T, Echner G, Kelleter L and Martišíková M (2021) Investigation of Suitable Detection Angles for Carbon-Ion Radiotherapy Monitoring in Depth by Means of Secondary-Ion Tracking. Front. Oncol. 11:780221. doi: 10.3389/fonc.2021.780221

The dose conformity of carbon-ion beam radiotherapy, which allows the reduction of the dose deposition in healthy tissue and the escalation of the dose to the tumor, is associated with a high sensitivity to anatomical changes during and between treatment irradiations. Thus, the monitoring of inter-fractional anatomical changes is crucial to ensure the dose conformity, to potentially reduce the size of the safety margins around the tumor and ultimately to reduce the irradiation of healthy tissue. To do so, monitoring methods of carbon-ion radiotherapy in depth using secondary-ion tracking are being investigated. In this work, the detection and localization of a small air cavity of 2 mm thickness were investigated at different detection angles of the mini-tracker relative to the beam axis. The experiments were conducted with a PMMA head phantom at the Heidelberg Ion-Beam Therapy Center (HIT) in Germany. In a clinic-like irradiation of a single field of 3 Gy (RBE), secondary-ion emission profiles were measured by a 2 cm^2 mini-tracker composed of two silicon pixel detectors. Two positions of the cavity in the head phantom were studied: in front and in the middle of the tumor volume. The significance of the cavity detection was found to be increased at smaller detection angles, while the accuracy of the cavity localization was improved at larger detection angles. Detection angles of 20° – 30° were found to be a good compromise for accessing both, the detectability and the position of the air cavity along the depth in the head of a patient.

Keywords: carbon-ion radiotherapy, *in-vivo* treatment monitoring, inter-fractional anatomical changes, secondary-ion tracking, beam fragmentation, silicon pixel detector, Timepix3

1 INTRODUCTION

There are several advantages of carbon ion radiotherapy (CIRT) over photon and proton RT. The narrow depth-dose deposition profile of carbon ions, as well as their higher LET and RBE compared to protons or photons can be used to deliver more conformal dose distributions to the tumor volume while sparing nearby organs at risk (1). However, the CIRT dose distribution is very

sensitive to treatment geometry variations such as anatomical changes or changes in the patient positioning. Those variations can lead to severe under-dosage of the tumor or over-dosage of healthy tissue (2). On-line and *in-vivo* monitoring methods of the dose distribution could allow potential inter-fractional changes to be detected, offering to make CIRT safer and more effective (3, 4).

Most of the proposed CIRT monitoring methods exploit the information on the dose distribution in the patient carried by products of nuclear interactions of the carbon-ion beam with the patient tissue. These products can be annihilation photons from β+ emitters, prompt gamma rays or prompt charged fragments (also known as secondary ions) (5). The developed CIRT monitoring methods use the distribution of these interaction products to detect the position of the primary carbon-ion beam in the patient. Even in the case when the correlation between nuclear products and dose is low, the measured nuclear product distributions of different treatment fractions can be directly compared to each other (or to Monte Carlo simulations) in order to draw conclusions on potential treatment variations (6).

This contribution investigates the secondary-ions-based method. It aims to quantify the influence of the detection angle on the performance of the cavity detection within a head phantom. As the secondary ion production is forward-peaked, i.e. they are mainly emitted in the direction of the primary carbon-ion beam, experimental configurations of secondary-ion-based monitoring methods use forward detection angles α with respect to the beam direction. Over the years, secondary-ions detection angles ranging from 0° (7, 8) to 90° (9) were investigated. Most of the recently published experiments have been measured at either 30° (10, 11), or at 60° and 90° (12–14). The first results of a clinical study were taken at a composite detection angle of 60° (horizontal plane) and 30° (vertical plane) relative to the beam direction (15). However, no systematic investigation of the influence of the detection angle on the performance of the detection system in a realistic clinical setting has been published to this date.

In this contribution, the efficiency of our secondary-ion-based monitoring system to detect a 2-mm-thick air cavity in a head phantom is investigated for different detection angles. Two metrics are used to identify the optimal detection angle for this specific set-up: the detectability of the changes induced by the air cavity, and the localization of the change along the depth in the head phantom. The detectability is quantified as a metric based on the measured deviation in the detected charged fragments. The localization is defined as the reconstructed cavity position. Additionally, the robustness of the method is investigated for two different cavity positions along the depth in the head phantom.

Detection angles from 10° to 50° in steps of 10° are investigated. The detectability is expected to improve with larger number of detected secondary ion tracks, i.e. to improve at smaller angles, while the localization is expected to improve with the spatial resolution, thus to be better at larger angles. This is because the spatial resolution is determined by Multiple Coulomb Scattering (MCS) of the fragments in the phantom (16, 17), which is projected onto the beams axis under the detection angle (12). However, the optimal angle for the detection of the secondary ion tracks is currently unknown.

2 MATERIALS AND METHODS

2.1 The Heidelberg Ion-Beam Therapy Center

The experiments were carried out at the Heidelberg Ion-Beam Therapy Center (HIT) in Germany (18, 19). At the HIT facility, carbon-ion irradiation can be performed in four rooms - three treatment rooms and one experimental room. Two treatment rooms have fixed horizontal beam lines while the third treatment room is equipped with a 360° revolving carbon-ion gantry. The experimental room, which is used for quality assurance and research, houses a horizontal beam line that is identical to those in the treatment rooms. The measurements of this study were performed in the experimental room. HIT offers 255 discrete energy steps ranging from 88.83 MeV/u to 430.10 MeV/u for carbon ions. These energy steps correspond to a range of penetration depths in water of 2 cm to 30 cm (20) with step sizes of 1 mm to 1.5 mm and adjustable beam sizes in 6 steps ranging from 3.4 mm to 13.4 mm FWHM.

To cover the three-dimensional tumor volume with the required dose, the HIT facility uses an active raster scanning system (20). This system involves the separation of the target volume into iso-energy slices (IES) that are irradiated slice-by-slice. The manipulation of the lateral beam spot position is performed with a magnetic scanning system. The beam nozzle includes a ripple filter for dose flattening in the spread-out Bragg peak and a beam application monitor system (BAMS), which registers the lateral pencil beam position, size and number of particles for each pencil-beam spot (21).

2.2 Head Phantom

For this work, a homogenous Poly(methyl methacrylate) (PMMA) cylinder was used as a surrogate for a patient head. The cylinder has a height of 90 mm and a diameter of 160 mm. At its center there is a cubic opening of $80 \times 80 \times 80$ mm^3 that could be filled with PMMA slabs as shown in **Figure 2**. The relative stopping power (RSP) of the head phantom, measured with a PTW Peakfinder Water Column (T34080 Bragg Peak chamber and TANDEM XDR electrometer) was found to be 1.163 for the cylinder and 1.151 for the PMMA slabs, both were thus comparable to the RSP of soft human tissues (22).

2.3 Treatment Plan

Using a clinical CT scanner (SIEMENS Sensation Open device) and the corresponding clinical imaging protocol for head patients, a CT image of the head phantom was acquired. Based on that, a CIRT treatment was designed using the Siemens syngo RT Planning system (Siemens Healthcare GmbH, Erlangen, Germany). The treatment plan targets a virtual spherical tumor (volume of 70.06 cm^3) centered in head phantom with a fraction dose of 3 Gy (RBE), comparable to a realistic clinic-like single-field CIRT fraction dose. The total number of primary carbon ions was 5.69×10^8, distributed

over 8356 raster points (scan grid distances of 2.0 mm × 2.0 mm), divided into 19 iso-energy slices (step width of 3.0 mm range in water) ranging from 167.66 to 239.45 MeV/u and with a beam spot size in air of 6 mm (FWHM).

2.4 Mini-Tracker

A mini-tracker (see **Figures 1**, **2**) made of two pixelated detectors was used to detect and track individual charged nuclear fragments. Each of the employed AdvaPIX TPX3 modules was equipped with a Timepix3 chip based on the hybrid semiconductor pixel detector technology developed within the Medipix3 Collaboration at CERN (23). The sensitive layer of each detector is 300 µm thick crystalline silicon with an area of 14×14 mm^2 divided into 256×256 pixels (pixel pitch of 55 µm). The time resolution of a single TPX3 module is 1.56 ns. The sensors were operated at a bias voltage of 10 V. This relatively low bias voltage causes a partial depletion of the silicon layer, which leads to a larger cluster size and thus enables an more precise hit position measurement based on the calculation of the energy-weighted center of mass of the cluster (24). The energy threshold was set to 3 keV, ensuring a noise-free data acquisition.

The distance between the two sensitive silicon layers was set to 25.5 mm (see **Figure 2**). The two TPX3 modules were connected *via* a synchronization cable and to a mini PC notebook *via* two USB 3.0 cables (see **Figure 1**). The detector settings and the data acquisition were controlled using the Pixet software (version 1.6.5.778) (25).

2.5 Experimental Set-Up

The following experimental set-up (see **Figure 1**) was used to measure individual secondary-ion tracks with a mini-tracker placed at different detection angles. The center of the head phantom, which was identical to the center of the tumor, was aligned to coincide with the isocenter of the experimental room. Individual secondary ions emerging from the head phantom were tracked by the mini-tracker placed behind the phantom at different positions defined by the detection angle α (10°, 20°, 30°, 40°, 50°) with respect to the beam direction and the distance *d* (12 cm, 16 cm and 34 cm, depending of the detection angle) to the isocenter, as illustrated in **Figure 2**. The mini-tracker axis was made to point at the isocenter in order to cover the region before and behind the tumor in the field-of-view. The standard distance from the front detector to the isocenter was 12 cm. In order to cope with the signal pile-up seen at smaller detection angles where the fluence rate increases rapidly, the mini-tracker module was positioned further away from the isocenter.

To mimic inter-fractional anatomical changes, a $2 \times 80 \times 80$ mm^3 PMMA slab in the head phantom was removed, creating an air cavity as indicated by the white slabs in the drawing of the head phantom (**Figure 2**). In this study, two different cavity positions were investigated: upstream of the tumor volume (at a depth of -40 mm relative to the isocenter) and at the isocenter (at a depth of 0 mm). Only a single air-cavity position was measured at a time.

Four kinds of measurements, corresponding to four treatment fractions (one reference fraction and three follow-up fractions), were performed at each investigated angle. The first fraction was defined as the reference fraction. The second fraction was a repetition of the first fraction, in order to investigate fraction-to-fraction variation of the signal in case that there are no internal geometry changes. In the third and fourth fractions, the air cavity was inserted at a depth of -40 and 0 mm, respectively. Mini-tracker and head phantom were not moved between measurements of different air-cavity positions.

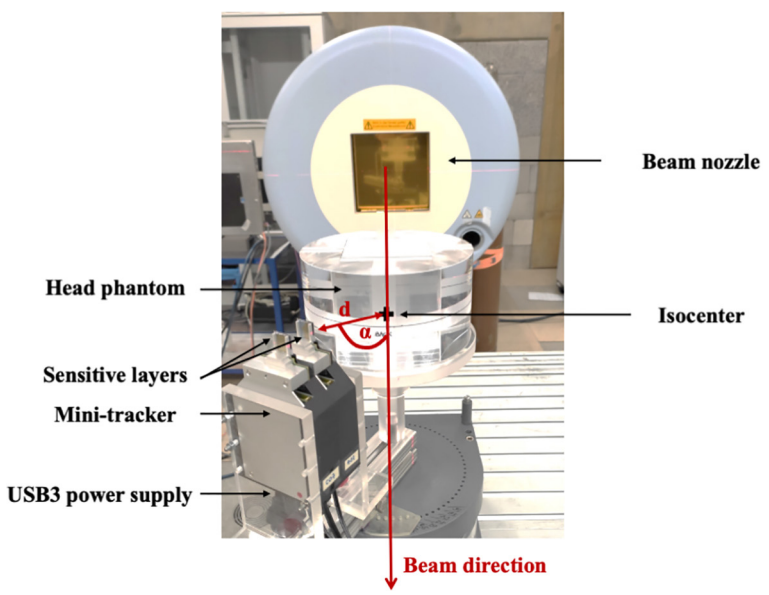

FIGURE 1 | A head phantom composed of PMMA was irradiated with a clinic-like carbon-ion treatment field. Charged fragments were detected by a mini-tracker based on two Timepix3 chips. Several positions of the mini-tracker, characterized by the distance d between the front detector and the isocenter as well as the angle α with respect to the beam direction, were investigated.

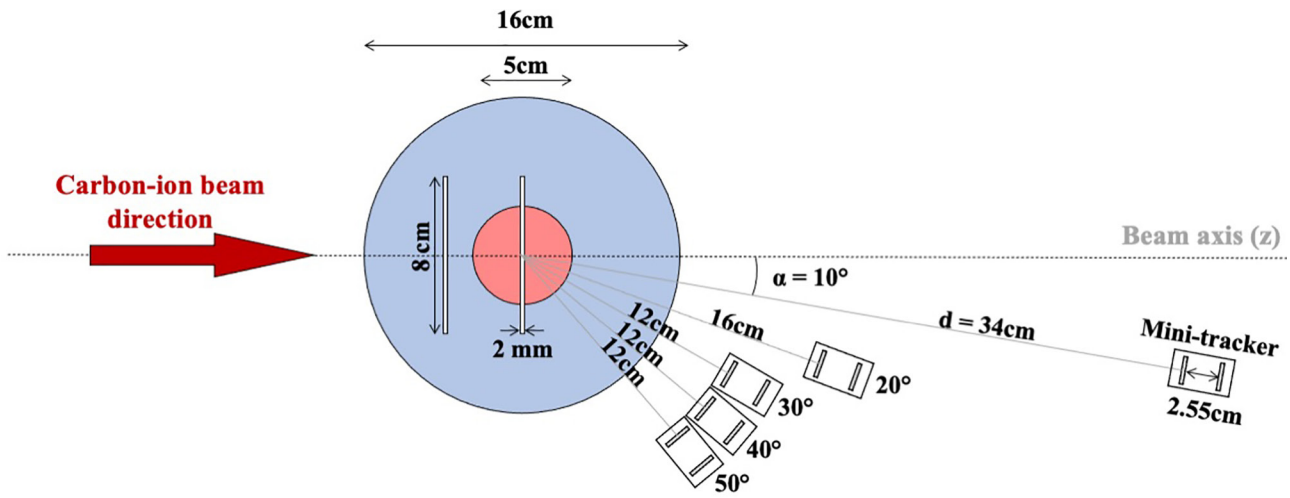

FIGURE 2 | Schematic top view of the experimental set-up. The blue circle represents the cylindrical head phantom and the red circle represents the irradiated spherical tumor volume. The vertical white bars represent the positions of the air cavity (either upstream of the tumor volume or at the isocenter). The distance between the room isocenter and the front detector of the mini-tracker is denoted as d and α is the angle of the mini-tracker axis with respect to the axis of the treatment field direction (beam axis). The following mini-tracker positions were investigated: 10° at a distance d of 34 cm, 20° at a distance of 16 cm, and 30°, 40°, and 50° at a distance of 12 cm.

In order to simulate a future detector upgrade with ≥8 mini-trackers, each measurement was repeated eight times and the obtained data was summed up. A larger detection area can be approximated by a repetition of the measurement because of the small size of the mini-tracker and the resulting small angular variance. The angular variance could be further reduced by arranging the mini-trackers on a circle with a constant detection angle relative to the beam axis, thus utilizing the angular symmetry of the fragment field.

2.6 Data Acquisition

For each of the two Timepix3 detectors in the mini-tracker, the measured raw data consist of a stream of pixel hits with the time of arrival (ToA) and the time over threshold (ToT) being recorded. Using in-house written Matlab[1] and C++ routines, the raw data was post-processed as follows: for each measured secondary ion hit, a so-called cluster was formed from the stream of measured pixels. Neighboring pixel signals within ±75 ns were grouped together as a cluster. The cluster size was defined as the number of pixels contained in a cluster, the cluster arrival time was defined as the minimum ToA of any pixel in the cluster. Clusters with a size of one single pixel were excluded from further data processing, as those were expected to represent noise or background radiation (photons or electrons) (26).

2.7 Data Analysis

2.7.1 Secondary-Ion Tracks and Emission Profiles

Coincident clusters measured within ±75 ns in both mini-tracker sensor layers were considered as hits caused by the same secondary ion. The straight line connecting the energy-weighted centers of mass of the coincident clusters in the two sensor layers was defined as a secondary ion track (26).

To approximate the origin of a secondary ion in the head phantom (the fragmentation vertex), a three-dimensional pencil-beam-based back-projection method was used (27). This back-projection method finds the line that represents the shortest distance between the extrapolated secondary ion track and the beam axis of the respective carbon-ion pencil beam at the time of the track detection. The middle point on this connecting line is defined as the origin of the secondary ion.

The angular projection uncertainty is a function of the uncertainty of the hit position and the distance between the detection layers. The uncertainty of the hit position was approximated as that of a uniform distribution in a pixel. On top of that comes the MCS angle in the front detector (1 mm Silicon), resulting in an estimated angular projection uncertainty of 0.072°+0.069°=0.141°. For comparison, the 1/e MCS angle of 200-MeV-protons travelling through 8 cm of PMMA is approximately 0.84° (28).

The histogram of the fragment origins along the beam axis is referred to as a secondary-ion (or fragment) emission profile. A bin size of 5 mm was used as a reasonable bin size. The effect of the bin size on the data analysis is investigated in section 3.2.4. The number of detected secondary ions in a bin is denoted as N, with the uncertainty being the square root of N (Poisson statistics).

Subsequently, the measured secondary-ion emission profiles were analyzed with different methods to investigate the impact of the air cavity on the radiation field distribution in the phantom. In particular the detectability and the localization of the air cavity were investigated for different positions of the mini-tracker.

2.7.2 Detectability of the Air Cavity

As the aim of the developed method is to compare the emission profiles of different treatment fractions, the difference between

[1] MATLAB, version 9.4.0 (R2018a). The MathWorks, Inc., Natick, Massachusetts, USA

the absolute fragment emission profiles of a follow-up fraction (with or without air cavity) and the reference fraction (without air cavity) was determined using: $Difference = N_{followUp} - N_{ref}$ with its uncertainty being $\sigma(Difference) = \sqrt{N_{followUp} + N_{ref}}$ where $N_{followUp}$ and N_{ref} represent the number of entries in a bin of the follow-up and reference emission profile, respectively.

To quantify the detectability of the inserted air cavity, the integral of the absolute differences along the depth covered by the head phantom was calculated:

$$Integral_{|followUp-ref|} = \sum_{head\ phantom} \left| N_{followUp} - N_{ref} \right|$$

Equation 1: Integral oft the absolute difference of two emission profiles.

$$\sigma(Integral_{|followUp-ref|}) = \sqrt{\sum_{head\ phantom} (N_{followUp} + N_{ref})}$$

Equation 2: Statistical uncertainty of the integral.

The absolute value allows positive as well as negative deviations to be taken into account. As a consequence, the integral of absolute values will not be equal to zero even in case of no significant deviation. Therefore, it must always be compared to a measurement without cavity in place. The detectability is defined as the number of combined standard deviations of the integral with air cavity above the integral without air cavity. The uncertainty of the detectability is calculated using Gaussian error propagation.

$$Detectability = \frac{Integral_{|cavity-ref|} - Integral_{|noCavity-ref|}}{\sqrt{\sigma(Integral_{|cavity-ref|})^2 - \sigma(Integral_{|noCavity-ref|})^2}}$$

Equation 3: Detectability of the air cavity.

2.7.3 Localization of the Air Cavity

In a first step to localize the air cavity, the minimum of the fragment emission profile is determined. Only bins from the start of the head phantom up to the distal end of the tumor volume (depth of -80 mm to +25 mm) are considered when searching for the minimum bin because only anatomical changes in this area can have an impact on the dose distribution.

The location of the air cavity along the depth of the head phantom is defined as the minimum of a second order polynomial drawn through the minimum bin and its two nearest neighbors. The polynomial does not represent a fit since the number of included bins (three) equals the number of degrees of freedom (also three). Instead, the polynomial is used to take into account the information on the minimum location that is included in the direct vicinity of the minimum bin, while simultaneously minimizing the bias from any assumption made on the shape of the minimum that would come with the fit of a function. The uncertainty on the location of the minimum was calculated using Gaussian error propagation.

The suggested procedure for finding the cavity location depends on the bin size since it always takes into account the same number of bins (three), regardless of their size. Therefore, the influence of the bin size on the reconstructed location of the air cavity was investigated by conducting the localization procedure for emission profiles with different bin sizes (see section 3.2.4).

3 RESULTS

3.1 Secondary-Ion Emission Profiles for Different Mini-Tracker Positions

The measured secondary-ion emission profiles were analyzed for each mini-tracker position shown in **Figure 2**. A comparison of the absolute as well as the normalized (to the integral) emission profiles is shown in **Figures 3A**, **B**, respectively. The absolute secondary-ion emission profiles in **Figure 3A** differ mainly in the total number of detected secondary-ion tracks. The number of detected tracks decreases with increasing detection angle, as expected. The relatively small increase in the number of tracks at 10° and 20° results from the larger distance of the mini-tracker to the isocenter, which was chosen in order to technically cope with the higher secondary-ion fluence close to the beam axis.

As visible in **Figure 3B**, due to the geometrical limit of the back-projection method (12), the sharpness of the normalized emission profile increases with increasing detection angle while the effect of Multiple Coulomb Scattering within the phantom, leading to an increased number of tracks that are wrongly back-projected in front of and behind the head phantom, decreases. For large detection angles, the maximum of the emission profile is located at a shallow depth, whereas for small detection angles the maximum is closer to the isocenter. This is a direct geometrical consequence of detection angle: the maximum fragment emission is expected at the entrance to the phantom (highest number and energy of carbon ions and smallest effective detection angle), but the emission profile is smeared out by the projection uncertainty, which increases with decreasing detection angle. The larger distance to the isocenter at small detection angles also contributes to the increase of the projection uncertainty. However, this effect is small in comparison because of the small pixel size of 55 μm.

3.2 Impact of an Air Cavity on the Secondary-Ion Emission Profiles For Different Mini-Tracker Positions

In this work, the impact of an inter-fractional change induced by a 2-mm-thick air cavity was analyzed in three ways. First, the change was visualized by calculating the difference between the secondary-ion emission profiles measured with and without the air cavity. In a next step, the detectability and localization of the air cavity were determined.

3.2.1 Secondary-Ion Emission Profiles With and Without Air Cavity

Secondary-ion emission profiles were measured using a mini-tracker placed at five different positions. As an extreme example with the lowest number of measured tracks, **Figure 4** shows the secondary-ion emission profiles for the mini-tracker positioned at an angle 50° and a distance of 120 mm from the isocenter.

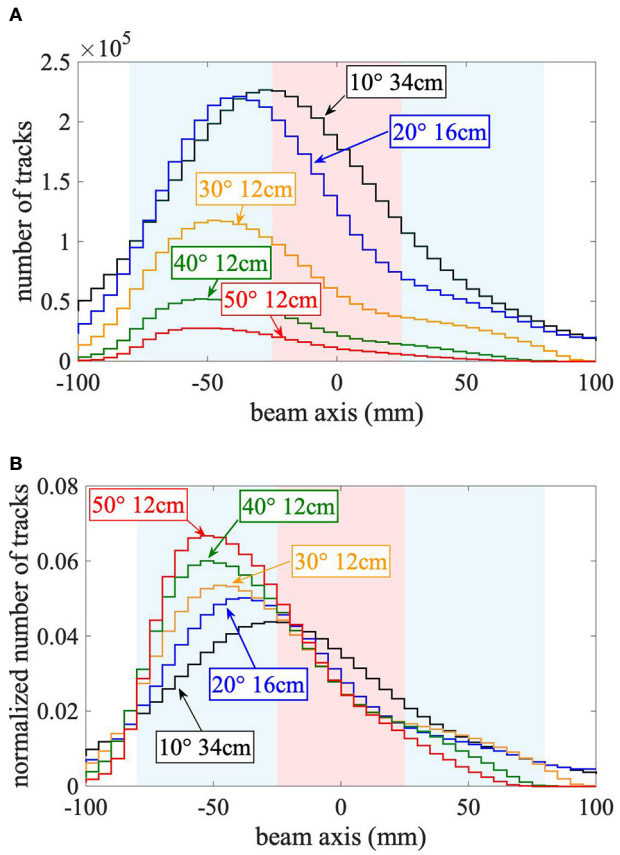

FIGURE 3 | **(A)** Absolute emission profiles. **(B)** Normalized emission profiles. **(A)** Absolute and **(B)** normalized (to the integral) secondary-ion emission profiles along the beam axis for each studied mini-tracker position without air cavity. The cylindrical head phantom (radius of 80 mm) is centered in the isocenter at a depth along the beam axis of 0 mm and is highlighted by the blue area. The spherical target volume (25 mm radius) is represented by the red area. The beam crosses the head phantom from left to right. The statistical uncertainties are plotted as uncertainty bands.

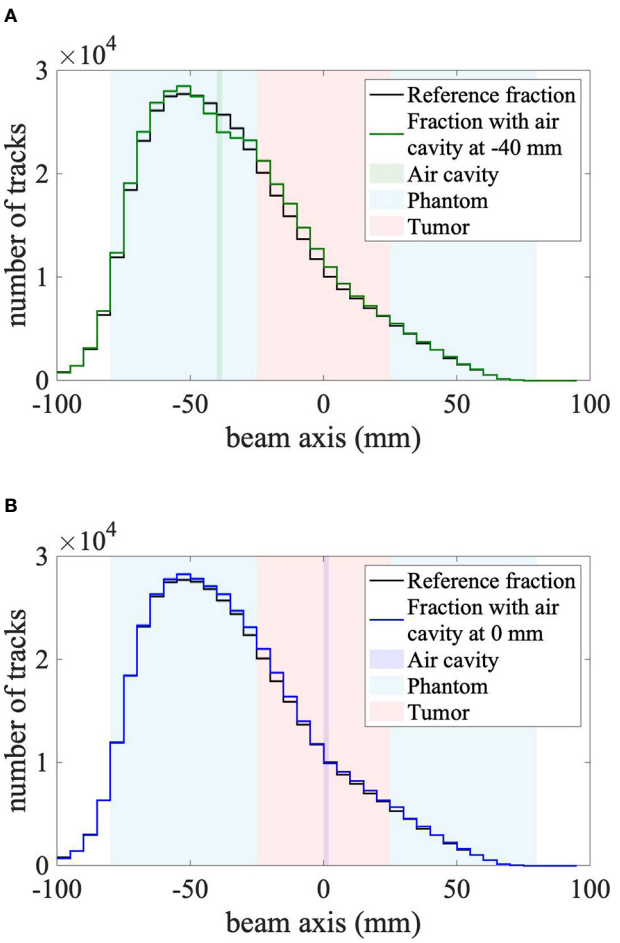

FIGURE 4 | **(A)** Air cavity at -40 mm (in front of the tumor). **(B)** Air cavity at 0 mm (center of the tumor). Secondary-ion emission profiles measured by the mini-tracker placed at an angle of 50° and a distance of 12 cm from the center of the target. The irradiation fraction with a cavity in front of the tumor volume (solid green line) is plotted on the left, whereas the irradiation fraction with a cavity in the middle of the tumor volume (solid blue line) is plotted on the right. The solid black line in both plots represents the reference fraction. Corresponding statistical uncertainties are plotted as uncertainty bands for each profile, which are smaller than the line width. The head phantom is centered at 0 mm and is represented by the blue area, the 25-mm-radius tumor volume is represented by the red area and the inserted air cavity is represented by the vertical green and blue band in **(A, B)**, respectively.

The shape of the measured secondary-ion emission profile is similar for all measured fractions. However, statistically significant differences between the reference irradiation fraction and the fractions with an inserted air cavity are present, particularly when the cavity is placed in front of the tumor volume. Compared to the reference fraction, the secondary-ion emission profile is higher in front of the air cavity, lower at the depth of the cavity and higher behind the cavity. These observations are consistent with (11), due to the expected effect of the air cavity on the primary carbon ions and the charged fragments: the carbon ions penetrate deeper when they cross a low-density region such as the air cavity, leading to a shift of the emission profile towards deeper positions, which explains the larger amount of detected fragments behind the air cavity. In the air cavity itself, fewer fragments are produced, leading to a dip in the secondary-ion emission profile at the depth of the air cavity. Those fragments produced in front of the air cavity have to cross less material in order to reach the mini-tracker, explaining the increased number of detected fragments from shallow depths. For further analysis, the differences between the reference fraction and the follow-up fractions are shown in **Figure 5**.

3.2.2 Difference of Fragment Emission Profiles

For all mini-tracker angles (**Figure 5**), it is observed that the difference between the absolute fragment emission profile without a cavity and the reference (dashed-dotted black curve) is compatible with zero (dotted black line) within its statistical uncertainties, showing the robustness of the method. For both cavity positions and all mini-tracker positions, the difference to

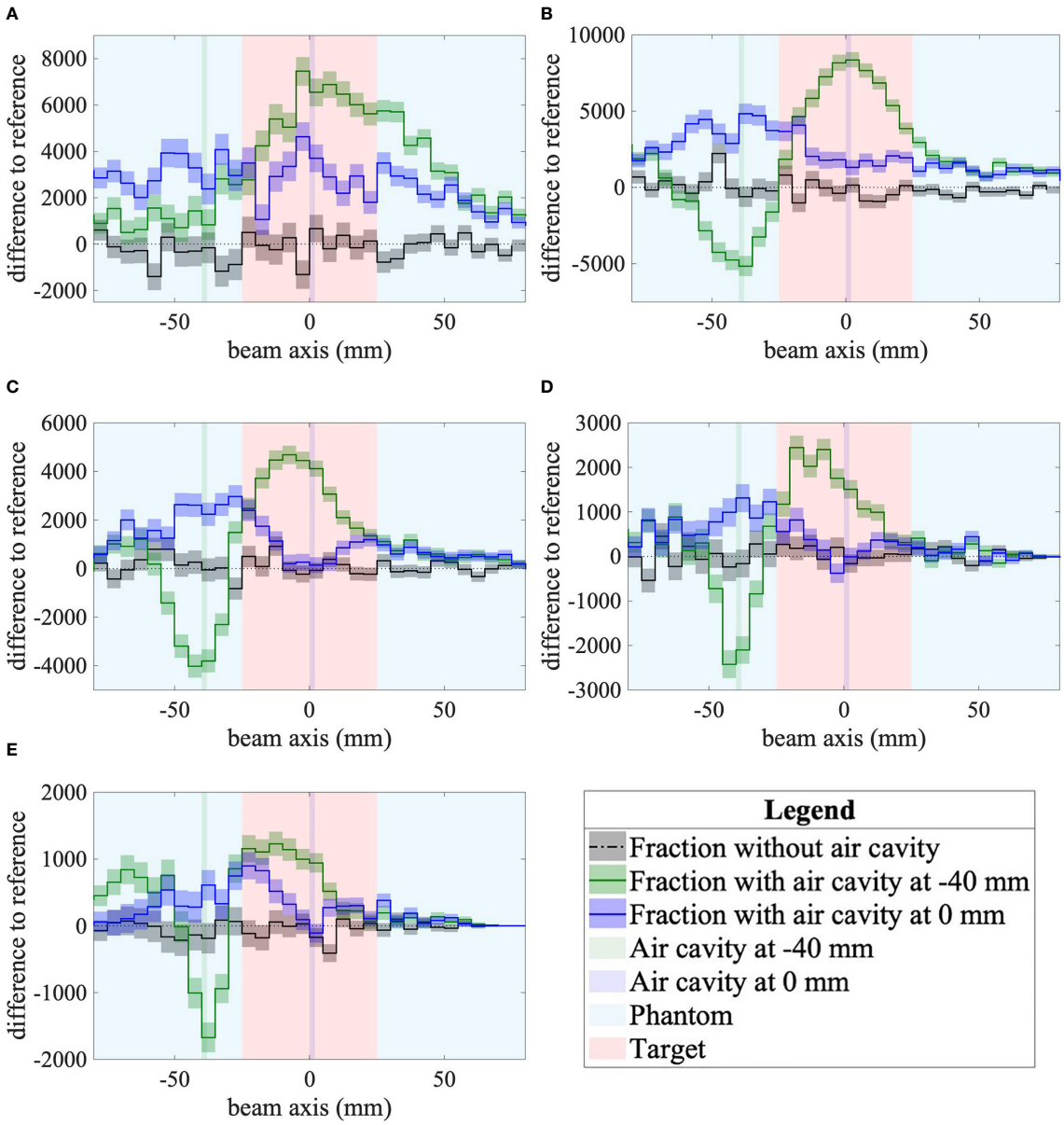

FIGURE 5 | **(A)** α=10°, d=34 cm. **(B)** α=20°, d=16 cm. **(C)** α=30°, d=12 cm. **(D)** α=40°, d=12 cm. **(E)** α=50°, d=12 cm. Differences to the reference of secondary-ion emission profiles for the three follow-up fractions as measured by the mini-tracker placed at different detection angles and distances to the isocenter. The difference between the reference fraction and the fraction without a cavity is shown as a dotted-dashed black line. The difference between the reference fraction and the fraction with a cavity in front of the tumor volume (depth of -40 mm) is plotted in green. The difference between the reference fraction and the fraction with a cavity in the middle of the tumor volume (0 mm) is plotted in blue. The statistical uncertainties are plotted as uncertainty bands for each curve. The plots show the data inside the 80-mm-radius head phantom, which is centered at 0 mm. The red area represents the 25-mm-radius tumor volume and the inserted air cavity is represented by the vertical green and blue bands.

the reference measured with an air cavity in place was found to be significantly different from zero, demonstrating qualitatively the detectability even for such a small variation of the phantom geometry.

For the air cavity inserted in front of the tumor, the difference profile reaches a minimum near the depth of the air cavity (-40 mm) for every detection angle except for 10°. The width of this minimum is found to decrease with increasing detection angle, as expected from the projection of the Multiple Coulomb Scattering on the beam axis.

A dip at the depth of the air cavity is visible when the air cavity is located in the isocenter for detection angles of 30° to 50°. It can happen that the dip does not represent an unambiguous minimum. This is partly due to the lower number of fragments of sufficient energy produced at this depth. Moreover, because of the lateral size of the air cavity (80×80 mm^2), fragments that are

produced in front of the air cavity and which cross the air cavity on their path to the mini-tracker are less likely to be absorbed because they cross less material. This explains the increased number of detected fragments in front of the air cavity. This effect partly compensates for the dip and makes the identification of the minimum more challenging.

3.2.3 Detectability of the Air Cavity

To quantify the detectability of the air cavity, the integral of the absolute difference between the fraction with/without air cavity and the reference fraction is calculated (**Figure 6A**). At every mini-tracker angle, the integral of the absolute difference between the fraction with an air cavity and the reference fraction (green circles and blue triangles) is significantly higher than the integral of the difference without a cavity (black squares). The integral increases with decreasing detection angle because of the larger number of detected secondary-ion tracks at small angles.

The detectability as defined in Equation 3 is shown in **Figure 6B**. The detectability can also be interpreted as the significance of the measurement. It is observed that the presence of the air cavity is detected for all mini-tracker positions and both air cavity locations with a detectability of more than four combined standard deviations. The detectability is maximized for a detection angle of 20° and 10° for a cavity position of -40 mm and 0 mm, respectively. This can be explained by the number of detected fragment tracks, which is maximized at small detection angles.

3.2.4 Localization of the Air Cavity

The measured position of the air cavity is defined as the minimum of a parabola drawn through the minimum bin and its both nearest neighbors (see section 2.7.3). **Figure 7** shows the reconstructed positions of the air cavity for two cavity locations and five detection angles. The error bars represent the statistical uncertainty of the minimum of the parabola. For all cavity positions and the mini-tracker positions between 20° and 50°, except for the cavity at 0 mm and the mini-tracker at 40°, the measured cavity position is in agreement with the actual cavity position within the statistical uncertainty of the measurement. It is observed that the localization fails for the smallest investigated detection angle of 10° due to the absence of a clear minimum in the difference of the emission profiles.

In order to quantify the influence of the bin size on the power of the method to localize the air cavity, the localization procedure was conducted for emission profiles with different bin sizes ranging from 3 to 7 mm in steps of 1 mm, besides the 5 mm used previously. The standard deviation of the resulting cavity positions is used as an estimate for the influence of the bin size on the localization. This systematic uncertainty is shown in **Figure 7** as colored error boxes centered on the markers. The localization is found to be more accurate (smaller systematic uncertainties) for air cavities located in front of the tumor. This is expected because more primary carbon ions cross those shallow air cavities, leading to a more pronounced minimum in the difference distribution.

It can be seen that even the influence of the bin size (i.e. the size of the error boxes) cannot explain the observed difference between the measured and the true cavity position at 10°. This difference is probably caused by the geometrical distortion of the emission profile at this small detection angle.

The large systematic uncertainty at a detection angle of 50° for the cavity position at the isocenter can be explained by the ambiguity of the minimum due to the lower number of measured tracks at this detection angle. Depending on the utilized bin size, the position of the minimum is reconstructed either too close to the isocenter or too close to the entrance to the phantom (see also difference plot in **Figure 5E**).

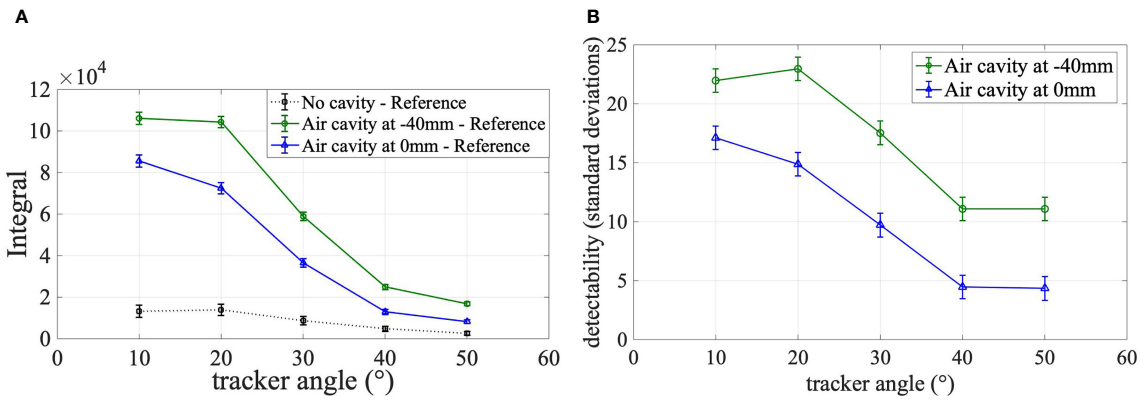

FIGURE 6 | **(A)** Integral of absolute differences, **(B)** Detectability. **(A)** Integral of the absolute difference between secondary-ion emission profiles of the reference fraction and the three follow-up fractions over the target area shown for all investigated mini-tracker positions. The integral of the difference between the reference fraction and the fraction without cavity is plotted as square black markers. The integral values between the reference fraction and the fraction with a cavity in front of the tumor volume are plotted as green circles. The integral between the reference fraction and the fraction with a cavity in the middle of the tumor volume is shown as blue triangles. **(B)** Detectability of the air cavity in units of combined standard deviations.

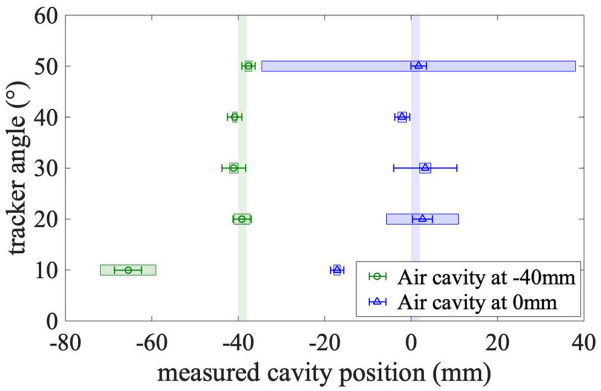

FIGURE 7 | Measured positions of the cavity for different detection angles. The measurement with an air cavity in front of the tumor volume (at -40 mm) is plotted as green circles. The blue triangles show the measurement with the cavity in the middle of the tumor volume (0 mm). The true positions of the air cavity are shown as the vertical green and blue bands. The error bars represent the statistical uncertainty. The colored boxes that are centered on the markers represent the systematic effect of the bin size.

4 DISCUSSION

This study employed a mini-tracker made of dead-time-free Timepix3 silicon pixel detectors to measure the charged fragments emerging from a homogeneous PMMA head phantom that is irradiated by a realistic carbon-ion treatment plan with a dose of 3 Gy (RBE). A dataset equivalent to eight mini-trackers with an active area of 2 cm^2 each was used to detect and localize an air cavity of 2 mm thickness and 80 × 80 mm^2 transverse area from different detection angles relative to the beam axis. The size of the investigated inter-fractional change is considerably smaller than in previously published studies that used inserts with a thickness of 10 mm (11), 28.5 mm (29) and 28 mm (30).

The suitability of different mini-tracker angles was investigated in terms of detectability and localization of the air cavity.

All investigated measurement settings in terms of the tracker position and the air cavity position resulted in a detectability above the significance threshold of three standard deviations. The larger number of detected secondary ions at small detection angles led to a strongly improved detectability (up to 23 standard deviations) compared with larger detection angles with 4 standard deviations at 40° and above. This shows the large technical potential of the used tracking method for a future use in clinical studies.

The detectability of the air cavity was found to be more significant when the cavity is located in front of the tumor in the path of the primary carbon ions, compared to a cavity located at the center of the tumor. Only cavities located in the primary carbon-ion beam path (in front of the Bragg peak) are relevant for the dose deposition in the tumor and changes in the high-dose-gradient region of the Bragg curve. Therefore, an increased sensitivity to shallower anatomical changes could be an asset of secondary-ion monitoring, leading to a lower number of false-positive detections.

The localization of the air cavity was found to be more accurate at larger detection angles, as expected from geometrical effects in the projection. Air cavities at shallow depths were found to be easier to localize because they cause a more pronounced minimum in the fragment emission profile. A limitation of this localization method is that it will fail if no unambiguous minimum can be identified, which can be the case if the number of measured fragment tracks is too small. The localization could be made more robust by introducing prior knowledge in the analysis, e.g. information about the location of natural cavities from the planning CT.

The proposed analysis uses non-normalized (absolute) fragment emission profiles. This is motivated by the fact that a noticeable difference in the number of measured fragment tracks between two treatment fractions would suggest an important change in the dose to the patient. Concerning the reproducibility of the irradiation, it was found in the presented measurements that the number of detected fragments is relatively constant: a maximum relative difference between repetitions of 0.5% was measured for the smallest number of detected fragments at a detection angle of 50°. Moreover, an analysis of the beam record files of the BAMS showed that the number of primary carbon ions between two irradiations of the same treatment plan has a relative standard deviation of 0.03%, whereas the observed systematic deviation from the number of carbon ions in the treatment plan was 0.4%. It is worth noting that our definition of the detectability takes into account the statistical fluctuation of the number of detected fragments by including a comparison to a no-cavity measurement (see Equation 3).

One aim of this study is to inform the design of a future detection system about the optimum detection angle. It was found that a compromise is to be made between detectability and localization of air cavities. The significance of the cavity detection is maximized at smaller detection angles, while the accuracy of the cavity localization is improved at medium-to-large detection angles. However, taking into account the detectability and localization as well as current hardware limitations (signal pile-up), the optimum detection angle for the presented system was found to be in the range from 20° to 40°. In further studies, a detection system with several mini-trackers placed at different detection angles could allow both parameters to be optimized simultaneously.

All measurements at a specific mini-tracker position were performed without moving the detector or the phantom. Therefore, the data does not include any inter-fractional positioning uncertainty of the mini-tracker. If too large, the positioning uncertainty could impair the performance of the method, leading to a false-positive detection of an inter-fractional anatomical change. Since the magnitude of the positioning uncertainty is determined by the mechanics of the positioning system, the impact of the positioning uncertainty has to be quantified once the final layout of a future detection system is designed. Based on the experience from prompt-gamma range-verification systems, the required positioning reproducibility is expected to be around 1 mm (31).

The observed large values of the detectability show that the effective detection area of 16 cm^2 is sufficient for the detection of small inter-fractional density changes. The measured number of fragments tracks was also sufficient for the accurate localization of the air cavity. However, the absolute number of detected fragment tracks depends also on the applied dose, the energies of the carbon-ion pencil beams as well as the amount of tissue that has to be crossed by the fragments before reaching the mini-tracker. The setting investigated in this work, where the tumor is located at the center of a head phantom and irradiated by a single field of 3 Gy (RBE), represents a best-case scenario in terms of fragment statistics. Therefore, even larger detection areas would further benefit the performance of the method, leading to smaller statistical uncertainties. Moreover, pointing the mini-tracker axis onto the region of interest in front of the tumor volume could increase the geometrical acceptance and therefore the number of detected fragments.

Future investigations of more realistic cavities in terms of shape, size, position, and composition, might lead to additional information for the geometrical design of future detection systems. Moreover, the size of changes, which can still be detected reliably in a more realistic heterogeneous anthropomorphic head phantom, needs to be investigated. The detection of a potential patient misalignment with respect to the carbon-ion beam (translations and rotations) should be addressed separately.

5 CONCLUSION

The aim of this work was to investigate the power of monitoring carbon ion radiotherapy using tracking of charged nuclear fragments in terms of detection and localization of a 2-mm-thick air cavity in a head-sized PMMA phantom. The performance of the method was analyzed as a function of the position of the mini-tracker. In contrast to previous publications focusing on single pencil beams, a treatment plan with a realistic dose (3 Gy (RBE)), dose rate and tumor size were used. This became possible thanks to the dead-time-free data acquisition of the Timepix3 detector. A dataset equivalent to eight mini-trackers, with an active area of 2 cm^2 each, was used.

It was found that the presence of the air cavity could be detected for both investigated cavity positions – in the Bragg curve plateau as well as in the center of the target – and for all the investigated detection angles (10° to 50°). The significance of the detection increases with decreasing detection angles – up to 23 standard deviations at 10°. The position of the cavity could be correctly localized within 2 mm, being within the statistical uncertainties, if detection angles ≥ 20° are used. It was found that the air cavity could be localized with higher accuracy and precision if it is located closer to the entrance to the phantom.

The presented results provide important information on the design of future detection systems to be used in clinical trials. Taking into account the ability of the detection system to detect and localize the investigated inter-fractional change, as well as the current hardware limitations, the optimum range of detection angles for the investigated system was found to be between 20° to 30°. The universality of this finding for clinical situations with targets in different depths has to be investigated in the future, ideally within real patient treatments.

DATA AVAILABILITY STATEMENT

The raw data supporting the conclusions of this article will be made available by the authors, without undue reservation.

AUTHOR CONTRIBUTIONS

LG-D and AS planned and performed the measurements, did the data analysis, and wrote the manuscript in the frame of their PhD and Bachelor theses, respectively. LG-D and AS share the first authorship of the manuscript. TG helped design the experiment and provided scientific advice. GE built the experimental setup. RF-B helped perform the measurements. LK helped perform the measurements, design the data analysis, and write the manuscript. MM came up with the original research idea, collected part of the funding, and supervised the scientific rigor of the study. LK and MM share the last authorship of the manuscript. All authors contributed to the article and approved the submitted version.

FUNDING

This publication is part of a common project of the DKFZ and HIT, supported by the National Center for Tumor Diseases Heidelberg (NCT). TG was funded by the Deutsche Forschungsgemeinschaft (DFG, German Research Foundation) – Project No.: 426970603.

ACKNOWLEDGMENTS

The authors would like to acknowledge Markus Winter (HIT) for the generation of the treatment plan and Stephan Brons (HIT) for support during the beam time.

REFERENCES

1. Mohamad O, Sishc BJ, Saha J, Pompos A, Rahimi A, Story MD, et al. Carbon Ion Radiotherapy: A Review of Clinical Experiences and Preclinical Research, With an Emphasis on DNA Damage/Repair. *Cancers (Basel)* (2017) 9(6):66. doi: 10.3390/cancers9060066
2. Fattori G, Riboldi M, Scifoni E, Krämer M, Pella A, Durante M, et al. Dosimetric Effects of Residual Uncertainties in Carbon Ion Treatment of Head Chordoma. *Radiother Oncol* (2014) 113(1):66–71. doi: 10.1016/j.radonc.2014.08.001
3. Kraan AC. Range Verification Methods in Particle Therapy: Underlying Physics and Monte Carlo Modelling. *Front Oncol* (2015) 5:150. doi: 10.3389/fonc.2015.00150
4. Muraro S, Battistoni G, Collamati F, De Lucia E, Faccini R, Ferroni F, et al. Monitoring of Hadrontherapy Treatments by Means of Charged Particle Detection. *Front Oncol* (2016) 6:177. doi: 10.3389/fonc.2016.00177

5. Parodi K, Polf JC. *In Vivo* Range Verification in Particle Therapy. *Med Phys* (2018) 45(11):e1036–50. doi: 10.1002/mp.12960
6. Smeets J, Roellinghoff F, Prieels D, Stichelbaut F, Benilov A, Busca P, et al. Prompt Gamma Imaging With a Slit Camera for Real-Time Range Control in Proton Therapy. *Phys Med Biol* (2012) 57, (11):3371–405. doi: 10.1088/0031-9155/57/11/3371
7. Henriquet P, Testa E, Chevallier M, Dauvergne D, Dedes G, Freud N, et al. Interaction Vertex Imaging (IVI) for Carbon Ion Therapy Monitoring: A Feasibility Study. *Phys Med Biol* (2012) 57(14):4655–69. doi: 10.1088/0031-9155/57/14/4655
8. Martisikova M, Jakubek J, Gwosch K, Hartmann B, Telsemeyer J, Pospisil S, et al. Monitoring of Ion Beam Energy by Tracking of Secondary Ions: First Measurements in a Patient-Like Phantom. *IEEE Nucl Sci Symposium Med Imaging Conf Rec (NSS/MIC) Phys Med Biol* (2012) 1914–7. doi: 10.1109/NSSMIC.2012.6551443
9. Agodi C, Battistoni G, Bellini F, Cirrone GAP, Collamati F, Cuttone G, et al. Charged Particle's Flux Measurement From PMMA Irradiated by 80 MeV/u Carbon Ion Beam. *Phys Med Biol* (2012) 57(18):5667–78. doi: 10.1088/0031-9155/57/18/5667
10. Gwosch K, Hartmann B, Jakubek J, Granja C, Soukup P, Jäkel O, et al. Non-Invasive Monitoring of Therapeutic Carbon Ion Beams in a Homogeneous Phantom by Tracking of Secondary Ions. *Phys Med Biol* (2013) 58(11):3755–73. doi: 10.1088/0031-9155/58/11/3755
11. Gaa T, Reinhart M, Hartmann B, Jakubek J, Soukup P, Jäkel O, et al. Visualization of Air and Metal Inhomogeneities in Phantoms Irradiated by Carbon Ion Beams Using Prompt Secondary Ions. *Physica Med* (2017) 38:140–47. doi: 10.1016/j.ejmp.2017.05.055
12. Piersanti L, Bellini F, Bini F, Collamati F, De Lucia E, Durante M, et al. Measurement of Charged Particle Yields From PMMA Irradiated by a 220 MeV/u 12c Beam. *Phys Med Biol* (2014) 59(7):1857–72. doi: 10.1088/0031-9155/59/7/1857
13. Mattei I, Bini F, Collamati F, De Lucia E, Frallicciardi PM, Iarocci, et al. Secondary Radiation Measurements for Particle Therapy Applications: Prompt Photons Produced by 4He, 12C and 16O Ion Beams in a PMMA Target. *Phys Med Biol* (2017) 62(4):1438–55. doi: 10.1088/1361-6560/62/4/1438
14. Mattei I, Battistoni G, Collini F, De Lucia E, Durante M, Fiore S, et al. Addendum: Measurement of Charged Particle Yields From PMMA Irradiated by a 220 MeV/u 12 C Beam. *Phys Med Biol* (2017) 62(21):8483–94. doi: 10.1088/1361-6560/aa8b35
15. Fischetti M, Baroni G, Battistoni G, Bisogni G, Cerello P, Ciocca, et al. Inter-Fractional Monitoring of 12 C Ions Treatments: Results From a Clinical Trial at the CNAO Facility. *Sci Rep* (2020) 10(1):20735. doi: 10.1038/s41598-020-77843-z
16. Bethe HA. Molière's Theory of Multiple Scattering. *Phys Rev* (1953) 89:1256. doi: 10.1103/PhysRev.89.1256
17. Gottschalk B, Koehler AM, Schneider RJ, Sisterson JM, Wagner MS. Multiple Coulomb Scattering of 160 MeV Protons. *Nucl Instruments Methods Phys Res B* (1993) 74(4):467–90. doi: 10.1016/0168-583X(93)95944-Z
18. Haberer T, Debus J, Eickhoff H, Jäkel O, Schulz-Ertner D, Weber U. The Heidelberg Ion Therapy Center. *Radiother Oncol* (2004) 73(Suppl2):S186–90. doi: 10.1016/s0167-8140(04)80046-x
19. Combs SE, Jäkel O, Haberer T, Debus J. Particle Therapy at the Heidelberg Ion Therapy Center (HIT) - Integrated Research-Driven University-Hospital-Based Radiation Oncology Service in Heidelberg, Germany. *Radiother Oncol* (2010) 95(1):41–4. doi: 10.1016/j.radonc.2010.02.016
20. Haberer T, Becher W, Schardt D, Kraft G. Magnetic Scanning System for Heavy Ion Therapy. *Nucl Instrum Methods Phys Res A* (1993) 330(1–2):296–305. doi: 10.1016/0168-9002(93)91335-K
21. Schoemers C, Feldmeier E, Naumann J, Panse R, Peters A, Haberer T. The Intensity Feedback System at Heidelberg Ion-Beam Therapy Centre. *Nucl Instrum Methods Phys Res A* (2015) 795:92–9. doi: 10.1016/j.nima.2015.05.054
22. Rietzel E, Schardt D, Haberer T. Range Accuracy in Carbon Ion Treatment Planning Based on CT-Calibration With Real Tissue Samples. *Radiat Oncol* (2007) 2(1):14. doi: 10.1186/1748-717X-2-14
23. Poikela T, Plosila J, Westerlund T, Campbell M, De Gaspari M, Llopart X, et al. Timepix3: A 65k Channel Hybrid Pixel Readout Chip With Simultaneous ToA/ToT and Sparse Readout. *J Instrumentation* (2014) 9(5):C05013. doi: 10.1088/1748-0221/9/05/C05013
24. Gehrke T, Burigo L, Arico G, Berke S, Jakubek J, Turecek D, et al. Energy Deposition Measurements of Single 1H, 4He and 12C Ions of Therapeutic Energies in a Silicon Pixel Detector. *J Instrumentation* (2017) 12(4):P04025. doi: 10.1088/1748-0221/12/04/P04025
25. Turecek D, Holy T, Jakubek J, Pospisil S, Vykydal Z. Pixelman: A Multi-Platform Data Acquisition and Processing Software Package for Medipix2, Timepix and Medipix3 Detectors. *J Instrumentation* (2011) 6(1):C01046. doi: 10.1088/1748-0221/6/01/C01046
26. Félix-Bautista R, Gehrke T, Ghesquière-Diérickx L, Reimold M, Amato C, Turecek D, et al. Experimental Verification of a Non-Invasive Method to Monitor the Lateral Pencil Beam Position in an Anthropomorphic Phantom for Carbon-Ion Radiotherapy. *Phys Med Biol* (2019) 64(17):175019. doi: 10.1088/1361-6560/ab2ca3
27. Ghesquière-Diérickx L, Félix-Bautista R, Schlechter A, Kelleter L, Reimold M, Echner G, et al. Detecting Perturbations of a Radiation Field Inside a Head-Sized Phantom Exposed to Therapeutic Carbon-Ion Beams Through Charged-Fragment Tracking. *Med Phys* (2021).
28. Highland VL. Some Practical Remarks on Multiple Scattering. *Nucl Instruments Methods* (1975) 129(2):497–9. doi: 10.1016/0029-554X(75)90743-0
29. Reinhart AM, Spindeldreier CK, Jakubek J, Martisikova M. Three Dimensional Reconstruction of Therapeutic Carbon Ion Beams in Phantoms Using Single Secondary Ion Tracks. *Phys Med Biol* (2017) 62:4884. doi: 10.1088/1361-6560/aa6aeb
30. Finck C, Karakaya Y, Reithinger V, Rescigno R, Baudot J, Constanzo, et al. Study for Online Range Monitoring With the Interaction Vertex Imaging Method. *Phys Med Biol* (2017) 62(24):9220–39. doi: 10.1088/1361-6560/aa954e
31. Richter C, Pausch G, Barczyk S, Priegnitz M, Keitz I, Thiele J, et al. First Clinical Application of a Prompt Gamma Based *In Vivo* Proton Range Verification System. *Radiother Oncol* (2016) 118(2):232–7. doi: 10.1016/j.radonc.2016.01.004

Conflict of Interest: The authors declare that the research was conducted in the absence of any commercial or financial relationships that could be construed as a potential conflict of interest.

Publisher's Note: All claims expressed in this article are solely those of the authors and do not necessarily represent those of their affiliated organizations, or those of the publisher, the editors and the reviewers. Any product that may be evaluated in this article, or claim that may be made by its manufacturer, is not guaranteed or endorsed by the publisher.

frontiers in Oncology

REVIEW
published: 30 November 2021
doi: 10.3389/fonc.2021.789079

Biological Rationale and Clinical Evidence of Carbon Ion Radiation Therapy for Adenoid Cystic Carcinoma: A Narrative Review

Pierre Loap[1,2,3], Barbara Vischioni[1], Maria Bonora[1], Rossana Ingargiola[1], Sara Ronchi[1], Viviana Vitolo[1], Amelia Barcellini[1], Lucia Goanta[4], Ludovic De Marzi[2,3,5], Remi Dendale[2,3], Roberto Pacelli[4], Laura Locati[6,7], Valentin Calugaru[2,3], Hamid Mammar[2,3], Stefano Cavalieri[6,7], Youlia Kirova[2,3] and Ester Orlandi[1]*

[1] Radiation Oncology Unit, Clinical Department, National Center for Oncological Hadrontherapy (CNAO), Pavia, Italy, [2] Department of Radiation Oncology, Institut Curie, Paris, France, [3] Proton Therapy Center, Institut Curie, Orsay, France, [4] Department of Advanced Biomedical Sciences, University of Naples "Federico II", Napoli, Italy, [5] Institut Curie, PSL Research University, University Paris Saclay, INSERM LITO, Orsay, France, [6] Medical Oncology Department, Fondazione IRCCS Istituto Nazionale dei Tumori, Milan, Italy, [7] Department of Oncology and Hemato-Oncology, University of Milan, Milan, Italy

Adenoid cystic carcinoma (ACC) is a rare, basaloid, epithelial tumor, arising mostly from salivary glands. Radiation therapy can be employed as a single modality for unresectable tumors, in an adjuvant setting after uncomplete resection, in case of high-risk pathological features, or for recurrent tumors. Due to ACC intrinsic radioresistance, high linear energy transfer (LET) radiotherapy techniques have been evaluated for ACC irradiation: while fast neutron therapy has now been abandoned due to toxicity concerns, charged particle beams such as protons and carbon ions are at present the beams used for hadron therapy. Carbon ion radiation therapy (CIRT) is currently increasingly used for ACC irradiation. The aim of this review is to describe the immunological, molecular and clinicopathological bases that support ACC treatment with CIRT, as well as to expose the current clinical evidence that reveal the advantages of using CIRT for treating ACC.

Keywords: adenoid cyst carcinoma, hadrontherapy, carbon ion radiotherapy (CIRT), tumor immunology, radioresistance

OPEN ACCESS

Edited by:
Thomas Tessonnier, Heidelberg University Hospital, Germany

Reviewed by:
Stefania Volpe, European Institute of Oncology (IEO), Italy
Alexandra Jensen, Uniklinikum Giessen und Marburg, Germany

***Correspondence:**
Pierre Loap
pierre.loap@gmail.com

Specialty section:
This article was submitted to Radiation Oncology, a section of the journal Frontiers in Oncology

Received: *04 October 2021*
Accepted: *15 November 2021*
Published: *30 November 2021*

Citation:
Loap P, Vischioni B, Bonora M, Ingargiola R, Ronchi S, Vitolo V, Barcellini A, Goanta L, De Marzi L, Dendale R, Pacelli R, Locati L, Calugaru V, Mammar H, Cavalieri S, Kirova Y and Orlandi E (2021) Biological Rationale and Clinical Evidence of Carbon Ion Radiation Therapy for Adenoid Cystic Carcinoma: A Narrative Review. Front. Oncol. 11:789079. doi: 10.3389/fonc.2021.789079

Abbreviations: ACC, Adenoid cystic carcinoma; CD, Cluster of differentiation; CIRT, Carbon ion radiation therapy; CSC, Cancer stem cell; CTA, Cancer-testis antigen; DC, Dendritic cell; EGFR, Epithelial growth factor receptor; EMT, Epithelial-mesenchymal transition; HN, Head and neck; IHC,Immunohistochemistry; IMRT, Intensity modulated radiation therapy; LC, Local control; LEM, Local effect model; LET, Linear energy transfer; MDSC, Myeloid-derived suppressor cells; mMKM, Modified microdosimetric kinetic model; OER, Oxygen enhancement ratio; OS, Overall survival; PBT, Proton beam therapy; PFS, Progression free survival; PNI, Perineural invasion; RBE, Relative biological effectiveness; RFS, Relapse free survival; RNA, Ribonucleic acid; RT, Radiation therapy; TAA, Tumor-associated antigen; TAM, Tumor-associated macrophages; TCD50, Tumor control dose 50; TF, Transcription factor; TMB, Tumor mutational burden; TME, Tumor microenvironment; TNA, Tumor-specific neo-antigens; VEGF, Vascular endothelial growth factor.

1 INTRODUCTION

Adenoid cystic carcinoma (ACC) is a rare tumor, which has a dual component of myoepithelial and ductal cells. Most of the ACCs arise from minor salivary glands, and account for about 10% of all malignant salivary tumors (1). Other involved head and neck (HN) sites include the external ear and the lacrimal glands. Less frequently, ACC might be diagnosed in non-HN sites, including the breasts, the lungs, the prostate gland, the esophagus, the cervix, the vulva or the skin (2–4). Overall, around 3000 cases have been identified between 1973 and 2007 in the US National Cancer Institute's Surveillance, Epidemiology and End Results (SEER) program (5) and around 2600 cases have been described between 1983 and 1994 in the European EUROCARE registry (6).

Photon beam radiotherapy (RT) technological developments gave a substantial contribution in HN patient prognosis improvement last decades especially in patients bearing squamous cell carcinoma (7). RT plays a key role in different phases of ACC management: in the adjuvant setting after surgery for potentially resectable cases or as a definitive modality for non-operable tumors; or in a reirradiation context for local recurrent disease (8). Due to the radioresistance of ACC, RT techniques using high linear energy transfer (LET) particles have been evaluated for more than 50 years, in particular fast neutron beams (9). However, the use of neutron beams, while efficient, has been abandoned for late toxicity due to the difficulty of obtaining an advantageous dose gradient between the target and the organs-at-risk. On the other hand, carbon ion radiation therapy (CIRT) harbors both the high LET of fast neutron beams and the specific spatial distribution of charged particle beams. Charged particle beams are characterized by a Bragg peak that deposits most of the dose in a very short path, the deepness of which depends on the start energy of the beam, allowing targeted irradiation. CIRT has consequently been increasingly evaluated for ACC irradiation during the last years.

To this date, no *in vitro* or preclinical study have specifically evaluated CIRT irradiation effects on ACC cell lines. Nevertheless, multiple immunological and biological properties justify ACC management with CIRT (**Table 1**). We reviewed the literature on the biological bases and the clinical evidence that support the use of CIRT in ACC management.

2 MOLECULAR RATIONALE OF CIRT FOR ACC

2.1 ACC Heterogeneity Represents a Challenge for Radiotherapy

2.1.1 ACC Is a Heterogeneous Group of Tumors From a Molecular Point of View

Based on whole-exome sequencing (WES) of 34 tumor samples from primary and metastatic ACC tumors isolated from eight patients, Liu et al. (10) demonstrated that there was an important spatial and temporal clonal diversity within and between primary and metastatic tumors. The average mutation rate was evaluated around 0.32 per million base pair and the incidence of shared mutations between primary and metastatic tumor samples was 21.9%; truncal genetic alterations included NOTCH pathway genes (such as NOTCH1 or SPEN) or the t (6, 9) translocation (MYB–NFIB fusion). Nevertheless, this apparent diversity of tumor mutations allows a variety of potential systemic targeted treatments. For instance, Ho et al. (11) demonstrated that tumoral activation of the VEGF/KIT/PDGFR pathway could be effectively targeted by anti-angiogenic agents (such as Axitinib), while the NOTCH-mutated ACCs could be specifically blocked

TABLE 1 | Biological rationale for adenoid cystic carcinoma (ACC) with carbon ion radiation therapy (CIRT).

ACC adverse characteristics	Molecular determinants	Biological rationale of CIRT
Tumor antigenicity	Low TMB	↗ tumor immunogenicity
Immunosurveillance escape	↗ PD-L2 and HLA-G expression ↘ ICAM-1 expression	↗ ICAM1
Immunotolerant microenvironment	↘ CD1a and CD83 infiltrate ↘ MDSC and M2 macrophage infiltrate T-cell exclusion phenotype	↗ DC ↘ M2 and MDSC ↗ proinflamattory cytokines ↗ CD8, ± NK
Hypoxia	↗ HIF1a expression VEGFA-mediated vascular mimicry	low OER ↘ tumorigenesis and angiogenesis
Stemness	↗ HSP27 expression ↗ Brachyury expression VEGF A, Nodal, Lefty, Oct-4, Pac6, Rex1, Nanog	Anti-tumor response on radioresistant tumor cell lines
Autophagy	ATG3, 4A, 5, PIK3R4, MAP1LC3B	
Perineural invasion	BNDF/TrkB; CCLR/CCR5; NGF/TrkA	↘ migration, invasion, adhesion ↘ cell mobility ↘ integrin expression
Tumoral heterogeneity	Biphasic tumor: ductal and myoepithelial components Molecular heterogeneity within/between primary tumors and metastatic disease	Anti-tumor response ± independent on tumoral heterogeneity

The rationale to use CIRT for ACC management is based on immunological, molecular, and pathological considerations, despite the fact that no in vitro *or preclinical study have specifically evaluated CIRT irradiation on ACC cell lines; CD, cluster of differentiation; DC, dendritic cell; HIF1a, hypoxia-inducible factor 1a; ICAM-1, intercellular adhesion molecule 1; MDSC, myeloid-derived suppressor cell; NK, natural killer cell; OER, oxygen enhancement ratio; TMB, tumor mutational burden; VEGF, vascular-endothelial growth factor.*

by agents targeted NOTCH pathway (such as Bronctictuzumab or AL101) (12, 13). NOTCH-mutated ACC are over-represented in solid variant and are associated with a higher rate of liver and bone metastases, as well as shorter relapse-free survival (RFS) and overall survival (OS) (12). The molecular diversity of ACC tumors is striking in a relapsed or a metastatic context (14). Up to 26.3% of relapsed or metastatic ACC patients are NOTCH-mutated, including 18.3% of activating NOTCH mutations, which have the poorest prognosis among all NOTCH mutations types. Ho et al. (14) further demonstrated that mutations in the KDM6A gene, which intervenes in chromatin remodeling, had a pejorative prognosis for relapsed or metastatic ACC, and that TERT pathway mutations were exclusive of NOTCH mutations and of MYB fusions. Consequently, it appeared that four distinct relapsed/metastatic ACC molecular subgroups could be proposed, based on the presence of NOTCH, TERT mutations and MYB fusion: MYB-mutated/NOTCH-mutated; MYB-mutated/other mutations; MYB wild-type/NOTCH-mutated and MYB-mutated/TERT-mutated.

2.1.2 ACC Is a Heterogeneous Group of Tumors From an Anatomopathological Point of View

ACC is characterized by a biphasic composition made of ductal cells (characterized by CK7 protein expression) and myoepithelial cells (characterized by CK5/6, P63, P40, D2-40, Calponin, a-SMA, S-100, and vimentin protein expression). The histological tumoral organization defines three ACC variants based on the predominant anatomopathological pattern: cribriform, tubular (both characterized by CK7 protein expression), or solid pattern (characterized by a glandular architecture and a loss of myoepithelial differentiation). Solid patterns usually have a higher Ki67 index. Multiple histological grading systems have been proposed based on the estimated proportion of the solid pattern component [Perzin grading using a 30% threshold (15), Spiro grading using a 50% threshold (16)]. It should be noted, however, that Van Weert et al. (17) recently demonstrated that the mere presence of solid components, independently of its proportion, was a negative prognostic factor. Bell et al. (18) evidenced that the c-Kit protein was systematically expressed, and EGFR was consistently negative, in the solid ACC subtype. C-Kit expression was limited to inner ductal epithelial cells, and EGFR expression was restrained to the outer myoepithelial cells, the latter being found in the majority of tubular and cribriform ACC patterns.

2.1.3 CIRT Anti-Tumor Efficiency Is Not Influenced by Tumor Heterogeneity

Based on three cellular sublines of resistant prostate tumors in murine models, Glowa et al. (19) demonstrated that the values of the tumor control dose 50 (TCD50) differed significantly less for CIRT than for photon RT. They concluded that response to CIRT was relatively independent on the molecular and histological tumoral heterogeneity. Additionally, Masunaga et al. (20) found that quiescent tumor cells were more sensitive to CIRT than to photon RT. They suggested that CIRT anti-tumor efficacy could be relatively independent from intra-tumoral cellular heterogeneity, resulting from the co-existence of quiescent and proliferative cell populations in various proportions.

2.2 ACC Radioresistance Properties Might Be Overcome by CIRT

ACC are radioresistant tumors. The main molecular actors of ACC EMT and radioresistance features are provided in **Table 2**.

2.2.1 Epithelial-Mesenchymal Transition and Cancer Stem Cell Properties Are Related to ACC Radioresistance

Wang et al. (21) demonstrated that hypoxic conditions promoted ACC epithelial-mesenchymal transition (EMT) and cancer stem cell (CSC) properties. Molecular actors of ACC EMT and stemness were characterized by Chen et al. (22) who found that HSP27 protein overexpression increased cell migration and invasion properties and induced an up-regulation of Snail 1 and Prrx1, which are potent EMT regulators. Expectedly, increased HSP27 levels in ACC correlated with radioresistance of ACC cell lines *in vitro*; it was also found that high HSP27 expression in ACC had a poor prognosis value. Finally, acquisition of CSC properties in ACC correlated with increased expression of CD133 and CD44. Shimoda et al. (23) further evidenced stemness was a generic characteristic of metastatic ACC cells, which express stemness-related transcription factors (TF) (such

TABLE 2 | Notable molecular actors of ACC stemness and radioresistance properties.

Molecular actor		Roles in ACC radioresistance
BNIP3	BCL2/adenovirus E1B 19 kDa protine-interacting protein 3	Apoptotic Bcl-2 protein. Intervenes in autophagosome formation; can induce autophagic cell death.
Brachyury		Transcription factor. Represses expression of adhesion molecules which promotes epithelial mesenchymal transition (EMT)
CD133/ CD44		CD133: Surface glycoproteine. Marker of cancer stem cells. CD44: Surface glycoprotein. Intervenes in cellular interactions and cell adhesion
HIF1α	Hypoxia-inducible factor 1-alpha	Transcription factor (subunit) responsive to oxygen level. Induces cell proliferation and survival
HSP27	Heat Shock Protein 27	Chaperone protein. Has an anti-apoptotic role and a cytoprotection function under stress conditions; modulates reactive oxygen species
MAP1LC3B	Microtubule-associated proteins 1A/1B light chain 3B	Ubiquitin-like protein. Selects substrate for autophagic degradation
Snail	Zinc finger protein SNAI1	Transcription factor. Represses expression of adhesion molecules which promotes EMT

as Nodal, Lefty, Oct-4, Pac6, Rex1, and Nanog). In particular, the T-box Brachyury TF was highly expressed in clinical ACC samples and was found to regulate both EMT and CSC properties of ACC. Kobayashi et al. (24) further demonstrated that a knock-out of the Brachyury gene in ACC cells lines with short hairpin RNA (shRNA) suppressed both tumor chemoresistance and radioresistance *in vitro*.

2.2.2 ACCs Are Characterized by Hypoxia Markers

De Mendoça et al. (25) demonstrated that ACCs were associated with high Hypoxia-Inducible Factor (HIF) 1α expression levels compared with normal salivary gland, which is expressed in the absence of adequate tissular oxygenation. Liu et al. (26) further observed that salivary ACC had an up-regulation of autophagy-related genes (such as ATG3, 4A, 5, PIK3R4, and MAP1LC3B), controlled by HIF1α. It should be recalled that hypoxia-induced autophagy is a notable actor of resistance to anti-tumor treatments, including radiation therapy (27). Chen et al. (28) demonstrated that BNIP3, a regulator of hypoxia-induced autophagy, was expressed by 63.1% of ACCs, and that BNIP3 in ACC cell lines could be induced *in vitro* by hypoxia. Another notable consequence of ACC hypoxia was to induce tumoral vascular mimicry and cell migration invasion as a response to VEGF-A secretion (21, 29).

2.2.3 CIRT Is Valuable for Radioresistant and Hypoxic Tumors

Peschke et al. (30) found on murine models of radioresistant prostate carcinomas that the TCD50 were 32.9 Gy for CIRT and 75.7 Gy for photon RT for single dose irradiation, and 38.0 Gy for CIRT and 90.6 Gy for photon radiotherapy for multiple-dose irradiation. This observation suggested that CIRT was more potent than photon radiotherapy for intrinsically radioresistant tumors, which is the case for ACC. In addition, Grimes et al. (31) evidenced that carbon ion beams had a lower oxygen enhancement ratio (OER) than proton beams, in particular towards the Bragg peak where the LET substantially increased for carbon beams, making CIRT valuable in case of hypoxic tumors. Nevertheless, Antonovic et al. (32) underlined that hypoxia could anyhow influence the outcome of CIRT because of the non-negligible OER of the low LET contributions in the spread-out Bragg peak (SOBP). Taking into account inter-fraction local oxygenation changes, occurring after tumor shrinkage (even for hypoxic tumors), CIRT OER was estimated around 1.2. Finally, using a glioma model, Liu et al. (33) demonstrated that CIRT superiority in tumorigenesis and angiogenesis inhibition compared with photon beams, resulted from modulation of VEGF level in the tumor micro-environment (TME).

2.3 CIRT May Control ACC Tumoral Invasion Properties

2.3.1 Perineural Invasion Is a Characteristic Feature of ACC Local Malignancy

ACCs are characterized by an elevated propensity to locally invade surrounding tissues through perineural invasion (PNI). Shan et al. (34) demonstrated that the BDNF/TrkB axis plays a causative role in ACC PNI. Gao et al. (35) found that the CCL5/CCR5 axis increases salivary ACC PNI invasion and that blocking this chemokine axis inhibited perineural invasion in ACC cell lines. CCR5 chemokine receptor expression was elevated in salivary ACC tissue samples. Kobayashi et al. (36) observed that NGF and TrkA signaling contributed to PNI, and that both were expressed in around 65% of ACC patients.

2.3.2 CIRT Might Control Tumoral Invasion

Fujita et al. (37) demonstrated that CIRT irradiation decreased tumor cell mobility through a process involving ubiquitinoylation and proteasome destruction of Rac1 and RhoA proteins. Rieken et al. (38) also found that CIRT decreased tumor integrin expression 24h after irradiation, and significantly reduced glioma cell migration. Matsumoto et al. (39) observed that CIRT could reduce the metastatic abilities of malignant melanoma cells (including cell migration, invasion, and adhesion), both *in vitro* and *in vivo*, in murine models.

3 IMMUNOLOGICAL RATIONALE OF CIRT FOR ACC

3.1 ACC Tumoral Immunology

3.1.1 ACC Cell Immunogenicity Is Limited to Few Tumor-Associated Antigens

ACC cells express few tumor-specific neo-antigens (TNA) against which specific anti-tumor immune responses could be directed, which is explained by their low tumoral mutation burden (TMB). Based on 60 ACC tumor samples, Ho et al. (40) estimated that ACC TMB was around 0.31 non-silent mutation per megabase. Nevertheless, TMB-high ACCs have already been described, either microsatellite-instable (MSI) or POLE-mutated, but these cases represent only a minority of ACC patients (41). Consequently, T-cell receptor (TCR) clonotype diversity in ACCs is usually lower than in most other solid tumor types and CD8 tumor-infiltrating lymphocytes (TIL) are rare (41). On the other hand, ACC cells express diverse types of tumor-associated antigens (TAA), in particular cancer-testis antigen (CTA). Based on 84 head and neck (HN) ACC tumor samples, Veit et al. (42) found that NY-ESO-1 and pan-MAGE CTA were significantly expressed in 57.1% and 31.2% of ACC patients, respectively. In addition, tumor expression of these two CTA has been found to be linked to a worse prognosis, since median overall survival (OS) was 282 months in the absence of NY-ESO-1 and pan-MAGE expression, 190.5 months when one of these two antigens was present, and only 90.5 months in case of simultaneous co-expression. Beppu et al. (43) estimated that MAGE-A CTA was detected in 60% of ACC tumors and represented an independent risk factor for locoregional recurrence. Finally, in addition to CTA, ACC also expresses less immunogenic tissue-differentiation TAA. Prostate-specific membrane antigen (PSMA) expression without predictive value was found in 94% of ACC patients (44).

3.1.2 ACC Cells Evade Immune Surveillance by Regulating the Expression of Membrane Receptors

Based on immunohistochemistry (IHC) analyses on 36 ACC tumor samples, Mosconi et al. (45) found that ACC expressed a high level of inhibitory immune membrane proteins, particularly PD-L2 and HLA-G. Notably, PD-L1 expression was systematically negative, and CTLA-4 expression was low, which are the targets of most current immune checkpoint inhibitors. PD-L2 expression has a prognosis value: Chang et al. (46) demonstrated that low PD-L2 expression was associated with a shorter RFS in a cohort of 70 patients with malignant salivary gland tumors (including 15 ACC). In addition, ACC cells have a reduced expression of ICAM-1 adhesion protein (47), and IHC analysis of tumor samples demonstrated reduced staining for surface antigens of T cells, NK cells, macrophage (TIA1 and CD68) (47), and antigen-presenting cells (APC) (CD1a and CD83) (45). It has consequently been proposed that the reduced ACC membrane expression of ICAM-1 might promote immune evasion by limiting the ICAM-1/LFA-1-mediated interaction between ACC cells and anti-tumoral immune cells. Conversely, high ICAM-1 expression was associated with a significantly better DFS for ACC (47).

3.1.3 ACC Tumoral Micro-Environment Is Characterized by a Pro-Tumoral Immune Polarization

ACC TME is characterized by a pro-tumoral polarization. Based on WES of 76 malignant salivary tumor samples, including ACC, myoepithelial carcinomas (MECA) and salivary duct carcinomas (SDC), Linxweiler et al. (48) demonstrated that ACC had the highest infiltration of M2-polarized tumor-associated macrophages (TAM) and of myeloid-derived suppressor cells (MDSC), among all types of salivary gland carcinomas. Simultaneously, ACC TME had the lowest infiltration of anti-tumoral immune cells, with a T-cell exclusion phenotype characterized by a limited population of innate immunity cells (NK cells, mast cell, neutrophils, macrophages, and eosinophils), of APC [dendritic cells (DC)], and lymphocytes (CD8 T cells; Th1, Th2, and Th17 CD4 T cells; follicular helper T cells; regulator T cells; γδ T cells; and B cells). Sridharan et al. (49) demonstrated that alterations in the PI3K and the WNT pathways (in particular, involving FGF17, BCL2, beta-catenin, and BAMBI genes) strongly correlated with a lack of immune-cell infiltrates in ACC TME. In addition, it was found that cytokine landscape of ACC TME contributed to its pro-tumoral properties: CCL2 chemokine produced by ACC cells recruit M2-polarized TAM, which, in response, increase tumor cell invasive and migrative properties by secreting glial cell line-derived neurotrophic factor (GDNF).

3.2 CIRT and Immune System Modulation

3.2.1 CIRT Increases Tumoral Cell Immunogenicity

Imadome et al. (50) found that CIRT upregulated stress-responsive genes and immunity-related cell-communication genes (notably ICAM1) in tumor cells. At the same time, CIRT increased gene expression of cytokines and chemokines. Six to 36 hours after CIRT irradiation, Ohkubo et al. (51) demonstrated that an increased expression of ICAM-1 membrane receptor could be observed, which interacts with APC through their LFA1 receptors, but which is usually downregulated in ACC tumors (47). Based on murine lung tumor models, it was demonstrated that combination of CIRT with DC inhibited the development of lung metastases (51), while Ando et al. (52) evidenced that CIRT increased tumor cells immunogenicity and DC activation to a higher level than photon beam radiotherapy, as evidenced by greater CD40 and IL-12 level.

3.2.2 CIRT Activates Adaptative Immunity

Hartman et al. (53) found *in vitro* that CIRT and photon beam radiotherapy had common radiobiological properties such as induction of cell cycle arrest, surface expression of immune-modulating molecules, and activation of cytotoxic lymphocytes. Nevertheless, other authors have suggested that CIRT-induced immune activation might be more potent. Spina et al. (54) demonstrated that CIRT could induce a more pro-inflammatory cytokine landscape compared with photon beam radiotherapy on mammary tumor cell lines: high levels of IL-2, IL-1β, and IFNγ were observed after CIRT (compared with an isolated IL-6 increase after photon radiotherapy). Simultaneously, CIRT induced an activated CD8 TIL phenotype in TME, as evidenced by high levels of granzyme B, IL-2, and TNFα expression, while the authors found that photon therapy decreased CD8 TILs. Takahashi et al. (55) demonstrated that, when combined with anti-PD-L1 and anti-CTLA-4 immunotherapies, CIRT substantially increased CD8 TIL infiltrates and HMGB-1 level, a potent danger-associated molecular pattern (DAMP), suggesting a rational therapeutic strategy combining immune checkpoint inhibitors with CIRT.

3.2.3 TME Acquires Anti-Tumoral Polarization After CIRT Irradiation

In a murine glioblastoma model, Chiblak et al. (56) demonstrated that CIRT reduced the population of M2-polarized TAM and MDSC while simultaneously increasing CD8 TILs, compared with photon beam radiotherapy. Xie et al. (57) further evidenced that low-dose whole-body CIRT of mice (up to 0.05Gy) might increase NK cell activity and induce an IFNγ pro-inflammatory cytokine signature. The propensity of CIRT to induce an immune-permissive anti-tumoral TME might be of significant interest for ACC management.

4 CLINICAL CONSIDERATIONS ON ACC IRRADIATION WITH CIRT

4.1 Photon RT Leads to Substantial Toxicity Due to Critical OAR Radiation Exposure

Photon radiotherapy for ACC management usually leads to unsatisfying exposure of organs-at-risk (OAR) with substantial toxicity. On the other hand, CIRT, taking advantage of a superior dose deposition characterized by a Bragg peak, increases OAR sparing.

4.1.1 OAR Toxicity for Head and Neck ACC Treated With Photon RT

Münter et al. (58) irradiated with intensity-modulated radiation therapy (IMRT) 17 ACC localized at the base of the skull or in maxillary sinuses with a median dose of 66Gy observed 20% of grade 3 mucositis. For sinonasal tumors (including 4 ACC patients) treated to the median dose of 70 Gy with IMRT, Madani et al. (59) also found non-negligible radiation-induced toxicity with 14.1% of grade 3 mucositis, 5.1% of grade 3 dysphagia, 5.1% of grade 3 dermatitis, and three cases of asymptomatic radio-necrosis. Lesueur et al. (60) evaluated that lachrymal ACC radiation therapy could be associated with brain radio-necrosis, bone exposure, radiation neuropathy, secondary glaucoma, and radiation neuropathy.

4.1.2 OAR Toxicity for Thoracic ACC Treated With Photon RT

Thoracic ACC RT exposes multiple OARs: the heart, the lungs, the esophagus, the trachea, and the thyroid. Out of 31 tracheal ACC patients treated with photon RT (mean dose of 62 Gy), Levy et al. (61) observed five tracheal stenoses, four dyspnea, five hypothyroidism, and four pericarditis. Je et al. (62) irradiated 13 tracheal ACC patients with photon RT (59.4 Gy in an adjuvant setting and 74.4 Gy in a definitive setting): two patients developed tracheal stenoses, and both died (abrupt respiratory failure after 1 year and tracheal infection after 13 years). Finally, Dracham et al. (63) treated 19 tracheal ACC patients with photon RT (50 Gy for adjuvant and 67.8 Gy for definitive setting) and observed seven grade ≥2 acute pneumonitis and two grade 3 esophagitis.

4.1.3 OAR Toxicity for Digestive and Pelvic ACC Treated With Photon RT

The largest cohort of Bartholin's gland ACC has been reported by Cardosi et al. (2) consisting of 12 patients treated with surgery; seven patients underwent adjuvant RT. One vulva radio-necrosis was observed, followed by a grade 5 sepsis, and one patient developed concomitant digestive and urinary fistulas. It should be recalled that fistulas have a significant impact on the quality of life of the patient. Zelga et al. (64)demonstrated that the simplest and safest treatment of radiation-induced rectovaginal fistulas was a fecal diversion with an ileostomy. While cardia (65) and esophageal (3) ACC exist, no report of RT-induced toxicity with photon RT has been published to this date; nevertheless, CIRT is expected to reduce radiation exposure to the unaffected digestive tract and to the heart.

4.2 Evidence of CIRT by ACC Tumor Site

4.2.1 Materials and Methods

A search was conducted on the PubMed, Medline, Google Scholar, Cochrane library and Web of Science databases using the following keywords: ["particle therapy" or "hadrontherapy" or "carbon ion" or "CIRT" or "heavy ion" or "ion beam" or "ion radiation"] and ["adenoid cystic carcinoma" OR "ACC"]. Search was independently conducted by PL and EO. Inclusion criteria, defined using the PICOS framework, were the following: clinical studies (trials, prospective or retrospectives studies, and case reports) evaluating CIRT for ACC, in any setting, and reporting toxicity and efficacy data. Exclusion criteria were pre-clinical or purely dosimetric studies. References from the selected studies were screened for potential additional articles.

4.2.2 Head and Neck (Primary Tumor)

The current clinical experience of CIRT for ACC is summarized in the **Table 3**. CIRT has been evaluated as a sole modality for definitive irradiation of head and neck ACC by Japanese centers. Mizoe et al. (67) evaluated the efficacy of 64 Gy(RBE) on 236 patients with head and neck cancers, including 69 ACC (mostly from the paranasal sinuses), with 5-year LC and OS of 73% and 68%, respectively. Sulaiman et al. (68) retrospectively described the outcome of all ACC patients treated in the four active CIRT facilities in Japan treated between 2003 and 2014. Overall, 289 ACC patients were treated with a median CIRT dose of 64 Gy (RBE) (ranging between 55.2 Gy(RBE) and 70.4 Gy(RBE)); 2-year OS, PFS, LC were 94%; 68% and 88%, respectively. Two patients died from bleeding ulcers, and 15% of all patients developed grade ≥3 toxicity. Ikawa et al. (71) observed 5-year LC and OS of 78.8% and 58.3% in a cohort of 74 oral non-squamous cell carcinomas, including 34 ACC patients, treated with doses ranging from 57.6 to 64 Gy(RBE). Analyses of specific tumoral localization demonstrated the efficacy of CIRT for ACC arising from the nasopharynx (72) (2-year LC: 88%), from the paranasal sinuses (73)(5-year LC: 51%), from the tongue (74)(5-year LC: 92%), from the parotid (66) (5-year LC: 74.5%), or from the lacrimal gland (69)(5-year LC: 62%).

An alternative approach has been evaluated at the Heidelberg Ion-Beam Therapy Center, using CIRT as a boost to conventional photon radiotherapy. In 2004, Schulz-Ertner et al. (70) obtained a 3-year LC of 62% on a series of 21 patients affected by head and neck unfavorable and locally advanced ACC, using an 18 Gy(RBE) CIRT boost coupled to photon radiotherapy delivering 54 Gy. Similarly, using CIRT as an 18-24 Gy(RBE) boost to IMRT photon radiotherapy (50-56Gy), Akbaba et al. (76) treated 59 nasopharyngeal ACC patients to a 2-year LC, distant PFS and OS of 83% 81% and 87%. Seven patients developed acute grade 3 toxicities (mucositis, dysphagia, and odynophagia) and four patients had late grade 3 toxicities (locked jaw, tympanic effusion, and hypopituitarism). Akbaba et al. (75) treated 227 patients for sinonasal ACC with an 18-24 Gy(RBE) CIRT boost added to IMRT radiotherapy (48-56Gy). With a median follow-up of 50 months, 3-year local control was 79% when treated in a definitive context and 82% when treated in an adjuvant setting. Acute toxicity was observed for 34.4% of the patients in a definitive setting and for 41.6% in an adjuvant setting. CIRT as a boost to IMRT has also been evaluated for laryngeal ACC (80), demonstrating an excellent local control on a cohort of eight ACC patients without any relapse at 24 months. Lacrimal ACC has also been treated with a CIRT boost (81), with a 2-year local control of 93%.

4.2.3 Head and Neck (Reirradiation)

Jensen et al. (82) re-irradiated 52 recurrent head and neck ACC with a median dose of 51 Gy(RBE). Median follow-up was 14 months; one-year local and distant controls were 70.3% and 72.6%

TABLE 3 | Clinical studies evaluating carbon ion radiation therapy (CIRT) for adenoid cystic carcinoma (ACC) irradiation.

Indication	Study	Year	Center	Type	Number	CIRT fractionation	Efficacy	Grade ≥3 toxicity	Grade 4-5 toxicity (detail)
Head and neck (diverse sites)	Schulz-Ertner et al. (66)	2004	Heidelberg	Retrospective	21 ACC (out of 152 tumors)	18 Gy(RBE) CIRT boost + 54 Gy photon RT.	3-year LRC: 62%. 3-year OS: 75%.	Acute: 2 pts. Late: 0 pt (10%). (ACC cohort)	Ø (ACC cohort)
	Mizoe et al. (64)	2011	NIRS	Phase II	69 ACC (out of 236 tumors)	57.6-64 Gy(RBE)/ 16 fr	5-year LC: 73%. 5-year OS: 68%.	Acute: 39 pts (56%). Late: 4 pts (6%).	4 G4 blindness (late).
	Sulaiman et al. (65)	2017	NIRS, Hyogo, Gunma, HIMAT	Retrospective	289 ACC	57.6-64 Gy(RBE)/ 16 fr	5-year LC: 68%. 5-year OS: 74%.	Acute: 92 pts (32%). Late: 48 pts (17%).	2 G5 hemorrhage, 9 G4 blindnesses, 1 G4 brain necrosis(late).
	Ikawa et al. (67)	2019	NIRS	Retrospective	34 ACC (out of 74 tumors)	57.6-64 Gy(RBE)/ 16 fr	5-year LC: 75.2%. 5-year OS: 65.7%.	Acute: 43 pts (58%). Late: 22 pts (30%) (10 G3 osteonecrosis). (Whole cohort)	3 G4 blindness (late). (Whole cohort)
Nasopharynx	Abe et al. (68)	2018	NIRS, Hyogo, Gunma, HIMAT	Retrospective	43 ACC	57.6-64 Gy(RBE)/ 16 fr	2-year LC: 88%. 2-year OS: 84%.	Acute: 14 pts (33%). Late: 9 pts (21%).	2 G5 pharyngeal hemorrhage, 1 G4 blindness (late).
	Akbaba et al. (69)	2019	Heidelberg	Retrospective	59 ACC	18-24Gy(RBE) CIRT boost + 50-56 Gy photon RT.	5-year LC: 49%. 5-year OS: 69%.	Acute: 7 pts (12%). Late: 4 pt (7%).	Ø
Paranasal sinuses	Akbaba et al. (70)	2019	Heidelberg	Retrospective	227 ACC	15-18Gy(RBE) CIRT boost + 48-56 Gy photon RT.	3-year LRC: 79% (primary) - 82% (postoperative). 3-year OS: 64% (primay) - 79% (postoperative).	Acute: 88 pts (39%). Late: 26 pts (11%).	Ø
	Hagiwara et al. (71)	2020	NIRS	Retrospective	22 ACC	57.6-64 Gy(RBE)/ 16 fr	5-year LC: 51%. 5-year OS: 62.7%.	Acute: 0 pts. Late: 9 pts (41%).	6 G4 blindness, 1 G4 brain necrosis (late).
Tongue	Koto et al. (72)	2016	NIRS	Retrospective	18 ACC	57.6-64 Gy(RBE)/ 16 fr	5-year LC: 92%. 5-year OS: 72%.	Acute: 10 pts (56%). Late: 3 pts (16.7%).	Ø
Parotid	Koto et al. (73)	2017	NIRS	Retrospective	16 ACC	57.6-64 Gy(RBE)/ 16 fr	5-year LC: 74.5%. 5-year OS: 70.1%.	Acute: 1 pt (6%). Late: 8 pts (50%).	1 G4 blindess (late).
Lacrimal gland	Hayashi et al. (74)	2018	NIRS	Retrospective	16 ACC (out of 33 tumors)	57.6-64 Gy(RBE)/ 16 fr	5-year LC: 62%. 5-year OS: 65%.	Acute: 0 pt. Late: 22 pts (67%). (Whole cohort)	12 G4 blindness, 2 G4 brain necrosis (late). (Whole cohort)
	Akbaba et al. (75)	2019	Heidelberg	Retrospective	18 ACC (out of 24 tumors)	18-24Gy(RBE) CIRT boost + 50-54 Gy photon RT.	5-year LC: 90%. 5-year OS: 94%.	Acute: 3 pts (13%). Late: 2 pt (8%). (Whole cohort)	Ø
Larynx	Akbaba et al. (76)	2018	Heidelberg	Retrospective	8 ACC (out of 15 tumors)	18-24Gy(RBE) CIRT boost + 50-54 Gy photon RT.	3-year LRC: 100%. 3-year OS: 100%.	Acute: 4 pts (27%). Late: 0 pt. (Whole cohort)	Ø
Tracheobronchial tree	Chen et al. (77)	2021	Shanghai	Retrospective	18 ACC	66-72.6 Gy(RBE)/ 22-23 fr	2-year LC: 100%. 2-year OS: 100%.	Acute: 0 pt. Late: 1 pt (6%).	1 G4 tracheal stenosis (late).
	Högerle et al. (78)	2019	Heidelberg	Retrospective	7 ACC treated with CIRT (out of 38 ACC)	24Gy(RBE) CIRT boost + 50-54 Gy photon RT (n=4). 60-63 Gy(RBE) (n=2)	1-year LC: 100%. 1-year OS: 100%.	Acute: 1 pt (14%). Late: 0 pt. (CIRT cohort)	1 G4 stomatitis (acute).
Bartholin's gland	Bernhardt et al. (79)	2018	Heidelberg	Retrospective	1 ACC	24Gy(RBE) CIRT boost + 50 Gy photon RT	NA	Ø	Ø

(Continued)

TABLE 3 | Continued

Indication	Study	Year	Center	Type	Number	CIRT fractionation	Efficacy	Grade ≥3 toxicity	Grade 4-5 toxicity (detail)
Reirradiation (Head and neck, diverse sites)	Jensen et al. (80)	2015	Heidelberg	Retrospective	48 ACC	51 [36-74] Gy (RBE)	1-year LC: 70.3%. 1-year OS: 81.8%.	Acute: 0 pt. Late: 8 pt (6.5%). (Whole cohort)	2 G4 carotid artery haemorrhage (late).
	Held et al. (81)	2019	Heidelberg	Retrospective	124 ACC (out of 229 tumors)	51 [30-66] Gy (RBE)	1-year LC: 60%. 1-year OS: 72%.	Acute: 7 pt. Late: 18 pt. (Whole cohort)	2 G4 laryngeal edema (acute). 2 G4 blindness, 1 brain necrosis, 1 vascular hemorrhage (late). (Whole cohort)
	Hayashi et al. (82)	2019	NIRS	Retrospective	17 ACC (out of 48 tumors)	54 [40-64] Gy (RBE)	2-year LC: 40.5%. 2-year OS: 59.6%.	Acute: 4 pt. Late: 25 pt. (Whole cohort)	1 G5 brain necrosis, 9 G4 blindness, 1 G4 brain necrosis, 1 G4 infection, 1 G4 arterial injury (late). (Whole cohort)
	Vischioni et al. (83)	2020	CNAO	Retrospective	38 ACC (out of 51 tumors)	60 [45-68.8] Gy (RBE)	2-year PFS: 52.2%. 2-year OS: 64%.	Acute: 2 pt (3.9%). Late: 3 pt (17.5%). (Whole cohort)	Ø

G, grade; LC, local control; LRC, locoregional control; OS, overall survival; PFS, progression-free survival; pts, patients.

respectively. Held et al. (83) re-irradiated 124 ACC, in a cohort of 229 patients (54%) with recurrent head and neck cancers. The median reirradiation dose was 51 Gy(RBE). Median PFS and OS were respectively 24.2 months and 26.1 months. Hayashi (84) evaluated CIRT reirradiation on 17 ACC on a cohort of 48 patients with recurrent head and neck tumors. The median reirradiation doses ranged between 40.0 Gy(RBE) and 64 Gy(RBE) in 8 to 16 fractions. The median follow-up was 27.1 months; two-year local control, locoregional control, PFS and OS were 40.5%, 33.5%, 29.4% and 59.6% respectively. There was 10.4% of acute grade 3 toxicity and 37.5% of late grade 3 toxicity, including one grade 5 central nervous system necrosis. Finally, Vischioni et al. (85) evaluated CIRT re-irradiation on 38 ACC in a cohort of 51 patients (75%). The median prescription dose was 60 Gy(RBE). The median follow-up was 19 months; two-year PFS and OS were 52.2% and 64%. Two other studies have CIRT for head and neck recurrent tumor re-irradiation, but ACC histologies only represented a minority of the included cases: Combs et al. (77), who treated four ACC on a cohort of 28 patients, and Gao et al. (78) with 10 ACC on a cohort of 141 patients.

4.2.4 Thoracic, Abdomen and Pelvis

Chen et al. (86) treated 18 patients with tracheobronchial adenoid cystic carcinoma with definitive CIRT treatment. Prescription doses ranged between 66 Gy(RBE) and 72 Gy(RBE). With a median FU of 20.7 months, the overall response rate (ORR) was 88.2%, and the 2-year OS, local control rate, and PFS were respectively 100%, 100%, and 61.4%. One G4 tracheal stenosis was observed, but no other grade 3 toxicity. Högerle et al. (79) treated six patients with tracheal ACC with CIRT (four patients received CIRT as a targeted boost added to photon irradiation); one patient was treated in an adjuvant setting, while six patients received definitive CIRT treatment. Prescription doses ranged between 60 Gy(RBE) and 74.4 Gy(RBE). One-year OS, freedom from local progression, and freedom from distant progression were both 100%. One grade 4 stomatitis was observed, but no other G3 toxicity. CIRT has also been proposed for gynecological ACC (87), but available clinical data is limited; to this date, only one patient seems to have been treated for a Bartholin's gland ACC, with a 24 Gy(RBE) CIRT boost added to IMRT (50 Gy) (88).

4.3 Present and Future Considerations for CIRT Practice

4.3.1 Treatment Planning System Considerations

Molinelli et al. (89) evaluated the possible prescription corrections in CIRT planning when comparing the modified microdosimetric kinetic model (mMKM) and the local effect model (LEM) relative biological effectiveness (RBE) models; overall, a 64 Gy(RBE) prescribed to the target volumes based on the mMKM model was found to be close to that of 68.8 Gy (RBE) with the LEM model. A new calculation of the OAR dose constraints, adapted to the RBE calculation model was therefore recommended in order to enhance the target control probability, such as for brain stem and optic pathway (90, 91).

For a full CIRT irradiation, ACC is generally irradiated with a sequential strategy consisting of a first phase of nine to ten fractions to a low-risk volume (including the surgical bed and zones at risk of perineural spread), followed by a second phase of six to seven fractions to a high risk volume (boost), with a unique nominal dose per fraction, according to the protocol adopted in Japan since 1997 (67). In this context, CIRT is usually delivered with a limited number of beams, typically two or three, achieving both a high conformation and an improved normal tissue sparing. However, in the absence of isocentric CIRT gantry, only fixed beam irradiations are available (which is for instance the case at CNAO) and it is difficult to change the beam arrangement between the two sequential phases: as a consequence, part of the low-risk volume receives unintended dose from the beam paths of the boost phase. A simultaneous integrated boost (SIB) approach is thus being evaluated at CNAO, in comparison to the sequential protocol, to improve the dose distribution of the two target volumes.

Robust planning is of prime importance for CIRT, to take into account range and positioning uncertainties (92). Finally, the use

of Monte-Carlo algorithms combined with GPU-running processors make it possible to carry out extremely fast calculations, thus allowing the combination of accurate physical dose computation with biological effects modelling as well as inverse planning for CIRT, with a reasonable calculation time (93).

4.3.2 Monitoring Tumoral Response and Anatomical Changes

The predicted range of carbon ion beams should be calculated as precisely as possible during treatment planning and treatment delivery. While small errors in margins quantification with photon RT leads to target underdosage, such errors with CIRT may have critical consequences; due to the sharp dose diminution at the distal edge of the Bragg peak, parts of the tumor might not receive any dose. The location of the distal dose fall-off notably depends on anatomical modifications, and minor anatomical changes might consequently negatively affect target coverage as well as substantially increase OAR toxicity. For head and neck ACC irradiation, where multiple nearby OARs have critical functions, CIRT might thus benefit from advanced techniques to monitor tumor response and potential anatomical changes during irradiation. This could for example be conveniently done by systematic CT scan reevaluations, the implementation of image guided CIRT, or robust planning. The dosimetric interest of adaptative planning for CIRT, relying on daily CT imaging, has been demonstrated for pancreatic irradiation (94) and might be conveniently implemented in the near future in clinical practice for hadrontherapy, possibly relying on automatic tools (95, 96). Fiorina et al. (97) demonstrated that in-beam positron emission tomography (PET) imageries allowed detection of morphological changes for head and neck proton therapy in clinical practice; while the primary fluence is lower in CIRT which introduces additional uncertainties compared to proton treatments, such devices have been successfully evaluated in phantoms for CIRT (98, 99) with a 1mm to 2mm agreement on the range prediction.

5 DISCUSSION

We have detailed the rationale to use CIRT for ACC management, based on immunological, molecular, and pathological considerations, even though no *in vitro* or preclinical study have specifically evaluated CIRT irradiation on ACC cell lines to date. In addition, clinical data demonstrate that CIRT is associated with superior local control compared to conventional photon radiotherapy. In the future, further improvement of the outcomes of ACC treatment with CIRT may be possible by personalizing the treatment by taking into account ACC molecular and pathological features. Vered et al. (100) found that around 85% of ACC expressed EGFR receptors, which motivated the use of anti-EGFR systemic therapies in addition to radiation therapy, as radiosensitizers and to increase micrometastatic disease control. Adeberg et al. (101) recently evaluated adjunction of Cetuximab to photon radiation therapy (54 Gy) with a CIRT boost [24 Gy(RBE)], in 33 head and neck ACC patients. The toxicity was noticeable since 17% of the patients developed grade 3 rashes, 22% grade 3 radiation dermatitis and 48% grade 3 mucositis, but tumoral control was encouraging with a three-year DFS and OS of 67% and 90%, respectively. The ongoing NCT02942693 trial is a 2-arm study evaluating six weeks of Apatinib, an anti-VEGFR2 drug, followed by mixed irradiation with 56 Gy in photons and 15 Gy(RBE) in carbons. Immunotherapy combined with CIRT, although potentially attractive, considering the immunomodulatory effects of CIRT, is not currently evaluated in clinical trials.

However, CIRT might face competition with low-LET RT techniques for ACC management in the future. Takagi et al. (102) evaluated the outcome of 40 ACC patients treated with proton beam therapy (PBT) and 40 patients treated with CIRT; no difference between PBT and CIRT were observed in terms of OS, PFS, or local control at 5 years. However, in addition to the inherent weakness of a retrospective non-randomized comparison, there was a significant difference in the equivalent dose prescription between treatment groups in favor of PBT. Patient selection for CIRT (instead of PBT) must consequently be defined; NTCP or dosimetric considerations could be used. In some specific cases, fear of adverse events in case of rapid tumor shrinkage second to CIRT irradiation might justify considering normofractionated PBT irradiation. Reirradiation with photon stereotactic radiotherapy has been evaluated for relapsed head and neck ACC patients (103), with a total dose of 30 Gy in 5 fractions: the 3-year LC of 49% was lower than that observed with CIRT (possibly due to the relatively low prescribed dose), but this technique might be easily implemented in radiotherapy centers where hadrontherapy is not available. Other ongoing trials comparing CIRT with low-LET RT techniques include the ETOILE trial (NCT02838602) comparing CIRT and PBT or photon radiotherapy for radioresistant tumors, including ACC, and the COSMIC trial (NCT04214366) comparing CIRT with a mix of CIRT and photon beam radiotherapy for ACC. In addition, financial sustainability is an issue that may weigh against CIRT compared with other low-LET techniques. Jensen et al. (104) estimated that IMRT with a carbon boost might have a mean survival benefit of 0.86 years for a single head and neck ACC, with an incremental cost-effectiveness ratio of 20.638€ per year.

Finally, other high-LET techniques are currently being investigated for ACC, such as boron neutron capture therapy (BNCT), currently under development in various European and Asian centers. Kato et al. (105) treated one ACC patient to a dose of 14Gy, which was well-tolerated without any grade ≥2 toxicity. Other reports include Kankaanranta et al. (106), who re-irradiated four inoperable recurrent ACC and Aihara et al. (107), who treated four inoperable head and neck ACC (including two recurrent diseases). This latter reported complete response for all patients within 6 months, a median OS of 32 months and no grade ≥3 toxicity.

6 CONCLUSION

The use of CIRT for ACC management is motivated by immunological, molecular and clinicopathological considerations.

Although no prospective randomized trials have been published to this date and might not be easily feasible, due to the rarity of ACCs and the scarce availability of particle beam RT facilities, clinical studies demonstrated that CIRT was well tolerated and associated with a substantial tumor control in diverse clinical situations, especially in advanced unresectable stages. Current technical developments ensure safe treatments.

AUTHOR CONTRIBUTIONS

Conceptualization: PL, BV, YK, and EO. Methodology: PL, BV, YK, and EO. Writing: PL. Review and Editing: PL, BV, MB, RI, SR, VV, AB, LG, LM, RD, RP, LL, VC, HM, SC, YK, and EO. Supervision: BV, YK, and EO. All authors contributed to the article and approved the submitted version.

REFERENCES

1. Coca-Pelaz A, Rodrigo JP, Bradley PJ, Vander Poorten V, Triantafyllou A, Hunt JL, et al. Adenoid Cystic Carcinoma of the Head and Neck–An Update. *Oral Oncol* (2015) 51:652–61. doi: 10.1016/j.oraloncology.2015.04.005
2. Cardosi RJ, Speights A, Fiorica JV, Grendys EC, Hakam A, Hoffman MS. Bartholin's Gland Carcinoma: A 15-Year Experience. *Gynecol Oncol* (2001) 82:247–51. doi: 10.1006/gyno.2001.6304
3. Cerar A, Jutersek A, Vidmar S. Adenoid Cystic Carcinoma of the Esophagus. A Clinicopathologic Study of Three Cases. *Cancer* (1991) 67:2159–64. doi: 10.1002/1097-0142(19910415)67:8<2159::aid-cncr2820670826>3.0.co;2-e
4. Bishop J, Thompson LDR, Wakely P, Weinreb I. *AFIP Atlas: Tumors of the Salivary Glands. fifth series* Vol. 5. Arlington VA: ARP Press.
5. Ellington CL, Goodman M, Kono SA, Grist W, Wadsworth T, Chen AY, et al. Adenoid Cystic Carcinoma of the Head and Neck: Incidence and Survival Trends Based on 1973-2007 Surveillance, Epidemiology, and End Results Data. *Cancer* (2012) 118:4444–51. doi: 10.1002/cncr.27408
6. Ciccolallo L, Licitra L, Cantú G, Gatta G. EUROCARE Working Group. Survival From Salivary Glands Adenoid Cystic Carcinoma in European Populations. *Oral Oncol* (2009) 45:669–74. doi: 10.1016/j.oraloncology.2008.10.010
7. Gatta G, Botta L, Sánchez MJ, Anderson LA, Pierannunzio D, Licitra L. EUROCARE Working Group: Prognoses and Improvement for Head and Neck Cancers Diagnosed in Europe in Early 2000s: The EUROCARE-5 Population-Based Study. *Eur J Cancer* (2015) 51:2130–43. doi: 10.1016/j.ejca.2015.07.043
8. Orlandi E, Iacovelli NA, Bonora M, Cavallo A, Fossati P. Salivary Gland. Photon Beam and Particle Radiotherapy: Present and Future. *Oral Oncol* (2016) 60:146–56. doi: 10.1016/j.oraloncology.2016.06.019
9. Pötter R, Prott FJ, Micke O, Haverkamp U, Wagner W, Willich N. Results of Fast Neutron Therapy of Adenoid Cystic Carcinoma of the Salivary Glands. *Strahlenther Onkol* (1999) 175(Suppl 2):65–8. doi: 10.1007/BF03038892
10. Liu B, Mitani Y, Rao X, Zafereo M, Zhang J, Zhang J, et al. Spatio-Temporal Genomic Heterogeneity, Phylogeny, and Metastatic Evolution in Salivary Adenoid Cystic Carcinoma. *J Natl Cancer Inst* (2017) 109. doi: 10.1093/jnci/djx033
11. Ho AL, Dunn L, Sherman EJ, Fury MG, Baxi SS, Chandramohan R, et al. A Phase II Study of Axitinib (AG-013736) in Patients With Incurable Adenoid Cystic Carcinoma. *Ann Oncol* (2016) 27:1902–8. doi: 10.1093/annonc/mdw287
12. Ferrarotto R, Mitani Y, Diao L, Guijarro I, Wang J, Zweidler-McKay P, et al. Activating NOTCH1 Mutations Define a Distinct Subgroup of Patients With Adenoid Cystic Carcinoma Who Have Poor Prognosis, Propensity to Bone and Liver Metastasis, and Potential Responsiveness to Notch1 Inhibitors. *J Clin Oncol* (2017) 35:352–60. doi: 10.1200/JCO.2016.67.5264
13. Ferrarotto R, Wirth LJ, Muzaffar J, Rodriguez CP, Xia B, Perez CA, et al. 919mo ACCURACY a Phase II Trial of AL101, a Selective Gamma Secretase Inhibitor, in Subjects With Recurrent/Metastatic (R/M) Adenoid Cystic Carcinoma (ACC) Harboring Notch Activating Mutations (Notchmut). *Ann Oncol* (2020) 31:S663. doi: 10.1016/j.annonc.2020.08.1034
14. Ho AS, Ochoa A, Jayakumaran G, Zehir A, Mayor CV, Tepe J, et al. Genetic Hallmarks of Recurrent/Metastatic Adenoid Cystic Carcinoma. *J Clin Invest* (2019) 129:4276–89. doi: 10.1172/JCI128227
15. Perzin KH, Gullane P, Clairmont AC. Adenoid Cystic Carcinomas Arising in Salivary Glands: A Correlation of Histologic Features and Clinical Course. *Cancer* (1978) 42:265–82. doi: 10.1002/1097-0142(197807)42:1<265::aid-cncr2820420141>3.0.co;2-z
16. Spiro RH, Huvos AG, Strong EW. Adenoid Cystic Carcinoma of Salivary Origin. A Clinicopathologic Study of 242 Cases. *Am J Surg* (1974) 128:512–20. doi: 10.1016/0002-9610(74)90265-7
17. van Weert S, van der Waal I, Witte BI, Leemans CR, Bloemena E. Histopathological Grading of Adenoid Cystic Carcinoma of the Head and Neck: Analysis of Currently Used Grading Systems and Proposal for a Simplified Grading Scheme. *Oral Oncol* (2015) 51:71–6. doi: 10.1016/j.oraloncology.2014.10.007
18. Bell D, Roberts D, Kies M, Rao P, Weber RS, El-Naggar AK. Cell Type-Dependent Biomarker Expression in Adenoid Cystic Carcinoma: Biologic and Therapeutic Implications. *Cancer* (2010) 116:5749–56. doi: 10.1002/cncr.25541
19. Glowa C, Karger CP, Brons S, Zhao D, Mason RP, Huber PE, et al. Carbon Ion Radiotherapy Decreases the Impact of Tumor Heterogeneity on Radiation Response in Experimental Prostate Tumors. *Cancer Lett* (2016) 378:97–103. doi: 10.1016/j.canlet.2016.05.013
20. Masunaga S, Ando K, Uzawa A, Hirayama R, Furusawa Y, Koike S, et al. The Radiosensitivity of Total and Quiescent Cell Populations in Solid Tumors to 290 MeV/u Carbon Ion Beam Irradiation *in vivo*. *Acta Oncol* (2008) 47:1087–93. doi: 10.1080/02841860701821999
21. Wang H-F, Wang S-S, Zheng M, Dai L-L, Wang K, Gao X-L, et al. Hypoxia Promotes Vasculogenic Mimicry Formation by Vascular Endothelial Growth Factor A Mediating Epithelial-Mesenchymal Transition in Salivary Adenoid Cystic Carcinoma. *Cell Prolif* (2019) 52:e12600. doi: 10.1111/cpr.12600
22. Chen W, Ren X, Wu J, Gao X, Cen X, Wang S, et al. HSP27 Associates With Epithelial-Mesenchymal Transition, Stemness and Radioresistance of Salivary Adenoid Cystic Carcinoma. *J Cell Mol Med* (2018) 22:2283–98. doi: 10.1111/jcmm.13510
23. Shimoda M, Sugiura T, Imajyo I, Ishii K, Chigita S, Seki K, et al. The T-Box Transcription Factor Brachyury Regulates Epithelial–Mesenchymal Transition in Association With Cancer Stem-Like Cells in Adenoid Cystic Carcinoma Cells. *BMC Cancer* (2012) 12:377. doi: 10.1186/1471-2407-12-377
24. Kobayashi Y, Sugiura T, Imajyo I, Shimoda M, Ishii K, Akimoto N, et al. Knockdown of the T-Box Transcription Factor Brachyury Increases Sensitivity of Adenoid Cystic Carcinoma Cells to Chemotherapy and Radiation *In Vitro*: Implications for a New Therapeutic Principle. *Int J Oncol* (2014) 44:1107–17. doi: 10.3892/ijo.2014.2292
25. de Mendonça RP, Chemelo GP, Mitre GP, Branco DC, da Costa NMM, Tuji FM, et al. Role of Hypoxia-Related Proteins in Adenoid Cystic Carcinoma Invasion. *Diagn Pathol* (2020) 15:47. doi: 10.1186/s13000-020-00967-3
26. Liu C, Li S, Pang F, Wu H, Chai L, Liang C, et al. Autophagy-Related Gene Expression Regulated by HIF-1α in Salivary Adenoid Cystic Carcinoma. *Oral Dis* (2019) 25:1076–83. doi: 10.1111/odi.13058
27. Greijer AE, van der Wall E. The Role of Hypoxia Inducible Factor 1 (HIF-1) in Hypoxia Induced Apoptosis. *J Clin Pathol* (2004) 57:1009–14. doi: 10.1136/jcp.2003.015032
28. Chen Z, Wu H, Huang S, Li W, Zhang S, Zheng P, et al. Expression of BNIP3 and its Correlations to Hypoxia-Induced Autophagy and Clinicopathological Features in Salivary Adenoid Cystic Carcinoma. *Cancer Biomark* (2015) 15:467–75. doi: 10.3233/CBM-150474
29. Wei X, Chen Y, Jiang X, Peng M, Liu Y, Mo Y, et al. Mechanisms of Vasculogenic Mimicry in Hypoxic Tumor Microenvironments. *Mol Cancer* (2021) 20:7. doi: 10.1186/s12943-020-01288-1
30. Peschke P, Karger CP, Scholz M, Debus J, Huber PE. Relative Biological Effectiveness of Carbon Ions for Local Tumor Control of a Radioresistant

Prostate Carcinoma in the Rat. *Int J Radiat Oncol Biol Phys* (2011) 79:239–46. doi: 10.1016/j.ijrobp.2010.07.1976
31. Grimes DR. Estimation of the Oxygen Enhancement Ratio for Charged Particle Radiation. *Phys Med Biol* (2020) 65:15NT01. doi: 10.1088/1361-6560/ab9371
32. Antonovic L, Lindblom E, Dasu A, Bassler N, Furusawa Y, Toma-Dasu I. Clinical Oxygen Enhancement Ratio of Tumors in Carbon Ion Radiotherapy: The Influence of Local Oxygenation Changes. *J Radiat Res* (2014) 55:902–11. doi: 10.1093/jrr/rru020
33. Liu Y, Liu Y, Sun C, Gan L, Zhang L, Mao A, et al. Carbon Ion Radiation Inhibits Glioma and Endothelial Cell Migration Induced by Secreted VEGF. *PloS One* (2014) 9:e98448. doi: 10.1371/journal.pone.0098448
34. Shan C, Wei J, Hou R, Wu B, Yang Z, Wang L, et al. Schwann Cells Promote EMT and the Schwann-Like Differentiation of Salivary Adenoid Cystic Carcinoma Cells *via* the BDNF/TrkB Axis. *Oncol Rep* (2016) 35:427–35. doi: 10.3892/or.2015.4366
35. Gao T, Shen Z, Ma C, Li Y, Kang X, Sun M. The CCL5/CCR5 Chemotactic Pathway Promotes Perineural Invasion in Salivary Adenoid Cystic Carcinoma. *J Oral Maxillofac Surg* (2018) 76:1708–18. doi: 10.1016/j.joms.2018.02.009
36. Kobayashi K, Ando M, Saito Y, Kondo K, Omura G, Shinozaki-Ushiku A, et al. Nerve Growth Factor Signals as Possible Pathogenic Biomarkers for Perineural Invasion in Adenoid Cystic Carcinoma. *Otolaryngol Head Neck Surg* (2015) 153:218–24. doi: 10.1177/0194599815584762
37. Fujita M, Imadome K, Shoji Y, Isozaki T, Endo S, Yamada S, et al. Carbon-Ion Irradiation Suppresses Migration and Invasiveness of Human Pancreatic Carcinoma Cells MIAPaCa-2 *via* Rac1 and RhoA Degradation. *Int J Radiat Oncol Biol Phys* (2015) 93:173–80. doi: 10.1016/j.ijrobp.2015.05.009
38. Rieken S, Habermehl D, Wuerth L, Brons S, Mohr A, Lindel K, et al. Carbon Ion Irradiation Inhibits Glioma Cell Migration Through Downregulation of Integrin Expression. *Int J Radiat Oncol Biol Phys* (2012) 83:394–9. doi: 10.1016/j.ijrobp.2011.06.2004
39. Matsumoto Y, Furusawa Y, Uzawa A, Hirayama R, Koike S, Ando K, et al. Antimetastatic Effects of Carbon-Ion Beams on Malignant Melanomas. *Radiat Res* (2018) 190:412–23. doi: 10.1667/RR15075.1
40. Ho AS, Kannan K, Roy DM, Morris LGT, Ganly I, Katabi N, et al. The Mutational Landscape of Adenoid Cystic Carcinoma. *Nat Genet* (2013) 45:791–8. doi: 10.1038/ng.2643
41. Wang F, Xie X, Song M, Ji L, Liu M, Li P, et al. Tumor Immune Microenvironment and Mutational Analysis of Tracheal Adenoid Cystic Carcinoma. *Ann Transl Med* (2020) 8:750. doi: 10.21037/atm-20-3433
42. Veit JA, Heine D, Thierauf J, Lennerz J, Shetty S, Schuler PJ, et al. Expression and Clinical Significance of MAGE and NY-ESO-1 Cancer-Testis Antigens in Adenoid Cystic Carcinoma of the Head and Neck. *Head Neck* (2016) 38:1008–16. doi: 10.1002/hed.24403
43. Beppu S, Ito Y, Fujii K, Saida K, Takino H, Masaki A, et al. Expression of Cancer/Testis Antigens in Salivary Gland Carcinomas With Reference to MAGE-A and NY-ESO-1 Expression in Adenoid Cystic Carcinoma. *Histopathology* (2017) 71:305–15. doi: 10.1111/his.13226
44. Klein Nulent TJW, Valstar MH, Smit LA, Smeele LE, Zuithoff NPA, de Keizer B, et al. Prostate-Specific Membrane Antigen (PSMA) Expression in Adenoid Cystic Carcinoma of the Head and Neck. *BMC Cancer* (2020) 20:519. doi: 10.1186/s12885-020-06847-9
45. Mosconi C, de Arruda JAA, de Farias ACR, Oliveira GAQ, de Paula HM, Fonseca FP, et al. Immune Microenvironment and Evasion Mechanisms in Adenoid Cystic Carcinomas of Salivary Glands. *Oral Oncol* (2019) 88:95–101. doi: 10.1016/j.oraloncology.2018.11.028
46. Chang H, Kim JS, Choi YJ, Cho J-G, Woo J-S, Kim A, et al. Overexpression of PD-L2 Is Associated With Shorter Relapse-Free Survival in Patients With Malignant Salivary Gland Tumors. *Onco Targets Ther* (2017) 10:2983–92. doi: 10.2147/OTT.S134589
47. Shirai A, Furukawa M, Yoshizaki T. Expression of Intercellular Adhesion Molecule (ICAM)-1 in Adenoid Cystic Carcinoma of the Head and Neck. *Laryngoscope* (2003) 113:1955–60. doi: 10.1097/00005537-200311000-00019
48. Linxweiler M, Kuo F, Katabi N, Lee M, Nadeem Z, Dalin MG, et al. The Immune Microenvironment and Neoantigen Landscape of Aggressive Salivary Gland Carcinomas Differ by Subtype. *Clin Cancer Res* (2020) 26:2859–70. doi: 10.1158/1078-0432.CCR-19-3758
49. Sridharan V, Gjini E, Liao X, Chau NG, Haddad RI, Severgnini M, et al. Immune Profiling of Adenoid Cystic Carcinoma: PD-L2 Expression and Associations With Tumor-Infiltrating Lymphocytes. *Cancer Immunol Res* (2016) 4:679–87. doi: 10.1158/2326-6066.CIR-16-0031
50. Imadome K, Iwakawa M, Nojiri K, Tamaki T, Sakai M, Nakawatari M, et al. Upregulation of Stress-Response Genes With Cell Cycle Arrest Induced by Carbon Ion Irradiation in Multiple Murine Tumors Models. *Cancer Biol Ther* (2008) 7:208–17. doi: 10.4161/cbt.7.2.5255
51. Ohkubo Y, Iwakawa M, Seino K-I, Nakawatari M, Wada H, Kamijuku H, et al. Combining Carbon Ion Radiotherapy and Local Injection of α-Galactosylceramide-Pulsed Dendritic Cells Inhibits Lung Metastases in an *In Vivo* Murine Model. *Int J Radiat Oncol Biol Phys* (2010) 78:1524–31. doi: 10.1016/j.ijrobp.2010.06.048
52. Ando K, Fujita H, Hosoi A, Ma L, Wakatsuki M, Seino K, et al. Intravenous Dendritic Cell Administration Enhances Suppression of Lung Metastasis Induced by Carbon-Ion Irradiation. *J Radiat Res* (2017) 58:446–55. doi: 10.1093/jrr/rrx005
53. Hartmann L, Schröter P, Osen W, Baumann D, Offringa R, Moustafa M, et al. Photon Versus Carbon Ion Irradiation: Immunomodulatory Effects Exerted on Murine Tumor Cell Lines. *Sci Rep* (2020) 10:21517. doi: 10.1038/s41598-020-78577-8
54. Spina CS, Tsuruoka C, Mao W, Sunaoshi MM, Chaimowitz M, Shang Y, et al. Differential Immune Modulation With Carbon-Ion Versus Photon Therapy. *Int J Radiat Oncol Biol Phys* (2021) 109:813–8. doi: 10.1016/j.ijrobp.2020.09.053
55. Takahashi Y, Yasui T, Minami K, Tamari K, Hayashi K, Otani K, et al. Carbon Ion Irradiation Enhances the Antitumor Efficacy of Dual Immune Checkpoint Blockade Therapy Both for Local and Distant Sites in Murine Osteosarcoma. *Oncotarget* (2019) 10:633–46. doi: 10.18632/oncotarget.26551
56. Chiblak S, Tang Z, Lemke D, Knoll M, Dokic I, Warta R, et al. Carbon Irradiation Overcomes Glioma Radioresistance by Eradicating Stem Cells and Forming an Antiangiogenic and Immunopermissive Niche. *JCI Insight* (2019) 4:e123837. doi: 10.1172/jci.insight.123837
57. Xie Y, Zhang H, Wang YL, Zhou QM, Qiu R, Yuan ZG, et al. Alterations of Immune Functions Induced by 12C6+ Ion Irradiation in Mice. *Int J Radiat Biol* (2007) 83:577–81. doi: 10.1080/09553000701481774
58. Münter MW, Schulz-Ertner D, Hof H, Nikoghosyan A, Jensen A, Nill S, et al. Inverse Planned Stereotactic Intensity Modulated Radiotherapy (IMRT) in the Treatment of Incompletely and Completely Resected Adenoid Cystic Carcinomas of the Head and Neck: Initial Clinical Results and Toxicity of Treatment. *Radiat Oncol* (2006) 1:17. doi: 10.1186/1748-717X-1-17
59. Madani I, Bonte K, Vakaet L, Boterberg T, De Neve W. Intensity-Modulated Radiotherapy for Sinonasal Tumors: Ghent University Hospital Update. *Int J Radiat Oncol Biol Phys* (2009) 73:424–32. doi: 10.1016/j.ijrobp.2008.04.037
60. Lesueur P, Rapeaud E, De Marzi L, Goudjil F, Levy C, Galatoire O, et al. Adenoid Cystic Carcinoma of the Lacrimal Gland: High Dose Adjuvant Proton Therapy to Improve Patients Outcomes. *Front Oncol* (2020) 10:135. doi: 10.3389/fonc.2020.00135
61. Levy A, Omeiri A, Fadel E, Le Péchoux C. Radiotherapy for Tracheal-Bronchial Cystic Adenoid Carcinomas. *Clin Oncol (R Coll Radiol)* (2018) 30:39–46. doi: 10.1016/j.clon.2017.10.012
62. Je HU, Song SY, Kim DK, Kim Y-H, Jeong S-Y, Back GM, et al. Choi EK. A 10-Year Clinical Outcome of Radiotherapy as an Adjuvant or Definitive Treatment for Primary Tracheal Adenoid Cystic Carcinoma. *Radiat Oncol* (2017) 12:196. doi: 10.1186/s13014-017-0933-6
63. Dracham C, Khosla D, Kapoor R, Dey T, Periasamy K, Elangovan A, et al. Expanding Role of Radiotherapy in Adenoid Cystic Carcinoma of the Tracheobronchial Tree: A New Horizon. *Tumori* (2021) 3008916211012461. doi: 10.1177/03008916211012461
64. Zelga P, Tchórzewski M, Zelga M, Sobotkowski J, Dziki A. Radiation-Induced Rectovaginal Fistulas in Locally Advanced Gynaecological Malignancies-New Patients, Old Problem? *Langenbecks Arch Surg* (2017) 402:1079–88. doi: 10.1007/s00423-016-1539-4
65. Zhou Y, Zang Y, Xiang J, Tang F, Chen Z. Adenoid Cystic Carcinoma of the Cardia: Report of a Rare Case and Review of the Chinese Literature. *Oncol Lett* (2014) 8:726–30. doi: 10.3892/ol.2014.2153

66. Koto M, Hasegawa A, Takagi R, Ikawa H, Naganawa K, Mizoe J-E, et al. Definitive Carbon-Ion Radiotherapy for Locally Advanced Parotid Gland Carcinomas. *Head Neck* (2017) 39:724–9. doi: 10.1002/hed.24671
67. Mizoe J-E, Hasegawa A, Jingu K, Takagi R, Bessyo H, Morikawa T, et al. Results of Carbon Ion Radiotherapy for Head and Neck Cancer. *Radiother Oncol* (2012) 103:32–7. doi: 10.1016/j.radonc.2011.12.013
68. Sulaiman NS, Demizu Y, Koto M, Saitoh J-I, Suefuji H, Tsuji H, et al. Multicenter Study of Carbon-Ion Radiation Therapy for Adenoid Cystic Carcinoma of the Head and Neck: Subanalysis of the Japan Carbon-Ion Radiation Oncology Study Group (J-CROS) Study (1402 Hn). *Int J Radiat Oncol Biol Phys* (2018) 100:639–46. doi: 10.1016/j.ijrobp.2017.11.010
69. Hayashi K, Koto M, Ikawa H, Ogawa K, Kamada T. Efficacy and Safety of Carbon-Ion Radiotherapy for Lacrimal Gland Carcinomas With Extraorbital Extension: A Retrospective Cohort Study. *Oncotarget* (2018) 9:12932–40. doi: 10.18632/oncotarget.24390
70. Schulz-Ertner D, Nikoghosyan A, Thilmann C, Haberer T, Jäkel O, Karger C, et al. Results of Carbon Ion Radiotherapy in 152 Patients. *Int J Radiat Oncol Biol Phys* (2004) 58:631–40. doi: 10.1016/j.ijrobp.2003.09.041
71. Ikawa H, Koto M, Hayashi K, Tonogi M, Takagi R, Nomura T, et al. Feasibility of Carbon-Ion Radiotherapy for Oral non-Squamous Cell Carcinomas. *Head Neck* (2019) 41:1795–803. doi: 10.1002/hed.25618
72. Abe T, Ohno T, Koto M, Demizu Y, Suefuji H, Tsuji H, et al. A Multi-Institutional Retrospective Study of Carbon-Ion Radiotherapy for non-Squamous Cell Malignant Tumors of the Nasopharynx: Subanalysis of Japan Carbon-Ion Radiation Oncology Study Group Study 1402 HN. *Cancer Med* (2018) 7:6077–83. doi: 10.1002/cam4.1884
73. Hagiwara Y, Koto M, Bhattacharyya T, Hayashi K, Ikawa H, Nemoto K, et al. Long-Term Outcomes and Toxicities of Carbon-Ion Radiotherapy in Malignant Tumors of the Sphenoid Sinus. *Head Neck* (2020) 42:50–8. doi: 10.1002/hed.25965
74. Koto M, Hasegawa A, Takagi R, Ikawa H, Naganawa K, Mizoe J-E, et al. Evaluation of the Safety and Efficacy of Carbon Ion Radiotherapy for Locally Advanced Adenoid Cystic Carcinoma of the Tongue Base. *Head Neck* (2016) 38 Suppl 1:E2122–6. doi: 10.1002/hed.24397
75. Akbaba S, Ahmed D, Mock A, Held T, Bahadir S, Lang K, et al. Treatment Outcome of 227 Patients With Sinonasal Adenoid Cystic Carcinoma (ACC) After Intensity Modulated Radiotherapy and Active Raster-Scanning Carbon Ion Boost: A 10-Year Single-Center Experience. *Cancers (Basel)* (2019) 11:E1705. doi: 10.3390/cancers11111705
76. Akbaba S, Ahmed D, Lang K, Held T, Mattke M, Hoerner-Rieber J, et al. Results of a Combination Treatment With Intensity Modulated Radiotherapy and Active Raster-Scanning Carbon Ion Boost for Adenoid Cystic Carcinoma of the Minor Salivary Glands of the Nasopharynx. *Oral Oncol* (2019) 91:39–46. doi: 10.1016/j.oraloncology.2019.02.019
77. Combs SE, Kalbe A, Nikoghosyan A, Ackermann B, Jäkel O, Haberer T, et al. Carbon Ion Radiotherapy Performed as Re-Irradiation Using Active Beam Delivery in Patients With Tumors of the Brain, Skull Base and Sacral Region. *Radiother Oncol* (2011) 98:63–7. doi: 10.1016/j.radonc.2010.10.010
78. Gao J, Hu J, Guan X, Yang J, Hu W, Kong L, et al. Salvage Carbon-Ion Radiation Therapy For Locoregionally Recurrent Head and Neck Malignancies. *Sci Rep* (2019) 9:4259. doi: 10.1038/s41598-019-39241-y
79. Högerle BA, Lasitschka F, Muley T, Bougatf N, Herfarth K, Adeberg S, et al. Primary Adenoid Cystic Carcinoma of the Trachea: Clinical Outcome of 38 Patients After Interdisciplinary Treatment in a Single Institution. *Radiat Oncol* (2019) 14:117. doi: 10.1186/s13014-019-1323-z
80. Akbaba S, Lang K, Held T, Bulut OC, Mattke M, Uhl M, et al. Accelerated Hypofractionated Active Raster-Scanned Carbon Ion Radiotherapy (CIRT) for Laryngeal Malignancies: Feasibility and Safety. *Cancers (Basel)* (2018) 10: E388. doi: 10.3390/cancers10100388
81. Akbaba S, Lang K, Held T, Herfarth K, Rieber J, Plinkert P, et al. Carbon-Ion Radiotherapy in Accelerated Hypofractionated Active Raster-Scanning Technique for Malignant Lacrimal Gland Tumors: Feasibility and Safety. *Cancer Manag Res* (2019) 11:1155–66. doi: 10.2147/CMAR.S190051
82. Jensen AD, Poulakis M, Nikoghosyan AV, Chaudhri N, Uhl M, Münter MW, et al. Re-Irradiation of Adenoid Cystic Carcinoma: Analysis and Evaluation of Outcome in 52 Consecutive Patients Treated With Raster-Scanned Carbon Ion Therapy. *Radiother Oncol* (2015) 114:182–8. doi: 10.1016/j.radonc.2015.01.002
83. Held T, Windisch P, Akbaba S, Lang K, El Shafie R, Bernhardt D, et al. Carbon Ion Reirradiation for Recurrent Head and Neck Cancer: A Single-Institutional Experience. *Int J Radiat Oncol Biol Phys* (2019) 105:803–11. doi: 10.1016/j.ijrobp.2019.07.021
84. Hayashi K, Koto M, Ikawa H, Hagiwara Y, Tsuji H, Ogawa K, et al. Feasibility of Re-Irradiation Using Carbon Ions for Recurrent Head and Neck Malignancies After Carbon-Ion Radiotherapy. *Radiother Oncol* (2019) 136:148–53. doi: 10.1016/j.radonc.2019.04.007
85. Vischioni B, Dhanireddy B, Severo C, Bonora M, Ronchi S, Vitolo V, et al. Reirradiation of Salivary Gland Tumors With Carbon Ion Radiotherapy at CNAO. *Radiother Oncol* (2020) 145:172–7. doi: 10.1016/j.radonc.2020.01.004
86. Chen J, Mao J, Ma N, Wu K-L, Lu J, Jiang G-L. Definitive Carbon Ion Radiotherapy for Tracheobronchial Adenoid Cystic Carcinoma: A Preliminary Report. *BMC Cancer* (2021) 21:734. doi: 10.1186/s12885-021-08493-1
87. Barcellini A, Gadducci A, Laliscia C, Imparato S, Vitolo V, Preda L, et al. Adenoid Cystic Carcinoma of Bartholin's Gland: What Is the Best Approach? *Oncology* (2020) 98:513–9. doi: 10.1159/000506485
88. Bernhardt D, Sterzing F, Adeberg S, Herfarth K, Katayama S, Foerster R, et al. Bimodality Treatment of Patients With Pelvic Adenoid Cystic Carcinoma With Photon Intensity-Modulated Radiotherapy Plus Carbon Ion Boost: A Case Series. *CMAR* (2018) 10:583–8. doi: 10.2147/CMAR.S148395
89. Molinelli S, Bonora M, Magro G, Casale S, Dale JE, Fossati P, et al. RBE-Weighted Dose in Carbon Ion Therapy for ACC Patients: Impact of the RBE Model Translation on Treatment Outcomes. *Radiother Oncol* (2019) 141:227–33. doi: 10.1016/j.radonc.2019.08.022
90. Dale JE, Molinelli S, Vischioni B, Vitolo V, Bonora M, Magro G, et al. Brainstem NTCP and Dose Constraints for Carbon Ion RT—Application and Translation From Japanese to European RBE-Weighted Dose. *Front Oncol* (2020) 10:531344. doi: 10.3389/fonc.2020.531344
91. Dale JE, Molinelli S, Vitolo V, Vischioni B, Bonora M, Magro G, et al. Optic Nerve Constraints for Carbon Ion RT at CNAO - Reporting and Relating Outcome to European and Japanese RBE. *Radiother Oncol* (2019) 140:175–81. doi: 10.1016/j.radonc.2019.06.028
92. Wolf M, Anderle K, Durante M, Graeff C. Robust Treatment Planning With 4D Intensity Modulated Carbon Ion Therapy for Multiple Targets in Stage IV non-Small Cell Lung Cancer. *Phys Med Biol* (2020) 65:215012. doi: 10.1088/1361-6560/aba1a3
93. Qin N, Shen C, Tsai M-Y, Pinto M, Tian Z, Dedes G, et al. Full Monte Carlo-Based Biologic Treatment Plan Optimization System for Intensity Modulated Carbon Ion Therapy on Graphics Processing Unit. *Int J Radiat Oncol Biol Phys* (2018) 100:235–43. doi: 10.1016/j.ijrobp.2017.09.002
94. Li Y, Kubota Y, Okamoto M, Shiba S, Okazaki S, Matsui T, et al. Adaptive Planning Based on Single Beam Optimization in Passive Scattering Carbon Ion Radiotherapy for Patients With Pancreatic Cancer. *Radiat Oncol* (2021) 16:111. doi: 10.1186/s13014-021-01841-2
95. Li X, Quan EM, Li Y, Pan X, Zhou Y, Wang X, et al. A Fully Automated Method for CT-On-Rails-Guided Online Adaptive Planning for Prostate Cancer Intensity Modulated Radiation Therapy. *Int J Radiat Oncol Biol Phys* (2013) 86:835–41. doi: 10.1016/j.ijrobp.2013.04.014
96. Sun B, Yang D, Lam D, Zhang T, Dvergsten T, Bradley J, et al. Toward Adaptive Proton Therapy Guided With a Mobile Helical CT Scanner. *Radiotherapy Oncol* (2018) 129:479–85. doi: 10.1016/j.radonc.2018.08.021
97. Fiorina E, Ferrero V, Baroni G, Battistoni G, Belcari N, Camarlinghi N, et al. Detection of Interfractional Morphological Changes in Proton Therapy: A Simulation and *In Vivo* Study With the INSIDE In-Beam PET. *Front Phys* (2021) 8:578388. doi: 10.3389/fphy.2020.578388
98. Sun L, Hu W, Lai S, Shi L, Chen J. *In Vivo* 3-D Dose Verification Using PET/CT Images After Carbon-Ion Radiation Therapy. *Front Oncol* (2021) 11:621394. doi: 10.3389/fonc.2021.621394
99. Pennazio F, Battistoni G, Bisogni MG, Camarlinghi N, Ferrari A, Ferrero V, et al. Carbon Ions Beam Therapy Monitoring With the INSIDE in-Beam PET. *Phys Med Biol* (2018) 63:145018. doi: 10.1088/1361-6560/aacab8
100. Vered M, Braunstein E, Buchner A. Immunohistochemical Study of Epidermal Growth Factor Receptor in Adenoid Cystic Carcinoma of Salivary Gland Origin. *Head Neck* (2002) 24:632–6. doi: 10.1002/hed.10104
101. Adeberg S, Akbaba S, Lang K, Held T, Verma V, Nikoghosyan A, et al. The Phase 1/2 ACCEPT Trial: Concurrent Cetuximab and Intensity Modulated

Radiation Therapy With Carbon Ion Boost for Adenoid Cystic Carcinoma of the Head and Neck. *Int J Radiat Oncol Biol Phys* (2020) 106:167–73. doi: 10.1016/j.ijrobp.2019.09.036

102. Takagi M, Demizu Y, Hashimoto N, Mima M, Terashima K, Fujii O, et al. Treatment Outcomes of Particle Radiotherapy Using Protons or Carbon Ions as a Single-Modality Therapy for Adenoid Cystic Carcinoma of the Head and Neck. *Radiother Oncol* (2014) 113:364–70. doi: 10.1016/j.radonc.2014.11.031
103. Karam SD, Snider JW, Wang H, Wooster M, Lominska C, Deeken J, et al. Reirradiation of Recurrent Salivary Gland Malignancies With Fractionated Stereotactic Body Radiation Therapy. *J Radiat Oncol* (2012) 1:147–53. doi: 10.1007/s13566-012-0010-6
104. Jensen AD, Debus J. Cost-Effectiveness Analysis (CEA) of IMRT Plus C12 Boost vs IMRT Only in Adenoid Cystic Carcinoma (ACC) of the Head and Neck. *Radiat Oncol* (2019) 14:194. doi: 10.1186/s13014-019-1395-9
105. Kato I, Ono K, Sakurai Y, Ohmae M, Maruhashi A, Imahori Y, et al. Effectiveness of BNCT for Recurrent Head and Neck Malignancies. *Appl Radiat Isot* (2004) 61:1069–73. doi: 10.1016/j.apradiso.2004.05.059
106. Kankaanranta L, Seppälä T, Koivunoro H, Saarilahti K, Atula T, Collan J, et al. Boron Neutron Capture Therapy in the Treatment of Locally Recurred Head-and-Neck Cancer: Final Analysis of a Phase I/II Trial. *Int J Radiat Oncol Biol Phys* (2012) 82:e67–75. doi: 10.1016/j.ijrobp.2010.09.057
107. Aihara T, Morita N, Kamitani N, Kumada H, Ono K, Hiratsuka J, et al. BNCT for Advanced or Recurrent Head and Neck Cancer. *Appl Radiat Isot* (2014) 88:12–5. doi: 10.1016/j.apradiso.2014.04.007

Conflict of Interest: The authors declare that the research was conducted in the absence of any commercial or financial relationships that could be construed as a potential conflict of interest.

Publisher's Note: All claims expressed in this article are solely those of the authors and do not necessarily represent those of their affiliated organizations, or those of the publisher, the editors and the reviewers. Any product that may be evaluated in this article, or claim that may be made by its manufacturer, is not guaranteed or endorsed by the publisher.

frontiers in Oncology

REVIEW
published: 09 December 2021
doi: 10.3389/fonc.2021.780025

Future Developments in Charged Particle Therapy: Improving Beam Delivery for Efficiency and Efficacy

Jacinta Yap[1]*, *Andrea De Franco*[2] *and Suzie Sheehy*[1]

[1] School of Physics, University of Melbourne, Melbourne, VIC, Australia, [2] IFMIF Accelerator Development Group, Rokkasho Fusion Institute, National Institutes for Quantum Science and Technology, Aomori, Japan

The physical and clinical benefits of charged particle therapy (CPT) are well recognized. However, the availability of CPT and complete exploitation of dosimetric advantages are still limited by high facility costs and technological challenges. There are extensive ongoing efforts to improve upon these, which will lead to greater accessibility, superior delivery, and therefore better treatment outcomes. Yet, the issue of cost remains a primary hurdle as utility of CPT is largely driven by the affordability, complexity and performance of current technology. Modern delivery techniques are necessary but limited by extended treatment times. Several of these aspects can be addressed by developments in the beam delivery system (BDS) which determines the overall shaping and timing capabilities enabling high quality treatments. The energy layer switching time (ELST) is a limiting constraint of the BDS and a determinant of the beam delivery time (BDT), along with the accelerator and other factors. This review evaluates the delivery process in detail, presenting the limitations and developments for the BDS and related accelerator technology, toward decreasing the BDT. As extended BDT impacts motion and has dosimetric implications for treatment, we discuss avenues to minimize the ELST and overview the clinical benefits and feasibility of a large energy acceptance BDS. These developments support the possibility of advanced modalities and faster delivery for a greater range of treatment indications which could also further reduce costs. Further work to realize methodologies such as volumetric rescanning, FLASH, arc, multi-ion and online image guided therapies are discussed. In this review we examine how increased treatment efficiency and efficacy could be achieved with improvements in beam delivery and how this could lead to faster and higher quality treatments for the future of CPT.

Keywords: particle therapy, accelerators, large energy acceptance, energy layer switching time, rescanning, FLASH, arc therapy, beam delivery

OPEN ACCESS

Edited by:
Stewart Mac Mein, German Cancer Research Center (DKFZ), Germany

Reviewed by:
Marco Durante, GSI Helmholtz Center for Heavy Ion Research, Germany
Håkan Nyström, Skandion Clinic, Sweden
Lei Dong, University of Pennsylvania, United States

***Correspondence:**
Jacinta Yap
jacinta.yap@unimelb.edu.au

Specialty section:
This article was submitted to Radiation Oncology, a section of the journal Frontiers in Oncology

Received: *20 September 2021*
Accepted: *16 November 2021*
Published: *09 December 2021*

Citation:
Yap J, De Franco A and Sheehy S (2021) Future Developments in Charged Particle Therapy: Improving Beam Delivery for Efficiency and Efficacy. Front. Oncol. 11:780025. doi: 10.3389/fonc.2021.780025

1 INTRODUCTION

Access to charged particle therapy is growing rapidly worldwide. As a therapeutic modality CPT is now well established, where proton beam therapy (PBT) is the most common type. Where available, PBT is often standard practice, particularly for pediatric cases and specific tumor types [ocular, head and neck tumors (1)]. CPT has an important prospective role in reducing the growing cancer

burden on a global scale, and its impact could be significant (2) however, its full potential is yet to be realized. Overcoming this requires improvements in two key areas: improving efficacy and decreasing cost.

CPT offers benefits over and above standard radiotherapy (RT) for palliative or curative treatments, offering not just physical dose escalation but also biological advantage. Yet in terms of efficacy, we cannot capitalize fully on increased radiobiological effectiveness of charged particles at present, primarily due to limitations in knowledge (3). For this reason, existing programmes of research are investigating the underlying mechanisms of CPT in terms of fundamental chemical, biological and cellular processes (4–9) to try to understand the roles of these processes in determining clinical outcomes (10–12). Nonetheless, the superior physical properties of charged particles are evident as the characteristic '*Bragg Peak*' (BP) enables a precise dose distribution and an improved therapeutic window.

The second reason we cannot yet fully exploit the efficacy of CPT is due to technological limitations. Advanced techniques and technological improvements for CPT seek to deliver higher quality treatments with increased conformity as these translate to long-term benefits. However some of these improvements would increase, rather than decrease, the cost of the treatment.

In terms of cost (or efficiency) the gap between conventional X-ray photon RT (XRT) and CPT still exists due to the many challenges to be addressed: affordability, complexity and limitations with current technology all restrict the utility of CPT. Developments in accelerators and related technologies, beam delivery methods, verification tools, and increased clinical experience have seen growth in the number of facilities. Although availability has surged in recent years with several vendors offering competitive and commercial turn-key solutions, high capital and operational costs are still a primary issue. Many potential areas of improvement have been well identified (13–21). In general, the potential for cost reduction can be considered by decreasing the facility and machine size, operational complexities, treatment times, increasing the treatment workflow efficiency and hence throughput.

However, simply making the treatment cheap and widespread is not enough. Both efficiency and efficacy need to be improved, in other words, even in an ideal world of low-cost and widespread availability of facilities, the maximum possible clinical benefit of CPT will only be achievable if existing technical limitations are overcome. Of course, there are many improvements which can be implemented with current systems to improve treatment efficacy and cost. Yet these will be restricted by – both technological and systems-based – capabilities of the BDS: developments are necessary to better deliver CPT, at future facilities and with advanced methodologies.

Presently, the majority of CPT treatments use active pencil beam scanning (PBS), involving the intricate delivery of several thousand overlapping narrow beams, resulting in highly conformal dose distributions. Most clinical indications are treated with PBS however the lengthy beam delivery time is consequential. During treatment the beam is scanned across the target site, requiring the accelerator complex, control system and diagnostic instruments to adjust. A key bottleneck in this process is the energy layer switching time.

The slow ELST is due to technical constraints and is a prevalent issue: it can account for a majority of the BDT (22, 23). The beam moves relatively quickly across the tumor transversely, but often takes much longer to switch the beam in depth. This extends the beam-on time and long overall irradiation times can increase dose uncertainties. This is a key problem for cases where the tumor site itself may also move, for example during lung treatments, interplay effects caused by respiratory motion are unavoidable. Although different motion management approaches such as gating, rescanning and tracking can be performed, the clinical implications reduce the utility of CPT, especially for particular indications (11). Moreover, as the high dose BP region is a motivation for using CPT, sensitivity to changes in range are especially important – for heavy ions this is even greater – which impairs benefits attained from the physical and radiobiological advantages (24, 25).

There are many factors which govern the overall cost and efficacy of treatment and we identify one key underlying aspect: the beam delivery. Complimentary to the accelerator complex, the beam delivery system contributes significantly to the BDT and thus overall treatment time, forming the primary focus of this review. The scope of this review is to look at the technology pertaining to the BDS, broadly covering those aspects of the system which impact the dose delivery process and treatment time[1]. We review the challenges and developments needed for the BDS and related accelerator technology with the outlook of decreasing the BDT. The clinical feasibility, impact on the delivery process and potential benefits of different approaches are examined. We focus on the perspective of minimizing the ELST, its contribution and the implication of extended BDT on treatment. Lastly, we examine aspects to deliver emerging and future treatment paradigms such as FLASH, arc, multi-ion and image guided therapy.

2 BEAM DELIVERY

The beam produced by the accelerator must be shaped and modified to deliver the dose to the target site. This involves changing the distribution of the spatial (lateral) and energy (longitudinal) spread and also often the time structure, i.e. beam modification in four-dimensions. The objective of the BDS is to deliver this beam with the required parameters prescribed by the treatment plan. In this review we define the BDS as the components after the accelerator complex which determines how the beam is shaped, transported and ultimately delivered to the patient for treatment. This encompasses the beam transport lines (BTL), diagnostic instrumentation, energy selection systems (ESS), treatment line (gantry or fixed delivery

[1]Existing recommendations and requirements for technological improvements have been primarily focused on PBT, which precede developments for CPT with heavier ions due to greater clinical experience. We include many references to PBT for readers to explore these where relevant.

line) and treatment head. For brevity, we focus mainly on the BTL, treatment line and delivery system for PBS (**Figure 1**).

Treatments can take anywhere from a few minutes to more than half an hour, depending on the tumor type, size and complexity of the plan. This is determined by the BDT, additional activities including patient set-up (immobilisation, imaging, unload etc.) and equipment related checks (couch positioning, beam checks, readying beam devices etc.). The BDT consists of the actual irradiation '*beam-on*' time and the '*beam-off*' time, spent requesting and waiting on the beam after adjustments or between fields.

A quantitative analysis of PBT treatments by Suzuki et al. (26) reported that approximately 80% of treatment time was spent on these additional activities with the remaining 20% contributed by the BDT. Total treatment time is shown to increase with the number of fields; complex cases required the same amount of time to carry out patient-related activities but accrued larger contributions from equipment checks and the BDT. Reductions in these latter aspects have more potential to improve the efficiency as patient-related process times can vary widely, depend on the physical and clinical condition of the patient and cannot necessarily be improved with technology. Furthermore, shorter treatment times are preferred not just for cost but also due to difficulty of immobilisation and set-up of patients for 30 minutes or longer. As discussed by Nystrom & Paganetti et al. (13), a faster BDT can result in a significant gain in treatment efficiency, particularly for multi-room facilities with high waiting times. Evidently, any increase in treatment efficiency is valuable.

Decreasing BDT is complex as prescribed treatment plans are not standardized: the BDS, accelerator and other systems vary at each facility and the delivery efficiency depends on numerous technology-related factors. Facilities have different equipment vendors, number of rooms, delivery systems etc. and often adopt different processes: these characteristics all influence the delivery procedures implemented (27). Meanwhile the treatment plan calculates the number of spots and layers to deliver the required dose distribution to the target volume. Nystrom & Paganetti et al. (13) state the three main components which constitute the delivery time for a treatment field: time to irradiate a spot, time to move between spots and the time to change beam energy. Speeding up any of these components can shorten BDT however they are not independent variables. Delivering a faster treatment is not straightforward; it is not solely dependent on the capabilities of the BDS itself but is a multi-faceted problem. The contributing factors which impact the dose delivery and BDT are illustrated in **Figure 2**.

2.1 Pencil Beam Scanning

The planned dose distribution determines the requested parameters within the limits of the source, accelerator and beam transport lines, including the beam energies, size at isocentre, intensities and delivery channels. Each different configuration can total to thousands of available beam combinations (28), these multiple beams produce a 3D dose distribution where the entire process can amount to long treatment times. For PBS delivery, the beam is magnetically deflected across the tumor in the transverse plane across one layer or an iso-energy slice (IES), then adjusted longitudinally to a shorter depth (typically a decrease in proton range of 5 mm in water) and repeated (**Figure 3**).

Different scanning techniques (spot, raster and line/continuous) may be used with optimization methods to deliver the beam and irradiate each layer. Spot and raster scanning is usually dose driven, where progression through the spots occur when the prescribed number of protons have been delivered. Continuous line scanning moves the beam according to a calculated path dependent on time and consequently, may be

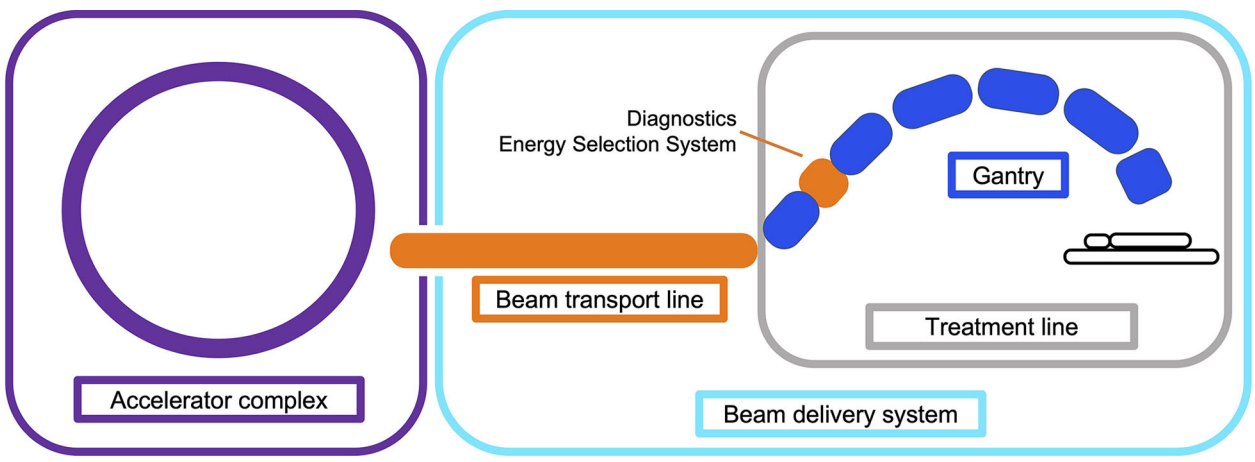

FIGURE 1 | Illustration overviewing the main components in a CPT treatment facility. The BDS is shown to include the BTL (beam instrumentation and devices which may alter the energy or shape of the beam) and treatment line (fixed line or here, a gantry).

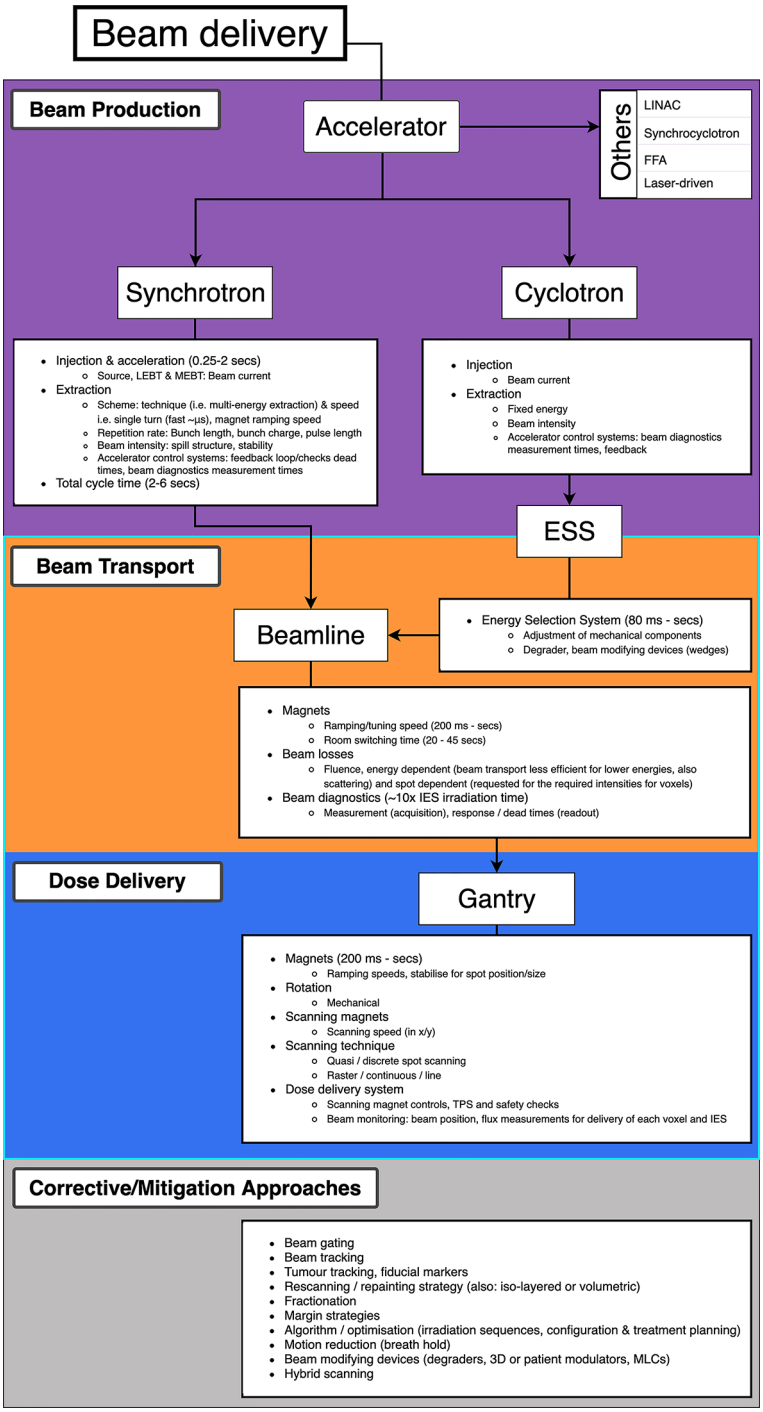

FIGURE 2 | Overview of PBS beam delivery and different motion mitigation strategies. Breakdown of contributions to the BDT from the beam production, beam transport and dose delivery processes.

affected by beam current variations (29). This requires a continuous beam, where the quick delivery also makes it more challenging to validate and monitor (13). For all techniques, the dose is painted such that the accumulation of the distribution in both planes results in sufficient tumor volume coverage (**Figure 4**).

2.2 BDT Time Components

The delivery of a field combines multiple aspects of the BDS: if we consider only the beam delivery process, this can be approximated to include the $[T_1]$ transverse scanning, $[T_2]$ energy adjustment and $[T_3]$ systematic dead times (**Figure 5**).

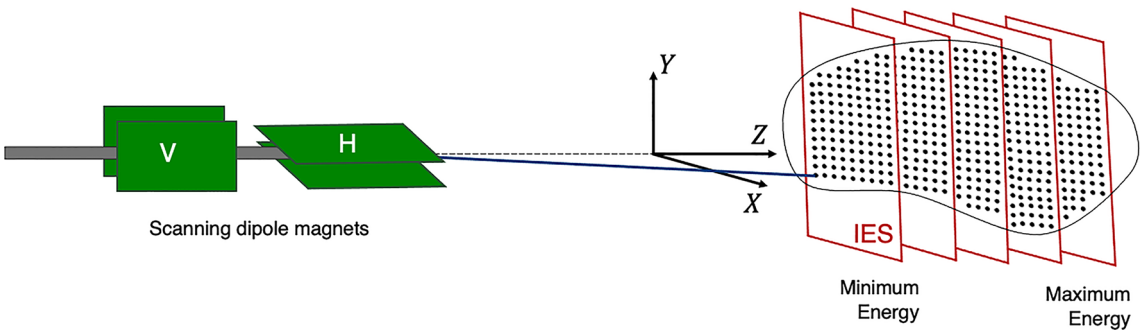

FIGURE 3 | Active PBS. The BDS delivers a conformal dose distribution to the treatment volume by scanning the beam along a calculated path in the transverse plane. The beam energy is then adjusted to change the depth (typically lower in energy), switching to a proximal IES, scanning through subsequent layers.

These estimations are provided (within applicable orders of magnitude) as based on broadly reported values.

The $[\mathbf{T_{1A}}]$ staying or '*dwell*' time at a position varies according to the intended amount of dose (and extracted beam intensity); it can be down to 0.1 ms (30) however is likely to be of the order of 1's ms (31). The $[\mathbf{T_{1B}}]$ transition time to the next position can be ~3 ms (29, 32) or ~10 ms between raster points (33). For line scanning, $[\mathbf{T_{1C}}]$ could be 5 ms for a line and $[\mathbf{T_{1D}}]$ 5 ms to move to the next line (34). Irradiation time for a single IES $[\mathbf{T_1}]$ depends on the size of the distribution: it increases linearly with the number of spots, likely needing at least ~100 ms.

$[\mathbf{T_2}]$ ranges from 80 ms to a few seconds (16), faster energy modulation is possible with cyclotrons and synchrocyclotrons, and slower direct energy adjustments with synchrotrons. This is discussed in detail later in Section 3.2; the fastest reported ELSTs are listed in **Table 1**.

$[\mathbf{T_3}]$ ionization chamber measurement times average ~0.1 ms (13, 28). ACS and diagnostic safety checks ensure correct beam parameters (spot size, position, intensity etc.). As reported by Schoemers et al. (41), measurement times are a bottom line limit across the BDS and similarly for continuous scanning, the lower bound is determined by the instrumentation speed (21); at least 1 ms for an IES is required.

The BDT is a function of the irradiation sequencing and indeed, a larger tumor volume or higher number of IES recruits more of these actions $[\mathbf{T_{1-3}}]$, amounting to a longer BDT. Independently, the irradiation time is also determined by the intensity of the beam produced by the accelerator (16, 41). As a standard (PBT) clinical minimum, most facilities have the capability of delivering dose rates of 2 Gy/min to a 1 L volume, 10–20 cm deep (42). This equates to beam currents of 100's nA at the patient, varying for accelerator type. However, even at facilities which are able to achieve higher dose rates, there are practical limitations with operation at higher intensities (Section 3.1).

3 LIMITATIONS AND AVENUES FOR IMPROVEMENTS

3.1 Accelerators

The timing structure of delivered beams varies significantly between different types of accelerators, as they have different

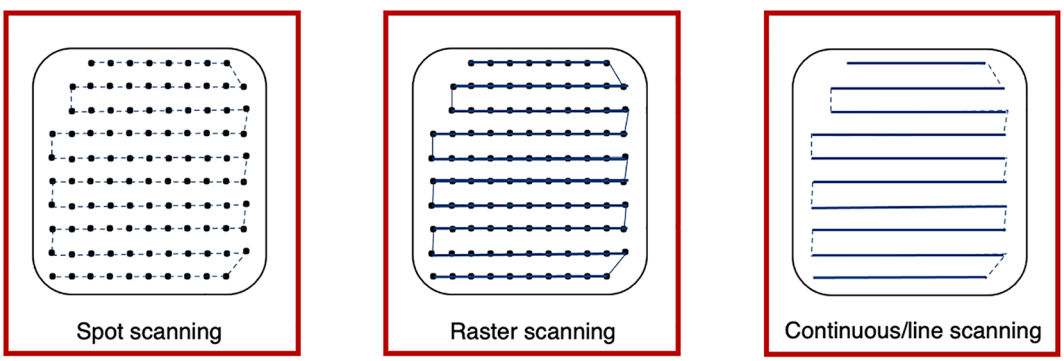

FIGURE 4 | Spot, raster and continuous line scanning patterns for PBS delivery. Spots and solid lines indicate beam-on irradiation and dashed lines indicate movement with beam-off. For spot scanning, the beam is turned off between movement to the next spot but remains on for the whole delivery in raster scanning. For continuous line scanning, the dose is delivered across a linear path (rather than as spots) and may be turned off between movement to subsequent lines.

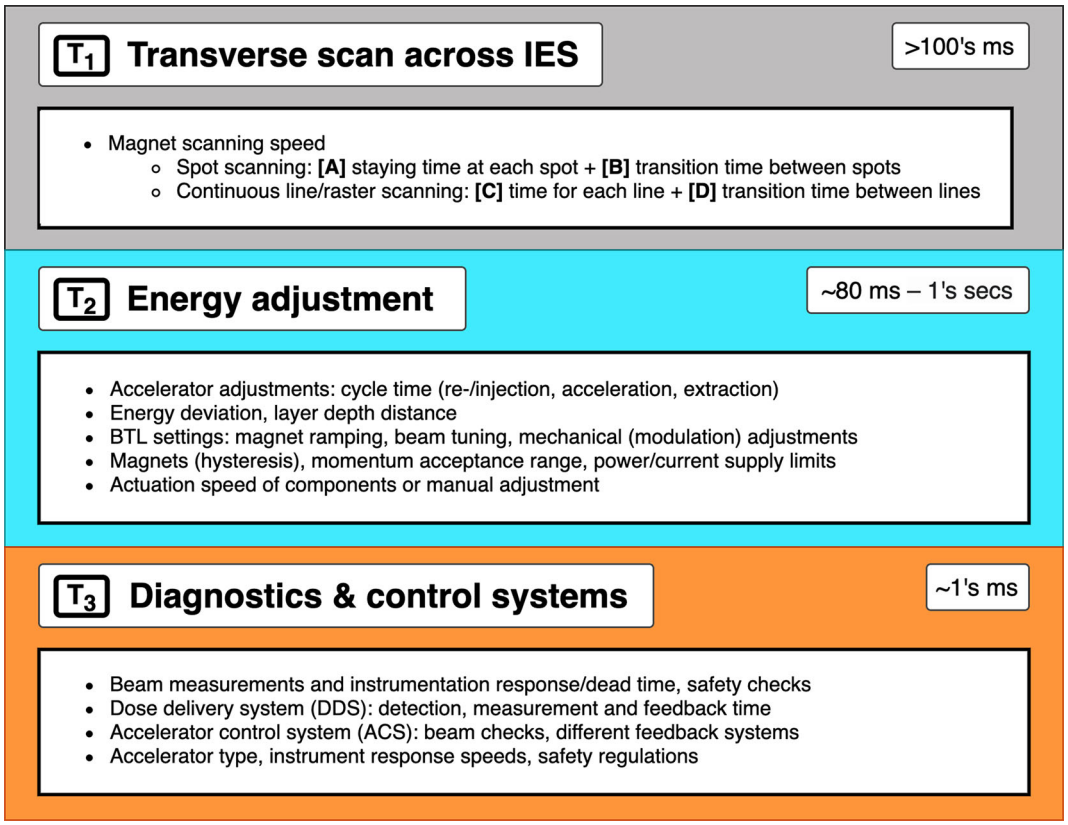

FIGURE 5 | Major BDS components and corresponding factors which contribute to BDT.

technological and safety limitations. In this section we present the main operational patterns and optimization challenges for synchrotrons, cyclotrons, synchrocyclotrons and other accelerators that may soon be available for PBT or CPT facilities (**Figure 6**).

3.1.1 Synchrotrons

The most common operation pattern for synchrotrons starts by injecting a beam pulse from a radiofrequency quadrupole (RFQ) and linear accelerator (LINAC) at up to ~5 MeV/u (order of 10–100 μs) of ~10^{11} protons (or ~10^{9} carbon ions) into the main synchrotron ring. The beam is accelerated in ~1 s to the desired energy, then slowly but continuously extracted and transported to the irradiation room to treat a specific treatment slice. While extraction processes are typically capable to deliver the entire accumulated charge in <100 ms, the process is intentionally extended to safely match the maximum supported scanning speeds in the transverse plane.

After delivery to one IES is completed, the particles still circulating in the synchrotron are dumped and all the magnets of the main ring are ramped to their maximum current and back to injection levels in typically ~1–2 s. This process, often called '*magnet washing*' (~100's ms), ensures reproducibility of the magnetic field in the presence of hysteresis of ferromagnetic

TABLE 1 | Reported minimum ELSTs ([T2]) for currently used clinical cyclotron, slow cycling synchrotron and synchrocyclotron accelerators.

	Accelerator type		
	Cyclotron	**Synchrotron**	**Synchrocyclotron**
Energy layer switching times – fastest reported	PSI G2: 80 ms G3: 200 ms	HIMAC MEE: 220 ms Hybrid: 100 ms	Mevion S250i 50 ms
Modulation method	ESS, degrader (carbon wedges)	MEE (>3 cm depths) and range shifters (<3 cm)	Motorised modulator plates (lexan/polycarbonate), 2.1 mm depth change
References	(35, 36)	(37–39)	(40)

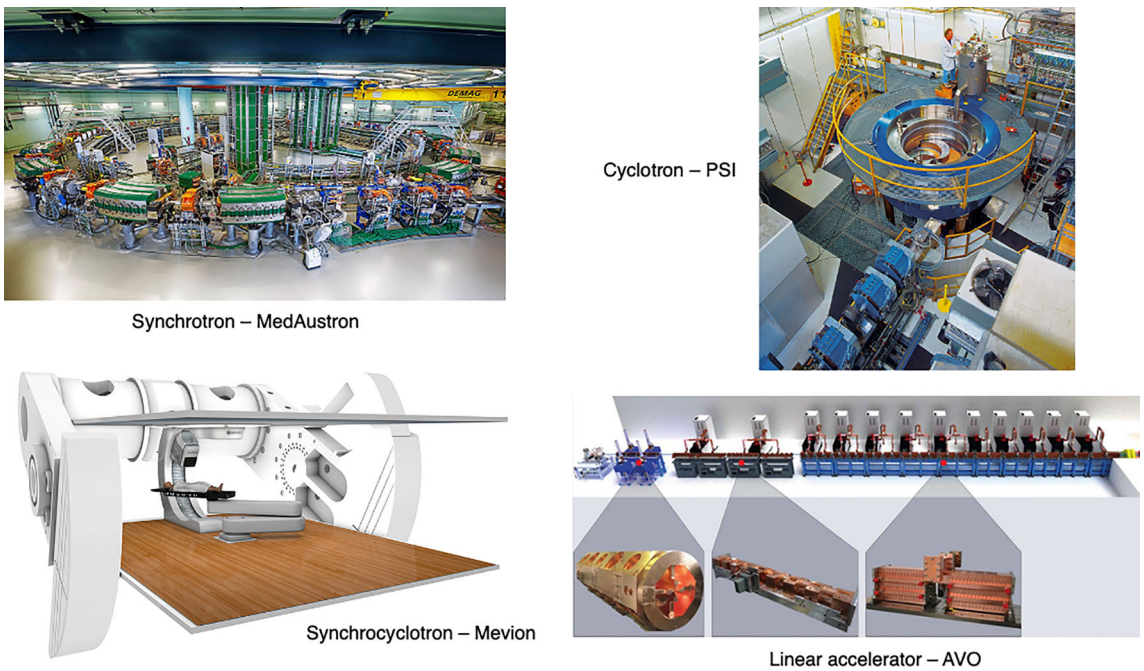

FIGURE 6 | Synchrotron at the MedAustron facility (43) and COMET cyclotron (for PBT) at PSI (44). Gantry-mounted Mevion S250i synchrocyclotron (Mevion Medical Systems, Inc.). Depiction of the AVO LIGHT LINAC with the radiofrequency quadrupole, side coupled drift tube LINAC and coupled cavity LINAC sections highlighted (45).

components. If the number of particles injected into the synchrotron is not sufficient to deliver the required dose at the specific energy, more pulses will be injected, accelerated, and delivered. For injection pulses of the order of ~10^{11} protons, only the treatment of large lesions (>1 L) in combination with hypofractionation requires more than one injection for the IES. The total time required to change energy (or refill the main ring) is of the order of ~2–4 s.

Two significant technological solutions exist which can drastically reduce the time required to change energy or refill the ring. This can be shortened to ~1–2 s by decreasing the time required to wash the magnets by employing an active regulation of the magnet power supply output, based on live measurement of the magnetic field (46, 47). However the technology necessary for active regulation of quadrupoles or sextupoles has not yet been implemented in clinical machines.

Another technique is called multiple energy extraction (MEE) operation (or extended flattop operation) and aims to reducing only (but drastically) the time required to change energy. In MEE (48) the beam can be extracted across several energy levels in a single spill; this enables the delivery of successive IES without needing to wait for re-/acceleration. The unused part of the beam circulating after completion of a slice is re-accelerated (or decelerated) instead of being dumped in preparation for a re-injection. Although the process is not completely lossless, it requires only roughly ~100 ms (37, 49) to change beam energy[2].

[2]The energy change is fixed to a single direction.

Younkin et al. (50) performed a study to quantify BDT savings with MEE implemented at a synchrotron PBT facility, finding an average BDT reduction of 35%. The ELST was reduced by ~90% from ~2 s to 200 ms with MEE. Additional savings could also be achieved by improving charge, extraction limits and charge recapture rates: these depend on the performance and limits of the synchrotron[3].

The extraction mechanism most often used in synchrotron ion beam therapy facilities is based around two methods: a slow resonant mechanism which is usually driven by a transverse excitation [RF knockout (RF-KO) (51, 52)] or a longitudinally slowly induced energy change [Betatron magnet (47, 53, 54)]. For slow resonant extraction, the beam can be kept bunched throughout the extraction process, making re-acceleration (or deceleration) a delicate but feasible process. However, this produces fundamentally different beam distributions in the horizontal and vertical plane. This requires an optics matching stage in the BTL, often realized by inserting a thin foil that spreads the beam to equalize the particle distributions. The foil orientation might also require mechanical adjustment at different energies, potentially limiting the ELST[4].

[3]In this scenario the re-injection times are also not improved from the typical operation mode.

[4]Another arguably more elegant method is the use of a rotator (55) which physically rotates a set of magnets to match the optics for different gantry angles, requiring no additional time for energy switching (apart from the magnetic field setting in the BTL).

The second technique requires the de-bunching of the beam, which makes further re-acceleration (or deceleration) theoretically possible (RF front acceleration), but extremely challenging, loss prone and potentially time consuming. Facilities not originally designed for MEE operation exhibit the trend to implement RF-KO first rather than attempting other retro-fitted techniques (56–58). The direction of energy change is typically fixed (e.g. always increases or decreases), because an up-down energy scanning would violate the reproducibility of the main ring magnetic field due to hysteresis effects. A magnetic field active regulation control would be necessary for this feature.

Alternative extraction techniques which are compatible with bunched beams are based on optics changes often used in larger synchrotrons for non-clinical applications (59). These could be applied in the future but so far promise limited advantages for small machines dedicated to therapy. The limited benefits offered by MEE operations for hypofractionated treatments can be overcome by increasing the particle filling of the ring.

It is not uncommon for an IES to host a vast dynamic range of dose among its spots. If the beam intensity is kept constant, it has to be as low as necessary to fulfil a minimum dwell time on the lowest rated spot. Synchrotrons that adopt RF-KO can regulate the extraction speed of the accumulated charge spot-by-spot, with fast feedforward loops (60, 61). The properties of the beam are largely independent of the strength of the field applied. This feature can reduce the BDT considerably and is already implemented in most of the latest generation commercial solutions.

Although it is not the focus of this work, it is worth mentioning that synchrotrons are often chosen by therapy centres also for their capability and ease of delivering multiple particle species (proton, He, C, O, etc.), assuming multiple ion sources are used for each species. The time required to switch particle species is driven by the change and stabilization of the field in the injector and low/medium energy BTL magnets. In some tests at NIRS-QST this was chosen to be ~20 s (62) but could potentially be reduced to only a few seconds with a dedicated design and development of the source, injector and overall control system (63).

3.1.2 Cyclotrons & Synchrocyclotrons

The most common choice for PBT is the cyclotron (mostly isochronous cyclotrons), which accelerates protons to a single (maximum) energy[5]. The beam is typically available as a continuous wave beam with a micro-bunch structure of 100's MHz. As the extraction energy is fixed, material must be inserted in the beamline to change the energy. This produces large losses [i.e. >99% of the beam can be lost (66)] especially when selecting lower energies, resulting in a radioactive hot spot and a beam with a very large distribution of energies, not suitable for precise 3D conformal dose delivery. Therefore, an ESS usually follows the energy degrader, consisting of several devices (degraders i.e. carbon or graphite wedges, collimators, slits, magnets, diagnostics etc.) which are necessary to modify the beam for the correct parameters for treatment. The transmission, quality and distribution of the beam is affected by interactions with objects in the beam path (the increase in distal penumbra from the energy spread can be up to 10 mm) (16). The optics is designed to create a section with a large dispersion, where slits are inserted to trim the beam and reduce the energy spread.

Compared to synchrotrons, the time taken to mechanically insert the beam modifying devices is relatively quick (~10's ms) for small energy adjustments. The use of actuated static wedges with time compensation and fast deflecting magnets (range adaptation) is reported to be the fastest method, changing energies in less than 20 ms (67). At PSI the wedge positioning takes 50 ms; Pedroni et al. (35) report the fastest energy modulation times are achievable on gantry 2 (G2) at 80 ms. Delays are caused by stabilization of the dipole magnets in the BTL and gantry. The direction of the energy change is not limited by the accelerator (can change up and down in any sequence), but the reproducibility of the magnetic field in the ESS. Thehysteresis of ferromagnetic components in the BTL typically restricts fast energy change to one direction only, with a magnet wash required before each direction swap. The BDS magnets must be ramped to accommodate different energies: the time taken to vary and reset the magnetic fields in the BDS determine the ELST time. This also holds true for synchrotron facilities however, the times required for energy changes with the accelerator far surpass these at present.

Spot-by-spot intensity modulation (as done with synchrotrons) is possible, but more complex to achieve for cyclotrons and LINACs because they do not accumulate charge. The dose rate can be regulated by either modifying the extracted current from the ion source or by forcefully reducing the transmission throughout the accelerator. Although many parameters can be found in every design that could achieve this goal, it is extremely difficult to avoid affecting other beam properties at the same time (68, 69), especially in the very wide dynamic range (2 orders of magnitude) required to fully exploit this feature.

Superconducting synchrocyclotrons produce a pulsed beam (few μs, every 1–2 ms) as they are not isochronous (42, 70). Only one or a few pulses-per-spot is usually necessary. Synchrocyclotrons can bypass the limiting constraints of the BDS magnets with single room systems (for PBT) where the accelerator is gantry-mounted and the entire machine rotates around the patient. Energy changes are performed using an energy modulation system; like a regular cyclotron this comprises polycarbonate plates, range shifters, absorbers or other devices which physically attenuate the beam (71, 72). ELSTs as fast as ~50 ms, for changes of 2.1 mm in water equivalent thickness have been achieved (40). Although synchrocyclotrons have a smaller footprint and fast energy modulation, the achievable beam parameters and pulse structure are insufficient for continuous PBS delivery (13).

3.1.3 LINACs, Laser-Driven & Fixed Field Alternating Gradient Accelerators

Linear accelerators are already ubiquitous in hospitals as compact sources for conventional XRT. Using a LINAC for

[5] Although designs for cyclotrons dedicated to particle therapy with He or C exist (64, 65), no facility has so far been developed yet.

protons or ions is more challenging: they are physically much larger, in part because the velocity of the particles changes significantly in the clinical energy range, thus the physical length of accelerating gaps must accommodate for this throughout the accelerator. A proposed LINAC-based solution from Advanced Oncotherapy (73) includes: a high-frequency RF quadrupole design at 750 MHz, originating from CERN, and a side-coupled 3 GHz LINAC for the high-energy accelerating section originating from the TERA foundation (74, 75). Above a threshold minimum energy (~70 MeV for protons),modular cavities are used to enable the LINAC to change energy. This is an unusual LINAC design, but enables the beam energy to be precisely regulated pulse-by-pulse at rates of ~200 Hz. This translates into a minimum time for energy change of just 5 ms (16). Technology capable of supporting kHz pulse rates for lower ELSTs exists. A LINAC is capable of switching energy in any direction but the remaining bottleneck would be the magnetic reproducibility in the BDS.

Recent studies on clinical suitability for LINACs show that the production of a stable spot size with energy can result in increased conformity particularly for deep tumors (76), and the ability to vary spot size on demand while delivering protons at FLASH dose rates could lead to LINACs having greater conformity and larger tumor volume capability compared to cyclotrons (77).

Additionally, LINAC designs could also be adjusted to accelerate different particle species, where particle switching times are limited by magnetic field changes and stabilisation in the ion source and low energy section. Cavities with increasingly higher accelerating gradients are being designed and proposed, exploiting synergies with accelerators developed for high energy particle physics experiments. This trend could also contribute to shrinking the injector stage of synchrotrons. Although the most pursued R&D is a reduction of the facility footprint, LINACs capable of accelerating orders of magnitude larger currents of protons and light ions to ~10 MeV exist or are being developed[6] (79–81).

Another concept which has been considered are laser-driven accelerators. Although much interest has been generated since the early 2000s, progress has been slower than initially anticipated, primarily due to limitations in laser repetition rate, beam intensity, control and reproducibility (82). Proposals exist to use laser-driven ions both as a pre-accelerator into a synchrotron (83) – in which case beam delivery aspects remain as they are at present – or more radically to replace the entire magnetic beam delivery system with an optical one (84). Compared to conventional ion sources, laser-driven beams have large energy spread or even an exponential energy distribution over the full energy range and large divergence, which makes efficient beam transport very challenging (85). A realistic implementation would likely require a beam capture, ESS, collimation and BDS. Existing studies focusing on protons only have proposed high field (>8 T) pulsed solenoids for beam capture, although in some cases a conventional quadrupole triplet could be considered (86, 87). This latter option faces challenges in controlling ion species, energy spread, energy control and other aspects (88).

Alternatively, a potential future option is the Fixed Field Alternating Gradient (FFA) accelerator, which has static (in time) magnets but a beam orbit which spirals slightly outward with increasing beam energy[7]. Unlike the cyclotron, the energy range of the FFA is in principle limitless, so heavier ions including carbon can also be accelerated to clinical energies.

FFAs have many potential applications as they can be compact in size, with fast acceleration and high beam current (89). The largest limitation is that this technology is less well-established than synchrotrons or cyclotrons: few accelerator physicists, engineers and component suppliers are familiar with this type of machine. However, they were first proposed back in the 1960s and have been developing rapidly in the last two decades. A number of FFAs have been constructed, the most relevant being the two 150 MeV proton FFAs constructed in the early 2000s in Japan (90) with 100 Hz repetition rates which have been the subject of detailed beam studies and characterisation (91). New designs for proton and ion therapy, including superconducting designs, have not yet been prototyped or constructed.

In general this type of accelerator produces a pulsed beam. This leads to a key advantage of the FFA for charged particle therapy: fast variable energy extraction, usually with single-turn extraction[8]. Extraction can occur at any time in the acceleration process, dictating the beam energy. A second advantage is that the FFA removes magnet ramping, overcoming hysteresis or magnet washing issues, so the pulse repetition rate of the FFA can be much higher than a synchrotron: a rate of 1 kHz was the goal of a 2010 design study PAMELA (Particle Accelerator for MEdicaL Applications) (92). This is vastly different to the few seconds (<1 Hz) for a regular synchrotron or 50–70 Hz for a rapid cycling synchrotron. This rapid pulse rate has a remarkable feature of enabling pulse-by-pulse flexibility across the entire clinical energy range without limitation in energy step or direction, with a choice of particle species. This could reduce the ELST to the order of ms and also enable the possibility of interleaved treatment pulses (carbon or proton) and imaging (high energy proton) pulses delivered through the same BDS.

Removing restrictions in energy variation imposed by existing technologies could open up treatment options that are impossible at present. Nonetheless, taking full advantage of the rapid energy changes enabled by FFAs, LINACs or other machines with fast energy variation would require the BTL and/or gantry to be able to accept and deliver the extracted beam.

3.2 Energy Layer Switching Time

The transverse motion of the beam can be sped up by using continuous scanning methods and with faster dipole magnets. As discussed by Flanz & Paganetti et al. (13) scanning dipoles from

[6] An extreme example is LIPAc (78) which has already demonstrated the acceleration of 5 MeV, 125 mA deuteron beam which is ~50 times more than the currents typically injected in synchrotrons for therapy.

[7] FFA is a method of designing accelerator optics and can be applied also to beamlines and gantries.

[8] Slow extraction may be possible, but has not been studied in detail.

3–100 Hz are used clinically but capabilities also depend on their size, distance from the patient as well as inductance and power supply considerations. Additionally, speeds are restricted by the viability of currently available beam instrumentation tools to accurately and rapidly, measure and record dose rates.

While the transverse scanning magnets are relatively fast; it can take ~100 times longer to move the beam the same distance longitudinally. Decreasing the time to change energies between IES is a challenging issue. It is not just a singular aspect of the delivery process but is governed by several factors: primarily the accelerator and the BDS. The ELST ranges widely across facilities and can be up to an order of magnitude longer than the time it takes to scan across an IES. A comparison of minimum baseline figures for clinical accelerators are shown in **Table 1**.

If we consider the breakdown of time components again (Section 2.2), the BDT can be approximated by summing the different contributions. Assuming some general conditions (uniform, continuous beam intensity) with a typical PBS [$\mathbf{T_{1A+B}}$] spot delivery speed of 6.67 ms/spot [i.e. 150 spots/s; PSI report 5 ms/spot = 200 spots/s (93)]. As a practical example, we take values from a robust IMPT "standard clinical plan" for an oropharyngeal case, averaged for 5 patients over 3 fields (94) where 700 spots are needed over 42 layers. Therefore, a BDT estimate[9] with a typical ELST (1 s), for a single field irradiation: $42\times[\mathbf{T_1}$ = 113 ms] + $41\times[\mathbf{T_2}$ = 1 s] + $42\times[\mathbf{T_3}$ = 2 ms] = 45.84 s.

For comparison, if a fast ELST (80 ms) is instead applied: $42\times[\mathbf{T_1}$ = 113 ms] + $41\times[\mathbf{T_2}$ = 80 ms] + $42\times[\mathbf{T_3}$ = 2 ms] = 8.12 s. Evidently, this results in a much shorter BDT; particularly for complex cases with many layers which may also need rescanning, there is an accumulation of time saved for each IES. The increasing penalty for longer ELSTs on BDT for this case is illustrated in **Figure 7**.

Several studies have been performed which examine the time components quantitatively and evaluate the impact of the ELST on BDT, as a means to improve treatment delivery efficiency. Shen et al. (22) carried out a detailed analysis to model the BDT at a synchrotron PBT facility based on operational parameters including the ELST, average scanning speeds, spill rate, charge and extraction time, magnet preparation and verification time. The average ELST across the energy range and scanning speeds in x and y were reported as 1.91 s, 5.9 m/s and 19.3 m/s, respectively. Values determined by the model were compared with log files from a large range of delivered patient treatments to calculate the contributions to BDT. The ELST was identified as the most dominant contributor to BDT at 71%; reducing this time would greatly improve beam utility during delivery.

All components of the PBT treatment process were also comprehensively analyzed by Suzuki et al. (26) to evaluate the use factor and efficiency of beam delivery parameters for different disease sites. Although there are numerous factors, the BDS largely governs treatment efficiency which is asserted as the most important factor as it is directly related to utility and availability. For facilities which operate a busy schedule, reducing BDT can enable greater throughput; at this clinic, a 1 min reduction in BDT for a single field accumulated to treating an equivalent 10 more prostate patients a day. This can also lower costs as treatment costs scale with the total time spent by the patient in the treatment room (13).

Increasing throughput is an important consideration to improve the availability of CPT. A sensitivity analysis of daily throughput capacity – and therefore efficiency of PBS treatments – was subsequently performed at the same facility by Suzuki et al. (23). Several parameters in the treatment process were similarly studied; the BDT was reduced to the sum of the ELST and spot delivery time as a function of the treatment volume, dependent on the disease site. The ELST was reported as 2.1 s and accounted for 70–90% of the BDT for the majority of tumor volumes (<1 L). Although for this case the BDT is limited by the accelerator, a reduction in the waiting times can greatly decrease BDT: the ELST as well as room switching time account fora large part of the total treatment time. Increasing the uptime by minimizing beam-off time can significantly improve throughput (95). Nystrom and Paganetti et al. (13) emphasize that improvements in this area will have the greatest efficiency gain and that a shorter BDT will have the greatest impact on facilities with multiple rooms.

An optimization which could further reduce BDT is by splitting the beam for delivery to multiple different rooms simultaneously. This is more realistically achievable with accelerators carrying a microbunched beam structure. In this case transverse RF fields could be used to induce initial beam separation in transport lines. However, high beam intensities and continuous, reliable operation require additional degraders and shielding. The complexity and cost of the facility, ACS and other systems would nonetheless increase considerably and safety must also comply with medical standards (13, 96). Developments in the BDS and accelerator technology are needed for this; a more practical pursuit could be to optimize processes surrounding treatment set-up, room scheduling and utilization.

3.3 Beam Delivery Systems, Gantries & Fixed Beamlines

At clinical facilities, the ELST typically approaches the order of seconds with a commercially available BDS, much longer than the baseline values reported in **Table 1**. The time delays to change the magnetic parameters of the beamline are a bottleneck for cyclotron facilities; for synchrotrons, the use of MEE has been implemented in specific instances but is not yet universal (50). Nonetheless, it is clear that the ELST is contingent on magnet ramping speeds and will be prohibitive, particularly when considering emerging developments in the field. In fact, the cost of accelerators is in general lower than the BDS so improvements in accelerators alone will not be sufficient for CPT to reach levels of XRT adoption (25). Accordingly, Myers et al. (18) have advocated that progress with accelerators need to be matched by the BDS in order to accommodate for fast energy variation. Two possibilities are suggested: the use of superior magnets or alternatively, to increase the energy acceptance range. The first option would involve low inductance magnets that require large currents and therefore higher build and running costs. The second option has been considered frequently in

[9] Simple additive estimation where N is the number of IES, BDT = $(N)\mathbf{T_1}+(N-1)\mathbf{T_2}+(N)\mathbf{T_3}$.

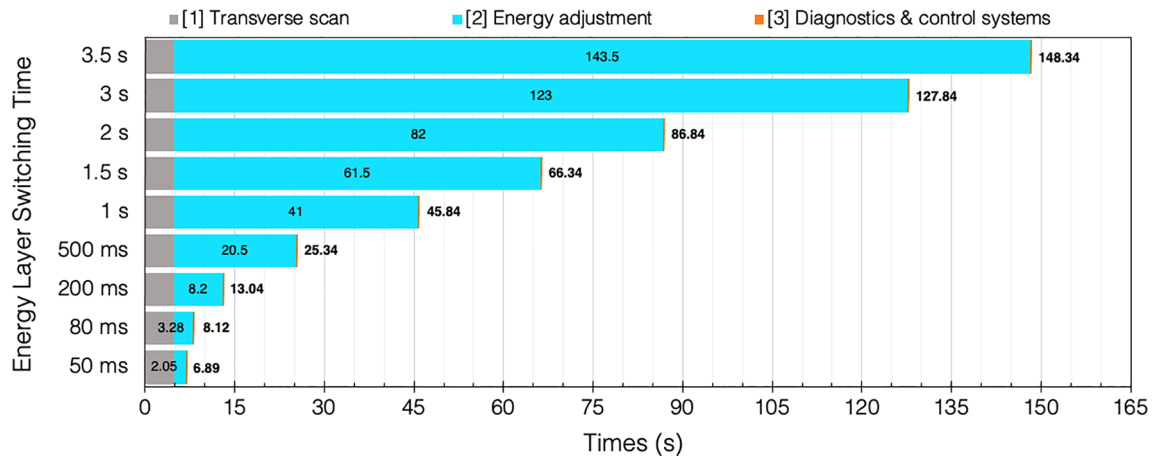

FIGURE 7 | BDT estimates and timing contributions for an example head and neck case (94) given a range of clinical ELSTs [T2]. Transvers scan [T1 = 4.76 s] and system dead times [T3 = 0.08 s] are assumed constant for each of the 42 IES.

literature (96–98) and is becoming more of a possibility with the realization of superconducting (SC) technology and advanced magnet designs.

The BDS contributes to a significant share of the capital and total cost for a CPT facility (24, 25) so future iterations must be designed to reduce operational and construction costs. The BDS must be able to transport the beam with high accuracy (sub-mm precision), at different specific energies and deliver the correct dose distribution reproducibly. For systems which possess a gantry, the downstream section of the BDS comprises of series of magnets to bend and transport the beam to isocentre with the required treatment parameters. The entire gantry rotates to deliver the beam from multiple entry angles. Consequently, the gantry (**Figure 8**) is a physically large and complex mechanical structure: this amounts to considerable costs associated with the weight, size, construction and operation. Most modern proton facilities have gantries in order to deliver PBS which achieves the highest quality of treatment.

For heavier ions, costs are much higher as the gantry must accommodate particles with larger beam rigidities and added physical constraints introduce greater probability of errors (99). Currently there are only a few facilities which deliver carbon-ion beam therapy (CIBT) using a gantry: HIT, Heidelberg, Germany has a gantry which has a footprint of 6.5 m × 25 m (radius × length), weighing ~670 t (100–102) and HIMAC, QST, Japan has a SC gantry, 5.5 m × 13 m weighing ~300 t (103, 104). A second generation, compact SC gantry with a smaller 4 m × 5.1 m footprint was also developed with Toshiba (105). Heavy ion facilities which do not employ a gantry are limited to delivery with fixed beamlines.

The use of SC magnets can dramatically decrease the weight and size of the gantry as higher fields (necessary for >1.8 T) can be achieved with comparatively fewer and smaller magnets. However, the costs for the magnets themselves and the operation of cooling systems may not be economical (98).

These further challenges and costs associated with delivering heavier ions with a gantry hinder its practicality. As such, the question of the necessity of a gantry itself has now been raised: Flanz & Paganetti et al. (13) propose that the simplest way to reduce costs is to remove the gantry completely and in place have

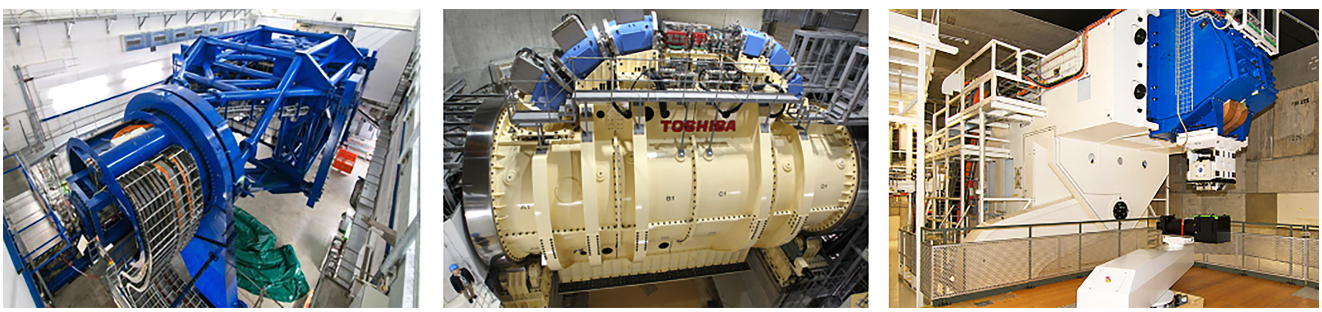

FIGURE 8 | Gantry installations at HIT (106) and HIMAC, QST (104) for CIBT. PSI PBT Gantry 2 (Photo: Paul Scherrer Institute/Markus Fischer).

a fixed beamline. A PBT study by Yan et al. (107) indicates that for several disease sites (PBS head and neck cases), treatments could effectively be delivered gantry-less, requiring only a few fields with fixed geometries. There are other potential benefits to removing the gantry besides lower costs (maintenance, commissioning and also construction i.e. shielding) and the use of upright chairs is now being reconsidered. Seated positioning is typical for ocular treatments and for some specific disease sites; it was also historically the method used at pioneering facilities yet with less success than supine treatments (108). Now, with the advent of modern delivery techniques, superior dose distributions can be achieved with seated treatments and clinical advantages with better immobilisation have also been reported (109). The use of vertical CT enables imaging of patients with the same treatment position for treatment planning and positioning errors can also be corrected with geometrical adjustments of the chair (i.e. changing pitch) (14). This could be particularly effective for tumor sites which are difficult to treat due to motion and could also provide better patient comfort.

A study by Sheng et al. (110) report that rotational and translational positioning with a 6D treatment chair is comparable in alignment precision and reproducibility to a standard robotic treatment couch. Clinical tests of this chair were performed by Sun et al. (111) to verify treatment and workflow feasibility. As optimal plans are possible with only a few fields, it is suggested that beam selection is more significant to the achievable dose distribution than the available number of fields or angles. Additional imaging is also required to ensure correct patient positioning however results showed similar intrafractional deviation to treatments in a lying position. The increased physical demand of a seated treatment indicated the need for better immobilisation procedures; an interesting prospect is if motion or positioning differences could be further reduced. Nevertheless, overall patient comfort is an important consideration for upright treatments and Mazal et al. (109) list several cases where there could be advantages, such as increased ease with patient anesthesia or airway management. Furthermore, the increased availability of physical space with a fixed beamline also enables greater flexibility with the beam optics and delivery components. This could allow the BDS to produce a beam with a wider range of characteristics (field size, spot size, scanning capabilities etc.) as the optical design and inclusion of auxiliary devices can be reconsidered without the conditions imposed by the rotational and mechanical constraints of the gantry. Similarly, another significant benefit is the prospect of enhanced integration with imaging; improved conformity and registration between imaging modalities and the possibility of online imaging systems. This technology is currently being commercially developed and the option of upright treatments with a gantry-less system in clinical practice may soon be a possibility.

3.3.1 Energy Acceptance Range

The energy acceptance – or momentum acceptance – is a limiting factor in existing beamlines and gantries. A typical momentum acceptance range is ±1% (approximately ±2% energy acceptance), equating to changes of 5 mm in water equivalent depth; this is the usual spacing between each adjacent IES. This acceptance band is a technical limit corresponding to the maximum deviation from nominal beam momentum which can stably be transported by the optics. Any such momentum deviation produces a change in trajectory (via dispersion) and the configuration of the magnetic elements determines the particle beam dynamics and stable range.

Presently, the settings of all the BDS magnets must be changed synchronously for each IES, whilst considering AC losses and hysteresis effects, requiring several checks and settling time for field stability (98). This preserves the correct beam parameters at isocentre and ramping typically occurs in one direction to reduce complexities. SC magnets with high ramp rates also experience issues with eddy currents, but their use in the BDS for heavier ions appears necessary in order to minimize size and weight. Increasing the momentum acceptance range enables the BDS to transport various beams with the same fixed magnet settings and therefore minimal dependence on their field ramping capabilities.

Several designs for PBT have been proposed which use achromatic beam optics to suppress dispersion effects, reporting momentum acceptance ranges of ±3% by Gerbershagen et al. (112), ±15% by Nesteruk et al. (113) and ±25% by Wan et al. (114). For heavy ions, large acceptance can be achieved with new SC magnet designs (canted-cosine-theta combined function magnets) (14).

Another optical configuration which enables a large energy acceptance (LEA) is the FFA concept (Section 3.1.3). With non-scaling FFA optics, combined function dipole and quadrupole magnets can be arranged in repeated cells in an alternating gradient configuration, resulting in strong focusing in both planes with small dispersion. This is stable for a wide range of energies and enables beam traversal along the beamline at multiple physical positions within the same fixed magnetic fields. Due to the low dispersion, small aperture magnets can be constructed, minimizing size and construction costs. Multiple designs using FFA optics have been reported by Trbojevic et al. (115, 116) with a momentum acceptance range of approximately ±20–30% using SC magnets for both PBT and CIBT. Alternatively, novel Halbach type permanent magnets have been designed for a PBT gantry (**Figure 9**) with a footprint of ~2.2 m × 7m, accepting up to ±35% (117, 118).

Alternative gantry designs to allow rapid beam delivery also include a novel method using high field SC magnets to produce a toroidal field capable of delivering beams from multiple directions in a fixed, steady state, '*GaToroid*' gantry (119). This removes the mechanical and time constraints typically required to change angle and energy. However, there may be limitations with the number of delivery angles, field size and challenges in achieving positional accuracy. Furthermore, several aspects with the design, engineering, field configuration, beam transport and optical modelling are still under development.

In general, increasing the energy acceptance of a BDS to enable a LEA suggests many benefits. Several aspects must be considered for future application of a LEA BDS in clinical facilities. The parameters of the magnets and the configuration

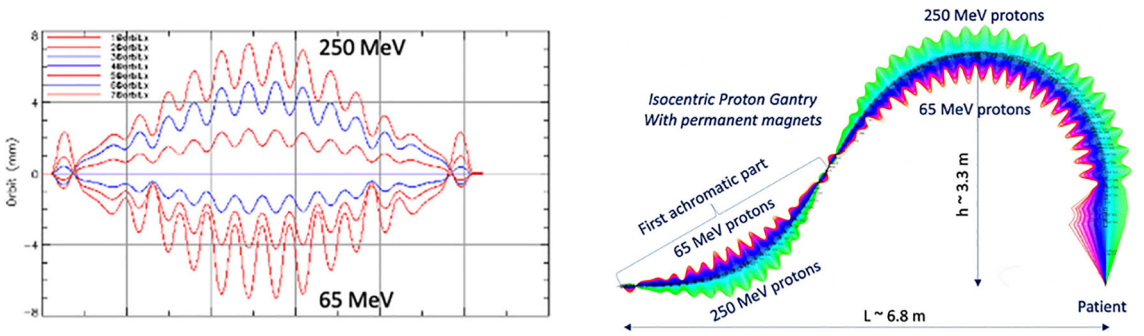

FIGURE 9 | Orbit shape with varying energy (left) showing an energy acceptance range of 65–250 MeV. Orbit offsets within the permanent FFA gantry for PBT (right). Note the orbit offsets with energy are magnified for clarity in the right hand image and are around 15 mm, as shown on the left (117).

of the optics design determine both the costs of the BDS and characteristics of the beam. This introduces a trade-off between the complexity and technical constraints imposed on the design and the achievable acceptance range: there must be an optimal range for which there will be maximal benefit. For example, Nesteruk et al. (113) describes that a ±30% energy acceptance band can provide ~70% of patient treatments at PSI without the energy modulation requiring a setting change. The design and optimisation process will likely be driven by this requirement which will outline the cost benefit, particularly for the delivery of other particle types and heavier ions.

This also raises the question of the appropriate source-to-axis distance and positioning of scanning magnets either upstream or downstream (17). What is clear is that in a novel BDS the parameters of the delivered beam must be clinically acceptable: energy spread (relates to range and beam penumbra), quality, size and shape (reproducible for every energy), position (spots must be positioned within precise margins) and also transmission (relates to particle rate for IES scans and current regulation with off-momentum particles). These properties must be consistent across the entire energy range and conform to performance and safety standards: rapid and accurate delivery cannot impinge on patient safety. Additional components (ripple filter, scattering foils etc.) may be necessary to moderate several beam characteristics upstream of the BDS (13, 120).

The build of any BDS must be as robust as existing commercial systems (mechanically and operationally) and accommodate all the necessary components (beam diagnostics, nozzle, ESS etc.). For integration, the BDS needs to consider modularity for possible retrofitting or replacement of parts. Fundamentally, one must expect a lighter or smaller physical structure, also a simpler system in terms of functionality, servicing and tuning; these improvements along with cheaper running costs will further assist to lower overall expense.

The adaptation of current control systems to manage a larger energy range is currently being explored. A recent study at PSI by Fattori et al. (121) demonstrates the clinical possibilities enabled by an increased momentum band to deliver PBS with real time tracking and enhanced rescanning capabilities. The prospect of energy meandering – ramping beamline magnets bidirectionally (up and down) – to further decrease the BDT is also presented. This combined with optimization of the energy sequencing and layering offers higher flexibility and uptime in terms of the duty cycle (93, 122).

3.4 Motion and Treatment Efficacy

The discussed benefits of decreased BDT have so far centered around the gain in delivery efficiency and therefore treatment efficiency or cost. Arguably however, the more compelling argument of a faster BDT is the potential of better treatment efficacy: treatment quality can be correlated to the efficiency of delivery (27). Future CPT facilities will need to be able to operate with shorter BDTs whilst ideally providing better quality treatments. As the BDT is dominated by the ELST, the accumulation of delays for each IES results in extended irradiation times; scanning sequences within 3–5 s or longer correspond with the respiration cycle and the effects of this motion are consequential for treatment (123).

3.4.1 Interplay Effects

For PBS in CPT, there is an inherent challenge of utilizing the BP due to uncertainties in the range and physiologic motion which compromise any dosimetric advantages. Heavy ions have regions of elevated LET and therefore greater sensitivity, this makes it more challenging to treat a wide range of indications, especially for moving tumors. The issue of motion during PBS delivery is twofold: both the target site and the beam deviate in position simultaneously, resulting in degraded dose distributions, '*extitinterplay effects*'. Effects differ as dependent on the accelerator type, BDS and dose delivery characteristics (124).

Interplay effects (**Figure 10**) cause regional dose in homogeneities due to under- and over-dosage, resulting in differences from the planned treatment distributions in each fraction. The clinical implications of interplay effects are well known (125–127) and require a variety of motion mitigation strategies; many are commonly used in practice and more are also being developed. It is frequently recommended that a shorter BDT can decrease the extent of or even prevent interplay effects, if

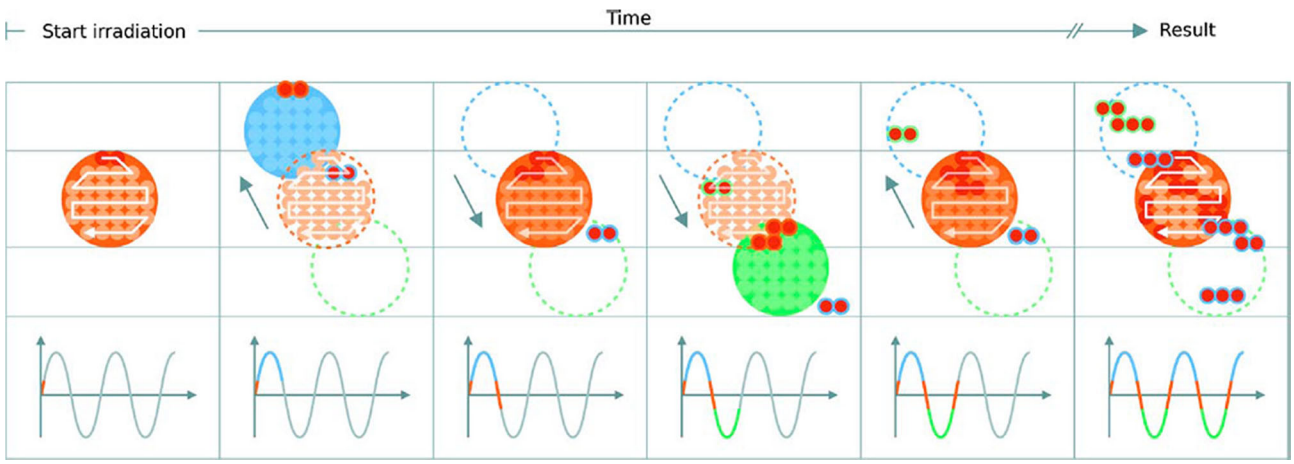

FIGURE 10 | Delivery of a single IES with target motion (phases of movement are indicated by the plot and shown in blue, orange and green). The initially determined scan path in the target volume is shown in red. The raster scanned spots are translated outside the target due to motion which results in progressive degradation of the dose distribution. Reproduced from (124) with permission from IOP.

the BDS is capable of delivering the dose sufficiently fast. The overall length of treatment is important: shorter irradiation times are ideal to reduce the amount of intrafractional motion yet to correct for interplay effects, more fractions are beneficial. It may seem like these are in conflict as each occur at the detriment of the other however, the key factor is again the BDT itself: high dosimetric quality has been demonstrated to be achievable even with higher delivery efficiency (27).

3.4.2 Management & Mitigation

A shorter BDT is attainable by reducing the burden of long ELSTs: the longer the duration, the greater the need to minimize its impact. Work by Van De Water et al. (94) investigated the effect of a shorter BDT on plan quality by using a self-developed method with their treatment planning system to minimize number of layers required to deliver a treatment with robust optimization. It was shown that the BDT could be reduced by up to 40% for a range of different disease sites without compromising treatment quality. Other methods to decrease the BDT include: increasing the IES spacing (128), varying the size of spots (129), using a range of non-uniform sizes (13), changing the dose grid size or spotspacing (130), optimizing spot sequencing (131), scan path (132), or multiple criteria i.e. different weighted spots or resampling for selective placement of spots (27, 133).

Cao et al. (134) also present an energy layer optimization method which increased the delivery efficiency whilst maintaining dosimetric quality. Each of these has varying effects on dosimetric metrics such as homogeneity, conformity indices or equivalent uniform dose. However, some associated benefits are not quantifiable, such as patient comfort and further biological effects which may also contribute to better treatment outcomes. The purpose of any motion mitigation approach is to preserve conformity but simultaneously maintain treatment time duration (124). All of these corrective optimization tools are designed to work around existing limitations in technology and if a new, faster BDS and accelerator system were made available, would either become obsolete, or could be made even more powerful to the benefit of both treatment efficiency and efficacy.

There are also a range of common techniques which have been translated from XRT to CPT, including 4D planning and delivery (135–137); a comprehensive overview is presented by Bertholet et al. (138). A simple method is to implement safety margins in treatment planning, expanding the clinical target volume to a planning target volume to account for uncertainties and dose delivery errors (139). However, this has been demonstrated to be insufficient for complex intensity modulated PBT plans (140) and more robust methods are necessary to lessen adverse effects caused by the steep dose gradients and motion. Managing these is a highly complex task and a variety of motion mitigation strategies are applied by different facilities; these are summarized in detail in (141–143). Some specific approaches include: breath-hold (144), beam tracking (33), gating (145) which can also be combined with rescanning (31, 146). The use of physical equipment to shape the beam has also been re-examined using ridge filters (147, 148), 3D modulators (149) and other beam shaping (150) or modulating devices (151). Equivalent to passive scattering, the entire field can then be delivered almost instantaneously which thus negates the effects of interplay (1).

3.4.3 Rescanning

In addition to beam gating and tracking, rescanning – also termed repainting (152) – is a primary method used to mitigate intrafractional motion through repeated irradiation. Pencil beams are particularly sensitive to motion and as this movement is generally periodic, dose errors can be statistically averaged out by increasing the number of fractions (153). A minimum number of rescans must be performed for added benefit (154), particularly for mobile sites such as the liver and lungs (127). Notably, the

effect itself depends on the patient and beam parameters such as the direction, scan speed and path: characteristics determined by the accelerator and BDS. Bert et al. (124) mention that by choosing favorable parameters, the severity of interplay effects can be lowered and quasi-eliminated if scan speeds are sufficiently quick. The significant concern with rescanning and other mitigation techniques is that they can extend treatment to unacceptable lengths of time. Even at facilities which offer fast dynamic energy modulation, the accumulation of BDT still surpass time limits defined by the respiration cycle. The potential benefit of a faster BDS is the higher rescanning ability: this is specifically dependent on capabilities of the BDS, primarily its efficiency and the applied methods of delivery (29).

Another issue with rescanning is if motion of the beam and patient are synchronized: this jeopardizes the averaging effect. This can be avoided by ensuring delivery across the entire respiration cycle (i.e. phase controlled rescanning or breath-sampled rescanning) or introducing variations in the scan path by delays or randomness (142). There are several different patterns by which rescanning is performed (**Figure 11**), most commonly it is done akin to typical delivery, by painting repeatedly across an IES before moving onto the next consecutive layer (layered rescanning). An alternative method is to move through the different layers first, returning to the same IES to paint subsequent distributions (volumetric rescanning).

Volumetric rescanning (VR) is not employed clinically due to long ELSTs which make it impractical. Studies suggest several benefits as it enables additional scan paths and can alter the temporal correlation between beam and organ motion (141). Modifying the rescanning pattern to break the coherence of the beam structure with the periods of motion is an indicator of effectiveness; Bernatowicz et al. (155) demonstrated in a comparative study that outcomes may be less dependent on when the irradiation occurs during the respiratory phase, if VR is performed. The magnitude of the motion amplitude and duty cycle also impact the effectiveness, which can be machine specific (156); VR appears more sensitive to motion irregularity however this is likely due to extended ELST and treatment times (157). A study by Zenklusen et al. (152) suggests that combining VR with a fast delivery technique such as continuous line scanning can be an attractive method if it is possible to irradiate the entire volume within a single breath hold.

4 EMERGING APPLICATIONS

The field of CPT is evolving rapidly and the limitations of even state-of-the-art technology are becoming apparent; the possibility of volumetric rescanning and other advanced techniques require the BDS to be able to deliver efficiently with fast energy modulation. A recent review by Mazal et al. (109) outline several of these proposed CPT approaches to reduce associated uncertainties, complexities and cost. We specifically examine technological constraints and discuss BDS improvements as relevant for FLASH and arc therapy.

4.1 FLASH

The goal for treatment is to be able to irradiate the tumor sufficiently while sparing healthy tissue. This is represented by the therapeutic index (TI) and indicates the ratio between the probability of tumor control to normal tissue complication: improvements in delivery methodologies and treatment efficacy seek to increase the TI. There is always a trade-off with increasing the amount of dose delivered to the tumor, as normal tissue is simultaneously exposed to damaging radiation. Hyperfractionation and different approaches are commonly used in RT to vary the length of treatments to reduce toxicity and support the recovery of healthy tissue. Alternatively, some radioresistant tumors also respond well with hypofractionation. It is well established that the dose rate and irradiation time has an effect on cell response (158, 159) although it varies widely, dependent on biological parameters and the linear energy transfer (LET) related to the particle type (160). For certain conditions, a minimal dose rate effect has been observed; this has prompted a surge of recent research activity to reconsider applicable irradiation time scales for better therapeutic outcomes.

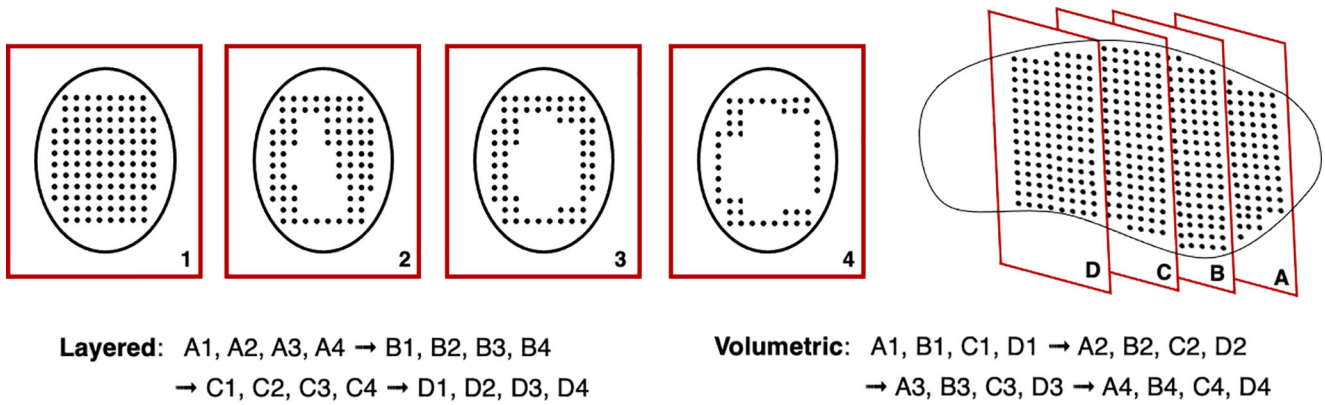

FIGURE 11 | Possible example IES pattern sequences for layered and volumetric rescanning.

As such, the shift to ultra high '*FLASH*' dose rates (≥40 Gy/s in ~100 ms) (161) has gained significant interest and may have the potential to revolutionise RT. The promise of FLASH therapy suggests an increased TI due to biological advantages by a reduction of normal tissue complications *via* the tissue sparing FLASH effect (162). Although the effect is dependent on spatio-temporal factors, the provision of FLASH RT may favor delivery with certain particle types based on technological compatibility and applicable physical parameters. However, the specific biological mechanisms are complex and still yet to be clearly identified (163–165). These drive the technical requirements necessary to induce the benefits and achieve clinical feasibility: the '*beam parameter space*' determines the applicable radiation conditions such as the beam structure and particle type, yet much remains under investigation (166, 167).

The necessary accelerator and beam delivery developments required to deliver FLASH with clinical protons are detailed extensively by Jolly et al. (42). Alongside this is also the need for better instrumentation systems which can operate proficiently under FLASH conditions (168). A fundamental challenge is achieving the requisite FLASH beam parameters for PBS delivery with clinical accelerator systems, given safety restrictions (169). The generated beam intensity must be sufficiently high to realize the minimum effective FLASH dose rate and simultaneously, provide adequate coverage and conformity over the applicable fields. It has been easier to modify existing clinical LINACs to deliver FLASH with electron beams (170). For ion beams there are difficulties with reaching the required dose rates, which demand an increase in beam current by several orders of magnitude for rapid irradiation of a clinically relevant volume. A number of CPT facilities have been able to modify their accelerators (mostly isochronous cyclotrons and synchrocyclotrons) for FLASH with proton beams (171), and photon beams have been studied at large scale synchrotron research facilities (172). FLASH with different ions such as carbon and helium is also being examined (173–175).

For conventional synchrotrons, one of the challenges is to be able to store enough particles in the main ring to deliver the entire field, as the time required for a single re-injection and acceleration is typically considerably longer than 500 ms. Systems theoretically capable of injecting into the main ring at a suitable energy with a charge exceeding requirements do exist (78). However, developments in this direction are in opposition to the goal of footprint and cost reduction, as larger and more expensive equipment is generally necessary. When a large amount of particles is injected in the main ring at once, the interaction among the particles start to be less and less negligible. Although strategies exist to keep this space charge effect under control, the effect is accentuated in smaller radius synchrotrons.

A study by Zou et al. (176) assessed the limitations experienced with cyclotrons by analyzing the main machine parameters which influence delivery. The authors demonstrate that it is impossible to deliver FLASH dose rates fully across the planned $5 \times 5 \times 5 \times cm^3$ SOBP region due to BDS dead times: magnet scanning speeds and significantly, the ELST. Nine IES scans were required and although applying a standard 1.5 s ELST was too slow, even the fastest clinical ELSTs of 50 ms and 80 ms, were also insufficient. High doses were achieved in the central beam spot axis but at the lateral edges, a significant portion fell below nominal levels. This spread of dose across the beam spot is a noted difficulty with delivering FLASH using PBS however the necessary instantaneous, mean or threshold dose over a region of interest, has not yet been quantitatively defined (177). The impact of deadtimes is also unclear, as PBS parameters (components in Section 2.2) determine the dose output and timing (178). Hybrid delivery schemes and 3D modulation devices have been suggested for reaching FLASH dose rates across the entire volume however higher beam intensities are needed to compensate particle losses.

Near instantaneous delivery should be targeted given the indicative 100 ms time frame necessary for the FLASH effect: this will also negate the effects of intrafractional motion. This rapid delivery of FLASH combined with image guidance is also being developed into a next generation, treatment modality: Pluridirectional High-energy Agile Scanning Electronic Radiotherapy (PHASER) (179). The platform consists of a novel high gradient LINAC structure, distributed RF network for 16 non-coplanar beamlines in place of a gantry, where the electron beam is steered onto the X-ray source and collimated into fine channels. This could enable the delivery of high intensity, modulated XRT beams from multiple angles with fast energy changes (300 ns) for FLASH.

Clinical FLASH trials have also commenced (180, 181) yet there is limited implementation due to many challenges: the technological requirements push the boundaries of and surpass current capabilities. Multiple experimental setups have been developed (182–185) investigating the applicability of these adaptations at clinical PBT facilities. Passive scattering systems with cyclotrons can deliver a SOBP with sufficient mean dose rates but face difficulties reaching larger fields given transmission losses. Improvements are needed for depth and lateral modulation: it is still unclear what optimal beam parameters (time structure, profile, range, uniformity, field size etc.) will be feasible in practice (167).

Furthermore, as ensuring precise beam delivery and positioning is difficult, transmission or '*shoot-through*' FLASH (186) with protons is performed where exploitation of the BP may be considered redundant to maintain a high, effective mean dose rate whilst also resulting in the FLASH effect (184). Several transmission studies have been reported (177, 178, 187) as this method is achievable with current technologies. This bypasses the need for additional beam modification devices, minimizing range uncertainties and delivery requirements. However, increased tissue sparing, dose conformity and other clinical benefits require use of the BP alongside multiple fields of different energies (188). There may also be further radiobiological advantages but this and the FLASH induced responses specific to different radiation types are still being explored.

4.2 Arc Therapy

The endeavor to speed up treatment times has recently renewed interest in arc therapy which is already a mainstream modality in XRT (i.e. Volumetric Modulated Arc Therapy, VMAT). Radiation is delivered to the patient as the gantry rotates

rather than with multiple fields of differently angled, fixed beams. It is possible to achieve higher quality XRT plans with VMAT and a significantly faster BDT than with multiple static beams (189). This concept applied to PBT is termed proton arc therapy (PAT) (190), combined with PBS, spot-scanning proton arc (SPArc) (191) and with other ions (helium and carbon), spot-scanning hadron arc (SHarc) therapy (192). This delivery technique is highly complex and a fundamental challenge again lies with the capacity of the BDS: it must deliver reliably and continuously along rotational arcs, with the ability to switch quickly between energy layers (193).

In PAT (**Figure 12**), a spot scanned beam is delivered in a continuous arc which effectively dilutes the impact of range uncertainties, achieving a conformal dose distribution with also a reduction in standard entrance dose (195). This allows greater flexibility in positioning high dose regions along the beam path and the potential for a much shorter BDT (15). Ding et al. (196) have shown that good conformity and the possibility of a lower integral dose could be achieved with SParc however, treatment plans must be optimized for robustness and efficiency (194, 197, 198). Significant savings in BDT were reported (191) with continuous arc delivery however this is not yet clinically possible with current technology, due to complexities with gantry rotation and long ELSTs.

As an alternative, conventional (step-and-shoot) spot delivery was suggested with a moving couch for fixed beamlines as well as better timing synchronization. Carabe-Fernandez et al. (193) emphasized that although more investigation is needed, PAT has potential particularly for certain indications (brain tumors). Once again, in PAT the delivery efficiency is determined by the BDS and improvements are required such as better stability with beam current, positioning and fast energy switching. Single energy fields can reduce BDT such as in proton monoenergetic arc therapy (PMAT) (194), showing acceptable coverage and plan quality. However, partial arcs of varying energies have been proposed for better biological (LET) optimization with complex geometries (199). As the total BDT is a limiting factor (195), quicker ELSTs can shorten treatment times which will also lessen dosimetric constraints due to a dependence on single fields.

Additionally, the possibility of an increased dose in the target volume with PAT may not translate to a higher degree of conformity however could exploit radiobiological advantages further by increasing the TI (199, 200). As with multi-ion radiotherapy (MIRT), combining different particle types for an effective mix of low- and high-LET regions could generate a higher dosimetric quality plan by utilizing favorable characteristics. A planning study by Mein et al. (192) evaluates SHarc with different field configurations using proton, helium and carbon ion beams (**Figure 13**). The results demonstrate several possible clinical benefits such as a lower dose bath, minimization of high-LET components on critical structures and better tumor control with normal tissue toxicity reduction. The use of multiple beam energies offer further gain over single or two-field plans however there are clear, unresolved technical hurdles with the present BDS and gantry systems which prevent the actualization of this technique.

5 DISCUSSION AND FUTURE DIRECTIONS

It is contended that CPT will be a widely adopted modality once costs are comparable to XRT. Global prevalence is growing and new and exciting advancements are on the horizon: delivery methodologies, novel design concepts and greater biological advantages. The current landscape encourages exploration of future long- and intermediate-term approaches which will allow CPT to exceed the ceiling achieved by state-of-the-art XRT (15). Evidently, next generation technologies and facilities are needed to address present challenges in CPT.

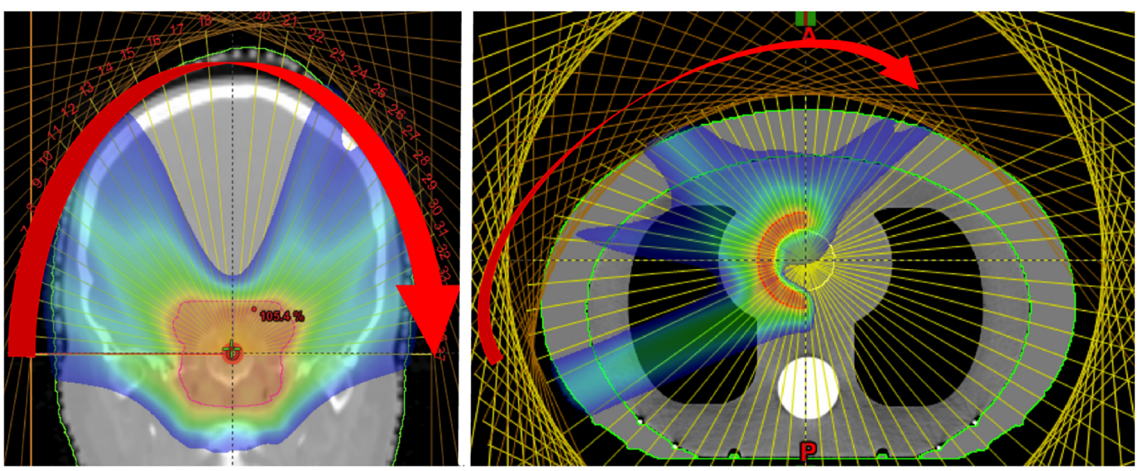

FIGURE 12 | Dose distributions obtained from the delivery of mono-energetic PAT. Coronal view of 37 fields for a brain tumor treatment, applied by a couch rotation every 5° (left). Axial view of a tissue equivalent lung phantom using 35 fields, also 5° rotation (right). Reproduced from (194) with permission from IOP.

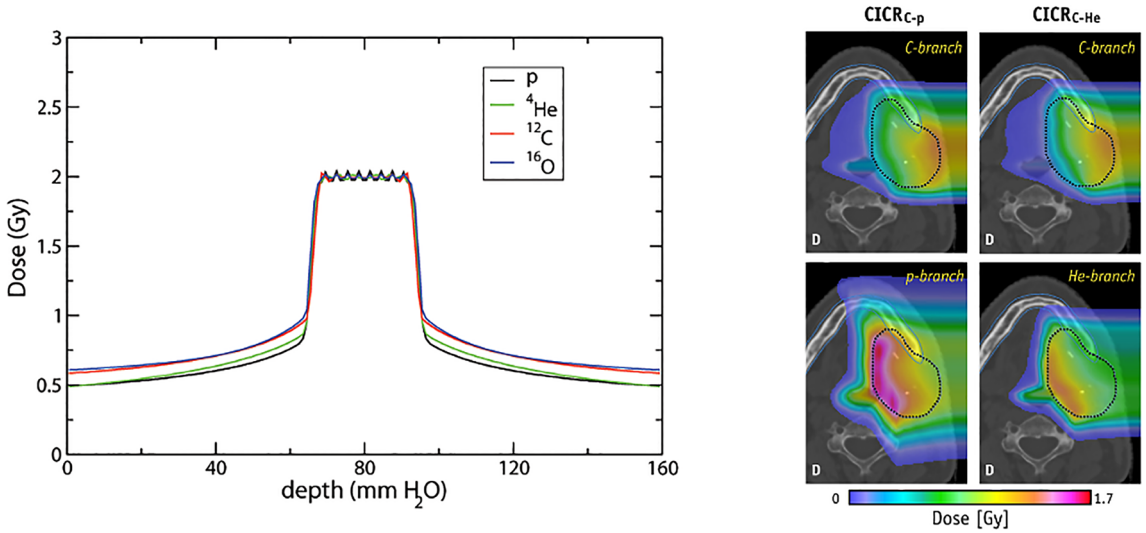

FIGURE 13 | Conformal distributions can be produced by applying opposed fields using different particle types, optimizing for physical dose (left) (201). Combining beams of multiple particle types can generate distinctly different dose distributions, by positioning a chosen particle branch (p or He) at the distal end of the field (202). Images distributed under CC BY 4.0, BY-NC-ND.

Several innovative concepts of delivery have emerged which offer hope of full exploitation of the unique advantages offered by CPT. However, among the multitude of prospective improvements for beam delivery, there is a common underlying goal, to address challenges surrounding treatment time. This is complex as it encompasses more than the BDS and technology, as was examined in Section 2. A shorter BDT results in not only a shorter treatment time, but is also consequential in terms of costs and treatment quality. The constraint imposed by the long ELST is a distinct hurdle in minimizing the BDT: alleviating this would result in better treatment efficiency by reducing involved costs, increasing throughput, also improving treatment efficacy.

Gantries account for the largest expense of facilities and more compact systems have been designed for CPT however the general ambition has been mostly for size and cost reduction. Fundamentally, these hinge on the optical design and the parameters of the magnets, new possibilities are becoming feasible with SC technology however limitations and issues with ramping speeds still persist. Nevertheless, an alternative approach is to improve the beam transport capabilities of the BDS and redesign the optics to increase the overall momentum acceptance range; this has the potential to have a significant impact on treatment by eliminating the ELST dependency on technological bounds, thus shrinking the BDT. The feasibility of a LEA BDS as a solution to decrease the BDT is discussed in Section 3.3.1. The prospect of a LEA BDS raises several challenges but has the possibility of achieving higher quality treatments at lower incurred costs, however would need to be supplemented by further technological improvements throughout. Recent developments with accelerators and possibilities to further decrease the BDT are discussed in Section 3.1.

The ELST handicap on BDT is almost entirely dependent on technological limits: a myriad of different methods must be used in the clinic in order to provide effective treatments to circumvent existing capabilities. These add onto the delivery scheme and workflow; treatment planning optimization is required or the BDS must be adapted to directly change the beam energy using mechanical components. This includes various approaches outside of the BDS such as patient specific devices as well as different accelerator feedback and extraction schemes. A shorter BDT has a significant clinical benefit and the impact of motion and interplay effects must be mitigated using various strategies, described in Section 3.4. Many of the mentioned approaches could also effectively reduce BDT and improve conformity if implemented during the planning optimization process in general clinical practice (13).

A faster BDT and energy switching also drives developments toward a future BDS capable of delivering treatments for a wider range of indications, also with advanced techniques. Several emerging applications are anticipated in the near future which will require an improved BDS for successful delivery such as FLASH and arc therapy. Several other anticipated developments in CPT are not discussed in detail but are also mentioned for context. Faster irradiation times go hand in hand with the need to ensure that treatments are still delivered with the necessary requirements of safety and precision. The importance of robust planning is also arguably higher for CPT than XRT but more challenging due to the physical uncertainties, geometrical in homogeneities and inter- and intra-fractional motion. This is again significant when considering different particle types. CIBT

is expanding in addition to MIRT possibilities using beams of helium, oxygen, lithium etc. (201, 203) which could further increase treatment efficacy. The combination of different ions offers a realm of new possibilities, by tailoring the desired LET and radiobiological attributes for different cancer sites. Optimization of these dose regions can offer more stable distributions and effective treatments (**Figure 13**), such as using lower-LET particles for the sharper dose fall-off and higher-LET beams for hypoxic or radioresistant tumors (204).

MIRT is still a developing modality and technical limitations are primarily due to difficulties with the ion sources and long switching times. Considerations are also necessary with the acceleration and beam transport, as it is more difficult to deliver beams of heavier ions given the associated beam dynamics, mechanical and physical requirements (205). The accelerator complex and BDS will need to be able to accommodate the range of different particle types; this may be selective based on characteristics such as mass and charge [i.e. mass-to-charge ratio ≤3 (206)]. For MIRT treatments, the beams are expected to be arranged such that the high dose regions fall appropriately within the target volume, hence this corresponds to different beam energies for each individual particle type.

The method of delivery must also be gauged, techniques such as minibeams and spatially fractionated RT are suggested (6). Moreover, as the ion switching and ELST restrictions currently cause long BDTs, MIRT treatments have firstly been studied in a single field arrangement (202) and opposed fields (63). The clinical flexibility and advantages are demonstrated however it is worth to note that technological possibilities may only allow sequential irradiation: this raises questions about throughput, quality assurance requirements, interplay effects, motion mitigation and fractionation schedules. The unknowns with the biological effects are also crucial, aside from the uncertainties with modelling and determination of treatment outcomes, the irradiation time structure and the division of the BDT between sources and fractions may introduce considerations with radiobiological chronicity (204).

Simultaneous delivery with mixed beams is complex however has been performed for online monitoring and range verification with helium and carbon (206, 207), exploiting the difference between BPs: carbon ions were used for treatment and helium for simultaneous imaging. Mixed fields are practically limited to synchrotron facilities as cyclotrons aren't able to achieve the acceleration requirements for heavier ions at clinical treatment depths, also the presence of an ESS changes the particle energy and velocity ratio (208). Nonetheless, the strengths of MIRT and fundamentally CPT, can be achieved when limiting factors with delivery and motion are resolved; another important element with this is the need for precision imaging (209).

Online, volumetric imaging for (also adaptive) treatment planning, continuous patient monitoring, motion compensation and 4D treatment delivery is not yet readily clinically available for CPT; the value of these however have a higher potential for benefit in comparison with XRT (210). A promising avenue for this is with MRI guided PBT (MRPT), which has the capability of providing fast real-time imaging with superior soft-tissue contrast without the drawback of additional radiation exposure (211). This approach is also still being developed however there are several complex challenges with integrating MRI technology with a PBT system. The influence of the MRI magnetic field affects the trajectory of the proton beam, interfering with both the delivered dose distribution and resulting image quality. Corrections are required to compensate for the beam deflection and deviations in the treatment plan, dependent on the MR magnet field strength (212, 213). The associated technological concerns relate to beam delivery and decoupling the PBS beamline from the MRI magnet: this requires an entirely new BDS design which can accommodate the physical and geometrical aspects of both systems (214–216). The use of multi-modal approaches for enhanced imaging is also of interest and combining i.e. CT with MRPT has exhibited benefits (13, 217).

6 CONCLUDING REMARKS

The primary hurdle with CPT remains a question of cost, its availability and accessibility is still driven by the balance between cost and benefit: progressive improvements will contribute to decreasing the cost however future growth will depend on the extent of benefit (24). This is also influenced by various factors such as patient selection, clinical trials and scientific evidence. CPT still favors shorter treatments as it is difficult to immobilize patients for larger or complex lesions requiring extended treatment times (i.e. >30 mins). Increasing the range of accepted indications for treatment and capitalising on biological benefits (i.e. reducing fractions) supports the pursuit of reaching the same cost-effective levels as XRT (218, 219).

However, there are several challenges which impact the delivery efficiency and efficacy of treatments in CPT. We have reviewed the existing technical limitations related to the BDS and accelerator, identifying potential avenues for development in CPT. Focusing on the BDS, enhancements such as a LEA could reduce the limiting impact of the ELST on the BDT and shorten treatment times. This supports potential benefits such as cost reduction by expanding the utility of CPT and increasing the throughput of faster and higher quality treatments. Fast energy variation would also offer the capability of delivering advanced methodologies such as volumetric rescanning, FLASH and arc therapy. Improvements in beam delivery and related technologies enable the possibility of a future with cheaper, faster, precise and more effective CPT treatments.

AUTHOR CONTRIBUTIONS

JY and SS: conception and design of the study. JY: literature review, manuscript preparation, writing, editing and figures. AF: writing and review. SS: writing, review, editing and figures. All authors contributed to the article and approved the submitted version.

FUNDING

This work was supported by the William Stone Trust Fund and the Laby Foundation.

ACKNOWLEDGMENTS

SS would also like to acknowledge the generous support of the Baker Foundation and ANSTO.

REFERENCES

1. Engelsman M, Schwarz M, Dong L. Physics Controversies in Proton Therapy. *Semin Radiat Oncol* (2013) 23:88–96. doi: 10.1016/j.semradonc.2012.11.003
2. Bortfeld TR, de Viana MF, Yan S. The Societal Impact of Ion Beam Therapy. *Z fur Medizinische Physik* (2020) 31(2):6–8. doi: 10.1016/j.zemedi.2020.06.007
3. Schaue D, Mcbride WH. Opportunities and Challenges of Radiotherapy for Treating Cancer. *Nat Rev Clin Oncol* (2015) 12:527–40. doi: 10.1038/nrclinonc.2015.120
4. Lühr A, von Neubeck C, Pawelke J, Seidlitz A, Peitzsch C, Bentzen SM, et al. "Radiobiology of Proton Therapy": Results of an International Expert Workshop. *Radiother Oncol* (2018) 128:56–67. doi: 10.1016/j.radonc.2018.05.018
5. Held KD, Kawamura H, Kaminuma T, Paz AES, Yoshida Y, Liu Q, et al. Effects of Charged Particles on Human Tumor Cells. *Front Oncol* (2016) 6:23. doi: 10.3389/fonc.2016.00023
6. Tinganelli W, Durante M. Carbon Ion Radiobiology. *Cancers* (2020) 12:1–43. doi: 10.3390/cancers12103022
7. Lomax ME, Folkes LK, O'Neill P. Biological Consequences of Radiation-Induced DNA Damage: Relevance to Radiotherapy. *Clin Oncol* (2013) 25:578–85. doi: 10.1016/j.clon.2013.06.007
8. Durante M. New Challenges in High-Energy Particle Radiobiology. *Br J Radiol* (2014) 87. doi: 10.1259/bjr.20130626
9. Vitti ET, Parsons JL. The Radiobiological Effects of Proton Beam Therapy: Impact on DNA Damage and Repair. *Cancers* (2019) 11:946. doi: 10.3390/cancers11070946
10. Durante M, Debus J. Heavy Charged Particles: Does Improved Precision and Higher Biological Effectiveness Translate to Better Outcome in Patients? *Semin Radiat Oncol* (2018) 28:160–7. doi: 10.1016/j.semradonc.2017.11.004
11. Durante M, Orecchia R, Loeffler JS. Charged-Particle Therapy in Cancer: Clinical Uses and Future Perspectives. *Nat Rev Clin Oncol* (2017) 14:483–95. doi: 10.1038/nrclinonc.2017.30
12. Rackwitz T, Debus J. Clinical Applications of Proton and Carbon Ion Therapy. *Semin Oncol* (2019) 46:226–32. doi: 10.1053/j.seminoncol.2019.07.005
13. Paganetti H, Beltran C, Both S, Dong L, Flanz J, Furutani K, et al. Roadmap: Proton Therapy Physics and Biology. *Phys Med Biol* (2021) 66:05RM01. doi: 10.1088/1361-6560/abcd16
14. Durante M, Debus J, Loeffler JS. Physics and Biomedical Challenges. *Nat Rev Phys* (2021) 0123456789:777–90. doi: 10.1038/s42254-021-00368-5
15. Schreuder AN, Shamblin J. Proton Therapy Delivery : What is Needed in the Next Ten Years? *Br J Radiol* (2019) 2020). doi: 10.1259/bjr.20190359
16. Farr JB, Flanz JB, Gerbershagen A, Moyers MF. New Horizons in Particle Therapy Systems. *Med Phys* (2018) 45:e953–83. doi: 10.1002/mp.13193
17. Schippers JM, Lomax A, Garonna A, Parodi K. Can Technological Improvements Reduce the Cost of Proton Radiation Therapy? *Semin Radiat Oncol* (2018) 28:150–9. doi: 10.1016/j.semradonc.2017.11.007
18. Myers S, Degiovanni A, Farr JB. Future Prospects for Particle Therapy Accelerators. *Rev Accelerator Sci Technol* (2019) 10:49–92. doi: 10.1142/s1793626819300056
19. Owen H, Lomax A, Jolly S. Current and Future Accelerator Technologies for Charged Particle Therapy. *Nucl Instruments Methods Phys Research Section A: Accelerators Spectrometers Detectors Associated Equip* (2016) 809:96–104. doi: 10.1016/j.nima.2015.08.038
20. Lomax A. What Will the Medical Physics of Proton Therapy Look Like 10 Yr From Now? A Personal View. *Med Phys* (2018) 45:e984–93. doi: 10.1002/mp.13206
21. Flanz J, Bortfeld T. Evolution of Technology to Optimize the Delivery of Proton Therapy: The Third Generation. *Semin Radiat Oncol* (2013) 23:142–8. doi: 10.1016/j.semradonc.2012.11.006
22. Shen J, Tryggestad E, Younkin JE, Keole SR, Furutani KM, Kang Y, et al. Technical Note: Using Experimentally Determined Proton Spot Scanning Timing Parameters to Accurately Model Beam Delivery Time. *Med Phys* (2017) 44:5081–8. doi: 10.1002/mp.12504
23. Suzuki K, Palmer MB, Sahoo N, Zhang X, Poenisch F, MacKin DS, et al. Quantitative Analysis of Treatment Process Time and Throughput Capacity for Spot Scanning Proton Therapy. *Med Phys* (2016) 43:3975–86. doi: 10.1118/1.4952731
24. Loeffler JS, Durante M. Charged Particle Therapy-Optimization, Challenges and Future Directions. *Nat Rev Clin Oncol* (2013) 10:411–24. doi: 10.1038/nrclinonc.2013.79
25. Durante M, Paganetti H. Nuclear Physics in Particle Therapy: A Review. *Rep Prog Phys* (2016) 79. doi: 10.1088/0034-4885/79/9/096702
26. Suzuki K, Gillin MT, Sahoo N, Zhu XR, Lee AK, Lippy D. Quantitative Analysis of Beam Delivery Parameters and Treatment Process Time for Proton Beam Therapy. *Med Phys* (2011) 38:4329–37. doi: 10.1118/1.3604153
27. Müller BS, Wilkens JJ. Prioritized Efficiency Optimization for Intensity Modulated Proton Therapy. *Phys Med Biol* (2016) 61:8249–65. doi: 10.1088/0031-9155/61/23/8249
28. Lazarev V, Chubarov O, Emhofer S, Franzini G, Göller S, Robin A, et al. Technical Overview of the Siemens Particle Therapy Accelerator. *IPAC 2011 - 2nd Int Particle Accelerator Conf* (2011) 3577–9.
29. Klimpki G, Zhang Y, Fattori G, Psoroulas S, Weber DC, Lomax A, et al. The Impact of Pencil Beam Scanning Techniques on the Effectiveness and Efficiency of Rescanning Moving Targets. *Phys Med Biol* (2018) 63:aacd27. doi: 10.1088/1361-6560/aacd27
30. Furukawa T, Inaniwa T, Sato S, Shirai T, Takei Y, Takeshita E, et al. Performance of the NIRS Fast Scanning System for Heavy-Ion Radiotherapy. *Med Phys* (2010) 37:5672–82. doi: 10.1118/1.3501313
31. Schätti A, Zakova M, Meer D, Lomax AJ. The Effectiveness of Combined Gating and Re-Scanning for Treating Mobile Targets With Proton Spot Scanning. An Experimental and Simulation-Based Investigation. *Phys Med Biol* (2014) 59:3813–28. doi: 10.1088/0031-9155/59/14/3813
32. Zhang Y, Huth I, Weber DC, Lomax AJ. A Statistical Comparison of Motion Mitigation Performances and Robustness of Various Pencil Beam Scanned Proton Systems for Liver Tumour Treatments. *Radiother Oncol* (2018) 128:182–8. doi: 10.1016/j.radonc.2018.01.019
33. Saito N, Bert C, Chaudhri N, Gemmel A, Schardt D, Durante M, et al. Speed and Accuracy of a Beam Tracking System for Treatment of Moving Targets With Scanned Ion Beams. *Phys Med Biol* (2009) 54:4849–62. doi: 10.1088/0031-9155/54/16/001
34. Pedroni E, Bearpark R, Böhringer T, Coray A, Duppich J, Forss S, et al. The PSI Gantry 2: A Second Generation Proton Scanning Gantry. *Z fur Medizinische Physik* (2004) 14:25–34. doi: 10.1078/0939-3889-00194
35. Pedroni E, Meer D, Bula C, Safai S, Zenklusen S. Pencil Beam Characteristics of the Next-Generation Proton Scanning Gantry of PSI: Design Issues and Initial Commissioning Results. *Eur Phys J Plus* (2011) 126:1–27. doi: 10.1140/epjp/i2011-11066-0
36. Koschik A, Baumgarten C, Bula C, Duppich J, Gerbershagen A, Grossmann M, et al. PSI Gantry 3: Integration of a New Gantry Into an Existing Proton Therapy Facility. In: *IPAC 2016 - Proceedings of the 7th International Particle Accelerator Conference*. Busan, Korea: JACoW Publishing (2016). p. 1927–9.
37. Mizushima K, Furukawa T, Iwata Y, Hara Y, Saotome N, Saraya Y, et al. Performance of the HIMAC Beam Control System Using Multiple-Energy Synchrotron Operation. *Nucl Instruments Methods Phys Research Section B: Beam Interact Materials Atoms* (2017) 406:347–51. doi: 10.1016/j.nimb.2017.03.051
38. Noda K, Furukawa T, Fujimoto T, Hara Y, Inaniwa T, Iwata Y, et al. Recent Progress and Future Plans of Heavy-Ion Cancer Radiotherapy With HIMAC. *Nucl Instruments Methods Phys Research Section B: Beam Interact Materials Atoms* (2017) 406:374–8. doi: 10.1016/j.nimb.2017.04.021
39. Noda K. Beam Delivery Method for Carbon-Ion Radiotherapy With the Heavy-Ion Medical Accelerator in Chiba. *Int J Particle Ther* (2016) 2:481–9. doi: 10.14338/IJPT-15-00041.1

40. Vilches-Freixas G, Unipan M, Rinaldi I, Martens J, Roijen E, Almeida IP, et al. Beam Commissioning of the First Compact Proton Therapy System With Spot Scanning and Dynamic Field Collimation. *Br J Radiol* (2020) 93:20190598. doi: 10.1259/bjr.20190598
41. Schoemers C, Feldmeier E, Naumann J, Panse R, Peters A, Haberer T. The Intensity Feedback System at Heidelberg Ion-Beam Therapy Centre. *Nucl Instruments Methods Phys Research Section A: Accelerators Spectrometers Detectors Associated Equip* (2015) 795:92–9. doi: 10.1016/j.nima.2015.05.054
42. Jolly S, Owen H, Schippers M, Welsch C. Technical Challenges for FLASH Proton Therapy. *Physica Med* (2020) 78:71–82. doi: 10.1016/j.ejmp.2020.08.005
43. CERN. *Medaustron Facility* (2021). Available at: https://cds.cern.ch/images/CERN-HOMEWEB-PHO-2021-020-1 (Accessed 20-9-2021).
44. PSI. *COMET Cyclotron* (2021). Available at: https://www.psi.ch/en/protontherapy/comet-cyclotron (Accessed 20-9-2021).
45. Degiovanni A, Stabile P, Ungaro D. LIGHT: A Linear Accelerator for Proton Therapy. In: *North American Particle Accelerator Conf.(Napac'16)*, vol. 2016. Chicago, IL, USA (2017). p. 1282–6.
46. Cee R, Feldmeier E, Galonska M, Haberer T, Peters A, Scheloske S. The First Magnetic Field Control (B-Train) to Optimize the Duty Cycle of a Synchrotron in Clinical Operation. *Conf Proc C* (2012) 1205201:3503–5.
47. Falbo L, Bressi E, Pezzetta M, Priano C. Btrain Calibration With RF-Master Method. *9th Int Particle Accelerator Conf* (2018) 679–82. doi: 10.18429/JACoW-IPAC2018-TUPAF011
48. Iwata Y, Kadowaki T, Uchiyama H, Fujimoto T, Takada E, Shirai T, et al. Multiple-Energy Operation With Extended Flattops at HIMAC. *Nucl Instruments Methods Phys Research Section A: Accelerators Spectrometers Detectors Associated Equip* (2010) 624:33–8. doi: 10.1016/j.nima.2010.09.016
49. Mizushima K, Katagiri K, Iwata Y, Furukawa T, Fujimoto T, Sato S, et al. Experimental Studies of Systematic Multiple-Energy Operation at HIMAC Synchrotron. *Nucl Instruments Methods Phys Research Section B: Beam Interact Materials Atoms* (2014) 331:243–7. doi: 10.1016/j.nimb.2013.12.033
50. Younkin JE, Bues M, Sio TT, Liu W, Ding X, Keole SR, et al. Multiple Energy Extraction Reduces Beam Delivery Time for a Synchrotron-Based Proton Spot-Scanning System. *Adv Radiat Oncol* (2018) 3:412–20. doi: 10.1016/j.adro.2018.02.006
51. Noda K, Furukawa T, Shibuya S, Uesugi T, Muramatsu M, Kanazawa M, et al. Advanced Rf-Ko Slow-Extraction Method for the Reduction of Spill Ripple. *Nucl Instruments Methods Phys Research Section A: Accelerators Spectrometers Detectors Associated Equip* (2002) 492:253–63. doi: 10.1016/S0168-9002(02)01319-0
52. Krantz C, Cee R, Faber F, Feldmeier E, Fischer T, Galonska M, et al. Slow Extraction Techniques at the Marburg Ion-Beam Therapy Centre. *9th International Particle Accelerator Conference* (2018) 1084–6. doi: 10.18429/JACoW-IPAC2018-TUPAL036
53. Badano L, Benedikt M, Bryant PJ, Crescenti M, Holy P, Maier AT, et al. Proton-Ion Medical Machine Study (PIMMS). *Strahlentherapie und Onkologie* (1999) 1:1–4. doi: 10.1007/BF03038873
54. Pullia M, Bressi E, Falbo L, Priano C, Rossi S, Viviani C. Betatron Core Driven Slow Extraction at CNAO and MedAustron. *7th Int Particle Accelerator Conf* (2016) TUPMR037. doi: 10.18429/JACoW-IPAC2016-TUPMR037
55. Dorda U, Benedikt M, Bryant P. Layout and Optics of the Medaustron High Energy Beam Transfer Line. *Proceedings of IPAC2011* San Sebastián, Spain (2011) 3484–6.
56. Savazzi S, Bressi E, Debernardi G, Falbo L, Lante V, Meliga P, et al. Implementation of RF-KO Extraction at CNAO. *10th Int Particle Accelerator Conf* (2019) THPMP010. doi: 10.18429/JACoW-IPAC2019-THPMP010
57. De Franco A, Böhlen TT, Farinon F, Kowarik G, Kronberger M, Kurfürst C, et al. UPGRADE STUDY OF THE MedAustron ION BEAM CENTER. *Proc Int Particle Accelerator Conf 2017* (2017) 4619–22.
58. De Franco A, Adler L, Farinon F, Gambino N, Guidoboni G, Kowarik G. Slow Extraction Optimization at the MedAustron Ion Therapy Center: Implementation of Front End Acceleration and RF Knock Out. *9th Int Particle Accelerator Conf* (2018) 453–6. doi: 10.18429/JACoW-IPAC2018-MOPML025
59. Kain V, Velotti FM, Fraser MA, Goddard B, Prieto J, Stoel LS, et al. Resonant Slow Extraction With Constant Optics for Improved Separatrix Control at the Extraction Septum. *Phys Rev Accel. Beams* (2019) 22:101001. doi: 10.1103/PhysRevAccelBeams.22.101001
60. Schoemers C, Feldmeier E, Naumann J, Panse R, Peters A, Haberer T. Patient-Specific Intensity-Modulation of a Slowly Extracted Beam at the Hit-Synchrotron. *Int Particle Accelerators Conf 2013* (2013) 2944–46.
61. Sato S, Furukawa T, Noda K. Dynamic Intensity Control System With Rf-Knockout Slow-Extraction in the Himac Synchrotron. *Nucl Instruments Methods Phys Res Section A: Accelerators Spectrometers Detectors Associated Equip* (2007) 574:226–31. doi: 10.1016/j.nima.2007.01.174
62. Mizushima K, Furukawa T, Iwata Y, Muramatsu M, Sato S, Hara Y, et al. Experimental Verification of Beam Switching Operation for Multiple-Ion Therapy Applications at HIMAC. *Nucl Instruments Methods Phys Research Section B: Beam Interact Materials Atoms* (2019) 459:115–9. doi: 10.1016/j.nimb.2019.09.008
63. Sokol O, Krämer M, Hild S, Durante M, Scifoni E. *Phys Med Biol* (2019) 64. doi: 10.1088/1361-6560/aafe40
64. Jongen Y, Abs M, Blondin A, Kleeven W, Zaremba S, Vandeplassche D, et al. Iba-Jinr 400 Mev/U Superconducting Cyclotron for Hadron Therapy. *Nuclear Instruments and Methods in Physics Research Section A: Accelerators, Spectrometers, Detectors and Associated Equipment* (2010) 624:47–53. doi: 10.1016/j.nima.2010.09.028
65. Jongen Y. Review on Cyclotrons for Cancer Therapy. Lanzhou, China: Proceedings of CYCLOTRONS 2010 (2010), 398–403.
66. Maradia V, Meer D, Weber DC, Lomax AJ, Schippers JM, Psoroulas S. A New Emittance Selection System to Maximize Beam Transmission for Low-Energy Beams in Cyclotron-Based Proton Therapy Facilities With Gantry. *Med Phys* (2021) 1–10. doi: 10.1002/mp.15278
67. Chaudhri N, Saito N, Bert C, Franczak B, Steidl P, Durante M, et al. Ion-Optical Studies for a Range Adaptation Method in Ion Beam Therapy Using a Static Wedge Degrader Combined With Magnetic Beam Deflection. *Phys Med Biol* (2010) 55:3499–513. doi: 10.1088/0031-9155/55/12/015
68. Gambino N, Myalsky S, Adler L, Franco AD, Ecker F, Guidoboni G, et al. Impact of Ion Source Stability for a Medical Accelerator. *J Instrument* (2019) 14:C05017–7. doi: 10.1088/1748-0221/14/05/c05017
69. Psoroulas S, Fernandez Carmona P, Meer D, Weber DC. On-Line Dynamic Beam Intensity Control in a Proton Therapy Cyclotron. *Cyclotrons 2019* (2019) 148–51. doi: 10.18429/JACoW-Cyclotrons2019-TUB04
70. Pearson E, Abs M, Henrotin S, Kleeven W, Van de Walle J, Verbruggen P, et al. The New Iba Superconducting Synchrocyclotron (S2c2): From Modelling to Reality. Eleventh I*nternational Topical Meeting or Nuclear Applications of Accelerators at Bruges, Belgium* (2013).
71. Kang M, Pang D. Commissioning and Beam Characterization of the First Gantry-Mounted Accelerator Pencil Beam Scanning Proton System. *Med Phys* (2020) 47:3496–510. doi: 10.1002/mp.13972
72. Zhao T, Sun B, Grantham K, Rankine L, Cai B, Goddu SM, et al. Commissioning and Initial Experience With the First Clinical Gantry-Mounted Proton Therapy System. *J Appl Clin Med Phys* (2016) 17:24–40. doi: 10.1120/jacmp.v17i2.5868
73. Cartlidge E. *Proton Therapy Goes Slimline* (2018). Available at: https://physicsworld.com/a/proton-therapy-goes-slimline/ (Accessed 9-9-21).
74. Benedetti S, Grudiev A, Latina A. High Gradient Linac for Proton Therapy. *Phys Rev Accel Beams* (2017) 20:40101. doi: 10.1103/PhysRevAccelBeams.20.040101
75. De Martinis C, Giove D, Amaldi U, Berra P, Crandall K, Mauri M, et al. Acceleration Tests of a 3 GHz Proton Linear Accelerator (LIBO) for Hadrontherapy. *Nucl Instruments Methods Phys Research Section A: Accelerators Spectrometers Detectors Associated Equip* (2012) 681:10–5. doi: 10.1016/j.nima.2012.04.017
76. Farr J, Kolano A, Aumon S, Degiovanni A, Caldara M, Valloni A. Proton LINAC Transverse Beam Scanning Performance Implications for Therapeutic Quality Improvement. *Int J Radiat Oncol Biol Phys (Elsevier Inc)* (2020) 108:e351. doi: 10.1016/j.ijrobp.2020.07.2334
77. Kolano A, Degiovanni A, Farr J. Investigation on the PBS FLASH Beam Delivery Technique Using a Proton Linac. *Int J Radiat Oncol Biol Phys (Elsevier Inc)* (2020) 108:e331. doi: 10.1016/j.ijrobp.2020.07.791

78. Kondo K, Akagi T, Arranz F, Bazin N, Bellan L, Bolzon B, et al. Validation of the Linear IFMIF Prototype Accelerator (Lipac) in Rokkasho. *Fusion Eng Design* (2020) 153:111503. doi: 10.1016/j.fusengdes.2020.111503
79. Garoby R. Status and Plans of the ESS Neutron Source. *JPS Conf Proc* (2021) 33:11003. doi: 10.7566/JPSCP.33.011003
80. Cara P, Heidinger R, O'hira S, Sakamoto K, Kasugai A, Knaster J, et al. The Linear IFMIF Prototype Accelerator (Lipac) Design Development Under the European-Japanese Collaboration. *Proceedings of IPAC2016* Busan, Korea (2016) 985–8.
81. Vretenar M, Bauche J, Baudrenghien P, Body Y, Brunner O, Buzio M. Linac4 Design Report, CERN Yellow Reports: Monographs. (2020) 6/2020: (Geneva: CERN). doi: 10.23731/CYRM-2020-006
82. Linz U, Alonso J. Laser-Driven Ion Accelerators for Tumor Therapy Revisited. *Phys Rev Accelerators Beams* (2016) 19:1–8. doi: 10.1103/PhysRevAccelBeams.19.124802
83. Ding J, Schumacher D, Jahn D, Blažević A, Roth M. Simulation Studies on Generation, Handling and Transport of Laser-Accelerated Carbon Ions. *Nucl Instruments Methods Phys Res Section A: Accelerators Spectrometers Detectors Associated Equip* (2018) 909:168–72. doi: 10.1016/J.NIMA.2018.02.103
84. Bulanov SV, Daido H, Esirkepov TZ, Khoroshkov VS, Koga J, Nishihara K, et al. Feasibility of Using Laser Ion Accelerators in Proton Therapy. *AIP Conf Proc* (2004) 740:414–29. doi: 10.1063/1.1843524
85. Nürnberg F, Friedman A, Grote DP, Harres K, Logan BG, Schollmeier M, et al. Warp Simulations for Capture and Control of Laser-Accelerated Proton Beams. *J Physics: Conf Ser* (2010) 244:22052. doi: 10.1088/1742-6596/244/2/022052
86. Hofmann I, ter Vehn JM, Yan X, Orzhekhovskaya A, Yaramyshev S. Collection and Focusing of Laser Accelerated Ion Beams for Therapy Applications. *Phys Rev Special Topics - Accelerators Beams* (2011) 14:31304. doi: 10.1103/PhysRevSTAB.14.031304
87. Hofmann I, Meyer-Ter-Vehn J, Yan X, Al-Omari H. Chromatic Energy Filter and Characterization of Laser-Accelerated Proton Beams for Particle Therapy. *Nucl Instruments Methods Phys Research Section A: Accelerators Spectrometers Detectors Associated Equip* (2012) 681:44–54. doi: 10.1016/j.nima.2012.04.022
88. Bolton PR. The Integrated Laser-Driven Ion Accelerator System and the Laser-Driven Ion Beam Radiotherapy Challenge. *Nucl Instruments Methods Phys Research Section A: Accelerators Spectrometers Detectors Associated Equip* (2016) 809:149–55. doi: 10.1016/J.NIMA.2015.08.070
89. Sheehy S. *Fixed Field Alternating Gradient Accelerators (FFA)* (2019). Available at: http://www.icfa-bd.org/Newsletter_76_htmlversion/BDN-Fixed-Field-Alternating-Gradient-Accelerators-(FFA).html (Accessed 10-9-2021).
90. Uesugi T, Mori Y, Horii H, Kuriyama Y, Mishima K, Osanai A, et al. FFAGS for the ERIT and ADS Projects at KURRI. *EPAC 2008 - Contributions to Proc* (2008) 1013–5.
91. Sheehy SL, Kelliher DJ, Machida S, Rogers C, Prior CR, Volat L, et al. Characterization Techniques for Fixed-Field Alternating Gradient Accelerators and Beam Studies Using the KURRI 150 MeV Proton FFAG. *Prog Theor Exp Phys* (2016) 2016). doi: 10.1093/ptep/ptw086
92. Peach KJ, Aslaninejad M, Barlow RJ, Beard CD, Bliss N, Cobb JH, et al. Conceptual Design of a Nonscaling Fixed Field Alternating Gradient Accelerator for Protons and Carbon Ions for Charged Particle Therapy. *Phys Rev Special Topics - Accelerators Beams* (2013) 16:1–34. doi: 10.1103/PhysRevSTAB.16.030101
93. Safai S, Bula C, Meer D, Pedroni E. Improving the Precision and Performance of Proton Pencil Beam Scanning. *Trans Cancer Res* (2012) 1:196–206. doi: 10.3978/j.issn.2218-676X.2012.10.08
94. Van De Water S, Kooy HM, Heijmen BJ, Hoogeman MS. Shortening Delivery Times of Intensity Modulated Proton Therapy by Reducing Proton Energy Layers During Treatment Plan Optimization. *Int J Radiat Oncol Biol Phys* (2015) 92:460–8. doi: 10.1016/j.ijrobp.2015.01.031
95. Aitkenhead AH, Bugg D, Rowbottom CG, Smith E, Mackay RI. Modelling the Throughput Capacity of a Single-Accelerator Multitreatment Room Proton Therapy Centre. *Br J Radiol* (2012) 85:1263–72. doi: 10.1259/bjr/27428078
96. Schippers JM, Lomax AJ. Emerging Technologies in Proton Therapy. *Acta Oncol* (2011) 50:838–50. doi: 10.3109/0284186X.2011.582513
97. Owen H, Holder D, Alonso J, Mackay R. Technologies for Delivery of Proton and Ion Beams for Radiotherapy. *Int J Modern Phys A* (2013) 29:1–54. doi: 10.1142/S0217751X14410024
98. Gerbershagen A, Calzolaio C, Meer D, Sanfilippo S, Schippers M. The Advantages and Challenges of Superconducting Magnets in Particle Therapy. *Superconductor Sci Technol* (2016) 29. doi: 10.1088/0953-2048/29/8/083001
99. Strodl T, Pavlovič M, Seemann R, Murín J. Advanced Concepts for Particle-Therapy Accelerators. *EPAC 2008 - Contributions to Proc (Genoa Italy)* (2008) 1821–3.
100. Fuchs R, Weinrich U, Sust E. Assembly of the Carbon Beam Gantry at the Heidelberg Ion Therapy (HIT) Accelerator. *Proc EPAC08 (Genoa)* (2008) 1839–41.
101. Schardt D, Elsässer T, Schulz-Ertner D. Heavy-Ion Tumor Therapy: Physical and Radiobiological Benefits. *Rev Modern Phys* (2010) 82:383–425. doi: 10.1103/RevModPhys.82.383
102. Haberer T, Debus J, Eickhoff H, Jäkel O, Schulz-Ertner D, Weber U. The Heidelberg Ion Therapy Center. *Radiother Oncol* (2004) 73:186–90. doi: 10.1016/S0167-8140(04)80046-X
103. Iwata Y, Noda K, Murakami T, Shirai T, Furukawa T, Fujita T, et al. Development of a Superconducting Rotating-Gantry for Heavy-Ion Therapy. *Nucl Instruments Methods Phys Research Section B: Beam Interact Materials Atoms* (2013) 317:793–7. doi: 10.1016/j.nimb.2013.03.050
104. Iwata Y, Fujita T, Furukawa T, Hara Y, Matsuba S, Mizushima K, et al. Superconducting Gantry for Carbon-Ion Radiotherapy. *IPAC 2018: ninth Int Particle Accelerator Conf* (2018) 1232–6. doi: 10.18429/JACoW-IPAC2018-TUZGBF1
105. Iwata Y, Fujita T, Fujimoto T, Furukawa T, Hara Y, Kondo K, et al. Development of Carbon-Ion Radiotherapy Facilities at NIRS. *IEEE Trans Appl Superconductivity* (2018) 28:1–7. doi: 10.1109/TASC.2017.2785835
106. Pullia M, Ebskamp F. Introduction to Gantries and Comparison of Gantry Design. *Academia Industry Matching Event Superconductivity Accelerators Med Appl* (2016).
107. Yan S, Lu HM, Flanz J, Adams J, Trofimov A, Bortfeld T. Reassessment of the Necessity of the Proton Gantry: Analysis of Beam Orientations From 4332 Treatments at the Massachusetts General Hospital Proton Center Over the Past 10 Years. *Int J Radiat Oncol Biol Phys* (2016) 95:224–33. doi: 10.1016/j.ijrobp.2015.09.033
108. Rahim S, Korte J, Hardcastle N, Hegarty S, Kron T, Everitt S. Upright Radiation Therapy—A Historical Reflection and Opportunities for Future Applications. *Front Oncol* (2020) 10:213. doi: 10.3389/fonc.2020.00213
109. Mazal A, Vera Sanchez JA, Sanchez-Parcerisa D, Udias JM, España S, Sanchez-Tembleque V, et al. Biological and Mechanical Synergies to Deal With Proton Therapy Pitfalls: Minibeams, FLASH, Arcs, and Gantryless Rooms. *Front Oncol* (2021) 10:613669. doi: 10.3389/fonc.2020.613669
110. Sheng Y, Sun J, Wang W, Stuart B, Kong L, Gao J, et al. Performance of a 6D Treatment Chair for Patient Positioning in an Upright Posture for Fixed Ion Beam Lines. *Front Oncol* (2020) 10:122. doi: 10.3389/fonc.2020.00122
111. Sun J, Kong L, Chen Z, You D, Mao J, Guan X, et al. Clinical Implementation of a 6D Treatment Chair for Fixed Ion Beam Lines. *Front Oncol* (2021) 11:694749. doi: 10.3389/fonc.2021.694749
112. Gerbershagen A, Meer D, Schippers JM, Seidel M. A Novel Beam Optics Concept in a Particle Therapy Gantry Utilizing the Advantages of Superconducting Magnets. *Z fur Medizinische Physik* (2016) 26:224–37. doi: 10.1016/j.zemedi.2016.03.006
113. Nesteruk KP, Calzolaio C, Meer D, Rizzoglio V, Seidel M, Schippers JM. Large Energy Acceptance Gantry for Proton Therapy Utilizing Superconducting Technology. *Phys Med Biol* (2019) 64. doi: 10.1088/1361-6560/ab2f5f
114. Wan W, Brouwer L, Caspi S, Prestemon S, Gerbershagen A, Schippers JM, et al. Alternating-Gradient Canted Cosine Theta Superconducting Magnets for Future Compact Proton Gantries. *Phys Rev Special Topics - Accelerators Beams* (2015) 18:103501. doi: 10.1103/PhysRevSTAB.18.103501
115. Trbojevic D, Parker B, Keil E, Sessler AM. Carbon/proton Therapy: A Novel Gantry Design. *Phys Rev Special Topics - Accelerators Beams* (2007) 10:1–6. doi: 10.1103/PhysRevSTAB.10.053503
116. Trbojevic D, Morozov V. Innovative Superconducting non Scaling Fixed Field Alternating Gradient Isocentric Gantry for Carbon Cancer Therapy. *Proc IPAC2011* (2011) 2544–6.

117. Trbojevic D, Brooks S, Roser T, Tsoupas N. Superb Fixed Field Permanent Magnet Proton Therapy Gantry *. *Proc IPAC2021 (JACoW Publishing)* (2021) 1405–8. doi: 10.18429/JACoW-IPAC2021-TUPAB030
118. Trbojevic D, Brooks S, Lou W, Parker B, Tsoupas N. Permanent Halbach Magnet Proton and Superconducting Carbon Cancer Therapy Gantries. *IPAC 2017: eighth Int Particle Accelerator Conf* (2017) 4679–82.
119. Bottura L, Felcini E, De Rijk G, Dutoit B. GaToroid: A Novel Toroidal Gantry for Hadron Therapy. *Nucl Instruments Methods Phys Research Section A: Accelerators Spectrometers Detectors Associated Equip* (2020) 983:164588. doi: 10.1016/j.nima.2020.164588
120. Takada Y, Kobayashi Y, Yasuoka K, Terunuma T. A Miniature Ripple Filter for Filtering a Ripple Found in the Distal Part of a Proton SOBP. *Nucl Instruments Methods Phys Research Section A: Accelerators Spectrometers Detectors Associated Equip* (2004) 524:366–73. doi: 10.1016/j.nima.2004.01.069
121. Fattori G, Zhang Y, Meer D, Weber DC, Lomax AJ, Safai S. The Potential of Gantry Beamline Large Momentum Acceptance for Real Time Tumour Tracking in Pencil Beam Scanning Proton Therapy. *Sci Rep* (2020) 10:1–13. doi: 10.1038/s41598-020-71821-1
122. Actis O, Mayor A, Meer D, Weber DC. Precise Beam Delivery for Proton Therapy With Dynamic Energy Modulation. *J Physics: Conf Ser* (1067) 2018). doi: 10.1088/1742-6596/1067/9/092002
123. Seco J, Robertson D, Trofimov A, Paganetti H. Breathing Interplay Effects During Proton Beam Scanning: Simulation and Statistical Analysis. *Phys Med Biol* (2009) 54:283–94. doi: 10.1088/0031-9155/54/14/N01
124. Bert C, Grözinger SO, Rietzel E. Quantification of Interplay Effects of Scanned Particle Beams and Moving Targets. *Phys Med Biol* (2008) 53:2253–65. doi: 10.1088/0031-9155/53/9/003
125. Bortfeld T, Jiang SB, Rietzel E. Effects of Motion on the Total Dose Distribution. *Semin Radiat Oncol* (2004) 14:41–51. doi: 10.1053/j.semradonc.2003.10.011
126. Lambert J, Suchowerska N, McKenzie DR, Jackson M. Intrafractional Motion During Proton Beam Scanning. *Phys Med Biol* (2005) 50:4853–62. doi: 10.1088/0031-9155/50/20/008
127. Dowdell S, Grassberger C, Sharp GC, Paganetti H. Interplay Effects in Proton Scanning for Lung: A 4d Monte Carlo Study Assessing the Impact of Tumor and Beam Delivery Parameters. *Phys Med Biol* (2013) 58:4137–56. doi: 10.1088/0031-9155/58/12/4137
128. Kang JH, Wilkens JJ, Oelfke U. Non-Uniform Depth Scanning for Proton Therapy Systems Employing Active Energy Variation. *Phys Med Biol* (2008) 53:149–55. doi: 10.1088/0031-9155/53/9/N01
129. Grassberger C, Dowdell S, Lomax A, Sharp G, Shackleford J, Choi N, et al. Motion Interplay as a Function of Patient Parameters and Spot Size in Spot Scanning Proton Therapy for Lung Cancer. *Int J Radiat Oncol Biol Phys* (2013) 86:380–6. doi: 10.1016/j.ijrobp.2013.01.024
130. Hillbrand M, Georg D. Assessing a Set of Optimal User Interface Parameters for Intensity-Modulated Proton Therapy Planning. *J Appl Clin Med Phys* (2010) 11:93–104. doi: 10.1120/jacmp.v11i4.3219
131. Li H, Zhu XR, Zhang X. Reducing Dose Uncertainty for Spot-Scanning Proton Beam Therapy of Moving Tumors by Optimizing the Spot Delivery Sequence. *Int J Radiat Oncol Biol Phys* (2015) 93:547–56. doi: 10.1016/j.ijrobp.2015.06.019
132. Kang JH, Wilkens JJ, Oelfke U. Demonstration of Scan Path Optimization in Proton Therapy. *Med Phys* (2007) 34:3457–64. doi: 10.1118/1.2760025
133. Van De Water S, Kraan AC, Breedveld S, Schillemans W, Teguh DN, Kooy HM, et al. Improved Efficiency of Multi-Criteria IMPT Treatment Planning Using Iterative Resampling of Randomly Placed Pencil Beams. *Phys Med Biol* (2013) 58:6969–83. doi: 10.1088/0031-9155/58/19/6969
134. Cao W, Lim G, Liao L, Li Y, Jiang S, Li X, et al. Proton Energy Optimization and Reduction for Intensity-Modulated Proton Therapy. *Phys Med Biol* (2014) 54:6341–54. doi: 10.1088/0031-9155/59/21/6341
135. Keall P. 4-Dimensional Computed Tomography Imaging and Treatment Planning. *Semin Radiat Oncol* (2004) 14:81–90. doi: 10.1053/j.semradonc.2003.10.006
136. Keall PJ, Mageras GS, Balter JM, Emery RS, Forster KM, Jiang SB, et al. The Management of Respiratory Motion in Radiation Oncology Report of AAPM Task Group 76. *Med Phys* (2006) 33:3874–900. doi: 10.1118/1.2349696
137. Graeff C. Motion Mitigation in Scanned Ion Beam Therapy Through 4D-Optimization. *Physica Med* (2014) 30:570–7. doi: 10.1016/j.ejmp.2014.03.011
138. Bertholet J, Knopf A, Eiben B, McClelland J, Grimwood A, Harris E, et al. Real-Time Intrafraction Motion Monitoring in External Beam Radiotherapy. *Phys Med Biol* (2019) 64:1–33. doi: 10.1088/1361-6560/ab2ba8
139. Albertini F, Hug EB, Lomax AJ. Is it Necessary to Plan With Safety Margins for Actively Scanned Proton Therapy? *Phys Med Biol* (2011) 56:4399–413. doi: 10.1088/0031-9155/56/14/011
140. Lomax AJ. Intensity Modulated Proton Therapy and its Sensitivity to Treatment Uncertainties 2: The Potential Effects of Inter-Fraction and Inter-Field Motions. *Phys Med Biol* (2008) 53:1043–56. doi: 10.1088/0031-9155/53/4/015
141. Rietzel E, Bert C. Respiratory Motion Management in Particle Therapy. *Med Phys* (2010) 37:449–60. doi: 10.1118/1.3250856
142. Bert C, Durante M. Motion in Radiotherapy: Particle Therapy. *Phys Med Biol* (2011) 56:R113–44. doi: 10.1088/0031-9155/56/16/R01
143. Mori S, Knopf AC, Umegaki K. Motion Management in Particle Therapy. *Med Phys* (2018) 45:e994–e1010. doi: 10.1002/mp.12679
144. Gorgisyan J, Munck af Rosenschold P, Perrin R, Persson GF, Josipovic M, Belosi MF, et al. Feasibility of Pencil Beam Scanned Intensity Modulated Proton Therapy in Breath-Hold for Locally Advanced Non-Small Cell Lung Cancer. *Int J Radiat Oncol Biol Phys* (2017) 99:1121–8. doi: 10.1016/j.ijrobp.2017.08.023
145. Vedam SS, Keall PJ, Kini VR, Mohan R. Determining Parameters for Respiration-Gated Radiotherapy. *Med Phys* (2001) 28:2139–46. doi: 10.1118/1.1406524
146. Zhang Y, Knopf A, Tanner C, Lomax AJ. Online Image Guided Tumour Tracking With Scanned Proton Beams: A Comprehensive Simulation Study. *Phys Med Biol* (2014) 59:7793–817. doi: 10.1088/0031-9155/59/24/7793
147. Matsuura T, Fujii Y, Takao S, Yamada T, Matsuzaki Y, Miyamoto N, et al. Development and Evaluation of a Short-Range Applicator for Treating Superficial Moving Tumors With Respiratory-Gated Spot-Scanning Proton Therapy Using Real-Time Image Guidance. *Phys Med Biol* (2016) 61:1515–31. doi: 10.1088/0031-9155/61/4/1515
148. Courneyea L, Beltran C, Tseung HSWC, Yu J, Herman MG. Optimizing Mini-Ridge Filter Thickness to Reduce Proton Treatment Times in a Spot-Scanning Synchrotron System. *Med Phys* (2014) 41. doi: 10.1118/1.4876276
149. Simeonov Y, Weber U, Penchev P, Ringbæk TP, Schuy C, Brons S, et al. 3D Range-Modulator for Scanned Particle Therapy: Development, Monte Carlo Simulations and Experimental Evaluation. *Phys Med Biol* (2017) 62:7075–96. doi: 10.1088/1361-6560/aa81f4
150. Moteabbed M, Yock TI, Depauw N, Madden TM, Kooy HM, Paganetti H. Impact of Spot Size and Beam-Shaping Devices on the Treatment Plan Quality for Pencil Beam Scanning Proton Therapy. *Int J Radiat Oncol Biol Phys* (2016) 95:190–8. doi: 10.1016/j.ijrobp.2015.12.368
151. Sánchez-Parcerisa D, Pourbaix JC, Ainsley CG, Dolney D, Carabe A. Fast Range Switching of Passively Scattered Proton Beams Using a Modulation Wheel and Dynamic Beam Current Modulation. *Phys Med Biol* (2014) 59:19–26. doi: 10.1088/0031-9155/59/7/N19
152. Zenklusen SM, Pedroni E, Meer D. A Study on Repainting Strategies for Treating Moderately Moving Targets With Proton Pencil Beam Scanning at the New Gantry 2 at PSI. *Phys Med Biol* (2010) 55:5103–21. doi: 10.1088/0031-9155/55/17/014
153. Phillips MH, Pedroni E, Blattmann H, Boehringer T, Coray A, Scheib S. Effects of Respiratory Motion on Dose Uniformity With a Charged Particle Scanning Method. *Phys Med Biol* (1992) 37:223–34. doi: 10.1088/0031-9155/37/1/016
154. Grassberger C, Dowdell S, Sharp G, Paganetti H. Motion Mitigation for Lung Cancer Patients Treated With Active Scanning Proton Therapy. *Med Phys* (2015) 42:2462–9. doi: 10.1118/1.4916662
155. Bernatowicz K, Lomax AJ, Knopf A. Comparative Study of Layered and Volumetric Rescanning for Different Scanning Speeds of Proton Beam in Liver Patients. *Phys Med Biol* (2013) 58:7905–20. doi: 10.1088/0031-9155/58/22/7905
156. Gut P, Krieger M, Lomax T, Weber DC, Hrbacek J. Combining Rescanning and Gating for a Time-Efficient Treatment of Mobile Tumors Using Pencil Beam Scanning Proton Therapy. *Radiother Oncol* (2021) 160:82–9. doi: 10.1016/j.radonc.2021.03.041

157. Zhang Y, Huth I, Wegner M, Weber DC, Lomax AJ. An Evaluation of Rescanning Technique for Liver Tumour Treatments Using a Commercial PBS Proton Therapy System. *Radiother Oncol* (2016) 121:281–7. doi: 10.1016/j.radonc.2016.09.011
158. Hall EJ. Radiation Dose-Rate: A Factor of Importance in Radiobiology and Radiotherapy. *Br J Radiol* (1972) 45:81–97. doi: 10.1259/0007-1285-45-530-81
159. Hall EJ, Brenner DJ. The Dose-Rate Effect Revisited: Radiobiological Considerations of Importance in Radiotherapy. *Int J Radiat Oncol Biol Phys* (1991) 21:1403–14. doi: 10.1016/0360-3016(91)90314-T
160. Wozny AS, Alphonse G, Battiston-Montagne P, Simonet S, Poncet D, Testa E, et al. Influence of Dose Rate on the Cellular Response to Low- and High-LET Radiations. *Front Oncol* (2016) 6:58. doi: 10.3389/fonc.2016.00058
161. Favaudon V, Caplier L, Monceau V, Pouzoulet F, Sayarath M, Fouillade C, et al. Ultrahigh Dose-Rate FLASH Irradiation Increases the Differential Response Between Normal and Tumor Tissue in Mice. *Sci Trans Med* (2014) 6:245ra93–245ra93. doi: 10.1126/scitranslmed.3008973
162. Durante M, BräUer-Krisch E, Hill M. Faster and Safer? FLASH Ultra-High Dose Rate in Radiotherapy. *Br J Radiol* (2018) 91:6–9. doi: 10.1259/bjr.20170628
163. de Kruijff RM. FLASH Radiotherapy: Ultra-High Dose Rates to Spare Healthy Tissue. *Int J Radiat* (2020) 96:419–23. doi: 10.1080/09553002.2020.1704912
164. Wilson JD, Hammond EM, Higgins GS, Petersson K. Ultra-High Dose Rate (FLASH) Radiotherapy: Silver Bullet or Fool's Gold? *Front Oncol* (2020) 9:1563. doi: 10.3389/fonc.2019.01563
165. Hughes JR, Parsons JL. Flash Radiotherapy: Current Knowledge and Future Insights Using Proton-Beam Therapy. *Int J Mol Sci* (2020) 21:1–14. doi: 10.3390/ijms21186492
166. Bourhis J, Montay-Gruel P, Gonçalves Jorge P, Bailat C, Petit B, Ollivier J, et al. Clinical Translation of FLASH Radiotherapy: Why and How? *Radiother Oncol* (2019) 139:11–7. doi: 10.1016/j.radonc.2019.04.008
167. Esplen N, Mendonca MS, Bazalova-Carter M. Physics and Biology of Ultrahigh Dose-Rate (FLASH) Radiotherapy: A Topical Review. *Phys Med Biol* (2020) 65. doi: 10.1088/1361-6560/abaa28
168. Nesteruk KP, Psoroulas S. FLASH Irradiation With Proton Beams : Beam Characteristics and Their Implications for Beam Diagnostics. *Appl Sci* (2021) 11. doi: 10.3390/app11052170
169. van de Water S, Safai S, Schippers JM, Weber DC, Lomax AJ. Towards FLASH Proton Therapy: The Impact of Treatment Planning and Machine Characteristics on Achievable Dose Rates. *Acta Oncol* (2019) 58:1463–9. doi: 10.1080/0284186X.2019.1627416
170. Lempart M, Blad B, Adrian G, Bäck S, Knöös T, Ceberg C, et al. Modifying a Clinical Linear Accelerator for Delivery of Ultra-High Dose Rate Irradiation. *Radiother Oncol* (2019) 139:40–5. doi: 10.1016/j.radonc.2019.01.031
171. Nesteruk KP, Togno M, Grossmann M, Lomax AJ, Weber DC, Schippers JM, et al. Commissioning of a Clinical Pencil Beam Scanning Proton Therapy Unit for Ultra-High Dose Rates (FLASH). *Med Phys* (2021) 48:4017–26. doi: 10.1002/mp.14933
172. Kim MM, Darafsheh A, Schuemann J, Dokic I, Lundh O, Zhao T. Development of Ultra-High Dose Rate (FLASH) Particle Therapy. *IEEE Trans Radiat Plasma Med Sci* (2021) 7311:1–12. doi: 10.1109/TRPMS.2021.3091406
173. Zakaria AM, Colangelo NW, Meesungnoen J, Azzam EI, Plourde MÉ, Jay-Gerin JP. Ultra-High Dose-Rate, Pulsed (FLASH) Radiotherapy With Carbon Ions: Generation of Early, Transient, Highly Oxygenated Conditions in the Tumor Environment. *Radiat Res* (2020) 593:587–93. doi: 10.1667/RADE-19-00015.1
174. Weber UA, Scifoni E, Durante M. FLASH Radiotherapy With Carbon Ion Beams. *Med Phys* (2021) 00:1–19. doi: 10.1002/mp.15135
175. Tessonnier T, Mein S, Walsh DW, Schuhmacher N, Liew H, Cee R, et al. FLASH Dose Rate Helium Ion Beams: First *In Vitro* Investigations. *Int J Radiat Oncol Biol Phys (Elsevier)* (2021) 111:1011–22. doi: 10.1016/j.ijrobp.2021.07.1703
176. Zou W, Diffenderfer ES, Cengel KA, Kim MM, Avery S, Konzer J, et al. Current Delivery Limitations of Proton PBS for FLASH. *Radiother Oncol* (2021) 155:212–8. doi: 10.1016/j.radonc.2020.11.002
177. Kang M, Wei S, Isabelle Choi J, Simone CB, Lin H. Quantitative Assessment of 3D Dose Rate for Proton Pencil Beam Scanning FLASH Radiotherapy and its Application for Lung Hypofractionation Treatment Planning. *Cancers* (2021) 13:1–14. doi: 10.3390/cancers13143549
178. van Marlen P, Dahele M, Folkerts M, Abel E, Slotman BJ, Verbakel W. Ultra-High Dose Rate Transmission Beam Proton Therapy for Conventionally Fractionated Head and Neck Cancer: Treatment Planning and Dose Rate Distributions. *Cancers* (2021) 13:1–12. doi: 10.3390/cancers13081859
179. Maxim PG, Tantawi SG, Loo BW. PHASER: A Platform for Clinical Translation of FLASH Cancer Radiotherapy. *Radiother Oncol* (2019) 139:28–33. doi: 10.1016/j.radonc.2019.05.005
180. Bourhis J, Sozzi WJ, Jorge PG, Gaide O, Bailat C, Duclos F, et al. Treatment of a First Patient With FLASH-Radiotherapy. *Radiother Oncol* (2019) 139:18–22. doi: 10.1016/j.radonc.2019.06.019
181. National Library of Medicine (US). *Feasibility Study of FLASH Radiotherapy for the Treatment of Symptomatic Bone Metastases (FAST-01)* (2020). Available at: https://clinicaltrials.gov/ct2/show/NCT04592887 (Accessed 2021-10-27).
182. Patriarca A, Fouillade C, Auger M, Martin F, Pouzoulet F, Nauraye C, et al. Experimental Set-Up for FLASH Proton Irradiation of Small Animals Using a Clinical System. *Int J Radiat Oncol Biol Phys* (2018) 102:619–26. doi: 10.1016/j.ijrobp.2018.06.403
183. Beyreuther E, Brand M, Hans S, Hideghéty K, Karsch L, Leßmann E, et al. Feasibility of Proton FLASH Effect Tested by Zebrafish Embryo Irradiation. *Radiother Oncol* (2019) 139:46–50. doi: 10.1016/j.radonc.2019.06.024
184. Diffenderfer ES, Verginadis II, Kim MM, Shoniyozov K, Velalopoulou A, Goia D, et al. Design, Implementation, and in Vivo Validation of a Novel Proton FLASH Radiation Therapy System. *Int J Radiat Oncol Biol Phys* (2020) 106:440–8. doi: 10.1016/j.ijrobp.2019.10.049
185. Darafsheh A, Hao Y, Zwart T, Wagner M, Catanzano D, Williamson JF, et al. Feasibility of Proton FLASH Irradiation Using a Synchrocyclotron for Preclinical Studies. *Med Phys* (2020) 47:4348–55. doi: 10.1002/mp.14253
186. Verhaegen F, Wanders RG, Wolfs C, Eekers D. Considerations for Shoot-Through FLASH Proton Therapy. *Phys Med Biol* (2021) 66:06NT01. doi: 10.1088/1361-6560/abe55a
187. Diffenderfer ES, Sørensen BS, Mazal A, Carlson DJ. The Current Status of Pre-Clinical Proton Flash Radiation and Future Directions. *Med Phys* (2021) 1–16. doi: 10.1002/mp.15276
188. van Marlen P, Dahele M, Folkerts M, Abel E, Slotman BJ, Verbakel WF. Bringing FLASH to the Clinic: Treatment Planning Considerations for Ultrahigh Dose-Rate Proton Beams. *Int J Radiat Oncol Biol Phys* (2020) 106:621–9. doi: 10.1016/j.ijrobp.2019.11.011
189. Holt A, Van Gestel D, Arends MP, Korevaar EW, Schuring D, Kunze-Busch MC, et al. Multi-Institutional Comparison of Volumetric Modulated Arc Therapy vs. Intensity-Modulated Radiation Therapy for Head-and-Neck Cancer: A Planning Study. *Radiat Oncol* (2013) 8:1–11. doi: 10.1186/1748-717X-8-26
190. Sandison GA, Papiez E, Block C, Morphis J. Phantom Assessment of Lung Dose From Proton Arc Therapy. *Int J Radiat Oncol Biol Phys* (1997) 38:891–7. doi: 10.1016/S0360-3016(97)00059-X
191. Ding X, Li X, Zhang JM, Kabolizadeh P, Stevens C, Yan D. Spot-Scanning Proton Arc (SPArc) Therapy: The First Robust and Delivery-Efficient Spot-Scanning Proton Arc Therapy. *Int J Radiat Oncol Biol Phys* (2016) 96:1107–16. doi: 10.1016/j.ijrobp.2016.08.049
192. Mein S, Tessonnier T, Kopp B, Harrabi S, Abdollahi A, Debus J, et al. Spot-Scanning Hadron Arc (SHArc) Therapy: A Study With Light and Heavy Ions. *Adv Radiat Oncol* (2021) 6:100661. doi: 10.1016/j.adro.2021.100661
193. Carabe-Fernandez A, Bertolet-Reina A, Karagounis I, Huynh K, Dale RG. Is There a Role for Arcing Techniques in Proton Therapy? *Br J Radiol* (2020) 93:20190469. doi: 10.1259/bjr.20190469
194. Sanchez-Parcerisa D, Kirk M, Fager M, Burgdorf B, Stowe M, Solberg T, et al. Range Optimization for Mono- and Bi-Energetic Proton Modulated Arc Therapy With Pencil Beam Scanning. *Phys Med Biol* (2016) 61:N565–74. doi: 10.1088/0031-9155/61/21/N565
195. Seco J, Gu G, Marcelos T, Kooy H, Willers H. Proton Arc Reduces Range Uncertainty Effects and Improves Conformality Compared With Photon Volumetric Modulated Arc Therapy in Stereotactic Body Radiation Therapy

for non-Small Cell Lung Cancer. *Int J Radiat Oncol Biol Phys* (2013) 87:188–94. doi: 10.1016/j.ijrobp.2013.04.048
196. Ding X, Li X, Qin A, Zhou J, Yan D, Stevens C, et al. Have We Reached Proton Beam Therapy Dosimetric Limitations?–A Novel Robust, Delivery-Efficient and Continuous Spot-Scanning Proton Arc (SPArc) Therapy is to Improve the Dosimetric Outcome in Treating Prostate Cancer. *Acta Oncol* (2018) 57:435–7. doi: 10.1080/0284186X.2017.1358463
197. Gu W, Ruan D, Lyu Q, Zou W, Dong L, Sheng K. A Novel Energy Layer Optimization Framework for Spot-Scanning Proton Arc Therapy. *Med Phys* (2020) 47:2072–84. doi: 10.1002/mp.14083
198. Liu G, Li X, Zhao L, Zheng W, Qin A, Zhang S, et al. A Novel Energy Sequence Optimization Algorithm for Efficient Spot-Scanning Proton Arc (SPArc) Treatment Delivery. *Acta Oncol* (2020) 59:1178–85. doi: 10.1080/0284186X.2020.1765415
199. Bertolet A, Carabe A. Proton Monoenergetic Arc Therapy (PMAT) to Enhance LETd Within the Target. *Phys Med Biol* (2020) 65. doi: 10.1088/1361-6560/ab9455
200. Carabe A, Karagounis IV, Huynh K, Bertolet A, François N, Kim MM, et al. Radiobiological Effectiveness Difference of Proton Arc Beams Versus Conventional Proton and Photon Beams. *Phys Med Biol* (2020) 65. doi: 10.1088/1361-6560/ab9370
201. Tommasino F, Scifoni E, Durante M. New Ions for Therapy. *Int J Particle Ther* (2015) 2:428–38. doi: 10.14338/ijpt-15-00027.1
202. Kopp B, Mein S, Dokic I, Harrabi S, Böhlen TT, Haberer T, et al. Development and Validation of Single Field Multi-Ion Particle Therapy Treatments. *Int J Radiat Oncol Biol Phys* (2020) 106:194–205. doi: 10.1016/j.ijrobp.2019.10.008
203. Kirkby KJ, Kirkby NF, Burnet NG, Owen H, Mackay RI, Crellin A, et al. Heavy Charged Particle Beam Therapy and Related New Radiotherapy Technologies: The Clinical Potential, Physics and Technical Developments Required to Deliver Benefit for Patients With Cancer. *Br J Radiol* (2020) 2020:13. doi: 10.1259/bjr.20200247
204. Ebner DK, Frank SJ, Inaniwa T, Yamada S, Shirai T. The Emerging Potential of Multi-Ion Radiotherapy. *Front Oncol* (2021) 11:624786. doi: 10.3389/fonc.2021.624786
205. Yap JSL, Higgins E, Sheehy S. Preliminary Study of a Large Energy Acceptance FFA Beam Delivery System for Particle Therapy. *Proc IPAC2021* (2021) 1256–9. doi: 10.18429/JACoW-IPAC2021-MOPAB417
206. Volz L, Kelleter L, Brons S, Burigo L, Graeff C, Niebuhr NI, et al. Experimental Exploration of a Mixed Helium/Carbon Beam for Online Treatment Monitoring in Carbon Ion Beam Therapy. *Phys Med Biol* (2020) 65:0–14. doi: 10.1088/1361-6560/ab6e52
207. Mazzucconi D, Agosteo S, Ferrarini M, Fontana L, Lante V, Pullia M, et al. Mixed Particle Beam for Simultaneous Treatment and Online Range Verification in Carbon Ion Therapy: Proof-Of-Concept Study. *Med Phys* (2018) 45:5234–43. doi: 10.1002/mp.13219
208. Jolly S, Volz L, Graeff C, Kelleter L, Pullia M, Schoemers C, et al. Enhancing Particle Therapy Through The Use Of Mixed Ion Beams. *Proc IPAC2021 (Campinas Brazil)* (2021).
209. Schaub L, Harrabi SB. Debus J. Particle Therapy in the Future of Precision Therapy. *Br J Radiol* (2020) 93:20200183. doi: 10.1259/bjr.20200183
210. Li Y, Kubota Y, Tashiro M, Ohno T. Value of Three-Dimensional Imaging Systems for Image-Guided Carbon Ion Radiotherapy. *Cancers* (2019) 11:1–13. doi: 10.3390/cancers11030297
211. Hoffmann A, Oborn B, Moteabbed M, Yan S, Bortfeld T, Knopf A, et al. MR-Guided Proton Therapy: A Review and a Preview. *Radiat Oncol* (2020) 15:1–13. doi: 10.1186/s13014-020-01571-x
212. Moteabbed M, Schuemann J, Paganetti H. Dosimetric Feasibility of Real-Time MRI-Guided Proton Therapy. *Med Phys* (2014) 41:1–11. doi: 10.1118/1.4897570
213. Oborn BM, Dowdell S, Metcalfe PE, Crozier S, Mohan R, Keall PJ. Proton Beam Deflection in MRI Fields: Implications for MRI-Guided Proton Therapy. *Med Phys* (2015) 42:2113–24. doi: 10.1118/1.4916661
214. Oborn BM, Dowdell S, Metcalfe PE, Crozier S, Mohan R, Keall PJ. Future of Medical Physics: Real-Time MRI-Guided Proton Therapy: Real-Time. *Med Phys* (2017) 44:e77–90. doi: 10.1002/mp.12371
215. Schellhammer SM, Hoffmann AL, Gantz S, Smeets J, van der Kraaij E, Quets S, et al. Integrating a Low-Field Open MR Scanner With a Static Proton Research Beam Line: Proof of Concept. *Phys Med Biol* (2018) 63. doi: 10.1088/1361-6560/aaece8
216. Gantz S, Hietschold V, Hoffmann AL. Characterization of Magnetic Interference and Image Artefacts During Simultaneous in-Beam MR Imaging and Proton Pencil Beam Scanning. *Phys Med Biol* (2020) 65. doi: 10.1088/1361-6560/abb16f
217. Bernatowicz K, Peroni M, Perrin R, Weber DC, Lo+.max A. Four-Dimensional Dose Reconstruction for Scanned Proton Therapy Using Liver 4dct-MRI. *Int J Radiat Oncol Biol Phys* (2016) 95:216–23. doi: 10.1016/j.ijrobp.2016.02.050
218. Smith GL, Ganz PA, Bekelman JE, Chmura SJ, Dignam JJ, Efstathiou JA, et al. Promoting the Appropriate Use of Advanced Radiation Technologies in Oncology: Summary of a National Cancer Policy Forum Workshop. *Int J Radiat Oncol Biol Phys* (2017) 97:450–61. doi: 10.1016/j.ijrobp.2016.10.042
219. Peeters A, Grutters JP, Pijls-Johannesma M, Reimoser S, De Ruysscher D, Severens JL, et al. How Costly is Particle Therapy? Cost Analysis of External Beam Radiotherapy With Carbon-Ions, Protons and Photons. *Radiother Oncol* (2010) 95:45–53. doi: 10.1016/j.radonc.2009.12.002

Conflict of Interest: The authors declare that the research was conducted in the absence of any commercial or financial relationships that could be construed as a potential conflict of interest.

Publisher's Note: All claims expressed in this article are solely those of the authors and do not necessarily represent those of their affiliated organizations, or those of the publisher, the editors and the reviewers. Any product that may be evaluated in this article, or claim that may be made by its manufacturer, is not guaranteed or endorsed by the publisher.

frontiers in Oncology

ORIGINAL RESEARCH
published: 13 December 2021
doi: 10.3389/fonc.2021.772580

In Silico Feasibility Study of Carbon Ion Radiotherapy With Simultaneous Integrated Boost for Head and Neck Adenoid Cystic Carcinoma

Edoardo Mastella[1], Silvia Molinelli[1], Giuseppe Magro[1], Stefania Russo[1], Maria Bonora[1], Sara Ronchi[1], Rossana Ingargiola[1], Alexandra D. Jensen[2,3], Mario Ciocca[1], Barbara Vischioni[1†] and Ester Orlandi[1†]*

[1] Clinical Department, National Center for Oncological Hadrontherapy (CNAO), Pavia, Italy, [2] Department of Radiation Oncology, University Hospitals Gießen and Marburg (UKGM), Gießen, Germany, [3] FB20 (Medicine), Philipps University Marburg, Marburg, Germany

OPEN ACCESS

Edited by:
Susanne Rogers,
Aarau Cantonal Hospital, Switzerland

Reviewed by:
Francesco Tommasino,
University of Trento, Italy
Yosuke Takakusagi,
Kanagawa Cancer Center, Japan
Lai Wei,
The Ohio State University,
United States

***Correspondence:**
Edoardo Mastella
edoardo.mastella@cnao.it

†These authors have contributed equally to this work

Specialty section:
This article was submitted to Radiation Oncology, a section of the journal Frontiers in Oncology

Received: 08 September 2021
Accepted: 11 November 2021
Published: 13 December 2021

Citation:
Mastella E, Molinelli S, Magro G, Russo S, Bonora M, Ronchi S, Ingargiola R, Jensen AD, Ciocca M, Vischioni B and Orlandi E (2021) In Silico Feasibility Study of Carbon Ion Radiotherapy With Simultaneous Integrated Boost for Head and Neck Adenoid Cystic Carcinoma. Front. Oncol. 11:772580. doi: 10.3389/fonc.2021.772580

Purpose: In carbon ion radiotherapy (CIRT), a simultaneous integrated boost (SIB) approach has not been fully exploited so far. The feasibility of a CIRT-SIB strategy for head and neck adenoid cystic carcinoma (ACC) patients was investigated in order to improve treatment planning dose distributions.

Methods and Materials: CIRT plans of 10 ACC patients treated at the National Center for Oncological Hadrontherapy (CNAO, Pavia, Italy) with sequential boost (SEQ) irradiation and prescription doses of 41.0 Gy [relative biological effectiveness (RBE)]/10 fractions to low-risk (LR) clinical target volume (CTV) plus 24.6 Gy(RBE)/6 fractions to the high-risk (HR) CTV were re-planned with two SIB dose levels to the LR-CTV, namely, 48.0 Gy(RBE) and 54.4 Gy(RBE). While planning with SIB, the HR-CTV coverage had higher priority, with fixed organ-at-risk dose constraints among the SIB and SEQ plans. The homogeneity and conformity indexes were selected for CTV coverage comparison. The biologically effective dose (BED) was calculated to compare the different fractionation schemes.

Results: Comparable HR-CTV coverage was achieved with the treatment approaches, while superior conformality and homogeneity were obtained with the SIB technique in both CTVs. With the SEQ, $SIB_{48.0}$, and $SIB_{54.4}$, the LR-CTV median doses were respectively 50.3%, 11.9%, and 6.0% higher than the prescriptions. Significant reductions of the median and near-maximum BEDs were achieved with both SIB dose levels in the LR-CTV.

Conclusions: The SIB approach resulted in highly conformal dose distributions with the reduction of the unintended dose to the LR-CTV. A prescription dose range for the LR-CTV will be clinically defined to offer tailored personalized treatments, according to the clinical and imaging characteristics of the patients.

Keywords: simultaneous integrated boost (SIB), carbon ion radiation therapy (CIRT), head and neck cancer, adenoid cystic carcinoma (ACC), radiobiological models

INTRODUCTION

Simultaneous integrated boost (SIB)–intensity-modulated radiation therapy (IMRT) has been one of the major technical photon-based RT innovations in the last 20 years.

For head and neck (HN) squamous cell carcinomas (SCCs), moderately accelerated IMRT techniques using SIB, usually at 2.12–2.2 and 1.7–2 Gy per fraction to the high-risk clinical target volume (HR-CTV) and low-risk (LR) CTV, respectively, in 30–33 fractions, with or without systemic therapy, have been largely adopted in clinical practice and within several prospective clinical trials, with similar results in terms of toxicity and oncologic outcome (1), whereas hypofractionated chemoradiation schedule with more than 2.4 Gy per fraction requires more caution to avoid severe toxicity (2).

For other non-SCC histologic tumor types historically known to be radioresistant, such as adenoid cystic carcinomas (ACCs) or other salivary gland cancers (SGCs), low linear energy transfer (LET) RT has not shown adequate local control, especially in the radical setting. Treatment outcome has recently improved with photon IMRT at doses of at least 70 Gy, with acceptable local control in patients with unresectable SGCs, especially in comparison with 3D techniques, since IMRT allows to better optimize the dose delivery, while reducing doses to the organs at risk (OARs) when escalating the dose to the target (3). ACC remains a major challenge for radiation oncologists, since it requires very high total doses to increase the probability to be cured. Moreover, its horseshoe shape is often anatomically complex, embracing or intersecting radiosensitive structures and following neural pathways (4). In recent years, strong evidence has been produced to support treatment with high-LET carbon ion RT (CIRT) for unresected ACC or after uncomplete surgical resection (5–11). Pencil beam scanning (PBS)-CIRT has entered the clinical practice for the treatment of ACC with beneficial effects on the outcome, in light of specific physical properties (allowing highly conformal dose distributions) and superior relative biological effectiveness (RBE) by at least a 1.5- to 3-fold factor in comparison with photons (5–11). Furthermore, CIRT has been shown to be effective even in more complex radioresistant scenarios, such as reirradiation of inoperable ACC (12) or of radiation-induced SGC (13), highlighting the need of further efforts to offer tailored personalized treatments, including particle therapy, to improve survival in cases of peculiar radioresistant phenotypes (14).

Until now, at our Institution (National Center for Oncological Hadrontherapy, CNAO, Pavia, Italy) (15), the PBS-CIRT standard approach for the treatment of ACC has been a sequential strategy consisting of a first phase of nine to 10 fractions to the LR-CTV followed by a second phase of six to seven fractions to the HR-CTV, with a unique nominal dose per fraction, according to the protocol adopted in Japan since 1997 (16). Japanese data of ACC CIRT treatments have recently been reported in a multicenter retrospective series with excellent results in terms of tumor local control and normal tissue toxicity (8). PBS-CIRT is usually delivered with a limited number of beams, typically two to three, achieving both high dose conformation and normal tissue sparing. However, with fixed-beam irradiation (horizontal and vertical directions at CNAO, where no isocentric gantry is available), it is very difficult to significantly change the beam arrangement between the two sequential phases; therefore part of the LR-CTV receives unintended dose from the beam paths of the boost phase.

In this paper, we investigated a SIB approach in comparison with our standard protocol for ACC patients treated with sequential boost (here called SEQ), in order to improve the actual dose distribution of the two target volumes currently delivered sequentially. While doing this, some aspects need to be taken into account, starting from the radiobiological model adopted in the treatment planning system (TPS) for RBE-weighted dose (DRBE) calculation. In fact, it is undoubtable that in CIRT, the radiobiological model has a strong impact on the dose delivered to the patient (17, 18). For ACC, a local effect model (LEM)-based (DRBE|LEM) prescription of 68.8 Gy(RBE) in 16 fractions to the HR-CTV was initially adopted to mimic the reference modified microdosimetric kinetic model (mMKM)-based (DRBE|MKM) prescription of 64 Gy(RBE) (19) adopted from HN clinical trial experience with CIRT in Japan. From the beginning of 2017, a slightly lower DRBE|LEM prescription of 65.6 Gy(RBE) has been used for patients at risk of major toxicity at our center. Since the majority of failures in our series were within the HR-CTV region due to the underdosage of the HR-CTV possibly due to the dose constraints to the OARs, we have hypothesized here that the total dose to the LR-CTV was enough to control microscopic tumor spread. In the view of a future clinical trial to implement the treatment of ACC patients, we aimed here to *in silico* investigate the feasibility of a SIB strategy instead of the standard SEQ protocol, comparing SIB plans with the original SEQ versions, in terms of target coverage, dose homogeneity, and dose conformality, in the two RBE abovementioned frames currently in clinical use worldwide. To our best knowledge, this is the first study that evaluates a SIB strategy for HN ACC patients treated with CIRT.

MATERIALS AND METHODS

Patient Data

A retrospective dataset of 10 HN ACC patients was used: five ACC with parotid gland tumors and five originating from the minor salivary glands of paranasal sinuses/lacrimal glands were selected for the present analysis. These patients were consecutively treated at CNAO in a curative intent between October 2019 and September 2020 with CIRT in 16 fractions, delivered over 4 weeks according to our current SEQ strategy. The main patient clinical and treatment data are reported in **Table 1**.

HR-CTV was defined as the macroscopic gross tumor volume (GTV) with a margin of 3–5 mm, whereas the LR-CTV included a margin of 2–5 mm around the HR-CTV and the perineural or compartmental spread of the disease. The mean LR-CTV was 272.1 ± 141.6 cm^3, while the mean HR-CTV was 112.0 ± 84.1 cm^3. Ethical approval by the institutional review board

TABLE 1 | Clinical information of the adenoid cystic carcinoma patients.

Patient	Site	T N M*	LR-CTV		HR-CTV	
			Volume [cm^3]	No. of beams	Volume [cm^3]	No. of beams
P1	LG	cT4cN0	195.8	2	50.1	2
P2	PS	cT4aN0	618.2	3	301.9	2
P3	LG	cT4cN0	188.1	2	62.1	2
P4	LG	cT4bN0	174.3	2	50.0	2
P5	PS	cT4aNo	216.0	2	98.0	2
P6	PG	pT3cN0	189.1	2	60.2	1
P7	PG	cT3N1	342.4	2	179.9	2
P8	PG	cT4aN0	384.4	3	186.9	2
P9	PG	pT3cNo	238.8	2	71.5	2
P10	PG	pT3cN0	174.1	2	59.6	2

CTV, clinical target volume; LR, low risk; HR, high risk; LG, lacrimal glands; PS, paranasal sinuses; PG, parotid glands.
**Cancer staging according to the Union for International Cancer Control (UICC) TNM Classification of Malignant Tumors (8th Edition).*

was obtained for this study, and all patients gave their written consent (CNAO study number OSS-26-2021).

Sequential Boost Treatment Plans

Clinical delivered plans were optimized using RayStation-V8.1.2.5 TPS (RaySearch Laboratories AB, Stockholm, Sweden), with a prescribed dose of 4.1 Gy(RBE)|LEM/fraction. For the two sequential phases, beam arrangement and couch setup were selected depending on the target location. The first phase of the delivered treatment was planned with two beams for eight out of 10 patients and with three beams for the two other patients, while the SEQ (second phase) was planned with two beams for nine out of 10 patients and with one beam for the other patient (see **Table 1**). Our standard beam scanning parameters were used (20). Robust optimization (21) was performed using our standard settings: ± 3% range uncertainty, 2-mm isotropic isocenter shift. The LEM version I (22) was firstly used to calculate the DRBE|LEM with a α β ratio of 2 Gy. The prescribed dose of the first phase was 41.0 Gy(RBE) in 10 fractions to the median LR-CTV. A SEQ phase of 24.6 Gy(RBE)|LEM was then delivered in six more fractions to the median HR-CTV, reaching a total prescription DRBE|LEM of 65.6 Gy(RBE). In the plan optimization, the highest priority was sparing the brainstem and the optic pathways (at least the optic chiasm and the contra-lateral optic to preserve mono-lateral vision), with dose constraints derived from Dale et al. (23, 24). CTV coverage was thus increased as much as possible without exceeding the constraints of the OARs reported above. The main planning goals for volumes of interest are summarized in **Table 2**.

TABLE 2 | Main planning goals for volumes of interest.

	Structures	Planning goals
CTVs	All CTVs	D95% ≥ 95%
		D98% ≥ 90%
	HR-CTV	D2% ≤ 103%
OARs	Brainstem	D1% ≤ 40 Gy(RBE)
	Optic pathways	D1% ≤ 45 Gy(RBE)
		D20% ≤ 37 Gy(RBE)
	Temporal and frontal lobes	D2cc < 54 Gy(RBE)

Note. CTV, clinical target volume; HR, high risk; OAR, organ at risk; D%, dose to % of the volume of interest.

Simultaneous Integrated Boost Treatment Plans

The delivered SEQ treatment plans were compared with two SIB fractionation schemes with different low dose levels: 54.4 Gy (RBE) ("$SIB_{54.4}$") and 48.0 Gy(RBE) ("$SIB_{48.0}$") to the median LR-CTV in 16 fractions and a high dose level of 65.6 Gy(RBE) to the HR-CTV. Thus, nominal dose per fraction to LR-CTV was 3.4 Gy (RBE) in $SIB_{54.4}$ and 3.0 Gy(RBE) in $SIB_{48.0}$. These prescription doses were investigated as they resulted in a nominal LR-CTV biologically effective dose (BED) comparable with the SEQ approach when using the different RBE models (see the section *Treatment Plan Evaluation*). The median LR-CTV was defined as the volume of the LR-CTV minus HR-CTV. The same beam arrangements and scanning parameters of the first phase of the SEQ plan were used, together with the same robustness settings. In the SIB plans, priority was given to the HR-CTV coverage to reproduce a dose–volume histogram (DVH) similar to the SEQ keeping fixed the same OAR dose constraints. A total of 20 SIB plans were optimized by the same experienced planner.

Modified Microdosimetric Kinetic Model Dose Translation

Being our clinical protocols derived from the CIRT protocols tested in clinical trials in Japan (17) and thus our approach ensued from the mMKM-based experience (19), all SEQ and SIB absorbed dose distributions were translated into mMKM doses using the V6.99 research RayStation version, previously commissioned for our beamline (19). A total of 40 plans were recalculated.

Treatment Plan Evaluation

The SEQ and SIB techniques were firstly compared in terms of DVH-based metrics. In particular, the near-minimum (D98%), the median (D50%), and the near-maximum (D2%) doses were chosen as dose-summarizing parameters (DSPs) for CTV coverage evaluation, as recommended by the International Commission on Radiation Units and Measurements (ICRU) 78 (25). The DSPs were normalized to the corresponding prescriptions. For mMKM doses, the nominal prescriptions were obtained through the relations calculated in Fossati et al.

and Wang et al. (17, 26). The doses/fractions of 4.1, 3.4, and 3.0 Gy(RBE)|LEM corresponded to 3.5, 2.6, and 2.2 Gy(RBE)|mMKM, respectively. Dose evaluators for the LR-CTV were referred to the LR-CTV minus the HR-CTV.

The homogeneity index (HI) and conformity index (CI) of the CTVs were evaluated as recommended by the ICRU 93 (27) and were calculated for the whole treatment similarly to Orlandi et al. (28):

$$HI = \frac{D2\,\% - D98\,\%}{Dprescription} \quad (1)$$

$$CI = \frac{TV_{D98\,\%}}{CTV} \quad (2)$$

where TV is the total volume encompassed by the D98%.
Differences of the DSP were calculated as SIB minus SEQ plans:

$$\Delta DSP = DSP_{SIB} - DSP_{SEQ} \quad (2)$$

Afterwards, we calculated the BED to compare the different fractionation schemes similarly to Kawashiro et al. (29):

$$BED_{\alpha/\beta} = nd\left(1 + \frac{d}{\alpha/\beta}\right) \quad (3)$$

where α and β are coefficients of the linear-quadratic model, n is the number of fractions, and d is the dose per fraction. For the SEQ approach, the total BED was the sum of the single-phase BEDs. We assumed a α/β ratio of 3 for ACC. The SEQ prescription of 41.0 Gy(RBE)|LEM in 10 fractions for the LR-CTV corresponded to a BED of 97.0 Gy(RBE), while the SIB levels of 48.0 and 54.4 Gy(RBE)|LEM in 16 fractions corresponded to a BED of 96.0 Gy(RBE) and 116.1 Gy(RBE). When translating to mMKM, the nominal BEDs of the first phase of the SEQ, $SIB_{48.0}$, and $SIB_{54.4}$ were respectively 75.8, 61.0, and 77.7Gy(RBE).

The equivalent dose in 2-Gy(RBE) fractions (EQD2) was also calculated as

$$EQD2_{\alpha/\beta} = \frac{BED_{\alpha/\beta}}{1 + \frac{2}{\alpha/\beta}} \quad (4)$$

Statistical significance of the dosimetric parameters was assessed with the non-parameter Wilcoxon signed-rank test, using MATLAB-based software (version R2018a, The MathWorks Inc., Natick, MA, USA). A significance level of 5% was chosen (p-value <0.05). In the *post-hoc* analysis, the significance level was corrected using the Bonferroni method based on the number of multiple tests conducted (n = 5 for the DSPs; n = 3 for the BEDs).

RESULTS

Figure 1 shows the dose distributions of a representative case (P6) obtained with the SEQ and SIB approaches: the top panel corresponds to LEM doses and the bottom panel to mMKM doses.

Figure 2 shows the DVHs of the HR-CTV and the LR-CTV of P6 achieved with the SEQ and SIB techniques.

The mean values of the DSP are reported in **Table 3**, obtained with both the LEM and the mMKM for the different treatment approaches. The values were normalized to the corresponding prescriptions.

All optimized plans concern the OAR dose constraints reported in **Table 2**.

After Bonferroni correction of five tests, comparable HR-CTV coverage was found between LEM-based SEQ and SIB plans ($SIB_{48.0}$: p = 0.014 for both D98% and D2%; $SIB_{54.4}$: p = 0.13 and p = 0.38 for D98% and D2%). On average, a very slight decrease of −1.8% was observed in the D98% with the $SIB_{48.0}$, which was on average compliant with the optimization goal (D95% ≥ 95% and D2% ≤ 103% of the prescribed dose). HR-CTV dose inhomogeneity slightly increased with the SIB, while the HI values of the LR-CTV decreased significantly for both SIB dose levels. With the SEQ approach, 50% of the LR-CTV received on average a dose 50.3% higher than the prescription, while differences between LR-CTV median and prescribed doses were reduced to 11.9% and 6.0% for $SIB_{48.0}$ and $SIB_{54.4}$, respectively.

Dose inhomogeneity was slightly higher for ACC of paranasal sinuses/lacrimal glands than parotid glands cases due to the target location closer to critical structures. In particular, for ACC of paranasal sinuses/lacrimal glands, the average HI values of the HR(LR)-CTV were 0.06 ± 0.02 (0.68 ± 0.09), 0.07 ± 0.03 (0.30 ± 0.05), and 0.08 ± 0.02 (0.45 ± 0.03) for the SEQ, $SIB_{54.4}$, and $SIB_{48.0}$, respectively (see **Supplementary Table S1**).

The CI values of both CTVs were significantly reduced with the SIB, indicating a better conformality of this technique with respect to the SEQ.

As expected, DRBE became more inhomogeneous when translating into mMKM doses (19), with an increase of the HI in both CTVs for all treatment approaches (see **Table 3**). However, mMKM ΔDSP between the SIB and SEQ techniques decreased for HR-CTV, with respect to LEM, with comparable HR-CTV coverage for all optimization approaches. In particular, the p-values of the $SIB_{48.0}$ and $SIB_{54.4}$ were respectively 0.065 (0.87) and 0.39 (0.77) for D98% (D2%).

The mMKM dose distributions confirmed the superior conformality of the SIB technique in both CTVs. When considering the LR-CTV, the dose distributions of the SIB were also more homogeneous, with the best homogeneity and conformality obtained with the $SIB_{54.4}$.

All the dose distributions of the paranasal sinuses/lacrimal glands group were slightly more inhomogeneous than the parotid gland group, as highlighted with the LEM. For these patients, the average HI values of the HR(LR)-CTV were 0.21 ± 0.07 (0.92 ± 0.10), 0.19 ± 0.05 (0.60 ± 0.07), and 0.20 ± 0.04 (0.87 ± 0.06) for the SEQ, $SIB_{54.4}$, and $SIB_{48.0}$, respectively (see **Supplementary Table S2**).

The mean values of the BED calculated with both RBE models are summarized in **Table 4**.

After Bonferroni correction of three tests, a significant decrease of the BED(D98%)|LEM was found with the $SIB_{48.0}$ in the HR-CTV (p = 0.014), together with slight increase of the BED

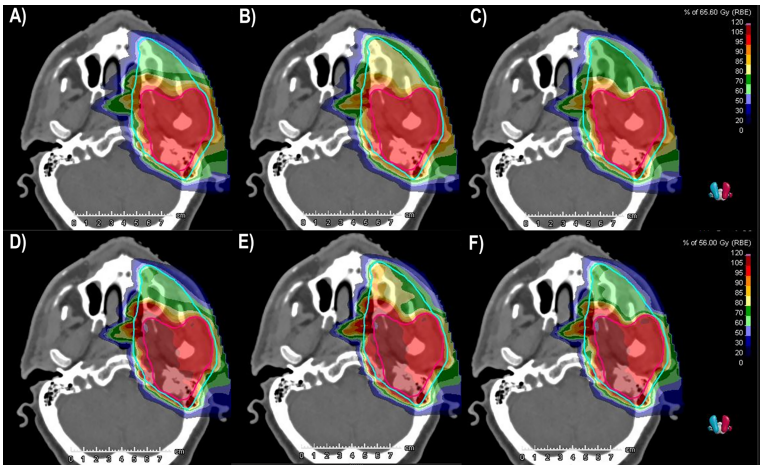

FIGURE 1 | LEM and mMKM dose distributions calculated for patient P6. The top (bottom) panel corresponds to LEM (mMKM) doses: **(A, D)** SEQ approach. **(B, E)** $SIB_{54.4}$. **(C, F)** $SIB_{48.0}$. The HR-CTV and LR-CTV are delineated in purple and light blue, respectively. The isodoses were normalized to the HR-CTV prescriptions. LEM, local effect model; mMKM, modified microdosimetric kinetic model; SEQ, sequential boost; SIB, simultaneous integrated boost; HR-CTV, high-risk clinical target volume; LR-CTV, low-risk clinical target volume.

(D2%)|LEM (p = 0.01). When translated into mMKM doses, these values were comparable: p = 0.065 for BED(D98%)|mMKM and p = 0.92 for BED(D2%)|mMKM. When considering the LR-CTV, the BEDs calculated for the median doses were significantly lower for both SIB dose levels and RBE models with respect to the SEQ plans (p = 0.002).

With the LEM, the near-minimum BED(D98%)|LEM was comparable between the SEQ and $SIB_{48.0}$ (p = 0.19), while a statistically significant increase was found for $SIB_{54.4}$ plans (p = 0.002).

Opposite to the LEM, with the mMKM, a significant difference was found in the BED(D98%)|mMKM of the LR-CTV for the $SIB_{48.0}$ (p = 0.002), while the BED(D98%)|mMKM of the $SIB_{54.4}$ was comparable with the SEQ (p = 0.13).

Statistically significant decreases of the BED(D2%)|mMKM were observed for both SIB dose levels (p = 0.002), with a reduction of about 10 Gy(RBE).

The mean values of the EQD2 calculated for the three treatment approaches and both RBE models are reported in **Supplementary Table S3**.

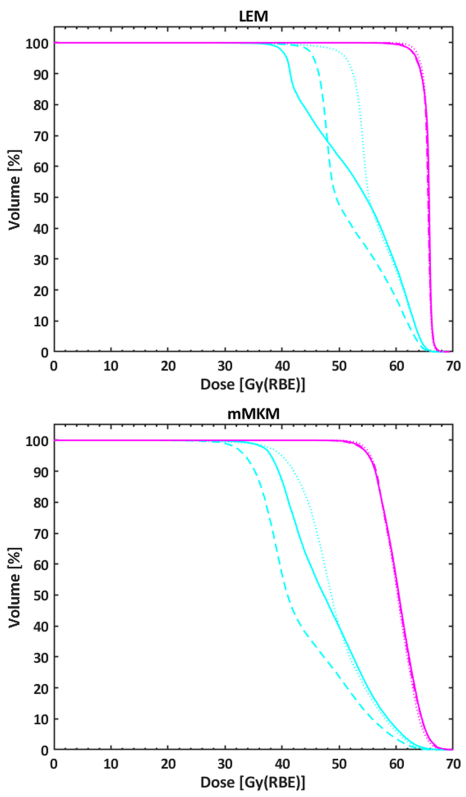

FIGURE 2 | DVHs of the HR-CTV (purple line) and the LR-CTV (light blue line) of P6 achieved with the SEQ (solid line), the $SIB_{54.4}$ (dotted line), and the $SIB_{48.0}$ (dashed line) approaches. The top (bottom) panel corresponds to LEM (mMKM) doses. DVH, dose–volume histogram; HR-CTV, high-risk clinical target volume; LR-CTV, low-risk clinical target volume; SEQ, sequential boost; SIB, simultaneous integrated boost; LEM, local effect model; mMKM, modified microdosimetric kinetic model.

DISCUSSION

Our CIRT prescription doses were defined with the aim of reproducing the National Institute of Radiological Sciences (NIRS) clinical results, with long follow-up available that provides reassuring conclusions on long-term toxicity. The RBE model currently in clinical use at NIRS is the mMKM. At the time of this study, no commercial TPS provided clinical mMKM doses, and the European experience was primarily based on the LEM model. Therefore, using the same fractionation schemes of the NIRS, we corrected the LEM-based prescription doses for the RBE dependence as described in Fossati et al. for

TABLE 3 | Mean values (± 1 standard deviation) of the target coverage achieved with the three treatment approaches, reported for both radiobiological calculation models.

		HR-CTV					LR-CTV				
		D98% [%]	D50% [%]	D2% [%]	HI	CI	D98% [%]	D50% [%]	D2% [%]	HI	CI
LEM	SEQ	97.2 ± 2.1	100.0 ± 0.0	101.5 ± 0.8	0.04 ± 0.03	1.38 ± 0.23	100.0 ± 1.5	150.3 ± 11.9	166.3 ± 8.4	0.66 ± 0.08	1.56 ± 0.13
	$SIB_{54.4}$	96.2 ± 2.3	100.0 ± 0.0	101.7 ± 0.6	0.05 ± 0.03	**1.06 ± 0.07**	**91.2 ± 3.3**	**106.0 ± 5.7**	**120.7 ± 1.0**	**0.30 ± 0.03**	**1.19 ± 0.13**
	$SIB_{48.0}$	95.4 ± 2.2	100.0 ± 0.0	102.0 ± 0.5	0.07 ± 0.03	**0.99 ± 0.04**	**92.2 ± 2.3**	**111.9 ± 10.6**	**136.6 ± 1.6**	**0.44 ± 0.02**	**1.33 ± 0.12**
mMKM	SEQ	98.7 ± 2.2	106.6 ± 1.8	117.6 ± 4.7	0.19 ± 0.06	1.78 ± 0.36	105.4 ± 2.8	153.8 ± 20.9	191.3 ± 11.2	0.86 ± 0.11	1.50 ± 0.16
	$SIB_{54.4}$	97.7 ± 2.5	106.2 ± 1.7	116.4 ± 2.7	0.19 ± 0.04	**1.39 ± 0.19**	**91.5 ± 4.5**	**118.8 ± 11.9**	**149.4 ± 3.8**	**0.58 ± 0.05**	**1.39 ± 0.13**
	$SIB_{48.0}$	96.9 ± 2.1	106.6 ± 1.7	116.9 ± 2.2	0.20 ± 0.03	**1.27 ± 0.15**	**90.0 ± 3.5**	**122.8 ± 19.9**	**175.2 ± 4.3**	0.85 ± 0.05	1.47 ± 0.11

The values were normalized to the corresponding prescriptions. Statistically significant differences between the SEQ and SIB approaches are shown in bold (p-values are statistically significant after Bonferroni correction of five tests, $p < 0.01$).
CTV, clinical target volume; HR, high risk; LR, low risk; D%, dose to % of the CTV; HI, homogeneity index; CI, conformity index; LEM, local effect model; mMKM, modified microdosimetric kinetic model; SEQ, sequential boost; SIB, simultaneous integrated boost.

simple geometric configuration (17). The practically feasible way to deliver treatment plans as close as possible, from a clinical point of view, to NIRS practice was to minimize the physical dose differences between the two RBE models. Conversion factors ranging from 1.04 to 1.15 were initially adopted to translate DRBE|mMKM into the DRBE|LEM prescription dose levels that deliver the closest absorbed dose. Prudentially, no correction was applied to OAR constraints. Prescription dose conversion factors increase as the mMKM prescribed dose per fraction decreases. A new approach combining Monte Carlo simulations was then implemented for real patient data in order to further verify the consistency of our conversion factors (18). Our group has recently investigated the impact of RBE modelling on treatment outcomes of a series of 78 ACC patients treated between 2013 and 2016 with the SEQ approach (19). The study highlighted that the majority of the recurrences could be explained by inadequate HR-CTV coverage, mainly due to conservative dose constraints to the OARs. New constraints for the brainstem and optic pathways were then defined to improve target coverage and dose homogeneity in treatment planning, considering the uncertainties in dose biological modelling translation of Japanese protocols to LEM (23, 24). Until now, no increment in normal tissue complications has been observed in our treated patients with the adoption of new dose limits for OARs (30). In this study, with these new OAR constraints, we have evaluated for 10 ACC patients the dose distribution of a SIB treatment in comparison with the actual clinical scenario of SEQ volume, with the aim of improving the tumor dose conformation while reducing the unintended dose to the LR volume and related probability of complications.

In addition, the SIB technique is known to be a more practical and efficient treatment approach (31). A single optimization process is needed, thus facilitating the optimizer in the search for the optimal solution balancing target coverage and OAR sparing over the whole treatment. Moreover, the clinical workflow would benefit from the SIB strategy, e.g., in the patient-specific quality assurance process or in case of treatment adaptation.

Only Kawashiro et al. (29) investigated a SIB treatment using PBS-CIRT, although it is the more convenient procedure, to our best knowledge. In their *in silico* study, the authors evaluated a SIB strategy for pancreatic cancer to increase tumor dose while sparing OARs. Their analysis suggested the feasibility of dose escalation using the SIB satisfying the dose constraints for OARs, underlying that the SIB technique has the potential to deliver higher doses to the tumor, without substantially increasing the dose to OARs. Of course, their results should be confirmed in future patient clinical trials.

We investigated two different SIB prescriptions that resulted in a nominal LR-CTV BED comparable with the SEQ approach when using the different RBE models. As recently underlined in Molinelli et al. (32), in CIRT, a combined multimodel RBE-based optimization could play a key role in the enhancement of the

TABLE 4 | Mean values (± 1 standard deviation) of the biologically effective dose (BED) obtained with the three treatment approaches, reported for both radiobiological calculation models.

		HR-CTV			LR-CTV		
		BED (D98%) [Gy(RBE)]	BED (D50%) [Gy(RBE)]	BED (D2%) [Gy(RBE)]	BED (D98%) [Gy(RBE)]	BED (D50%) [Gy(RBE)]	BED (D2%) [Gy(RBE)]
LEM	SEQ	148.4 ± 5.3	155.3 ± 0.0	158.9 ± 2.1	87.6 ± 5.5	135.6 ± 11.0	156.8 ± 1.3
	$SIB_{54.4}$	146.1 ± 5.1	155.3 ± 0.0	159.4 ± 1.4	**100.9 ± 5.5**	**127.1 ± 10.2**	155.5 ± 2.1
	$SIB_{48.0}$	**144.1 ± 5.1**	155.3 ± 0.0	**160.2 ± 1.3**	85.0 ± 3.1	**114.4 ± 16.9**	155.1 ± 2.9
mMKM	SEQ	119.0 ± 4.1	134.0 ± 3.4	156.3 ± 10.0	71.1 ± 4.8	112.4 ± 14.2	152.5 ± 6.3
	$SIB_{54.4}$	117.1 ± 4.6	133.2 ± 3.3	153.7 ± 5.5	68.4 ± 4.8	**100.8 ± 16.3**	**142.7 ± 5.6**
	$SIB_{48.0}$	115.7 ± 3.8	134.0 ± 3.4	154.7 ± 4.5	**52.6 ± 2.8**	**83.1 ± 22.0**	**141.0 ± 5.3**

Statistically significant differences between the SEQ and SIB approaches are shown in bold (p-values are statistically significant after Bonferroni correction of three tests, $p < 0.017$).
CTV, clinical target volume; HR, high risk; LR, low risk; LEM, local effect model; mMKM, modified microdosimetric kinetic model; SEQ, sequential boost; SIB, simultaneous integrated boost.

therapeutic ratio for radioresistant tumors. In particular, the lower SIB dose level, i.e., DRBE|LEM prescription of 48.0 Gy(RBE), resulted in a nominal LR-CTV BED comparable with the LEM-based SEQ approach: BED($SIB_{48.0}$)|LEM = 96.0 Gy(RBE) *vs.* BED (SEQ)|LEM = 97.0 Gy(RBE). As the prescription dose conversion factors to correct for differences in the RBE model increase for lower doses per fraction (17, 18), we also examined a higher SIB dose level, i.e., 54.4 Gy(RBE), which maintains a similar mMKM-based LR-CTV nominal BED of the SEQ plan: BED($SIB_{54.4}$)| mMKM = 77.7 Gy(RBE) *vs.* BED(SEQ)|mMKM = 75.8 Gy(RBE).

The sample size of this work was small for practical reasons. However, most of the studies that compare dosimetric data in RT include between 10 and a few hundred patients, as reported by Chaikh et al. (33). Of course, a greater number of patients would be needed to strengthen our results. A limitation of the statistical analysis could be that a paired test was adopted, thus increasing the probability of finding statistical significance even when the actual difference is low in absolute values. However, as the Wilcoxon signed-rank test does not require a normal distribution and does not consider the size of the difference, it particularly fits for RT dosimetric comparison, since the data are "naturally" paired (33). Another limitation could be that using multiple summarizing parameters could inflate the false-positive rate. Therefore, the Bonferroni correction was computed to avoid inflating type 1 error probability (33).

In the plan optimization, with the $SIB_{48.0}$, we obtained a slightly lower D98%|LEM of the HR-CTV even respecting the planning goals, probably due to the high dose gradient between the CTV prescription dose levels. A superior conformality was obtained with the SIB technique in both CTVs, together with an improved homogeneity and a significant reduction in the biological median and near-maximum doses to the LR-CTV. The $SIB_{54.4}$ achieved the best homogeneity and conformality with both RBE models.

Plan robustness may be an issue in extremely modulated plans, especially in the paranasal sinuses. Our clinical protocol foresees periodic re-evaluation CT scans every other week or whenever deemed necessary according to patients' status and daily imaging.

As expected, a higher BED to the 98% of the LR-CTV was obtained with the $SIB_{54.4}$ when using the LEM, with an average value comparable with photon-based RT with a prescription dose of 60 Gy (34). On the other hand, this value turned out to be comparable with that of the SEQ approach when translating to mMKM. Predictably, with the SIB approach, the LR-CTV was more sensitive to the translation between LEM and mMKM (see **Figure 2** and **Table 4**) as a result of the lower prescribed dose per fraction (e.g., higher conversion factors between the models).

The issue of the effective clinical dose to the LR volume and perineural spread for ACC tumors has been deeply investigated in photon-based RT (34). When considering both BED and EQD2 values of the $SIB_{48.0}$ and $SIB_{54.4}$, both dose levels would be equally acceptable when treating ACC tumors, depending on the prognostic factors.

In consideration of the near-minimum BED obtained with the mMKM and of the superior dose distributions achieved with the $SIB_{54.4}$, we believe that for future clinical trials of CIRT in ACC patients, the 54.4 Gy(RBE)|LEM dose level could assure adequate tumor control in case of positive margin along the nerve, whereas the 48.0 Gy(RBE)|LEM dose level could have adequate efficacy in case of elective perineural irradiation or microscopic focal intratumor perineural invasion (PNI), maintaining a low toxicity profile.

Furthermore, concerning the fractionation scheme, adopting the SIB strategy instead of the sequential approach would allow to maintain a high dose/fraction (4.1 Gy(RBE)|LEM/fraction) for the more radioresistant GTV in the HR-CTV, lowering the fraction dose for the microscopic disease (3.0–3.4 Gy(RBE)|LEM/fraction) embedded within the normal OARs of the LR-CTV.

A limitation of this study is that a retrospective dataset was used and a greater number of patients would strengthen these results. Only five ACC of paranasal sinuses/lacrimal glands were selected where the HR-CTV is closer/adjacent to critical organs (e.g., brainstem and optic pathways). However, as the HR-CTV prescription dose was the same between the two treatment approaches, the OAR dose constraints of the SIB plans corresponded to the total SEQ approach and for this reason were not reported in this analysis.

CONCLUSION

In conclusion, this study investigated the SIB feasibility for CIRT in HN ACC for both the LEM and mMKM radiobiological models. The advantage of the SIB approach would be a better dose conformality with the reduction of the unintended dose to the LR-CTV in comparison with the standard strategy of SEQ. A prescription dose range for the LR-CTV will be clinically defined to offer tailored personalized treatments, according to the clinical and imaging characteristics of the patients.

DATA AVAILABILITY STATEMENT

The original contributions presented in the study are included in the article/**Supplementary Material**. Further inquiries can be directed to the corresponding author.

ETHICS STATEMENT

The studies involving human participants were reviewed and approved by the institutional review board (CNAO study number OSS-26-2021). The patients/participants provided their written informed consent to participate in this study. Written informed consent was obtained from the individual(s) for the publication of any potentially identifiable images or data included in this article.

AUTHOR CONTRIBUTIONS

EM, SM, and EO contributed to the conception and design of the study. EM, MB, and BV organized the database. EM and GM performed the statistical analysis. EM and EO wrote the first

draft of the manuscript. SM and BV wrote sections of the manuscript. EM, SM, GM, SRu, MB, SRo, RI, AJ, MC, BV, and EO contributed to the manuscript revision and read and approved the submitted version. All authors contributed to the article and approved the submitted version.

SUPPLEMENTARY MATERIAL

The Supplementary Material for this article can be found online at: https://www.frontiersin.org/articles/10.3389/fonc.2021.772580/full#supplementary-material

REFERENCES

1. De Felice F, Bonomo P, Sanguineti G, Orlandi E. Moderately Accelerated Intensity-Modulated Radiation Therapy Using Simultaneous Integrated Boost: Practical Reasons or Evidence-Based Choice? A Critical Appraisal of Literature. *Head Neck* (2020) 42(11):3405–14. doi: 10.1002/hed.26400
2. Iqbal MS, Morgan D, West N, Paterson C. Hypofractionated Chemoradiation (2.75 Gy Per Fraction) in Head and Neck Cancer: Extreme Caution Required. *Oral Oncol* (2021) 120:105261. doi: 10.1016/j.oraloncology.2021.105261
3. Spratt DE, Salgado LR, Riaz N, Doran MG, Tam M, Wolden S, et al. Results of Photon Radiotherapy for Unresectable Salivary Gland Tumors: Is Neutron Radiotherapy's Local Control Superior? *Radiol Oncol* (2014) 48(1):56–61. doi: 10.2478/raon-2013-0046
4. Orlandi E, Iacovelli NA, Bonora M, Cavallo A, Fossati P. Salivary Gland. Photon Beam and Particle Radiotherapy: Present and Future. *Oral Oncol* (2016) 60:146–56. doi: 10.1016/j.oraloncology.2016.06.019
5. Jensen AD, Nikoghosyan A, Windemuth-Kieselbach C, Debus J, Münter MW. Combined Treatment of Malignant Salivary Gland Tumours With Intensity-Modulated Radiation Therapy (IMRT) and Carbon Ions: COSMIC. *BMC Cancer* (2010) 10:546. doi: 10.1186/1471-2407-10-546
6. Jensen AD, Nikoghosyan AV, Poulakis M, Höss A, Haberer T, Jäkel O, et al. Combined Intensity-Modulated Radiotherapy Plus Raster-Scanned Carbon Ion Boost for Advanced Adenoid Cystic Carcinoma of the Head and Neck Results in Superior Locoregional Control and Overall Survival. *Cancer* 121 (17):3001–9. doi: 10.1002/cncr.29443
7. Jensen AD, Poulakis M, Nikoghosyan AV, Welzel T, Uhl M, Federspil PA, et al. High-LET Radiotherapy for Adenoid Cystic Carcinoma of the Head and Neck: 15 Years' Experience With Raster-Scanned Carbon Ion Therapy. *Radiotherapy Oncol* (2016) 118(2):272–80. doi: 10.1016/j.radonc.2015.05.010
8. Koto M, Hasegawa A, Takagi R, Ikawa H, Naganawa K, Mizoe JE, et al. Evaluation of the Safety and Efficacy of Carbon Ion Radiotherapy for Locally Advanced Adenoid Cystic Carcinoma of the Tongue Base. *Head Neck* (2016) 38(Suppl 1):E2122–6. doi: 10.1002/hed.24397
9. Sulaiman NS, Demizu Y, Koto M, Saitoh JI, Suefuji H, Tsuji H, et al. Multicenter Study of Carbon-Ion Radiation Therapy for Adenoid Cystic Carcinoma of the Head and Neck: Subanalysis of the Japan Carbon-Ion Radiation Oncology Study Group (J-CROS) Study (1402 Hn). *Int J Radiat Oncol Biol Phys* (2018) 100(3):639–46. doi: 10.1016/j.ijrobp.2017.11.010
10. Koto M, Demizu Y, Saitoh JI, Suefuji H, Tsuji H, Okimoto T, et al. Definitive Carbon-Ion Radiation Therapy for Locally Advanced Sinonasal Malignant Tumors: Subgroup Analysis of a Multicenter Study by the Japan Carbon-Ion Radiation Oncology Study Group (J-CROS). *Int J Radiat Oncol Biol Phys* (2018) 102(2):353–61. doi: 10.1016/j.ijrobp.2018.05.074
11. Akbaba S, Ahmed D, Mock A, Held T, Bahadir S, Lang K, et al. Treatment Outcome of 227 Patients With Sinonasal Adenoid Cystic Carcinoma (ACC) After Intensity Modulated Radiotherapy and Active Raster-Scanning Carbon Ion Boost: A 10-Year Single-Center Experience. *Cancers* (2019) 11(11):1705. doi: 10.3390/cancers11111705
12. Vischioni B, Dhanireddy B, Severo C, Bonora M, Ronchi S, Vitolo V, et al. Reirradiation of Salivary Gland Tumors With Carbon Ion Radiotherapy at CNAO. *Radiotherapy Oncol* (2020) 145:172–7. doi: 10.1016/j.radonc.2020.01.004
13. Romanello DA, Imamguliyeva Z, Cavalieri S, Vischioni B, Gandola L, Iannalfi A, et al. Multidisciplinary Management of Radiation-Induced Salivary Gland Carcinomas in the Modern Radiotherapy Era. *Cancers* (2020) 12(12):3769. doi: 10.3390/cancers12123769
14. Ronchi S, Mastella E, Vischioni B, Bonora M, Orlandi E. Therapeutic Challenges in Radiation-Induced Salivary Gland Cancers. *Curr Opin Otolaryngol Head Neck Surg* (2021) 29(2):120–5. doi: 10.1097/MOO.0000000000000694
15. Rossi S. The National Centre for Oncological Hadrontherapy (CNAO): Status and Perspectives. *Physica Med* (2015) 31(4):333–51. doi: 10.1016/j.ejmp.2015.03.001
16. Mizoe JE, Hasegawa A, Jingu K, Takagi R, Bessyo H, Morikawa T, et al. Results of Carbon Ion Radiotherapy for Head and Neck Cancer. *Radiotherapy Oncol* (2012) 103(1):32–7. doi: 10.1016/j.radonc.2011.12.013
17. Fossati P, Molinelli S, Matsufuji N, Ciocca M, Mirandola A, Mairani A, et al. Dose Prescription in Carbon Ion Radiotherapy: A Planning Study to Compare NIRS and LEM Approaches With a Clinically-Oriented Strategy. *Phys Med Biol* (2012) 57(22):7543–54. doi: 10.1088/0031-9155/57/22/7543
18. Molinelli S, Magro G, Mairani A, Matsufuji N, Kanematsu N, Inaniwa T, et al. Dose Prescription in Carbon Ion Radiotherapy: How to Compare Two Different RBE-Weighted Dose Calculation Systems. *Radiotherapy Oncol* (2016) 120(2):307–12. doi: 10.1016/j.radonc.2016.05.031
19. Molinelli S, Bonora M, Magro G, Casale S, Dale JE, Fossati P, et al. RBE-Weighted Dose in Carbon Ion Therapy for ACC Patients: Impact of the RBE Model Translation on Treatment Outcomes. *Radiotherapy Oncol* (2019) 141:227–33. doi: 10.1016/j.radonc.2019.08.022
20. Mirandola A, Molinelli S, Vilches Freixas G, Mairani A, Gallio E, Panizza D, et al. Dosimetric Commissioning and Quality Assurance of Scanned Ion Beams at the Italian National Center for Oncological Hadrontherapy. *Med Phys* (2015) 42(9):5287–300. doi: 10.1118/1.4928397
21. Fredriksson A, Forsgren A, Hårdemark B. Minimax Optimization for Handling Range and Setup Uncertainties in Proton Therapy. *Med Phys* (2011) 38(3):1672–84. doi: 10.1118/1.3556559
22. Kramer M, Scholz M. Treatment Planning for Heavy-Ion Radiotherapy: Calculation and Optimization of Biologically Effective Dose. *Phys Med Biol* (2000) 45(11):3319–30. doi: 10.1088/0031-9155/45/11/314
23. Dale JE, Molinelli S, Vitolo V, Vischioni B, Bonora M, Magro G, et al. Optic Nerve Constraints for Carbon Ion RT at CNAO – Reporting and Relating Outcome to European and Japanese RBE. *Radiotherapy Oncol* (2019) 140:175–81. doi: 10.1016/j.radonc.2019.06.028
24. Dale JE, Molinelli S, Vischioni B, Vitolo V, Bonora M, Magro G, et al. Brainstem NTCP and Dose Constraints for Carbon Ion RT—Application and Translation From Japanese to European RBE-Weighted Dose. *Front Oncol* (2020) 10:531344. doi: 10.3389/fonc.2020.531344
25. Prescribing, Recording, and Reporting Proton-Beam Therapy. *J ICRU* (2007) 7(2). doi: 10.1093/jicru/ndm021
26. Wang W, Huang Z, Sheng Y, Zhao J, Shahnazi K, Zhang Q, et al. RBE-Weighted Dose Conversions for Carbon Ionradiotherapy Between Microdosimetric Kinetic Model and Local Effect Model for the Targets and Organs at Risk in Prostate Carcinoma. *Radiotherapy Oncol* (2020) 144:30–6. doi: 10.1016/j.radonc.2019.10.005
27. Prescribing, Recording, and Reporting Light Ion Beam Therapy. *J ICRU* (2019) 16(1):1–2. doi: 10.1093/jicru/ndy029
28. Orlandi E, Giandini T, Iannacone E, De Ponti E, Carrara M, Mongioj V, et al. Radiotherapy for Unresectable Sinonasal Cancers: Dosimetric Comparison of Intensity Modulated Radiation Therapy With Coplanar and non-Coplanar Volumetric Modulated Arc Therapy. *Radiotherapy Oncol* (2014) 113(2):260–6. doi: 10.1016/j.radonc.2014.11.024
29. Kawashiro S, Mori S, Yamada S, Miki K, Nemoto K, Tsuji H, et al. Dose Escalation Study With Respiratory-Gated Carbon-Ion Scanning Radiotherapy Using a Simultaneous Integrated Boost for Pancreatic Cancer: Simulation With Four-Dimensional Computed Tomography. *Br J Radiol* (2017) 90 (1072):20160790. doi: 10.1259/bjr.20160790
30. Ronchi S, Vischioni B, Bonora M, Barcellini A, Locati LD, Castelnuovo P, et al. Managing Locally Advanced Adenoid Cystic Carcinoma of the Head and Neck During the COVID-19 Pandemic Crisis: Is This the Right Time for Particle Therapy? *Oral Oncol* (2020) 106:104803. doi: 10.1016/j.oraloncology.2020.104803

31. Orlandi E, Palazzi M, Pignoli E, Fallai C, Giostra A, Olmi P. Radiobiological Basis and Clinical Results of the Simultaneous Integrated Boost (SIB) in Intensity Modulated Radiotherapy (IMRT) for Head and Neck Cancer: A Review. *Crit Rev Oncology/Hematology* (2010) 73(2):111–25. doi: 10.1016/j.critrevonc.2009.03.003
32. Molinelli S, Magro G, Mairani A, Allajbej A, Mirandola A, Chalaszczyk A, et al. How LEM-Based RBE and Dose-Averaged LET Affected Clinical Outcomes of Sacral Chordoma Patients Treated With Carbon Ion Radiotherapy. *Radiotherapy oncology: J Eur Soc Ther Radiol Oncol* (2021) 163:209–14. doi: 10.1016/J.RADONC.2021.08.024
33. Chaikh A, Giraud JY, Perrin E, Bresciani JP, Balosso J. The Choice of Statistical Methods for Comparisons of Dosimetric Data in Radiotherapy. *Radiat Oncol* (2014) 9(1). doi: 10.1186/1748-717X-9-205
34. Bakst RL, Glastonbury CM, Parvathaneni U, Katabi N, Hu KS, Yom SS. Perineural Invasion and Perineural Tumor Spread in Head and Neck Cancer. *Int J Radiat Oncol Biol Phys* (2019) 103(5):1109–24. doi: 10.1016/j.ijrobp.2018.12.009

Conflict of Interest: The authors declare that the research was conducted in the absence of any commercial or financial relationships that could be construed as a potential conflict of interest.

Publisher's Note: All claims expressed in this article are solely those of the authors and do not necessarily represent those of their affiliated organizations, or those of the publisher, the editors and the reviewers. Any product that may be evaluated in this article, or claim that may be made by its manufacturer, is not guaranteed or endorsed by the publisher.

frontiers in Oncology

ORIGINAL RESEARCH
published: 11 February 2022
doi: 10.3389/fonc.2021.808216

Two-Year Toxicity and Efficacy of Carbon Ion Radiotherapy in the Treatment of Localized Prostate Cancer: A Single-Centered Study

Ping Li[1,2,3], *Zhengshan Hong*[1,2,3], *Yongqiang Li*[2,3,4], *Shen Fu*[5,6] *and Qing Zhang*[1,2,3]*

[1] Department of Radiation Oncology, Shanghai Proton and Heavy Ion Center, Shanghai, China, [2] Shanghai Engineering Research Center of Proton and Heavy Ion Radiation Therapy, Shanghai, China, [3] Shanghai Key Laboratory of Radiation Oncology, Shanghai, China, [4] Department of Medical Physics, Shanghai Proton and Heavy Ion Center, Shanghai, China, [5] Key Laboratory of Nuclear Physics and Ion-Beam Application (MOE), Fudan University, Shanghai, China, [6] Department of Radiation Oncology, Shanghai Concord Cancer Hospital, Shanghai, China

OPEN ACCESS

Edited by:
Giuseppe Magro,
National Center of Oncological Hadrontherapy, Pavia, Italy

Reviewed by:
Hirokazu Makishima,
University of Tsukuba, Japan
Stefania Russo,
National Center of Oncological Hadrontherapy, Italy

***Correspondence:**
Qing Zhang
zhangqing_sphic@163.com

Specialty section:
This article was submitted to Radiation Oncology, a section of the journal Frontiers in Oncology

Received: 03 November 2021
Accepted: 27 December 2021
Published: 11 February 2022

Citation:
Li P, Hong Z, Li Y, Fu S and Zhang Q (2022) Two-Year Toxicity and Efficacy of Carbon Ion Radiotherapy in the Treatment of Localized Prostate Cancer: A Single-Centered Study. Front. Oncol. 11:808216. doi: 10.3389/fonc.2021.808216

Background: We aimed at determining the safety and feasibility of spot-scanning carbon ion radiotherapy (CIRT) for patients with localized prostate cancer.

Methods: We enrolled 118 patients with localized prostate cancer who underwent treatment with spot-scanning CIRT at the Shanghai Proton and Heavy Ion Center (SPHIC) from January 2016 to December 2020. The dose was gradually increased from relative biological effectiveness (RBE)-weighted dose (D_{RBE}) = 59.2–65.6 Gy in 16 fractions. The primary endpoint was the occurrence of acute and late toxicities, while the secondary endpoints were biochemical relapse-free survival (bRFS), distant metastasis-free survival (DMFS), prostate cancer-specific survival (PCSS), and overall survival (OS).

Results: The median follow-up time was 30.2 months (4.8–62.7 months). Acute grade 1 and 2 genitourinary (GU) toxicities were 15.3% and 18.6%, while acute grade 1 and 2 gastrointestinal (GI) toxicities were 2.5% and 0%, respectively. Late grade 1 and 2 GU toxicities were 4.2% and 1.7%, respectively. No late GI toxicity was observed. Moreover, there were no cases of severe acute or late toxicity (≥ grade 3). No significant association were observed between the factors and the acute GU toxicities, except for clinical target volume (CTV) ($p = 0.031$) on multivariate analysis. The 2-year bRFS, DMFS, PCSS, and OS were 100%, 100%, 100%, and 98.8%, respectively.

Conclusion: The 2-year outcomes were encouraging, providing additional and useful information on the feasibility and safety of spot-scanning CIRT for treating prostate cancer. Thus, we recommend long-term follow-up and prospective multicentered studies to reinforce the role of CIRT in the management of localized prostate cancer.

Keywords: prostate cancer, carbon ion radiotherapy, spot scanning, local effect model, toxicity

INTRODUCTION

Radiotherapy is a radical treatment option for localized prostate cancer. Randomized studies have demonstrated that dose-escalated radiotherapy improves cancer control (1, 2). However, increasing the dose leads to concerns about the toxicities in organs at risks (OARs), such as the rectum and bladder. Thus, if the dose to the prostate can be increased without increasing the dose to the OARs, the treatment outcome and quality of life of patients will be improved.

Carbon ion radiotherapy (CIRT) can minimize radiation dose to OARs while increasing the biologically effective dose delivery to the prostate (3, 4). According to the data from the Particle Therapy Co-operative Group (https://www.ptcog.ch/) on June 2021, approximately 40,000 patients have been treated with CIRT in 12 carbon ion centers worldwide. The higher relative biological effectiveness (RBE) and greater cytocidal effect of CIRT on cancer cells make it more beneficial over conventional radiotherapy (5). Additionally, carbon ion beams produce the Bragg peak through the release of enormous energy at the end of their range (6), maximizing the destructive energy delivered to the tumor site while minimizing unwanted damage to the surrounding normal tissues (7, 8). These properties make CIRT theoretically efficient in improving tumor control and reducing radiation-related toxicity.

The first CIRT clinical trial for prostate cancer was started in Chiba, Japan in 1995 (8). This phase I/II dose escalation study established the efficacy and safety of CIRT. The following studies in Japan further confirmed the effectiveness of the CIRT with 16-fraction regimens (4, 9). However, different models were used to predict the RBE at different institutes. Two major RBE models have been applied clinically in CIRT: the Japanese model [the original mixed beam model and the modified micro-dosimetric kinetic model (MKM)] and Helmholtzzentrum für Schwerionenforschung GmbH (GSI) model [local effect model (LEM)] (10, 11). Comparative studies showed that the LEM predicts a 5%–15% higher RBE in the spread-out Bragg peak of a carbon ion beam, relative to the MKM (12). Similarly, findings from previous studies revealed that the RBE-weighted doses using MKM for targets and OARs should be converted to LEM doses using conversion curves for prostate cancer treated with CIRT (13). This hampers the exchange of experience between different CIRT facilities by the use of disparate RBE models. Thus, assessing the dose needed when using LEM model to achieve results similar to those reported by Japanese facilities will be of great value.

In 2014, the Shanghai Proton and Heavy Ion Center (SPHIC) started the first prostate cancer CIRT treatment in China. Till January 2021, more than 300 patients with prostate cancer have undergone particle therapy at our institute, including patients with localized prostate cancer, oligo-metastatic prostate cancer, prostate cancer with pelvic lymph node metastasis, and postoperative prostate cancer. To establish the optimal dose for CIRT in LEM model, dose-escalated clinical trials of CIRT for patients with localized prostate cancer began in January 2016 at our center (NCT02739659 and NCT04724577). The purpose of this study was to assess the 2-year toxicity, biochemical relapse-free survival (bRFS), distant metastasis-free survival (DMFS), prostate cancer-specific survival (PCSS), and overall survival (OS) of the 118 patients treated with CIRT in 16 fractions.

PATIENTS AND METHODS

Study Design and Patient Eligibility

We consecutively enrolled 118 patients with localized prostate cancer treated with 16 fractions CIRT at SPHIC between January 2016 and December 2020 through a retrospective design. Patients were included if they meet the following: (1) histological diagnosis of prostate adenocarcinoma, (2) cT1N0M0 to cT4N0M0 according to the 7th American Joint Committee on Cancer (AJCC) classification, (3) Karnofsky Performance Score ≥70, (4) without any previous surgery or radiotherapy for prostate cancer, and (5) the presence of written informed consent. We excluded patients who did not meet all of the aforementioned criteria.

The study was approved by the Institutional Review Board of SPHIC (Approval Number 180620EXP-02). Eligible patients gave their written informed consent for CIRT and for future anonymous use. All patients were treated by spot-scanning CIRT combined with or without hormone therapy in our institute. According to the National Comprehensive Cancer Network (NCCN) guidelines, patients with low-risk prostate cancer had no hormone therapy, while intermediate-risk patients received 4–6 months of hormone therapy, and high/very high-risk patients received hormone therapy for 2–3 years. The hormone therapy regimens were combined androgen blockade.

Carbon Ion Radiotherapy

Methods for preparing the bladder and rectum, immobilizing the patients, and setting clinical target volume (CTV) and planning target volume (PTV) have been described (14). Briefly, the CTV routinely included the prostate and seminal vesicle (seminal vesicle was excluded for low-risk patients), and pelvic lymph nodes were excluded from this study. Two opposite lateral beams were used for each fraction treatment. CIRT was given once a day, five fractions per week. The treatment position was adjusted before each fraction with orthogonal X-ray scans as image guide. Since May 2020, the daily in-room computed tomography (CT) was applied to guide the CIRT. The prescription was performed in terms of RBE-weighted dose (D_{RBE}). RBE was calculated by the treatment planning system (Syngo), using the LEM model. The carbon ion was administered at a five-dose regimen of D_{RBE} = 59.2/60.8/62.4/64/65.6 Gy in 16 fractions. OARs required for all the patients were the rectum and the bladder. The dose constraints of the rectum are as follow: Dmax (the max dose) <105% prescription dose (PD), V_{60} [volume receiving ≥ 60 Gy < 3 cc], V_{55} [volume receiving ≥ 55 Gy < 7 cc, and V_{50} [volume receiving ≥ 50 Gy] < 10 cc, which were referred from our previous dose conversion study (13, 14). The dose constraints on the bladder were Dmax <105% PD and V_{60}

[volume receiving ≥ 60 Gy] < 10%, V_{55} [volume receiving ≥ 55 Gy] < 15%, and V_{30} [volume receiving ≥ 30 Gy] < 30%.

Follow-Up

To closely monitor the patients, the patients' follow-up was performed every week during treatment, and every 3 months until 3 years after CIRT, then sixth monthly until further notice. A rise in prostate-specific antigen (PSA) by at least 2 ng/ml above the nadir (the Phoenix definition) is considered as biochemical failure (15). For each patient, baseline parameters for genitourinary (GU) and gastrointestinal (GI) functions were assessed and acute, and late toxicities were scored by a physician using Common Terminology Criteria for Adverse Events v.4.03 and Radiation Therapy Oncology Group (RTOG) Classification (16). Acute toxicities are defined as side effects occurring within 3 months after the start of CIRT. Toxicities that occurred 3 months after the start of CIRT were considered late toxicities.

Statistics

The bRFS, DMFS, PCSS, and OS were evaluated using the Kaplan–Meier method. The bRFS, DMFS, PCSS, and OS were calculated from the start date of CIRT. The chi-square test was used to examine the difference in acute GU toxicities between the low-dose [D_{RBE} = 59.2–60.8 Gy] and high-dose [D_{RBE} = 62.4–65.6 Gy] groups. Logistic and Cox regression identified univariate and multivariate associations between toxicities and clinical/dosimetric characteristics. A two-sided $p < 0.05$ was considered statistically significant. All the analyses were performed using SPSS software (version 22.0; IBM Corp.).

RESULTS

Patients Characteristics

Table 1 shows the characteristics of the included patients. Their median age of the patients was 71 years old (range, 46–86 years). The median follow-up time was 30.2 months (4.8–62.7 months). According to the 7th AJCC classification, the number of patients with T1, T2, T3, and T4 was 5 (4.2%), 94 (79.7%), 17 (14.4%), and 2 (1.7%), respectively. The number of patients with Gleason score of 6, 7, and ≥8 was 32 (27.1%), 46 (39.0%), and 40 (33.9%), respectively. Before treatment, 45 patients had a PSA level <10 ng/ml, 42 had a PSA level ranging from 10 to 20 ng/ml, and 31 had a PSA level >20 ng/ml. According to the NCCN guideline, the number of patients at low-risk, intermediate-risk, and high/very-high risk patients was 9 (7.6%), 45 (38.1%), and 64 (54.2%), respectively. The number of patients irradiated with an RBE-weighted dose of 59.2, 60.8, 62.4, 64.0, and 65.6 Gy was 43 (36.4%), 10 (8.5%), 9 (7.6%), 25 (21.2%), and 31 (26.3%), respectively. All patients completed their spot-scanning CIRT.

Acute Toxicities

All patients were included in the analysis of acute and late toxicities. The acute toxicities are summarized in **Table 2**. The incidences of grades 1 and 2 acute GU toxicities were 15.3% and 18.6%, respectively. Moreover, eight (15.1%) and five (9.4%)

TABLE 1 | Patients' characteristics.

Characteristics	D_{RBE} = 59.2 Gy	D_{RBE} = 60.8 Gy	D_{RBE} = 62.4 Gy	D_{RBE} = 64.0 Gy	D_{RBE} = 65.6 Gy	Total
Patient number	43 (36.4%)	10 (8.5%)	9 (7.6%)	25 (21.2%)	31 (26.3%)	118(100%)
BED (α/β = 1.5 Gy)	205.2 Gy	214.8 Gy	224.6 Gy	237.4 Gy	244.9 Gy	NA
Age (year)						
Median (range)	69 (50–84)	73 (69–79)	68 (62–74)	72 (47–86)	73 (50–86)	71 (46–86)
T stage						
T1	4 (9.3%)	0 (0%)	0 (0%)	0 (0%)	1 (3.2%)	5 (4.2%)
T2	32 (74.4%)	8 (80.0%)	8 (88.9%)	22 (88.0%)	24 (77.4%)	94 (79.7%)
T3	5 (11.6%)	2 (20.0%)	1 (11.1%)	3 (12.0%)	6 (19.4%)	17 (14.4%)
T4	2 (4.7%)	0 (0%)	0 (0%)	0 (0%)	0 (0%)	2 (1.7%)
Initial PSA (ng/ml)						
<10	13 (30.2%)	5 (50.0%)	4 (44.4%)	10 (40.0%)	13 (41.9%)	45 (38.1%)
≥10 and ≤20	16 (37.2%)	2 (20.0%)	2 (22.2%)	11 (44.0%)	11 (35.5%)	42 (35.6%)
>20	14 (32.6%)	3 (30.0%)	3 (33.3%)	4 (16.0%)	7 (22.6%)	31 (26.3%)
Gleason Score						
6	13 (30.2%)	3 (30.0%)	2 (22.2%)	4 (16.0%)	10 (29.1%)	32 (27.1%)
7	19 (44.2%)	3 (30.0%)	4 (44.4%)	8 (32.0%)	12 (40.0%)	46 (39.0%)
≥8	11 (25.6%)	4 (40.0%)	3 (33.3%)	13 (52.0%)	9 (30.9%)	40 (33.9%)
Risk (NCCN)						
Low	4 (9.3%)	0 (0%)	1 (11.1%)	1 (4.0%)	3 (9.7%)	9 (7.6%)
Intermediate	14 (32.6%)	4 (40.0%)	3 (33.3%)	10 (40.0%)	14 (45.2%)	45 (38.1%)
High/Very High	25 (58.1%)	6 (60.0%)	5 (55.6%)	14 (56.0%)	14 (45.2%)	64 (54.2%)
Complications						
Diabetes mellitus	7 (16.3%)	0 (0%)	1 (11.1%)	7 (28.0%)	4 (12.9%)	19 (16.1%)
Internal use of anticoagulanti	6 (14.0%)	0 (0%)	0 (0%)	3 (12.0%)	4 (12.9%)	13 (11.0%)
TURP	4 (9.3%)	1 (10%)	0 (0%)	2 (8.0%)	3 (9.7%)	10 (8.5%)

BED, biological equivalent dose; RBE, relative biological effectiveness; D_{RBE}, RBE weighted dose; PSA, prostate-specific antigen; NCCN, National Comprehensive Cancer Network; TURP, transurethral resection of the prostate; Na, not applicable.

patients developed grade 1 and 2 acute GU toxicities in the low-dose group, respectively, while 10 (15.4%) and 17 (26.2%) patients developed grade 1 and 2 acute GU toxicities in the high-dose group, respectively. The incidence of grade 2 acute GU toxicities of the high-dose group was higher than the low-dose group, although not significantly (p = 0.059). There were no significant differences in the frequency of acute GU toxicities, including hematuria, urinary frequency, urgency, retention, and urinary tract pain between the two groups (**Table 2**). CTV volume, bladder V60, V61, V62, and V63 were associated with ≥ grade 1 acute GU toxicities on univariate analysis, but only CTV volume was associated with ≥ grade 1 acute GU toxicities on multivariate analysis (**Table 3**).

Three (2.5%) patients developed grade 1 acute GI toxicities: one patient in the low-dose group and two patients in the high-dose group ($p = 0.683$). There were no significant differences in the frequency of acute GI toxicities manifested by symptoms, such as hematochezia and diarrhea. No patients demonstrated grade 2 or worse acute GI toxicity.

Late Toxicities

Grade 1 late GU toxicities did not differ significantly between the low-dose group [2 (3.2%) of 62 patients] and the high-dose group [2 (3.6%) of 56 patients] ($p = 0.158$). Five patients developed grade 1 late GU toxicities; three patients presented with urinary frequency, and two patients presented with microscopic hematuria. Moreover, two patients developed grade 2 late GU toxicity (gross hematuria). No grade ≥3 late GU toxicity was observed across the groups. Furthermore, no patient suffered from late GI toxicity within the follow-up period (**Table 4**).

Efficacy

The median follow-up time was 30.2 months (4.8–62.7 months). At the end of follow-up, five patients developed biochemical relapse, two patients received re-biopsy, but there was no evidence of tumor cells, and the PSA were stable without any treatment, such as hormone therapy. One patient received hormone therapy immediately after the diagnosis of PSA

TABLE 2 | Acute toxicity between low-dose and high-dose groups.

Total dose	D_{RBE} = 59.2–60.8 Gy (n = 53)				D_{RBE} = 62.4–65.6 Gy (n = 65)				*P* value
Toxicity (grade)	**0**	**1**	**2**	**≥ 3**	**0**	**1**	**2**	**≥ 3**	
GU									
Max toxicity	40 (75.5%)	8 (15.1%)	5 (9.4%)	0 (0%)	38 (58.5%)	10 (15.4%)	17 (26.2%)	0 (0%)	0.059
Urinary frequency	43 (81.1%)	5 (9.4%)	5 (9.4%)	0 (0%)	41 (63.1%)	9 (13.8%)	15 (23.1%)	0 (0%)	0.081
Urinary urgency	47 (88.7%)	3 (5.7%)	3 (5.7%)	0 (0%)	57 (87.7%)	2 (3.1%)	6 (9.2%)	0 (0%)	0.622
Urinary tract pain	52 (98.1%)	1 (1.9%)	0 (0%)	0 (0%)	62 (95.4%)	1 (1.5%)	2 (3.1%)	0 (0%)	0.433
Hematuria	51 (96.2%)	2 (3.8%)	0 (0%)	0 (0%)	61 (93.8%)	3 (4.6%)	1 (1.5%)	0 (0%)	0.644
Urinary retention	52 (98.1%)	0 (0%)	1 (1.9%)	0 (0%)	60 (92.3%)	3 (4.6%)	2 (3.1%)	0 (0%)	0.258
GI									
Max toxicity	52 (98.1%)	1 (1.9%)	0 (0%)	0 (0%)	63 (96.4%)	2 (3.6%)	0 (0%)	0 (0%)	0.683
Hematochezia	52 (98.1%)	1 (1.9%)	0 (0%)	0 (0%)	64 (98.2%)	1 (1.8%)	0 (0%)	0 (0%)	0.884
Diarrhea	53 (100%)	0 (0%)	0 (0%)	0 (0%)	64 (98.2%)	1 (1.8%)	0 (0%)	0 (0%)	0.364

GU, genitourinary; GI, gastrointestinal.

TABLE 3 | Univariate and multivariate clinical and DVH associations with acute GU toxicities (≥ grade 1).

Variable	Univariate Cox regression		Multivariate Cox regression	
	OR (95% CI)	***p*-value**	**OR (95% CI)**	***p*-value**
Age	1.001 (0.956–1.047)	0.976	1.003 (0.952–1.056)	0.925
Diabetes mellitus	1.531 (0.509–4.605)	0.448	3.703 (0.881–15.564)	0.074
Internal use of anticoagulant	0.559 (0.174–1.790)	0.327	0.370 (0.077–1.775)	0.214
TURP	2.171 (0.439–10.745)	0.342	1.871 (0.275–12.730)	0.522
CTV volume	1.016 (1.004–1.029)	0.011	1.016 (1.001–1.031)	0.031
Bladder volume	1.005 (0.997–1.013)	0.212	1.002 (0.992–1.013)	0.673
Bladder Dmax	1.105 (0.985–1.240)	0.090	1.038 (0.919–1.173)	0.549
Bladder V30	1.022 (0.983–1.063)	0.275	0.878 (0.463–1.664)	0.690
Bladder V40	1.030 (0.982–1.080)	0.224	1.031 (0.319–3.336)	0.959
Bladder V50	1.045 (0.982–1.111)	0.164	1.700 (0.489–5.912)	0.404
Bladder V55	1.059 (0.985–1.138)	0.122	0.503 (0.167–1.513)	0.221
Bladder V60	1.092 (1.004–1.187)	0.040	1.311 (0.443–3.881)	0.624
Bladder V61	1.106 (1.006–1.215)	0.038	1.193 (0.147–9.673)	0.869
Bladder V62	1.129 (1.009–1.264)	0.034	0.701 (0.135–3.647)	0.672
Bladder V63	1.178 (1.019–1.362)	0.027	1.432 (0.642–3.192)	0.380
Bladder V65	1.227 (0.908–1.658)	0.182	0.762 (0.442–1.313)	0.328

DVH, dose–volume histograms; GU, genitourinary.

TABLE 4 | Late toxicities between the low- and high-dose groups.

Dose regimens	Number of patients	Number of patients (%) with GU toxicity grade				p-value	Number of patients (%) with GI toxicity grade				p-value
		0	1	2	≥3		0	1	2	≥3	
D_{RBE} = 59.2–60.8Gy	53	52 (98.1%)	1 (1.9%)	0 (0%)	0 (0%)	0.158	53 (100%)	0 (0%)	0 (0%)	0 (0%)	NA
D_{RBE} = 62.4–65.6Gy	65	59 (90.8%)	4 (6.2%)	2 (3.1%)	0 (0%)		65 (100%)	0 (0%)	0 (0%)	0 (0%)	
Total	118	111 (94.1%)	5 (4.2%)	2 (1.7%)	0 (0%)		118 (100%)	0 (0%)	0 (0%)	0 (0%)	

GU, genitourinary; GI, gastrointestinal, NA, not applicable.

failure. Two patients who were classified as high- and very-high risk groups experienced bone metastases at 27.4 and 32.1 months after CIRT, respectively. A 72-year-old patient died at 20.6 months after CIRT due to cerebrovascular accident. No patient died of prostate cancer throughout the observation period. The 2-year bRFS, DMFS, PCSS, and OS was 100%, 100%, 100%, and 98.8%, respectively (**Figure 1**). The 2-year bRFS in low-, intermediate-, and high-/very-high risk groups was 100%, 100%, and 100%, respectively (p = 0.782) (**Figure 2**).

DISCUSSION

The improvement in biochemical relapse-free and OS of patients with prostate cancer was found to be dose dependent (17, 18). Several studies have shown the great potential of CIRT in the management of prostate cancer (3, 4, 8, 9), most from Japanese institutes. However, the biological model used in Europe and our center (LEM model) were different from that used in the Japanese institutes (MKM model) (19). Previous studies reveal that the RBE-weighted doses at our center are too conservative compared with those in Japanese institutes (13). The clinical study also found that the 5-year local control (71%) of skull base chordoma treated with CIRT at Centro Nazionale di Adroterapia Oncologica was inferior to the results reported by Japanese centers (76%–92%) using the same prescription dose, and they found that 92% of the local recurrences were attributable to suboptimal target dose in regions close to the brainstem or optic pathways (12, 20, 21). These studies indicated that the prescription dose from Japanese experiences for prostate cancer could not be replicated. Until now, the optimal dose for CIRT with LEM model in localized prostate cancer is not clear yet.

The first dose escalation clinical trial of CIRT for prostate cancer occurred in Japan. The 5-year bRFS of the 57.6 Gy in a 16-fraction regimen was 88.5% (9). In a multi-institutional study, which collected and re-analyzed data from prospective clinical trials conducted in three institutions in Japan, the 5-year bRFS in low-risk, intermediate-risk, and high-risk patients was 92%, 89%, and 92%, respectively (4). At first, 63/66 Gy in 23/24 fractions

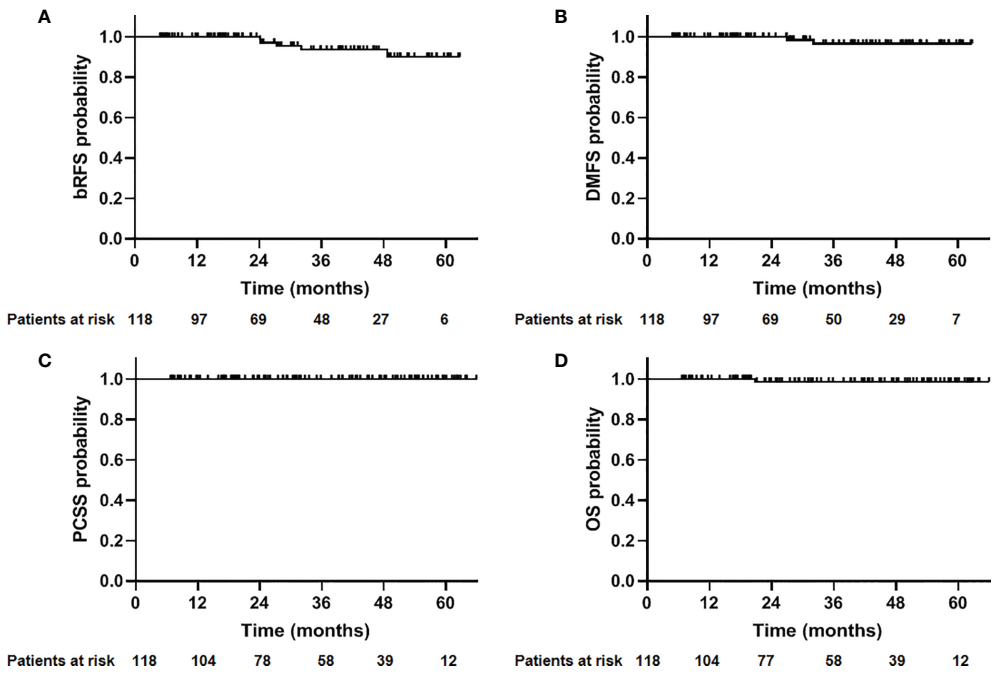

FIGURE 1 | Outcome of 118 patients with prostate cancer treated with CIRT. **(A)** Biochemical relapse-free survival (bRFS); **(B)** distant metastasis free survival (DMFS); **(C)** prostate cancer-specific survival (PCSS); **(D)** overall survival (OS).

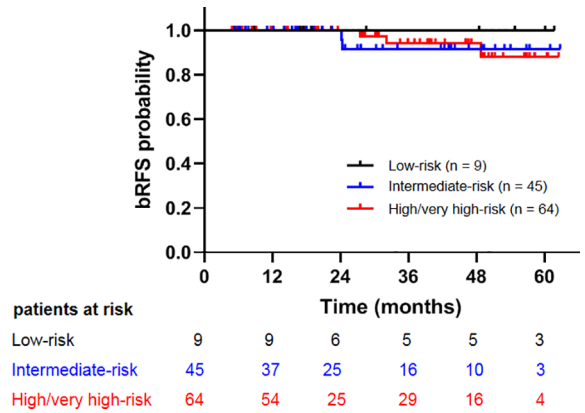

FIGURE 2 | Comparison of biochemical relapse free survival among patients with low-, intermediate-, and high-/very high-risk prostate cancer.

was applied to treat patients with prostate cancer in our institute. The dose regimens were well tolerated and without any ≥ grade 2 late GI and GU toxicities. In this study, we retrospectively evaluated the safety and feasibility of CIRT for patients with localized prostate cancer. By this, 118 patients treated by CIRT in our institute achieved satisfactory short-term biochemical control without developing serious adverse events.

In this study, 118 patients were treated with D_{RBE} = 59.2 Gy (n = 43), 60.8 Gy (n = 10), 62.4 Gy (n = 9), 64.0 Gy (n = 25), and 65.6 Gy (n = 31). Five patients developed biochemical relapse, all of which received 59.2Gy group. No patient in the ≥60.8 Gy groups developed biochemical relapse within the follow-up period. The comparative analysis for efficacy between low- and high-dose groups was not performed due to the relatively short follow-up time. The prescribed dose was D_{RBE} = 57.6 Gy in 16 fractions in the National Institute of Radiobiological Science, Japan. Our previous study showed that 3.60 Gy per fraction for 16 fractions in MKM could be converted to 4.21 Gy per fraction for 16 fractions in LEM (13). Hence, further evaluation of the efficacy of the fixed dose at 65.6 Gy in 16 fractions regimen in LEM model system is highly recommended.

In terms of acute toxicity, according to results from the RTOG 0126 clinical trial (22), in 751 patients treated with 79.2 Gy photon therapy, the incidence of grade 1–3 acute GU toxicity was 19%, 16%, and 1%, respectively, and the incidence of grade 1–and 3 acute GI toxicity was 7%, 7%, and <1%, respectively. Moreover, 91 patients were treated with D_{RBE} = 66 Gy in 20 fractions carbon ion or proton in the Ion Prostate Irradiation (IPI) study from Heidelberg Ion-Beam Therapy Center (HIT) (23), and the incidence of grade 1–3 acute GU toxicity was 34.1%, 17.6%, and 0%, respectively, and that of grade 1–3 acute GI toxicity was 60.4%, 7.7%, and 2.2%, respectively. In our study, patients in the high-dose group seem to experience higher rates of acute grade 2 GU toxicities than those in the low-dose group (26.2% vs. 9.4%). No ≥ grade 3 GU toxicity was observed in both groups. The incidence of acute GU toxicities in our study is consistent with that found in 79.2 Gy arms in the RTOG 0126 study but lower than that of the IPI study. The incidence of acute GI toxicity in our study is rare and significantly lower than that of the IPI study. A possible explanation for these differences may lie in that half of the patients received proton therapy in IPI, while daily in-room CT was applied to every patient with prostate cancer in our center since 2020. The association between the prognostic factors and the acute toxicities has been investigated in this study. We found that CTV volume was associated with acute GU toxicities. Previous studies also revealed that patients with large prostate volumes have a great risk of irritative/obstructive symptoms (particularly dysuria) in the acute radiotherapy phase (24). This may be due to the fact that a greater bladder volume was irradiated and lower urinary bother score before CIRT for patient with large prostate was observed. Therefore, for patients with large prostate in our center, neoadjuvant hormone therapy is often recommended to reduce prostate volume.

Late toxicities tend to be more problematic than acute toxicities in radiotherapy for prostate cancer. The incidence rates of late grade 2 and 3 GU toxicities after radiotherapy were 11% and 3%, respectively, in the RTOG 0126 trial (79.2Gy arm) (22). According to the results of a multi-institutional study from the Japan Carbon Ion Radiation Oncology Study Group (J-CROS), which analyzed 2,157 patients treated with CIRT, the incidence rates of late grade 2 and 3 GU toxicities were 4.2% and 0%, respectively (4). In this study, the incidence rates of late grade 2 and 3 GU toxicities were 1.7% and 0%, respectively. The incidence rates of late grade 2 and 3 GI toxicities were 16% and 5%, respectively, in the RTOG 0126 trial (79.2 Gy arm). The incidence rates of late grade 2 and 3 GU toxicities were 0.5% and 0%, respectively, in the J-CROS trial, which were more favorable than photon therapy. In our study, no patient suffered from GI toxicity within the follow-up period, probably due to the short follow-up time. Ishikawa's study showed that 81% of late toxicities occurred within 2 years after CIRT. The median follow-up time of patients in the low- and high-dose groups was 49 and 17 months, respectively (25). Therefore, toxicities were evaluated for a sufficient period in the low-dose group but not in the high-dose group.

This study had several limitations. First, the results were retrospectively analyzed from a single institution. A phase II study with a fixed dose of D_{RBE} = 65.5 Gy in 16 fractions is ongoing at our center. However, multicenter prospective studies are warranted to validate the safety and efficacy of carbon ion with the LEM model. Second, with 30.2 months follow-up, we could only assess acute and early late toxicities but not the long-term outcomes. Third, the sample size was small. Hence, the recruitment of more patients and a longer follow-up period are highly recommended.

CONCLUSIONS

In conclusion, the short-term results of spot-scanning carbon ion therapy for localized prostate cancer were encouraging. Our results provide additional and useful information on the feasibility and

safety of CIRT with LEM model for patients with localized prostate cancer. Longer follow-up periods and multicenter prospective studies are warranted to confirm the biochemical control and survival benefit of this promising technique.

DATA AVAILABILITY STATEMENT

The raw data supporting the conclusions of this article will be made available by the authors, without undue reservation.

ETHICS STATEMENT

The studies involving human participants were reviewed and approved by Shanghai Proton and Heavy Ion Center Institutional Reviewer Board. The patients/participants provided their written informed consent to participate in this study.

AUTHOR CONTRIBUTIONS

PL, SF, and QZ conceived and designed the study. PL contributed data analysis and reagents. YL performed the physical data analysis. PL and ZH participated in patient treatment and follow-up. PL wrote the manuscript. SF and QZ reviewed the manuscript and contributed to the final version of the manuscript. All authors contributed to the article and approved the submitted version.

FUNDING

Funding for this study was provided by the National Natural Science Foundation of China (81773225), Shanghai Municipal Health Commission (No. 201940121), and Pudong New Area Science and Technology Development Foundation (No. PKJ2020-Y52).

REFERENCES

1. Dearnaley DP, Jovic G, Syndikus I, Vincent K, Cowan RA, Graham JD, et al. Escalated-Dose Versus Control-Dose Conformal Radiotherapy for Prostate Cancer: Long-Term Results From the MRC RT01 Randomised Controlled Trial. *Lancet Oncol* (2014) 15:464–73. doi: 10.1016/S1470-2045(14)70040-3
2. Heemsbergen WD, Al-Mamgani A, Slot A, Dielwart MF, Lebesque JV. Long-Term Results of the Dutch Randomized Prostate Cancer Trial: Impact of Dose-Escalation on Local, Biochemical, Clinical Failure, and Survival. *Radiother Oncol* (2014) 110:104–9. doi: 10.1016/j.radonc.2013.09.026
3. Takakusagi Y, Katoh H, Kano K, Anno W, Tsuchida K, Mizoguchi N, et al. Preliminary Result of Carbon-Ion Radiotherapy Using the Spot Scanning Method for Prostate Cancer. *Radiat Oncol* (2020) 15(1):127. doi: 10.1186/s13014-020-01575-7
4. Nomiya T, Tsuji H, Kawamura H, Ohno T, Toyama S, Shioyama Y, et al. A Multi-Institutional Analysis of Prospective Studies of Carbon Ion Radiotherapy for Prostate Cancer: A Report From the Japan Carbon Ion Radiation Oncology Study Group (J-CROS). *Radiother Oncol* (2016) 121(2):288–93. doi: 10.1016/j.radonc.2016.10.009
5. Tinganelli W, Durante M. Carbon Ion Radiobiology. *Cancers (Basel)* (2020) 12(10):3022. doi: 10.3390/cancers12103022
6. Shioyama Y, Tsuji H, Suefuji H, Sinoto M, Matsunobu A, Toyama S, et al. Particle Radiotherapy for Prostate Cancer. *Int J Urol* (2015) 22(1):33–9. doi: 10.1111/iju.12640
7. Schulz-Ertner D. Tsujii H. Particle Radiation Therapy Using Proton and Heavier Ion Beams. *J Clin Oncol* (2007) 25(8):953–64. doi: 10.1200/JCO.2006.09.7816
8. Akakura K, Tsujii H, Morita S, Tsuji H, Yagishita T, Isaka S, et al. Phase I/II Clinical Trials of Carbon Ion Therapy for Prostate Cancer. *Prostate* (2004) 58(3):252–8. doi: 10.1002/pros.10328
9. Ishikawa H, Tsuji H, Kamada T, Yanagi T, Mizoe J, Kanai T, et al. Carbon Ion Radiation Therapy for Prostate Cancer: Results of a Prospective Phase II Study. *Radiother Oncol* (2006) 81(1):57–64. doi: 10.1016/j.ijrobp.2012.01.072
10. Fossati P, Molinelli S, Matsufuji N, Ciocca M, Mirandola A, Mairani A, et al. Dose Prescription in Carbon Ion Radiotherapy: A Planning Study to Compare NIRS and LEM Approaches With a Clinically-Oriented Strategy. *Phys Med Biol* (2012) 57(22):7543–54. doi: 10.1088/0031-9155/57/22/7543
11. Fossati P, Matsufuji N, Kamada T, Karger CP. Radiobiological Issues in Prospective Carbon Ion Therapy Trials. *Med Phys* (2018) 45(11):e1096–110. doi: 10.1002/mp.12506
12. Koto M, Ikawa H, Kaneko T, Hagiwara Y, Hayashi K, Tsuji H. Long-Term Outcomes of Skull Base Chordoma Treated With High-Dose Carbon-Ion Radiotherapy. *Head Neck* (2020) 42(9):2607–13. doi: 10.1002/hed.26307
13. Wang WW, Huang ZJ, Sheng YS, Zhao JF, Shahnazi K, Zhang Q, et al. RBE-Weighted Dose Conversions for Carbon Ionradiotherapy Between Microdosimetric Kinetic Model and Local Effect Model for the Targets and Organs at Risk in Prostate Carcinoma. *Radiother Oncol* (2020) 144:30–6. doi: 10.1016/j.radonc.2019.10.005
14. Li YQ, Li P, Hsi W, Hong ZS, Fu S, Zhang Q. Normal Tissue Complication Probability (NTCP) Models of Acute Urinary Toxicity (AUT) Following Carbon Ion Radiotherapy (CIRT) for Prostate Cancer. *Radiother Oncol* (2021) 156:69–79. doi: 10.1016/j.radonc.2020.12.009
15. Roach M, Hanks G, Thames HCJR, Schellhammer P, Shipley WU, Sokol GH, et al. Defining Biochemical Failure Following Radiotherapy With or Without Hormonal Therapy in Men With Clinically Localized Prostate Cancer: Recommendations of the RTOG-ASTRO Phoenix Consensus Conference. *Int J Radiat Oncol Biol Phys* (2006) 65(4):965–74. doi: 10.1016/j.ijrobp.2006.04.029
16. Cox JD, Stetz J, Pajak TF. Toxicity Criteria of the Radiation Therapy Oncology Group (RTOG) and the European Organization for Research and Treatment of Cancer (EORTC). *Int J Radiat Oncol Biol Phys* (1995) 31(5):1341–6. doi: 10.1016/0360-3016(95)00060-C
17. Kuban DA, Tucker SL, Dong L, Starkschall G, Huang EH, Cheung MR, et al. Long-Term Results of the M. D. Anderson Randomized Dose-Escalation Trial for Prostate Cancer. *Int J Radiat Oncol Biol Phys* (2008) 70(1):67–74. doi: 10.1016/j.ijrobp.2007.06.054
18. Kalbasi A, Li J, Berman A, Swisher-McClure S, Marc Smaldone M, Uzzo RG, et al. Dose-Escalated Irradiation and Overall Survival in Men With Nonmetastatic Prostate Cancer. *JAMA Oncol* (2015) 1(7):897–906. doi: 10.1001/jamaoncol.2015.2316
19. Molinelli S, Magro G, Mairani A, Matsufuji N, Kanematsu N, Inaniwa T, et al. Dose Prescription in Carbon Ion Radiotherapy: How to Compare Two Different RBE-Weighted Dose Calculation Systems. *Radiother Oncol* (2016) 120(2):307–12. doi: 10.1016/j.radonc.2016.05.031
20. Iannalfi A, D'Ippolito E, Riva G, Molinelli S, Gandini S, Viselner G, et al. Proton and Carbon Ions Radiotherapy in Skull Base Chordomas: A Prospective Study Based on a Dual Particle and a Patient-Customized Treatment Strategy. *Neuro Oncol* (2020) 22(9):1348–58. doi: 10.1093/neuonc/noaa067
21. Takagi M, Demizu Y, Nagano F, Terashima K, Fujii O, Jin D, et al. Treatment Outcomes of Proton or Carbon Ion Therapy for Skull Base Chordoma: A Retrospective Study. *Radiat Oncol* (2018) 13(1):232. doi: 10.1186/s13014-018-1173-0

22. Michalski JM, Moughan J, Purdy J, Bosch W, Bruner DW, Bahary JP, et al. Effect of Standard vs Dose-Escalated Radiation Therapy for Patients With Intermediate-Risk Prostate Cancer. *JAMA Oncol* (2018) 4(6):e180039. doi: 10.1001/jamaoncol.2018.0039
23. Habl G, Uhl M, Katayama S, Kessel KA, Hatiboglu G, Hadaschik B, et al. Acute Toxicity and Quality of Life in Patients With Prostate Cancer Treated With Protons or Carbon Ions in a Prospective Randomized Phase II Study–The IPI Trial. *Int J Radiat Oncol Biol Phys* (2016) 95(1):435–43. doi: 10.1016/j.ijrobp.2016.02.025
24. Pinkawa M, Fischedick K, Asadpour B, Gagel B, Piroth MD, Nussen S. Eble MJ Toxicity Profile With a Large Prostate Volume After External Beam Radiotherapy for Localized Prostate Cancer. *Int J Radiat Oncol Biol Phys* (2008) 70(1):83–9. doi: 10.1016/j.ijrobp.2007.05.051
25. Ishikawa H, Tsuji H, Kamada T, Hirasawa N, Yanagi T, Mizoe JE, et al. Risk Factors of Late Rectal Bleeding After Carbon Ion Therapy for Prostate Cancer. *Int J Radiat Oncol Biol Phys* (2006) 66(4):1084–91. doi: 10.1016/j.ijrobp.2006.06.056

Conflict of Interest: The authors declare that the research was conducted in the absence of any commercial or financial relationships that could be construed as a potential conflict of interest.

frontiers in Oncology

ORIGINAL RESEARCH
published: 25 February 2022
doi: 10.3389/fonc.2022.812961

Evaluation of the Response of HNSCC Cell Lines to γ-Rays and ^{12}C Ions: Can Radioresistant Tumors Be Identified and Selected for ^{12}C Ion Radiotherapy?

Lianghao Ding[1‡], Brock J. Sishc[1‡], Elizabeth Polsdofer[1‡], John S. Yordy[1†], Angelica Facoetti[2], Mario Ciocca[2], Debabrata Saha[1], Arnold Pompos[1], Anthony J. Davis[1] and Michael D. Story[1]*

[1] Univeristy of Texas Southwestern Medical Center, Department of Radiation Oncology, Dallas, TX, United States, [2] Medical Physics Unit & Research Department, Foundazione Centro Nazionale di Adroterapia Oncologica (CNAO), Pavia, Italy

Head and neck squamous cell carcinoma (HNSCC) is the sixth most common malignancy worldwide. Thirty percent of patients will experience locoregional recurrence for which median survival is less than 1 year. Factors contributing to treatment failure include inherent resistance to X-rays and chemotherapy, hypoxia, epithelial to mesenchymal transition, and immune suppression. The unique properties of ^{12}C radiotherapy including enhanced cell killing, a decreased oxygen enhancement ratio, generation of complex DNA damage, and the potential to overcome immune suppression make its application well suited to the treatment of HNSCC. We examined the ^{12}C radioresponse of five HNSCC cell lines, whose surviving fraction at 3.5 Gy ranged from average to resistant when compared with a larger panel of 38 cell lines to determine if ^{12}C irradiation can overcome X-ray radioresistance and to identify biomarkers predictive of ^{12}C radioresponse. Cells were irradiated with ^{12}C using a SOBP with an average LET of 80 keV/μm (CNAO: Pavia, Italy). RBE values varied depending upon endpoint used. A 37 gene signature was able to place cells in their respective radiosensitivity cohort with an accuracy of 86%. Radioresistant cells were characterized by an enrichment of genes associated with radioresistance and survival mechanisms including but not limited to G2/M Checkpoint MTORC1, HIF1α, and PI3K/AKT/MTOR signaling. These data were used in conjunction with an *in silico*-based modeling approach to evaluate tumor control probability after ^{12}C irradiation that compared clinically used treatment schedules with fixed RBE values vs. the RBEs determined for each cell line. Based on the above analysis, we present the framework of a strategy to utilize biological markers to predict which HNSCC patients would benefit the most from ^{12}C radiotherapy.

Keywords: carbon ion radiotherapy, head and neck squamous cell carcinoma, radioresistance, relative biological effectiveness, prediction of radioresponse

OPEN ACCESS

Edited by:
Stewart Mac Mein, German Cancer Research Center (DKFZ), Germany

Reviewed by:
Bouchra Tawk, Heidelberg University Hospital, Germany
Michael Orth, LMU Munich University Hospital, Germany
Jason Luke Parsons, University of Liverpool, United Kingdom

****Correspondence:***
Michael D. Story
Michael.Story@UTSouthwestern.edu

[†]Present address:
John S. Yordy, Valley Radiation Therapy Center, Palmer, AK, United States

[‡]These authors share first authorship

Specialty section:
This article was submitted to Radiation Oncology, a section of the journal Frontiers in Oncology

Received: *10 November 2021*
Accepted: *31 January 2022*
Published: *25 February 2022*

Citation:
Ding L, Sishc BJ, Polsdofer E, Yordy JS, Facoetti A, Ciocca M, Saha D, Pompos A, Davis AJ and Story MD (2022) Evaluation of the Response of HNSCC Cell Lines to γ-Rays and ^{12}C Ions: Can Radioresistant Tumors Be Identified and Selected for ^{12}C Ion Radiotherapy? Front. Oncol. 12:812961. doi: 10.3389/fonc.2022.812961

INTRODUCTION

The potential therapeutic advantage of particle radiotherapy was recognized in the 1940s and was based upon the physical properties of the energy deposition patterns of said particles. Since that time, particle therapy has continuously developed predominantly based upon advances in engineering, imaging, and physics. The first dedicated clinical heavy ion therapy center was opened in 1994, and this facility focused on the use of accelerated carbon ions because of the physical and biological advantages over photons and protons including steeper lateral dose penumbra at greater depths in the body, a higher LET which results in a higher relative biological effectiveness (RBE) and took into account the experience gained at the Lawrence Berkeley Laboratory where the initial results for the use of heavy charged particles as a cancer therapy took place (1–4).

Since then, carbon ion radiotherapy (CIRT) has been used against intracranial cancers, head and neck cancers, primary and metastatic lung cancers, gastrointestinal tumors, sarcomas, prostate cancer, breast cancer, and pediatric cancers at what has grown to become 12 carbon centers across the globe, although none currently exist in the USA. CIRT has been shown to exert a strong antitumor effect in tumors resistant to conventional photon therapy; however, some tumor sites have been less amenable to therapy over concerns for the response of adjacent normal tissues. Whereas, the efficacy of CIRT has been shown for nonsquamous tumors like mucosal melanomas (5, 6), adenocarcinomas and sarcoma (7, 8), and adenoid cystic carcinomas (9, 10); in tumors that are considered radioresistant or chemoresistant, the use of CIRT for squamous cell carcinomas, the most common type of head and neck cancer, has been limited (11–13).

Given the technologic advances in recent years for proton and heavy ion radiotherapy, the potential benefit from the increased conformity of charged particles and higher LETs seen with ^{12}C ions against head and neck squamous cell carcinoma (HNSCC) of the oral cavity, larynx, pharynx, and nasopharynx in a fashion that is beneficial for sparing organs at risk such as tissues of the oral cavity, the spinal cord, or bony structures like the mandible and vertebrae has been considered and acted upon. For example, the multi-institutional *in silico* trial designated ROCOCO describes the benefits of particle therapy and in particular CIRT, in a trial of reirradiation for recurrent HNSCC (14). In that study, comparing reductions in mean dose to organs at risk, particle therapy—using protons and carbon ions, both achieved reductions in complications with a dosimetric benefit for carbon ions over protons which they attributed to conformity, that is, dose to the normal tissue as suggested by other studies (15–17).

CIRT facilities have a highly limited capacity to treat the millions of individuals who are diagnosed with cancer each year, and even with new facilities coming online, it remains a limited medical resource where patients should be stratified in order to optimize the use and efficiency of CIRT. Tumors of the head and neck should be ideal for the use of CIRT because head and neck regions have functionally important anatomic sites amenable to dose conformality and the additional cell killing effects of high LET radiations, particularly for low LET-resistant (photon and proton) tumors. Furthermore, identification of patients as potentially radioresistant by omics or other analysis that requires tumor sampling, is less complicated in H&N cancers based upon ease of access to tumor tissue.

Intuitively, DNA repair-related biomarkers would be particularly useful for predicting radiotherapy and chemoradiotherapy outcomes for HNSCC. Ku80, a mediator of DSB repair, was established as the first candidate DNA repair biomarker to show potential predictive value for head and neck radiotherapy in a cohort of archival HNSCC specimens from irradiated patients (18). In this series, Ku80 was overexpressed in half of tumors, and its expression was independent of all clinical and genetic covariates examined. Ku80 overexpression was an independent predictor for both locoregional failure and mortality following radiotherapy ($p < 0.01$) conferring a 9-fold greater risk of mortality at 2 years. Furthermore, using a battery of HNSCC cell lines, tumor growth and metastatic potential were determined in an orthotopic model of oral tongue cancer, including how TP53 mutations influence tumor growth and metastasis (19) and how disruptive mutations in TP53 lead to treatment failure by inhibiting radiation-induced senescence (20). Besides the identification of Ku80 and TP53 as potential negative prognostic indicator in HNSCC, Eschrich et al., using the Radiosensitivity Index (RSI) in a retrospective study of HNSCC treated with radiochemotherapy identified a radiosensitive cohort of patients that saw improved locoregional control (21). However, as argued here, identifying tumors that are likely radioresistant would seem more appropriate for the selection of patients to be treated by CIRT.

Towards that goal of defining radioresistance for patient triage, 38 HNSCC cell lines were collected and interrogated for their γ-ray radioresponse *via* clonogenic survival. An approximately 4-fold range of radiosensitivity as measured by SF2 or SF3.5 was determined. At the molecular level, these 38 cell lines have been assayed for basal gene and miRNA expression as well as DNA methylation, and our future goal is to integrate gene expression, miRNA expression, and methylation patterns with cell survival to characterize radioresponse.

However, for this study, these 38 HNSCC cell lines were agnostically divided into 4 groups, radiosensitive, moderately radiosensitive, moderately radioresistant and radioresistant, based on SF3.5 values. A signature of 37 genes built from the basal gene expression of each cell line was then developed that could stratify these cell lines into their respective radiosensitivity cohorts with 86% accuracy. From these 38 cell lines, five were chosen to characterize the behavior of moderately radioresistant and radioresistant cell lines to ^{12}C ion exposures to determine the radioresponse to ^{12}C ions, calculate RBE values using different endpoints, and model tumor control probabilities for a series of dose and fraction combinations to expose the variability in tumor control probability when a fixed RBE is used as opposed to a personalized RBE within a radioresistant population of HNSCC tumor cell lines.

METHODS

HNSCC Cell Culture

HNSCC cell lines were cultured in Dulbecco's modified essential media (D-MEM) supplemented with 10% Fetal Plus brand fetal bovine serum (FBS, Atlas Biologicals, Fort Collins, CO, USA),

penicillin/streptomycin solution (Sigma Aldrich, St. Louis, MO, USA). All cell lines were authenticated by genotyping and validated as negative for mycoplasma contamination by the Molecular Diagnostics Core Services at the Dana Farber Cancer Center, Boston, MA. All cell culture was conducted in incubators at 37°C in ambient 5% CO_2. See **Table 1** for additional information such as the anatomical site from which the cell line was derived and other information.

HNSCC Tumor Gene Expression Microarray Dataset

An expression microarray dataset (GEO accession number GSE 67614) that was generated from 102 tumor samples collected from patients treated with a consistent protocol of surgery followed by radiotherapy based upon a prospective trial that evaluated pathologic risk features, total combined treatment duration, and postoperative radiation therapy (23) was used to evaluate the expression of genes and molecular pathways identified from the cell line gene expression data. The patient pool from which these tumors were isolated were 34% stage III and 54% stage IV, i.e., predominantly high risk, and were divided into cohorts representing those for whom their disease recurred locally/regionally (LR), had distant metastasis (DM), and who showed no evidence of disease (NED). HPV status was not determined directly; however, p16 positivity was seen in samples representing 11 patients and were split 6:5 in the recurrent setting vs. those designated as having no evidence of disease.

Photon Irradiations

Photon irradiation was conducted at the University of Texas Southwestern Medical Center using a J. L. Shepherd sealed horizontal ^{137}Cs-sourced irradiator or at the MD Anderson Cancer Center using the "NASAtron" ^{137}Cs irradiator. Dosimetry for these sealed source irradiators was validated on an annual basis. Briefly, for the J. L. Shepherd, irradiator cells in culture were placed on a 360° platform revolving at 13 RPM, irradiated, removed from the irradiator, and immediately returned to the incubator. For the

TABLE 1 | Characteristics of HNSCC cell lines.

Cell line	SF2	SF3.5	P.E.	Anatomical location
584A2	0.45	0.119	0.03	Larynx
CAL-27	0.459	0.248	0.07	Oral cavity
FADU	0.622	0.346	0.44	Hypopharynx
HN30	0.476	0.179	0.38	Pharynx
HN31	0.542	0.265	0.11	LN (HN30)
HN4	0.652	0.307	0.15	REC (larynx)
HN5	0.709	0.414	0.65	REC (oral cavity)
JHU011	0.447	0.19	0.1	REC (larynx)
JHU022	0.442	0.188	0.16	LN (larynx)
JHU029	0.482	0.196	0.25	Larynx
MDA1386LN	0.359	0.117	0.2	LN (MDA1386TU)
MDA1386TU	0.574	0.248	0.08	Hypopharynx
MDA686LN	0.617	0.319	0.02	LN (MDA686TU)
MDA686TU	0.624	0.339	0.08	Oropharynx
MDA886LN	0.342	0.131	0.03	LN (larynx)
OSC19	0.502	0.241	0.03	LN (oral cavity)
PCI13	0.522	0.31	0.03	Oral cavity
PCI-15A	0.342	0.108	0.08	Hypopharynx
PCI-15B	0.392	0.095	0.13	LN (PCI-15A)
PJ34	0.507	0.263	0.14	Oral cavity
SCC15	0.456	0.183	0.07	Oral cavity
SCC25	0.529	0.232	0.09	Oral cavity
SCC4	0.667	0.362	0.24	Oral cavity
SCC61	0.74	0.465	0.64	Oral cavity
SCC9	0.73	0.44	0.28	Oral cavity
Sqccy1	0.688	0.345	0.81	Oral cavity
TR146	0.554	0.256	0.09	REC (oral cavity)
Tul38	0.575	0.332	0.12	Oral cavity
UMSCC1	0.671	0.358	0.58	REC (oral cavity)
UMSCC11A	0.473	0.225	0.02	Larynx
UMSCC14B	0.449	0.152	0.35	REC (UMSCC14A)
UMSCC17A	0.232	0.056	0.14	Larynx
UMSCC17B	0.415	0.168	0.26	E) CT (UMSCC17A)
UMSCC22A	0.473	0.176	0.12	Hypopharynx
UMSCC22B	0.434	0.113	0.07	LN (UMSCC22A)
UMSCC25	0.656	0.372	0.47	LN (larynx)
UMSCC47[a]	0.259	0.075	0.09	Oral cavity
UMSCC4	0.63	0.342	0.2	Oropharynx

[a]*HVP positive. EXT, extension into adjacent tissue; REC, recurrence; LN, lymph node. Anatomical location taken from Zhao et al. (22).*

NASAtron irradiations, the source was vertically above the stage and there was no sample rotation. Both devices had dose rates of ~3.25 Gy/min.

^{12}C Ion Irradiations

All ^{12}C irradiations took place at the Centro Nazionale di Adroterapia Oncologica (CNAO) facility in Pavia, Italy. Cells were irradiated in T12.5 cm flasks while immersed in a water bath at 37°C using CNAO's clinical, therapeutic quality, pencil beam scanning ^{12}C-ion beam. A spread-out Bragg peak (SOBP) was created to assure a homogenous (± 2.5%) physical dose. The beam quality has been previously characterized (24) and adheres to the recommendations of a NCI special panel on particle beam characterization (25). The dimensions of the SOBP were 17 cm in width, 7 cm in height, and 2 cm in depth. Cells were centered in the SOBP within a leucite holder with cells set back-to-back such that the depth of the cells in the upstream flask was 80 mm water equivalent depth (WED) while the position of cells in the downstream flask was 84 mm of WED. LETs at the positions where the cells were aligned were 74.1 and 89.3 keV/μm, respectively. (No difference in biological response was seen based upon position.) The entrance LET was 16.4 keV/μm at a depth of 0.15 mm. The physical dose rate was typically 0.60 Gy/min.

Irradiation of Cells With a Carbon Ion SOBP

To ensure a consistent SOBP, cells were suspended in a circulating water phantom maintained at 37°C in sealed T-12.5 flasks filled to the neck with complete cell culture medium containing 2% FBS for a roughly 5-min pre-exposure. This configuration provided a complete liquid/plastic interface with no ion deflection due to the presence of air. Immediately after irradiation, 2% FBS-containing media was aspirated and replaced with 5 ml of complete media containing 10% FBS for incubation.

Clonogenic Cell Survival Assays

Cells undergoing log phase growth at roughly 70%–80% maximum cell culture density were trypsinized and then seeded into T-12.5 flasks at low density in complete growth medium 8 h prior to irradiation. Five minutes prior to irradiation with either γ-rays or carbon ions, cell culture flasks were filled to the neck with complete growth media containing 2% FBS. Cells were irradiated with doses of 1, 2, 4, 6, and 8 Gy of γ-rays, or 0.5, 1, 2, 4, and 6 Gy carbon ions. Following irradiation, growth medium containing 2% FBS was immediately aspirated and replaced with growth medium containing 10% FBS and dishes were allowed to incubate for ~10 population doublings based on cell-specific doubling times. The use of media with 2% FBS was simply to limit the overall volume of FBS that would be used if media containing 10% FBS was used to completely fill the T12.5 flasks for only a few minutes as was necessary at CNAO. (See above.) Using 2% FBs for such a limited time had no effect on cell growth or radioresponse.

Following incubation, cultures were rinsed with phosphate-buffered saline at a pH of 7.4 and fixed in a solution of 0.5% crystal violet and 10% methanol in water. After staining and drying, colonies were counted to determine the number of surviving cells following irradiation. Only colonies identified as having more than 50 cells per colony were scored as surviving, and the surviving fraction was determined by dividing the number of colonies by the product of the plating efficiency of the cell line multiplied by the number of cells seeded.

Survival Curve Fits

Survival curves were fitted based upon the Repairable Conditionally Repairable (RCR) Model as described in Equation 1 where d is the dose per fraction and a, b, and c are parameters determined using a curve fitting algorithm (26).

$$S(d) = e^{-ad} + bde^{-cd} \tag{1}$$

The γ-ray survival assays were performed at least twice for each cell line. If the coefficient of variation at 2 Gy was greater than 25%, they were repeated.

RBE Calculations

RBE values were calculated by comparing a radiosensitivity value from ^{137}Cs exposures (reference) to that same radiosensitivity value determined from ^{12}C exposures (test) as in **Equation 2**.

$$\text{RBE} = \frac{\text{Dose,reference}}{\text{Dose,test}} \tag{2}$$

Radiosensitivity parameters included:

Dose at 10% Survival

The dose at $SF_{10\%}$ was calculated using values generated with the RCR model as described in Equation 1.

$\bar{D}_{\text{parm}}$

$\bar{D}$ was calculated using the parameters of the RCR model as shown in Equation 3 (26).

$$\bar{D} = \frac{1}{a} + \frac{b}{c^2} \tag{3}$$

$\bar{D}_{\text{AUC}}$

Here, $\bar{D}$ is calculated using a trapezoidal method of the area under the curve (AUC) of the survival curve assay. The trapezoidal method is similar to a Reimann sum with the exception that the area is approximated using trapezoids as opposed to rectangles.

Limiting slope, D_0

The limiting slope, D_0, represents the linear portion of the RCR fit located at the distal end of the survival curve. D_0 was calculated by plotting the linear portion of the RCR line of best fit in MATLAB and using a linear to calculate the slope. The relationship between the slope of the linear portion and D_0 is given in Equation 4.

$$D_0 = \frac{-1}{\text{slope}} \tag{4}$$

Transcriptomic Analysis of HNSCC Cell Lines and Tissues

Labeling and Hybridization of Microarrays

The tumor data set was generated using Illumina Whole Genome HumanWG6 v2 arrays (GEO accession number GSE67614). The v3 Illumina Expression BeadChip was used to generate transcriptome profiles for the HNSCC cell lines. Each RNA sample with 0.5 μg of total RNA was amplified using the Illumina TotalPrep RNA amplification kit with biotin UTP (Enzo) labeling. The Illumina TotalPrep RNA amplification kit uses T7 oligo(dT) primer to generate single-stranded cDNA followed by a second-strand synthesis to generate double-stranded cDNA which is then column purified. *In vitro* transcription was done to synthesize biotin-labeled cRNA using T7 RNA polymerase. The cRNA was column purified and then checked for size and yield using the Bio-Rad Experion system. A total of 1.5 μg of cRNA was hybridized for each array using the standard Illumina protocols with streptavidin-Cy3 (Amersham, Amersham, UK) being used for detection. Slides were scanned on an Illumina Beadstation. Summarized expression values for each probe sets were generated using BeadStudio 3.1 (Illumina Inc., San Diego, CA, USA).

Preprocessing and Data Analysis for Gene Expression Profiling

The Illumina BeadChip expression data were background subtracted and quantile–quantile normalized across samples using the MBCB algorithm (27–29). Normalized gene expression values were used for all the subsequent analysis. The clustering analysis was performed by calculating Euclidean distances and clustered by average method using the hclust function from the R base package.

Classification of Radiosensitivity Groups in HNSCC Cell Lines Using Gene Expression Profiles

The gene expression values from 38 HNSCC cell lines were ranked by *p*-values generated from an *F*-test using the R limma package. The top-ranked genes corresponded to those that significantly changed in more than one of the radiosensitivity groups. Feature selection was performed by incrementally expanding the gene list from 4 to 500 from the top of the gene ranking. Classification models were built using a support vector machine (SVM) algorithm and the models were validated using a 10-fold repeated cross-validation.

Molecular Pathway Analysis

Functional pathway analysis was performed using the Gene Set Enrichment Analysis (GSEA 4.0.1) and Ingenuity Pathways Analysis (IPA) online software packages. Genes were ranked by *p*-values calculated from moderated *t*-test using the R limma package. The R limma analysis was performed to compare resistant cell lines vs. other cell lines or tumors where there was local recurrence (LR) vs. tumors where there was NED in patients treated with postoperative radiotherapy. A false-discovery rate (FDR) <0.4 was used as a cutoff for significantly enriched pathways and then interrogated against the GSEA Hallmark Pathways by Leading Edge Analysis for pathway enrichment using the metrics of *p*-value, FDR, and Normalized Enrichment Scores, whereas the IPA analysis focused on pathways were enriched based upon a Fisher's test with a *p*-value of 0.05 used as a cutoff. *Z*-scores for these pathways were then calculated with negative scores representing downregulation and positive scores representing upregulation of a given pathway.

Tumor Control Probability

The calculation of tumor control probability (TCP) is adapted from Antonovic et al. (30) and is summarized in **Equation 5** where N_{vox} is the number of voxels in an *in silico* tumor, N_i is the number of cells in voxel i, and $S_{i,j}$ *(d,L,pO2)* is the surviving fraction in voxel i at fraction j with dose d, oxygen partial pressure pO_2, and LET L.

$$\text{TCP} = \exp\left\{-\sum_{i=1}^{N_{\text{vox}}} N_i \prod_{j=1}^{n} S_{i,j}(d, L, pO_2)\right\} \tag{5}$$

A spherical tumor with a radius of 0.6203 cm (total volume 1 cm^3) was assumed to contain 10^8 cells distributed equally across the voxels in the *in silico* tumor simulation. The survival model utilized is the Repairable Conditionally Repairable (RCR) model which can account for changes in survival due to dose, LET, and partial oxygenation, as shown in **Equation 6**.

$$S(d, L, pO_2) = e^{-a(L)d/\tilde{O}(L,pO_2)} + b(L)d/\tilde{O}(L, pO_2)e^{-c(L)d/\tilde{O}(L,pO_2)} \tag{6}$$

As only the effect of dose on survival was accounted for **Equation 5** was simplified to **Equation 7** and **Equation 6** was simplified to **Equation 1**.

$$\text{TCP} = \exp\left\{-\sum_{i=1}^{N_{\text{vox}}} N_i \prod_{j=1}^{n} S_{i,j}(d)\right\} \tag{7}$$

To take into account the effect of dose per fraction and the number of fractions on survival, **Equation 1** was modified to **Equation 8** where d is the dose per fraction and n is the number of fractions. In each simulation, the dose per fraction, d, is kept constant and the number of fractions, n, is varied to generate a TCP curve.

$$S(d) = (e^{ad} + bde^{-cd})^n \tag{8}$$

RESULTS

A collection of 38 HNSCC cell lines was tested for radioresponse *via* clonogenic cell survival. Surviving fraction at 2 and 3.5 Gy (SF2, SF3.5, respectively) was determined based upon the fitted values for SF2 and SF3.5 from the survival curves. The cell lines were clustered into four groups based upon Euclidean distances using the SF3.5 values for each cell line as depicted in **Figure 1**. Those groups are described as sensitive (S), moderately sensitive (MS), moderately resistant (MR), and resistant (R). The cluster is

accompanied by the cell line identity and the respective SF3.5 values. SF3.5 was chosen based upon the conclusions of Johansen et al. (31), who suggest SF3.5 as more representative of radiosensitivity where a larger dose per fraction might be used as in stereotactic ablative radiotherapy (SAbR) or CIRT.

To determine whether there were differences in gene expression underlying these radiosensitivity cohorts, an SVM model was trained using the most significantly changed genes. As depicted in **Figure 2A**, a 37-gene panel could place the cell lines within their respective radiosensitivity cohort with an accuracy of 86%. **Figure 2B** represents the SF3.5 for the cell lines directly above in **Figure 2A** and reflects the trend in cell line radioresponse from radioresistant on the left to radiosensitive on the right. Furthermore, if cell line segregation was adjusted to identify the three radioresistant lines from all others, only 13 genes were required (**Figure 2C**). Genes segregating the R cohort include those associated with radio/chemoresistance (GAGE12C, GAGE2E, SPINK1), metabolic processes (PNLIPRP3), proliferation migration, invasion and metastasis (PARM1, CDH12, CYYR1, GAGE12C), and inhibition of apoptosis (SPINK1).

GSEA and IPA were used to examine differences in Hallmark Pathways (GSEA) and canonical pathway signaling (IPA). As shown in **Figure 3**, when the R cohort was compared with all others, cholesterol metabolism, G2M checkpoint, PI3K/AKT/MTOR, and MTORC1 pathways were enriched with Normalized Enrichment Scores being 1.5988, 1.7422, 1.258, and 1.363, respectively. IPA pathway analysis identified HIF1a and ERK/MAPK pathways as upregulated along with a number of other pathways that were up- or downregulated based upon *Z*-scores.

These same pathways were then interrogated in a gene expression dataset derived from 102 flash-frozen HNSCC tumor specimens from patients treated by postoperative radiotherapy (PORT) using a consistent treatment protocol (23, 32, 33). The gene expression data from 49 patients characterized as having NED and 35 patients characterized as having had LR were used. As shown in **Figure 3**, the GSEA

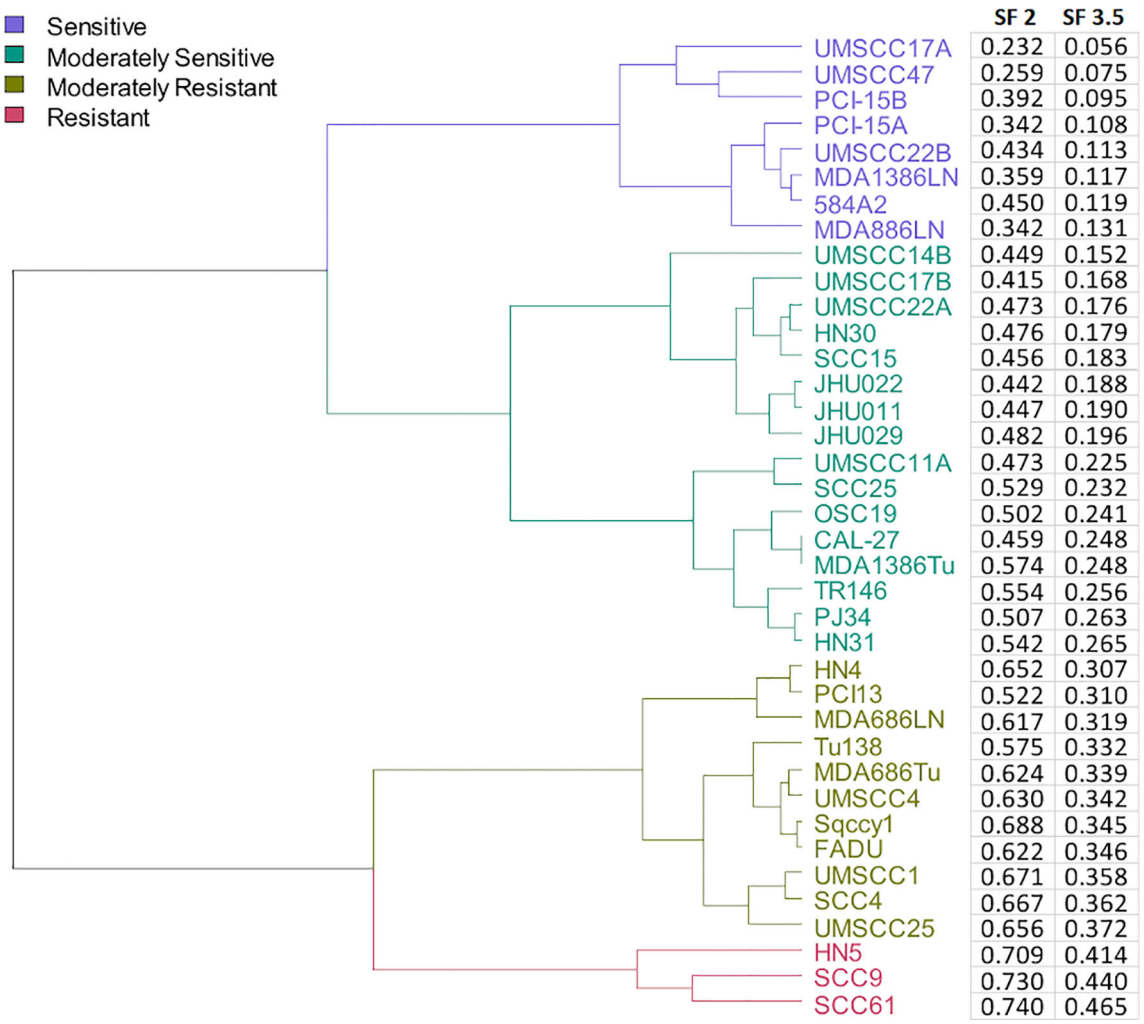

FIGURE 1 | Dendrogram of cell lines clustered by their radiosensitivity at 3.5 Gy and agnostically grouped into 4 clusters based upon radiosensitivity.

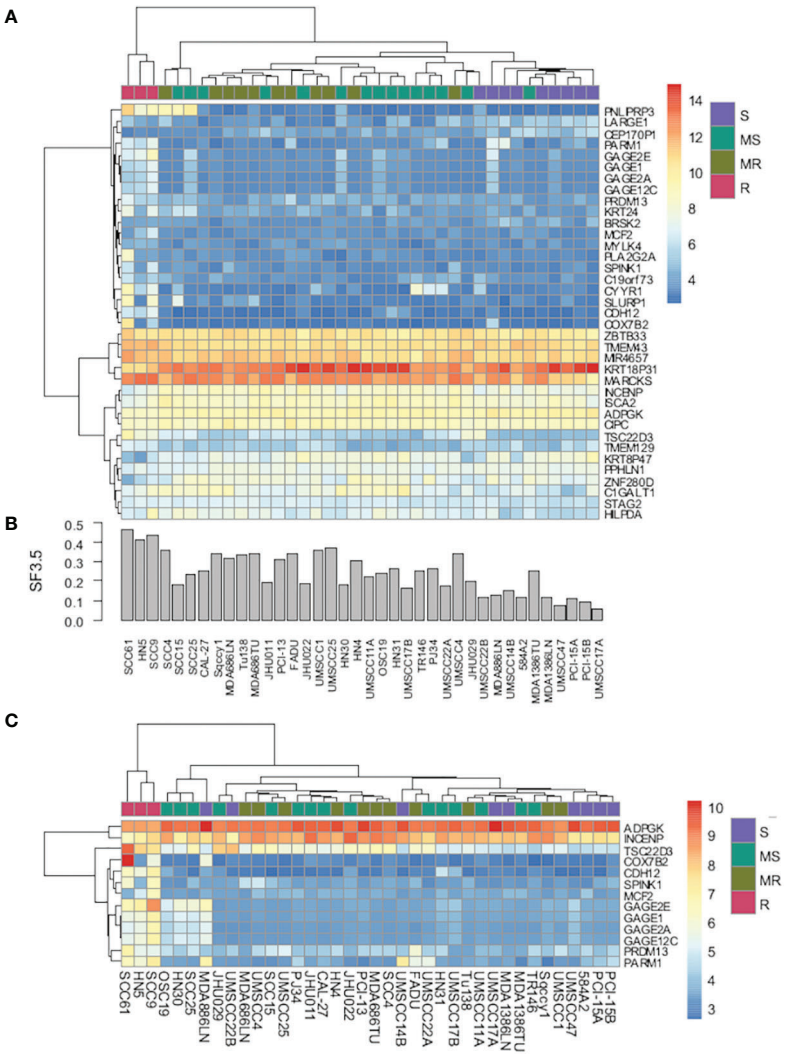

FIGURE 2 | **(A)** Heat map of gene expression using a 37-gene signature that segregates cell lines by radiosensitivity cluster. **(B)** Bar chart of radiosensitivity (SF3.5) for each cell line. **(C)** Heat map of gene expression using a 13-gene signature that segregates radioresistant cells from all other cell lines.

Hallmark Pathway cholesterol metabolism, G2M checkpoint, PI3K/AKT/MTOR, and MTORC1 were also enriched in the LR group when compared with those designated NED. Not surprisingly, their Normalized Enrichment Scores were somewhat lower than that seen in the cell lines.

Next, we examined the ^{12}C radioresponse of five HNSCC cell lines whose SF3.5 ranged from average to resistant when compared with the larger panel of 38 cell lines to determine if ^{12}C irradiation can overcome radioresistance. Radiation survival curves were generated using ^{137}Cs as a low LET radiation and ^{12}C ions were generated by the Carbon Therapy Center in Pavia, Italy (CNAO). The cell lines SqCC/Y1 and UMSCC1 were chosen to represent the range of SF3.5 in the MR group with an emphasis on the high end of response; HN31 represents the highest SF3.5 in the MS cohort; and HN5 and SCC9 represent the R cohort. Survival curves for these cell lines are seen in **Figure 4**. The RBE for ^{12}C ions was calculated at: 10% survival; by mean inactivation dose ($\bar{D}$) using the parameters of the repair-conditionally repairable curve fitting algorithm (26); $\bar{D}$ using a Reimann sum approach; and the limiting slopes (D_0) for each cell line. Those values are found in **Table 2**.

Using the survival data for both γ-rays and clinical ^{12}C ions from the five HNSCC cell lines, TCP curves were generated based upon Antonovic etal. (30). The calculation of TCP differs slightly from the study of Antonovic et al. (30) in that the tumor model created was fully oxygenated and the LET is fixed. Fractionation schedules (IMRT, ^{12}C) were based upon schedules used in recurrent H&N cancers treated at the Shanghai and Heidelberg Heavy Ion radiotherapy facilities (34, 35) where we chose an RBE value of 3, which is in line with that used clinically, as well as the RBE values determined for each cell line. These TCP curves are depicted in **Figure 5**.

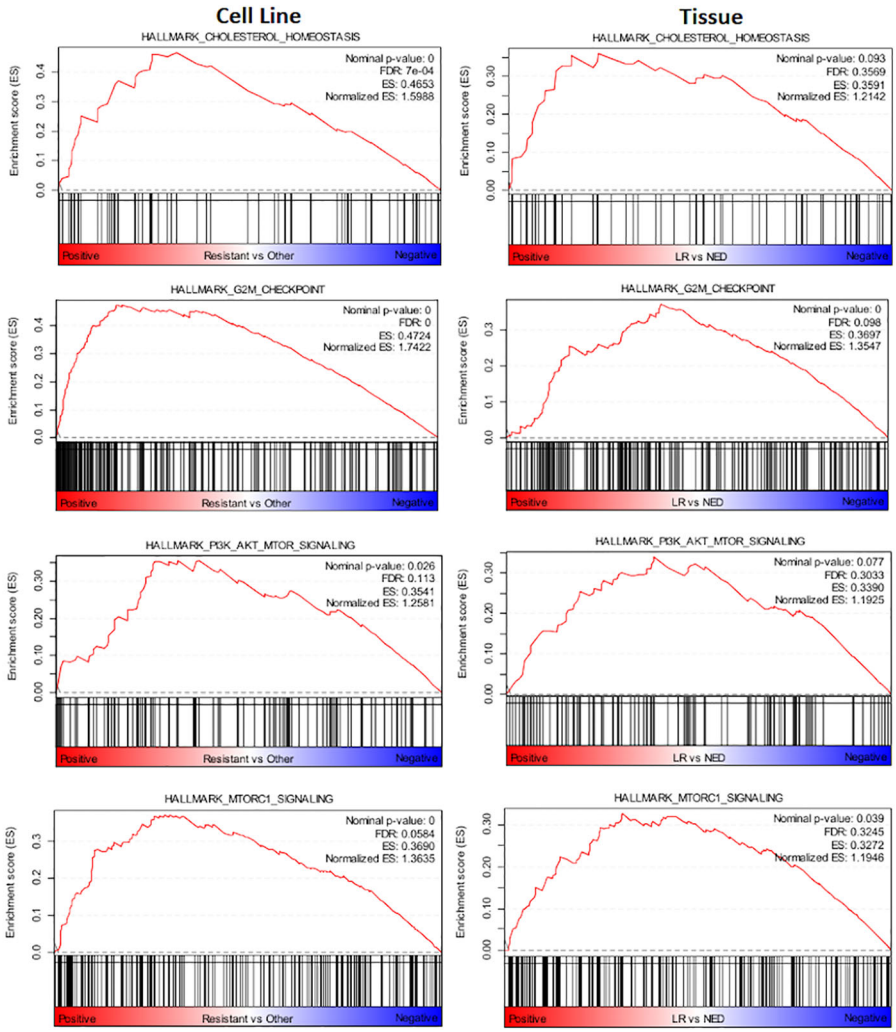

	LR vs NED	R vs All Other
HIF1α Signaling	1.63	1.61
ERK/MAPK Signaling	1.51	1.62
Tumor Microenvironment Pathway	1.67	1.2
Production of Nitric Oxide and Reactive Oxygen Species in Macrophages	0.71	1.43
mTOR Signaling	1	1.02
NF-κB Activation by Viruses	1	0.48
ILK Signaling	1.34	0.71
Role of CHK Proteins in Cell Cycle Checkpoint Control	-2	-0.45
AMPK Signaling	2	0.41
CDK5 Signaling	-1.41	-0.22
LPS-stimulated MAPK Signaling	0.45	0.42

FIGURE 3 | Identification of key signaling pathways that segregate radioresistant cells from others and comparison with key signaling pathways identified in HNSCC tumors treated by PORT and classified by their treatment response: no evidence of disease (NED) and local recurrence (LR).

Lastly, in **Figure 6**, TCP curves representative of each cell line using the physical dose (solid line) and the GyE dose (red dashed line) are plotted, which represent the expected TCP using a generic RBE of 3. The blue dashed line in each curve represents the physical dose necessary to accomplish the same TCP as the generic RBE of 3. The differences in physical dose would represent the "underdosing" of radioresistant tumors and are found in **Table 3**.

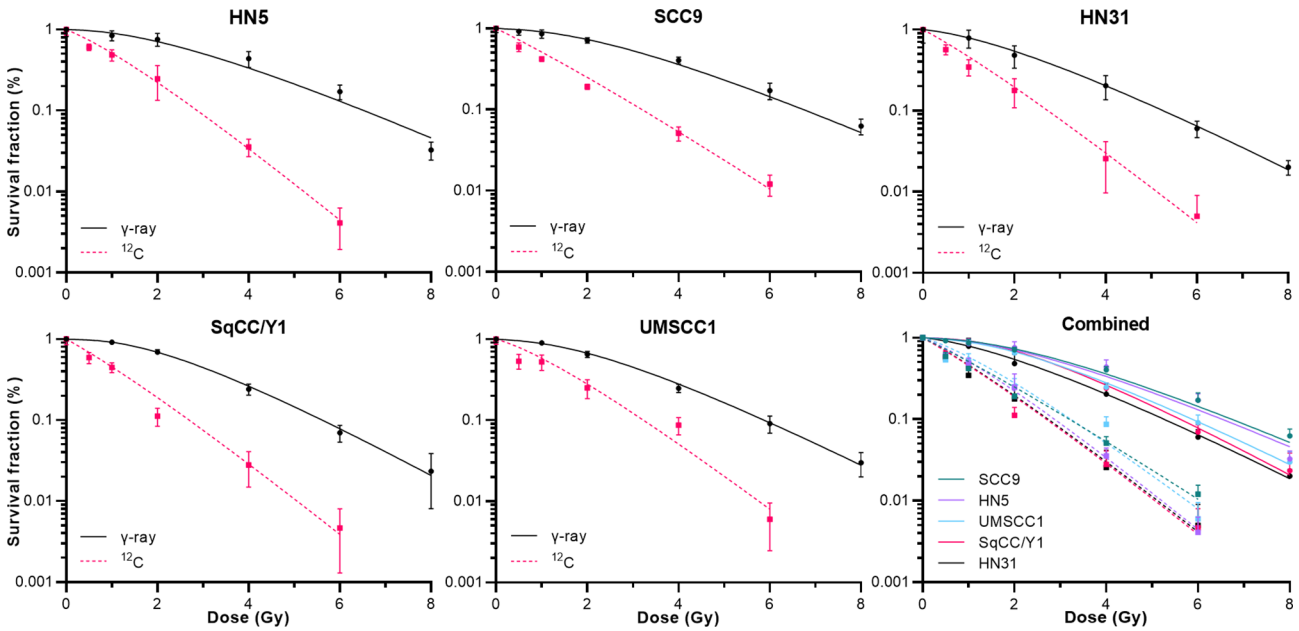

FIGURE 4 | Clonogenic cell survival for the 5 cell lines described in **Table 2** when irradiated by either γ-rays or ^{12}C at 400 Mev/u. The lower right panel shows all data combined.

TABLE 2 | Limiting slopes, mean inactivation doses, and RBEs using different methods of determination.

Cell line	$RBE_{SF10\%}$	$RBE\bar{D}_{parm}$	$RBE\bar{D}_{AUC}$	RBE_{D0}
SCC9	2.11	2.55	2.55	1.51
HN5	2.27	2.61	2.56	1.93
UMSCC1	1.83	2.09	2.07	1.50
SqCC/Y1	2.08	2.58	2.57	1.51
HN31	1.92	2.14	2.12	1.61
Average	2.04	2.39	2.37	1.61
Std dev	0.17	0.26	0.25	0.18
CV	0.08	0.11	0.11	0.11

$RBE_{SF10\%}$, RBE calculated using 10% survival; $RBE\bar{D}_{parm}$, RBE calculated using mean inactivation dose derived from RCR parameters; $RBE\bar{D}_{AUC}$, RBE calculated using mean inactivation dose derived from Reimann sum; RBE_{D0}, RBE calculated as ratio of limiting slopes.

DISCUSSION

HNSCC is the sixth most prevalent cancer in the world, and despite many treatment options, local or regional recurrence is still as high as 30%–50% after surgery or surgery plus radiochemotherapy. The alternatives for recurrent HNSCC include surgery with or without adjuvant radiochemotherapy with survival rates of 40%–66% (36), but the rates of grade 3 or grade 4 toxicities can be as high as 40% (37–41) with only 1 in 3 patients surviving reirradiation without recurrence or severe complications (42).

The high total doses from prior radiotherapy limit the total dose acceptable for reirradiation based upon the toxicity to organs at risk. However, a retrospective analysis of patients treated at the Heidelberg Ion-beam Therapy Center (HIT) by reirradiation for recurrent HNSCC with CIRT developed little in the way of either acute or late severe (>Grade III) toxicity (35) using a median total dose of 51 GyE in 3 GyE fractions. The Shanghai Proton and Heavy Ion Center in a trial of recurrent HNSCC found similar results (34). Late toxicities (> Grade III) were seen in 7.1% of patients as compared to HIT where late toxicities occurred in 14.5% of patients. The primary tumor sites in these two series of patients were vastly different with Shanghai for instance having ~83% of cases represented by squamous carcinomas (nasopharyngeal cancer representative of 78% of all cases) while only 28% of the HIT cohort was squamous carcinoma. These differences in patient population likely drive the differences in toxicity profiles and compare well to reirradiation trials for head and neck cancers using proton therapy where late toxicities ranged from 7% to 8%, 20%, and 24.6%, respectively (43–45).

The comparable overall improvements in late normal tissue toxicities in H&N cancers treated with CIRT suggest the potential for overall improvements in outcome in primary and recurrent disease as well as the potential for dose escalation in tumors identified as radioresistant. Also, given the limitations of access,

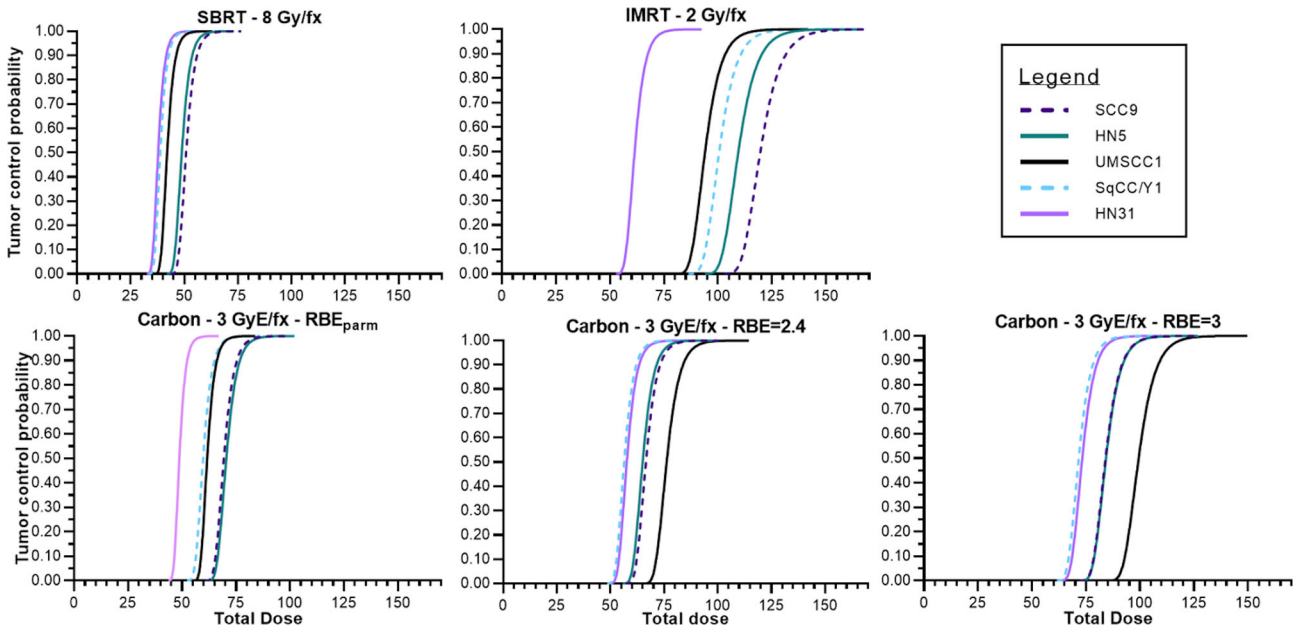

FIGURE 5 | Tumor control probabilities for various treatment modalities across the panel of HNSCC cell lines assuming no hypoxia, tumors that are a volume of 1 cm and containing 10^8 tumor cells. Photon IMRT, SAbR, ^{12}C using a fixed RBE to determine GyE, ^{12}C using the RBE associated with the cell line used for tumor modeling.

if patients with tumors that are radioresistant can be identified, the argument could be made to treat those patients where possible with ^{12}C ions. Radioresistant HNSCC can be manifested *via* a number of mechanisms, the predominant mechanism being hypoxia, but resistance may also be through acquired mechanisms of enhanced DNA repair, abrogation of apoptosis or through the development of a tolerogenic immune environment. ^{12}C ions—or for that matter other ions separately or in combination—should at least partially overcome these limitations.

Determining radioresistance in a clinically useful manner is not straightforward as there are currently no clinically useful biomarkers of radioresistance in HNSCC with the possible exception of HPV status. Because of the ease with which tumors can be biopsied in H&N cancers, an omics approach is feasible. To test this approach, 38 HNSCC tumor cell lines were tested for radiosensitivity *via* clonogenic survival. Basal gene expression analysis was then tested as a surrogate for clonogenic survival and found to be capable of segregating the most radioresistant cell lines from the other cell lines. Furthermore, the gene expression patterns in these radioresistant cell lines supported their classification as radioresistant. Besides identifying some of the more commonly identified genes and pathways associated with radioresistance, one of the more intriguing finds is the increased expression of the GAGE genes. These genes are not expressed in normal tissue with the exception of testes. In tumors, members of this family (GAGE1 and 2) are CD4+T cell antigens, attracting T cells into tumors. GAGE12 family members have been shown to increase both radio- and chemoresistance and metastasis (46–48). Other genes identified included SPINK1, an inhibitor of apoptosis that has been associated with chemoresistance (49, 50), and PARM1 which is an androgen-related gene that drives tumor proliferation (51, 52). Mechanistic analysis of any role for the genes in HNSCC radioresistance is warranted.

Assuming that one will be able to identify radioresistance so that patients could be triaged to receive ^{12}C ion therapy is of little benefit if this cohort of patients is then not treated to full potency. That potency is based upon an understanding of the dose equivalence for a given situation—or individual. Unlike stochastic processes such as radiation-induced carcinogenesis which uses the Seivert (Sv) for dose equivalent, dose equivalent for ^{12}C radiotherapy is described as GyEq, GyE, or GyRBE because there is no unit definition for dose equivalent in a deterministic setting. GyEq relies on the determination of the RBE for a given endpoint. The earliest determinations of RBE, still used today, were based upon cell survival in mostly rodent (CHO) cell lines and the human radioresistant salivary tumor cell line HSG, which was determined to be contaminated with HeLa cells (53, 54). The initial ^{12}C scattered beam at NIRS was normalized to the dose-averaged LET at 80 KeV/μm using their clinical neutron RBE of 3.0 as they were equally effective (55). This along with their experience with neutron exposures led them to use this value in their NIRS treatment planning system across all tumor sites. However, it is likely that "clinical RBE" is not a fixed value and should be personalized where possible. Furthermore, RBE can be a poor descriptor of the radiobiology associated with charged particle therapy as there are many factors that determine a RBE value, and it suffers from the inability to make direct comparisons from one method of determination to another or treatment regime to another (26, 30, 56). Therefore, we determined the

TABLE 3 | Comparisons of GyE based upon use of a fixed RBE vs. the actual RBE for a given cell line and the dose differential for a tumor control probability of 70%.

Cell line	Dose (GyE) if RBE = 3	Physical dose (Gy)	Dose (GyE) if actual RBE used	RBE (actual)	Difference in total GyE (fixed RBE vs. actual)
SCC9	86.9	28.9	73.9	2.55	13
HN5	87.2	29	75.9	2.61	11.3
UMSCC1	102.8	34.2	71.5	2.09	31.3
SqCC/Y1	74.1	24.7	63.7	2.58	10.4
HN31	75.8	25.2	54	2.14	21.8

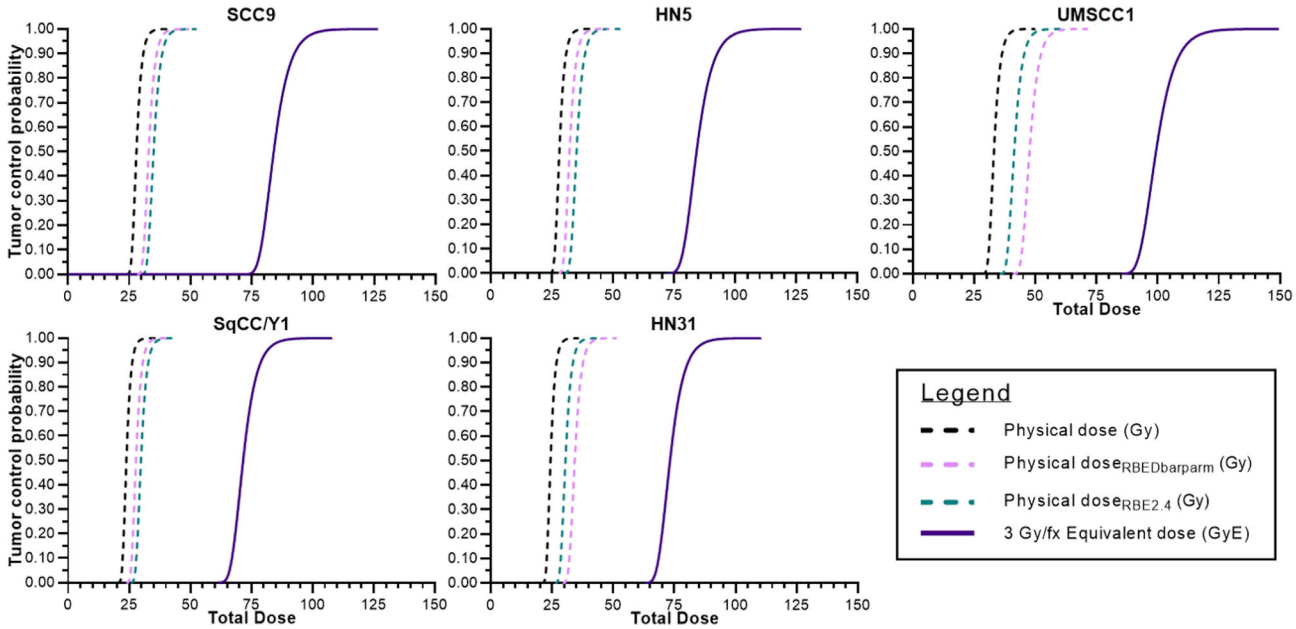

FIGURE 6 | Tumor control probabilities for each cell line after ^{12}C ion radiotherapy: left line is physical dose; far right line represents TCP when a clinical dose equivalent (GyE) based upon a fixed RBE is used; and the intermediate dashed line is the physical dose necessary to achieve the same TCP as the far right curve. The interval between the two physical doses is the underdosing for each tumor. That value at a TCP of 70% is seen in **Table 3**.

^{12}C RBE in a small cohort of moderate to radioresistant cell lines using multiple endpoints and then applied the survival and RBE values to model tumor control probability and asked whether individualization of RBE could be consequential when compared to a generic value.

Figure 5 depicts tumor control probability curves for the 5 tumor cell lines. Dose fractionation schemes include a standard 2 Gy/fraction scheme, a SAbR fractionation scheme of 8 Gy per fraction, and a 3 GyE per fraction approach (generic RBE of 3). As expected, TCP varied according to the radiosensitivity of the tumor with the most resistant tumors requiring greater overall total doses to achieve the modeled tumor cure. The TCP curves for the HN31, which is intermediate in radiosensitivity, is far to the left of the more radioresistant lines in the upper left panel (IMRT 2 Gy/fraction) and at 60–70 Gy total dose TCP is roughly between 30% and 90%. The remaining TCP curves for the more radioresistant cells falls well outside with total doses of 90–120 Gy required to achieve 50% control. Total doses for the TCP of a SAbR regimen are far less but also suffer from a lack of efficacy for very radioresistant tumors and would be expected to be constrained by an increased risk for normal tissue complications. The TCP curves for ^{12}C, because this is GyE and uses a more conventional fraction size, is comparable with the conventional 2 Gy/fraction regimen. The SabR approach with ^{12}C ions may be more effective for carbon ions but suffers the same complications as a conventional SAbR approach within the radioresistant subset.

In **Figure 6**, we attempted to determine the underdosing for a given tumor if a fixed RBE vs. an individually determined RBE was used. TCP curves include (a) the TCP using the generic RBE of 3 for each cell line from **Figure 5**; (b) the 12C physical dose associated with the TCP determined using the generic RBE; and (c) the physical dose if the TCP curve based upon an RBE of 3 were modified by the RBE determined for each cell line. That difference in the physical dose curves could be considered as an "underdosing" of ^{12}C physical dose and it is consequential in that it reflects the need to understand the intrinsic radioresistance for a given tumor. Those values of "underdosing" at a TCP of 70% are given in **Table 3**.

In this manuscript, we have attempted to draw attention to the need for individualizing therapy based upon the intrinsic radioresponse of a tumor. Head and neck squamous cells were used because of the recent trials where HNSCC are being treated

with ^{12}C and because HNSCC outcomes have seen little improvement. At least for cell lines, gene expression was able to segregate radioresistant tumor cell lines from cell lines less resistant. One could argue that 38 cell lines do not bring enough diversity of radiosensitivity as the most radioresistant cell lines were few in number. Also, while there was overlap in the enrichment of specific pathways in common between cell lines and tumors that were treated with PORT, it is evident that much work is needed, irrespective of the gene expression analysis.

Using five cell lines whose radiosensitivity ranged from moderate to resistant across the 38 cell line panel, the potential impact of intrinsic radiosensitivity was tested by determining TCP curves using various radiation regimens for both γ-ray and ^{12}C exposures. This exercise highlighted the potential for underdosing radioresistant tumors when generic rather than personalized RBEs were used, which would negate the impact of triaging patients with radioresistant tumors.

We understand that our TCP calculations reflect fully oxygenated tumors, did not reflect tumor response to varied LETs, etc., but our goal is more one of relative comparisons and not necessarily quantitative comparisons. What we require are data from actual tumors treated with curative intent using X-rays and ^{12}C ions with different dose and fractionation schedules and a realistic understanding of the impact of tumor hypoxia to challenge and ultimately improve upon the biophysical modeling of CIRT with the intent to ultimately personalize therapy.

DATA AVAILABILITY STATEMENT

The original contributions presented in the study are included in the article/supplementary materials. Further inquiries can be directed to the corresponding author.

AUTHOR CONTRIBUTIONS

MS conceived of and carried out experiments, wrote the manuscript, and led the research program. AD conceived of and carried out experiments, edited the manuscript, and participated intellectually. AP was responsible for radiation physics, helped develop the beam configuration, and wrote a portion of the manuscript. DS was partly responsible for designing and carrying out experiments. MC was responsible for 12C dosimetry, developing the SOBP for CNAO, and all physics aspects of 12C irradiation. AF was the CNAO biology contact person. She helped facilitate experiments and helped with the design of our irradiation setup at CNAO. JY was responsible for collecting the panel of H&N tumor cell lines, designed and carried out experiments to determine the X-ray survival parameters for these cells, and provided DNA and RNA for omics analysis. EP carried out additional survival X-ray survival curves, plotted all data, and calculated survival fits and tumor control probability curves. BS conceived of and carried out both X-ray and 12C experiments. He was involved in the interpretation of data and wrote sections of this manuscript. LD was responsible for all omics analysis, interpretation of that data, and wrote sections of the manuscript. All authors listed have made a substantial, direct, and intellectual contribution to the work and approved it for publication.

FUNDING

Funds were provided through the Department of Radiation Oncology Seed Grant Program to MS as well as the David A. Pistenmaa M.D., Ph.D. Distinguished Chair in Radiation Oncology to MS. The funders were not involved in the study design, collection, analysis, interpretation of data, the writing of this article or the decision to submit it for publication.

REFERENCES

1. Castro JR, Quivey JM, Lyman JT, Chen GT, Phillips TL, Tobias CA. Radiotherapy With Heavy Charged Particles at Lawrence Berkeley Laboratory. *J Can Assoc Radiol* (1980) 31:30–4.
2. Blakely EA, Faddegon B, Tinkle C, Bloch C, Dominello M, Griffin RJ, et al. Three Discipline Collaborative Radiation Therapy (3DCRT) Special Debate: The United States Needs at Least One Carbon Ion Facility. *J Appl Clin Med Phys* (2019) 20:6–13. doi: 10.1002/acm2.12727
3. Malouff TD, Mahajan A, Krishnan S, Beltran C, Seneviratne DS, Trifiletti DM. Carbon Ion Therapy: A Modern Review of an Emerging Technology. *Front Oncol* (2020) 10:82. doi: 10.3389/fonc.2020.00082
4. Tinganelli W, Durante M. Carbon Ion Radiobiology. *Cancers (Basel)* (2020) 12. doi: 10.3390/cancers12103022
5. Yanagi T, Mizoe JE, Hasegawa A, Takagi R, Bessho H, Onda T, et al. Mucosal Malignant Melanoma of the Head and Neck Treated by Carbon Ion Radiotherapy. *Int J Radiat Oncol Biol Phys* (2009) 74:15–20. doi: 10.1016/j.ijrobp.2008.07.056
6. Demizu Y, Fujii O, Terashima K, Mima M, Hashimoto N, Niwa Y, et al. Particle Therapy for Mucosal Melanoma of the Head and Neck. A Single-Institution Retrospective Comparison of Proton and Carbon Ion Therapy. *Strahlenther Onkol* (2014) 190:186–91. doi: 10.1007/s00066-013-0489-9
7. Jingu K, Tsujii H, Mizoe JE, Hasegawa A, Bessho H, Takagi R, et al. Carbon Ion Radiation Therapy Improves the Prognosis of Unresectable Adult Bone and Soft-Tissue Sarcoma of the Head and Neck. *Int J Radiat Oncol Biol Phys* (2012) 82:2125–31. doi: 10.1016/j.ijrobp.2010.08.043
8. Koto M, Hasegawa A, Takagi R, Sasahara G, Ikawa H, Mizoe JE, et al. Feasibility of Carbon Ion Radiotherapy for Locally Advanced Sinonasal Adenocarcinoma. *Radiother Oncol* (2014) 113:60–5. doi: 10.1016/j.radonc.2014.09.009
9. Schulz-Ertner D, Didinger B, Nikoghosyan A, Jakel O, Zuna I, Wannenmacher M, et al. Optimization of Radiation Therapy for Locally Advanced Adenoid Cystic Carcinomas With Infiltration of the Skull Base Using Photon Intensity-Modulated Radiation Therapy (IMRT) and a Carbon Ion Boost. *Strahlenther Onkol* (2003) 179:345–51. doi: 10.1007/s00066-003-1071-7
10. Takagi M, Demizu Y, Hashimoto N, Mima M, Terashima K, Fujii O, et al. Treatment Outcomes of Particle Radiotherapy Using Protons or Carbon Ions as a Single-Modality Therapy for Adenoid Cystic Carcinoma of the Head and Neck. *Radiother Oncol* (2014) 113:364–70. doi: 10.1016/j.radonc.2014.11.031
11. Mizoe JE, Tsujii H, Kamada T, Matsuoka Y, Tsuji H, Osaka Y, et al. Dose Escalation Study of Carbon Ion Radiotherapy for Locally Advanced Head-and-Neck Cancer. *Int J Radiat Oncol Biol Phys* (2004) 60:358–64. doi: 10.1016/j.ijrobp.2004.02.067
12. Mizoe JE, Hasegawa A, Jingu K, Takagi R, Bessyo H, Morikawa T, et al. Results of Carbon Ion Radiotherapy for Head and Neck Cancer. *Radiother Oncol* (2012) 103:32–7. doi: 10.1016/j.radonc.2011.12.013
13. Morimoto K, Demizu Y, Hashimoto N, Mima M, Terashima K, Fujii O, et al. Particle Radiotherapy Using Protons or Carbon Ions for Unresectable Locally Advanced Head and Neck Cancers With Skull Base Invasion. *Jpn J Clin Oncol* (2014) 44:428–34. doi: 10.1093/jjco/hyu010
14. Eekers DBP, Roelofs E, Jelen U, Kirk M, Granzier M, Ammazzalorso F, et al. Benefit of Particle Therapy in Re-Irradiation of Head and Neck Patients.

Results of a Multicentric in Silico ROCOCO Trial. *Radiother Oncol* (2016) 121:387–94. doi: 10.1016/j.radonc.2016.08.020
15. Weber U, Kraft G. Comparison of Carbon Ions Versus Protons. *Cancer J* (2009) 15:325–32. doi: 10.1097/PPO.0b013e3181b01935
16. Grun R, Friedrich T, Kramer M, Zink K, Durante M, Engenhart-Cabillic R, et al. Assessment of Potential Advantages of Relevant Ions for Particle Therapy: A Model Based Study. *Med Phys* (2015) 42:1037–47. doi: 10.1118/1.4905374
17. Gamez ME, Patel SH, Mcgee LA, Sio TT, Mcdonald M, Phan J, et al. A Systematic Review on Re-Irradiation With Charged Particle Beam Therapy in the Management of Locally Recurrent Skull Base and Head and Neck Tumors. *Int J Part Ther* (2021) 8:131–54. doi: 10.14338/IJPT-20-00064.1
18. Moeller BJ, Yordy JS, Williams MD, Giri U, Raju U, Molkentine DP, et al. DNA Repair Biomarker Profiling of Head and Neck Cancer: Ku80 Expression Predicts Locoregional Failure and Death Following Radiotherapy. *Clin Cancer Res* (2011) 17:2035–43. doi: 10.1158/1078-0432.CCR-10-2641
19. Sano D, Xie TX, Ow TJ, Zhao M, Pickering CR, Zhou G, et al. Disruptive TP53 Mutation is Associated With Aggressive Disease Characteristics in an Orthotopic Murine Model of Oral Tongue Cancer. *Clin Cancer Res* (2011) 17:6658–70. doi: 10.1158/1078-0432.CCR-11-0046
20. Skinner HD, Sandulache VC, Ow TJ, Meyn RE, Yordy JS, Beadle BM, et al. TP53 Disruptive Mutations Lead to Head and Neck Cancer Treatment Failure Through Inhibition of Radiation-Induced Senescence. *Clin Cancer Res* (2012) 18:290–300. doi: 10.1158/1078-0432.CCR-11-2260
21. Eschrich SA, Pramana J, Zhang H, Zhao H, Boulware D, Lee JH, et al. A Gene Expression Model of Intrinsic Tumor Radiosensitivity: Prediction of Response and Prognosis After Chemoradiation. *Int J Radiat Oncol Biol Phys* (2009) 75:489–96. doi: 10.1016/j.ijrobp.2009.06.014
22. Zhao M, Sano D, Pickering CR, Jasser SA, Henderson YC, Clayman GL, et al. Assembly and Initial Characterization of a Panel of 85 Genomically Validated Cell Lines From Diverse Head and Neck Tumor Sites. *Clin Cancer Res* (2011) 17:7248–64. doi: 10.1158/1078-0432.CCR-11-0690
23. Ang KK, Trotti A, Brown BW, Garden AS, Foote RL, Morrison WH, et al. Randomized Trial Addressing Risk Features and Time Factors of Surgery Plus Radiotherapy in Advanced Head-and-Neck Cancer. *Int J Radiat Oncol Biol Phys* (2001) 51:571–8. doi: 10.1016/S0360-3016(01)01690-X
24. Mirandola A, Molinelli S, Vilches Freixas G, Mairani A, Gallio E, Panizza D, et al. Dosimetric Commissioning and Quality Assurance of Scanned Ion Beams at the Italian National Center for Oncological Hadrontherapy. *Med Phys* (2015) 42:5287–300. doi: 10.1118/1.4928397
25. Durante M, Paganetti H, Pompos A, Kry SF, Wu X, Grosshans DR. Report of a National Cancer Institute Special Panel: Characterization of the Physical Parameters of Particle Beams for Biological Research. *Med Phys* (2019) 46:e37–52. doi: 10.1002/mp.13324
26. Lind BK, Persson LM, Edgren MR, Hedlof I, Brahme A. Repairable-Conditionally Repairable Damage Model Based on Dual Poisson Processes. *Radiat Res* (2003) 160:366–75. doi: 10.1667/0033-7587(2003)160[0366:RRDMBO]2.0.CO;2
27. Ding LH, Xie Y, Park S, Xiao G, Story MD. Enhanced Identification and Biological Validation of Differential Gene Expression via Illumina Whole-Genome Expression Arrays Through the Use of the Model-Based Background Correction Methodology. *Nucleic Acids Res* (2008) 36:e58. doi: 10.1093/nar/gkn234
28. Xie Y, Wang X, Story M. Statistical Methods of Background Correction for Illumina BeadArray Data. *Bioinformatics* (2009) 25:751–7. doi: 10.1093/bioinformatics/btp040
29. Chen M, Xie Y, Story M. An Exponential-Gamma Convolution Model for Background Correction of Illumina BeadArray Data. *Commun Stat Theory Methods* (2011) 40:3055–69. doi: 10.1080/03610921003797753
30. Antonovic L, Dasu A, Furusawa Y, Toma-Dasu I. Relative Clinical Effectiveness of Carbon Ion Radiotherapy: Theoretical Modelling for H&N Tumours. *J Radiat Res* (2015) 56:639–45. doi: 10.1093/jrr/rrv016
31. Johansen J, Bentzen SM, Overgaard J, Overgaard M. Relationship Between the In Vitro Radiosensitivity of Skin Fibroblasts and the Expression of Subcutaneous Fibrosis, Telangiectasia, and Skin Erythema After Radiotherapy. *Radiother Oncol* (1996) 40:101–9. doi: 10.1016/0167-8140(96)01777-X
32. Giri U, Ashorn CL, Ramdas L, Stivers DN, Coombes K, El-Naggar AK, et al. Molecular Signatures Associated With Clinical Outcome in Patients With High-Risk Head-and-Neck Squamous Cell Carcinoma Treated by Surgery and Radiation. *Int J Radiat Oncol Biol Phys* (2006) 64:670–7. doi: 10.1016/j.ijrobp.2005.08.032
33. Keck MK, Zuo Z, Khattri A, Stricker TP, Brown CD, Imanguli M, et al. Integrative Analysis of Head and Neck Cancer Identifies Two Biologically Distinct HPV and Three non-HPV Subtypes. *Clin Cancer Res* (2015) 21:870–81. doi: 10.1158/1078-0432.CCR-14-2481
34. Gao J, Hu J, Guan X, Yang J, Hu W, Kong L, et al. Salvage Carbon-Ion Radiation Therapy For Locoregionally Recurrent Head and Neck Malignancies. *Sci Rep* (2019) 9:4259. doi: 10.1038/s41598-019-39241-y
35. Held T, Windisch P, Akbaba S, Lang K, El Shafie R, Bernhardt D, et al. Carbon Ion Reirradiation for Recurrent Head and Neck Cancer: A Single-Institutional Experience. *Int J Radiat Oncol Biol Phys* (2019) 105:803–11. doi: 10.1016/j.ijrobp.2019.07.021
36. Pulte D, Brenner H. Changes in Survival in Head and Neck Cancers in the Late 20th and Early 21st Century: A Period Analysis. *Oncologist* (2010) 15:994–1001. doi: 10.1634/theoncologist.2009-0289
37. Duprez F, Madani I, Bonte K, Boterberg T, Vakaet L, Derie C, et al. Intensity-Modulated Radiotherapy for Recurrent and Second Primary Head and Neck Cancer in Previously Irradiated Territory. *Radiother Oncol* (2009) 93:563–9. doi: 10.1016/j.radonc.2009.10.012
38. Giro C, Berger B, Bolke E, Ciernik IF, Duprez F, Locati L, et al. High Rate of Severe Radiation Dermatitis During Radiation Therapy With Concurrent Cetuximab in Head and Neck Cancer: Results of a Survey in EORTC Institutes. *Radiother Oncol* (2009) 90:166–71. doi: 10.1016/j.radonc.2008.09.007
39. Werbrouck J, De Ruyck K, Duprez F, Veldeman L, Claes K, Van Eijkeren M, et al. Acute Normal Tissue Reactions in Head-and-Neck Cancer Patients Treated With IMRT: Influence of Dose and Association With Genetic Polymorphisms in DNA DSB Repair Genes. *Int J Radiat Oncol Biol Phys* (2009) 73:1187–95. doi: 10.1016/j.ijrobp.2008.08.073
40. Riaz N, Hong JC, Sherman EJ, Morris L, Fury M, Ganly I, et al. A Nomogram to Predict Loco-Regional Control After Re-Irradiation for Head and Neck Cancer. *Radiother Oncol* (2014) 111:382–7. doi: 10.1016/j.radonc.2014.06.003
41. Takiar V, Garden AS, Ma D, Morrison WH, Edson M, Zafereo ME, et al. Reirradiation of Head and Neck Cancers With Intensity Modulated Radiation Therapy: Outcomes and Analyses. *Int J Radiat Oncol Biol Phys* (2016) 95:1117–31. doi: 10.1016/j.ijrobp.2016.03.015
42. Hoebers F, Heemsbergen W, Moor S, Lopez M, Klop M, Tesselaar M, et al. Reirradiation for Head-and-Neck Cancer: Delicate Balance Between Effectiveness and Toxicity. *Int J Radiat Oncol Biol Phys* (2011) 81:e111–118. doi: 10.1016/j.ijrobp.2011.01.004
43. Mcdonald MW, Zolali-Meybodi O, Lehnert SJ, Estabrook NC, Liu Y, Cohen-Gadol AA, et al. Reirradiation of Recurrent and Second Primary Head and Neck Cancer With Proton Therapy. *Int J Radiat Oncol Biol Phys* (2016) 96:808–19. doi: 10.1016/j.ijrobp.2016.07.037
44. Phan J, Sio TT, Nguyen TP, Takiar V, Gunn GB, Garden AS, et al. Reirradiation of Head and Neck Cancers With Proton Therapy: Outcomes and Analyses. *Int J Radiat Oncol Biol Phys* (2016) 96:30–41. doi: 10.1016/j.ijrobp.2016.03.053
45. Romesser PB, Cahlon O, Scher ED, Hug EB, Sine K, Deselm C, et al. Proton Beam Reirradiation for Recurrent Head and Neck Cancer: Multi-Institutional Report on Feasibility and Early Outcomes. *Int J Radiat Oncol Biol Phys* (2016) 95:386–95. doi: 10.1016/j.ijrobp.2016.02.036
46. Lee EK, Song KA, Chae JH, Kim KM, Kim SH, Kang MS. GAGE12 Mediates Human Gastric Carcinoma Growth and Metastasis. *Int J Cancer* (2015) 136:2284–92. doi: 10.1002/ijc.29286
47. Gjerstorff MF, Terp MG, Hansen MB, Ditzel HJ. The Role of GAGE Cancer/Testis Antigen in Metastasis: The Jury is Still Out. *BMC Cancer* (2016) 16:7. doi: 10.1186/s12885-015-1998-y
48. Nin DS, Wujanto C, Tan TZ, Lim D, Damen JMA, Wu KY, et al. GAGE Mediates Radio Resistance in Cervical Cancers via the Regulation of Chromatin Accessibility. *Cell Rep* (2021) 36:109621. doi: 10.1016/j.celrep.2021.109621
49. Chen F, Long Q, Fu D, Zhu D, Ji Y, Han L, et al. Targeting SPINK1 in the Damaged Tumour Microenvironment Alleviates Therapeutic Resistance. *Nat Commun* (2018) 9:4315. doi: 10.1038/s41467-018-06860-4

50. Xu L, Lu C, Huang Y, Zhou J, Wang X, Liu C, et al. SPINK1 Promotes Cell Growth and Metastasis of Lung Adenocarcinoma and Acts as a Novel Prognostic Biomarker. *BMB Rep* (2018) 51:648–53. doi: 10.5483/BMBRep.2018.51.12.205
51. Fladeby C, Gupta SN, Barois N, Lorenzo PI, Simpson JC, Saatcioglu F, et al. Human PARM-1 Is a Novel Mucin-Like, Androgen-Regulated Gene Exhibiting Proliferative Effects in Prostate Cancer Cells. *Int J Cancer* (2008) 122:1229–35. doi: 10.1002/ijc.23185
52. Charfi C, Levros LCJr., Edouard E, Rassart E. Characterization and Identification of PARM-1 as a New Potential Oncogene. *Mol Cancer* (2013) 12:84. doi: 10.1186/1476-4598-12-84
53. Capes-Davis A, Theodosopoulos G, Atkin I, Drexler HG, Kohara A, Macleod RA, et al. Check Your Cultures! A List of Cross-Contaminated or Misidentified Cell Lines. *Int J Cancer* (2010) 127:1–8. doi: 10.1002/ijc.25242
54. Matsumoto Y, Matsuura T, Wada M, Egashira Y, Nishio T, Furusawa Y. Enhanced Radiobiological Effects at the Distal End of a Clinical Proton Beam: In Vitro Study. *J Radiat Res* (2014) 55:816–22. doi: 10.1093/jrr/rrt230
55. Kanai T, Endo M, Minohara S, Miyahara N, Koyama-Ito H, Tomura H, et al. Biophysical Characteristics of HIMAC Clinical Irradiation System for Heavy-Ion Radiation Therapy. *Int J Radiat Oncol Biol Phys* (1999) 44:201–10. doi: 10.1016/S0360-3016(98)00544-6
56. Toma-Dasu I, Dasu A, Brahme A. Dose Prescription and Optimisation Based on Tumour Hypoxia. *Acta Oncol* (2009) 48:1181–92. doi: 10.3109/02841860903188643

Conflict of Interest: The authors declare that the research was conducted in the absence of any commercial or financial relationships that could be construed as a potential conflict of interest.

Publisher's Note: All claims expressed in this article are solely those of the authors and do not necessarily represent those of their affiliated organizations, or those of the publisher, the editors and the reviewers. Any product that may be evaluated in this article, or claim that may be made by its manufacturer, is not guaranteed or endorsed by the publisher.

frontiers in Oncology

ORIGINAL RESEARCH
published: 02 March 2022
doi: 10.3389/fonc.2022.829502

Dosimetric and Clinical Risk Factors for the Development of Maxillary Osteoradionecrosis in Adenoid Cystic Carcinoma (ACC) Patients Treated With Carbon Ion Radiotherapy

Barbara Vischioni[1], Stefania Russo[1], Martino Meuli[2], Maria Bonora[1], Sara Ronchi[1], Rossana Ingargiola[1], Anna Maria Camarda[3,4], Sara Imparato[1], Lorenzo Preda[1,2,5], Mario Ciocca[1], Silvia Molinelli[1] and Ester Orlandi[1]*

[1] Radiation Oncology Clinical Department, National Center for Oncological Hadrontherapy, Pavia, Italy, [2] Department of Clinical, Surgical, Diagnostic and Pediatric Sciences, University of Pavia, Pavia, Italy, [3] Division of Radiotherapy, Istituto Europeo di Oncologia (IEO) European Institute of Oncology, Istituto di Ricovero e Cura a Carattere Scientifico (IRCCS), Milan, Italy, [4] Department of Oncology and Hemato-Oncology, University of Milan, Milan, Italy, [5] Radiology Institute, Fondazione Istituto di Ricovero e Cura a Carattere Scientifico (IRCCS) Policlinico San Matteo, Pavia, Italy

OPEN ACCESS

Edited by:
Thomas Tessonnier, Heidelberg University Hospital, Germany

Reviewed by:
Tatsuya Ohno, Gunma University, Japan
Thomas Held, Heidelberg University Hospital, Germany

***Correspondence:**
Barbara Vischioni
barbara.vischioni@cnao.it

Specialty section:
This article was submitted to Radiation Oncology, a section of the journal Frontiers in Oncology

Received: *05 December 2021*
Accepted: *04 February 2022*
Published: *02 March 2022*

Citation:
Vischioni B, Russo S, Meuli M, Bonora M, Ronchi S, Ingargiola R, Camarda AM, Imparato S, Preda L, Ciocca M, Molinelli S and Orlandi E (2022) Dosimetric and Clinical Risk Factors for the Development of Maxillary Osteoradionecrosis in Adenoid Cystic Carcinoma (ACC) Patients Treated With Carbon Ion Radiotherapy. Front. Oncol. 12:829502. doi: 10.3389/fonc.2022.829502

Background: The present study aims to evaluate dosimetric and clinical risk factors for the development of maxillary osteoradionecrosis (ORN) in head and neck adenoid cystic carcinoma (ACC) patients treated with carbon ion radiotherapy (CIRT).

Methods: Clinical data and treatment plans of ACC patients, consecutively treated from January 2013 to September 2016 within the phase II clinical trial CNAO S9/2012/C, were retrospectively reviewed. ORN and other treatment-related toxicity were graded according to the Common Terminology Criteria for Adverse Events (CTACE), version 4.0. The maxillary bone was contoured on the planning CT, and only patients receiving more than 10% of the prescription dose at their maxilla were considered for the analysis (67 patients). The volumes of maxilla receiving doses from 10 Gy (RBE) to 60 Gy (RBE) (V_D), with an increment of 10 Gy (RBE), and additional clinical factors were correlated to the incidence of ORN with univariate analysis (Chi-square test). The logistic regression model was subsequently applied for multivariate analysis. Treatment plans calculated with a local effect model (LEM)-based optimization were recalculated with the modified microdosimetric kinetic model (MKM), and compared with literature data from the Japanese experience.

Results: The median time interval from the start of CIRT to ORN appearance was 24 months (range, 8–54 months). Maxillary ORN was observed in 11 patients (16.4%). Grade 1 ORN was observed in 2 patients (18.1%), G2 in 4 (36.3%), G3 in 4 (36.3%) and G4 in 1 (9.3%). From univariate analysis, the site of the tumor, the presence of teeth within the PTV and acute mucositis correlated with the development of maxillary ORN. V_D were significantly higher for all the dose levels tested in patients with maxillary ORN than

patients without necrosis, according to both radiobiological models. The multivariate analysis showed that V60 significantly correlated with ORN risk.

Conclusion: The volume of maxilla irradiated with high dose values was relevant for ORN development in our cohort of ACC patients. These results are in line with previously published data obtained with a different radiobiological model. Our findings might be helpful to prevent the risk of ORN in patients receiving CIRT.

Keywords: ACC, maxillary osteonecrosis, carbon ion radiotherapy, risk factors, late toxicity

INTRODUCTION

Osteoradionecrosis (ORN) is described as a chronic wound that fails to heal with bone exposure. It is a treatment related complication primarily reported in the head and neck population treated with radiotherapy (RT) frequently associated with a substantial morbidity causing pain and infection. The pathophysiology of its occurrence is linked to the hypoxia, hypocellularity, and hypo vascularity that follow a RT course (1). There are several risk factors that have been reported to favor ORN in patients undergoing RT, for example alcohol and tobacco consumption, dental and periodontal status deterioration, trauma after dental extractions, oral implantology, insufficient body mass index, general comorbidities such as diabetes, and anti-inflammatory or anti-coagulant therapy (2). Treatment related factors that might be linked to ORN are technique of irradiation, dosimetric parameters, fractionation schedule, extension of irradiated volumes, and concomitant chemotherapy (3).

The incidence of ORN of the mandible when irradiating parotid tumors and also at the skull base when irradiating tumors localized at the nasopharynx, has decreased in recent years with the transition from 2 and 3D-RT to the modern intensity modulated-RT (IMRT), since the more localized deposition of the higher doses to the tumor target in respect to the surrounding normal tissues (4, 5). In this regard, carbon ion RT (CIRT) has shown its superiority in dosimetric studies in delivering tumoricidal dose while sparing the surrounding normal tissues, due to the sharp penumbra of the therapeutic beams. Furthermore, the radiobiological properties of CIRT that causes not repairable DNA damage not cell cycle specific nor oxygen dependent (6), have advocated its therapeutic use for radioresistant tumors, such as adenoid cystic carcinoma (ACC). The gold standard treatment for ACC is radical surgical resection followed by post-operative RT (7). In case of unresectable locally advanced tumors or with tumor macroscopic persistence after surgical resection or patient contraindication to surgery (8–10), or reirradiation (11), CIRT has been recently shown to have higher efficacy compared to conventional photon RT (12).

While numerous clinical and physical factors have been reported to be associated with ORN development after photon RT, the risk factors for maxillary ORN after CIRT are still under investigation. Sasahara et al. (13) reported V50 as a good predictor of ORN in multivariate analysis in a series of 63 malignant radioresistant tumors (namely, 24 ACC) treated with CIRT at a prescribed dose of 57.6 Gy (RBE) in 16 fractions, with passive beam delivery. RBE-weighted dose calculation was based on the semi-empirical model by Kanai et al. (14), while the modified microdosimetric kinetic model (MKM) is currently used for pencil beam scanning in Japan (15). The two models have been validated for consistency, and only the latter will be adopted here for comparison against available literature data.

The aim of the present study was to identify dosimetric and non-dosimetric risk factors correlated to ORN development for head and neck ACC patients treated at CNAO (National Center for Oncological Hadrontherapy, Pavia, Italy) with CIRT delivered with curative intent. At CNAO the local effect model (LEM—version I) is employed for RBE calculation as in other European CIRT centers (16), with treatment protocols derived from the Japanese experience (17), after mice and cell experiments to assure comparable radiobiological efficacy of the CNAO carbon ion beam to the reference CIRT beam of the NIRS Hadrontherapy Center in Japan (18). The impact of RBE conversion from MKM to LEM on prescription doses and organ at risk (OAR) constraints was extensively reported for different CIRT cancer indications, including ACC (19). Only MKM model-based analysis on ORN has been reported so far for patients with head and neck tumors (13), while here we directly investigate risk factors for ORN development when irradiating head and neck patients with CIRT by using the LEM model. The findings from the present study might be helpful to prevent ORN risk at the maxilla in patients receiving CIRT in facilities where the LEM is used for treatment of patients in 16 fractions, directly estimating the dose that might be delivered without causing ORN, and thus avoiding the deterioration of quality of life reported for example when ORN evolves into oronasal fistula (20). Furthermore, in our study the identification of other clinical and treatment related risk factors predisposing to ORN might be helpful to assess ORN risk in the head and neck population undergoing CIRT and plan adequate follow up schedule with possible preventive measures.

MATERIAL AND METHODS

Study Protocol Design

The present study is a retrospective, observational study, a subanalysis of the prospective phase II clinical trial ongoing

from January 2013 to September 2016 at CNAO (CNAO S9/2012/C) to assess safety and feasibility of CIRT with radical intent for ACC patients with partially resected tumors (R1/R2 margins), or unresectable tumors, or unfit to surgery (21). CNAO's Ethics Committee formally approved the present research protocol CNAO OSS/19/2020, and the patient consents for the research participation were properly collected and stored. The primary endpoint of the present study was to evaluate the dose of CIRT associated with the development of ORN at the maxillary bone in the ACC patients treated at CNAO with CIRT according to the LEM model. Secondary endpoints were the correlation of ORN in our series with the patient clinical and treatment characteristics to describe possible factors that might predict bone toxicity after CIRT.

Patient's Baseline and Follow-Up Data

A total of 128 patients with head and neck ACC consecutively treated with CIRT along with their diagnostic imaging and treatment plan data were screened for selection in the present study. Only the patients with at least more than 10% of the total prescription dose of 68.8 Gy (RBE) to their maxilla were selected for the analysis as detailed in Sasahara et al. (13). On the other side, patients with tumor invading the maxillary bone before CIRT, or with maxillary recurrence after CIRT, were excluded to avoid confounding factors for ORN assessment. At the end, 67 patients, 35 women (52.2%) and 32 men (47.8%) were considered for the analysis. The mean age of the studied population at the beginning of the CIRT course was of 55 years. Patients clinical and tumor characteristics (namely, anamnestic data that have been reported to impact on ORN except for osteoporosis), and data related to previous surgery and CIRT toxicity, were collected and detailed in **Table 1**. Most of the tumors were in the sinonasal area (35.8%). The other sites involved were the parotid glands (20.9%), the pharynx (17.9%), the submandibular glands (13.4%), the oral cavity (9%), and the external auditory channel (3%). Tumors were all re-staged following the 8th edition of TNM staging system (AJCC/UICC). Prior to therapy, the patients were adequately informed about the possible risks of maxillary ORN as

TABLE 1 | Patients clinical and tumor characteristics.

Clinical factors	**Subgroup**	**N (%)**
Age	<57	33 (49.3)
	≥57	34 (50.7)
Sex	Male	32 (47.8)
	Female	35 (52.2)
Diabetes	Yes	6 (9.0)
	No	61 (91.0)
Autoimmune disease	Yes	2 (3.0)
	No	65 (97.0)
Hypertension	Yes	19 (28.4)
	No	48 (71.6)
Tumor characteristics	**Subgroup**	**N (%)**
Tumor Site	Sinonasal	24 (35.8)
	Others	43 (64.2)
T Stage	T1	5 (7.5)
	T2	15 (22.4)
	T3	6 (9.0)
	T4	41 (61.2)
N Stage	N0	62 (92.5)
	N1	2 (3.0)
	N2	3 (4.5)
M Stage	No	61 (91.0)
	Lungs	5 (7.5)
	Liver	1 (1.5)
Surgery before CIRT	Yes	43 (64.2)
	No	24 (35.8)
Margins status at surgical report	RX	8 (11.9)
	R1	31 (46.3)
	R2	4 (6.0)
	No Surgery	24 (35.8)
Residual tumor disease (Pre CIRT MRI)	Yes	30 (44.8)
	No	37 (55.2)
Toxicity after CIRT	**Subgroup**	**N (%)**
Maximum acute toxicity during Follow Up	G0	0 (0.0)
	G1	17 (25.4)
	G2	37 (55.2)
	G3	13 (19.4)
Acute mucositis	Yes (G1-G4)	49 (73.1)
	No (G0)	18 (26.9)
Maxillary ORN	Yes	11 (16.4)
	No	56 (83.6)

a side effect after irradiation. As of institutional practice, a complete dental examination and a dental–periodontal prophylaxis were requested. If indicated, atraumatic extraction of dental elements with a poor prognosis was performed at least 10 days prior to treatment. For each patient, a dental health certificate stating the good dental health was mandatory to start CIRT. No patient underwent bisphosphonates or concomitant systemic treatment during CIRT or adjuvant chemotherapy after CIRT. After CIRT patients were regularly followed up every 3 months for at least 2 years, then every 6 months since the fifth year, with magnetic resonance imaging (MRI) examination and fibroscopic local examination, with a staging total body Computed Tomography (CT) once per year. The diagnosis of maxillary ORN relied on the clinical symptoms reported by each patient, the oral-maxillo-facial physical examination, and the imaging scan acquired during the follow up reviewed by a senior radiologist. In case of maxillary ORN a maxillo-facial CT scan was also performed along with the follow up MRI to further study the affected bone. Acute and late toxicities were collected at each follow up clinical visit and scored according to the Common Terminological Criteria for Adverse Events (CTCAE), version 4 (22), including bone toxicity.

Carbon Ion RT Treatment Planning and Dose-Volume Histogram Analysis

A set of 2 mm thickness CT scan was acquired for treatment planning. Patients were immobilized with a personalized thermoplastic head–neck–shoulder mask equipped with bite-blocks and fixation points to the couch as previously reported (23). After the simulation CT, a MRI was acquired in the same setup condition. The gross tumor volume (GTV) was first outlined based on the morphological analysis of the planning CT after registration with MRI, namely, the primary tumor lesion or the surgical tumor bed, and the metastatic lymph nodes. The high-risk clinical target volume 1 (CTV1) was delineated by including the GTV and a minimum of 5 mm margin in all directions to cover the microscopic extent of the lesion. A larger CTV2 (including the CTV1) with the anatomical area at risk of perineural spread along the cranial nerves up to the skull base was also outlined. Irradiation to prophylactic lymph nodes was omitted. PTV1 and PTV2 were created, adding a 2 mm margin at each CTV. The total prescription dose was 68.8 Gy (RBE) in 16 fractions over 4 weeks (4.3 Gy (RBE)/fraction, 4 fractions/week). CTV2 was irradiated with a dose of 38.7 Gy (RBE) and the high-risk CTV1 was irradiated up to the total prescribed dose. Patients were treated with 2 to 4 fields with active pencil beam scanning technique. Treatment plans were optimized with Syngo PT (Siemens AG Healthcare, Erlangen, Germany) treatment planning system (TPS), and the LEM I model was used for RBE-weighted dose calculation with an ideal α/β ratio of 2 Gy. For this study, all treatment plans were recalculated with a research version of Raystation TPS (V6.99, Raysearch, Stockholm, Sweden), which provides both LEM I and MKM for RBE-weighted dose calculation.

The radiological morphology of the maxillary bone was first studied and then manually contoured on planning CT for each patient. The delineation of maxillary volumes included the alveolar process, the palatine process and the roots of the upper teeth in their own alveoli as previously reported (13). Pterygoid processes, sinus cavities and the crowns of the upper teeth were excluded. The mean maxillary volume in the patient series was 26.2 ml (range: 11.1–42 ml). The absolute maxillary volumes receiving doses D ranging from 10 to 60 Gy (RBE) were extracted from the dose volume histograms (DVHs) of the patients, and were expressed as V_D doses (V10, V20, V30, V40, V50, and V60), for both LEM and MKM calculated plans. For each V_D parameter of the LEM-based plans, the median value was calculated over the entire patient cohort, and patients dichotomized accordingly, to test the correlation with the incidence of ORN. Furthermore, the patient cohort was divided into two groups according to the appearance of ORN, and the average DVHs were calculated for both groups and radiobiological models (LEM and MKM). In the work by Sasahara et al., the absolute maxillary volume receiving 50 Gy (RBE) ($V50_{MKM}$) was found significant for the onset of ORN. We therefore extracted the $V50_{MKM}$ for each patient, from the MKM-DVH, and calculated the corresponding LEM-based dose received by the same volume of maxilla in each delivered plan, to compare our treated population with literature dosimetric data (13). For each LEM-based patient treatment plan, the presence of teeth in the irradiated PTV was recorded for analysis.

Statistical Analysis

The Chi-square test was performed to investigate both clinical and dosimetric variables as predictors of ORN risk. For statistically significant variables only, the strength of association was estimated by Cramer's V. The Kaplan–Meier method was adopted to evaluate the cumulative incidence of late post-radiation bone effects with respect to the only statistically significant variables in the univariate analysis. The difference that was observed between the cumulative incidence curves was compared with the Log-rank test. P-values <0.05 were considered statistically significant. The logistic regression model was subsequently applied to assess how the baseline risk of developing ORN varied according to the presence/absence of several given variables, namely, the V_D in 10 Gy (RBE) increments (V10–V60) extracted from the LEM-based calculated plans, and statistically significant clinical factors. To increase the power of our logistic regression model, we then limited the variables in the analysis to the V_D in 10 Gy (RBE) increments and the ORN incidence. If the estimated odds ratio was >1, the variable was assumed to be a risk factor because it increased the baseline risk. SPSS ver.19 software (IBM SPSS, IBM Corporation, Somers, NY) was used for statistics.

RESULTS

Maxillary ORN and Risk Factors

The median follow-up time was of 50 months (range 8–82 months). ORN was observed in 11 patients (16.4%) with a median time to ORN development of 24 months (range 8–54 months). Grade 1 ORN was observed in 2 patients (18.1%), G2 in 4 (36.3%), G3 in 4 (36.3%), and G4 ORN in 1 patient (9.3%). In

this latter case the patient had a microbial infection at the sphenoid bone not properly managed, and the necrosis expanded up to the right carotid channel approximately 10 months after CIRT. To avoid fatal bleeding due to carotid blow out, the patient had to perform carotid artery coiling. At the last follow up, the patient was alive without evidence of disease, and his necrosis stable. In 6 patients ORN started at the bone close to the teeth alveoli, and in one case followed the loss of one dental element. Majority of the cases had stable ORN at the last follow up (81.8%). In 2 cases with G3 ORN a surgical sequestrotomy was performed, while in one case the defect was repaired with a temporal muscle flap. Furthermore, 3 patients in the series took advantage of hyperbaric chamber treatment to stabilize the progression of their G2 necrosis after intermittent cycles of antibiotics for recurrent infections of the necrotic area.

On univariate analysis, the tumor site, and acute mucositis ≥G1 developed during CIRT were found to be statistically associated with maxillary ORN (**Table 2**). Majority of the patients with ORN had a tumor located in the sinonasal area (p-value 0.035). Among patients treated with CIRT who did not experience acute mucositis, none had maxillary ORN. Among those with acute mucositis, however, 22.4% also had a late effect of maxillary toxicity (p-value 0.028). Log-rank tests for these factors confirmed that the difference between the Kaplan–Meier curves was statistically significant. In fact, tumors located in the sinonasal area had a higher probability of developing ORN over time (p-value 0.053), as for patients experiencing acute mucositis during CIRT compared to the others (p-value 0.040).

Dose-Volume Risk Factors and Comparison With Published Data

In **Table 3** are reported the median cut-off value for V10–V60 and the V_D correlation with the ORN incidence in our series as extracted from the LEM-based patients treatment plans. On univariate analysis, all the V_D were statistically associated with maxillary ORN (V10, V20, V30, V40, V50, V55, and V60) together with the presence of teeth in the irradiated PTV. The incidence of ORN always occurred in patients where the maxillary volume received dose higher than or equal to the median cut-off. **Figure 1** shows an example of one of the patients in the series that experienced ORN along with the screenshot from its treatment plans (**Figure 1**). Log-rank tests for all the V_D confirmed that the survival function from ORN decreases as the irradiated maxillary volume increases, both for low and high dose levels (data not shown). Among those patients who had no upper teeth within the PTV, none reported ORN. Among those who had maxillary teeth within the PTV, 36.7% suffered from maxillary ORN after CIRT (p-value <0.001).

Considering all the V_D, the tumor site, the presence of teeth within the PTV and acute mucositis, the logistic regression model identified only $V60_{LEM}$ as a significant variable in differential risk compared with baseline risk (Hazard Ratio = 1.431, p = <0.001, 95% CI 1,194–1,716). The risk of developing ORN increased by 43.1% if a maxillary volume ≥0.6 ml was covered with at least 60 Gy (RBE) dose. When limiting the variables in the regression analysis to the V_D in 10 Gy (RBE) increments to increase the power of prediction, the $V60_{LEM}$ was still identified as independent factor significantly associated to the ORN development in our series.

When the cohort of the patients was divided into two groups according to the appearance of ORN, the average maxillary dose received by patients with ORN was higher at all volume levels, in both RBE languages (**Figure 2** for both LEM and MKM treatment plans). In **Figure 3** we have shown the cumulative incidence of CIRT-related ORN over time in our series when ranking the patients according to the $V60_{LEM}$.

TABLE 2 | Correlation of relevant patients clinical and tumor characteristics and ORN at univariate analysis.

Clinical Factors	Subgroup	ORN rate N (%)	p-value
Age	<57	8 (24.2)	0.089
	≥57	3 (8.8)	
Sex	Male	5 (15.6)	0.867
	Female	6 (17.1)	
Diabetes	Yes	1 (16.7)	0.986
	No	10 (16.4)	
Autoimmune Disease	Yes	0 (0)	0.525
	No	11 (16.9)	
Hypertension	Yes	2 (10.5)	0.413
	No	9 (18.8)	
Tumor Characteristics	**Subgroup**	**ORN rate (%)**	**p-value**
Tumor Site	Sinonasal	7 (29.2)	0.035
	Others	4 (9.3)	
T Stage	T1	0 (0)	0.303
	T2–T4	11 (17.7)	
Surgery Before CIRT	Yes	6 (14,0)	0.466
	No	5 (20.8)	
Residual Tumor Disease (Pre CIRT MRI)	Yes	5 (16.7)	0.588
	No	1 (7.7)	
Toxicity After CIRT	**Subgroup**	**ORN rate (%)**	**p-value**
Acute Mucositis	G1–G4	11 (22.4)	0.028
	G0	0 (0)	

TABLE 3 | Univariate analysis of dichotomized dosimetric factors from LEM-based calculated treatment plans to assess dose-volume relationship and risk of maxillary ORN.

V-DOSE	Subgroup	ORN (%)	p-value
V10	<8.6	0	<0.001
	≥8.6	32.4	
V20	<5.5	0	<0.001
	≥5.5	32.4	
V30	<4.4	0	<0.001
	≥4.4	32.4	
V40	<2.9	0	<0.001
	≥2.9	32.4	
V50	<1.0	0	0.001
	≥1.0	31.4	
V60	<0.6	0	0.001
	≥0.6	31.4	
Teeth in PTV	Yes	36.7	<0.001
	No	0	

Teeth within the PTV were considered a risk factor for analysis.

Finally, as for comparison with previous literature dosimetric data acquired with the MKM radiobiological model (13), the LEM-based dose received by the $V50_{MKM}$ of each patient in our cohort averaged over the patient population, was 55 Gy (RBE) ± 2 SD.

DISCUSSION

Bone necrosis is an important side effect, not only when irradiating with conventional photon RT, but also after CIRT. Here we analyzed for the first time the risk factors for ORN development in patients treated with LEM-based CIRT. Although we had a small sample of patients and of ORN events, we have still shown in our series the relevance of dosimetric parameters in predicting ORN risk after CIRT, with both the biological models mostly used in CIRT facilities worldwide for treatment planning, the LEM and MKM model.

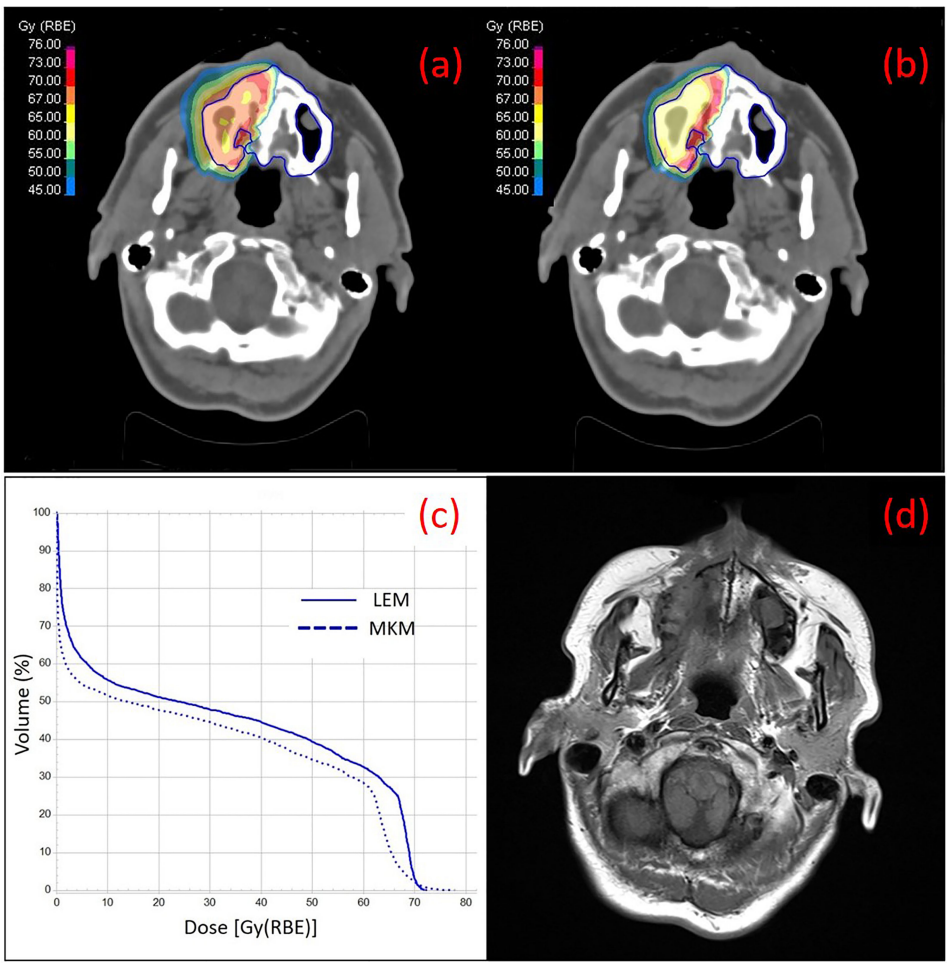

FIGURE 1 | Treatment plans on the simulation CT of one of the patients of the series with ACC at the right nasal cavity with color wash of the most representative isodoses at the maxilla (contoured in blue), calculated with LEM **(A)** and MKM **(B)** radiobiological model, are shown. The irradiation geometry consisted of 2 beam ports with couch rotation of 165°C and 180°C. In **(C)** the DVH curves for the maxilla calculated with LEM and MKM are depicted. In **(D)** a T1-weighted axial image taken from the 2 years post-CIRT MRI of the same patient is depicted with typical imaging features of maxillary Grade 1 necrosis.

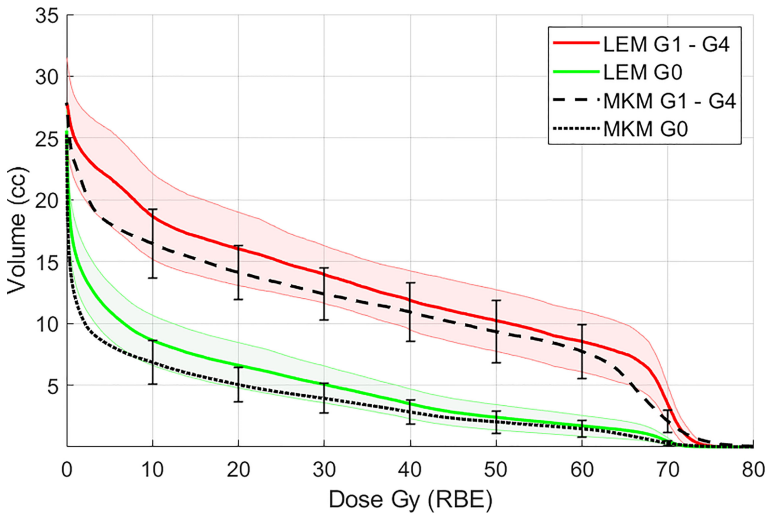

FIGURE 2 | Mean maxillary volumes at incremental dose levels from 10 to 60 Gy (RBE) calculated with the LEM model in patients with ORN (G1–G4, red solid line) vs patients without ORN (G0, green solid line). In black the maxilla DVH averaged for all the patients for the MKM model is also presented. Shaded bands and vertical error bars represent 2 SEM (Standard Error of the Mean) for the LEM and MKM model, respectively.

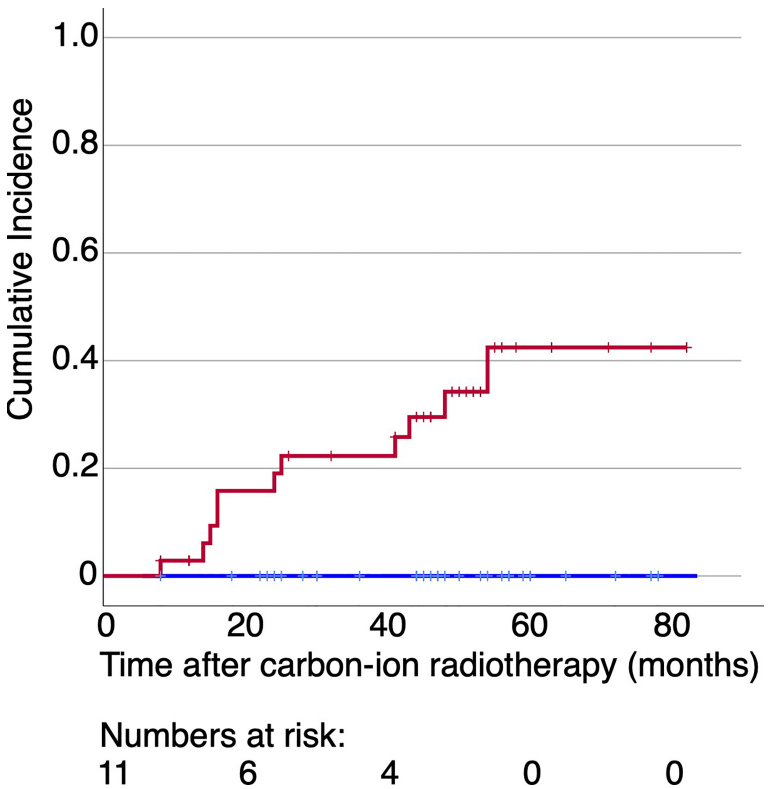

FIGURE 3 | Cumulative incidence of CIRT-related ORN over time for the patients irradiated with more than 60 Gy (RBE) at 0.6 ml of their maxilla (red line) or not (blue line) with data extracted form LEM-based treatment plans. No patients experienced ORN in case the dose to 0.6 ml of their maxilla was below 60 Gy (RBE).

Tumor treatment, especially when curative, must not disregard ORN risk to preserve patient quality of life. However, sparing dose to the maxilla, should never be prioritized at the cost of target coverage.

With a similar study design, in Sasahara et al. the $V50_{MKM}$ was found to be a risk factor at multivariate analysis, along with the presence of teeth in the PTV, in a series with different radioresistant tumors including ACC treated with CIRT at a prescription dose of 57.6 Gy (RBE) (13). As pointed out in Musha et al., the adjustment for the RBE model is necessary in CIRT facilities outside Japan (24), when investigating for dosimetric factors predisposing to toxicity such as ORN. As part of our investigation, here we wanted to translate the $V50_{MKM}$, significant factor for ORN reported for the Japanese series (13), into the corresponding V_D extrapolated from our LEM optimized plans recalculated with the MKM Japanese radiobiological model. In our patient population, $V50_{MKM}$ corresponded to $V55_{LEM}$. The statistical significance of 55 Gy (RBE) was not explicitly tested, but it is in good agreement with the dose value resulting significant at our multivariate analysis ($V60_{LEM}$), considering all the uncertainties involved. As a limit, several sources of dose deviation need to be considered when comparing clinical outcomes from patient series treated with different techniques, such as the beam delivery, the different beam number per fraction and beam arrangements, physical and RBE-weighted dose calculation uncertainties, the small number of patients, and different clinical characteristics (19). Furthermore, the power of the multivariate analysis presented here is low because of the small number of ORN events. Indeed, we might consider this study as a pilot trial, and for the future we aim at increasing the number of patients to produce more solid data on the clinical and dosimetric factors predisposing to ORN.

The relevance of the high doses when irradiating with CIRT in comparison to photon RT was pointed out in Ikawa et al., where 76 patients with oral nonsquamous cell carcinoma treated with CIRT at mostly with 64 Gy (RBE) prescription dose in 16 fractions equivalent to 89.6 Gy (RBE) at a fractionation of 2 Gy (RBE) per fraction, experienced 11.8% G3 ORN requiring surgery (25). Furthermore, in Naganawa et al. reporting on CIRT in 19 patients with oral malignant mucosal melanoma treated with 57.6 Gy (RBE) prescription dose in 16 fractions, all Grade 2 and 3 ORN were derived from the alveolar bone in the high dose–irradiated volume. Despite this, the mean $V50_{MKM}$ of the maxilla or mandible was 12.5 ml (range, 0–23.4 ml) for patients with Grade 0–1, and 12.5 ml (range, 3.1–22.3 ml) for patients with Grade 2–3 ORN, respectively, with a difference not statistically significant (26).

The impact of lower doses after CIRT on the mandible ORN onset has been recently reported to be significant when irradiating tumors localized at the oral cavity and oropharynx, for the $V30_{MKM}$–$V45_{MKM}$ at the mandible, and in case of $V10_{MKM}$–$V30_{MKM}$ to the teeth (24). In our study, all the V_D ($V10_{LEM}$–$V60_{LEM}$) tested at univariate analysis were statistically correlated with the occurrence of ORN. Maxillary ORN cases occurred in the subgroup of patients with V_D larger than- or equal- to the median volume for that DVH as it has been reported also in Sasahara et al. although with a different biological model (13). This indicates that the risk of ORN in our analysis of LEM-based calculated treatment plans might be enhanced both for larger bone volumes exposed to a low dose bath (<50 Gy (RBE)), and for smaller bone volumes exposed to a high dose >55 Gy (RBE). This finding might be translated into the importance of maximizing the dose conformity at the tumor target while sparing sensitive organs for toxicity, such as the maxilla, minimizing the volume receiving high doses to the maxilla in the range $V55_{LEM}$–$V60_{LEM}$, and the dose bath at lower doses. In this regard, CIRT in general for its physical and biological peculiarities, and the spot scanning beam delivery technique, might represent an advantage as postulated in Ikawa et al. when treating radioresistant tumors that requires high doses (25). In our series, even if the latency time for the ORN onset was similar as in Sasahara et al. (13), ORN incidence was less probable, not only because of the shorter follow up time in our series (50 vs 79 months), but possibly for the active spot scanning technique (vs passive beam) routinely employed at CNAO for treatments.

Not surprisingly, in our study with ACC in different locations in the maxillofacial area, ORN was mainly found after CIRT at the sinonasal site. In this regard, in Koto et al., over the 458 patients with sinonasal malignancies treated with different CIRT prescription doses but more frequently with 64 Gy (RBE) in 16 fractions, maxillary ORN was the most frequent late toxicity together with visual impairment, with G3 ORN reported in 18 patients (4%) and grade 2 in 36 (8%) (27).

In our series, the presence of superior dental elements within the PTV correlated with the onset and development of maxillary ORN at univariate analysis. In Bhattacharyya et al. the number of teeth irradiated with more than 50 Gy (RBE) was a significant independent risk factor for the development of oronasal fistula, which is also a late complication of CIRT. In order to reduce the risk, the authors suggested minimizing the number of teeth at a maximum of 2 within the volume irradiated with more than 50 Gy (RBE) (20). These data, together with data with conventional photon RT on the impact of dental infection on ORN incidence (28), confirm the benefit of pre-CIRT prophylactic dental avulsion and oral hygiene control before CIRT and during follow up adopted in CIRT facilities around the world, and at our center. Acute mucositis developed during the CIRT course (also significantly correlated with ORN in our series) together with the high radiation dose to the maxilla alveolar bone portion, might lead to superficial and then deep periodontal disease, gingival recession with increase susceptibility to infection with progressive bone injury leading to ORN (24). The elimination of odontostomatological risk factors (traumatic, inflammatory, and infectious events) and not, before the start of CIRT and during follow up, is of considerable importance for the outcome of the treatments and the quality of life of the patients. Time management of teeth extractions should also be strictly observed both before and after CIRT, and dental extraction protocol should be based on the individual plan isodose maps in case is not avoidable. As previously reported, teeth extraction or surgical procedure whenever not amenable should be performed not earlier than 1 year after CIRT to avoid ORN

progression to soft tissue and skin, and more serious sequelae with related deterioration of quality of life (29). According to the median time of onset of maxillary ORN in our analysis, it would be advisable to wait at least for 24 months after CIRT before any bone intervention. Conservative measures are recommended for early stage ORN, reserving surgery at later stages when no other medical options are available.

In our series, we investigated also pre-CIRT surgery as risk factor for ORN. According to Marunick et al., pre-RT surgical risk involves tissue trauma, reduced blood supply, cell death, collagen lysis, and greater metabolic challenge to repair. Surprisingly, here postoperative CIRT was not correlated with increased ORN risk differently from Marunick et al., where only the 4 patients included in the study who had jointly received both definitive tumor resection and neutron RT developed ORN at the residual maxillary orbital complex (30).

In summary, among all the toxicities of patients treated with CIRT in the head and neck area, ORN is one of the most serious and debilitating chronic post-treatment sequelae. Here, we have pointed out the $V55_{LEM}$–$V60_{LEM}$ irradiated volumes as most important factor correlated with ORN. The limitations of our study include the small patient number and the short follow up. For the future, clinical trials with larger patients' number and longer follow up are warranted. Based on our experience enriched by literature data, we might further summarize the recommendations for the optimal strategies to reduce ORN risk onset when irradiating tumors at the skull base, especially in facilities using the LEM-based CIRT: 1) to perform dental examination and prophylactic extraction procedures before CIRT if necessary, and close dentist follow up for all the 2-year period after CIRT more at risk of developing ORN, especially in case of patients with the maxilla covered for large volume by dose higher than 55 Gy (RBE); 2) to maximize the dose conformity to the maxilla by reducing volumes irradiated with dose higher than 55 Gy (RBE) and the dose bath below 50 Gy (RBE); 3) to avoid teeth in the PTV especially if the tumor does not involve the maxilla, and in case it is inevitable, to include not more than 2 teeth in the high dose PTV; 4) to prefer conservative measures and avoid surgical traumatic procedures after ORN onset. In case of unamenable necrosectomy after CIRT, our recommendation might be to remove the bone around the necrotic tissue by including at least the $V55_{LEM}$ isodose and higher, in order to facilitate tissue post-surgical healing.

DATA AVAILABILITY STATEMENT

The raw data supporting the conclusions of this article will be made available by the authors, without undue reservation.

ETHICS STATEMENT

The studies involving human participants were reviewed and approved by the Ethical committee San Matteo Hospital, Pavia (Italy). The patients/participants provided their written informed consent to participate in this study.

AUTHOR CONTRIBUTIONS

Conceptualization: BV, SR, and EO. Methodology and statistics: BV, SR, SM, EO, MM, and SR. Writing: MM and BV. Review and Editing: BV, SR, MM, MB, SRO, RI, AMC, SI, LP, MC, SM, and EO. Supervision: BV and EO. All authors listed have made a substantial, direct, and intellectual contribution to the work and approved it for publication.

REFERENCES

1. Marx RE. Osteoradionecrosis: A New Concept of its Pathophysiology. *J Oral Maxillofac Surg* (1983) 41(5):283–8. doi: 10.1016/0278-2391(83)90294-x
2. Leonetti JP, Weishaar JR, Gannon D, Harmon GA, Block A, Anderson DE. Osteoradionecrosis of the Skull Base. *J Neurooncol* (2020) 150(3):477–82. doi: 10.1007/s11060-020-03462-3
3. Tsai CJ, Hofstede TM, Sturgis EM, Garden AS, Lindberg ME, Wei Q, et al. Osteoradionecrosis and Radiation Dose to the Mandible in Patients With Oropharyngeal Cancer. *Int J Radiat Oncol Biol Phys* (2013) 85(2):415–20. doi: 10.1016/j.ijrobp.2012.05.032
4. Wahl MJ. Osteoradionecrosis Prevention Myths. *Int J Radiat Oncol Biol Phys* (2006) 64(3):661–9. doi: 10.1016/j.ijrobp.2005.10.021
5. Lee AW, Ng WT, Chan LL, Hung WM, Chan CC, Sze HC, et al. Evolution of Treatment for Nasopharyngeal Cancer–Success and Setback in the Intensity-Modulated Radiotherapy Era. *Radiother Oncol* (2014) 110(3):377–84. doi: 10.1016/j.radonc.2014.02.003
6. Tinganelli W, Durante M. Carbon Ion Radiobiology. *Cancers (Basel)* (2020) 12(10):3022. doi: 10.3390/cancers12103022
7. Orlandi E, Iacovelli NA, Bonora M, Cavallo A, Fossati P. Salivary Gland. Photon Beam and Particle Radiotherapy: Present and Future. *Oral Oncol* (2016) 60:146–56. doi: 10.1016/j.oraloncology.2016.06.019
8. Sulaiman NS, Demizu Y, Koto M, Saitoh JI, Suefuji H, Tsuji H, et al. Multicenter Study of Carbon-Ion Radiation Therapy for Adenoid Cystic Carcinoma of the Head and Neck: Subanalysis of the Japan Carbon-Ion Radiation Oncology Study Group (J-CROS) Study (1402 Hn). *Int J Radiat Oncol Biol Phys* (2018) 100(3):639–46. doi: 10.1016/j.ijrobp.2017.11.010
9. Akbaba S, Bostel T, Lang K, Bahadir S, Lipman D, Schmidberger H, et al. Large German Multicenter Experience on the Treatment Outcome of 207 Patients With Adenoid Cystic Carcinoma of the Major Salivary Glands. *Front Oncol* (2020) 10:593379. doi: 10.3389/fonc.2020.593379
10. Ronchi S, Vischioni B, Bonora M, Barcellini A, Locati LD, Castelnuovo P, et al. Managing Locally Advanced Adenoid Cystic Carcinoma of the Head and Neck During the COVID-19 Pandemic Crisis: Is This the Right Time for Particle Therapy? *Oral Oncol* (2020) 106:104803. doi: 10.1016/j.oraloncology.2020.104803
11. Vischioni B, Dhanireddy B, Severo C, Bonora M, Ronchi S, Vitolo V, et al. Reirradiation of Salivary Gland Tumors With Carbon Ion Radiotherapy at CNAO. *Radiother Oncol* (2020) 145:172–7. doi: 10.1016/j.radonc.2020.01.004
12. Loap P, Vischioni B, Bonora M, Ingargiola R, Ronchi S, Vitolo V, et al. Biological Rationale and Clinical Evidence of Carbon Ion Radiation Therapy for Adenoid Cystic Carcinoma: A Narrative Review. *Front Oncol* (2021) 11:789079. doi: 10.3389/fonc.2021.789079
13. Sasahara G, Koto M, Ikawa H, Hasegawa A, Takagi R, Okamoto Y, et al. Effects of the Dose-Volume Relationship on and Risk Factors for Maxillary Osteoradionecrosis After Carbon Ion Radiotherapy. *Radiat Oncol* (2014) 9 (1):92. doi: 10.1186/1748-717X-9-92
14. Kanai T, Endo M, Minohara S, Miyahara N, Koyama-ito H, Tomura H, et al. Biophysical Characteristics of HIMAC Clinical Irradiation System for Heavy-Ion Radiation Therapy. *Int J Radiat Oncol Biol Phys* (1999) 44(1):201–10. doi: 10.1016/s0360-3016(98)00544-6

15. Inaniwa T, Furukawa T, Kase Y, Matsufuji N, Toshito T, Matsumoto Y, et al. Treatment Planning for a Scanned Carbon Beam With a Modified Microdosimetric Kinetic Model. *Phys Med Biol* (2010) 55(22):6721–37. doi: 10.1088/0031-9155/55/22/008
16. Krämer M, Jäkel O, Haberer T, Kraft G, Schardt D, Weber U. Treatment Planning for Heavy-Ion Radiotherapy: Physical Beam Model and Dose Optimization. *Phys Med Biol* (2000) 45(11):3299–317. doi: 10.1088/0031-9155/45/11/313
17. Molinelli S, Magro G, Mairani A, Matsufuji N, Kanematsu N, Inaniwa T, et al. Dose Prescription in Carbon Ion Radiotherapy: How to Compare Two Different RBE-Weighted Dose Calculation Systems. *Radiother Oncol* (2016) 120(2):307–12. doi: 10.1016/j.radonc
18. Facoetti A, Vischioni B, Ciocca M, Ferrarini M, Furusawa Y, Mairani A, et al. *In Vivo* Radiobiological Assessment of the New Clinical Carbon Ion Beams at CNAO. *Radiat Prot Dosimet* (2015) 166(1-4):379–82. doi: 10.1093/rpd/ncv145
19. Molinelli S, Bonora M, Magro G, Casale S, Dale JE, Fossati P, et al. RBE-Weighted Dose in Carbon Ion Therapy for ACC Patients: Impact of the RBE Model Translation on Treatment Outcomes. *Radiother Oncol* (2019) 141:227–33. doi: 10.1016/j.radonc.2019.08.022
20. Bhattacharyya T, Koto M, Ikawa H, Hayashi K, Hagiwara Y, Tsuji H. Assessment of Risk Factors Associated With Development of Oronasal Fistula as a Late Complication After Carbon-Ion Radiotherapy for Head and Neck Cancer. *Radiother Oncol* (2020) 144:53–8. doi: 10.1016/j.radonc.2019.10.015
21. Bonora M, Vischioni B, Caivano D, Hasegawa A, Vitolo V, Ronchi S. EP-1189 Adenoid Cystic Carcinoma Of The Head And Neck Treated With Carbon Ion Radiotherapy At CNAO. *Radiother Oncol* (2019) 133:S659. doi: 10.1016/S0167-8140(19)31609-3
22. *Common Terminology Criteria for Adverse Events (CTCAE) Protocol Development CTEP*. Available at: https://ctep.cancer.gov/protocolDevelopment/electronic_applications/ctc.htm (Accessed on 15 July 2021).
23. Tuan J, Vischioni B, Fossati P, Srivastava A, Vitolo V, Iannalfi A, et al. Initial Clinical Experience With Scanned Proton Beams at the Italian National Center for Hadrontherapy (CNAO). *J Radiat Res* (2013) 54 Suppl 1(Suppl 1):i31–42. doi: 10.1093/jrr/rrt036
24. Musha A, Shimada H, Kubo N, Kawamura H, Okano N, Sato H, et al. Clinical Features and Dosimetric Evaluation of Carbon Ion Radiation-Induced Osteoradionecrosis of Mandible in Head and Neck Tumors. *Radiother Oncol* (2021) 161:205–10. doi: 10.1016/j.radonc.2021.06.022
25. Ikawa H, Koto M, Hayashi K, Tonogi M, Takagi R, Nomura T, et al. Feasibility of Carbon-Ion Radiotherapy for Oral non-Squamous Cell Carcinomas. *Head Neck* (2019) 41(6):1795–803. doi: 10.1002/hed.25618
26. Naganawa K, Koto M, Takagi R, Hasegawa A, Ikawa H, Shimozato K, et al. Organizing Committee for the Working Group for Head-And-Neck Cancer. Long-Term Outcomes After Carbon-Ion Radiotherapy for Oral Mucosal Malignant Melanoma. *J Radiat Res* (2017) 58(4):517–22. doi: 10.1093/jrr/rrw117
27. Koto M, Demizu Y, Saitoh JI, Suefuji H, Tsuji H, Okimoto T, et al. Definitive Carbon-Ion Radiation Therapy for Locally Advanced Sinonasal Malignant Tumors: Subgroup Analysis of a Multicenter Study by the Japan Carbon-Ion Radiation Oncology Study Group (J-CROS). *Int J Radiat Oncol Biol Phys* (2018) 102(2):353–61. doi: 10.1016/j.ijrobp.2018.05.074
28. Wang TH, Liu CJ, Chao TF, Chen TJ, Hu YW. Risk Factors for and the Role of Dental Extractions in Osteoradionecrosis of the Jaws: A National-Based Cohort Study. *Head Neck* (2017) 39(7):1313–21. doi: 10.1002/hed.24761
29. Dell'Era V, Aluffi Valletti P, Garzaro G, Garzaro M. Maxillo-Mandibular Osteoradionecrosis Following C-Ion Radiotherapy: Clinical Notes and Review of Literature. *Eur J Inflammation* (2020) 18:1–6. doi: 10.1177/2058739220934562
30. Marunick MT, Bahu SJ, Aref A. Osteoradionecrosis of the Maxillary-Orbital Complex After Neutron Beam Radiotherapy. *Otolaryngol Head Neck Surg* (2000) 123(3):224–8. doi: 10.1067/mhn.2000.107403

Conflict of Interest: The authors declare that the research was conducted in the absence of any commercial or financial relationships that could be construed as a potential conflict of interest.

Publisher's Note: All claims expressed in this article are solely those of the authors and do not necessarily represent those of their affiliated organizations, or those of the publisher, the editors and the reviewers. Any product that may be evaluated in this article, or claim that may be made by its manufacturer, is not guaranteed or endorsed by the publisher.

frontiers in Oncology

REVIEW
published: 09 March 2022
doi: 10.3389/fonc.2022.806153

Management of Motion and Anatomical Variations in Charged Particle Therapy: Past, Present, and Into the Future

Julia M. Pakela[1], *Antje Knopf*[2,3], *Lei Dong*[1], *Antoni Rucinski*[4] *and Wei Zou*[1]*

[1] Department of Radiation Oncology, University of Pennsylvania, Philadelphia, PA, United States, [2] Department of Radiation Oncology, University Medical Center Groningen, University of Groningen, Groningen, Netherlands, [3] Department I of Internal Medicine, Center for Integrated Oncology Cologne, University Hospital of Cologne, Cologne, Germany, [4] Institute of Nuclear Physics, Polish Academy of Sciences, Krakow, Poland

OPEN ACCESS

Edited by:
Stewart Mac Mein,
German Cancer Research Center (DKFZ), Germany

Reviewed by:
Lennart Volz,
Helmholtz Association of German Research Centres (HZ), Germany
Jingjing Dougherty,
Mayo Clinic Florida, United States
Chia-ho Hua,
St. Jude Children's Research Hospital, United States

***Correspondence:**
Wei Zou
Wei.Zou@pennmedicine.upenn.edu

Specialty section:
This article was submitted to Radiation Oncology, a section of the journal Frontiers in Oncology

Received: 31 October 2021
Accepted: 04 February 2022
Published: 09 March 2022

Citation:
Pakela JM, Knopf A, Dong L, Rucinski A and Zou W (2022) Management of Motion and Anatomical Variations in Charged Particle Therapy: Past, Present, and Into the Future. Front. Oncol. 12:806153. doi: 10.3389/fonc.2022.806153

The major aim of radiation therapy is to provide curative or palliative treatment to cancerous malignancies while minimizing damage to healthy tissues. Charged particle radiotherapy utilizing carbon ions or protons is uniquely suited for this task due to its ability to achieve highly conformal dose distributions around the tumor volume. For these treatment modalities, uncertainties in the localization of patient anatomy due to inter- and intra-fractional motion present a heightened risk of undesired dose delivery. A diverse range of mitigation strategies have been developed and clinically implemented in various disease sites to monitor and correct for patient motion, but much work remains. This review provides an overview of current clinical practices for inter and intra-fractional motion management in charged particle therapy, including motion control, current imaging and motion tracking modalities, as well as treatment planning and delivery techniques. We also cover progress to date on emerging technologies including particle-based radiography imaging, novel treatment delivery methods such as tumor tracking and FLASH, and artificial intelligence and discuss their potential impact towards improving or increasing the challenge of motion mitigation in charged particle therapy.

Keywords: motion management, 4DRT, pencil beam scanning (PBS), particle therapy, proton therapy

INTRODUCTION

The use of charged particles for radiation therapy (RT) represents a valuable treatment paradigm because their unique dose deposition properties, including maximum dose deposition at the Bragg peak and rapid distal falloff, allow for dose to be conformed tightly around the tumor while sparing normal tissues (1–6). However, these advantageous properties present a challenge in the presence of motion, because the same steep dose gradients which provide the benefit of lower integral dose in surrounding tissues are vulnerable to even small displacements in the patient geometry. In addition, because their range is dependent on tissues along the beam path, charged particles traveling through heterogenous tissues (such as in lung cancer) also suffer from dose deviations due to motion-induced range uncertainties (7).

Proton therapy is by far the most widely implemented form of charged particle therapy, with forty-one proton centers operating in the US and ninety-nine centers operating worldwide (8). Initial proton therapy systems were based on passive scattering, in which a scattered beam is passed through a range-modulating wheel [to determine the width of the spread-out Bragg peak (SOBP)] and a custom collimator and compensator (to laterally shape the beam and match the distal edge of the SOBP to that of the patient target). However, this scattering method is limited in its ability to conform dose to the proximal boundary of the target (9). Over time, a pencil beam scanning (PBS) method was developed which exhibited improved dose conformation around the target in comparison to passive scattering methods; dosimetric benefits of proton PBS have been verified across a diverse range of disease sites, including brain, esophageal, oropharyngeal, breast, and liver cancers (3, 6, 10–14). Proton PBS is performed by scanning a monoenergetic pencil beam over a grid of positions and repeating for multiple beam energies to create a SOBP with a varying span along the lateral direction. Treatments using PBS delivery utilize intensity modulation of the pencil beam spots and are optimized using one of two planning techniques. Single field uniform dose (SFUD) planning refers to a planning technique in which pencil beam weights are optimized independently for each field according to the planning objectives, resulting in treatment plans where each field contributes similar tumor coverage. Multi-field optimization (MFO) is a planning technique in which the pencil beam weights of every field are optimized simultaneously. Of these two planning methods, SFUD is more robust against motion because it only requires the consistency of anatomy during the treatment delivery of its own field. MFO requires the integrity of anatomy during the entire treatment session from all treatment fields; therefore, the potential impact of motion is more significant. PBS-based proton therapy is often referred to as intensity-modulated proton therapy (IMPT), which is created by simultaneously optimizing the beam intensity and energy for each spot/delivery unit. The addition to range uncertainties and sensitivity due to steep dose gradients at the distal end of the target, proton PBS presents an additional challenge for precise dose delivery under conditions of motion due to interplay effects between the scanning beam and intra-fractional motion in the patient anatomy (5, 15). The interplay of the proton and ion pencil beam scanning and organ motion has been shown to impact the target dose coverage in multiple disease sites (16–19). Recent lung cancer simulation studies found that interplay effects combined with small spot sizes (~3mm) resulted in a loss of 2-year local control of up to 18.5% ± 25.2% compared with the static cases for single fraction delivery; for multi-fractionation treatment significant loss of local control was observed only for large motion amplitudes (>30mm) (16). For esophageal cancer, a recent planning study found PBS proton therapy plans using posterior beams to be more robust against underdosage ($V95\%_{CTV}$ <97%) in comparison with IMRT, but interplay effects had an increasingly negative impact on the dose distribution as the number of simulated fractions was decreased below 10 (17). As the beam delivery time structures and intensities from various charged particle accelerators such as synchrotron or cyclotron are different (20), they can result in different interplay effects (21).

As of 2021, there currently exist twelve operating carbon-ion treatment centers with five more under construction (8, 22). Similar to protons, carbon and other heavier ions such as helium exhibit highly localized dose deposition at the Bragg peak. An additional advantage of treating with carbon ions (over photons and protons) is that they exhibit steeper lateral penumbra and higher linear energy transfer (LET), leading to increased relative biological effectiveness (RBE) (23). Like protons, carbon ions can be delivered either *via* passive scattering or pencil beam scanning; however, largely due to cost the majority of centers perform only fixed beam delivery, with only two capable of a full range of treatment angles through rotating gantry (24). A challenge of treating with carbon and other heavy ions is that the increased sharpness of the lateral penumbra in combination with the Bragg peak results in heightened dose uncertainties in the presence of motion. In addition, because carbon ions exhibit a distal tail of dose beyond the Bragg peak due to nuclear fragmentation, the potential for dose uncertainties distal to the target volume are of greater concern (24). Additionally, for carbon and heavier ions, RBE is nonlinear with respect to the absorbed dose level, particle energy, and atomic number (25), thus while it is typical to consider a constant RBE for proton radiotherapy (26), when considering the carbon ion interplay effects, the changing RBE along the beam path should be taken into consideration.

Motion management refers to techniques in RT which seek to mitigate the effects of inter- and intra-fractional motion. Causes of inter-fractional motion include weight loss, tumor shrinkage, and organ deformations such as those caused by changes in the volume of the rectum and bladder (27, 28). Inter-fractional motion occurs between fractions, typically separated by hours or days, and thus if correctly identified can be corrected with an established adaptive planning process. Intra-fractional motion is the result of respiration and to a lesser extent cardiac motion and peristalsis. Because intra-fractional motion occurs during treatment on a timescale of minutes to seconds, it represents a greater challenge. Imaging and treatment planning modalities which take into consideration time in addition to the 3-dimensional space of the patient are commonly referred to as 4D (e.g., 4DCT and 4DRT).

Motion management can generally be categorized into one of two strategies: 1) prevent or reduce anatomical motion, or 2) adapt treatment to motion during planning or delivery. The success of these strategies depends on access to imaging techniques which allow motion and/or dose deposition to be faithfully monitored and quantified. While much work has been done to address challenges in motion related to charged particle therapy, currently there is limited standardization of treatment protocols, with many centers developing their own unique standard of procedures and best practices (29). For example, in the case of proton therapy for thoracic cases, the Particle Therapy Co-Operative Group (PTCOG) Thoracic and Lymphoma Subcommittee has begun the work to define a set of guidelines

for best practices, but stress that it is still necessary for institutions to determine their own protocols, due to variations in technology across institutions as well as lack of commercialization for many solutions (9). Recommendations for control at other treatment sites are scarce.

This review seeks to provide an overview of current clinical practices for intra- and inter-fractional motion management in charged particle therapy as well as progress to date on emerging technologies that have potential to be used for or impact motion management. The remainder of this review is organized as follows: Section 2 provides an overview of the current state of the art in motion management implemented in clinical charged particle therapy, including motion reduction techniques at the major anatomical sites, imaging techniques for monitoring intra- and inter-fractional motion, as well as treatment planning, delivery, and plan evaluation mitigation strategies; Section 3 discusses promising ongoing research and emerging technologies in charged particle therapy which will either directly benefit or necessitate further innovations in motion management.

CLINICAL IMPLEMENTATION: THE CURRENT STATE OF THE ART

Motion Control Techniques at Simulation and Delivery

Motion control techniques consist of methods which seek to reduce patient motion and ensure consistent geometrical orientation during and between fractions.

Thorax and Upper Abdomen

In the thorax and upper abdomen, respiration is the most significant cause of intra-fractional anatomical variations. In thoracic tumors, motion control methods for proton therapy are recommended when a patient's target motion amplitude exceeds a pre-determined threshold (established per institution based on target location and treatment parameters) (9). Breath-hold is a standard technique for minimizing respiration-based movement during treatment delivery to the thorax and abdomen. Breath-hold involves patients temporarily suspending respiration at specific, reproducible lung volumes. Breath-hold techniques can be classified as *voluntary*, in which the patient is in control of their breathing (30), or *active*, in which the patient's airflow is temporarily blocked by a valve (31). A widely used commercial voluntary breath-hold system is the SDX Respiratory Gating System (DYN'R Medical Systems, Toulouse, France). The SDX system monitors the inspiration and expiration volume of a patient in real-time and provides visual display of the breathing-trace through patient-worn goggles. This allows the patient to perform consistently reproducible breath-holds at a specific volume for a specific duration of time. Typically, for thoracic cases, deep inspiration breath-hold (DIBH) is preferrable (holding in a deep breath at an individually determined volume threshold) because this increases the distance between the tumor and organs at risk. DIBH proton treatments to Hodgkin lymphoma and left breast cancer have shown significant reduction in lung and heart dose compared with the photon plans (32–34). High frequency percussive ventilation (HFPV) is an example of an active breath hold technique. In HFPV, the patient receives high frequency pressured pulses of air, causing suppression of respiratory motion and allowing for longer breath-holds. A drawback of HFPV is the requirement of anesthesia support, which may not be always available in radiation oncology. A recent study has also reported on the use of an enhanced deep inspiration breath hold (eDIBH), which involves passive, patient-controlled breath holds aided by preoxygenation, hyperventilation, and patient coaching to increase breath-hold times. eDIBH was found to reduce variability in lung volume and position in comparison with HFPV (35). Not all patients are candidates for breath-hold techniques. Patients with impaired respiratory function typical of advanced lung cancer may be physically unable to tolerate breath holds, while younger patients may be unable to follow instructions for voluntary breath-hold. Another limitation of breath-hold based motion management is it cannot account for inter-fractional anatomical changes, such as tumor shrinkage and lung density changes which can result in changes to the water equivalent path length (36).

Abdominal compression (AC) belts are a relatively inexpensive and easy-to-implement option for minimizing intra-fractional motion from respiration. For charged particle therapy, thin belts made of homogenous materials are preferred to ensure that the belt has a minimal and reproducible impact on the charged particle range (37). For PBS proton therapy, the use of AC has been shown to be valuable for reducing moderate to large motion during treatment of liver tumors (37, 38). Additionally, AC in combination with layered rescanning and respiratory gating has been clinically adopted for motion mitigation in carbon ion therapy (39). A limitation of compression belts is that the degree of compression applied is limited by individual patient tolerances, with some patients are unable to tolerate abdominal compression during treatment. The compression belt typically has fiducial markers and pressure meter to ensure consistent positioning of the belt during treatment. Nonetheless, it is recommended to avoid having particle beam passing through the device to avoid potential water equivalent thickness (WET) variations in the setup (38).

Lower Abdomen and Pelvic Regions

For the lower abdomen and pelvic regions, positioning techniques focus on reducing motion caused by volume changes in the rectum and bladder. Consistency of the position of bladder and rectal volume across and during treatment can be improved through hydration and voiding schedules (40, 41). Rectal balloons are used to immobilize the prostate and maintain the rectum at a consistent volume during simulation and treatment, reducing uncertainties from variable rectal filling and gas and allowing for smaller target margins and greater sparing of the rectum during external beam radiotherapy (42). For charged particle therapy, rectal balloons are inflated with water instead of air to maintain a consistent water equivalent pathlength (41); this removal of the rectal air cavity likely reduces the dosimetric benefit to the anterior rectal wall which is seen

with the air-based inflation used in photon therapy (42, 43). Recently, a rectal biodegradable hydrogel that is implanted between the prostate gland and the rectum was implemented in the clinic. For proton radiotherapy, the use of hydrogel provided improved rectal sparing and decreased late gastrointestinal toxicity compared with the use of a rectal balloon, suggesting that motion due to moderate rectal filling does not require intervention if adequate separation (8-13mm in this study) between prostate and rectum is achieved (44).

Imaging at Simulation and Delivery

Imaging technologies play a pivotal role in motion management for radiation therapy, allowing for the contouring of structures for treatment planning and providing a means to assess and monitor organ motion, either directly by imaging the motion of organs or *via* indirectly by imaging markers placed in tissue, e.g., fiducial markers. Computed tomography (CT) images are the gold-standard modality for treatment planning; however, CT images acquired during free breathing can suffer from motion artifacts, leading to uncertainty in the true delineation of boundaries between tumor, normal tissues, and organs at risk (45). For this reason, 4D computed tomography (4DCT) images, in which a series of CT images are acquired during different phases of the breathing cycle, have become a standard in treatment planning for thoracic and abdominal regions. One limitation of 4DCT is that irregularities in patient breathing during image acquisition leads to inherent uncertainties in how faithfully the final 4D images represent the patient's anatomy during respiration. Patients can also exhibit variations in their breathing cycle during day-to-day treatment; the intra-fractional motion patterns from respiration can themselves be subject to inter-fractional variations. For proton PBS therapy, weekly offline CT assessment are recommended for patients expected to experience inter-fractional changes (9). Because not all commercial treatment planning software supports multi-image planning, information from the 4DCT can be utilized for treatment planning by transforming the series of images into a single "representative" view of the patient, such as average intensity projection (AIP), maximum intensity projection (MIP) and mid-ventilation (MidV) (46).

Simulation for proton therapy treatment planning often involves fusion with tissue function-related positron emission tomography (PET) and magnetic resonance imaging (MRI) for target delineation. 4DPET provides information on tumor motion in addition to the metabolic information about the tumor structure and has been shown to be a valuable tool for target delineation in lung cancers (47). 4DMRI provides high contrast of soft tissues and has shown promise for motion-robust target delineation in both abdominal and lung cancers (48–50). A recent study further used 4DMRI and 3DCT to generate synthetic 4DCT for 4D dose calculation and interplay effect evaluation in pancreatic cancer (51).

Conventional cone-beam CT (CBCT) was first implemented for proton therapy for patient setup in 2012 (52). Daily CBCT adds valuable 3D anatomy information and soft tissue contrast in patient setup alignment compared to 2D kV imaging. It can also be used to identify inter-fractional tumor regression, weight loss, organ filling or atelectasis. Efforts have been made to enable CBCT for online adaptive planning for proton therapy (53–56), but it suffers from reduced image quality in comparison to CT due to restricted field of view, lower soft-tissue contrast, and inequivalent relation between CBCT voxel values and Hounsfield units. CT-on-Rails has also been investigated as an alternative to daily CBCT imaging for daily adaptive radiotherapy due to its ability to provide higher quality images at "near-treatment-position", though widespread adaption of CT-on-Rails is limited due to increased cost and larger footprint (57). Interested readers can find an in-depth discussion on radiological image guidance in particle therapy in the recent review by Landry and Hua (58).

Internal tumor motion during delivery can be monitored through implanted markers, such as electromagnetic sensors (59–61) and fiducial markers (62), with externally placed detectors. A benefit of EM systems or on-board imagers is that they do not require line-of-site and can thus also capture signal from internally placed markers. Tang et al. have used electromagnetic transponders to assess the intra-fractional prostate motion during PBS SFUD delivery (63). A major limitation of electromagnetic systems is that they are sensitive to distortions of the generated electromagnetic signal; a recent study found EM tracking systems unable to provide clinically useful measurements during proton therapy in the presence of gantry motion or when too close to a CT scanner (61). In addition, caution should be taken in the selection of the implanted markers for proton therapy to avoid image artifacts and dose disturbance (64).

Fluoroscopy with implanted markers can produce 2D images with high spatial and temporal resolution. Researchers at Hokkaido University in Japan have pioneered the clinical implementation of a gated proton PBS treatment system that utilizes fluoroscopy for real time tumor tracking through an internally placed gold fiducial marker (65–67). Aside from requiring an invasive placement, a potential risk is that the fiducial marker could migrate from its original placement during the course of treatment (68).

Another strategy for assessing tumor motion is to measure the patient's surface motion, which can then be used as a surrogate to infer the position and movement of the internal target (69). Surface imaging uses cameras/projectors mounted in the treatment room to capture pseudo-random light patterns projected on the patient surface to derive the patient surface change. It is non-ionizing and can monitor a large surface constantly from a distance; thus in addition correcting for inter-fractional motion during daily positioning, surface imaging is an attractive option for monitoring intra-fractional motion (70). A reported challenge of surface imaging in a clinical proton setting is that the layout of the therapy room can lead to restricted field of view or occlusion of the surface cameras at treatment gantry angle (71). Clinical applications of surface imaging for daily positioning of breast cancer proton therapy patients have been reported and found to achieve similar dosimetric accuracy to daily CBCT (70–72); however it was

noted that surface imaging alone can be insufficient to detect internal shifts of breast implants (71). Further surface imaging studies have noted limited correspondence between measured surface motion and internal target motion (73–75). Nevertheless, a recent technological assessment showed that optical tracking has better potential than electromagnetic tracking of embedded fiducial markers for use in PBS proton therapy (61).

Treatment Planning and Delivery

Many different strategies exist to account for patient motion during the treatment planning process or delivery itself. Mitigation during treatment planning and delivery is characterized by an approach of working with or around existing patient motion. These strategies rely on additional information input from imaging, either during simulation (in the case of treatment planning) or in real time during treatment delivery.

Motion-Encompassing Margins

One of the most widely used planning methods to account for expected patient motion in charged particle therapy is to delineate an additional margin around the tumor target, commonly denoted the internal target volume (ITV), which is defined as the overlay of boundaries for all (or a select subset of) CTV positions collected during 4DCT (76). While the use of ITVs alone is not considered adequate for motion management in PBS proton therapy due to range uncertainties and interplay effects, ITVs are recommended for use in combination with other motion mitigation strategies to account for any residual motion uncertainties (77). For example, for patients being treated with breath-hold, several breath-hold CT scans are performed during simulation to create an ITV that encompasses the variability of the breath-hold position for a particular patient. ITV structures can also be used in conjunction with compression belts under conditions of free breathing to account for residual motion. ITVs can be constructed using different methods based on 4DCT images, including Max/Min inhale-based, MIP-based, and MidV-based. In addition, the concept of using density overrides within and around the ITV has been shown in recent simulation studies to improve dose coverage when the target moves through regions of highly variable density (78, 79). Once an appropriate ITV has been determined, additional population-based margins reflecting setup and beam-specific range uncertainties are applied to generate a planning target for each beam (80).

Repainting

A unique challenge for particle therapy in the face of intra-fractional motion is the additional dose uncertainty caused by interplay effects between patient anatomical motion and the delivery sequence of the scanning beam. A mitigation method is to use repainting, which refers to a treatment delivery method applied for PBS by rescanning over the same spot positions multiple times (using an appropriately lower fraction of monitor units defined by the total number of repetitions) (81, 82). Studies on repainting for PBS proton therapy have found that this method improves dose homogeneity; however, interplay effects were found to be more pronounced for small tumor sizes, motion greater than 10mm, and small spot sizes (83, 84). Another recent study demonstrated that interplay effects due to motion could be further reduced using a novel repainting strategy in which the repaintings for a given energy layer (and by extension the repaintings for each spot position) are spread out evenly over the entire breathing cycle (85). This was accomplished by designing a flexible delivery schedule in which the number of times a given spot is repainted as a function of its assigned MU and the time it takes for the scanned beam to reach the given spot from its previous position, such that: 1) each spot is repainted as many times as possible, 2) repaintings for each spot are spread evenly over the breathing cycle, and 3) the total time to deliver a given energy layer is constricted to the length of the breathing cycle. One challenge for the repainting strategy is that it may encounter the minimum MU requirements because it requires the delivery of a smaller amount of dose multiple times. Sometimes it may only be possible to repaint the distal layers because they usually receive more dose.

Beam Angle Selection and Spot Size

In treatment planning, beam angle selection can help to minimize dose deviations by selecting beam orientations that are robust to motion. Proton range is sensitive to tissue variations along the beam path. Movement can cause tissue variation uncertainties that lead to dose deposition uncertainties. Thus, in selecting beam angles for proton therapy, it is advantageous to avoid large tissue density gradients in the beam path and to try to keep the beam angle parallel to the dominant direction of tumor motion (9). It is also important to avoid beam orientations such that the distal fall-off region of the proton range proximally borders an OAR, as range uncertainties could lead to unintended overdosing OAR or underdosing the CTV. Specific protocols for the selection of beam angles have been found to vary across facilities, but nevertheless follow these guidelines discussed above (76).

The pencil beam spot size, defined as the full width at half-maximum of the beam spot in air, has been identified as an additional beam parameter that impacts dosimetric deviations in PBS proton therapy (16, 63, 76). Specifically, larger spot sizes (~13 mm) have been shown to reduce the interplay effect compared with smaller spot sizes (~3mm) (16).

Respiratory Gating

Respiratory gating is a dynamic treatment delivery method used to ensure precise dose deposition in the presence of respiratory motion. In this technique, the treatment beam is turned on only when the patient is in a specific phase of their respiratory cycle. Gating methods can be performed in conjunction with breath-hold techniques or during free breathing; clinical use for charged particles has been described for several disease sites, including the lung, breast, and liver (86–89). Implementation of gating relies on the ability to accurately monitor patient motion during treatment delivery and on the ability for patients to perform reproducible breath holds or reproducible free-breathing cycles. Motion monitoring for charged particle gating is typically accomplished *via* external surface imaging (90). For PBS

proton therapy, a gating approach to treatment delivery in conjunction with real-time fluoroscopy imaging has been implemented and shown *via* simulation studies to be capable of significantly reducing mean liver dose while providing better target coverage in comparison with a free-breathing approach (66, 91). A limitation of beam gating for PBS-based therapies is that they can still suffer from interplay effects due to residual motion during the selected gating window; recent simulation studies suggest this can be mitigated through the use of laterally and longitudinally overlapping pencil beams or phase-controlled rescanning (92, 93). Another reported challenge to the clinical use of gating for PBS is balancing the gating window width with the duty cycle (ratio of beam-on time to overall treatment time). While a narrower window width provides improved motion mitigation, it can also lead to unacceptably long treatment times. A recent simulation study for PBS-based gated therapy of liver tumors found duty cycle dropped by as low as 10% when a small window width (3mm) was used for a gating-only approach (94). Gating in combination with repainting has been shown to be more efficient in motion mitigation than repainting alone (94, 95). Another challenge of implementing gating for proton therapy is that proton systems are subject to latency in beam control, meaning once a gating signal is detected from the patient, the treatment machine requires a delay to turn-on or turn-off the beam. This delay can sometimes be too long (150-200 ms in a 3-4 s breathing cycle) to perform reliable cycle-to-cycle beam delivery. For this reason, respiratory gating in particle therapy is usually performed in conjunction with breath-hold techniques, which provide a longer treatment window such that the beam's gate-lag time is insignificant.

4D and Robust Optimization

In radiation therapy, robust optimization (RO) can be used during the treatment planning process to design plans which are robust to the uncertainties associated with treatment delivery, including setup errors and patient motion. Traditionally for photons, such uncertainties in treatment planning have been accounted for by using an expanded margin around the CTV, called the planning target volume (PTV). In proton therapy, the additional presence of range uncertainties and, in the case of PBS, uncertainties from the interplay effect render the use of traditional margin-based solutions insufficient.

3DRO refers to a class of robust optimization techniques which account for patient setup and range uncertainties during treatment plan optimization. Implementations of 3DRO include probabilistic treatment planning, scenario-wise mini-max RO, and voxel-wise worst-case RO. In probabilistic optimization, setup and range uncertainty scenarios are randomly sampled from an assumed probability distribution to produce a large set of potential dose distributions (96, 97). This method is computationally expensive and requires prior knowledge of the probability distributions of the treatment conditions. Scenario-wise mini-max and voxel-wise worst-case RO evade these challenges by performing plan optimization based on either a smaller set of worst-case scenarios or a single worst-possible dose distribution (98–100). 4DRO can be considered an extension of 3DRO in that it also considers intra-fractional variations caused by organ motion such as respiration. Recent simulation studies have shown promising benefits of 4DRO for scanning proton therapy, including improved target coverage and improved robustness against interplay effects (100–102). In a study by Ge et al. comparing the performance between 3DRO and an in-house 4DRO system on a set of 10 lung cancer patients treated with IMPT, the 4DRO system was found to outperform both 3DRO and traditional PTV-based optimization methods in terms of dose homogeneity, CTV target coverage, and dose robustness considering setup uncertainties and patient motion (100). Another recent study published by Mastella et al. looked at the incorporation of gating with 4DRO for 20 lung cancer patients found that this 4DRO optimized gating approach resulted in significant reduction to lung dose while maintaining target coverage (102).

Studies have been performed for carbon ion 4D dose reconstruction and optimization. Reconstruction of the delivered 4D RBE dose needs to consider the tumor motion and temporal structure of the beam delivery (103). Eley et al. (104) worked on a 4D optimization approach for scanned beam tracking to reduce the dose to organs near the moving target. Graeff et al. (105) proposed a 4D optimization scheme that divides the target into sectors and to each of the sector with a delivers dedicated raster field corresponding to individual motion phases. Expanded carbon ion 4D-IMPT including the robust non-linear RBE-weighted optimization was also included (106, 107). For clinical application, it is essential to consider both the 4D treatment planning systems and 4D treatment control systems (108). 4DRO is currently commercially available through the RayStation treatment planning system (RaySearch Laboratories, Stockholm, Sweden) (109).

Plan Evaluation

Due to the interplay effect in proton PBS delivery, special considerations should be taken in evaluating PBS proton plans to ensure that the intended dose distribution can be delivered faithfully under conditions of anatomical motion. The guidelines provided by the Particle Therapy Co-Operative Group (PTCOG) Thoracic and Lymphoma Subcommittee recommended the use of a 4D phantom to evaluate motion interplay effects and the effectiveness of planned motion mitigation techniques, though at this time such a protocol is admittedly out of reach for most centers due to the expense of 4D phantoms (9), which have only recently become commercially available. In the same publication, the importance of continuous plan evaluation (through regular repeat 4DCT scans) to assess the need for plan adaption is also emphasized. Meijers et al. reported on a 4D dose reconstruction method which utilizes weekly repeated 4DCT scans in combination with treatment log files and breathing pattern records from each fraction (110, 111). This dose reconstruction method can be used to calculate dose accumulation on a per-fraction basis, allowing the clinical team to monitor motion-based dose degradation over the course of treatment and to help to trigger adaption when necessary. Recent studies have also reported on the implementation of tools designed for evaluation of PBS proton plans for moving targets. For example, Riberio et al. reported on the development and application of a plan

evaluation tool, 4D robust evaluation method (4DREM), which considers both setup errors as well as respiratory motion and the interplay effects (112), while Korevaar et al. developed a scenario-based plan evaluation method which allows for comparison between photon and proton plans (113). In another hand, fast 4D dose calculation with GPU-accelerated dose-engines enable potential clinical use and can be integrated into the optimization process (114–116). Another consideration for 4D dose calculation is that the temporal resolution used can impact the calculated final accumulated dose distribution, a recent simulation study found that the use of finer temporal resolutions for 4D dose calculations can help to reduce the over-estimation of interplay effects for hypo-fractionated treatments (19).

FUTURE TECHNOLOGIES

Advanced Imaging Techniques

A major directive in motion management is to develop methods that allow for high quality *in vivo* observation of internal anatomic structures during treatment fractions. 4D-CBCT has been recognized as a promising emerging technology in identifying intra-fractional motion at the time of treatment and has been investigated for photon therapy (117, 118). This technology potentially reduces the motion artifacts associated with 3D-CBCT and can be used for tumor motion verification when comparing with the planning 4DCT (119). Currently, there is a trade-off between image acquisition time and image quality, making it challenging for fast and reliable adaptive tumor target delineation and motion analysis with 4D-CBCT. Research investigations of image processing methods to improve 4D-CBCT image quality with reduced scan times are underway (120–123), and the commercial development of a dual-imaging proton treatment system with 4D-CBCT capability has been announced by Hitachi, with approval of the Japan's Pharmaceuticals and Medical Device Agency (PMDA) granted in 2020 (124).

Other imaging approaches provide promising alternatives for *in vivo* monitoring of anatomical changes and assessment of range uncertainties. One such developing imaging method for charged particle therapy is ion-based radiography, such as proton radiography (PR). PR involves measuring the residual energy of high energy protons after they have passed through the patient to construct a 2D image where each pixel represents the WET of the patient along the beam path at that position. PR has been proposed as a tool for quality control through *in vivo* proton range verification, as an aid for pre-treatment patient positioning, and even as a means to guide online plan adaptations (125, 126). The characterization of the WET accuracy, noise, and spatial resolution of a commercially developed prototype for clinical PR were reported (127, 128). Another PR system which measures individual proton depth-dose curves *via* a multi-layer ionization chamber was introduced and used to measure range uncertainties in proton pencil beams in a 4D porcine lung model; the findings supported the use of 3% range uncertainties for robust treatment planning in thoracic regions (129, 130). Proton-based fluoroscopy has also been proposed, and was investigated for range verification and monitoring of inter- and intra-fractional motion in lung tumors in a recent simulation study (131). Helium and carbon ion-based radiography systems have also been investigated in simulation and experimental studies, with carbon ions achieving the highest image quality at the cost of increased dose (132–134). A benefit of ion-based radiography is that it requires less dose in comparison with conventional x-ray radiography due to low fluence requirements and the Bragg peak not contributing to patient dose. A limitation of ion-based radiography is that particles must be able to fully penetrate the patient to acquire an image. Current clinical therapy systems can achieve a penetration depth of ~30cm, which may be insufficient for large patients for certain beam directions.

MRI-guided radiotherapy is an exciting imaging strategy for *in vivo* motion management during treatment because in addition to being non-ionizing, it provides excellent soft tissue contrast, high temporal resolution, and is capable of functional imaging (135, 136). While it has already been implemented for photon radiotherapy *via* the MR-linac, the application to charged particles is currently challenged by the need to mitigate the deflection of the treatment beam by the beamline magnetic field. Modelling on MR-integrated proton therapy for liver cancer has shown clear dosimetric benefits as well as significant reduction in normal tissue complication probability in comparison with other imaging modalities, including offline MR-guided proton therapy and MR-linac (137). Recent studies have made progress in quantifying the impact of the magnetic field on detectors for proton dosimetry and demonstrating the technical feasibility of low-field MR guidance on phantoms in a static research beam line (138, 139). Additional studies have investigated methods for calculating stopping power ratios from MRI to generate an MRI-based "synthetic" CT image for treatment planning and range verification (140). The first clinical MRI-proton system is scheduled to be built in 2022 at the OncoRay – National Center for Radiation Research in Oncology in Dresden, Germany (141).

Motion changes the ion beam path and alters the beam range. *In vivo* ion beam range can be potentially monitored by secondary particles generated during nuclear reactions of the ion beams with tissue (142). One set of the nuclear processes generates position emitters which annihilates into 511 keV photon pairs. Several in-beam PET designs were proposed to detect the proton range (143, 144). Its potential to assess the proton and carbon ion beam ranges was studied (145, 146). However, the limited PET spatial resolution and the biological washout of the nuclear activation confounds the analysis of the range from the PET images. Nonetheless, reconstructed time-resolved activities indicates its potential for online range verification during treatment (147).

Prompt gamma (PG) imaging is a technology that allows for *in vivo* proton range verification (on a spot-by-spot basis) during treatment delivery through the measurement of gamma rays created from nuclear interactions with protons passing through tissue.

The *in vivo* human applications of prompt gamma with passive scattering and PBS proton beams were reported (148, 149). One challenge of implementing PG imaging is that the number of photons needed to create a reliable signal (~10^8) exceeds the number of photons generated in most pencil beams for RT treatment. Potential solutions to this challenge include re-optimizing the treatment plan such that several of the pencil beams are boosted to reach this counting threshold, or aggregating the statistics from multiple neighbour pencil beams (at the cost of reduced resolution) (150). A recent simulation study by Tian et al. demonstrated under conditions of inter-fractional motion that a selective spot boosting method achieved tight <0.8 mm PG-dose correlation. This study further supports its proposed use for proton range monitoring (151).

Detection of the secondary charged particle emission in light-ions such as carbon ion beams was also proposed for beam range monitoring purposes (152); the capability of using charged secondary emission profiles to track ion beam range, spot position, and internal motion has been demonstrated in recent simulation studies (153, 154). It is realized by back-tracking and reconstructing the profile of the secondary emissions (155). The use of charged particles to detect lateral pencil beam position to a resolution of millimeters was reported recently in anthropomorphic head and neck phantom using a carbon ion beam (156). The INnovative Solutions for In-beam Dosimetry in hadronthErapy (INSIDE) collaboration has recently reported on the clinical trial for a carbon ion beam-range monitor and demonstrated the potential of this system to detect inter-fractional beam range variations which could be used to trigger re-simulation and adaptive replanning (157).

Another emerging technology for *in vivo* range verification is protoacoustics. Protoacoustics works by measuring the thermoacoustic pressure waves generated by the energy deposition of therapeutic protons in tissue. Like prompt gamma, protoacoustics is an attractive option for range verification in that it is derives its signal from the treatment beam itself, essentially utilizing free information from the patient's internal anatomy without the need for additional dose. In addition, a protoacoustic system can be implemented at low cost compared with other methods (158). Currently, the primary challenge in implementing protoacoustics as a mainstream technology is to develop methods for rapid and accurate translation of the acoustic pressure signal in heterogenous tissues into meaningful information about proton range, which is an active area of research (159, 160). Further work has also been done to characterize the dependencies of the protoacoustic signal on the proton pulse shape (161).

Novel Delivery Methods

Tumor tracking or "beam tracking" in radiotherapy refers to a delivery method in which the tumor position is actively tracked, and the treatment beam is modified in real-time to correct for intra-fractional motion. It has been described by previous reviews as one of the most promising but also the most technically challenging motion mitigation strategy for charged particles (162–164). Although tumor tracking has been achieved in the clinic for photon therapy, clinical implementation has yet to be realized for scanned ion beams due to additional technical challenges presented by charged particle treatment regimes. Unlike photon therapy in which tumor tracking can be achieved in the beam's eye view, tumor tracking with scanned ion beams requires 3D information as well as the ion beam delivery system's ability to change beam energy rapidly. Specifically, both the beam position and beam energy need to be rapidly modified to account for changes in the location of the tumor as well as the changes in the beam range caused by variations in depth and/or tissue composition in the beam path. Simulation studies have evaluated the robustness of tumor tracking systems for both carbon ion and proton scanned beams (165, 166). Ultrasound-guided tracking systems have also been explored (167, 168). Efforts have also been made to explore a motion-synchronized dose delivery system for ion therapy which carries the benefits of tumor tracking without the difficulties of implementation (169). In their study, Lis et al. created a 3D treatment plan on each of the 4D breathing phases. With anatomic motion monitoring, dynamic switching between plan libraries for tracking dose delivery was realized through an adaptive layer of software and hardware interfaces. Preliminary tests revealed acceptable dosimetric performance and safety characteristics. The system has the potential to deliver conformal, motion-compensated doses to the moving target.

Various novel beam setups have been proposed to aid in charged particle motion management. The use of a dual carbon-helium ion beam was proposed for carbon ion treatment with helium-guided imaging for range verification (170, 171). The rationale is that for a given energy, helium ions exhibit a range about three times that of carbon ions. This, in conjunction with the fact that both ions have approximately the same charge/mass ratio, means that both ions could be accelerated together in a synchrotron and delivered simultaneously, with the carbon depositing dose in the patient and the helium passing through the patient to a detector to provide online range estimation. Simulation studies using mixed beams have demonstrated the ability to detect range changes as small as 1 mm and detect changes in simulated rotations and bowel gas movement in anthropomorphic phantoms (172). Another novel beam delivery method is the use of radioactive ion treatment beams such as ^{11}C and ^{15}O, which could be utilized for improved PET imaging to achieve more accurate online range verification (173). Finally, patient orientation with respect to the ion beam can also be considered for reducing motion. Patient setup using an upright treatment posture has also been shown to reduce thoracic motion while increasing lung volume, and has been suggested as a potential motion mitigation strategy for lung cancer patients who cannot tolerate DIBH (174). A limitation of upright radiotherapy treatment posture is that for patient simulation it necessitates using a vertical CT to ensure accurate localization of anatomy between simulation and treatment; currently upright treatment of charged ion beams is limited to only a few centers (175).

Just as the evolution of proton therapy from passive scattering to scanned beam delivery presented new challenges in handling patient motion, future advancements in charged particle

treatment delivery will necessitate new innovations to ensure patient safety in the face of motion. One promising emerging radiation technology is FLASH radiation therapy. Defined as radiation therapy delivered in ultra-high dose rates (>40Gy/s), FLASH RT has been shown for *in vivo* animal models to achieve less toxicity for normal tissues while providing the same degree of tumor control (176–179). Multiple platforms (180) including proton clinical machines (181, 182) were able to generate FLASH beams, but biological and technological challenges remain to realize clinical FLASH delivery. Further work on understanding the FLASH mechanisms, as well as optimal treatment dose, dose rates, and fractionation scheme needs to be established (183–185). Shortened treatment delivery times resulting from FLASH dose rates would potentially alleviate concerns about intra-fraction motion, but this also means that any unaccounted-for setup uncertainties and motion will likely lead to the dose being delivered to a completely unexpected location with no opportunity to be mitigated. Thus, the FLASH treatment paradigm necessitates a revisit on current clinical motion management practice and the exploration on the limits to ensure safe and accurate dose delivery when considering the "snap" of motion during ultra-fast dose deliveries.

Arc therapy is an emerging technology in proton therapy in which the gantry is rotated continuously through a pre-selected arc during treatment delivery. ARC therapy for photons (VMAT) is a standard clinical tool with several different commercial systems available (186). In 2021, the commercial proton therapy vendor IBA announced a global DynamicARC consortium, signaling a shared commitment between industry and select clinical centers towards translating proton arc therapy into a commercially available system in the near future (187). While proton ARC therapy has yet to be adopted into standard clinical practice as of yet, its application has been investigated and shown promise in reducing treatment delivery times, improving dose conformality, and reducing dose to OARs in multiple treatment sites (188–190). Planning study was also performed for carbon-ion beams to show normal tissue sparing and mitigation on the hypoxia-related tumor radioresistance (191). Robustness against range uncertainties using proton ARC therapy was demonstrated (192, 193). However, a potential drawback of proton ARC therapy is that it results in increased low dose/low LET dose to normal tissues, which could increase the risk of secondary cancers (194). Different treatment delivery scheme and dose distribution in ARC therapy from traditional PBS delivery will need further studies to assess potential interplay between patient motion and the rotating treatment beam.

Artificial Intelligence

Artificial intelligence (AI) refers to technologies or machines which can perform tasks/calculations with human-like skill and cognition. Machine learning (ML) is a subcategory of AI relating to computer algorithms which can "learn" to perform a task without being explicitly programmed to do so. Machine learning, and in particular deep learning (DL), has found tremendous success in the past decade in many diverse fields, ranging from finance to automotive technologies, and to medicine (195). DL (also called deep machine learning) is a specific class of ML algorithms which is capable of learning higher-order abstract representations or "features" from raw input data, as opposed to classical ML algorithms which learn patterns from user defined ("handcrafted") features (196). There is no known theoretical basis for the required structure of an algorithm to achieve DL; in practice however, artificial neural networks, which by design perform a nonlinear mapping from input data to the desired output space, have achieved the best success to date. In radiation oncology, machine learning and deep learning have seen exponential growth in applications and are poised to revolutionize the field (197).

Deep learning applications have been investigated for inter-fractional motion management in charged particle therapy. Van der Heyden et al. presented a single detector, multi-energy proton radiography system which relied on artificial intelligence to filter out proton scatter (198). In addition, multiple studies have been reported which utilize deep learning as a tool to facilitate accurate proton dose calculation from daily CBCT images (121, 199–201). Elmahdy et al. also reported on a convolutional neural network (CNN)-based model for robust, automatic contour propagation in prostate cancer for online adaptive proton therapy (202).

Relating to intra-fractional motion management, many studies have been published which apply deep machine learning towards challenges of real-time target tracking for both charged particles as well as photons. For example, Hirai et al. introduced a CNN-based model for marker-less real-time tumor tracking which was tested retrospectively on lung and liver cancer patients who received fluoroscopic imaging during carbon ion therapy (203). Mylonas et al. reported on the use of another CNN-based architecture for real-time tracking of arbitrarily shaped fiducial markers in fluoroscopy images (204). The motivation behind this study was to allow for fiducial marker segmentation without the need for prior maker-characterization, sparing the patient of additional imaging dose. Zhao et al. proposed a deep learning-based method for pancreatic tumor localization without the use of fiducial markers (205). Kim et al. introduced a CNN-based deep learning model for predict future motion of proton therapy patients based on facial expressions (206). In another promising study, Lin et al. describe a "super-learner" model which combined traditional neural networks with decision tree-based ML algorithms to predict the range of patient thoracic motion during proton therapy based on initial diagnostic CT and EMR data (207).

A substantial roadblock to implementing deep learning models in the clinical workflow stems from issues relating to model interpretability. Specifically, the inherent complexity of deep learning algorithms makes it difficult to understand how the models think (hence why DL models are often referred to as "black boxes") (208). Though capable of high accuracy predictions, DL models are still sensitive to unintended bias in the training data. The ability to understand and interpret the results of clinical models is critical for ensuring patient safety and quality of care in the event that such models fail (209). To this

end, the task of developing interpretable machine learning models without sacrificing model performance is an active research topic (210–212). One approach in handling the ethical question of what role a non-human entity should be trusted to play in clinical decision making is to require algorithms to follow a "human in the loop" framework. In a human-in-the-loop framework, clinicians remain fully integrated in the decision making process by allowing for human-computer interactions by which clinicians provide feedback/information to aid in model development, and the resulting models in turn provide accountable, interpretable decision support to the clinician (208).

SUMMARY

In this review, we provided an overview of the current clinical treatment methods for motion management in charged particle therapy as well as future emerging technologies and methodologies. As the use of charged particle therapy becomes more widespread and new treatment delivery modalities arise, further work will be necessary to ensure robust and accurate dose delivery. For the case of inter-fractional motion, further progress is also necessary to develop adaptive planning protocols which are triggered for clinically significant anatomical changes and can be implemented within the time and resource constraints of a clinical setting. Another important task in this field is to continue the development of imaging and tracking systems which allow for accurate localization of the tumor and internal anatomy delivery at the treatment couch prior to delivery and in real time. One limitation of most studies on motion mitigation methods is that dosimetry is used the primary evaluation metric. Future studies which can connect motion mitigation methods to clinical outcomes would aid in accelerating standardization of care.

AUTHOR CONTRIBUTIONS

JP and WZ drafted the manuscript. AK, LD, and AR contributed with discussions, coordination, and critical revision of the manuscript. All authors contributed to the article and approved the submitted version.

ACKNOWLEDGMENTS

The authors would like to thank Katja Langen for reading the manuscript and providing insightful suggestions.

REFERENCES

1. Newhauser WD, Zhang R. The Physics of Proton Therapy. *Phys Med Biol* (2015) 60(8):R155–209. doi: 10.1088/0031-9155/60/8/R155
2. Chang JY, Zhang X, Wang X, Kang Y, Riley B, Bilton S, et al. Significant Reduction of Normal Tissue Dose by Proton Radiotherapy Compared With Three-Dimensional Conformal or Intensity-Modulated Radiation Therapy in Stage I or Stage III Non-Small-Cell Lung Cancer. *Int J Radiat Oncol Biol Phys* (2006) 65(4):1087–96. doi: 10.1016/j.ijrobp.2006.01.052
3. van de Water TA, Lomax AJ, Bijl HP, de Jong ME, Schilstra C, Hug EB, et al. Potential Benefits of Scanned Intensity-Modulated Proton Therapy Versus Advanced Photon Therapy With Regard to Sparing of the Salivary Glands in Oropharyngeal Cancer. *Int J Radiat Oncol Biol Phys* (2011) 79(4):1216–24. doi: 10.1016/j.ijrobp.2010.05.012
4. Loeffler JS, Durante M. Charged Particle Therapy—Optimization, Challenges and Future Directions. *Nat Rev Clin Oncol* (2013) 10(7):411–24. doi: 10.1038/nrclinonc.2013.79
5. De Ruysscher D, Chang JY. Clinical Controversies: Proton Therapy for Thoracic Tumors. *Semin Radiat Oncol* (2013) 23(2):115–9. doi: 10.1016/j.semradonc.2012.11.010
6. Durante M, Orecchia R, Loeffler JS. Charged-Particle Therapy in Cancer: Clinical Uses and Future Perspectives. *Nat Rev Clin Oncol* (2017) 14(8):483–95. doi: 10.1038/nrclinonc.2017.30
7. Lomax AJ. Intensity Modulated Proton Therapy and its Sensitivity to Treatment Uncertainties 2: The Potential Effects of Inter-Fraction and Inter-Field Motions. *Phys Med Biol* (2008) 53(4):1043–56. doi: 10.1088/0031-9155/53/4/015
8. *Particle Therapy Facilities in Clinical Operation (Last Update: (October 2021) [Internet]* (2021). Available at: https://www.ptcog.ch/index.php/facilities-in-operation.
9. Chang JY, Zhang X, Knopf A, Li H, Mori S, Dong L, et al. Consensus Guidelines for Implementing Pencil-Beam Scanning Proton Therapy for Thoracic Malignancies on Behalf of the PTCOG Thoracic and Lymphoma Subcommittee. *Int J Radiat Oncol Biol Phys* (2017) 99(1):41–50. doi: 10.1016/j.ijrobp.2017.05.014
10. Madani I, Lomax AJ, Albertini F, Trnková P, Weber DC. Dose-Painting Intensity-Modulated Proton Therapy for Intermediate- and High-Risk Meningioma. *Radiat Oncol* (2015) 10:72. doi: 10.1186/s13014-015-0384-x
11. Welsh J, Gomez D, Palmer MB, Riley BA, Mayankkumar AV, Komaki R, et al. Intensity-Modulated Proton Therapy Further Reduces Normal Tissue Exposure During Definitive Therapy for Locally Advanced Distal Esophageal Tumors: A Dosimetric Study. *Int J Radiat Oncol Biol Phys* (2011) 81(5):1336–42. doi: 10.1016/j.ijrobp.2010.07.2001
12. Shiraishi Y, Xu C, Yang J, Komaki R, Lin SH. Dosimetric Comparison to the Heart and Cardiac Substructure in a Large Cohort of Esophageal Cancer Patients Treated With Proton Beam Therapy or Intensity-Modulated Radiation Therapy. *Radiother Oncol* (2017) 125(1):48–54. doi: 10.1016/j.radonc.2017.07.034
13. Bhangoo RS, Mullikin TC, Ashman JB, Cheng TW, Golafshar MA, DeWees TA, et al. Intensity Modulated Proton Therapy for Hepatocellular Carcinoma: Initial Clinical Experience. *Adv Radiat Oncol* (2021) 6(4). doi: 10.1016/j.adro.2021.100675
14. Wang X, Krishnan S, Zhang X, Dong L, Briere T, Crane CH, et al. Proton Radiotherapy for Liver Tumors: Dosimetric Advantages Over Photon Plans. *Med Dosim* (2008) 33(4):259–67. doi: 10.1016/j.meddos.2007.04.008
15. Bert C, Herfarth K. Management of Organ Motion in Scanned Ion Beam Therapy. *Radiat Oncol* (2017) 12:170. doi: 10.1186/s13014-017-0911-z
16. Grassberger C, Dowdell S, Lomax A, Sharp G, Shackleford J, Choi N, et al. Motion Interplay as a Function of Patient Parameters and Spot Size in Spot Scanning Proton Therapy for Lung Cancer. *Int J Radiat Oncol Biol Phys* (2013) 86(2):380–6. doi: 10.1016/j.ijrobp.2013.01.024
17. Møller DS, Poulsen PR, Hagner A, Dufour M, Nordsmark M, Nyeng TB, et al. Strategies for Motion Robust Proton Therapy With Pencil Beam Scanning for Esophageal Cancer. *Int J Radiat Oncol Biol Phys* (2021) 111(2):539–48. doi: 10.1016/j.ijrobp.2021.04.040
18. Kraus KM, Heath E, Oelfke U. Dosimetric Consequences of Tumour Motion Due to Respiration for a Scanned Proton Beam. *Phys Med Biol* (2011) 56(20):6563–81. doi: 10.1088/0031-9155/56/20/003
19. Zhang Y, Huth I, Weber DC, Lomax AJ. Dosimetric Uncertainties as a Result of Temporal Resolution in 4D Dose Calculations for PBS Proton Therapy. *Phys Med Biol* (2019) 64(12):125005. doi: 10.1088/1361-6560/ab1d6f
20. Schippers JM. Beam Delivery Systems for Particle Radiation Therapy: Current Status and Recent Developments. *Rev Accelerator Sci Technol* (2009) 02(01):179–200. doi: 10.1142/9789814299350_0009
21. Zhang Y, Huth I, Weber DC, Lomax AJ. A Statistical Comparison of Motion Mitigation Performances and Robustness of Various Pencil Beam Scanned

Proton Systems for Liver Tumour Treatments. *Radiother Oncol* (2018) 128 (1):182–8. doi: 10.1016/j.radonc.2018.01.019
22. Group PTC-O. *Particle Therapy Facilities Under Construction*. (2021) Available at: https://www.ptcog.ch/index.php/facilities-under-construction.
23. Tsujii H, Kamada T, Shirai T, Noda K, Tsuji H, Karasawa K. *Carbon-Ion Radiotherapy Principles, Practices, and Treatment Planning. 1st ed* Vol. 2014. Springer Japan: Imprint: Springer (2014). p. 2014.
24. Malouff TD, Mahajan A, Krishnan S, Beltran C, Seneviratne DS, Trifiletti DM. Carbon Ion Therapy: A Modern Review of an Emerging Technology. *Front Oncol* (2020) 10(82). doi: 10.3389/fonc.2020.00082
25. Krämer M, Scholz M. Treatment Planning for Heavy-Ion Radiotherapy: Calculation and Optimization of Biologically Effective Dose. *Phys Med Biol* (2000) 45(11):3319–30. doi: 10.1088/0031-9155/45/11/314
26. Paganetti H, Botas P, Sharp GC, Winey B. Adaptive Proton Therapy. *Phys Med Biol* (2021) 66(22). doi: 10.1088/1361-6560/ac344f
27. Wang X, Yu M, Wang J, Zhong R, Shen Y, Zhao Y, et al. An Assessment of Interfractional Bladder, Rectum and Vagina Motion in Postoperative Cervical Cancer Based on Daily Cone-Beam Computed Tomography. *Mol Clin Oncol* (2016) 4(2):271–7. doi: 10.3892/mco.2015.704
28. Chen L, Paskalev K, Xu X, Zhu J, Wang L, Price RA, et al. Rectal Dose Variation During the Course of Image-Guided Radiation Therapy of Prostate Cancer. *Radiother Oncol* (2010) 95(2):198–202. doi: 10.1016/j.radonc.2010.02.023
29. Bolsi A, Peroni M, Amelio D, Dasu A, Stock M, Toma-Dasu I, et al. Practice Patterns of Image Guided Particle Therapy in Europe: A 2016 Survey of the European Particle Therapy Network (EPTN). *Radiother Oncol* (2018) 128 (1):4–8. doi: 10.1016/j.radonc.2018.03.017
30. Dueck J, Knopf AC, Lomax A, Albertini F, Persson GF, Josipovic M, et al. Robustness of the Voluntary Breath-Hold Approach for the Treatment of Peripheral Lung Tumors Using Hypofractionated Pencil Beam Scanning Proton Therapy. *Int J Radiat Oncol Biol Phys* (2016) 95(1):534–41. doi: 10.1016/j.ijrobp.2015.11.015
31. Wong JW, Sharpe MB, Jaffray DA, Kini VR, Robertson JM, Stromberg JS, et al. The Use of Active Breathing Control (ABC) to Reduce Margin for Breathing Motion. *Int J Radiat Oncol Biol Phys* (1999) 44(4):911–9. doi: 10.1016/S0360-3016(99)00056-5
32. Baues C, Marnitz S, Engert A, Baus W, Jablonska K, Fogliata A, et al. Proton Versus Photon Deep Inspiration Breath Hold Technique in Patients With Hodgkin Lymphoma and Mediastinal Radiation: A PLANNING COMPARISON OF DEEP INSPIRATION BREATH HOLD INTENSITY MODULATION RADIOTHERAPY AND INTENSITY MODULATED PROTON THERAPY. *Radiat Oncol* (2018) 13(1):122. doi: 10.1186/s13014-018-1066-2
33. Mondal D, Jhawar SR, Millevoi R, Haffty BG, Parikh RR. Proton Versus Photon Breath-Hold Radiation for Left-Sided Breast Cancer After Breast-Conserving Surgery: A Dosimetric Comparison. *Int J Part Ther* (2020) 7 (3):24–33. doi: 10.14338/IJPT-20-00026.1
34. Lee HL, Lim LH, Master Z, Wong SMM. The Role of Breath Hold Intensity Modulated Proton Therapy for a Case of Left-Sided Breast Cancer With IMN Involvement. How Protons Compare With Other Conformal Techniques? *Tech Innov Patient Support Radiat Oncol* (2020) 15:1–5. doi: 10.1016/j.tipsro.2020.03.001
35. Emert F, Missimer J, Eichenberger PA, Walser M, Gmür C, Lomax AJ, et al. Enhanced Deep-Inspiration Breath Hold Superior to High-Frequency Percussive Ventilation for Respiratory Motion Mitigation: A Physiology-Driven, MRI-Guided Assessment Toward Optimized Lung Cancer Treatment With Proton Therapy. *Front Oncol* (2021) 11:621350. doi: 10.3389/fonc.2021.621350
36. Mori S, Lu HM, Wolfgang JA, Choi NC, Chen GT. Effects of Interfractional Anatomical Changes on Water-Equivalent Pathlength in Charged-Particle Radiotherapy of Lung Cancer. *J Radiat Res* (2009) 50(6):513–9. doi: 10.1269/jrr.09032
37. Lin L, Souris K, Kang M, Glick A, Lin H, Huang S, et al. Evaluation of Motion Mitigation Using Abdominal Compression in the Clinical Implementation of Pencil Beam Scanning Proton Therapy of Liver Tumors. *Med Phys* (2017) 44(2):703–12. doi: 10.1002/mp.12040
38. Taunk NK, Burgdorf B, Dong L, Ben-Josef E. Simultaneous Multiple Liver Metastasis Treated With Pencil Beam Proton Stereotactic Body Radiotherapy (SBRT). *Int J Part Ther* (2021) 8(2):89–94. doi: 10.14338/IJPT-20-00085.1
39. Meschini G, Seregni M, Pella A, Ciocca M, Fossati P, Valvo F, et al. Evaluation of Residual Abdominal Tumour Motion in Carbon Ion Gated Treatments Through Respiratory Motion Modelling. *Physica Med* (2017) 34:28–37. doi: 10.1016/j.ejmp.2017.01.009
40. Eminowicz G, Motlib J, Khan S, Perna C, McCormack M. Pelvic Organ Motion During Radiotherapy for Cervical Cancer: Understanding Patterns and Recommended Patient Preparation. *Clin Oncol (R Coll Radiol)* (2016) 28 (9):e85–91. doi: 10.1016/j.clon.2016.04.044
41. Wroe AJ, Bush DA, Schulte RW, Slater JD. Clinical Immobilization Techniques for Proton Therapy. *Technol Cancer Res Treat* (2015) 14 (1):71–9. doi: 10.7785/tcrt.2012.500398
42. Teh BS, McGary JE, Dong L, Mai W-Y, Carpenter LS, Lu HH, et al. The Use of Rectal Balloon During the Delivery of Intensity Modulated Radiotherapy (IMRT) for Prostate Cancer: More Than Just a Prostate Gland Immobilization Device? *Cancer J* (2002) 8(6). doi: 10.1097/00130404-200211000-00039
43. Vargas C, Mahajan C, Fryer A, Indelicato D, Henderson RH, McKenzie C, et al. Rectal Dose–Volume Differences Using Proton Radiotherapy and a Rectal Balloon or Water Alone for the Treatment of Prostate Cancer. *Int J Radiat Oncol Biol Phys* (2007) 69(4):1110–6. doi: 10.1016/j.ijrobp.2007.04.075
44. Dinh TT, Lee HJJr., Macomber MW, Apisarnthanarax S, Zeng J, Laramore GE, et al. Rectal Hydrogel Spacer Improves Late Gastrointestinal Toxicity Compared to Rectal Balloon Immobilization After Proton Beam Radiation Therapy for Localized Prostate Cancer: A Retrospective Observational Study. *Int J Radiat Oncol Biol Phys* (2020) 108(3):635–43. doi: 10.1016/j.ijrobp.2020.01.026
45. Balter JM, Ten Haken RK, Lawrence TS, Lam KL, Robertson JM. Uncertainties in CT-Based Radiation Therapy Treatment Planning Associated With Patient Breathing. *Int J Radiat Oncol Biol Phys* (1996) 36 (1):167–74. doi: 10.1016/S0360-3016(96)00275-1
46. Wolthaus JWH, Schneider C, Sonke J-J, van Herk M, Belderbos JSA, Rossi MMG, et al. Mid-Ventilation CT Scan Construction From Four-Dimensional Respiration-Correlated CT Scans for Radiotherapy Planning of Lung Cancer Patients. *Int J Radiat Oncol Biol Phys* (2006) 65(5):1560–71. doi: 10.1016/j.ijrobp.2006.04.031
47. Sindoni A, Minutoli F, Pontoriero A, Iatì G, Baldari S, Pergolizzi S. Usefulness of Four Dimensional (4D) PET/CT Imaging in the Evaluation of Thoracic Lesions and in Radiotherapy Planning: Review of the Literature. *Lung Cancer* (2016) 96:78–86. doi: 10.1016/j.lungcan.2016.03.019
48. Krieger M, Giger A, Salomir R, Bieri O, Celicanin Z, Cattin PC, et al. Impact of Internal Target Volume Definition for Pencil Beam Scanned Proton Treatment Planning in the Presence of Respiratory Motion Variability for Lung Cancer: A Proof of Concept. *Radiother Oncol* (2020) 145:154–61. doi: 10.1016/j.radonc.2019.12.001
49. Li G, Liu Y, Nie X. Respiratory-Correlated (RC) vs. Time-Resolved (TR) Four-Dimensional Magnetic Resonance Imaging (4DMRI) for Radiotherapy of Thoracic and Abdominal Cancer. *Front Oncol* (2019) 9:1024. doi: 10.3389/fonc.2019.01024
50. Rabe M, Thieke C, Düsberg M, Neppl S, Gerum S, Reiner M, et al. Real-Time 4DMRI-Based Internal Target Volume Definition for Moving Lung Tumors. *Med Phys* (2020) 47(4):1431–42. doi: 10.1002/mp.14023
51. Dolde K, Zhang Y, Chaudhri N, Dávid C, Kachelrieß M, Lomax AJ, et al. 4DMRI-Based Investigation on the Interplay Effect for Pencil Beam Scanning Proton Therapy of Pancreatic Cancer Patients. *Radiat Oncol* (2019) 14(1):30. doi: 10.1186/s13014-019-1231-2
52. Veiga C, Janssens G, Teng C-L, Baudier T, Hotoiu L, McClelland JR, et al. First Clinical Investigation of Cone Beam Computed Tomography and Deformable Registration for Adaptive Proton Therapy for Lung Cancer. *Int J Radiat Oncol Biol Phys* (2016) 95(1):549–59. doi: 10.1016/j.ijrobp.2016.01.055
53. Landry G, Nijhuis R, Dedes G, Handrack J, Thieke C, Janssens G, et al. Investigating CT to CBCT Image Registration for Head and Neck Proton Therapy as a Tool for Daily Dose Recalculation. *Med Phys* (2015) 42 (3):1354–66. doi: 10.1118/1.4908223

54. Park YK, Sharp GC, Phillips J, Winey BA. Proton Dose Calculation on Scatter-Corrected CBCT Image: Feasibility Study for Adaptive Proton Therapy. *Med Phys* (2015) 42(8):4449–59. doi: 10.1118/1.4923179
55. Kurz C, Kamp F, Park YK, Zöllner C, Rit S, Hansen D, et al. Investigating Deformable Image Registration and Scatter Correction for CBCT-Based Dose Calculation in Adaptive IMPT. *Med Phys* (2016) 43(10):5635. doi: 10.1118/1.4962933
56. Veiga C, Janssens G, Baudier T, Hotoiu L, Brousmiche S, McClelland J, et al. A Comprehensive Evaluation of the Accuracy of CBCT and Deformable Registration Based Dose Calculation in Lung Proton Therapy. *Biomed Phys Eng Express* (2017) 3(1):015003. doi: 10.1088/2057-1976/3/1/015003
57. Nesteruk KP, Bobić M, Lalonde A, Winey BA, Lomax AJ, Paganetti H. CT-On-Rails Versus In-Room CBCT for Online Daily Adaptive Proton Therapy of Head-And-Neck Cancers. *Cancers (Basel)* (2021) 13(23):5991. doi: 10.3390/cancers13235991
58. Landry G, Hua C-h. Current State and Future Applications of Radiological Image Guidance for Particle Therapy. *Med Phys* (2018) 45(11):e1086–e95. doi: 10.1002/mp.12744
59. Sawant A, Smith RL, Venkat RB, Santanam L, Cho B, Poulsen P, et al. Geometric Accuracy and Latency of an Integrated 4d IMRT Delivery System Using Real-Time Internal Position Monitoring and Dynamic MLC Tracking. *Int J Radiat Oncol Biol Phys* (2008) 72(1):S27–S8. doi: 10.1016/j.ijrobp.2008.06.828
60. Ehrbar S, Perrin R, Peroni M, Bernatowicz K, Parkel T, Pytko I, et al. Respiratory Motion-Management in Stereotactic Body Radiation Therapy for Lung Cancer - A Dosimetric Comparison in an Anthropomorphic Lung Phantom (LuCa). *Radiother Oncol* (2016) 121(2):328–34. doi: 10.1016/j.radonc.2016.10.011
61. Fattori G, Safai S, Carmona PF, Peroni M, Perrin R, Weber DC, et al. Monitoring of Breathing Motion in Image-Guided PBS Proton Therapy: Comparative Analysis of Optical and Electromagnetic Technologies. *Radiat Oncol* (2017) 12(1):63–. doi: 10.1186/s13014-017-0797-9
62. Mao W, Wiersma RD, Xing L. Fast Internal Marker Tracking Algorithm for Onboard MV and kV Imaging Systems. *Med Phys* (2008) 35(5):1942–9. doi: 10.1118/1.2905225
63. Tang S, Deville C, Tochner Z, Wang KK, McDonough J, Vapiwala N, et al. Impact of Intrafraction and Residual Interfraction Effect on Prostate Proton Pencil Beam Scanning. *Int J Radiat Oncol Biol Phys* (2014) 90(5):1186–94. doi: 10.1016/j.ijrobp.2014.08.015
64. Reidel C-A, Schuy C, Horst F, Ecker S, Finck C, Durante M, et al. Fluence Perturbation From Fiducial Markers Due to Edge-Scattering Measured With Pixel Sensors for 12C Ion Beams. *Phys Med Biol* (2020) 65(8):085005. doi: 10.1088/1361-6560/ab762f
65. Shirato H, Shimizu S, Kunieda T, Kitamura K, van Herk M, Kagei K, et al. Physical Aspects of a Real-Time Tumor-Tracking System for Gated Radiotherapy. *Int J Radiat Oncol Biol Phys* (2000) 48(4):1187–95. doi: 10.1016/S0360-3016(00)00748-3
66. Shimizu S, Miyamoto N, Matsuura T, Fujii Y, Umezawa M, Umegaki K, et al. A Proton Beam Therapy System Dedicated to Spot-Scanning Increases Accuracy With Moving Tumors by Real-Time Imaging and Gating and Reduces Equipment Size. *PloS One* (2014) 9(4):e94971. doi: 10.1371/journal.pone.0094971
67. Yoshimura T, Shimizu S, Hashimoto T, Nishioka K, Katoh N, Inoue T, et al. Analysis of Treatment Process Time for Real-Time-Image Gated-Spot-Scanning Proton-Beam Therapy (RGPT) System. *J Appl Clin Med Phys* (2020) 21(2):38–49. doi: 10.1002/acm2.12804
68. Shirato H, Harada T, Harabayashi T, Hida K, Endo H, Kitamura K, et al. Feasibility of Insertion/Implantation of 2.0-Mm-Diameter Gold Internal Fiducial Markers for Precise Setup and Real-Time Tumor Tracking in Radiotherapy. *Int J Radiat Oncol Biol Phys* (2003) 56(1):240–7. doi: 10.1016/s0360-3016(03)00076-2
69. Freislederer P, Kügele M, Öllers M, Swinnen A, Sauer TO, Bert C, et al. Recent Advances in Surface Guided Radiation Therapy. *Radiat Oncol* (2020) 15(1):187. doi: 10.1186/s13014-020-01629-w
70. MacFarlane MJ, Jiang K, Mundis M, Nichols E, Gopal A, Chen S, et al. Comparison of the Dosimetric Accuracy of Proton Breast Treatment Plans Delivered With SGRT and CBCT Setups. *J Appl Clin Med Phys* (2021) 22 (9):153–8. doi: 10.1002/acm2.13357
71. Batin E, Depauw N, Jimenez RB, MacDonald S, Lu HM. Reducing X-Ray Imaging for Proton Postmastectomy Chest Wall Patients. *Pract Radiat Oncol* (2018) 8(5):e266–e74. doi: 10.1016/j.prro.2018.03.002
72. Depauw N, Batin E, Daartz J, Rosenfeld A, Adams J, Kooy H, et al. A Novel Approach to Postmastectomy Radiation Therapy Using Scanned Proton Beams. *Int J Radiat Oncol Biol Phys* (2015) 91(2):427–34. doi: 10.1016/j.ijrobp.2014.10.039
73. Walter F, Freislederer P, Belka C, Heinz C, Söhn M, Roeder F. Evaluation of Daily Patient Positioning for Radiotherapy With a Commercial 3D Surface-Imaging System (Catalyst™). *Radiat Oncol* (2016) 11(1):154. doi: 10.1186/s13014-016-0728-1
74. Carl G, Reitz D, Schönecker S, Pazos M, Freislederer P, Reiner M, et al. Optical Surface Scanning for Patient Positioning in Radiation Therapy: A Prospective Analysis of 1902 Fractions. *Technol Cancer Res Treat* (2018) 17:1533033818806002. doi: 10.1177/1533033818806002
75. Stanley DN, McConnell KA, Kirby N, Gutiérrez AN, Papanikolaou N, Rasmussen K. Comparison of Initial Patient Setup Accuracy Between Surface Imaging and Three Point Localization: A Retrospective Analysis. *J Appl Clin Med Phys* (2017) 18(6):58–61. doi: 10.1002/acm2.12183
76. Czerska K, Emert F, Kopec R, Langen K, McClelland JR, Meijers A, et al. Clinical Practice vs. State-of-the-Art Research and Future Visions: Report on the 4D Treatment Planning Workshop for Particle Therapy - Edition 2018 and 2019. *Phys Med* (2021) 82:54–63. doi: 10.1016/j.ejmp.2020.12.013
77. Knopf A, Bert C, Heath E, Nill S, Kraus K, Richter D, et al. Special Report: Workshop on 4D-Treatment Planning in Actively Scanned Particle Therapy—Recommendations, Technical Challenges, and Future Research Directions. *Med Phys* (2010) 37(9):4608–14. doi: 10.1118/1.3475944
78. Kang Y, Zhang X, Chang JY, Wang H, Wei X, Liao Z, et al. 4d Proton Treatment Planning Strategy for Mobile Lung Tumors. *Int J Radiat Oncol Biol Phys* (2007) 67(3):906–14. doi: 10.1016/j.ijrobp.2006.10.045
79. Visser S, Neh H, Oraboni Ribeiro C, Korevaar EW, Meijers A, Poppe B, et al. Assessment of a Diaphragm Override Strategy for Robustly Optimized Proton Therapy Planning for Esophageal Cancer Patients. *Med Phys* (2021) n/a(n/a). doi: 10.1002/mp.15114
80. van Herk M, Remeijer P, Rasch C, Lebesque JV. The Probability of Correct Target Dosage: Dose-Population Histograms for Deriving Treatment Margins in Radiotherapy. *Int J Radiat Oncol Biol Phys* (2000) 47(4):1121–35. doi: 10.1016/S0360-3016(00)00518-6
81. Phillips MH, Pedroni E, Blattmann H, Boehringer T, Coray A, Scheib S. Effects of Respiratory Motion on Dose Uniformity With a Charged Particle Scanning Method. *Phys Med Biol* (1992) 37(1):223–34. doi: 10.1088/0031-9155/37/1/016
82. Seco J, Robertson D, Trofimov A, Paganetti H. Breathing Interplay Effects During Proton Beam Scanning: Simulation and Statistical Analysis. *Phys Med Biol* (2009) 54(14):N283–94. doi: 10.1088/0031-9155/54/14/N01
83. Zhang Y, Huth I, Wegner M, Weber DC, Lomax AJ. An Evaluation of Rescanning Technique for Liver Tumour Treatments Using a Commercial PBS Proton Therapy System. *Radiother Oncol* (2016) 121(2):281–7. doi: 10.1016/j.radonc.2016.09.011
84. Kardar L, Li Y, Li X, Li H, Cao W, Chang JY, et al. Evaluation and Mitigation of the Interplay Effects of Intensity Modulated Proton Therapy for Lung Cancer in a Clinical Setting. *Pract Radiat Oncol* (2014) 4(6):e259–e68. doi: 10.1016/j.prro.2014.06.010
85. Poulsen PR, Eley J, Langner U, Simone CB, Langen K. Efficient Interplay Effect Mitigation for Proton Pencil Beam Scanning by Spot-Adapted Layered Repainting Evenly Spread Out Over the Full Breathing Cycle. *Int J Radiat Oncol Biol Phys* (2018) 100(1):226–34. doi: 10.1016/j.ijrobp.2017.09.043
86. Gelover E, Deisher AJ, Herman MG, Johnson JE, Kruse JJ, Tryggestad EJ. Clinical Implementation of Respiratory-Gated Spot-Scanning Proton Therapy: An Efficiency Analysis of Active Motion Management. *J Appl Clin Med Phys* (2019) 20(5):99–108. doi: 10.1002/acm2.12584
87. Nakajima K, Iwata H, Ogino H, Hattori Y, Hashimoto S, Toshito T, et al. Clinical Outcomes of Image-Guided Proton Therapy for Histologically Confirmed Stage I non-Small Cell Lung Cancer. *Radiat Oncol* (2018) 13 (1):199. doi: 10.1186/s13014-018-1144-5
88. Ebner DK, Tsuji H, Yasuda S, Yamamoto N, Mori S, Kamada T. Respiration-Gated Fast-Rescanning Carbon-Ion Radiotherapy. *Jpn J Clin Oncol* (2017) 47(1):80–3. doi: 10.1093/jjco/hyw144

89. Mori S, Karube M, Shirai T, Tajiri M, Takekoshi T, Miki K, et al. Carbon-Ion Pencil Beam Scanning Treatment With Gated Markerless Tumor Tracking: An Analysis of Positional Accuracy. *Int J Radiat Oncol Biol Phys* (2016) 95 (1):258–66. doi: 10.1016/j.ijrobp.2016.01.014
90. Zhang M, Zou W, Teo B-KK. Image Guidance in Proton Therapy for Lung Cancer. *Trans Lung Cancer Res* (2018) 7(2). doi: 10.21037/tlcr.2018.03.26
91. Matsuura T, Miyamoto N, Shimizu S, Fujii Y, Umezawa M, Takao S, et al. Integration of a Real-Time Tumor Monitoring System Into Gated Proton Spot-Scanning Beam Therapy: An Initial Phantom Study Using Patient Tumor Trajectory Data. *Med Phys* (2013) 40(7):071729. doi: 10.1118/1.4810966
92. Bert C, Gemmel A, Saito N, Rietzel E. Gated Irradiation With Scanned Particle Beams. *Int J Radiat OncologyBiologyPhysics* (2009) 73(4):1270–5. doi: 10.1016/j.ijrobp.2008.11.014
93. Furukawa T, Inaniwa T, Sato S, Tomitani T, Minohara S, Noda K, et al. Design Study of a Raster Scanning System for Moving Target Irradiation in Heavy-Ion Radiotherapy. *Med Phys* (2007) 34(3):1085–97. doi: 10.1118/1.2558213
94. Zhang Y, Knopf A-C, Weber DC, Lomax AJ. Improving 4D Plan Quality for PBS-Based Liver Tumour Treatments by Combining Online Image Guided Beam Gating With Rescanning. *Phys Med Biol* (2015) 60(20):8141–59. doi: 10.1088/0031-9155/60/20/8141
95. Schätti A, Zakova M, Meer D, Lomax AJ. The Effectiveness of Combined Gating and Re-Scanning for Treating Mobile Targets With Proton Spot Scanning. An Experimental and Simulation-Based Investigation. *Phys Med Biol* (2014) 59(14):3813–28. doi: 10.1088/0031-9155/59/14/3813
96. Unkelbach J, Chan TCY, Bortfeld T. Accounting for Range Uncertainties in the Optimization of Intensity Modulated Proton Therapy. *Phys Med Biol* (2007) 52(10):2755–73. doi: 10.1088/0031-9155/52/10/009
97. Unkelbach J, Bortfeld T, Martin BC, Soukup M. Reducing the Sensitivity of IMPT Treatment Plans to Setup Errors and Range Uncertainties *via* Probabilistic Treatment Planning. *Med Phys* (2009) 36(1):149–63. doi: 10.1118/1.3021139
98. Fredriksson A, Forsgren A, Hårdemark B. Minimax Optimization for Handling Range and Setup Uncertainties in Proton Therapy. *Med Phys* (2011) 38(3):1672–84. doi: 10.1118/1.3556559
99. Pflugfelder D, Wilkens JJ, Oelfke U. Worst Case Optimization: A Method to Account for Uncertainties in the Optimization of Intensity Modulated Proton Therapy. *Phys Med Biol* (2008) 53(6):1689–700. doi: 10.1088/0031-9155/53/6/013
100. Ge S, Wang X, Liao Z, Zhang L, Sahoo N, Yang J, et al. Potential for Improvements in Robustness and Optimality of Intensity-Modulated Proton Therapy for Lung Cancer With 4-Dimensional Robust Optimization. *Cancers (Basel)* (2019) 11(1):35. doi: 10.3390/cancers11010035
101. Liu W, Schild SE, Chang JY, Liao Z, Chang Y-H, Wen Z, et al. Exploratory Study of 4D Versus 3D Robust Optimization in Intensity Modulated Proton Therapy for Lung Cancer. *Int J Radiat Oncol Biol Phys* (2016) 95(1):523–33. doi: 10.1016/j.ijrobp.2015.11.002
102. Mastella E, Molinelli S, Pella A, Vai A, Maestri D, Vitolo V, et al. 4D Strategies for Lung Tumors Treated With Hypofractionated Scanning Proton Beam Therapy: Dosimetric Impact and Robustness to Interplay Effects. *Radiother Oncol* (2020) 146:213–20. doi: 10.1016/j.radonc.2020.02.025
103. Richter D, Saito N, Chaudhri N, Härtig M, Ellerbrock M, Jäkel O, et al. Four-Dimensional Patient Dose Reconstruction for Scanned Ion Beam Therapy of Moving Liver Tumors. *Int J Radiat Oncol Biol Phys* (2014) 89(1):175–81. doi: 10.1016/j.ijrobp.2014.01.043
104. Eley JG, Newhauser WD, Lüchtenborg R, Graeff C, Bert C. 4D Optimization of Scanned Ion Beam Tracking Therapy for Moving Tumors. *Phys Med Biol* (2014) 59(13):3431–52. doi: 10.1088/0031-9155/59/13/3431
105. Graeff C, Lüchtenborg R, Eley JG, Durante M, Bert C. A 4D-Optimization Concept for Scanned Ion Beam Therapy. *Radiother Oncol* (2013) 109 (3):419–24. doi: 10.1016/j.radonc.2013.09.018
106. Wolf M, Anderle K, Durante M, Graeff C. Robust Treatment Planning With 4D Intensity Modulated Carbon Ion Therapy for Multiple Targets in Stage IV non-Small Cell Lung Cancer. *Phys Med Biol* (2020) 65(21):215012. doi: 10.1088/1361-6560/aba1a3
107. Meschini G, Kamp F, Hofmaier J, Reiner M, Sharp G, Paganetti H, et al. Modeling RBE-Weighted Dose Variations in Irregularly Moving Abdominal Targets Treated With Carbon Ion Beams. *Med Phys* (2020) 47(7):2768–78. doi: 10.1002/mp.14135
108. Bert C, Herfarth K. Management of Organ Motion in Scanned Ion Beam Therapy. *Radiat Oncol* (2017) 12(1):170. doi: 10.1186/s13014-017-0911-z
109. *RayStation: Robustness in Treatment Planning: RaySearch Laboratories*. Available at: https://www.raysearchlabs.com/robustness-in-treatment-planning/#:~:text=RayStation%20utilizes%20a%20unique%20robust,the%20use%20of%20multiple%20images.
110. Meijers A, Knopf AC, Crijns APG, Ubbels JF, Niezink AGH, Langendijk JA, et al. Evaluation of Interplay and Organ Motion Effects by Means of 4D Dose Reconstruction and Accumulation. *Radiother Oncol* (2020) 150:268–74. doi: 10.1016/j.radonc.2020.07.055
111. Meijers A, Jakobi A, Stützer K, Guterres Marmitt G, Both S, Langendijk JA, et al. Log File-Based Dose Reconstruction and Accumulation for 4D Adaptive Pencil Beam Scanned Proton Therapy in a Clinical Treatment Planning System: Implementation and Proof-of-Concept. *Med Phys* (2019) 46(3):1140–9. doi: 10.1002/mp.13371
112. Ribeiro CO, Meijers A, Korevaar EW, Muijs CT, Both S, Langendijk JA, et al. Comprehensive 4D Robustness Evaluation for Pencil Beam Scanned Proton Plans. *Radiother Oncol* (2019) 136:185–9. doi: 10.1016/j.radonc.2019.03.037
113. Korevaar EW, Habraken SJM, Scandurra D, Kierkels RGJ, Unipan M, Eenink MGC, et al. Practical Robustness Evaluation in Radiotherapy – A Photon and Proton-Proof Alternative to PTV-Based Plan Evaluation. *Radiother Oncol* (2019) 141:267–74. doi: 10.1016/j.radonc.2019.08.005
114. Magro G, Mein S, Kopp B, Mastella E, Pella A, Ciocca M, et al. FRoG Dose Computation Meets Monte Carlo Accuracy for Proton Therapy Dose Calculation in Lung. *Physica Med* (2021) 86:66–74. doi: 10.1016/j.ejmp.2021.05.021
115. Gajewski J, Garbacz M, Chang C-W, Czerska K, Durante M, Krah N, et al. Commissioning of GPU–Accelerated Monte Carlo Code FRED for Clinical Applications in Proton Therapy. *Front Phys* (2021) 8:403. doi: 10.3389/fphy.2020.567300
116. Pepin MD, Tryggestad E, Wan Chan Tseung HS, Johnson JE, Herman MG, Beltran C. A Monte-Carlo-Based and GPU-Accelerated 4D-Dose Calculator for a Pencil Beam Scanning Proton Therapy System. *Med Phys* (2018) 45 (11):5293–304. doi: 10.1002/mp.13182
117. Zhang Y, Yin F-F, Ren L. First Clinical Retrospective Investigation of Limited Projection CBCT for Lung Tumor Localization in Patients Receiving SBRT Treatment. *Phys Med Biol* (2019) 64(10):10NT01–1. doi: 10.1088/1361-6560/ab1c0c
118. Qin A, Gersten D, Liang J, Liu Q, Grill I, Guerrero T, et al. A Clinical 3D/4D CBCT-Based Treatment Dose Monitoring System. *J Appl Clin Med Phys* (2018) 19(6):166–76. doi: 10.1002/acm2.12474
119. Thengumpallil S, Smith K, Monnin P, Bourhis J, Bochud F, Moeckli R. Difference in Performance Between 3D and 4D CBCT for Lung Imaging: A Dose and Image Quality Analysis. *J Appl Clin Med Phys* (2016) 17(6):97–106. doi: 10.1120/jacmp.v17i6.6459
120. den Otter LA, Chen K, Janssens G, Meijers A, Both S, Langendijk JA, et al. Technical Note: 4D Cone-Beam CT Reconstruction From Sparse-View CBCT Data for Daily Motion Assessment in Pencil Beam Scanned Proton Therapy (PBS-Pt). *Med Phys* (2020) 47(12):6381–7. doi: 10.1002/mp.14521
121. Kurz C, Maspero M, Savenije MHF, Landry G, Kamp F, Pinto M, et al. CBCT Correction Using a Cycle-Consistent Generative Adversarial Network and Unpaired Training to Enable Photon and Proton Dose Calculation. *Phys Med Biol* (2019) 64(22):225004. doi: 10.1088/1361-6560/ab4d8c
122. Bryce-Atkinson A, Marchant T, Rodgers J, Budgell G, McWilliam A, Faivre-Finn C, et al. Quantitative Evaluation of 4D Cone Beam CT Scans With Reduced Scan Time in Lung Cancer Patients. *Radiother Oncol* (2019) 136:64–70. doi: 10.1016/j.radonc.2019.03.027
123. Shieh CC, Gonzalez Y, Li B, Jia X, Rit S, Mory C, et al. SPARE: Sparse-View Reconstruction Challenge for 4D Cone-Beam CT From a 1-Min Scan. *Med Phys* (2019) 46(9):3799–811. doi: 10.1002/mp.13687
124. *Motion Management: 2-Axis and 4-Dimensional Cone Beam Ct*. Hitachi Ltd (2021). Available at: https://www.hitachi.com/businesses/healthcare/products-support/pbt/probeat/motion/index.html.

125. Schneider U, Pedroni E. Proton Radiography as a Tool for Quality Control in Proton Therapy. *Med Phys* (1995) 22(4):353–63. doi: 10.1118/1.597470
126. Schreuder AN, Shamblin J. Proton Therapy Delivery: What is Needed in the Next Ten Years? *Br J Radiol* (2019) 93(1107):20190359. doi: 10.1259/bjr.20190359
127. DeJongh EA, DeJongh DF, Polnyi I, Rykalin V, Sarosiek C, Coutrakon G, et al. Technical Note: A Fast and Monolithic Prototype Clinical Proton Radiography System Optimized for Pencil Beam Scanning. *Med Phys* (2021) 48(3):1356–64. doi: 10.1002/mp.14700
128. Sarosiek C, DeJongh EA, Coutrakon G, DeJongh DF, Duffin KL, Karonis NT, et al. Analysis of Characteristics of Images Acquired With a Prototype Clinical Proton Radiography System. *Med Phys* (2021) 48(5):2271–8. doi: 10.1002/mp.14801
129. Farace P, Righetto R, Meijers A. Pencil Beam Proton Radiography Using a Multilayer Ionization Chamber. *Phys Med Biol* (2016) 61(11):4078–87. doi: 10.1088/0031-9155/61/11/4078
130. Meijers A, Seller OC, Free J, Bondesson D, Seller Oria C, Rabe M, et al. Assessment of Range Uncertainty in Lung-Like Tissue Using a Porcine Lung Phantom and Proton Radiography. *Phys Med Biol* (2020) 65(15):155014. doi: 10.1088/1361-6560/ab91db
131. Han B, Xu XG, Chen GT. Proton Radiography and Fluoroscopy of Lung Tumors: A Monte Carlo Study Using Patient-Specific 4DCT Phantoms. *Med Phys* (2011) 38(4):1903–11. doi: 10.1118/1.3555039
132. Gianoli C, Göppel M, Meyer S, Palaniappan P, Rädler M, Kamp F, et al. Patient-Specific CT Calibration Based on Ion Radiography for Different Detector Configurations in (1)H, (4)He and (12)C Ion Pencil Beam Scanning. *Phys Med Biol* (2020) 65(24):245014. doi: 10.1088/1361-6560/aba319
133. Gehrke T, Amato C, Berke S, Martišíková M. Theoretical and Experimental Comparison of Proton and Helium-Beam Radiography Using Silicon Pixel Detectors. *Phys Med Biol* (2018) 63(3):035037. doi: 10.1088/1361-6560/aaa60f
134. Kopp B, Meyer S, Gianoli C, Magallanes L, Voss B, Brons S, et al. Experimental Comparison of Clinically Used Ion Beams for Imaging Applications Using a Range Telescope. *Phys Med Biol* (2020) 65 (15):155004. doi: 10.1088/1361-6560/ab87f6
135. Paganelli C, Whelan B, Peroni M, Summers P, Fast M, van de Lindt T, et al. MRI-Guidance for Motion Management in External Beam Radiotherapy: Current Status and Future Challenges. *Phys Med Biol* (2018) 63(22):22tr03. doi: 10.1088/1361-6560/aaebcf
136. Stemkens B, Paulson ES, Tijssen RHN. Nuts and Bolts of 4D-MRI for Radiotherapy. *Phys Med Biol* (2018) 63(21):21tr01. doi: 10.1088/1361-6560/aae56d
137. Moteabbed M, Smeets J, Hong TS, Janssens G, Labarbe R, Wolfgang JA, et al. Toward MR-Integrated Proton Therapy: Modeling the Potential Benefits for Liver Tumors. *Phys Med Biol* (2021) 66(19). doi: 10.1088/1361-6560/ac1ef2
138. Fuchs H, Padilla-Cabal F, Zimmermann L, Palmans H, Georg D. MR-Guided Proton Therapy: Impact of Magnetic Fields on the Detector Response. *Med Phys* (2021) 48(5):2572–9. doi: 10.1002/mp.14660
139. Schellhammer SM, Hoffmann AL, Gantz S, Smeets J, van der Kraaij E, Quets S, et al. Integrating a Low-Field Open MR Scanner With a Static Proton Research Beam Line: Proof of Concept. *Phys Med Biol* (2018) 63(23):23lt01. doi: 10.1088/1361-6560/aaece8
140. Liu R, Lei Y, Wang T, Zhou J, Roper J, Lin L, et al. Synthetic Dual-Energy CT for MRI-Only Based Proton Therapy Treatment Planning Using Label-GAN. *Phys Med Biol* (2021) 66(6):065014. doi: 10.1088/1361-6560/abe736
141. Freeman T. One Step Closer to Real-Time MR Imaging in Proton Therapy. *Phys World* (2021).
142. Knopf A-C, Lomax A. *In Vivo*proton Range Verification: A Review. *Phys Med Biol* (2013) 58(15):R131–R60. doi: 10.1088/0031-9155/58/15/R131
143. Surti S, Zou W, Daube-Witherspoon ME, McDonough J, Karp JS. Design Study of an *in Situ* PET Scanner for Use in Proton Beam Therapy. *Phys Med Biol* (2011) 56(9):2667–85. doi: 10.1088/0031-9155/56/9/002
144. Zhu X, El Fakhri G. Proton Therapy Verification With PET Imaging. *Theranostics* (2013) 3(10):731–40. doi: 10.7150/thno.5162
145. Kuess P, Helmbrecht S, Fiedler F, Birkfellner W, Enghardt W, Hopfgartner J, et al. Automated Evaluation of Setup Errors in Carbon Ion Therapy Using PET: Feasibility Study. *Med Phys* (2013) 40(12):121718. doi: 10.1118/1.4829595
146. Parodi K, Bortfeld T. A Filtering Approach Based on Gaussian-Powerlaw Convolutions for Local PET Verification of Proton Radiotherapy. *Phys Med Biol* (2006) 51(8):1991–2009. doi: 10.1088/0031-9155/51/8/003
147. Ferrero V, Fiorina E, Morrocchi M, Pennazio F, Baroni G, Battistoni G, et al. Online Proton Therapy Monitoring: Clinical Test of a Silicon-Photodetector-Based in-Beam PET. *Sci Rep* (2018) 8(1):4100. doi: 10.1038/s41598-018-22325-6
148. Richter C, Pausch G, Barczyk S, Priegnitz M, Keitz I, Thiele J, et al. First Clinical Application of a Prompt Gamma Based *In Vivo* Proton Range Verification System. *Radiother Oncol* (2016) 118(2):232–7. doi: 10.1016/j.radonc.2016.01.004
149. Xie Y, Bentefour EH, Janssens G, Smeets J, Vander Stappen F, Hotoiu L, et al. Prompt Gamma Imaging for In Vivo Range Verification of Pencil Beam Scanning Proton Therapy. *Int J Radiat Oncol Biol Phys* (2017) 99(1):210–8. doi: 10.1016/j.ijrobp.2017.04.027
150. Tian L, Huang Z, Janssens G, Landry G, Dedes G, Kamp F, et al. Accounting for Prompt Gamma Emission and Detection for Range Verification in Proton Therapy Treatment Planning. *Phys Med Biol* (2021) 66(5):055005. doi: 10.1088/1361-6560/abc939
151. Tian L, Landry G, Dedes G, Pinto M, Kamp F, Belka C, et al. A New Treatment Planning Approach Accounting for Prompt Gamma Range Verification and Interfractional Anatomical Changes. *Phys Med Biol* (2020) 65(9):095005. doi: 10.1088/1361-6560/ab7d15
152. Muraro S, Battistoni G, Collamati F, De Lucia E, Faccini R, Ferroni F, et al. Monitoring of Hadrontherapy Treatments by Means of Charged Particle Detection. *Front Oncol* (2016) 6(177). doi: 10.3389/fonc.2016.00177
153. Rucinski A, Rinaldi I, De Lucia E, Battistoni G, Collamati F, Faccini R, et al. Internal Motion Tracking Based on Charged Secondary Proton Emission (Poster). *4D Treat Plann Workshop* (2014).
154. Bey A, Ma J, Furutani KM, Herman MG, Johnson JE, Foote RL, et al. Nuclear Fragmentation Imaging for Carbon-Ion Radiation Therapy Monitoring: An In Silico Study. *Int J Part Ther* (2021). doi: 10.14338/IJPT-20-00040.1
155. Rucinski A, Battistoni G, Collamati F, De Lucia E, Faccini R, Fralliccardi PM, et al. Secondary Radiation Measurements for Particle Therapy Applications: Charged Particles Produced By4he And12c Ion Beams in a PMMA Target at Large Angle. *Phys Med Biol* (2018) 63(5):055018. doi: 10.1088/1361-6560/aaa36a
156. Félix-Bautista R, Gehrke T, Ghesquière-Diérickx L, Reimold M, Amato C, Turecek D, et al. Experimental Verification of a non-Invasive Method to Monitor the Lateral Pencil Beam Position in an Anthropomorphic Phantom for Carbon-Ion Radiotherapy. *Phys Med Biol* (2019) 64(17):175019. doi: 10.1088/1361-6560/ab2ca3
157. Fischetti M, Baroni G, Battistoni G, Bisogni G, Cerello P, Ciocca M, et al. Inter-Fractional Monitoring of C12 Ions Treatments: Results From a Clinical Trial at the CNAO Facility. *Sci Rep* (2020) 10(1):20735. doi: 10.1038/s41598-020-77843-z
158. Nie W, Jones KC, Petro S, Kassaee A, Sehgal CM, Avery S. Proton Range Verification in Homogeneous Materials Through Acoustic Measurements. *Phys Med Biol* (2018) 63(2):025036. doi: 10.1088/1361-6560/aa9c1f
159. Freijo C, Herraiz JL, Sanchez-Parcerisa D, Udias JM. Dictionary-Based Protoacoustic Dose Map Imaging for Proton Range Verification. *Photoacoustics* (2021) 21:100240. doi: 10.1016/j.pacs.2021.100240
160. Yu Y, Li Z, Zhang D, Xing L, Peng H. Simulation Studies of Time Reversal-Based Protoacoustic Reconstruction for Range and Dose Verification in Proton Therapy. *Med Phys* (2019) 46(8):3649–62. doi: 10.1002/mp.13661
161. Jones KC, Seghal CM, Avery S. How Proton Pulse Characteristics Influence Protoacoustic Determination of Proton-Beam Range: Simulation Studies. *Phys Med Biol* (2016) 61(6):2213–42. doi: 10.1088/0031-9155/61/6/2213
162. Rietzel E, Bert C. Respiratory Motion Management in Particle Therapy. *Med Phys* (2010) 37(2):449–60. doi: 10.1118/1.3250856
163. Knopf A, Nill S, Yohannes I, Graeff C, Dowdell S, Kurz C, et al. Challenges of Radiotherapy: Report on the 4D Treatment Planning Workshop 2013. *Physica Med* (2014) 30(7):809–15. doi: 10.1016/j.ejmp.2014.07.341

164. Riboldi M, Orecchia R, Baroni G. Real-Time Tumour Tracking in Particle Therapy: Technological Developments and Future Perspectives. *Lancet Oncol* (2012) 13(9):e383–e91. doi: 10.1016/S1470-2045(12)70243-7
165. Eley JG, Newhauser WD, Richter D, Lüchtenborg R, Saito N, Bert C. Robustness of Target Dose Coverage to Motion Uncertainties for Scanned Carbon Ion Beam Tracking Therapy of Moving Tumors. *Phys Med Biol* (2015) 60(4):1717–40. doi: 10.1088/0031-9155/60/4/1717
166. van de Water S, Kreuger R, Zenklusen S, Hug E, Lomax AJ. Tumour Tracking With Scanned Proton Beams: Assessing the Accuracy and Practicalities. *Phys Med Biol* (2009) 54(21):6549–63. doi: 10.1088/0031-9155/54/21/007
167. Krieger M, Giger A, Jud C, Duetschler A, Salomir R, Bieri O, et al. Liver-Ultrasound-Guided Lung Tumour Tracking for Scanned Proton Therapy: A Feasibility Study. *Phys Med Biol* (2021) 66(3):035011. doi: 10.1088/1361-6560/abcde6
168. Prall M, Kaderka R, Saito N, Graeff C, Bert C, Durante M, et al. Ion Beam Tracking Using Ultrasound Motion Detection. *Med Phys* (2014) 41 (4):041708. doi: 10.1118/1.4868459
169. Lis M, Newhauser W, Donetti M, Wolf M, Steinsberger T, Paz A, et al. A Modular System for Treating Moving Anatomical Targets With Scanned Ion Beams at Multiple Facilities: Pre-Clinical Testing for Quality and Safety of Beam Delivery. *Front Oncol* (2021) 11(323). doi: 10.3389/fonc.2021.620388
170. Mazzucconi D, Agosteo S, Ferrarini M, Fontana L, Lante V, Pullia M, et al. Mixed Particle Beam for Simultaneous Treatment and Online Range Verification in Carbon Ion Therapy: Proof-of-Concept Study. *Med Phys* (2018) 45(11):5234–43. doi: 10.1002/mp.13219
171. Graeff C, Weber U, Schuy C, Saito N, Volz L, Piersimoni P, et al. [OA027] Helium as a Range Probe in Carbon Ion Therapy. *Physica Med* (2018) 52:11. doi: 10.1016/j.ejmp.2018.06.099
172. Volz L, Kelleter L, Brons S, Burigo L, Graeff C, Niebuhr NI, et al. Experimental Exploration of a Mixed Helium/Carbon Beam for Online Treatment Monitoring in Carbon Ion Beam Therapy. *Phys Med Biol* (2020) 65(5):055002. doi: 10.1088/1361-6560/ab6e52
173. Durante M, Parodi K. Radioactive Beams in Particle Therapy: Past, Present, and Future. *Front Phys* (2020) 8:326. doi: 10.3389/fphy.2020.00326
174. Yang J, Chu D, Dong L, Court LE. Advantages of Simulating Thoracic Cancer Patients in an Upright Position. *Pract Radiat Oncol* (2014) 4(1):e53–e8. doi: 10.1016/j.prro.2013.04.005
175. Durante M, Debus J, Loeffler JS. Physics and Biomedical Challenges of Cancer Therapy With Accelerated Heavy Ions. *Nat Rev Phys* (2021) 3 (12):777–90. doi: 10.1038/s42254-021-00368-5
176. Wilson JD, Hammond EM, Higgins GS, Petersson K. Ultra-High Dose Rate (FLASH) Radiotherapy: Silver Bullet or Fool's Gold? *Front Oncol* (2020) 9:1563. doi: 10.3389/fonc.2019.01563
177. Montay-Gruel P, Petersson K, Jaccard M, Boivin G, Germond JF, Petit B, et al. Irradiation in a Flash: Unique Sparing of Memory in Mice After Whole Brain Irradiation With Dose Rates Above 100Gy/s. *Radiother Oncol* (2017) 124(3):365–9. doi: 10.1016/j.radonc.2017.05.003
178. Vozenin MC, De Fornel P, Petersson K, Favaudon V, Jaccard M, Germond JF, et al. The Advantage of FLASH Radiotherapy Confirmed in Mini-Pig and Cat-Cancer Patients. *Clin Cancer Res* (2019) 25(1):35–42. doi: 10.1158/1078-0432.CCR-17-3375
179. Vozenin MC, Hendry JH, Limoli CL. Biological Benefits of Ultra-High Dose Rate FLASH Radiotherapy: Sleeping Beauty Awoken. *Clin Oncol (R Coll Radiol)* (2019) 31(7):407–15. doi: 10.1016/j.clon.2019.04.001
180. Esplen N, Mendonca MS, Bazalova-Carter M. Physics and Biology of Ultrahigh Dose-Rate (FLASH) Radiotherapy: A Topical Review. *Phys Med Biol* (2020) 65(23):23tr03. doi: 10.1088/1361-6560/abaa28
181. Diffenderfer ES, Verginadis II, Kim MM, Shoniyozov K, Velalopoulou A, Goia D, et al. Design, Implementation, and in Vivo Validation of a Novel Proton FLASH Radiation Therapy System. *Int J Radiat Oncol Biol Phys* (2020) 106(2):440–8. doi: 10.1016/j.ijrobp.2019.10.049
182. Patriarca A, Fouillade C, Auger M, Martin F, Pouzoulet F, Nauraye C, et al. Experimental Set-Up for FLASH Proton Irradiation of Small Animals Using a Clinical System. *Int J Radiat Oncol Biol Phys* (2018) 102(3):619–26. doi: 10.1016/j.ijrobp.2018.06.403
183. Zou W, Diffenderfer ES, Cengel KA, Kim MM, Avery S, Konzer J, et al. Current Delivery Limitations of Proton PBS for FLASH. *Radiother Oncol* (2021) 155:212–8. doi: 10.1016/j.radonc.2020.11.002
184. Jolly S, Owen H, Schippers M, Welsch C. Technical Challenges for FLASH Proton Therapy. *Physica Med* (2020) 78:71–82. doi: 10.1016/j.ejmp.2020.08.005
185. van de Water S, Safai S, Schippers JM, Weber DC, Lomax AJ. Towards FLASH Proton Therapy: The Impact of Treatment Planning and Machine Characteristics on Achievable Dose Rates. *Acta Oncol* (2019) 58(10):1463–9. doi: 10.1080/0284186X.2019.1627416
186. Teoh M, Clark CH, Wood K, Whitaker S, Nisbet A. Volumetric Modulated Arc Therapy: A Review of Current Literature and Clinical Use in Practice. *Br J Radiol* (2011) 84(1007):967–96. doi: 10.1259/bjr/22373346
187. IBA Initiates Global DynamicARC Consortium for the Roll-Out of Proton Arc Therapy [Press Release]. (2021).
188. Chang S, Liu G, Zhao L, Dilworth JT, Zheng W, Jawad S, et al. Feasibility Study: Spot-Scanning Proton Arc Therapy (SPArc) for Left-Sided Whole Breast Radiotherapy. *Radiat Oncol* (2020) 15(1):232. doi: 10.1186/s13014-020-01676-3
189. Ding X, Li X, Zhang JM, Kabolizadeh P, Stevens C, Yan D. Spot-Scanning Proton Arc (SPArc) Therapy: The First Robust and Delivery-Efficient Spot-Scanning Proton Arc Therapy. *Int J Radiat Oncol Biol Phys* (2016) 96 (5):1107–16. doi: 10.1016/j.ijrobp.2016.08.049
190. Gu W, Ruan D, Lyu Q, Zou W, Dong L, Sheng K. A Novel Energy Layer Optimization Framework for Spot-Scanning Proton Arc Therapy. *Med Phys* (2020) 47(5):2072–84. doi: 10.1002/mp.14083
191. Mein S, Tessonnier T, Kopp B, Harrabi S, Abdollahi A, Debus J, et al. Spot-Scanning Hadron Arc (SHArc) Therapy: A Study With Light and Heavy Ions. *Adv Radiat Oncol* (2021) 6(3):100661. doi: 10.1016/j.adro.2021.100661
192. Carabe-Fernandez A, Bertolet-Reina A, Karagounis I, Huynh K, Dale RG. Is There a Role for Arcing Techniques in Proton Therapy? *Br J Radiol* (2020) 93 (1107):20190469. doi: 10.1259/bjr.20190469
193. Seco J, Gu G, Marcelos T, Kooy H, Willers H. Proton Arc Reduces Range Uncertainty Effects and Improves Conformality Compared With Photon Volumetric Modulated Arc Therapy in Stereotactic Body Radiation Therapy for non-Small Cell Lung Cancer. *Int J Radiat Oncol Biol Phys* (2013) 87 (1):188–94. doi: 10.1016/j.ijrobp.2013.04.048
194. Toussaint L, Indelicato DJ, Holgersen KS, Petersen JBB, Stokkevåg CH, Lassen-Ramshad Y, et al. Towards Proton Arc Therapy: Physical and Biologically Equivalent Doses With Increasing Number of Beams in Pediatric Brain Irradiation. *Acta Oncol* (2019) 58(10):1451–6. doi: 10.1080/0284186X.2019.1639823
195. Sejnowski TJ. *The Deep Learning Revolution*. Cambridge, MA: The MIT Press (2018).
196. LeCun Y, Bengio Y, Hinton G. Deep Learning. *Nature* (2015) 521 (7553):436–44. doi: 10.1038/nature14539
197. El Naqa I, Haider MA, Giger ML, Ten Haken RK. Artificial Intelligence: Reshaping the Practice of Radiological Sciences in the 21st Century. *Br J Radiol* (2020) 93(1106):20190855–. doi: 10.1259/bjr.20190855
198. van der Heyden B, Cohilis M, Souris K, de Freitas Nascimento L, Sterpin E. Artificial Intelligence Supported Single Detector Multi-Energy Proton Radiography System. *Phys Med Biol* (2021) 66(10):105001. doi: 10.1088/1361-6560/abe918
199. Lalonde A, Winey B, Verburg J, Paganetti H, Sharp GC. Evaluation of CBCT Scatter Correction Using Deep Convolutional Neural Networks for Head and Neck Adaptive Proton Therapy. *Phys Med Biol* (2020) 65(24):245022. doi: 10.1088/1361-6560/ab9fcb
200. Thummerer A, Seller Oria C, Zaffino P, Meijers A, Guterres Marmitt G, Wijsman R, et al. Clinical Suitability of Deep Learning Based Synthetic CTs for Adaptive Proton Therapy of Lung Cancer. *Med Phys* (2021) 48(12):7673–84. doi: 10.1002/mp.15333
201. Harms J, Lei Y, Wang T, McDonald M, Ghavidel B, Stokes W, et al. Cone-Beam CT-Derived Relative Stopping Power Map Generation *via* Deep Learning for Proton Radiotherapy. *Med Phys* (2020) 47(9):4416–27. doi: 10.1002/mp.14347
202. Elmahdy MS, Jagt T, Zinkstok RT, Qiao Y, Shahzad R, Sokooti H, et al. Robust Contour Propagation Using Deep Learning and Image Registration for Online Adaptive Proton Therapy of Prostate Cancer. *Med Phys* (2019) 46 (8):3329–43. doi: 10.1002/mp.13620
203. Hirai R, Sakata Y, Tanizawa A, Mori S. Real-Time Tumor Tracking Using Fluoroscopic Imaging With Deep Neural Network Analysis. *Physica Med* (2019) 59:22–9. doi: 10.1016/j.ejmp.2019.02.006

204. Mylonas A, Keall PJ, Booth JT, Shieh C-C, Eade T, Poulsen PR, et al. A Deep Learning Framework for Automatic Detection of Arbitrarily Shaped Fiducial Markers in Intrafraction Fluoroscopic Images. *Med Phys* (2019) 46(5):2286–97. doi: 10.1002/mp.13519
205. Zhao W, Shen L, Han B, Yang Y, Cheng K, Toesca DAS, et al. Markerless Pancreatic Tumor Target Localization Enabled By Deep Learning. *Int J Radiat Oncol Biol Phys* (2019) 105(2):432–9. doi: 10.1016/j.ijrobp.2019.05.071
206. Kim KH, Park K, Kim H, Jo B, Ahn SH, Kim C, et al. Facial Expression Monitoring System for Predicting Patient's Sudden Movement During Radiotherapy Using Deep Learning. *J Appl Clin Med Phys* (2020) 21 (8):191–9. doi: 10.1002/acm2.12945
207. Lin H, Zou W, Li T, Feigenberg SJ, Teo B-KK, Dong L. A Super-Learner Model for Tumor Motion Prediction and Management in Radiation Therapy: Development and Feasibility Evaluation. *Sci Rep* (2019) 9 (1):14868. doi: 10.1038/s41598-019-51338-y
208. Cui S, Tseng H-H, Pakela J, Ten Haken RK, El Naqa I. Introduction to Machine and Deep Learning for Medical Physicists. *Med Phys* (2020) 47(5): e127–e47. doi: 10.1002/mp.14140
209. Caruana R, Lou Y, Gehrke J, Koch P, Sturm M, Elhadad N. Intelligible Models for HealthCare: Predicting Pneumonia Risk and Hospital 30-Day Readmission. In: *Proceedings of the 21th ACM SIGKDD International Conference on Knowledge Discovery and Data Mining* Sydney, Australia:Association for Computing Machinery (2015).
210. Luo Y, Tseng H-H, Cui S, Wei L, Ten Haken RK, El Naqa I. Balancing Accuracy and Interpretability of Machine Learning Approaches for Radiation Treatment Outcomes Modeling. *BJR Open* (2019) 1 (1):20190021. doi: 10.1259/bjro.20190021
211. Philbrick KA, Yoshida K, Inoue D, Akkus Z, Kline TL, Weston AD, et al. What Does Deep Learning See? Insights From a Classifier Trained to Predict Contrast Enhancement Phase From CT Images. *AJR Am J Roentgenol* (2018) 211(6):1184–93. doi: 10.2214/AJR.18.20331
212. Seah JCY, Tang JSN, Kitchen A, Gaillard F, Dixon AF. Chest Radiographs in Congestive Heart Failure: Visualizing Neural Network Learning. *Radiology* (2019) 290(2):514–22. doi: 10.1148/radiol.2018180887

Conflict of Interest: The authors declare that the research was conducted in the absence of any commercial or financial relationships that could be construed as a potential conflict of interest.

frontiers in Oncology

ORIGINAL RESEARCH
published: 21 March 2022
doi: 10.3389/fonc.2022.826414

Including Volume Effects in Biological Treatment Plan Optimization for Carbon Ion Therapy: Generalized Equivalent Uniform Dose-Based Objective in TRiP98

Marco Battestini[1,2], *Marco Schwarz*[2,3]*, *Michael Krämer*[4] *and Emanuele Scifoni*[2]

[1] Department of Physics, University of Trento, Trento, Italy, [2] Trento Institute for Fundamental Physics and Applications (TIFPA), Istituto Nazionale di Fisica Nucleare (INFN), Trento, Italy, [3] Trento Proton Therapy Center, Azienda Provinciale per i Servizi Sanitari (APSS), Trento, Italy, [4] Biophysics Department, GSI - Helmholtzzentrum für Schwerionenforschung, Darmstadt, Germany

We describe a way to include biologically based objectives in plan optimization specific for carbon ion therapy, beyond the standard voxel-dose-based criteria already implemented in TRiP98, research planning software for ion beams. The aim is to account for volume effects—tissue architecture-dependent response to damage—in the optimization procedure, using the concept of generalized equivalent uniform dose (gEUD), which is an expression to convert a heterogeneous dose distribution (e.g., in an organ at risk (OAR)) into a uniform dose associated with the same biological effect. Moreover, gEUD is closely related to normal tissue complication probability (NTCP). The multi-field optimization problem here takes also into account the relative biological effectiveness (RBE), which in the case of ion beams is not factorizable and introduces strong non-linearity. We implemented the gEUD-based optimization in TRiP98, allowing us to control the whole dose–volume histogram (DVH) shape of OAR with a single objective by adjusting the prescribed $gEUD_0$ and the volume effect parameter a, reducing the volume receiving dose levels close to mean dose when $a = 1$ (large volume effect) while close to maximum dose for $a >> 1$ (small volume effect), depending on the organ type considered. We studied the role of $gEUD_0$ and a in the optimization, and we compared voxel-dose-based and gEUD-based optimization in chordoma cases with different anatomies. In particular, for a plan containing multiple OARs, we obtained the same target coverage and similar DVHs for OARs with a small volume effect while decreasing the mean dose received by the proximal parotid, thus reducing its NTCP by a factor of 2.5. Further investigations are done for this plan, considering also the distal parotid gland, obtaining a NTCP reduction by a factor of 1.9 for the proximal and 2.9 for the distal one. In conclusion, this novel optimization method can be applied to different OARs, but it achieves the largest improvement for organs whose volume effect is larger. This allows TRiP98 to perform a double level of biologically driven optimization for ion beams, including at the same time RBE-weighted dose and volume effects in inverse planning. An outlook is presented on the possible extension of this method to the target.

Keywords: volume effect in radiotherapy, generalized equivalent uniform dose (gEUD), TRiP98, carbon ion therapy, treatment plan optimization, biological treatment planning, normal tissue complication probability (NTCP)

OPEN ACCESS

Edited by:
Stewart Mac Mein, German Cancer Research Center (DKFZ), Germany

Reviewed by:
Sarah Brüningk, ETH Zürich, Switzerland
Niklas Wahl, German Cancer Research Center (DKFZ), Germany

***Correspondence:**
Marco Schwarz
marcosch@uw.edu

Specialty section:
This article was submitted to Radiation Oncology, a section of the journal Frontiers in Oncology

Received: *30 November 2021*
Accepted: *31 January 2022*
Published: *21 March 2022*

Citation:
Battestini M, Schwarz M, Krämer M and Scifoni E (2022) Including Volume Effects in Biological Treatment Plan Optimization for Carbon Ion Therapy: Generalized Equivalent Uniform Dose-Based Objective in TRiP98. Front. Oncol. 12:826414. doi: 10.3389/fonc.2022.826414

1 INTRODUCTION

In the last decades, the physical and radiobiological properties of charged particles have been extensively studied, as an alternative to the traditional photons in radiation therapy (1). It was in particular emphasized that ion beams heavier than protons combine both physical and biological advantages (2). Among these particles, carbon ions have now reached clinical use in a dozen of treatment centers around the world, and typically, they are used for tumors that are inoperable or resistant to traditional treatments (3). Their use is presently still limited, primarily because of economic and logistical reasons, but also due to greater difficulty in characterizing and modeling the physics and radiobiological effects of ion beams on the biological tissues (4).

In state-of-the-art centers like HIT (Heidelberg), CNAO (Pavia), MED-Austron (Wiener Neustadt), or HIMAC (Chiba), the dose is delivered in a so-called "raster scanning mode", which allows optimal flexibility for improved tumor three-dimensional dose shaping and sparing of healthy tissues. The scanning parameters and the resulting dose distribution are obtained using dedicated treatment planning systems (TPSs) accounting for both physical and biological effects of the particles. TRiP98 (TReatment plannIng for Particles), the GSI (Darmstadt) research planning software for ion beams (5, 6), was the first TPS of this type and served as a reference for the following ones. This software allows to determine the optimal 3D biological dose distribution for a specific patient, imposing a uniform dose for the tumor and a maximum dose objective for critical structures. TRiP98 was used clinically during the GSI therapy pilot project, which started in 1997 in collaboration with DKFZ (Heidelberg), the University Clinic Heidelberg, and the FZ Rossendorf (Dresden), when 440 patients have been treated with carbon ions in an 11-year span, in particular with head and neck cancers (7). After that, it has been extensively used and expanded until now, as an advanced research tool for biological treatment planning with ion beams, including among others multiple-field optimization (8), advanced relative biological effectiveness (RBE)-weighted dose algorithms (9), oxygen enhancement ratio (OER)-driven optimization (10), helium and oxygen beams characterization (11, 12), and multiple-ion optimization (13). Despite all these advanced implementations, the volume effect was never included in the TRiP98 optimization, which is only based on a single dose value to date, i.e., the prescribed dose for target and a maximum dose for organs at risk (OARs).

Organs and tissues have a biological architecture, allowing them to perform specific functions. Such architecture has consequences also on the response of healthy organs to radiation, which is more complex than the response of an ensemble of cells that behave independently from one another. A key aspect determining the response of organized biological tissue to ionizing radiation is the so-called volume effect (14), which can be qualitatively described as the capability of an organ to compensate the radiation damage to part of it as long as the rest of the organ is sufficiently spared. There have been different proposals in the literature on a quantitative description of the volume effect. At the moment, one of the most commonly used is the generalized equivalent uniform dose (gEUD) proposed by Niemierko (15), which is an expression based on a power law dose–effect relation converting a heterogeneous dose distribution into a homogeneous dose distribution with the same biological effect.

There is a strong rationale for including volume effects in treatment planning optimization, in particular for OARs showing large volume effects, such as the lung, liver or parotid glands. Furthermore, the inclusion of the volume effect is a stepping stone towards the definition of cost functions that directly optimize the most clinically relevant parameters concerning healthy tissues, i.e., the normal tissue complication probability (NTCP).

Such an approach, which goes in the direction of what is called biologically oriented treatment planning, was tested for photon radiotherapy in a number of studies (16–18), investigating different approaches to extend the objective function for efficiently minimizing the gEUD. Over the past 10 years, the availability of gEUD-based optimization for photon radiotherapy in clinical practice has significantly increased. The use of gEUD in plan optimization has been addressed already in 2012 by Allen et al. (19). Only recently a single attempt to translate it for carbon ion therapy was performed based on different formulations for the equivalent uniform dose (EUD) (20). The latter case in fact is complicated by the additional biological level involved in a carbon plan optimization, namely, the RBE, a strongly non-linear effect.

The purpose of this work is to include objectives related to the volume effect in plan optimization for carbon ion therapy, in addition to the standard voxel-dose-based criteria already implemented in TRiP98. This approach should allow to optimize the dose in a different way according to the type of organ considered, attempting to improve the sparing of critical structures and therefore reducing the probability of complications.

This paper is organized as follows: we first describe the link between tissue architecture and normal tissue response to radiation, and we present an expression for gEUD. We then introduce the optimization problem in TRiP98; in particular, we define the cost function, we describe how the dose is calculated, and we present the optimization algorithms used in this study. We discuss in detail the novel optimization method based on the gEUD implemented in TRiP98 for OARs, and we show some treatment planning examples, comparing the new gEUD-based approach with the standard voxel-dose-based method. Finally, we discuss possible additional implementations for the optimization of the target and developments towards direct NTCP-based optimization.

2 MATERIALS AND METHODS

2.1 Tissue Architecture and Volume Effect

When complex biological systems are considered, like tissues or organs, cells are organized in structures that are often called functional sub-units (FSUs), which may also be visible at the morphological level (e.g., in lung alveoli or kidney nephrons).

The volume effect can be interpreted as a consequence of the fact that FSUs can be organized in different ways in different organs (14). For instance, a small volume effect (i.e., the fact that the organ damage is determined by the maximum dose, even if delivered to a very small portion of the organ itself) is the consequence of FSUs organized in form of a chain. In this case, it is sufficient that a single element of the chain breaks down for the chain not to exist anymore. This is the reason why complications associated with a small volume effect are also referred to as "serial". In the case of complications with a large volume effect (e.g., radiation pneumonitis), where the mean dose is the parameter that best correlates with the outcome, the FSUs are instead organized as threads of a rope. In this case, the rope is still functional as long as a sufficient number of threads are working, thus the name of "parallel" complication.

The "parallel" and "serial" behaviors are simplifications. In reality, each organ, and even each complication for the same organ, will have its own specific volume effect, which can be anywhere between a purely serial and purely parallel behavior.

2.1.1 Generalized Equivalent Uniform Dose

The gEUD is an expression to convert a heterogeneous dose distribution into a uniform dose associated with the same biological effect (15); the conversion is based on a power law:

$$gEUD\,[Gy] = \left(\frac{1}{M}\sum_{i=1}^{M} D_i^a\right)^{\frac{1}{a}} \tag{1}$$

where D_i is the dose associated with the voxel i, M is the number of voxels of the anatomical structure considered, and a is the parameter quantifies the volume effect of the organ/tissue considered, and it is specific to each biological structure (or each type of complication). For $a \to -\infty \Rightarrow gEUD \to D_{min}$, for $a \to +\infty \Rightarrow g\text{EUD} \to D_{max}$, and a=1 $\Rightarrow gEUD = D_{mean}$. This phenomenological description can be applied to both tumors ($a < 0$) and normal tissues ($a < 0$).

In addition to representing a more realistic description of the dose–effect relation for healthy tissues, from an optimization perspective, the use of gEUD has the advantage of providing a single metric able to control the volume irradiated from 0 to maximum dose, while dose–volume histogram (DVH)-based optimization considers only one dose value per DVH point.

The benefits of the using gEUD in the optimization of treatment plans have been investigated in the case of photon therapy, for different TPS and using different types of optimization algorithms [see e.g., Wu et al. (16), Schwarz et al. (18), and Fogliata et al. (21)].

The goal of this kind of optimization is to achieve a reduction in dose to the OAR focusing on the dose range that matters the most for that specific organ or complication. For instance, in the case of organs where the probability of complication is related to the mean dose, the setting $a = 1$ implies that the optimizer will have the same incentive in achieving dose reduction anywhere between 0 and maximum dose. On the other hand, in the case of small volume effects, by setting $a >> 1$, the *gEUD* will be largely determined by the DVH shape at high doses, thus creating an incentive for the optimizer to reduce the dose mostly in that dose range.

2.1.2 Normal Tissue Complication Probability

The probability of encountering a radiotherapy side effect is typically quantified *via* NTCP models. Several NTCP models exist, and the so-called Lyman–Kutcher–Burman (LKB) model (22, 23) is the most commonly used so far. An additional advantage of the LKB model in the context of our work is that its formulation is consistent with the gEUD expression, and it is therefore possible to use it as a phenomenological description of the dose–effect relation for an OAR. In the LKB formulation, the NTCP is defined as

$$NTCP\,(u) = \frac{1}{\sqrt{2\pi}}\int_{-\infty}^{u} e^{-\frac{t^2}{2}}dt \tag{2}$$

where

$$u = \frac{gEUD - TD_{50}}{m \cdot TD_{50}} \tag{3}$$

TD_{50} is the whole organ dose corresponding to 50% complication probability and m is the slope of the dose–response curve at TD_{50}. Therefore, an organ that receives a heterogeneous dose, described by a DVH, has the same NTCP as if it was irradiated with a uniform dose equal to *gEUD*.

2.2 Optimization in TRiP98

A radiotherapy treatment plan for a patient is a calculated dose distribution that achieves a satisfactory balance between the tumor control probability and the sparing of healthy tissues. In actively scanned particle therapy, the dose is usually delivered using a raster scanning system, which maximizes the degrees of freedom available in dose delivery, and as a consequence in dose shaping. In order to generate a treatment plan, a computational engine like TRiP98 is used: this allows to optimize the vector of particle numbers $\vec{N}_{opt}$ for all rasterpoints from all fields in order to obtain a 3D dose distribution that respects the objectives imposed (plan optimization), taking into account patient data (CT images, volume of interest (VOI) contours, the prescribed and maximum doses for each VOI, etc.), beam data (number of fields, ion species, available energies, etc.), and also physics and radiobiology data (depth-dose distributions, particle energy spectra, RBE, etc.). The optimization task produces in the output the scanner parameters (beam energies, particle fluences and positions) and the patient plan (DVH, dose distribution, etc.). The crucial part of the production of an acceptable treatment plan is the optimization task. The TRiP98 structure is schematized in **Figure 1**.

2.2.1 Objective Function

The starting point of the optimization procedure is the definition of a cost function, which formalizes the treatment goals in a mathematical expression. In a clinically realistic case, these objectives are in conflict with each other, and the final dose distribution is the best achievable compromise given such objectives. In TRiP98, the available objectives are uniform dose to the target and an upper dose value for each OAR (5, 6). The TRiP98 cost function is defined as follows:

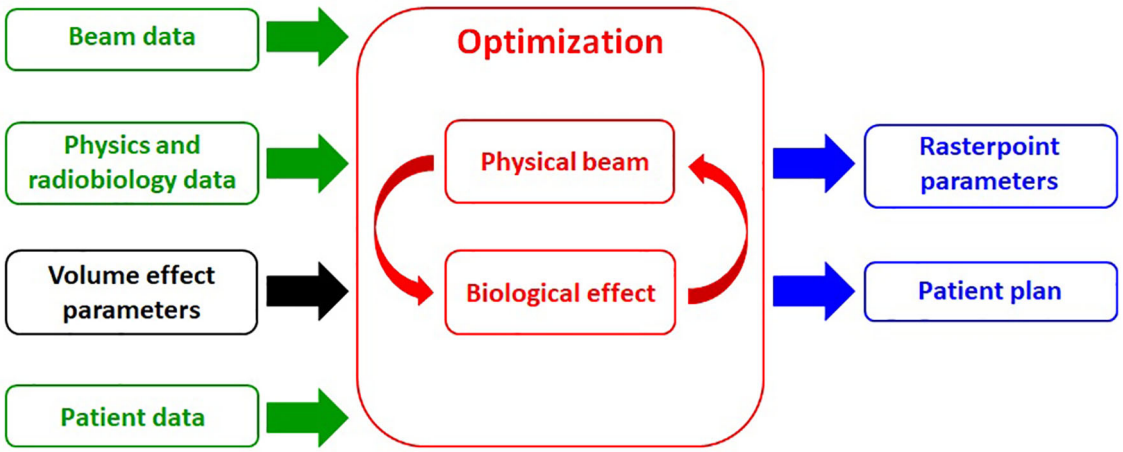

FIGURE 1 | Simplified flowchart structure of TRiP98: input data (green boxes), including the extension developed in this work, i.e., the implementation of a generalized equivalent uniform dose (gEUD)-based objective in the optimization procedure (black box); optimization task (red boxes); output data (blue boxes).

$$\chi^2_{D_{pre}/D_{\max}}(\vec{N}) = (w_T)^2 \sum_{i=1}^{M_T} \frac{\left(D_{pre} - D_i(\vec{N})\right)^2}{(\Delta D_{pre})^2} + (w_{OAR})^2 \sum_{i=1}^{M_{OAR}} \frac{\left(D_{\max} - D_i(\vec{N})\right)^2}{(\Delta D_{\max})^2} \theta_{D_{\max}} \quad (4)$$

where $\vec{N}$ is the vector of particle numbers; M_T and M_{OAR} are the total number of target and OAR voxels, respectively; D_{pre} and D_{max} are the prescribed dose per fraction for the target and the maximum dose per fraction for the OAR, respectively, where D_{max} is defined as a percentage of D_{pre}; $D_i(\vec{N})$ is the actual physical or biological dose per fraction at voxel i; ΔD_{pre} and ΔD_{max} are normalization factors, and they are usually imposed equal to $0.025 \cdot D_{pre}$ and $0.025 \cdot D_{max}$, respectively, where 0.025 is half of the estimated percental accuracy in dose calculation (5); w_T and w_{OAR} are the weight factors associated with each VOI; finally

$$\theta_{D_{\max}} = \theta(D_i(\vec{N}) - D_{\max}) = \begin{cases} 1, & D_i(\vec{N}) > D_{\max} \\ 0, & D_i(\vec{N}) \le D_{\max} \end{cases} \quad (5)$$

is a Heaviside function in order to penalize only overdosage of OAR voxels, unlike the target, where both under- and overdosages are penalized.

2.2.2 Dose Calculation

The interaction between a heavy ion beam and biological matter is very complex and leads to the creation of a mixed radiation field, due to the presence of ions with a very different linear energy transfer (LET) and the production of secondary particles caused by the fragmentation of the primary ions. The actual biological effect must be taken into account when calculating the dose in the case of a particle beam.

The physical dose (or absorbed dose) (5) at each voxel i is calculated as

$$D_i^{phys}(\vec{N}) = \vec{d}_i^T \cdot \vec{N} = \sum_j d_{ij} N_j \quad (6)$$

where $\vec{d}_i^T$ is the transposed column vector of the dose correlation matrix, whose elements d_{ij} represent the contribution from rasterpoint j to the dose at voxel i (8).

The biological dose (or RBE-weighted dose) in a voxel i is defined as the product between the physical dose D_i^{phys} and the relative biological effectiveness RBE_i (6):

$$D_i^{bio}(\vec{N}) = D_i^{phys}(\vec{N}) \cdot RBE_i(\vec{N}) \quad (7)$$

where the physical dose in each voxel i is the result of the superposition of several pencil beams (5), while RBE is a function of the tissue type and mixed radiation field, and it is calculated according to the local effect model (LEM) (6, 24–26).

Due to the stochastic nature of ion traversals and energy distributions, the biological damage for mixed radiation fields is estimated using Monte Carlo integration methods in the "classical" approach (6). Since this approach is very time-consuming, a faster method was developed, i.e., the so-called "low-dose" approximation (27), which allows to determine an analytical expression for the biological dose with an acceptable error of a few percent with respect to the "classical" approach in a therapeutic range of doses (6), i.e.,

$$D_{bio} = \begin{cases} \sqrt{\frac{-\ln S}{\beta_X} + \left(\frac{\alpha_X}{2\beta_X}\right)^2} - \left(\frac{\alpha_X}{2\beta_X}\right), & -\ln S \le -\ln S_t \\ \frac{-\ln S + \ln S_t}{s_{\max}} + D_t, & -\ln S > -\ln S_t \end{cases} \quad (8)$$

where the biological effect is

$$-\ln S = \begin{cases} (\bar{\beta} D_{phys} + \bar{\alpha}) D_{phys}, & D_{phys} \le D_t \\ (\bar{\beta} D_t + \bar{\alpha}) D_t + (D_{phys} - D_t) s_{\max}, & D_{phys} > D_t \end{cases} \quad (9)$$

where D_t and S_{max} are respectively the dose threshold and the maximum slope at high doses used by the LEM, determining the transition from the linear-quadratic to a purely linear region of response, S_t is the survival fraction at D_t, α_x and β_x are the X-ray coefficients of the dose–response curve, and $\bar{\alpha}$ and $\bar{\beta}$ are the mixed field coefficients, derived by a Zaider–Rossi weighting (28) of the α and β parameters of each particle type and energy, composing the beam (27).

2.2.3 Iterative Optimization Algorithms

The optimization problem consists in determining the optimal particle number for each spot *j*, i.e., the optimal dose distribution, *via* minimization of the cost function $\chi^2(\vec{N})$. This requires to deal with a couple of problems, such as several ten thousands of rasterpoints to be handled as free parameters, a minimum number of particles for each rasterspot due to the technological limitations of the raster scanner, the presence of the Heaviside functions in the cost function, and the non-linearity of the biological dose. All this makes it impossible to solve the problem analytically and forces the use of fast and efficient algorithms. Several optimization methods exist, approaching the problem in different ways. In TRiP98, the type of algorithms already implemented belong to *line search methods*, which are commonly used and are based on the gradient of the cost function with respect to the particle numbers $\nabla \chi^2(\vec{N})$.

The principle behind these iterative algorithms is as follows: at each iteration k, the vector of the particle numbers $\vec{N}_k$ is obtained such that the condition $\chi^2(\vec{N}_{k+1}) < \chi^2(\vec{N}_k)$ is true. The new particle numbers are calculated as

$$\vec{N}_{k+1} = \vec{N}_k + \mu_k \vec{h}_k \tag{10}$$

With this parametrization, the multidimensional optimization problem is reduced to the determination of a minimization direction $\vec{h}_k$ and the estimation of a stepsize μ_k along the search direction $\vec{h}_k$. Repeating this calculation for a certain number of iterations, the actual vector of the particle numbers $\vec{N}_k$ converges towards the optimal vector $\vec{N}_{opt}$. The starting values for particle numbers $\vec{N}_0$ are calculated during the preoptimization as described in Gemmel et al. (8).

Several iterative optimization algorithms are implemented in TRiP98. In this work, both the simplest one [steepest descent (SD)] (8), which consists in minimizing the cost function along its negative gradient, and the default one [Fletcher–Reeves variant of conjugated gradients (CGFR)] (9), which is faster because the minimization direction takes into account the previous successful iterations, have been employed. More details about iterative optimization algorithms used in this work and convergence tests are given in the **Supplementary Material (Section 1)**.

The optimal particle numbers can be obtained considering the two or more irradiation fields separately (single field optimization) or simultaneously (multiple field optimization) (8) during the optimization procedure. In particular, in this work, the second approach is used because it allows a better sparing of the critical biological structure, in particular for complex anatomy cases.

There are two methods to obtain the optimal particle numbers. The simplest approach consists in neglecting the variability of the biological effect, optimizing the absorbed dose, which depends in a linear way on the number of particles $\vec{N}$, i.e., the actual dose in the cost function is $D_i(\vec{N}) = D_i^{phys}(\vec{N})$ (physical optimization) (5). Instead, in the second approach, the actual dose is calculated according to equation 8, i.e., $D_i(\vec{N}) = D_i^{bio}(\vec{N})$, which depends in a non-linear way on the number of particles $\vec{N}$ (biological optimization) (6).

2.3 Implementation of Generalized Equivalent Uniform Dose-Based Optimization for Organs at Risk

The gEUD-based optimization allows to control the whole DVH shape of an OAR using a single objective, taking into account its volume effect in the optimization, by adjusting the prescribed value $gEUD_0$, i.e., the desired dose level to be reached for each OAR, and the volume effect parameter a, which quantifies the volume effect of the OAR considered. In order to do this, an additional term for each OAR in the original cost function, with a quadratic penalty, is implemented in TRiP98, namely,

$$\chi^2_{gEUD}(\vec{N}) = (w_{OAR})^2 \frac{(gEUD_0 - gEUD(\vec{N}))^2}{(\Delta gEUD_0)^2} \theta_{gEUD} \tag{11}$$

where

$$gEUD(\vec{N}) = \left(\frac{1}{M_{OAR}} \sum_{i=1}^{M_{OAR}} (D_i(\vec{N}))^a \right)^{\frac{1}{a}} \tag{12}$$

is the actual value, M_{OAR} is the total number of voxels for a single OAR, $\Delta gEUD_0 = 0.025\ gEUD_0$ is the normalization factor, w_{OAR} is the weight factor, and

$$\theta_{gEUD} = \theta(gEUD(\vec{N}) - gEUD_0) = \begin{cases} 1, & gEUD(\vec{N}) > gEUD_0 \\ 0, & gEUD(\vec{N}) \leq gEUD_0 \end{cases} \tag{13}$$

is a Heaviside function in order to penalize OAR with actual gEUD larger than the prescribed value $gEUD_0$.

Therefore, the total cost function is

$$\chi^2(\vec{N}) = \chi^2_{D_{pre}/D_{\max}}(\vec{N}) + \chi^2_{gEUD}(\vec{N}) \tag{14}$$

and it is possible to decide whether to optimize the dose distribution for a given organ by imposing a maximum dose or a prescribed gEUD and also to choose different values of D_{max} or $gEUD_0$ for each OAR considered.

In principle, by decreasing $gEUD_0$, one can achieve a lower $gEUD$ for a given organ, i.e., a larger sparing. The expected result of changes in a is to change the dose range where the organ sparing will be maximized: for example, selecting $a = 1$ the whole area under the DVH curve should be minimized, while for $a >> 1$, the best DVH will be obtained in terms of sparing at high doses.

In the following paragraphs, the solutions in the case of physical and biological optimization are presented.

2.3.1 Solution for Physical Optimization

The fundamental step to solve the optimization problem is the determination of the gradient of the cost function $\chi^2(\vec{N})$ with respect to the particle numbers $\vec{N}$. In the case of physical optimization, i.e., neglecting *RBE* in dose calculation, the gradient of the total cost function is calculated as

$$\nabla \chi^2(\vec{N}) = \nabla\chi^2_{D_{pre}/D_{\max}}(\vec{N}) + \nabla\chi^2_{gEUD}(\vec{N}) \tag{15}$$

where the voxel-dose-based term is

$$\begin{aligned}\nabla\chi^2_{D_{pre}/D_{\max}} &= -2(w_T)^2\sum_{i=1}^{M_T}\frac{(D_{pre}-D_i^{phys})}{(\Delta D_{pre})^2}\cdot\nabla D_i^{phys}\\ &-2(w_{OAR})^2\sum_{i=1}^{M_{OAR}}\frac{(D_{\max}-D_i^{phys})}{(\Delta D_{\max})^2}\cdot\nabla D_i^{phys}\cdot\theta_{D_{\max}}\end{aligned} \tag{16}$$

and the new gEUD-based term is

$$\begin{aligned}\nabla\chi^2_{gEUD} &= -2(w_{OAR})^2\,\frac{(gEUD_0-gEUD)}{(\Delta gEUD_0)^2}\left(\frac{1}{M_{OAR}}\right)^{\frac{1}{\alpha}}\\ &\times\left(\sum_{i=1}^{M_{OAR}}(D_i^{phys})^a\right)^{\frac{1}{\alpha}-1}\sum_{i=1}^{M_{OAR}}(D_i^{phys})^{a-1}\cdot\nabla D_i^{phys}\cdot\theta_{gEUD}\end{aligned} \tag{17}$$

Thanks to the chain rule in the derivation, the task becomes the calculation of the absorbed dose gradient for each voxel *i* from equation 6, which is calculated as $\nabla D_i^{phys} = \vec{d}_i^T$, where $\vec{d}_i^T$ is the transposed column vector of the dose correlation matrix already introduced.

The second important step is the determination of a scalar μ_k, i.e., the stepsize, for each iteration *k*, solving the following equation:

$$\frac{d\chi^2(\vec{N}_k+\mu_k\vec{h}_k)}{d\mu_k} = \frac{d\chi^2_{D_{pre}/D_{\max}}(\vec{N}_k+\mu_k\vec{h}_k)}{d\mu_k} + \frac{d\chi^2_{gEUD}(\vec{N}_k+\mu_k\vec{h}_k)}{d\mu_k} = 0 \tag{18}$$

for μ_k and for each iteration *k*, where the physical dose at iteration $k+1$ is calculated as $D_i^{phys}(\vec{N}_{k+1}) = \vec{d}_i^T\vec{N}_{k+1} = \vec{d}_i^T(\vec{N}_k + \mu_k\vec{h}_k)$.

In the case of physical optimization and for OARs with large volume effects, namely, considering $a = 1$, equation 18 is solved analytically because all terms are linear in μ_k. Instead, in the case of $a > 1$ due to the non-linearity of the gEUD-based term, we made two approximations: linearization of $gEUD(D_i^{phys}(\vec{N}_{k+1}))$ for small dose variation in each voxel *i*, i.e., $\mu_k\vec{d}_i^T\vec{h}_k \ll \vec{d}_i^T\vec{N}_k$, and large volume effect approximation, i.e., considering $a = 1$. The expression obtained for the stepsize μ_k^{phys}, in this case, is reported in the **Supplementary Material (Section 2)**.

2.3.2 Solution for Biological Optimization

Biological effectiveness and its relative variation for a high Z particle like carbon are not negligible. For this reason, we focused on biological optimization, which consists in considering the total cost function defined in equation 14, but where the actual dose $D_i(\vec{N})$ at each voxel *i* is calculated as the RBE-weighted dose D_i^{bio}, i.e., according to equation 7. The difficulty is that this expression is highly non-linear because both the absorbed dose D_i^{phys} and the RBE_i depend on the vector of particle numbers $\vec{N}$. An approach to solve the problem is now presented. As for the physical case, also for biological optimization, it is necessary to calculate the gradient of the total cost function and estimate the stepsize.

The expression of the gradient of the total cost function is the same as for the physical optimization case thanks to the chain rule in the derivation; the only difference is the presence of the biological dose gradient with respect to the number of particles:

$$\nabla D_i^{bio} = RBE_i\cdot\nabla D_i^{phys} + D_i^{phys}\cdot\nabla RBE_i \tag{19}$$

where the first term is the physical gradient component, while the second term is the biological gradient component.

There are several ways to calculate this gradient already implemented in TRiP98: the simplest approach is the classical method (6), in which ∇RBE_i is neglected, namely, the RBE is considered as a constant. However, in this way, the minimization direction is not optimally determined, and we may have accuracy problems during optimization. Therefore, the approach used in this work is based on the so-called "low-dose" approximation for a mixed radiation field (27), which allows to obtain an analytical expression for the biological dose and its gradient, according to equation 8, in a fast way.

The second element necessary to solve the optimization problem is the determination of a stepsize μ_k^{bio} for each iteration *k*, in principle solving equation 18. But due to the non-linearity of the biological dose with $\vec{N}$, it is not possible to obtain an analytical expression for the stepsize μ_k. For this reason, only an estimate of the true solution can be obtained, which approximately fulfills the equation.

The most common method used in TRiP98 is based on the calculation of the stepsize μ_k^{phys} solving equation 18; then, using "damping factor" *f*, an estimate of μ_k^{bio} for each iteration *k* is thus obtained as

$$\mu_{bio} = f\cdot\mu_{phys} \tag{20}$$

Testing different "damping factor" values, it is noticed that a reasonable value is $f = 0.5$, as it was reported in Gemmel et al. (8).

2.4 Patient and Plan Parameters

In order to study the role of the cost function parameters $gEUD_0$ and *a*, the gEUD-based optimization is tested considering a plan containing the proximal parotid gland as an OAR, in addition to the tumor (chordoma). Also the brainstem is considered, as an additional OAR, in order to have a clinically realistic plan. The tumor is irradiated using two nearly opposite fields, with (couch) angles −100° and 75°, according to the original plan. The uniform prescribed dose D_{pre} for the target is 3 Gy, according to the original prescription for a single fraction of the patient case, while the parotid is optimized with different combinations of $gEUD_0$ and *a* values. The SD algorithm was used.

The new gEUD-based optimization approach is tested for different sample plans of patients treated for head and neck cancers during the GSI pilot project. The tumor is a chordoma located in the skull base, while the typical OARs in this region are organs with a small volume effect, like the spinal cord, the

brainstem, the optic nerves, and the chiasm, for which the most important dose level is the maximum dose. But there are also important glands located in correspondence of the cheeks with a large volume effect, i.e., the parotid glands, for which the aim is to reduce the mean dose, in order to reduce the probability of complications (reduction of the salivary flow, speech and taste alterations, etc.). For all these plans, a multiple field optimization of the biological dose is performed, using the CGFR algorithm. Moreover, the plans obtained using the gEUD-based optimization are compared with the results coming from the standard voxel-dose-based approach. The prescriptions for the plans for both voxel-dose-based and gEUD-based optimization are reported in **Table 1**.

A typical situation of chordoma case is patient number 135 from the patient database of the GSI pilot project. This represents a very complex anatomical geometry, where the tumor is wrapped around the spinal cord, which is the OAR considered in this plan. This tumor is treated using two nearly opposite fields, with (couch) angles −100° and 104°, according to the original plan.

Another typical treatment plan is patient 335, which contains multiple OARs with small volume effects, like the spinal cord, the brainstem, the right and left optic nerves, the chiasm, but also the right parotid gland (proximal in this irradiation geometry), with a large volume effect. The tumor is irradiated using two nearly opposite fields, with (couch) angles −100° and 75°, according to the original plan.

A further investigation is done with this treatment plan. In fact, in the original plan for patient 335, only the proximal (right) parotid gland was considered. Therefore, the idea is to consider also the distal (left) parotid gland in order to see what happens if it is optimized using the gEUD-based approach. The aim is to reduce the mean dose received by both parotids. For this reason, an additional objective is considered for the left parotid in the definition of the total cost function; in particular, a volume effect parameter equal to 1 and a $gEUD_0$ equal to 0.60 Gy are used for both glands. The objectives for the other organs are the same as in the previous plan (see **Table 1**).

Additional results about patient plans optimization are reported in the **Supplementary Material (Section 3)**.

The estimates of NTCP presented in (29) for the parotids correspond to a dose per fraction of 2 Gy, while the dose per fraction prescribed in the optimization of our work is 3 Gy. This choice is due to the fact that the treatment plans considered in this work come from the GSI pilot project (which is a standard reference for TRiP98 implementations), and for this reason, we decided not to change the prescribed dose values. However, this deviation would only involve at most an underestimation of the improvement obtained in terms of NTCP with the new approach based on gEUD compared to the method based on the maximum dose. A possible way to solve this limitation is to calculate the mean dose to the parotids in terms of EQD2 and then to estimate their NTCP, i.e.,

$$EQD2 = D_{tot}\left(\frac{\alpha/\beta + D_{tot}/N_{frac}}{\alpha/\beta + 2\ Gy}\right) \tag{21}$$

where D_{tot} is the total dose, N_{frac} is the number of fractions, and α/β = 2 Gy in this case.

3 RESULTS

3.1 Role of the Cost Function Parameters

This section reports the results obtained for the study of the cost function parameters during the optimization, in particular $gEUD_0$ and a for an OAR. The patient considered has been described in Section 2.4.

The DVH in **Figure 2A** shows the dependence of the dose distributions for values of $gEUD_0$ between 0.80 and 0.40 Gy, for a fixed weight factor w_{OAR} = 20 and volume effect parameter a = 1. As expected, decreasing $gEUD_0$, the mean dose D_{mean} decreases from 0.81 to 0.44 Gy. Instead, the different impact on the DVH shape is visible in **Figure 2B**, using different values for the volume effect parameter a, with a = 1 minimizing the mean dose, while as a increases, this reduction shifts to regions of the DVH that receive higher doses (the maximum dose D_{max} decreases with increasing a, in particular from 2.69 Gy for a = 1 to 2.38 Gy for a = 10). It should be noted that in **Figure 2B** the $gEUD_0$ value is changed correspondingly to the variation of the a

TABLE 1 | Cost function parameters for plans 135 and 335.

Plan 135		
VOI	**Voxel-dose-based opt.**	**gEUD-based opt.**
Target	D_{pre} = 3.00 Gy, w_T = 1	D_{pre} = 3.00 Gy, w_T = 1
Spinal cord	D_{max} = 1.50 Gy, w_{OAR} = 1	$gEUD_0$ = 1.30 Gy, a = 20, w_{OAR} = 25
Plan 335		
VOI	**Voxel-dose-based opt.**	**gEUD-based opt.**
Target	D_{pre} = 3.00 Gy, w_T = 1	D_{pre} = 3.00 Gy, w_T = 1
Right parotid	D_{max} = 2.25 Gy, w_{OAR} = 1	$gEUD_0$ = 0.50 Gy, a = 1, w_{OAR} = 20
Brainstem	D_{max} = 2.25 Gy, w_{OAR} = 1	$gEUD_0$ = 1.90 Gy, a = 20, w_{OAR} = 20
Spinal cord	D_{max} = 1.80 Gy, w_{OAR} = 1	$gEUD_0$ = 1.40 Gy, a = 20, w_{OAR} = 20
Right optic nerve	D_{max} = 1.50 Gy, w_{OAR} = 1	$gEUD_0$ = 0.20 Gy, a = 20, w_{OAR} = 20
Left optic nerve	D_{max} = 1.50 Gy, w_{OAR} = 1	$gEUD_0$ = 1.30 Gy, a = 20, w_{OAR} = 20
Chiasm	D_{max} = 1.50 Gy, w_{OAR} = 1	$gEUD_0$ = 1.10 Gy, a = 20, w_{OAR} = 20

VOI, volume of interest; gEUD, generalized equivalent uniform dose.

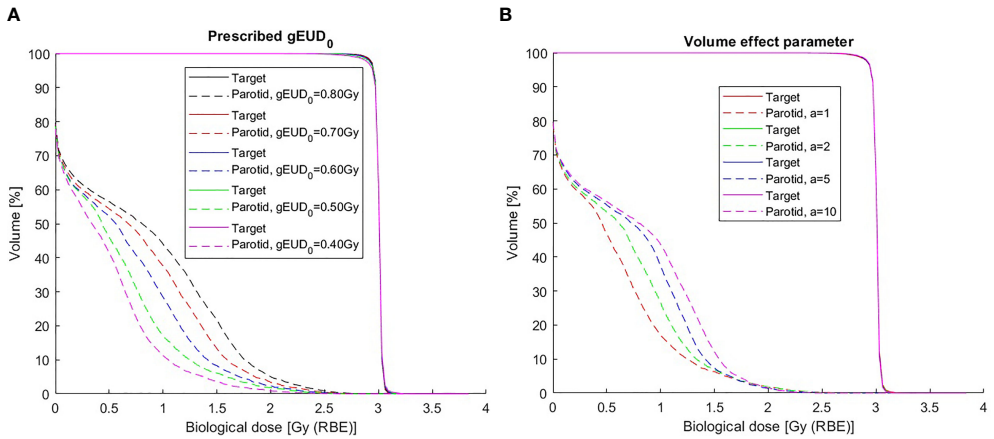

FIGURE 2 | Dose–volume histograms for a chordoma patient (same as in **Figure 3**). **(A)** For different $gEUD_0$ to the parotid. Cost function parameters: D_{pre} = 3.00 Gy, w_T = *1* (target); w_{OAR} = *20*, $gEUD_0$ = 0.80, 0.70, 0.60, 0.50, 0.40 Gy, and a= 1 (parotid). **(B)** For different a values of the parotid. Cost function parameters: D_{pre} = 3.00 Gy, w_T = *1* (target); w_{OAR} = *20*, ($gEUD_0$, a) = [(0.50 Gy, 1), (0.80 Gy, 2), (1.15 Gy, 5), (1.45 Gy, 10)] (parotid).

value to reflect the different regions of the optimization, by obtaining D_{max} values almost constant. All these parotid dose distributions are achievable without affecting the target dose. This effect is also visible in the 2D dose distributions (**Figure 3**).

Therefore, by appropriately choosing a pair of values for the volume effect parameter and for the prescribed gEUD, it is possible to finely control the shape of the DVH, depending on the type of biological architecture of the organ under consideration. Of course, the levels of control and variability of the DVH shape depend not on the gEUD parameters only but also on how the different components of the whole cost function interact with one another.

3.2 Comparison Between Voxel-Dose-Based and Generalized Equivalent Uniform Dose-Based Optimization

This section shows the results obtained for patient plans optimized with the gEUD-based and voxel-dose-based approach. The plan parameters have been described in Section 2.4.

In the case of patient number 135, from the gEUD values and the maximum doses obtained (**Table 2**) and from the DVHs (**Figure 4C**), it is evident that by using a volume effect parameter equal to 20, it is possible to obtain very similar plans using two different optimization approaches: in particular the *gEUD* values of the spinal cord are equivalent, and the target DVHs are identical. This is also confirmed by the dose distributions as shown in the CT slices in **Figures 4A, B**. The choice of a = 20 is due to the fact that the spinal cord is a typical serial organ and therefore requires a large volume effect parameter value. Furthermore, considering, for example, a = 15 or a = 25 in the optimization, the maximum dose is stable (D_{max} = 1.83 Gy and D_{max} = 1.79 Gy, respectively), and for this reason, the value a = 20 was chosen.

For patient number 335, observing the gEUD values and the maximum doses of the OARs coming from the optimization (**Table 3**), the DVHs (**Figure 5**), and the dose distributions (**Figure 6**), it is possible to conclude that the optimization of a complex plan, containing many biological structures with a small volume effect, using gEUD-based objectives is feasible; in particular, the DVHs of organs with a small volume effect are equivalent from a clinical point of view, but also the gEUD values for these organs, with a = 20, are the same.

In addition to that, the most important result obtained here is that the gEUD-based optimization allows to reduce the mean dose received by the proximal parotid gland, considering a volume effect parameter equal to 1 (see **Table 3**), without losing target coverage; it is also visible by observing the dose distributions in **Figure 6**. This is very important because the probability of a complication for this biological structure, i.e., the NTCP, is linked with the mean dose. Therefore, a gEUD reduction corresponds to a NTCP reduction. This is quantified using the LKB model for NTCP, according to equations 2 and 3, and considering the parameters proposed by Dijkema et al. (29), where n = a = 1 was fixed in the fit, and the values of TD_{50} and m and their 95% CIs were TD_{50} = 39.9 Gy (37.3–42.8) and m = 0.40 (0.34–0.51).

For this purpose, a complete treatment plan of 20 fractions of 3 Gy is considered. Then the NTCP curve for the right parotid is plotted as a function of the *gEUD* for a = 1, i.e., D_{mean}; furthermore, the NTCP values corresponding to the gEUD values obtained with the two optimization methods are calculated, and they are plotted in **Figure 7**. In particular, for this plan, the NTCP of the proximal parotid is reduced from 6.98% to 3.09%, i.e., by a factor of 2.3, using the gEUD-based optimization. This means a higher sparing of the parotid gland using this new optimization approach. Considering EQD2 calculation according to equation 21, the NTCP is reduced from 11.09% to 4.37%, i.e., by a factor of 2.5.

Considering both parotid glands for patient number 335, as can be seen from **Table 4** and from **Figures 8**, **9**, a mean dose reduction for both parotids is achieved using gEUD-based optimization instead of imposing a maximum dose for each gland. Note that a further reduction of the prescribed D_{max}, besides, it does not correlate directly with a mean dose reduction,

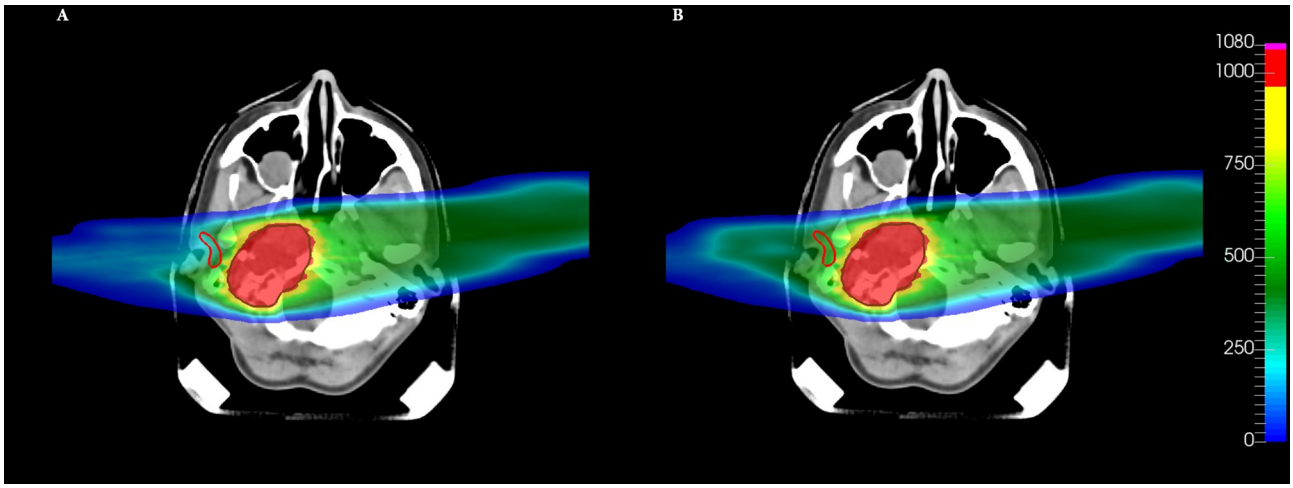

FIGURE 3 | Comparison of dose distributions on a CT slice for different volume effect parameters *a* of the parotid. Cost function parameters: **(A)** $gEUD_0$ = 0.50 Gy, *a* = 1 (red DVH in **Figure 2B**). **(B)** $gEUD_0$ = 1.45 Gy, *a* = 10 (violet DVH in **Figure 2B**). The target (brown contour) and the right parotid (red contour) are shown. The dose levels are plotted in per mil of the prescribed dose.

TABLE 2 | gEUD and other dosimetric indexes for the VOIs of plan 135.

Parameter	Voxel-dose-based opt.	gEUD-based opt.
	Target	
D_{min}	2.20 Gy	2.17 Gy
D_{max}	3.24 Gy	3.24 Gy
D_{mean}	3.00 Gy	3.00 Gy
CI	1.25	1.25
	Spinal cord	
gEUD (*a* = 20)	1.37 Gy	1.35 Gy
D_{max}	1.92 Gy	1.83 Gy

CI = volume 95% isodose / volume VOI.
gEUD, generalized equivalent uniform dose; OAR, organ at risk; VOI, volume of interest.

leads to a worsening of the target coverage, and we chose to compare plans with the same level of target coverage.

Furthermore, from the NTCP curve in **Figure 10**, a reduction of NTCP for both parotids can be seen, in particular from 6.98% to 4.03% for the proximal one and from 10.28% to 3.93% for the distal one, while considering EQD2 calculation according to equation 21, the NTCP is reduced from 11.10% to 4.37% (proximal parotid) and from 16.92% to 5.78% (distal parotid).

4 DISCUSSION

In this work, a possible approach of the gEUD-based optimization is implemented for the first time in TRiP98 as an alternative to the standard voxel-dose-based criteria. The resulting optimization method is able to account for RBE weighting of the dose and volume effects at the same time, i.e., a double level of biologically driven treatment planning.

From studying the cost function parameters during the optimization procedure, it emerges that it is possible to obtain different dose distributions for a given OAR using various combinations of prescription $gEUD_0$ and volume effect parameter *a*. In particular, as $gEUD_0$ decreases, it allows a greater sparing of the OAR considered, while as the parameter *a* increases, the DVH of the OAR takes very different shapes. For example, for *a* = 1, there is a decrease in the volume receiving doses close to the mean dose, while for a >> 1, there is a decrease in the volume receiving higher doses, as expected, thus showing high flexibility in planning criteria. This result is very important since gEUD is closely linked to the concept of NTCP, and therefore a decrease of gEUD leads to a reduction of NTCP. This is exactly what happens for patient plan 335 (**Figures 5**, **6**, **8**, **9**), where a reduction of *gEUD* for *a* = 1 in the case of the parotid involves a greater sparing of this gland and a reduction of the risk of complications quantified in terms of NTCP (**Figures 7**, **10**). Even more importantly, this occurs both considering the single parotid or both glands during the optimization and also without losing control of the target DVH. This means that, in principle, by choosing a reasonable combination of $gEUD_0$ and *a*, it is possible to reduce the probability of a complication for a given OAR by imposing a

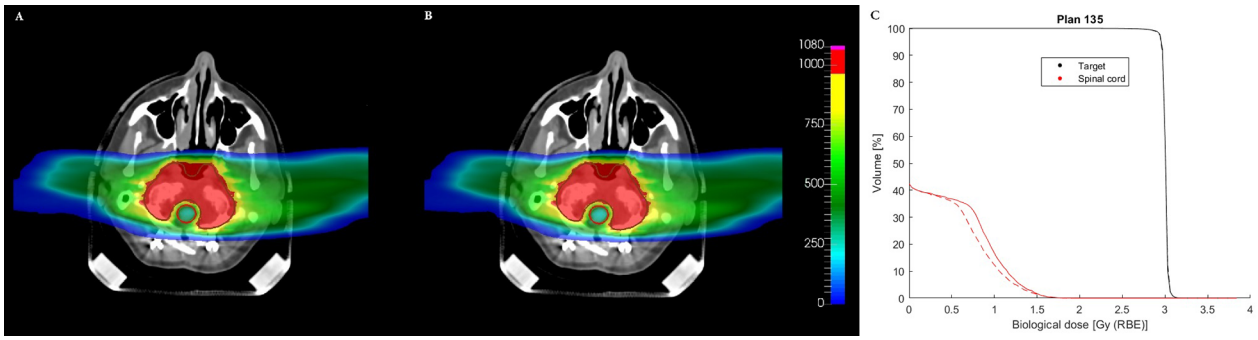

FIGURE 4 | Comparison of dose distributions on a CT slice for patient plan 135, obtained with **(A)** voxel-dose-based and **(B)** gEUD-based optimization. The target (brown contour) and the spinal cord (red contour) are shown. The dose levels are plotted in per mil of the prescribed dose. **(C)** Comparison of DVHs obtained with voxel-dose-based (solid line) and gEUD-based (dashed line) optimization for patient plan 135. gEUD, generalized equivalent uniform dose; DVH, dose–volume histogram.

TABLE 3 | gEUD, NTCP and other indexes for the VOIs of plan 335.

Parameter	Voxel-dose-based opt.	gEUD-based opt.
	Target	
D_{min}	2.52 Gy	2.16 Gy
D_{max}	3.17 Gy	3.39 Gy
D_{mean}	3.00 Gy	3.00 Gy
CI	1.24	1.27
	Right parotid	
gEUD (*a* = 1)	0.82 Gy	0.50 Gy
NTCP	11.09%	4.37%
D_{max}	2.51 Gy	2.80 Gy
	Brainstem	
gEUD (*a* = 20)	1.89 Gy	1.93 Gy
D_{max}	2.53 Gy	2.62 Gy
	Spinal cord	
gEUD (*a* = 20)	1.40 Gy	1.40 Gy
D_{max}	1.89 Gy	1.93 Gy
	Right optic nerve	
gEUD (*a* = 20)	0.22 Gy	0.19 Gy
D_{max}	0.29 Gy	0.25 Gy
	Left optic nerve	
gEUD (*a* = 20)	1.29 Gy	1.30 Gy
D_{max}	1.53 Gy	1.60 Gy
	Chiasm	
gEUD (*a* = 20)	1.08 Gy	1.04 Gy
D_{max}	1.44 Gy	1.39 Gy

CI = volume 95% isodose / volume VOI.
gEUD, generalized equivalent uniform dose; OAR, organ at risk; NTCP, normal tissue complication probability; VOI, volume of interest.

single objective during the optimization, formalizing it by a quadratic term during the definition of the cost function. Obviously, the effect of greater sparing of healthy organs will be more evident for organs with a large volume effect, as in the case of the parotid gland, compared to purely serial organs, in which the probability of complications is linked to the maximum dose, as for the spinal cord of patient plan 135 (**Figure 4**), where similar results are obtained using voxel-dose-based or gEUD-based optimization. But at the same time, this result can be seen as the possibility of using gEUD-based optimization for any type of organ, achieving improvements in the case of organs with large volume effect or similar results for organs with small volume effect with respect to the standard criteria, as in the present case, based on a maximum dose as an objective.

A possible limitation of this approach is that for many organs, there are no precise estimates for the volume effect parameter *a*, but only reasonable values from clinical studies. There is also a lack of knowledge of the specific tolerances for each organ in terms of gEUD. Therefore, it is necessary to test different combinations of $gEUD_0$ and *a* in order to identify the couple that leads to satisfactory results in terms of dose distributions and estimates of NTCP. On the other hand, a similar limitation is shared by the maximum dose criteria since such values are also associated with uncertainties.

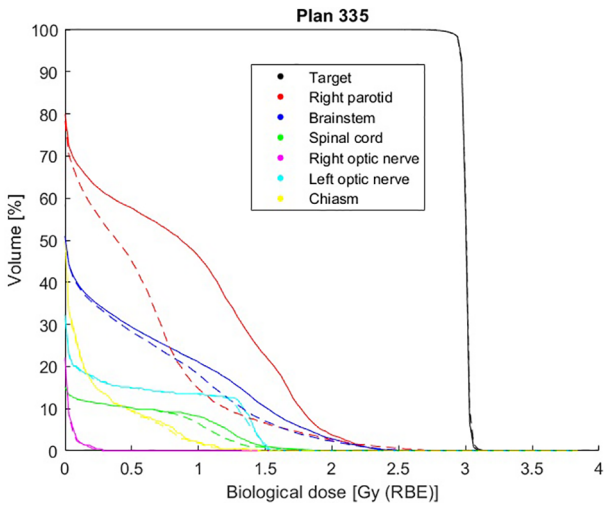

FIGURE 5 | Comparison of dose–volume histograms (DVHs) obtained with voxel-dose-based (solid line) and generalized equivalent uniform dose (gEUD)-based (dashed line) optimization for patient plan 335.

It should be also noted that the large improvement observed in **Figures 5**, **8** would be probably reduced when compared to a voxel-dose-based objective including several points. We decided to directly implement the gEUD-based optimization instead of the possibility to add several DVH point constraints considering also the arbitrarity of such points selection.

As described in Section 2.2.3, the optimization task in TRiP98 is based on iterative algorithms that belong to *exact line search methods*, which require the calculation of a minimization direction and a stepsize in an analytical way. This approach, due to the non-linearity of the problem, imposed the use of some specific approximations: the linearization of the gEUD-based objective (in Section 2.3.1) and the use of a "damping factor" (in Section 2.3.2) in order to obtain an analytical expression of the stepsize for biological optimization. A possible simplification of this approach could be, as an alternative, the implementation of a numerical approach, like the *backtracking line search method* [e.g., (30)]. The latter is a more general method to get an approximated value of the stepsize, which would not require the above specific choices. While we kept in this work the already implemented and highly tested analytical approach of TRiP98, future implementation of a numerical line search method could be in principle possible and useful.

Besides the ones here presented (SD and CGFR), there are alternative algorithms for non-linear optimization, such as BFGS (9), already implemented in TRiP98, and several others not yet implemented, such as *interior-point method* (31) and *sequential quadratic programming* (32). With this work, we wanted to implement a new optimization approach based on gEUD in TRiP98, while staying as close as possible to the already implemented optimization routines. The implementation of additional algorithms, however, could be evaluated in the future.

Furthermore, in principle, the gEUD-based quadratic cost function presented in this work could be applied independently of the optimization routine, previously mentioned, or the biological dose model used. For example, an alternative method for the optimization of the biological effect is the one proposed by Wilkens and Oelfke (33).

Optimization based on gEUD has been extensively studied in the case of photon therapy, as in Schwarz et al. (18) and in Fogliata et al. (21), which used a quadratic cost function similar to ours, and also in Wu et al. (16), where a logistic cost function was used, but much less in the case of particle therapy. In fact, the gEUD-based optimization has already been partially explored only by Brüningk et al. (20) in the case of carbon ion therapy.

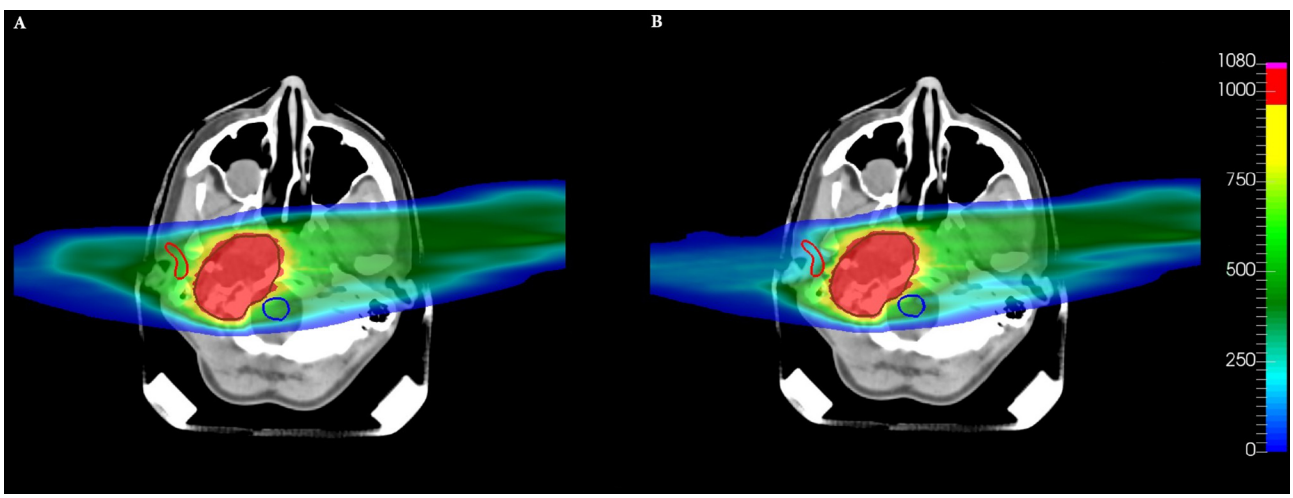

FIGURE 6 | Comparison of dose distributions on a CT slice for patient plan 335, obtained with **(A)** voxel-dose-based and **(B)** generalized equivalent uniform dose (gEUD)-based optimization. The target (brown contour), the right parotid (red contour), and the brainstem (blue contour) are shown. The dose levels are plotted in per mil of the prescribed dose.

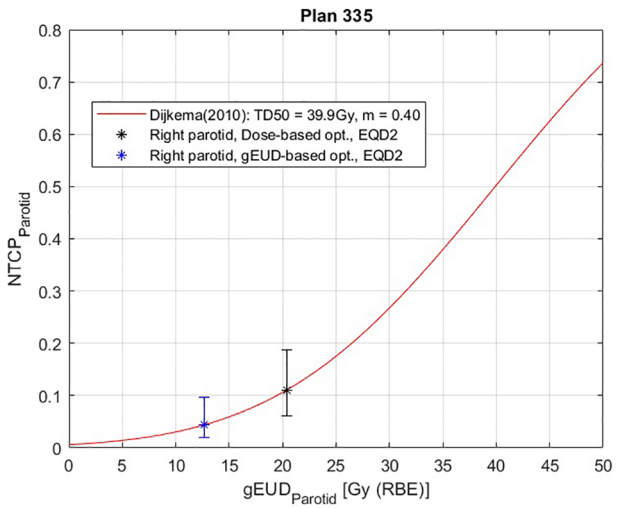

FIGURE 7 | Normal tissue complication probability (NTCP) curve for the right parotid gland of patient plan 335, calculated according to Lyman–Kutcher–Burman (LKB model) using the parameters obtained by Dijkema et al. (29). The error bars were calculated considering the maximum and minimum NTCP values coming from the combination of the extreme values of the parameters TD_{50} and m (95%CIs): TD_{50} = 37.3 Gy and m = 0.51 for the highest NTCP value, and TD_{50} = 42.8 Gy and m = 0.34 for the lowest NTCP. A therapeutic plan of 20 fractions of 3 Gy is considered, with EQD2 calculation.

Indeed, that study focused more on the equivalent uniform effect (EUE)-based optimization, using the approach proposed by Wilkens and Oelfke (33), comparing it also with the optimization based on RBE-weighted gEUD. Furthermore, the results shown there refer to organs with a small volume effect of a single plan. Finally, in that work, the influence of uncertainties in the volume effect parameter on the optimization outcome was investigated. Instead, in our work, we implemented a cost function with a quadratic penalty in RBE-weighted gEUD in order to maintain objectives on dose values and not on other quantities such as the EUE or NTCP. We decided to do this in order to make the new implementation an extension of the overall voxel-dose-based cost function of TRiP98. Moreover, in our work, a greater focus has been given to organs with a large volume effect, such as the parotid glands, in order to explore planning problems where the benefits of gEUD-based optimization are expected to be the largest. We also presented several treatment plans for which we compared voxel-dose-based optimization with the new gEUD-based approach. Finally, we also showed some technical details regarding the implementation of gEUD-based optimization, as well as some convergence tests in the **Supplementary Material**.

Another code, matRad (34), recently introduced the possibility to select a gEUD-based objective. It provides two options to perform biological optimization: the first one considers the biological effect-based optimization, according to Wilkens and Oelfke (33), while the second one takes into account the first implementation of RBE-weighted dose-based optimization used in TRiP98 (6). In our work instead, we employed the updated version of the RBE-weighted dose-based optimization, described in Krämer and Scholz (27) and Gemmel et al. (8), with the explicit inclusion of ∇RBE_i in the minimization, a feature that is not present in (6), as detailed in Section 2.3.2, but it is somehow implicitly accounted in (33). Another difference is that in matRad the absolute minimization of gEUD is proposed, while in our work, a prescription is defined and a quadratic objective is considered. Finally, in that work, no results from gEUD-based optimization are shown.

4.1 Outlook

Beyond the gEUD-based optimization of healthy organs, the next step would be to optimize also the target with gEUD: the idea is to use a negative value of a in order to control low dose levels, combined with the use of a positive a value to control high dose levels, treating the target as an OAR. This idea can be formalized mathematically defining a new cost function for the target composed of two terms that are dependent on gEUD, replacing the uniform dose objective, namely,

$$\chi_T^2(\vec{N}) = (w_T^{\min})^2 \frac{(gEUD_0^{\min} - gEUD^{\min}(\vec{N}))^2}{(\Delta gEUD_0^{\min})^2} \theta_{gEUD}^{\min} + (w_T^{\max})^2 \frac{(gEUD_0^{\max} - gEUD^{\max}(\vec{N}))^2}{(\Delta gEUD_0^{\max})^2} \theta_{gEUD}^{\max} \tag{22}$$

where the first term is for the minimum dose control, while the second one is for the maximum dose control, and

$$\theta_{gEUD}^{\min} = \theta(gEUD_0^{\min} - gEUD^{\min}(\vec{N})) = \begin{cases} 1, gEUD^{\min}(\vec{N}) < gEUD_0^{\min} \\ 0, gEUD^{\min}(\vec{N}) \geq gEUD_0^{\min} \end{cases}$$
$$\theta_{gEUD}^{\max} = \theta(gEUD^{\max}(\vec{N}) - gEUD_0^{\max}) = \begin{cases} 1, gEUD^{\max}(\vec{N}) > gEUD_0^{\max} \\ 0, gEUD^{\max}(\vec{N}) \leq gEUD_0^{\max} \end{cases} \tag{23}$$

are Heavyside functions in order to penalize the target if the actual gEUD values are smaller or larger than the prescribed values, respectively. In principle, using two gEUD objectives with two volume parameters does allow to control both high and low doses in the target. In theory, the advantage of this approach is to relax the objectives on the target, and when combined with the gEUD-based optimization of the OARs, it should allow for further sparing of them. Obviously, this should be demonstrated in clinical cases.

Another possible future step could be to move from the gEUD-based optimization of healthy organs to a direct NTCP-based optimization. As already mentioned above, in this work, we implemented a gEUD-based optimization because this is located in the dose space, and therefore, it is sufficient to integrate an additional term in the overall cost function to take into account the volume effect during the optimization task. Therefore, this allows to choose between optimization based on gEUD or on maximum dose depending on the type of OAR considered. Furthermore, given the close link between gEUD and NTCP as seen in equations 2 and 3, minimizing gEUD means also minimizing NTCP; this is also evident from the results obtained for patient 335, where the decrease in gEUD for the parotid glands corresponds to a reduction in the corresponding

TABLE 4 | gEUD, NTCP and other indexes for the VOIs of plan 335, considering both parotid glands.

Parameter	Voxel-dose-based opt.	gEUD-based opt.
	Target	
D_{min}	2.52 Gy	2.42 Gy
D_{max}	3.17 Gy	3.20 Gy
D_{mean}	3.00 Gy	3.00 Gy
CI	1.24	1.24
	Right parotid	
gEUD (*a* = 1)	0.82 Gy	0.60 Gy
NTCP	11.10%	5.94%
D_{max}	2.51 Gy	2.82 Gy
	Left parotid	
gEUD (*a* = 1)	0.98 Gy	0.59 Gy
NTCP	16.92%	5.78%
D_{max}	1.37 Gy	1.70 Gy
	Brainstem	
gEUD (*a* = 20)	1.89 Gy	1.94 Gy
D_{max}	2.53 Gy	2.62 Gy
	Spinal cord	
gEUD (*a* = 20)	1.40 Gy	1.40 Gy
D_{max}	1.89 Gy	1.95 Gy
	Right optic nerve	
gEUD (*a* = 20)	0.22 Gy	0.19 Gy
D_{max}	0.29 Gy	0.25 Gy
	Left optic nerve	
gEUD (*a* = 20)	1.29 Gy	1.30 Gy
D_{max}	1.54 Gy	1.58 Gy
	Chiasm	
gEUD (*a* = 20)	1.08 Gy	1.04 Gy
D_{max}	1.44 Gy	1.39 Gy

CI = volume 95% isodose / volume VOI.
gEUD, generalized equivalent uniform dose; OAR, organ at risk; NTCP, normal tissue complication probability; VOI, volume of interest.

NTCP. Instead, the NTCP-based optimization is located in the probability space, and it becomes necessary if we want to optimize the absolute risk of complication for an organ for which more complications are associated or if we want to minimize the probability of complications for multiple OARs. Kierkels et al. (35) proposed a method in order to consider multivariable NTCP models in treatment plan optimization in the case of photon therapy. They demonstrated the feasibility of using NTCP-based optimization in the case of head and neck cancer and compared this method with gEUD-based optimization, obtaining in both cases clinically acceptable plans with small differences. According to them, one of the advantages is that NTCP models combine multiple factors into a single objective, but at the same time, as described by Witte et al. (36), in order to use NTCP in the optimization task, it is necessary to implement a complex objective function. On the other hand, according to Wu et al. (17), one of the advantages of gEUD-based optimization over other methods, such as dose–volume-based or NTCP-based optimizations, is that it requires fewer planning parameters.

Finally, a combination of DVH-based and gEUD-based objectives may be of interest for specific OARs where DVH point constraints are commonly enforced in clinical practice.

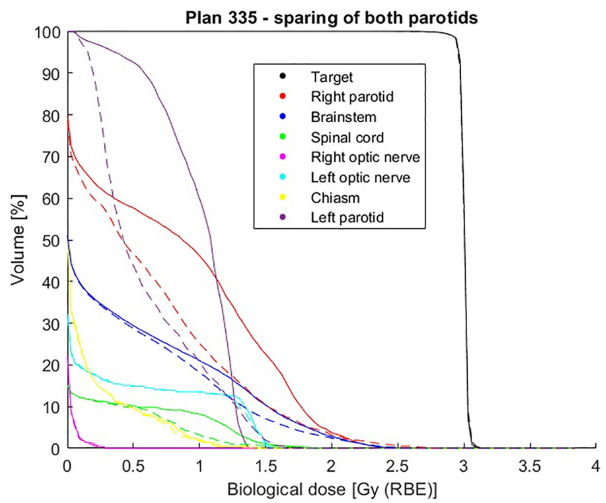

FIGURE 8 | Comparison of dose–volume histograms (DVHs) obtained with voxel-dose-based (solid line) and generalized equivalent uniform dose (gEUD)-based (dashed line) optimization for patient plan 335, considering both parotid glands.

5 CONCLUSIONS

In conclusion, we reported the first implementation of gEUD-based optimization in TRiP98 for carbon ion therapy, adding a new term in the cost function, in order to take into account for volume effects in the optimization task. The present

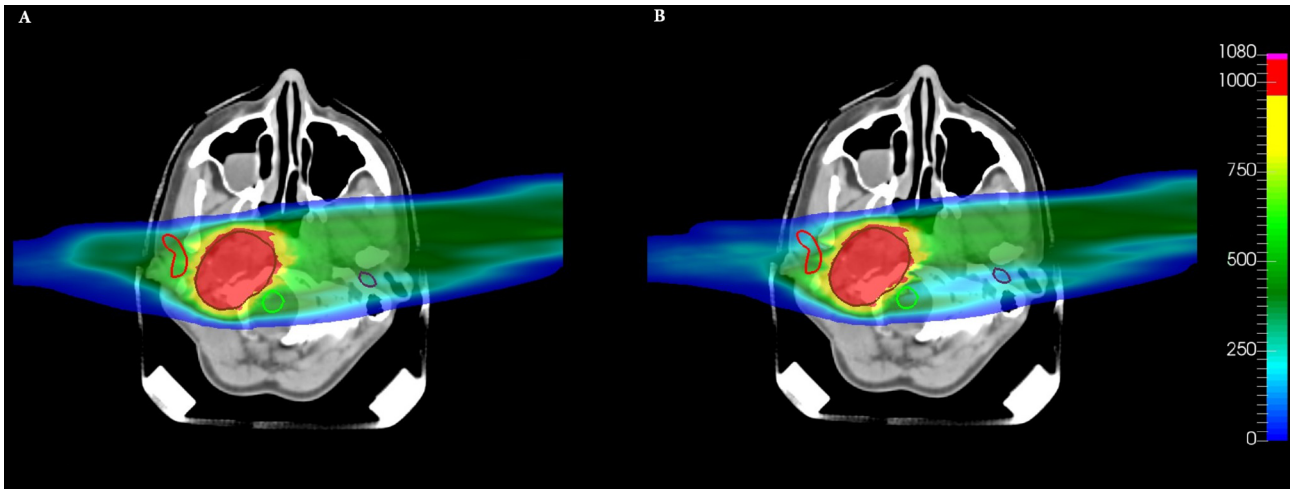

FIGURE 9 | Comparison of dose distributions on a CT slice for patient plan 335 considering both parotid glands, obtained with **(A)** voxel-dose-based and **(B)** generalized equivalent uniform dose (gEUD)-based optimization. The target (brown contour), the right parotid (red contour), the left parotid (violet contour), and the spinal cord (green contour) are shown. The dose levels are plotted in per mil of the prescribed dose.

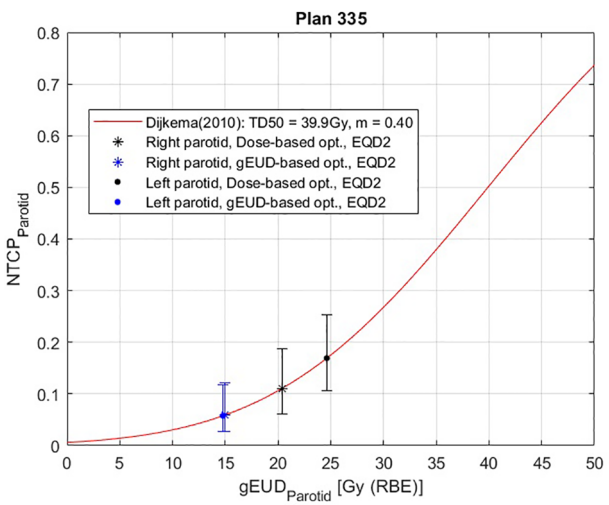

FIGURE 10 | Normal tissue complication probability (NTCP) curve for the parotid glands of patient plan 335, calculated according to Lyman–Kutcher–Burman (LKB) model, using the parameters obtained by Dijkema et al. (29). The error bars were calculated as before. A therapeutic plan of 20 fractions of 3 Gy is considered, with EQD2 calculation.

implementation, coupling organ structures with RBE-weighted dose consideration, allows a strong accounting of biological effects in particle beam treatment planning. In particular, it allows to control the whole DVH shape of an OAR using a single objective, reducing different dose levels depending on the value of the chosen volume effect parameter, i.e., increasing the sparing of the organ considered. In particular, for organs with a large volume effect, it is possible to reduce their NTCP. This approach could also be extended to the target, in principle to obtain a further sparing of healthy organs. Finally, the gEUD-based optimization seems to be an excellent compromise between not taking at all into account the volume effect (voxel-dose-based optimization) and the direct minimization of NTCP (NTCP-based optimization).

CODE AVAILABILITY STATEMENT

TRiP98 full documentation, including instructions for getting a stable version of the code on request by the main developer, is available on its official webpage http://bio.gsi.de/DOCS/trip98.html.

DATA AVAILABILITY STATEMENT

The raw data supporting the conclusions of this article will be made available by the authors, without undue reservation.

AUTHOR CONTRIBUTIONS

MB developed the novel code implementations, performed all the calculations, analyzed the data, and wrote the first draft of the manuscript. MS and ES conceived the work and supervised it. MK guided and assisted the TRiP98 code implementations. All the authors critically read and edited the manuscript.

FUNDING

This work was funded by INFN CSNV Call "MoVe IT", Modeling and verification for ion beam treatment planning.

ACKNOWLEDGMENTS

Dr. Olga Sokol is gratefully acknowledged for the technical support with graphical representations of TRiP98 data. Dr. Francesco Cordoni is thanked for the support and discussions on mathematical questions. Prof. Marco Durante is thanked for the inspiring discussions.

SUPPLEMENTARY MATERIAL

The Supplementary Material for this article can be found online at: https://www.frontiersin.org/articles/10.3389/fonc.2022.826414/full#supplementary-material

REFERENCES

1. Durante M, Orecchia R, Loeffler JS. Charged-Particle Therapy in Cancer: Clinical Uses and Future Perspectives. *Nat Rev Clin Oncol* (2017) 14:483–95. doi: 10.1038/nrclinonc.2017.30
2. Durante M, Debus J, Loeffler JS. Physics and Biomedical Challenges of Cancer Therapy With Accelerated Heavy Ions. *Nat Rev Phys* (2021) 3:777–90. doi: 10.1038/s42254-021-00368-5
3. Jermann M. *Particle Therapy Patient Statistics (Per End of 2019)* (2020) (Accessed 6-July-2021).
4. Malouff TD, Mahajan A, Krishnan S, Beltran C, Seneviratne DS, Trifiletti DM. Carbon Ion Therapy: A Modern Review of an Emerging Technology. *Front Oncol* (2020) 10:82. doi: 10.3389/fonc.2020.00082
5. Krämer M, Jäkel O, Haberer T, Kraft G, Schardt D, Weber U. Treatment Planning for Heavy-Ion Radiotherapy: Physical Beam Model and Dose Optimization. *Phys Med Biol* (2000) 45:3299–317. doi: 10.1088/0031-9155/45/11/313
6. Krämer M, Scholz M. Treatment Planning for Heavy-Ion Radiotherapy: Calculation and Optimization of Biologically Effective Dose. *Phys Med Biol* (2000) 45:3319–30. doi: 10.1088/0031-9155/45/11/314
7. Schulz-Ertner D, Karger CP, Feuerhake A, Nikoghosyan A, Combs SE, Jäkel O, et al. Effectiveness of Carbon Ion Radiotherapy in the Treatment of Skull-Base Chordomas. *Int J Radiat Oncol - Biol - Phys* (2007) 68:449–57. doi: 10.1016/j.ijrobp.2006.12.059
8. Gemmel A, Hasch B, Ellerbrock M, Weyrather WK, Krämer M. Biological Dose Optimization With Multiple Ion Fields. *Phys Med Biol* (2008) 53:6991–7012. doi: 10.1088/0031-9155/53/23/022
9. Horcicka M, Meyer C, Buschbacher A, Durante M, Krämer M. Algorithms for the Optimization of Rbe-Weighted Dose in Particle Therapy. *Phys Med Biol* (2013) 58:275–86. doi: 10.1088/0031-9155/58/2/275
10. Tinganelli W, Durante M, Hirayama R, Krämer M, Maier A, Kraft-Weyrather W, et al. Kill-Painting of Hypoxic Tumours in Charged Particle Therapy. *Sci Rep* (2015) 5:1–13. doi: 10.1038/srep17016
11. Krämer M, Scifoni E, Schuy C, Rovituso M, Tinganelli W, Maier A, et al. Helium Ions for Radiotherapy? Physical and Biological Verifications of a Novel Treatment Modality. *Med Phys* (2016) 43:1995–2004. doi: 10.1118/1.4944593
12. Sokol O, Scifoni E, Tinganelli W, Kraft-Weyrather W, Wiedemann J, Maier A, et al. Oxygen Beams for Therapy: Advanced Biological Treatment Planning and Experimental Verification. *Phys Med Biol* (2017) 62:7798. doi: 10.1088/1361-6560/aa88a0
13. Sokol O, Krämer M, Hild S, Durante M, Scifoni E. Kill Painting of Hypoxic Tumors With Multiple Ion Beams. *Phys Med Biol* (2019) 64:045008. doi: 10.1088/1361-6560/aafe40
14. Rodney Withers H, Taylor JMG, Maciejewski B. Treatment Volume and Tissue Tolerance. *Int J Radiat Oncol - Biol - Phys* (1988) 14:751–9. doi: 10.1016/0360-3016(88)90098-3
15. Niemierko A. A Generalized Concept of Equivalent Uniform Dose (Eud). *AAPM 1999 Conf Proc - Med Phys* (1999) 26:1100.
16. Wu Q, Mohan R, Niemierko A, Schmidt-Ullrich R. Optimization of Intensity-Modulated Radiotherapy Plans Based on the Equivalent Uniform Dose. *Int J Radiat Oncol - Biol - Phys* (2002) 52:224–35. doi: 10.1016/S0360-3016(01)02585-8
17. Wu Q, Djajaputra D, Wu Y, Zhou J, Liu HH, Mohan R. Intensity-Modulated Radiotherapy Optimization With Geud-Guided Dose–Volume Objectives. *Phys Med Biol* (2003) 48:279. doi: 10.1088/0031-9155/48/3/301
18. Schwarz M, Lebesque JV, Mijnheer BJ, Damen EMF. Sensitivity of Treatment Plan Optimisation for Prostate Cancer Using the Equivalent Uniform Dose (Eud) With Respect to the Rectal Wall Volume Parameter. *Radiother Oncol* (2004) 73:209–18. doi: 10.1016/j.radonc.2004.08.016
19. Allen Li X, Alber M, Deasy JO, Jackson A, Ken Jee KW, Marks LB, et al. The Use and Qa of Biologically Related Models for Treatment Planning: Short Report of the Tg-166 of the Therapy Physics Committee of the Aapm. *Med Phys* (2012) 39:1386–409. doi: 10.1118/1.3685447
20. Brüningk SC, Kamp F, Wilkens JJ. Eud-Based Biological Optimization for Carbon Ion Therapy. *Med Phys* (2015) 42:6248–57. doi: 10.1118/1.4932219
21. Fogliata A, Thompson S, Stravato A, Tomatis S, Scorsetti M, Cozzi L. On the Geud Biological Optimization Objective for Organs at Risk in Photon Optimizer of Eclipse Treatment Planning System. *J Appl Clin Med Phys* (2018) 19:106–14. doi: 10.1002/acm2.12224
22. Lyman JT. Complication Probability as Assessed From Dose–Volume Histograms. *Radiat Res* (1985) 104:S13–9. doi: 10.2307/3576626
23. Kutcher GJ, Burman C. Calculation of Complication Probability Factors for non-Uniform Normal Tissue Irradiation: The Effective Volume Method. *Int J Radiat Oncol - Biol - Phys* (1989) 16:1623–30. doi: 10.1016/0360-3016(89)90972-3
24. Scholz M, Kellerer AM, Kraft-Weyrather W, Kraft G. Computation of Cell Survival in Heavy Ion Beams for Therapy. The Model and its Approximation. *Radiat Environ Biophysics* (1997) 36:59–66. doi: 10.1007/s004110050055
25. Scholz M, Kraft G. Track Structure and the Calculation of Biological Effects of Heavy Charged Particles. *Adv Space Res* (1996) 18:5–14. doi: 10.1016/0273-1177(95)00784-C
26. Elsässer T, Weyrather WK, Friedrich T, Durante M, Iancu G, Krämer M, et al. Quantification of the Relative Biological Effectiveness for Ion Beam Radiotherapy: Direct Experimental Comparison of Proton and Carbon Ion Beams and a Novel Approach for Treatment Planning. *Int J Radiat Oncol - Biol - Phys* (2010) 78:1177–83. doi: 10.1016/j.ijrobp.2010.05.014
27. Krämer M, Scholz M. Rapid Calculation of Biological Effects in Ion Radiotherapy. *Phys Med Biol* (2006) 51:1959–70. doi: 10.1088/0031-9155/51/8/001
28. Zaider M, Rossi HH. The Synergistic Effects of Different Radiations. *Radiat Res* (1980) 83:732–9. doi: 10.2307/3575352
29. Dijkema T, Raaijmakers CPJ, Ten Haken RK, Roesink JM, Braam PM, Houweling AC, et al. Parotid Gland Function After Radiotherapy: The Combined Michigan and Utrecht Experience. *Int J Radiat Oncol - Biol - Phys* (2010) 78:449–53. doi: 10.1016/j.ijrobp.2009.07.1708
30. Yuan G, Lu X. A New Backtracking Inexact Bfgs Method for Symmetric Nonlinear Equations. *Comput Math Appl* (2008) 55:116–29. doi: 10.1016/j.camwa.2006.12.081
31. Breedveld S, van den Berg B, Heijmen B. An Interior-Point Implementation Developed and Tuned for Radiation Therapy Treatment Planning. *Comput Optimization Appl* (2017) 68:209–42. doi: 10.1007/s10589-017-9919-4
32. Fredriksson A, Forsgren A, Hårdemark B. Minimax Optimization for Handling Range and Setup Uncertainties in Proton Therapy. *Med Phys* (2011) 38:1672–84. doi: 10.1118/1.3556559
33. Wilkens JJ, Oelfke O. Fast Multifield Optimization of the Biological Effect in Ion Therapy. *Phys Med Biol* (2006) 51:3127–40. doi: 10.1088/0031-9155/51/12/009
34. Wieser HP, Cisternas E, Wahl N, Ulrich S, Stadler A, Mescher H, et al. Development of the Open-Source Dose Calculation and Optimization Toolkit Matrad. *Med Phys* (2017) 44:2556–68. doi: 10.1002/mp.12251
35. Kierkels RGJ, Korevaar EW, Steenbakkers RJHM, Janssen T, van't Veld AA, Langendijk JA, et al. Direct Use of Multivariable Normal Tissue

Complication Probability Models in Treatment Plan Optimisation for Individualised Head and Neck Cancer Radiotherapy Produces Clinically Acceptable Treatment Plans. *Radiother Oncol* (2014) 112:430–6. doi: 10.1016/j.radonc.2014.08.020

36. Witte MG, van der Geer J, Schneider C, Lebesque JV, Alber M, van Herk M. Imrt Optimization Including Random and Systematic Geometric Errors Based on the Expectation of Tcp and Ntcp. *Med Phys* (2007) 34:3544–55. doi: 10.1118/1.2760027

Conflict of Interest: The authors declare that the research was conducted in the absence of any commercial or financial relationships that could be construed as a potential conflict of interest.

Publisher's Note: All claims expressed in this article are solely those of the authors and do not necessarily represent those of their affiliated organizations, or those of the publisher, the editors and the reviewers. Any product that may be evaluated in this article, or claim that may be made by its manufacturer, is not guaranteed or endorsed by the publisher.

frontiers in Oncology

ORIGINAL RESEARCH
published: 25 March 2022
doi: 10.3389/fonc.2022.780784

A Data-Driven Fragmentation Model for Carbon Therapy GPU-Accelerated Monte-Carlo Dose Recalculation

Micol De Simoni[1,2], Giuseppe Battistoni[3], Angelica De Gregorio[1,2], Patrizia De Maria[4], Marta Fischetti[2,5], Gaia Franciosini[1,2], Michela Marafini[2,6], Vincenzo Patera[2,5], Alessio Sarti[2,5], Marco Toppi[5,7], Giacomo Traini[2], Antonio Trigilio[1,2] and Angelo Schiavi[2,5]*

[1] Department of Physics, University of Rome "Sapienza", Rome, Italy, [2] INFN (Istituto Nazionale di Fisica Nucleare) section of Roma 1, Rome, Italy, [3] INFN (Istituto Nazionale Fisica Nucleare) Section of Milano, Milano, Italy, [4] Department of Medico-Surgical Sciences and Biotechnologies, Post-Graduate School in Medical Physics, Rome, Italy, [5] Department of Scienze di Base e Applicate per l'Ingegneria (SBAI), University of Rome "Sapienza", Rome, Italy, [6] Museo Storico della Fisica e Centro Studi e Ricerche Enrico Fermi, Rome, Italy, [7] INFN Laboratori Nazionali di Frascati, Frascati, Italy

OPEN ACCESS

Edited by:
Thomas Tessonnier, Heidelberg Ion Beam Therapy Center, Heidelberg University Hospital, Germany

Reviewed by:
Chris Beltran, Mayo Clinic Florida, United States
Benedikt Kopp, Heidelberg University Hospital, Germany

***Correspondence:**
Marco Toppi
marco.toppi@uniroma1.it

Specialty section:
This article was submitted to Radiation Oncology, a section of the journal Frontiers in Oncology

Received: *21 September 2021*
Accepted: *04 February 2022*
Published: *25 March 2022*

Citation:
De Simoni M, Battistoni G, De Gregorio A, De Maria P, Fischetti M, Franciosini G, Marafini M, Patera V, Sarti A, Toppi M, Traini G, Trigilio A and Schiavi A (2022) A Data-Driven Fragmentation Model for Carbon Therapy GPU-Accelerated Monte-Carlo Dose Recalculation. Front. Oncol. 12:780784. doi: 10.3389/fonc.2022.780784

The advent of Graphics Processing Units (GPU) has prompted the development of Monte Carlo (MC) algorithms that can significantly reduce the simulation time with respect to standard MC algorithms based on Central Processing Unit (CPU) hardware. The possibility to evaluate a complete treatment plan within minutes, instead of hours, paves the way for many clinical applications where the time-factor is important. FRED (Fast paRticle thErapy Dose evaluator) is a software that exploits the GPU power to recalculate and optimise ion beam treatment plans. The main goal when developing the FRED physics model was to balance accuracy, calculation time and GPU execution guidelines. Nowadays, FRED is already used as a quality assurance tool in Maastricht and Krakow proton clinical centers and as a research tool in several clinical and research centers across Europe. Lately the core software has been updated including a model of carbon ions interactions with matter. The implementation is phenomenological and based on carbon fragmentation data currently available. The model has been tested against the MC FLUKA software, commonly used in particle therapy, and a good agreement was found. In this paper, the new FRED data-driven model for carbon ion fragmentation will be presented together with the validation tests against the FLUKA MC software. The results will be discussed in the context of FRED clinical applications to ^{12}C ions treatment planning.

Keywords: hadrontherapy, carbon ion (C12), fragmentation, fast MC, quality assurance (QA), graphics processing unit (GPU)

1 INTRODUCTION

In Particle therapy (PT) solid tumors are irradiated by means of accelerated charged particle beams (mainly protons and, more recently, carbon ions). The main advantage this technique with respect to the standard radiotherapy using X-rays/electron beams, is related to the different longitudinal energy release profiles. While photons longitudinal dose release is characterized by a slow

exponential decrease, for charged particles a sharp peak at the end of the path is observed, providing a more selective energy deposition. By conveniently controlling the Bragg Peak (BP) position by means of the beam energy tuning, it is possible to concentrate the dose to tumors and, at the same time, preserve the surrounding healthy tissues. In carbon ion therapy an important effect that has to be properly accounted for at the treatment planning stage is the contribution to the dose absorption distribution from nuclear fragments produced by the interaction of carbon ions with target nuclei. This process attenuates and mitigates the primary beam contribution while producing secondary fragments with an energy per nucleon comparable to that of the projectile. As a consequence, the total absorbed dose will have a non-negligible contribution due to secondary particles which have different biological effectiveness and range with respect to the primary beam, releasing the dose also in a tail beyond the BP. When comparing carbon ions and protons, it is also important to note that the BP of the former is more resolved and the absorbed dose distribution shows a better ratio between the peak and the plateau region. Another important difference is that photons have a sparse ionization density (low-LET radiation) and protons are considered to the photon-like beside their end-of-range path where they can reach high LET values, while carbon ions are high-LET particles all along their path. The achieved steep, when compared to conventional radiotherapy, dose gradients in PT demand accurate patient positioning and treatment planning to maximize the treatment efficacy. Patient treatment plans are obtained using a Treatment Planning System (TPS) software that provides, accordingly to medical prescriptions, the irradiation details for each particle beam in each field. The commercial TPS used in the clinical routine are mainly based on analytical algorithms that achieve a reduced computation time at the cost of a reduced accuracy in the dose maps calculations. Analytical TPSs have to be routinely tested through quality assurance (QA) tools to verify that the accelerators parameters have been calculated correctly for each patient. In several treatment centers the QA check is performed having the accelerator delivering the beam in a tank full of water following the TPS instructions and then measuring the dose in different target points with several ionization chambers. To improve the analytic TPS usually Monte-Carlo based TPS are employed (e.g. both RayStation and Varian AcurosPT provide full MC support). It has been demonstrated that the use of MC in PT could lead to a significant reduction in treatment planning safety margins (1), thanks to its accurate modelling and calculation of the dose absorbed by the tissues. MC simulations of proton treatment plans have previously been performed using well-established software packages such as FLUKA (2), GEANT4 and MCNP X (3). Despite the improvements that can be obtained by means of MC dose calculation, pencil-beam-based algorithms are widely used in clinical practice (4), mainly because of their high computational efficiency. On the other hand, the accuracy of a MC dose calculation is determined by the total number of particles used for the simulation, implying that a large number of particles, and long computational times, are needed to yield the desired level of precision. For that reason, the use of full MC simulations, especially in carbon therapy where also the secondary particles emitted need to be accounted for, is limited to the re-calculation of existing treatment plans for research studies, while it is not suitable for a routinely application in the TPS implementation and as QA tool for all patients (5). Despite the great efforts devoted to reducing the MC dose calculation time (6–9), the currently available algorithms and implementations still cannot match the clinical requirements.

The advent of general programming Graphics Processing Units (GPU) has prompted the development of MC algorithms that can significantly reduce the plan recalculation time (10–19) achieving an impressive speed gain compared to CPU-based calculations, profiting from algorithmic simplifications and hardware acceleration. Exploiting the GPU hardware, many vended TPS used for proton therapy now include MC tools (20–25). For carbon therapy, recently a tool called goCMC (GPU OpenCL Carbon Monte Carlo) (26) was developed.

In this framework, the FRED (Fast paRticle thErapy Dose evaluator) (27) software toolkit has been developed. It is a MC-based software optimized for GPU architecture that has been developed to recalculate and optimize external beams radio therapy treatment plans delivered using either protons, carbon ions, electrons or photons. FRED purpose is to rapidly recalculate a complete treatment plan within minutes, opening the way for many clinical applications where the time-factor is of paramount importance.

2 MATERIAL AND METHODS

The FRED core engine has been developed balancing accuracy, calculation time and GPU execution guidelines to achieve the best accuracy in the absorbed dose calculation while exploiting the GPU power to reduce the calculation time. To do so, the most effective physical models from the literature have been chosen, and a careful optimization has been carried out to achieve the needed precision in the dose calculation while avoiding the explicit computation and handling of processes that would result in negligible contributions while affecting the software tracking performance (e.g. atom excitation, the production and tracking of photons, etc.). To reduce the computational time of many physical processes, FRED relies on a library of pre-computed look-up tables. This approach performs extremely well on GPU cards where hardware interpolation can be exploited using the so-called Texture Units. The algorithms core structure is detailed elsewhere (27).

The handling of proton beams interaction with matter implemented within FRED is already at a mature stage, achieving a precision that matches the clinical requirements and allowed its use as a quality assurance tool in the centers of Maastricht and Krakow and as a research tool at several clinical and research centers in Europe (Krakow, Trento, Maastricht, Lyon and PSI). Carbon ion, electron and photon beams have been recently introduced as well for applications in carbon ion therapy, photon radiotherapy and IORT (IntraOperative

Radiation Therapy). In this contribution the newly developed data-driven tracking model of carbon ions will be described in detail.

The dose engine for carbon ions relies on three main building blocks that are used to simulate the particles interaction with matter: the ionization energy loss, the multiple scattering and the fragmentation model. The ionization energy loss and multiple scattering implemented in the carbon ions model are analogous to the ones used in FRED for protons (27). For what concerns the multiple coulomb scattering of carbon ion beams, the single Gaussian term included in Highland's formula (28) to account for such interactions is multiplied by a scaling factor f_{mcs}, following the approach documented in *Fippel and Soukup* (7). This factor was obtained by comparing FRED and FLUKA simulations of a single pencil beam in water with an energy in the center of the therapeutic range and with nuclear interactions switched off. The values obtained have been computed at different depths, energies and using different ion beams, resulting in values ranging from f_{mcs} = 1.29 (for 200 MeV/u alpha particles, computed at 15% of range) to f_{mcs} = 1.43 (for 300 MeV/u oxygen ions, computed at 90% of the range). For each transported charged particle, the best scaling factor was implemented as the one that gave the best lateral distribution of a single pencil beam at the BP placed at a reference depth of 15 cm in water.

The nuclear model, developed completely from scratch, has been parameterized using data already published and this is, as for now, a unique characteristic of FRED. The other available MC software implemented on a GPU hardware that is currently capable of handling carbon ions interactions [goCMC (26)] makes instead use of the information obtained from Geant4 simulations. In particular, for FRED, data used for the calculation of the fragmentation cross sections were extracted from the papers of *Tacheki* (29), *Zhang* (30) and *Kox* (31, 32). Data used for the sampling of the combination of fragments emitted, energy and angle distributions, were taken from the experiments at Ganil (laboratory of CAEN, France), where the fragmentation of carbon ions on thin targets (H, C, O, Al and Ti) has been studied (33, 34). The experiment provided data about the angular and energy cross-section of a carbon beam of 95 and 50 MeV/u and with detection angles in the range (-43°; 43°). To simulate all the energies of interest for carbon ion therapy [namely up to 400 MeV/u as in the case of CNAO center (35)], an algorithm to scale the energy and angle distribution as a function of the incident particle energy has been implemented. Whenever the data were missing, the predictions of the FRED model have been bench-marked instead, against the FLUKA MC.

2.1 Nuclear Model

The nuclear interactions of a given particle are handled in two separate steps. First, the probability that a nuclear interaction occurs is computed, taking into account each particle mass attenuation coefficient using the following equation:

$$\frac{\mu}{\rho} = \sum_i \frac{N_A w_i \sigma_t^i}{A_i} \quad (1),$$

where the sum is performed against all the elements of the target compound, μ is the attenuation coefficient, ρ is the material density, N_A is the number of Avogadro, w_i, A_i and σ_t^i are respectively the mass weight, the atomic mass and the total cross-section of nucleus-nucleus interactions of each i-th element of the target. The total cross-section is defined as the sum of the elastic and non-elastic cross-sections.

Elastic collisions are handled requiring kinetic energy and momentum conservation, and sampling the deflection angle in the center of mass frame. In the case of non-elastic collisions, no energy conservation is implied, the incident carbon ion track is removed from the simulation, and charged fragments are generated by means of a sampling procedure and queued for tracking.

2.1.1 Elastic Cross-Section

The elastic cross-section is explicitly accounted only if the carbon ion projectile interacts with a hydrogen nucleus, as the fragmentation process dominates for all heavier target nuclei. To handle the elastic interactions, we have exploited the center of mass reference system in which the carbon ion interactions with the proton target can be modeled using the data collected studying the reversed process (proton interactions with a carbon ion target).

The sampling of elastic cross-sections was done according to data available from the ENDF database [*ENDF/B-VII Incident-Proton Data* (36)], based on nuclear model calculations benchmarked against experimental data (37, 38).

The relationship between the carbon ion scattering angles, when it interacts with the hydrogen nucleus, in the center of mass and in the laboratory reference frames can be written as:

$$\cos\ (\theta_l) = \frac{A + \cos\ (\theta_c)}{\sqrt{A^2 + 2A\cos\ (\theta_c) + 1}} \quad (2),$$

where θ_l and θ_c are respectively the scattering angles in the laboratory and center of mass (CoM) reference frames, A is the atomic mass of the projectile and the atomic mass of the hydrogen has already been considered equal to 1 (39, 40). The carbon ion diffusion angle is hence extracted using, as input, an isotropic distribution computed in the CoM frame.

With the same procedure it is possible to calculate also the proton target deflection (ϕ_l):

$$\cos\ (\phi_l) = \frac{1 + \cos\ (\theta_c)}{\sqrt{2(1 + \cos\ (\theta_c))}} \quad (3),$$

The other parameter necessary for the description of the elastic interaction is the new energy of the projectile and of the target element(s). The kinetic energy in the laboratory system after the collision, $E_l{}'$, is:

$$E_l{}' = \frac{A^2 + 1 + 2A\cos\ (\theta_c)}{(A+1)^2} E_l$$

$$= \frac{1}{2}[(1+\alpha) + (1-\alpha)\cos\ (\theta_c)]E_l \quad (4)$$

where α equals to $\frac{(A-1)^2}{(A+1)^2}$ and E_l is the kinetic energy of the ion in the laboratory system before the collision. Similarly, in the laboratory system the energy of the proton E_l^p is:

$$E_l^p = \frac{2AE_l}{(A+1)^2}(1 - \cos\ (\theta_c)) \tag{5}$$

2.1.2 Non-Elastic Cross-Section

The non-elastic cross-section depends on the crossed material and on the type and energy of incident particle.

The cross-section of a nucleus projectile N_p (**Figure 1** left) interacting with a nucleus target N_t is obtained from a fit to existent carbon-carbon interactions data [*Takechi* (29), *Zhang* (30) and *Kox* (31, 32), **Figure 1** right]:

$$\sigma(N_p, N_t, E) = K(N_p, N_t, E)(1 - e^{\frac{-E}{E_c}})(p_0 + p_1 E + e^{p_2 - p_3 E}) \tag{6}$$

where $E_c = 30$ MeV, $p_0 = (762 \pm 7)$mb, $p_1 = (14.0 \pm 0.7) \times 10^{-4}$ mb MeV^{-1}, $p_2 = 6.7 \pm 0.8$ and $p_3 = (13.4 \pm 0.7) \times 10^{-3}$ MeV^{-1} have been obtained from the fit. $K(A_p, A_t, E)$ is a scaling factor that is needed whenever the projectile and target nuclei are different from carbon. In particular, the scaling has been obtained using the energy-dependent Kox formula (41–43) for the total cross-section σ_K in nucleus-nucleus reactions

$$K(N_p, N_t, E_{cm}) = \frac{\sigma_K(N_p, N_t, E_{cm})}{\sigma_K(^{12}C, ^{12}C, E_{cm})} \tag{7}$$

where $\sigma_K(^{12}C, ^{12}C, E_{cm})$ is Kox's cross-section for carbon on carbon interactions, while $\sigma_K(N_p, N_t, E_{cm})$ is the Kox's cross-section for a nucleus projectile N_p impinging on a nucleus target N_t.

This scaling law is used for every nucleus of the target except for hydrogen, for which the cross-section has been computed using the available data from ICRU (*International Commission on Radiation Units & Measurements*) (41). The comparison between the available data and the simulation performed using FRED is shown in **Figure 2**. The cross-sections are collected in pre-computed look-up tables that FRED reads and interpolates.

The fragmentation of secondary particles has been computed directly using the Kox formula (42–44). The simulation studies we performed clearly showed that the secondaries fragmentation gives a negligible contribution to the deposited dose. For that reason, by default, the algorithm only takes into account the primary particles fragmentation. We have although left the possibility, for the user interested in evaluating directly the impact of such contribution, to choose whether to enable the accounting for the secondary fragmentation contribution as well.

2.1.3 Fragmentation Model

The nuclear fragmentation process is still lacking a theoretical model capable of providing accurate and precise cross sections predictions. Interactions between the projectile and target nuclei are ultimately described by quantum electrodynamics (QED) but nuclear fragmentation interactions are many-body problems that defy present-day calculation methods at the most fundamental level. The lack of a fundamental theory has been addressed developing a semi-empirical model to describe nucleus-nucleus interactions. The details can be found in the next paragraph.

Sampling of the Target

The first step to simulate the fragmentation process in a given medium made of many materials is the choice of the actual nucleus of the target on which the fragmentation occurs. FRED computes such information from tables where a cumulative distribution (explained in detail here-after) is associated with each target used in the 95 MeV/u Ganil experiment and to each possible fragment emitted. To choose which combination of fragments will be emitted, it is necessary to know the nucleus hit by the carbon ion. This information is retrieved using the Kox's cross-section σ_K (42–44) and computing a cumulative distribution based on the probability for each nucleus to be hit:

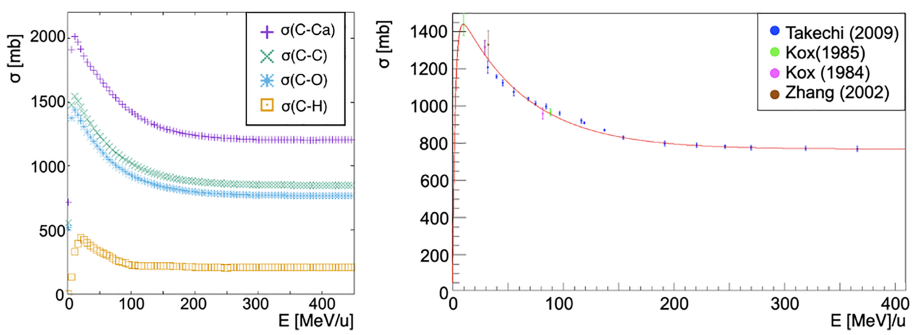

FIGURE 1 | On the left, cross-sections of a carbon ion beam as a function of the energy per nucleon of the projectile interacting with different targets: calcium (purple cross), carbon (green x), oxygen (blue asterisk), hydrogen (orange square). Each cross-section has been obtained as described by Eq. 6 with the exception of the hydrogen target for which the available ICRU data has been used (**Figure 2**). Cross section dependence on the energy per nucleon of the projectile is shown. On the right, fragmentation cross-section in carbon-carbon interactions in the energy range of interest for hadron therapy as a function of the total energy of the projectile. In red the fit to data from papers of *Takechi* (29), Zhang (30) and *Kox* (31, 32).

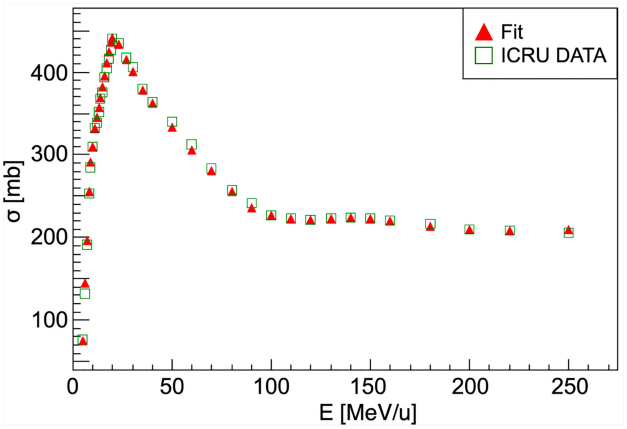

FIGURE 2 | Carbon-hydrogen fragmentation cross-section. For energies higher than 250 MeV/u the cross-section can be considered as nearly constant. Red triangles show the ICRU data fit result that is used in the FRED implementation. ICRU data (41) are represented as green squares.

$$P^i = \frac{n^i \sigma_K^i}{\sigma^{tot}} \tag{8}$$

where

$$\sigma^{tot} = \sum_{j=1}^{j=N} n^j \sigma_K^j \tag{9}$$

and σ_K^{tot} is the sum of the cross-sections of all the N nuclei of the target weighted by the occurrence n of each element. For hydrogen and carbon targets, the available cross-section from data is used. As an example, we list the definition of the probability of interaction on hydrogen and oxygen nuclei, $P(H)$ and $P(O)$ respectively, for a carbon ion impinging on a water target:

$$P(H) = \frac{2\sigma_{data}^H}{\sigma^{tot}}, P(O) = \frac{\sigma_K^O}{\sigma^{tot}} \tag{10}$$

$$\sigma^{tot} = 2\sigma_{data}^H + \sigma_K^O \tag{11}$$

where σ_{data}^H and σ_K^O are respectively the cross-sections for a hydrogen target, which is calculated by means of a data fit (**Figure 2**), and the Kox cross-section for an oxygen target. The Kox cross-section is used to compute the probability that an incident particle has an interaction with a given nucleus of crossed material. The algorithm extracts a uniform random number (0,1) to compare with the cumulative distributions in order to choose the element to be used for the fragmentation simulation.

Sampling of the Fragments

Once the target nucleus has been determined, the software computes the emission probabilities for each fragment using a look-up table. The isotopes with a non-negligible production cross section are: neutrons, ^{1}H, ^{2}H, ^{3}H, ^{3}He, ^{4}He, ^{6}He, ^{6}Li, ^{7}Li, ^{7}Be, ^{9}Be, ^{10}Be, ^{8}B, ^{10}B, ^{11}B, ^{10}C, ^{11}C and ^{12}C. The probability table has been computed using an iterative algorithm [*Newton Method* (45)] that allowed to reach a good agreement with the data published from the 95 MeV/u Ganil experiment. This iterative procedure was implemented to account for the experimental correlation between the different fragments production probabilities measured by Ganil. **Table 1** reports the results of the procedure, used for all the targets with the exception of hydrogen, for each isotope and elemental target in comparison with Ganil experiment measurements.

Since the Ganil experiment, as shown in **Table 1**, did not had any experimental access to the production of fragments heavier than ^{7}Be in the case of a hydrogen target, in that case the algorithm uses as input the cumulative distributions obtained from a FLUKA simulation[1] of the interactions of a 95 MeV/n carbon beam impinging on a thin target. The same holds also for the neutron production, absent in the Ganil data.

Outgoing particles from a heavy-ion fragmentation reaction are typically described as either "projectile" or "target" fragments. In the Ganil experiment, both types of fragments were detected and it was impossible to distinguish them. For that reason, both phenomena were considered to be present when using the cumulative distributions. The fragmentation production probabilities were also scaled to account for the non-negligible contribution from elastic scattering of ^{12}C isotopes. The simulation of each event proceeds using random numbers to sample, by means of the cumulative distributions previously described, the projectile fragments. The same procedure is used for the target fragmentation.

Once the complete set of fragments is defined, the energy and angle computation are obtained as described in the following section. If the sum of the energy of all projectile's and target's fragments is greater than the energy of the projectile, the software extracts a new set of fragments until mass, charge and energy are conserved. The most frequent fragments are neutrons, protons, deuterium and Helium-4 followed by lighter fragments.

[1]Version: 2020.0.10, using the default values provided by the HADROTHERAPY setting.

TABLE 1 | Production probabilities per isotope and for each elemental target reported in the Ganil experiment (33) and built for the code FRED.

	Probabilities [%]					
Frag	**(Ganil) H**	**(Fred) H**	**(Ganil) C**	**(Fred) C**	**(Ganil) O**	**(Fred) O**
n	–	1.4x10	–	6.5x10	–	6.0x10
^{1}H	52(8)	3.8x10	35(2)	1.0×10	38(4)	1.6×10
^{2}H	9(2)	5.0	16.3(0.8)	7.5	17(1)	8.8
^{3}H	2.0(0.4)	1.3	6.6(0.4)	6.1	6.5(0.7)	5.1
^{3}He	5.2(0.5)	3.0	7(1)	1.2	7.2(0.9)	1.7
^{4}He	25(10)	26	25(6)	6.4	22(7)	6.3
^{6}He	1.3(0.1)	3.6×10^{-2}	1.0(0.2)	1.7	1.0(0.4)	1.0
^{6}Li	1.5(0.8)	2.3	1.4(0.2)	2.5×10^{-1}	1.3(0.3)	2.8×10^{-1}
^{7}Li	1.0(0.2)	9.3×10^{-1}	1.2(0.2)	4.1×10^{-1}	1.2(0.3)	3.9×10^{-1}
^{7}Be	2.0(0.4)	1.6	1.0(0.2)	8.3×10^{-2}	1.0(0.2)	1.2×10^{-1}
^{9}Be	–	2.5×10^{-1}	$4(1)\times10^{-1}$	1.1×10^{-1}	$3.4(0.7)\times10^{-1}$	7.9×10^{-2}
^{10}Be	–	1.0×10^{-4}	$1.8(0.4)\times10^{-1}$	2.4×10^{-1}	$1.9(0.5)\times10^{-1}$	1.0×10^{-1}
^{8}B	–	1.5×10^{-1}	$1.3(0.4)\times10^{-1}$	1.3×10^{-2}	$1.2(0.5)\times10^{-1}$	1.4×10^{-2}
^{10}B	–	1.3	$10(3)\times10^{-1}$	8.9×10^{-2}	$9(6)\times10^{-1}$	8.6×10^{-2}
^{11}B	–	2.1	1.2(0.5)	2.0×10^{-1}	1(1)	1.8×10^{-1}
^{10}C	–	1.9×10^{-1}	$1.7(0.6)\times10^{-1}$	1.7×10^{-2}	$1.5(0.9)\times10^{-1}$	1.6×10^{-2}
^{11}C	–	3.9	1.1(0.4)	5.5×10^{-2}	1.0(0.7)	7.1×10^{-2}
^{12}C	–	5.9×10^{-1}	1.6(0.9)	4.3×10^{-2}	1.5(0.9)	7.9×10^{-2}

Sampling of Energy and Angular Distributions

When a projectile particle with a velocity v interacts with a fixed target, the produced projectile and target fragments have different angular and energy distributions. While projectile fragments are emitted mostly forward (small angles of emission) and have, on average, the same energy per nucleon of the projectile, target fragments have lower energies and their space distribution is more isotropic. *Golovkov and Matsufuji* (46, 47) observed that, to describe the energy and angular distributions of secondary fragments, Gaussian and exponential distributions are needed. The first one accounts for fragments produced by the projectile, while the latter one for the target fragmentation. In Ganil data the two contributions were mixed and could not be disentangled. In **Figures 3–5**, it is possible to observe an example of energy and angle distributions, in linear and logarithmic scales, for the six different fragments (^{1}H, ^{4}He, ^{6}Li, ^{7}Be, ^{11}B and ^{11}C) detected by the 95 MeV/u Ganil experiment after the interaction of a ^{12}C ion beam with hydrogen, carbon and oxygen targets respectively.

The measured fragment angles were in the range between 4° and 43°, while the applied energy threshold was fragment-dependent (ranging from 4 MeV for ^{1}H to 86.9 MeV for ^{12}C). The bi-dimensional phenomenological distribution, $f(E, \theta)$, built using a combination of Gaussian and exponential functions, which better describes the data is the following:

$$f(E,\theta) = A_1 e^{\alpha_E E + \alpha_\theta \theta} + A_2 e^{-\left(\frac{(E-<E>)^2}{2\sigma_E} + \frac{(\theta-<\theta>)^2}{2\sigma_\theta}\right)} \quad (12),$$

where A_1, A_2, α_E, α_θ, σ_E, σ_θ, $< E >$ and $< \theta >$ are respectively the different normalization factors of the projectile and target contributions, the empirical coefficients that take into account the target fragments energy and angle dependency and the mean and spread, in energy and angle, values describing the projectile fragments distributions. The parameters used in FRED are shown in **Tables 2–4** for hydrogen, carbon and oxygen target respectively.

The projectile fragments have an average energy per nucleon that is close to the projectile one (in this case 95 MeV/u) and their direction is peaked at zero degrees along the incoming beam direction. The target fragments angular distribution is instead almost isotropic and the energy is smaller than the energy of the projectile fragments. The contribution of the projectile fragments term becomes more important when the fragments are heavier. For the hydrogen fragments (^{1}H, ^{2}H and ^{3}H) the energy and angle of emission are extracted directly by Eq. 12 both for projectile and target fragmentation.

The reason of this choice is that, as it can be observed in **Figures 3–5**, the Gaussian and exponential distributions for these fragments are largely overlapping and they are not easily distinguishable. All other fragments are extracted from the Gaussian and the exponential distribution in case of projectile and target fragmentation respectively. For a hydrogen target (**Figure 3** and **Table 2**), with the exception of ^{1}H fragments, all the distributions have a predominant Gaussian component. This is because the target fragmentation can only produce a proton. The small exponential contribution can be explained as the cross-sections for the hydrogen target have been obtained by subtraction using the cross-sections of CH_2 and C targets. The distribution fitted in the experimental angular range [4°; 43°] is used to perform an extrapolation to cover the full [0°;180°] range in the angular sampling.

Extrapolation to Different Beam Energies

The angle and energy distributions collected by the Ganil experiment correspond to fragments produced by a carbon beam of 95 MeV/u. To consider every possible energy of the projectile, a scaling model has been implemented.

When sampling the projectile fragmentation, the emission energy per nucleon of the i-th fragment is scaled according to the following equation:

$$E^i[\mathrm{MeV/u}] = E^i_{95\mathrm{MeV/u}} \frac{E_{proj}[MeV/u]}{95[MeV/u]} (1-k) \quad (13)$$

where $E^i_{95\mathrm{MeV/u}}$ is the energy per nucleon extracted from the Gaussian distribution of the Ganil experiment and E_{proj} is the

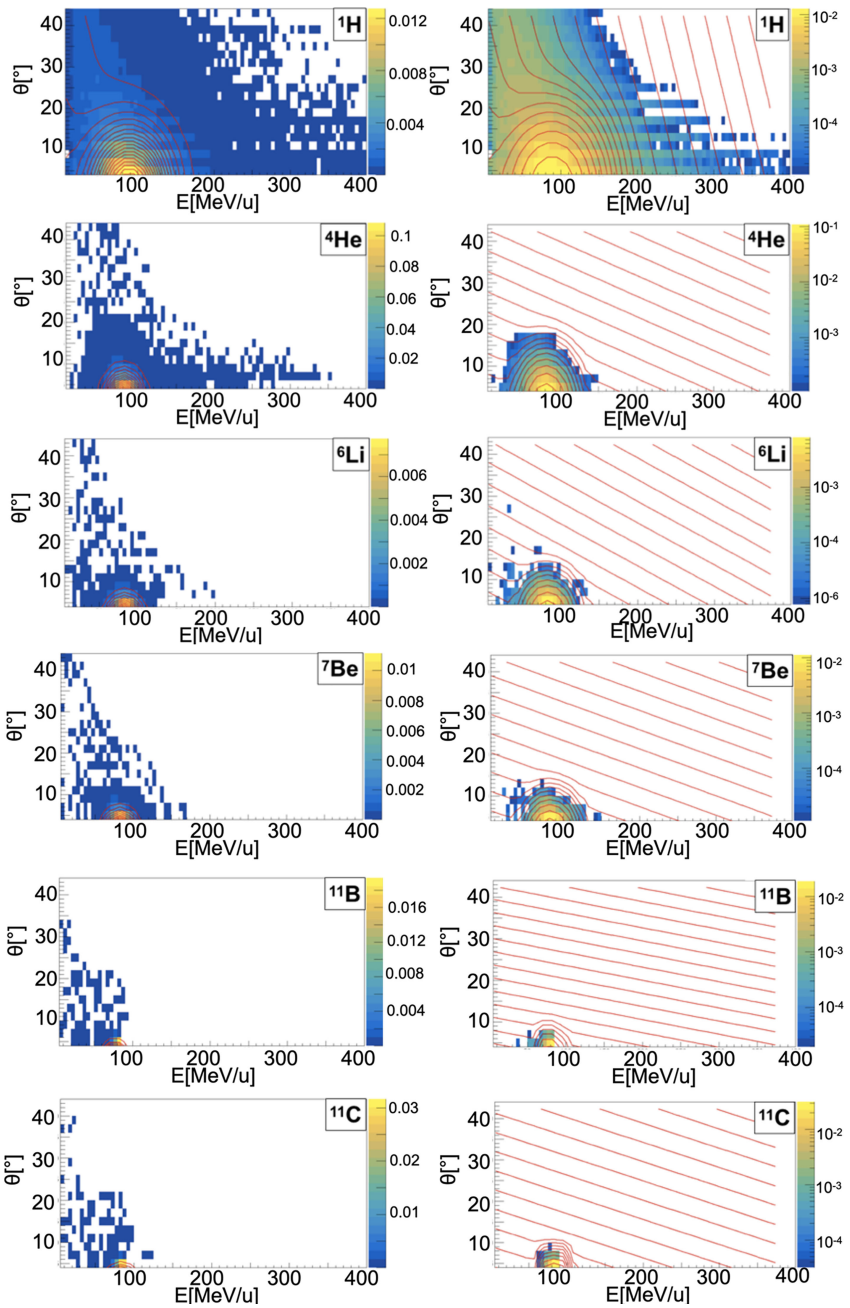

FIGURE 3 | Contour lines (red) of bidimensional fits of energy and angle distribution of different fragments produced by a 95 MeV/u carbon ion beam interacting with a hydrogen target. The color maps represent data taken from the 95 MeV/u Ganil experiment in linear (left) and logarithmic (right) scale.

energy per nucleon of the projectile. k is used to take into account that the fragments energy from the same event is correlated and that the total energy must not exceed the energy of the projectile:

$$k = c(1 - R) \tag{14}$$

where c is the correlation factor and R, for each i-th fragment, depends on the energy of the previous i-1 fragments:

$$R = \frac{E^i_{nucl}}{E_p} \tag{15}$$

$$E^i_{nucl} = \frac{\Sigma^{j=i}_{j=0} E_j A_j}{\Sigma^{j=i}_{j=0} A_j}. \tag{16}$$

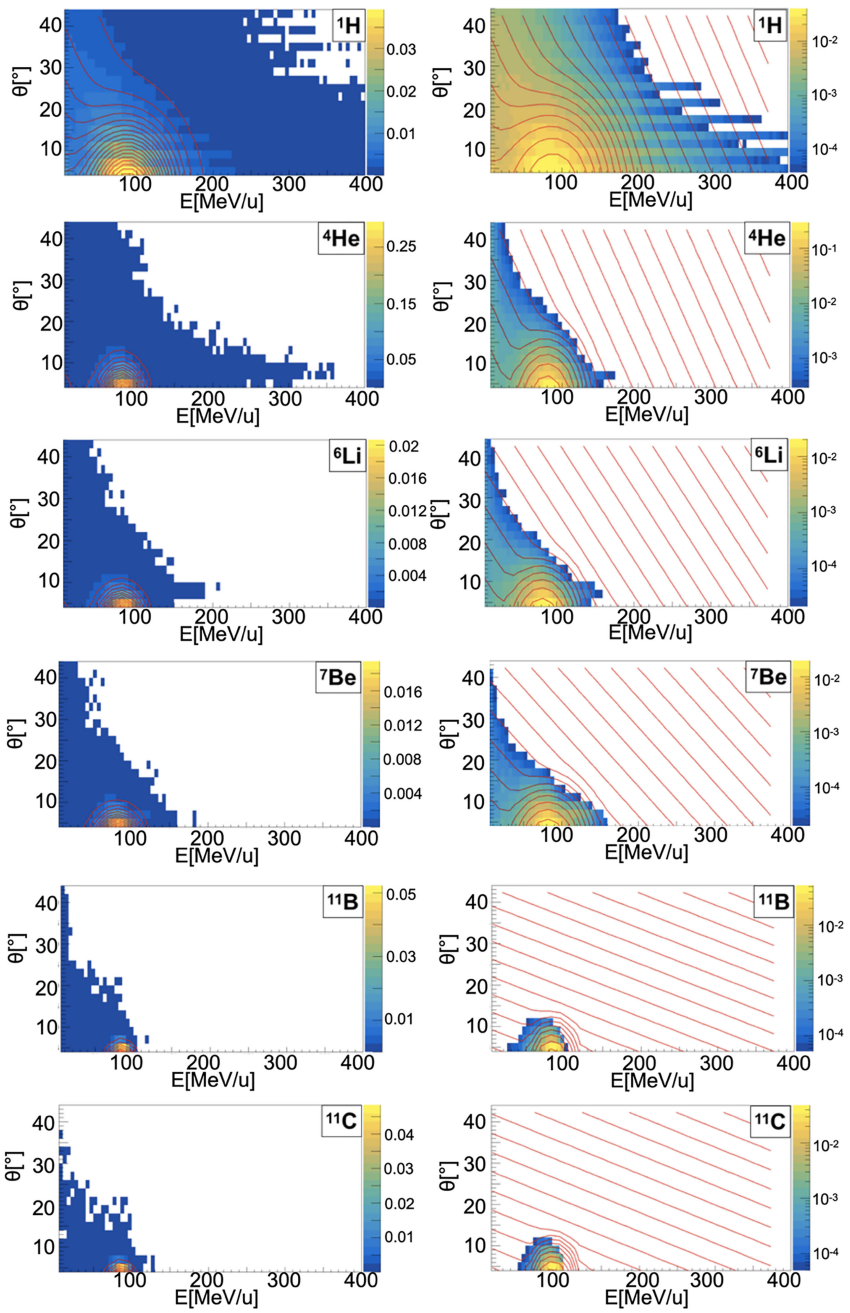

FIGURE 4 | Contour lines (red) of bidimensional fits of energy and angle distribution of different fragments produced by a 95 MeV/u carbon ion beam interacting with a carbon target. The color maps represent data taken from the 95 MeV/u Ganil experiment in linear (left) and logarithmic (right) scale.

E_j and A_j are the energy and the atomic number of the previous fragments in the current event.

For the results shown in this paper, the value implemented (c=0.4) was chosen in order to achieve the best agreement between FRED and FLUKA results.

With this linear dependence, the assumption that the average energy per nucleon of a projectile fragment is the same as that of the projectile itself is guaranteed. The sampling of the energy released to the target fragments is analogous to the one of the projectile but $E^i_{95\mathrm{Mev/u}}$ is extracted from the exponential distribution without any correlation factors.

The scaling factor for the angle of emission (θ) of the projectile fragment, can be computed according to:

$$|\vec{p}| \sin(\theta) = p_\perp \tag{17}$$

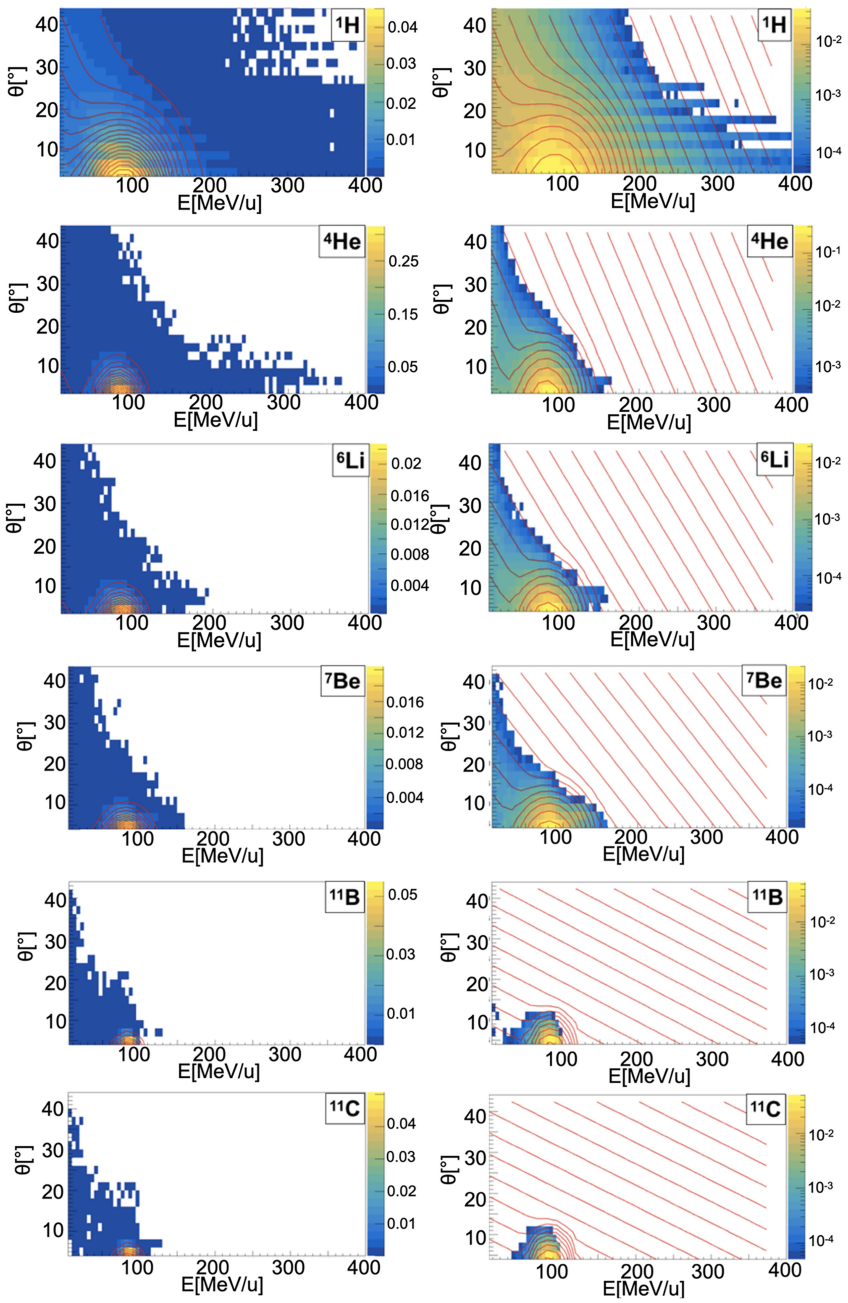

FIGURE 5 | Contour lines (red) of bidimensional fits of energy and angle distribution of different fragments produced by a 95 MeV/u carbon ion beam interacting with an oxygen target. The color maps represent data taken from the 95 MeV/u Ganil experiment in linear (left) and logarithmic (right) scale.

where $|\vec{p}|$ and $p_{\perp}$ are the fragment momentum magnitude and transverse momentum respectively and θ is the angle of $\vec{p}$ with respect to projectile direction. As the angles of emission of projectile fragments are small, it is possible to write:

$$\theta \sim \sin(\theta) = \frac{p_{\perp}}{|\vec{p}|}. \tag{18}$$

The fragment transverse momentum does not depend on the projectile energy. As a consequence, the dependence of the angle on the beam energy is only due to the denominator of Eq. 18:

$$\frac{\theta}{\theta_{95\mathrm{MeV}/u}} = \frac{|\vec{p}_{95\mathrm{MeV}/u}|}{|\vec{p}|} \tag{19}$$

where $\theta_{95MeV/u}$ is the angle extracted from the Gaussian distribution of the Ganil experiment and $|\vec{p}_{95\mathrm{MeV/u}}|$ is the corresponding momentum.

At therapeutic energies, $p \propto \sqrt{E}$ and hence the equation becomes:

$$\frac{\theta}{\theta_{95\mathrm{MeV}/u}} = \frac{\sqrt{E_{95\mathrm{MeV}/u}}}{\sqrt{E}} \tag{20}$$

where $E_{95MeV/u}$ and E are the fragments kinetic energies of the Ganil experiment and of the fragments emitted for a generic beam energy. Using the fragments energy scaling factor (Eq. 13), the relation between an angle of emission θ produced by a projectile of energy E_{proj} and the angle of Ganil data, $\theta^i_{95MeV/u}$, becomes

$$\theta^i = \theta^i_{95\mathrm{MeV/u}} \sqrt{\frac{95}{E_{proj}[MeV/u]}} \tag{21}$$

This scaling is not used for protons and neutrons since, checking the angular dependence with FLUKA, it has been observed that for those particles at the energies of interest for particle therapy applications the angle of emission is nearly energy-independent. The same scaling factor is also used for the angle of the target fragments.

3 RESULTS

The nuclear models implemented in FRED were tested against the results obtained with a full-MC simulation performed using

TABLE 2 | Parameters of Eq. 12 considering a 95 MeV/u carbon ion beams on a ^{1}H target.

Frag.	A_1	A_2	$< E >$	σ_E	$< \theta >$	σ_θ	α_E	α_θ
n	5.4×10^{-1}	4.9×10	9.3×10	3.3×10	0.0	9.7	1.0×10^{-2}	2.5×10^{-2}
^{1}H	5.4×10^{-1}	4.9×10	9.3×10	3.3×10	0.0	9.7	1.2×10^{-2}	2.5×10^{-2}
^{2}H	2.0×10^{-1}	7.5	8.1×10	2.3×10	0.0	8.2	2.2×10^{-2}	6.5×10^{-2}
^{3}H	7.8×10^{-2}	2.7	7.6×10	2.2×10	0.0	6.8	1.9×10^{-2}	1.8×10^{-1}
^{3}He	2.2×10^{-2}	7.6	9.6×10	2.7×10	0.0	6.2	1.8×10^{-2}	1.0×10^{-1}
^{4}He	9.8×10^{-3}	5.6×10	8.4×10	1.2×10	0.0	4.3	1.5×10^{-2}	1.8×10^{-1}
^{6}He	3.0×10^{-2}	3.1	7.8×10	1.4×10	0.0	4.0	2.6×10^{-2}	2.7×10^{-1}
^{6}Li	8.0×10^{-3}	4.5	8.4×10	1.1×10	0.0	3.4	1.9×10^{-2}	2.0×10^{-1}
^{7}Li	1.9×10^{-2}	3.3	7.9×10	8.6	0.0	3.2	2.0×10^{-2}	2.7×10^{-1}
^{7}Be	3.6×10^{-3}	6.6	8.5×10	1.1×10	0.0	3.1	1.7×10^{-2}	2.1×10^{-1}
^{9}Be	2.0×10^{-2}	1.3	8.2×10	7.3	0.0	3.0	2.3×10^{-2}	2.7×10^{-1}
^{10}Be	7.1×10^{-2}	3.8×10^{-1}	7.9×10	5.3	0.0	3.1	2.4×10^{-2}	3.2×10^{-1}
^{8}B	6.3×10^{-1}	8.3×10^{-3}	8.9×10	1.3×10	0.0	3.2	2.2×10^{-2}	1.6×10^{-1}
^{10}B	3.5×10^{-3}	1.3×10	8.3×10	6.5	0.0	2.5	1.9×10^{-2}	3.7×10^{-1}
^{11}B	1.1×10^{-2}	1.4	8.3×10	4.6	0.0	2.2	1.8×10^{-2}	5.8×10^{-1}
^{10}C	1.2×10^{-3}	3.7	8.8×10	7.2	0.0	2.3	1.8×10^{-2}	2.1×10^{-1}
^{11}C	5.0×10^{-4}	3.9×10	8.4×10	4.8	0.0	2.1	1.7×10^{-2}	3.0×10^{-1}
^{12}C	5.0×10^{-4}	9.3×10	8.3×10	3.6	0.0	9.2×10^{-1}	1.0×10^{-2}	2.0×10^{-1}

Parameters relative to the energy, **E***, are expressed in MeV/u while the one of the angle,* θ*, in degrees.*

TABLE 3 | Parameters of Eq. 12 considering a 95 MeV/u carbon ion beams on a ^{12}C target.

Frag.	A_1	A_2	$< E >$	σ_E	$< \theta >$	α_θ	α_E	α_θ
n	2.8×10^{-1}	1.0×10^{2}	9.3×10	3.7×10	0.0	1.0×10	1.2×10^{-2}	2.5×10^{-2}
^{1}H	2.8×10^{-1}	1.0×10^{2}	9.3×10	3.7×10	0.0	1.0×10	1.3×10^{-3}	2.6×10^{-2}
^{2}H	2.7×10^{-1}	5.4×10	8.1×10	2.6×10	0.0	8.9	2.6×10^{-2}	3.1×10^{-2}
^{3}H	2.6×10^{-1}	2.5×10	7.3×10	1.8×10	0.0	7.6	3.2×10^{-2}	5.7×10^{-2}
^{3}He	1.5×10^{-1}	3.6×10	9.2×10	2.9×10	0.0	7.0	3.1×10^{-2}	4.7×10^{-2}
^{4}He	7.4×10^{-2}	1.9×10^{2}	8.3×10	1.5×10	0.0	5.2	2.9×10^{-2}	8.0×10^{-2}
^{6}He	8.1×10^{-2}	1.0×10	7.8×10	1.7×10	0.0	5.4	3.0×10^{-2}	1.5×10^{-1}
^{6}Li	7.0×10^{-2}	1.3×10	8.4×10	1.4×10	0.0	4.4	2.7×10^{-2}	1.1×10^{-1}
^{7}Li	6.1×10^{-2}	1.3×10	7.9×10	1.3×10	0.0	4.2	3.1×10^{-2}	1.2×10^{-1}
^{7}Be	3.7×10^{-2}	1.2×10	8.3×10	1.6×10	0.0	4.2	2.6×10^{-2}	1.2×10^{-1}
^{9}Be	3.6×10^{-2}	5.7	8.3×10	1.1×10	0.0	3.7	2.5×10^{-2}	2.2×10^{-1}
^{10}Be	4.8×10^{-2}	3.0	8.2×10	9.3	0.0	3.6	2.4×10^{-2}	2.7×10^{-1}
^{8}B	1.8×10^{-2}	1.9	8.8×10	1.7×10	0.0	4.0	2.8×10^{-2}	1.5×10^{-1}
^{10}B	7.7×10^{-3}	1.9×10	8.6×10	9.3	0.0	3.2	2.3×10^{-2}	2.1×10^{-1}
^{11}B	8.4×10^{-3}	3.9×10	8.4×10	7.3	0.0	2.9	2.0×10^{-1}	3.0×10^{-1}
^{10}C	5.9×10^{-3}	3.5	8.8×10	9.5	0.0	3.1	1.9×10^{-2}	2.1×10^{-1}
^{11}C	3.4×10^{-3}	3.0	8.6×10	7.2	0.0	2.7	1.9×10^{-2}	2.6×10^{-1}
^{12}C	3.5×10^{-3}	6.5×10	8.8×10	4.9	0.0	2.3	1.6×10^{-2}	2.8×10^{-1}

Parameters relative to the energy, **E***, are expressed in MeV/u while the one of the angle,* θ*, in degrees.*

TABLE 4 | Parameters of Eq. 12 considering a 95 MeV/u carbon ion beams on a ^{16}O target.

Frag.	A_1	A_2	$< E >$	σ_E	$< \theta >$	α_θ	α_E	α_θ
n	3.0×10^{-1}	1.3×10^{2}	9.3×10	3.7×10	0.0	1.0×10	1.3×10^{-2}	2.4×10^{-2}
^{1}H	3.0×10^{-1}	1.3×10^{2}	9.3×10	3.7×10	0.0	1.0×10	1.3×10^{-2}	2.4×10^{-2}
^{2}H	3.0×10^{-1}	6.3×10	8.2×10	2.6×10	0.0	9.2	2.6×10^{-2}	3.0×10^{-2}
^{3}H	2.6×10^{-1}	2.8×10	7.3×10	1.8×10	0.0	7.9	3.2×10^{-2}	5.6×10^{-2}
^{3}He	1.5×10^{-1}	4.2×10	9.1×10	2.9×10	0.0	7.3	2.9×10^{-2}	4.3×10^{-2}
^{4}He	8.3×10^{-2}	2.1×10^{2}	8.3×10	1.5×10	0.0	5.3	2.9×10^{-2}	7.8×10^{-2}
^{6}He	8.1×10^{-2}	1.1×10	7.9×10	1.7×10	0.0	5.5	2.9×10^{-2}	1.4×10^{-1}
^{6}Li	7.9×10^{-2}	1.5×10	8.4×10	1.4×10	0.0	4.5	2.8×10^{-2}	1.0×10^{-1}
^{7}Li	6.3×10^{-2}	1.4×10	7.9×10	1.3×10	0.0	4.4	3.1×10^{-2}	1.1×10^{-1}
^{7}Be	3.9×10^{-2}	1.3×10	8.3×10	1.6×10	0.0	4.3	2.7×10^{-2}	1.1×10^{-1}
^{9}Be	3.1×10^{-2}	6.0	8.3×10	1.2×10	0.0	3.9	2.7×10^{-2}	1.8×10^{-1}
^{10}Be	5.5×10^{-2}	3.2	8.2×10	8.8	0.0	3.7	2.4×10^{-2}	2.4×10^{-1}
^{8}B	2.2×10^{-2}	2.1	8.9×10	1.7×10	0.0	4.1	2.9×10^{-2}	1.4×10^{-1}
^{10}B	7.7×10^{-3}	1.9×10	8.4×10	9.3	0.0	3.3	2.6×10^{-2}	1.7×10^{-1}
^{11}B	8.0×10^{-3}	3.1×10	8.5×10	7.1	0.0	2.9	2.1×10^{-2}	2.5×10^{-1}
^{10}C	8.8×10^{-3}	3.5	8.8×10	9.2	0.0	3.2	2.3×10^{-2}	2.0×10^{-1}
^{11}C	3.4×10^{-3}	3.0×10	8.6×10	7.1	0.0	2.8	2.0×10^{-2}	2.3×10^{-1}
^{12}C	3.4×10^{-3}	6.2×10	8.7×10	4.7	0.0	2.4	1.7×10^{-2}	3.0×10^{-1}

Parameters relative to the energy, **E**, *are expressed in MeV/u while the one of the angle,* **θ**, *in degrees.*

FLUKA. In particular, the longitudinal and lateral dose distribution obtained simulating the interactions of different beams with different targets have been compared in several configurations and projectiles. In this contribution, we report in detail the results obtained studying the carbon ions beam interactions with a water target and with a patient CT.

3.1 Single Pencil-Beam in Water

Figure 6 shows the depth-dose profiles obtained from a simulation performed using FRED, in which carbon ions with energies in the range of interest for PT applications (100-300 MeV/u) are interacting with a water target. The target dimensions are 10 cm × 10 cm × 40 cm ($x \times y \times z$) with a voxel size of 0.5 mm in all the directions. The incident beam in all the cases was directed along z.

The same distributions have been obtained using a FLUKA simulation and the results have been compared. In particular, the curves shown in **Figure 6** correspond to single pencil-beams of mono-energetic carbon ions.

The absorbed dose per primary is shown, from a simulation performed using 10^8 primary ions to minimize the statistical fluctuations. The profiles closely overlap and, in particular, the agreement of the absorbed dose at the peak between FRED and FLUKA simulations is very good. The relative difference between FRED and FLUKA predictions is always within 2.5% when computing the integral absorbed dose over the whole depth in the 100-300 MeV/u energy range, with the best agreement achieved at 100 MeV/u (relative difference = 0.05%).

The agreement between FRED and FLUKA, studied using the same scoring grid and the same number of primaries, is shown in

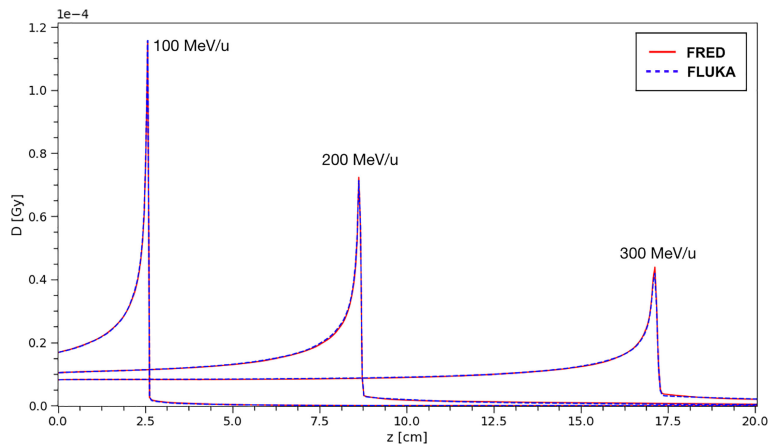

FIGURE 6 | The absorbed dose integrated over the longitudinal axis for carbon ion beams in water at different energies. The absorbed dose per primary particle was obtained simulationg 10^8 primaries. Comparison between FRED (red continuous line) and FLUKA (blue dotted line) simulations, with the same scoring grid, and the same number of primaries is presented.

Figure 7. A single pencil beam of 200 MeV/u has been simulated along the beam axis (longitudinal) and at the BP position (lateral).

The position chosen for the BP corresponds to the maximum of the dose observed in FLUKA and FRED simulations. With the same scoring grid, the two simulations predict the BP in the same voxel. The lateral transverse profiles show, in linear and logarithmic scale, the tails of the distribution, mainly due to nuclear interactions. Observing the lateral and longitudinal profiles, we can conclude that the present implementation of multiple Coulomb scattering, of nuclear elastic scattering and the angular distribution of secondary fragments are capable of reproducing the main features of the dose distribution.

3.2 SOBP in Water

After having studied the dose released by a single pencil beam, the next step was to assess agreement also for a Spread-out Bragg Peak (SOBP) composed by pencil-beams of different energies.

This is a more interesting benchmark considering the purpose of the software. In particular, we have simulated a SOBP corresponding to a 5 cm cuboid starting at a depth of 10 cm with ~2 Gy of physical dose in the center. It has been simulated in a water phantom of dimensions 5 cm × 5 cm × 20 cm ($x \times y \times z$) and with a voxel size of 0.5 × 0.5 × 0.2 mm^3 both with FLUKA and FRED. The incident beams were along z direction.

To obtain the cuboid, 31 energy layers from 219.0 to 277.5 MeV/u, with ~10^8 primaries per layer, have been simulated with a total of ~1.5 × 10^9 primary particles. In **Figure 8**, the longitudinal and lateral distribution of the SOBP are shown. The relative difference between the absorbed dose simulated by FRED and FLUKA is below 1.5%. The relative difference with respect to FLUKA predictions is within 0.2% of the total absorbed dose.

The gamma-index test has also been performed to quantify the dose distributions agreement. In **Figure 8**, the γ-index test obtained comparing FLUKA and FRED is shown. The gamma-index is strongly dependent on the statistical uncertainty, inherent to MC, which may (artificially) improve the γ pass-rate. However, it has been observed that 10^7 primaries are enough to reduce the statistical uncertainty contribution to a negligible level.

As already observed in **Figure 8**, the dose deposited in FRED is slightly lower than the one predicted by FLUKA. However, the γ-index 2mm/3% pass-rate is 99.89% with a global cutoff of 5% of the maximum dose. This result is very good and demonstrates that FRED can be successfully used in the clinical practice.

3.3 Heterogeneous Materials

To validate the FRED simulation results in heterogeneous materials, we used an anthropomorphic phantom (**Figure 9**). We delivered the same SOBP used in the previous paragraph on a head-and-neck CT, using the same calibration curve to convert HU into the material density both in FRED and in FLUKA. The CT has a voxel size of 2 mm in each direction. The 2mm/3% gamma-index between FRED and FLUKA dose distributions is 99.89% with threshold of 5%.

4 PERFORMANCE ON GPU

Once the good quality of the FRED simulation has been assessed performing a comparison with another state-of-the-art simulation software (FLUKA) the other important aspect that has to be quantified is the computation time. In **Table 5**, the time performances for different architectures are reported for the FLUKA and FRED simulations. Mono-energetic carbon beams

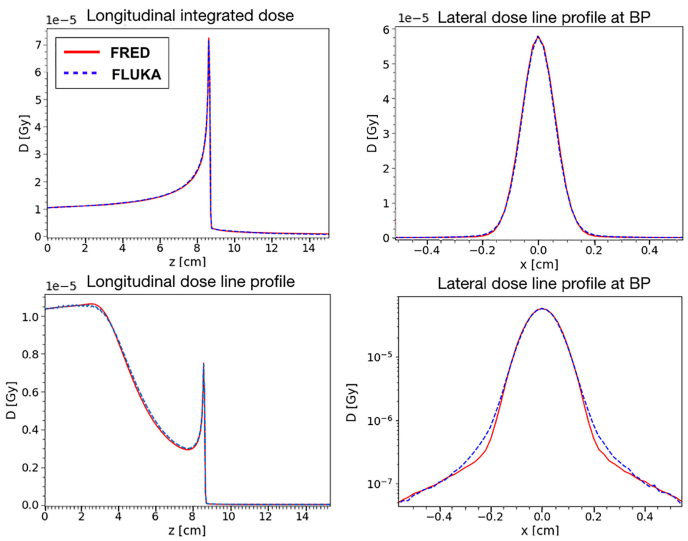

FIGURE 7 | Absorbed dose in water for a 200 MeV/u carbon ion beam simulated with FRED (red continuous line) and FLUKA (blue dotted line) with the same scoring grid and the same number of primaries. On the left, it is possible to observe the absorbed dose integrated over the longitudinal axis (top) and central axis profile along beam axis (bottom). On the right, the lateral axis profile at 8.6 cm of depth in linear scale (top right) and logarithmic (bottom right) scale. This position is the one corresponding to the maximum value of the dose (BP) both in the FLUKA and the FRED simulations.

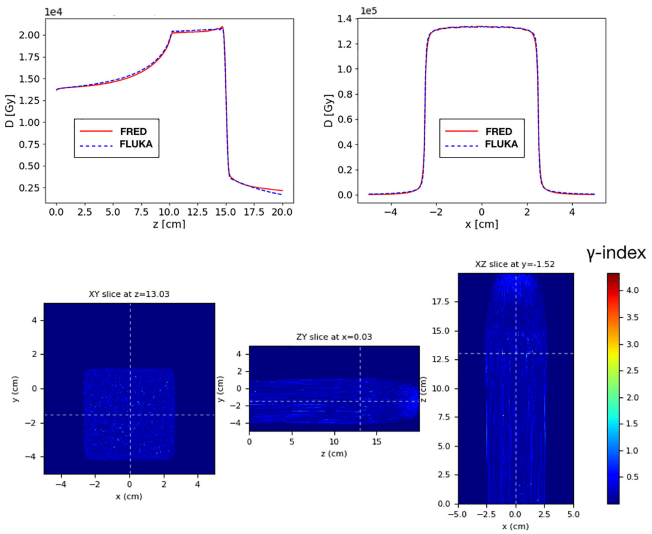

FIGURE 8 | Top: longitudinal (left) and lateral (right) integrated dose distributions for a SOBP in water. FRED (red continuous line) and FLUKA (blue dotted line) simulations are shown using the same scoring grid (voxel size: 0.5 × 0.5 × 0.2 mm^3), and the same number of primary particles (10^8). Bottom: the corresponding γ-index distribution is shown. The γ-index 2mm/3% pass rate is 99.89%. The maximum value of the γ-index is 4.3, while the mean value is 0.21. The γ-index xy slice (left) shows the γ-index distribution at z = 13 cm, which is in the peak region of the SOBP, while the other slices (center and right) are centered in x (0 cm) and y (-1.5 cm).

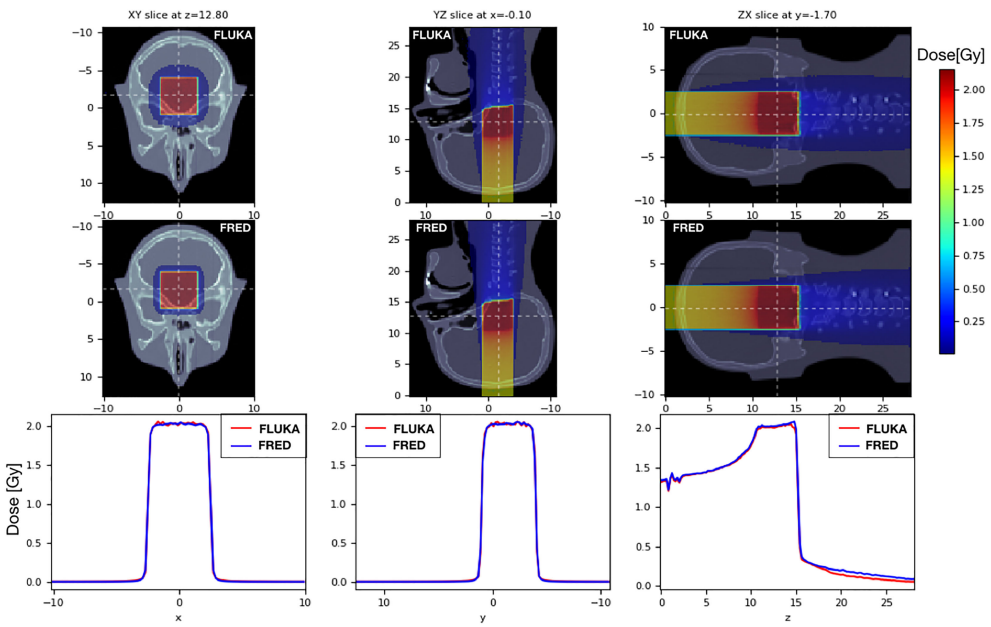

FIGURE 9 | On the left the dose distribution on the XY slice at z = 12.80 cm is shown. On the center pictures, there is the dose distribution on the YZ slice centered in x. On the right, the longitudinal dose distribution on the ZX slice at z=-1.7cm is shown. The projection of the 2D figures is shown on the bottom figures. Comparison between FRED (figures on the top and blue line) and FLUKA (figures on the bottom and red line) simulations, with the same scoring grid (2 mm), and the same number of primary particles (10^6) is shown.

interactions in water (target 20 cm × 20 cm × 20 cm with a 2 mm cubic voxels) were the subjects for the simulations.

As it can be observed, FRED is nearly 10 times faster than FLUKA when running on the same hardware (single CPU, Intel Xeon E5-2687W at 3,1 GHz) exploiting the simplification of the implemented physics models. The tracking rate decreases with increasing energy, as expected, since a carbon ion with more energy is subject to more interactions and its average path through the medium is longer.

As shown, running on GPU (NVIDIA Geforce RTX 3090) the gain in terms of time is about three orders of magnitude with

TABLE 5 | Computing times for different hardware architectures simulating a monoenergetic carbon ion beam at 100 (top) and 300 (bottom) MeV/u in a water target (20 cm × 20 cm× 20 cm) with 2 mm cubic voxels.

100 MeV/u			
MC	**Hardware**	**Primary/s**	**μs/primary**
FLUKA	single CPU core	0.7 k	1400
FRED	single CPU core	4.2 k	240
FRED	single GPU card	2000 k	0.5
300 MeV/u			
MC	**Hardware**	**Primary/s**	**μs/primary**
FLUKA	single CPU core	0.3 k	3000
FRED	single CPU core	3 k	300
FRED	single GPU card	2500 k	0.4

We used a motherboard with Intel Xeon E5-2687W CPU at 3,1 GHz to test the CPU performances, while we used a NVIDIA Geforce RTX 3090 for the GPU.

respect to single CPU execution. No significant changes to the structure of the original GPU algorithm (27) were necessary, besides the implementation of the nuclear fragmentation model for carbon described in Section 2.1. Carbon fragmentation is a relatively rare event with respect to tracing step-by-step all charged particles in a simulation. As such, the impact on the tracking rate is mostly due to the number of complete particle histories that have to be simulated per primary carbon ion. On the same GPU card and with similar geometry and scoring conditions, the typical tracking rate for a proton beam is about 5 million primary/s. The performance observed in the case of carbon ions is affected by the increased number of particles that have to be simulated. In the therapeutic energy range, such number has already been evaluated, and hence our fragmentation model generates on average 2 to 4 charged fragments per primary carbon.

5 CONCLUSION

In this contribution, we have presented a fast-MC software capable of simulating, with clinical precision, particle therapy carbon ion treatments. The nuclear fragmentation model has been developed parametrizing existent data and applying energy and angle re-scaling to estimate fragments energies in the range where data are missing. The model was based directly on experimental data, in order to ease its update whenever new or updated results will be available from experiments. For example, data from the FOOT experiment (48, 49) focusing on the study of nuclear fragmentation, will be available soon. This is the main difference between FRED and the GPU MC goCMC that has been developed starting from Geant4. In addition, by comparing the results of FRED, obtained from data, with the full-MC FLUKA, already clinically validated, there is a double check on the accuracy of the implemented model.

Results obtained when comparing FRED with FLUKA are satisfactory, especially for low energies which are the most used in PT and, in particular, for head-and-neck tumors. The relative difference between the total dose in single pencil beams in FRED and FLUKA predictions is always within 2.5% in the 100-300 MeV/u energy range. Simulating a SOBP in water the relative difference of the dose distribution is within 1.4%. For both the SOBP in water and in heterogeneous material we obtained an almost 100% pass rate for 2mm/3% gamma-index.

Beside the successful implementation of the nuclear model, capable of clinical precision when computing the absorbed dose in particle therapy conditions, FRED also achieved an impressive improvement in computing time, with respect to conventional full MC software solutions. Exploiting the parallel programming power of GPU architectures, FRED is capable of tracking millions of primary particles per second on a single GPU card. The observed gain in processing time, when comparing to the FLUKA full MC, was nearly a factor ~2000, depending on the energy of the primary beam. Using FRED in combination with GPU hardware, it is possible to process a complete treatment plan within minutes instead of days, opening the way for the use of FRED, not only for protons, but also as quality assurance tool in carbon therapy especially for the head-and-neck tumors that require lower beam energy. Comparing the time performance of FRED with the GPU MC goCMC we observed consistent results. The next step will be to compare the accuracy of FRED dose recalculation against commissioning data and commercial TPS at CNAO in order to achieve a clinical validation for carbon therapy applications.

DATA AVAILABILITY STATEMENT

The original contributions presented in the study are included in the article/supplementary material. Further inquiries can be directed to the corresponding author.

AUTHOR CONTRIBUTIONS

MDS: wrote the main manuscript text. MDS, VP, AnS, and GB: developed the nuclear model described in the paper. GB, MF, GT, and GF: provided FLUKA simulations used to compare the FRED model. AlS, MM, MT, and AT: provided the information about cross-sections found in literature and contributed to the interpretation of the work. PDM: provided the raster file for the SOBP and information about the clinical practice. All authors contributed to the article and approved the submitted version.

REFERENCES

1. Paganetti H. Range Uncertainties in Proton Therapy and the Role of Monte Carlo Simulations. *Phys Med Bio* (2012) 57:r99–117. doi: 10.1088/0031-9155/57/11/R99
2. Parodi K. Clinical CT-Based Calculations of Dose and Positron Emitter Distributions in Proton Therapy Using the Fluka Monte Carlo Code. *Phys Med Biol* (2007) 52:3369–87. doi: 10.1088/0031-9155/52/12/004
3. Titt U, Bednarz B, Paganetti H. Comparison of Mcnp X And Geant 4 Proton Energy Deposition Predictions for Clinical Use. *Phys Med Biol* (2012) 57:6381–93. doi: 10.1088/0031-9155/57/20/6381
4. Scaffner B, Pedroni E, Lomax A. Dose Calculation Models for Proton Treatment Planning Using a Dynamic Beam Delivery System: An Attempt to Include Density Heterogeneity Effects in the Analytical Dose Calculation. *Phys Med Bio* (1999) 44:27–41. doi: 10.1088/0031-9155/44/1/004
5. Paganetti H, Jiang H, Parodi K, Slopsema R, Engelsman M. Clinical Implementation of Full Monte Carlo Dose Calculation in Proton Beam Therapy. *Phys Med Bio* (2008) 53:4825–53. doi: 10.1088/0031-9155/53/17/023
6. Kohno R, Takada Y, Sakae T, Terunuma T, Matsumoto K, Nohtomi A, et al. Experimental Evaluation of Validity of Simplified Monte Carlo Method in Proton Dose Calculations. *Phys Med Biol* (2003) 48:1277–88. doi: 10.1088/0031-9155/48/10/303
7. Fippel M, Soukup M. A Monte Carlo Dose Calculation Algorithm for Proton Therapy. *Med Phys* (2004) 31:2263–73. doi: 10.1118/1.1769631
8. Li JS, Shahine B, Fourkal E, Ma CM. A Particle Track-Repeating Algorithm for Proton Beam Dose Calculation. *Phys Med Biol* (2005) 50:1001–10. doi: 10.1088/0031-9155/50/5/022
9. Yepes P, Randeniya S, Taddei PJ, Newhauser WD. Monte Carlo Fast Dose Calculator for Proton Radiotherapy: Application to a Voxelized Geometry Representing a Patient with Prostate Cancer. *Phys Med Biol* (2009) 54:N21–8. doi: 10.1088/0031-9155/54/1/N03
10. Jia X, Ziegenhein P, Jiang SB. GPU-Based High-Performance Computing for Radiation Therapy. *Phys Med Biol* (2014) 59:151–82. doi: 10.1088/0031-9155/59/4/R151
11. Jia X, Lou Y, Li R, Song WY, Jiang SB. GPU-Based Fast Cone Beam CT Reconstruction from Undersampled and Noisy Projection Data *via* Total Variation. *Phys Med Biol* (2010) 37:1757–60. doi: 10.1118/1.3371691
12. Giantsoudi D, Schuemann J, Jia X, Dowdell S, Jiang S, Paganetti H. Validation of a GPU-based Monte Carlo Code (gPMC) for Proton Radiation Therapy: Clinical Cases Study. *Phys Med Biol* (2015) 60:2257–69. doi: 10.1088/0031-9155/60/6/2257
13. Xu F, Mueller K. Accelerating Popular Tomographic Reconstruction Algorithms on Commodity PC graphics Hardware. *IEEE Trans Nucl Sci* (2005) 52:654–63. doi: 10.1109/TNS.2005.851398
14. Sharp GC, Kandasamy N, Singh H, Folkert M. GPU-Based Streaming Architectures for Fast Cone-Beam CT Image Reconstruction and Demons Deformable Registration. *Phys Med Biol* (2007) 16:5771–83. doi: 10.1088/0031-9155/52/19/003
15. Yan GR, Tian J, Zhu S, Dai Y, Qin C. Fast Cone-Beam CT image Reconstruction using GPU Hardware. *J X-Ray Sci Technol* (2008) 16:225–34.
16. Gu X, Choi D, Men C, Pan H, Majumdar A, Jiang SB. GPU-Based Ultra Fast Dose Calculation Using a Finite Size Pencil Beam Model. *Phys Med Biol* (2009) 54:6287–97. doi: 10.1088/0031-9155/54/20/017
17. Gu X, Pan H, Yun Liang RC, Yang D, et al. Implementation and Evaluation of Various Demons Deformable Image Registration Algorithms on a GPU. *Phys Med Biol* (2010) 55:207–19. doi: 10.1088/0031-9155/55/1/012
18. Hissoiny S, Ozell B, Després P. Fast Convolution-Superposition Dose Calculation on Graphics Hardware. *Med Phys* (2009) 36:1998–2005. doi: 10.1118/1.3120286
19. Samant SS, Xia J, Muyan-Ozcelik P, Owens JD. High Performance Computing for Deformable Image Registration: Towards A New Paradigm in Adaptive Radiotherapy. *Med Phys* (2008) 35:3546–53. doi: 10.1118/1.2948318
20. Men C, Gu X, Choi D, Majumdar A, Zheng Z, Mueller K, et al. GPU-Based Ultra Fast IMRT Plan Optimization. *Phys Med Biol* (2009) 54:6565–73. doi: 10.1088/0031-9155/54/21/008
21. Men C, Jia X, Jiang SB. GPU-Based Ultra-Fast Direct Aperture Optimization for Online Adaptive Radiation Therapy. *Phys Med Biol* (2010) 55:4309–19. doi: 10.1088/0031-9155/55/15/008
22. Men C, Romeijn HE, Jia X, Jiang SB. Ultrafast Treatment Plan Optimization for Volumetric Modulated Arc Therapy (VMAT). *Med Phys* (2010) 37:5787–91. doi: 10.1118/1.3491675
23. WanChanTseung H, et al. A Fast GPU-based Monte Carlo Simulation of Proton Transport with Detailed Modeling of Nonelastic Interactions. *Med Phys* (2015) 42:2967–78. doi: 10.1118/1.4921046
24. WanChanTseung H, et al. Clinically Applicable Monte Carlo–based Biological Dose Optimization for the Treatment of Head and Neck Cancers With Spot-Scanning Proton Therapy. *Int J Radiat Oncol Biol Physics* (2016) 95:1535–43. doi: 10.1016/j.ijrobp.2016.03.041
25. Beltran C, Jia Y, Slopsema R, Yeung D, Li Z. A Simplified Methodology to Produce Monte Carlo Dose Distributions in Proton Therapy. *J Appl Clin Med Phys* (2014) 15:2–10. doi: 10.1120/jacmp.v15i4.4413
26. Qin N, Pinto M, Tian Z, Dedes G, Pompos A, Jiang SB, et al. Initial Development of goCMC: A GPU-Oriented Fast Cross-Platform Monte Carlo Engine for Carbon Ion Therapy. *Phys Med Bio* (2017) 62:3682–99. doi: 10.1088/1361-6560/aa5d43
27. Schiavi A, Senzacqua M, Pioli S, Mairani A, Magro G, Molinelli S, et al. Fred: A GPU-Accelerated fast-Monte Carlo Code for Rapid Treatment Plan Recalculation in Ion Beam Therapy. *Phys Med Biol* (2017) 62:7482–504. doi: 10.1088/1361-6560/aa8134
28. Highland L. Some Practical Remarks on Multiple Scattering. *Nucl Instruments Methods* (1975) 129:497–9. doi: 10.1016/0029-554X(75)90743-0
29. Takechi M, Fukuda M, Mihara M, Tanaka K, Chinda T, Matsumasa T, et al. Reaction Cross Sections at Intermediate Energies and Fermi-Motion Effect. *Nucl Phys* (2009) 79:061601. doi: 10.1103/PhysRevC.79.061601
30. Zhang HY, Shenac W, Ren Z, Ma Y, Jiang W, Zhu Z, et al. Measurement of Reaction Cross Section for Proton-Rich Nuclei (A<30) at Intermediate Energies. *Nucl Phys* (2002) 707:303. doi: 10.1016/S0375-9474(02)01007-2
31. Kox S, Gamp A, Cherkaoui R, Cole AJ, Longequeue N, Menet J, et al. Direct Measurements of Heavy-Ion Total Reaction Cross Sections at 30- And 83-MeV/Nuclon. *Nucl Phys* (1984) 420:162. doi: 10.1016/0375-9474(84)90663-8
32. Kox S, Gamp A, Perrin C, Arvieux J, Bertholet R, Bruandet J, et al. Transparency Effects in Heavy-Ion Collisions Over the Energy Range 100300 MeV/Nuclon. *Phys Lett* (1985) 159:15. doi: 10.1016/0370-2693(85)90110-8
33. Dudouet J, Juliani D, Labalme M, Cussol D, Angelique JC, Braunn B, et al. Double-Differential Fragmentation Cross-Section Measurements of 95 MeV/Nucleon *C* Beams on Thin Targets for Hadron Therapy. *Phys Med Biol* (2013) 159:24606. doi: 10.1103/PhysRevC.88.024606
34. Divay C, Colin J, Cussol D, Finck C, Karakaya Y, Labalme M, et al. Differential Cross Section Measurements for Hadron Therapy: 50 MeV/Nucleon *C* Reactions on H, C, O, A1, and *Ti* Targets. *Phys Rev C* (2017) 95:044602. doi: 10.1103/PhysRevC.95.044602
35. Franzini G. Final Design and Features of the B-Train System of CNAO. *Proc IPAC* (2010) 9:1–3. doi: 10.18429/JACoW-IPAC2018-TUPAF011
36. Chadwick MB, Herman M, Obložinský P. Nuclear Data for Science and Technology: Cross Sections, Covariances, Fission Product Yields and Decay Data. *ENDF/B-VII.1 Nucl Data Sheets* (2011) 112:2887–996. doi: 10.1016/j.nds.2011.11.002. Special Issue on ENDF/B-VII.1 Library.
37. Chadwick MB, Young PG. Proton Nuclear Interactions Up to 250 MeV for Radiation Transport Simulations of Particle Therapy. *Proc Int Particle Ther Meeting PTCOG XXIV* (1996) 13:89–93.
38. Chadwick MB, Herman M, Obložinský P. High-Energy Nuclear Data Libraries for Accelerator-Driven Technologies: Calculational Method for Heavy Recoils. *Proc. of 2nd Int. Conf on Accelerator Driven Transmutation Technology and Applications*, Kalmar, Sweden (1996). pp. 483–9.
39. Bernard JA. Kinematics of Elastic Neutron Scattering. *Neutron Sci Reactor Phys* (2006) 14:22.05. (MIT Course).
40. Henry AF. *Nuclear-Reactor Analysis*. Cambridge, MA: MIT Press (1975).
41. Malmer C. Nuclear Data for Neutron and Proton Radiotherapy and For Radiation Protection. *ICRU Rep 63 Med Phys* (2001) 28:861–861. doi: 10.1118/1.1369116

42. Kox S, Gamp A, Perrin C, Arvieux J, Bertholet R, Bruandet JF, et al. Trends of Total Reaction Cross Sections for Heavy Ion Collisions in the Intermediate Energy Range. *Phys Rev C* (1987) 33:1678–91. doi: 10.1103/PhysRevC.35.1678
43. Ivanchenko V, Bagulya A, Bakr S, Bandieramonte M, Bernard D, Bordage M-C, et al. Progress of Geant4 Electromagnetic Physics Developments and Applications. *EPJ Web Conf* (2019) 214:2046. doi: 10.1051/epjconf/201921402046
44. Allison J, Amako K, Apostolakis J, Arce P, Asai M, Aso T, et al. Recent Developments in Geant4. *Nucl Instruments Methods Phys Res Section A: Accelerators Spectrometers Detectors Associated Equip* (2016) 835:186–225. doi: 10.1016/j.nima.2016.06.125
45. Griva I, Nash S, Sofer A. *Linear and Non Linear Optimization*. Cambridge Press (2009).
46. Golovkov M, Aleksandrov D, Chulkov l, Kraus G, Schardt D. Fragmentation of 270 A MeV Carbon Ions in Water. st International Week on Hadrontherapy: Advances in Hadrontherapy GSI-97-08.U Amaldi, B Larsson and Y Lemoigne. ed. *Excerpta Medica, Int. Congr. Series* Elsevier Science (1997) 1144:316–24.
47. Matsufuji N, Komori M, Sasaki H, Akiu K, Ogawa M, Fukumura A, et al. Spatial Fragment Distribution from a Therapeutic Pencil-Like Carbon Beam in Water. *Phys Med Biol* (2004) 50:3393–403. doi: 10.1088/0031-9155/50/14/014
48. Kraan AC, Zarrella R, Alexandrov A, Alpat B, Ambrosi G, Argirò S, et al. Charge Identification of Nuclear Fragments With the FOOT Time-Of-Flight System. *Nucl Instruments Methods Phys Research Section A: Accelerators Spectrometers Detectors Associated Equip* (2021) 1001:165206. doi: 10.1016/j.nima.2021.16520
49. Battistoni G, Toppi M, Patera V, Collaboration TF. Measuring the Impact of Nuclear Interaction in Particle Therapy and in Radio Protection in Space: the FOOT Experiment. *Front Phys* (2021) 8:1–20. doi: 10.3389/fphy.2020.568242

Conflict of Interest: The authors declare that the research was conducted in the absence of any commercial or financial relationships that could be construed as a potential conflict of interest.

Publisher's Note: All claims expressed in this article are solely those of the authors and do not necessarily represent those of their affiliated organizations, or those of the publisher, the editors and the reviewers. Any product that may be evaluated in this article, or claim that may be made by its manufacturer, is not guaranteed or endorsed by the publisher.

frontiers | Frontiers in Oncology

ORIGINAL RESEARCH
published: 19 May 2022
doi: 10.3389/fonc.2022.804036

Redefine the Role of Spot-Scanning Proton Beam Therapy for the Single Brain Metastasis Stereotactic Radiosurgery

Sheng Chang[1,2†], Gang Liu[2,3†], Lewei Zhao[2], Weili Zheng[2], Di Yan[2], Peter Chen[2], Xiangpan Li[1], Kunyu Yang[3], Rohan Deraniyagala[2], Craig Stevens[2], Inga Grills[2], Prakash Chinnaiyan[2], Xiaoqiang Li[2] and Xuanfeng Ding[2]*

[1] Department of Radiation Oncology, Renmin Hospital, Wuhan University, Wuhan, China, [2] Department of Radiation Oncology, Beaumont Health System, Royal Oak, MI, United States, [3] Cancer Center, Union Hospital, Tongji Medical College, Huazhong University of Science and Technology, Wuhan, China

OPEN ACCESS

Edited by:
Stewart Mac Mein,
German Cancer Research Center (DKFZ), Germany

Reviewed by:
Laura Toussaint,
Aarhus University Hospital, Denmark
Xiaorong Ronald Zhu,
University of Texas MD Anderson Cancer Center, United States
Dante Amelio,
The Trento Proton Therapy Centre, Italy
Marco Cianchetti,
Azienda Provinciale per i Servizi Sanitari (APSS), Italy

***Correspondence:**
Xuanfeng Ding
xuanfeng.ding@beaumont.edu

[†]These authors have contributed equally to this work

Specialty section:
This article was submitted to Radiation Oncology, a section of the journal Frontiers in Oncology

Received: 28 October 2021
Accepted: 14 April 2022
Published: 19 May 2022

Citation:
Chang S, Liu G, Zhao L, Zheng W, Yan D, Chen P, Li X, Yang K, Deraniyagala R, Stevens C, Grills I, Chinnaiyan P, Li X and Ding X (2022) Redefine the Role of Spot-Scanning Proton Beam Therapy for the Single Brain Metastasis Stereotactic Radiosurgery. Front. Oncol. 12:804036. doi: 10.3389/fonc.2022.804036

Purpose: To explore the role of using Pencil Beam Scanning (PBS) proton beam therapy in single lesion brain stereotactic radiosurgery (SRS), we developed and validated a dosimetric in silico model to assist in the selection of an optimal treatment approach among the conventional Volumetric Modulated Arc Therapy (VMAT), Intensity Modulated Proton Therapy (IMPT) and Spot-scanning Proton Arc (SPArc).

Material and Methods: A patient's head CT data set was used as an in *silico* model. A series of targets (volume range from 0.3 cc to 33.03 cc) were inserted in the deep central and peripheral region, simulating targets with different sizes and locations. Three planning groups: IMPT, VMAT, and SPArc were created for dosimetric comparison purposes and a decision tree was built based on this in *silico* model. Nine patients with single brain metastases were retrospectively selected for validation. Multiple dosimetric metrics were analyzed to assess the plan quality, such as dose Conformity Index (CI) (ratio of the target volume to 100% prescription isodose volume); R50 (ratio of 50% prescription isodose volume to the target volume); V_{12Gy} (volume of brain tissue minus GTV receiving 12 Gy), and mean dose of the normal brain. Normal tissue complication probability (NTCP) of brain radionecrosis (RN) was calculated using the Lyman-Kutcher-Burman (LKB) model and total treatment delivery time was calculated. Six physicians from different institutions participated in the blind survey to evaluate the plan quality and rank their choices.

Results: The study showed that SPArc has a dosimetric advantage in the V_{12Gy} and R50 with target volumes > 9.00 cc compared to VMAT and IMPT. A significant clinical benefit can be found in deep centrally located lesions larger than 20.00 cc using SPArc because of the superior dose conformity and mean dose reduction in healthy brain tissue. Nine retrospective clinical cases and the blind survey showed good agreement with the in *silico* dosimetric model and decision tree. Additionally, SPArc significantly reduced the treatment delivery time compared to VMAT (SPArc 184.46 ± 59.51s vs. VMAT: 1574.78 ± 213.65s).

Conclusion: The study demonstrated the feasibility of using Proton beam therapy for single brain metastasis patients utilizing the SPArc technique. At the current stage of technological development, VMAT remains the current standard modality of choice for single lesion brain SRS. The *in silico* dosimetric model and decision tree presented here could be used as a practical clinical decision tool to assist the selection of the optimal treatment modality among VMAT, IMPT, and SPArc in centers that have both photon and proton capabilities.

Keywords: single brain metastasis, stereotactic radiosurgery, spot-scanning, proton arc therapy, intensity modulated proton therapy, volumetric modulated arc therapy, brain radionecrosis

INTRODUCTION

Stereotactic Radiosurgery (SRS) is a non-invasive alternative treatment method for brain metastases (BM) (1, 2). It can be delivered through several modalities, such as Gamma Knife, Cyberknife, conventional radiotherapy linear accelerators (linac-based SRS), or passive-scattering proton beam therapy (3–5). Brain radionecrosis (RN) is one of the major side effects. It was reported that this long-term complication had been linked to V_{12Gy} (the volume of healthy brain tissue irradiated with 12 Gy) of the brain tissue (6–8). Some studies suggested that keeping V_{12Gy} below 8.5 cc could reduce the risk of brain RN (5, 7, 9). Current practice in many centers is to follow stepwise prescription schemes according to the size of the lesion, with generally lower doses for larger lesions (10–14). Importantly, local control is highly dependent on the prescribed dose and negatively associated with target volume in photon therapy due to the significant exit dose (5, 11–13). The ability to deliver ablative doses of radiation, particularly to patients with large brain tumors, is often limited by this constraint to spare an adequate volume of normal brain. For a target diameter of more than 3 cm, it has been recommended to use fractionated treatment other than single-fraction SRS to mitigate the radiation-induced toxicity (15, 16).

Proton beam therapy offers the potential clinical benefit to further spare healthy brain tissue by taking advantage of its unique physical characteristic, "Bragg Peak," in which the rapid dose fall-off offers zero dose beyond the target's distal edge. The pencil beam scanning (PBS) technique, which delivers the proton treatment *via* spot by spot and energy layer by layer, significantly improves the dose conformity at the proximal region compared to the passive-scattering technique (17, 18). Recently, such treatment methodology has been adopted by most of the new proton therapy centers (19). However, due to the large in-air spot size, the PBS technique has a much larger lateral penumbra than the passive-scattering technique or photon radiotherapy techniques such as IMRT or VMAT (20, 21). This critical physics parameter limits its clinical implementation in the single fractionation brain SRS where a sharp gradient dose fall-off is desired to protect adjacent healthy tissue or organs (22–24). To our best of knowledge, there is no report of using PBS for brain SRS to date. Thus, there is an immediate need to address this challenge and continue to develop the PBS technique to meet such clinical needs.

In 2016, Spot-scanning proton arc (SPArc) therapy was proposed by Ding et al. to improve the dosimetric plan quality of PBS while making the arc therapy efficient, robust, and compatible with the current PBS technique without major hardware modifications (25). This new concept has recently been integrated into an existing clinical system as the prototype proton arc machine (26). Previous studies have demonstrated its potential clinical benefits in the conventional treatment fraction for head and neck, brain, prostate, lung, spine, and breast cancer patients, compared to the IMPT (27–33). However, no studies have been conducted to exploit the potential dosimetric benefits and feasibility in brain SRS. We hypothesized that by taking advantage of the degree of freedom through arc(s) trajectory, SPArc might have the flexibility and the optimization freedom to balance the sharp distal fall-off and larger lateral penumbra to provide an optimal dosimetric plan quality and treatment solution for a single target brain SRS compared to the conventional VMAT and IMPT. We aimed to build a dosimetric prediction model through an *in silico* planning study with a variety of tumor sizes and locations compared among the SPArc, IMPT, and VMAT plans. The validation tests were then performed through clinical patient datasets previously treated by single-fraction (SSRT) and fractionated stereotactic radiotherapy (FSRT) and then followed by a blind survey of clinicians worldwide. To our best knowledge, this is the first comprehensive study to build an *in silico* dosimetric model to assist the clinical decision-making among three treatment modalities, including IMPT, VMAT, and SPArc for single BM SRS.

METHODS AND MATERIALS

In Silico Brain SRS Dosimetric Model

A patient's CT image and structure set were used as an *in silico* head phantom to develop a brain SRS dosimetric model to assist the optimal treatment modality selection. A spherical-shaped target, Gross Tumor Volume (GTV) (0.3 cc), was inserted in the deep central and peripheral region of the CT. The deep central targets are located at a depth of 5.65 cm from the brain surface

and the peripheral region targets are located at a depth of 1.06 cm from the brain surface. The GTV was then expanded with a uniform margin every 2mm increments, corresponding to a different target volume (from 0.3 cc to 33.03 cc) (**Figure 1**). The target volume extending outside of the brain structure was excluded. Three treatment modalities IMPT, VMAT, and SPArc were generated in Raystation ver. 9A using the same planning robust optimization parameters (2mm setup and 3.5% range uncertainty for proton planning and 2mm setup uncertainty for VMAT planning). Each VMAT plan consisted of two coplanar and two non-coplanar arcs with 6MV photon. The coplanar arcs were rotated clockwise from 181°–179° and rotated counterclockwise from 179°–181°, two non-coplanar arcs were placed at couch angles of 45° and 315°. The SPArc plan consisted of one coplanar and two non-coplanar arcs. The couch positions and arc rotations of the two non-coplanar arcs were the same as those of VMAT, while the 3-field IMPT was delivered with two posterior oblique fields along with a vertex field (Gantry angle of 90 and couch angle of 270) (**Table S1**). Range shifter was used in the IMPT plan but not in the SPArc plan due to the sufficient degree of freedom. For SPArc, three arcs were used with a sampling frequency of 2.5° per control point. In other words, the SPArc plan consists of a total of 288 beam angles. Both SPArc and IMPT used the same physics beam model based on IBA ProteusONE® with an energy range from 70MeV to 227.7MeV. For more beam specific parameters, the study used RayStation's default setting such as the automatic energy layer spacing and spot spacing for optimization in both the IMPT and SPArc planning groups (**Figure S1**). The prescription was 18 Gy (RBE) in 1 fx, with at least 96% of GTV receiving a full prescription dose in the worst-case scenario robustness evaluation. Multiple dosimetric metrics were analyzed to assess the plan quality, such as dose Conformity Index (CI) (ratio of the target volume to 100% prescription isodose volume); R50 (atio of 50% prescription isodose volume to the target volume); V_{12Gy} (Volume of normal brain tissue irradiated with at least 12 Gy); and mean dose of the normal brain. The normal brain tissue was defined as brain tissue minus GTV.

Clinical Validation Tests

To validate the *in silico* brain SRS model, nine patients with single brain metastasis previously treated by single or multi-fraction SRS at our institution were retrospectively included in the study. The target volumes and previous clinical prescribed doses (Gy) and fraction are detailed in **Table 1** for each of the nine patients, in which two patients received fractionated brain SRS (FSRT) due to the size and location of the lesion. All CT-data sets with corresponding structure contours were transferred from gamma plan™ to Raystation 9A and replanned with IMPT, VMAT, and SPArc with prescription 18 Gy in one fraction. These nine cases were separated into two groups based on the location: four deep central and five peripheral located targets. The GTVs volume ranges from 1.66 cc–28.65 cc. The target CI, R50, mean dose of the brain, and V_{12Gy} of the cases were analyzed and compared to the brain SRS dosimetric model (**Table 2**). We generated a brain SRS decision tree based on tumor size and location using the *in silico* model.

Normal Tissue Complication Probability of Brain Necrosis

In this study, the normal brain was defined as the whole brain minus the GTV, and we evaluated the normal tissue complication probability (NTCP) of brain necrosis by using the Lyman-Kutcher-Burman (LKB) model (34) The single-fraction doses were converted to equivalent 2 Gy per fraction total doses using the linear-quadratic model assuming an α/β ratio of 2 Gy for normal tissue (35).

$$\mathrm{NTCP} = \frac{1}{\sqrt{2\pi}} \int_{-\infty}^{t} e^{-\frac{x^2}{2}} dx \tag{1}$$

$$t = \frac{D - TD_{50}}{m \times TD_{50}} \tag{2}$$

where TD_{50} is the tolerance dose for a 50% complication probability for uniform doses to the organ and m is a dimensionless parameter for determining the slope of the

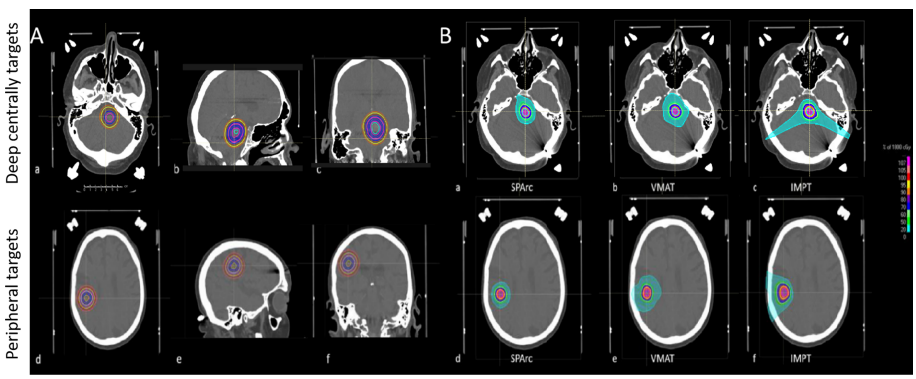

FIGURE 1 | **(A)** Target's locations and sizes (from 0.3cc to 33.03cc) in the brain SRS dosimetric model. Deep centrally located targets (a, b, c); Peripheral targets (d, e, f). **(B)** A representative transverse view of dose distributions among SPArc, IMPT, and VMAT on the 0.3cc target. Deep centrally located 0.3cc target (a) SPArc, (b) VMAT, (c) IMPT; Peripheral 0.3cc target (d) SPArc, (e) VMAT, (f) IMPT.

TABLE 1 | Target size and previous clinical prescription for the 9 patients included in this SRS study comparison.

Patient	Tumor location	Tumor volume (cc)	Previous Clinical prescription dose and fraction
#1	deep central region	1.66	21Gy/1f
#2	peripheral region	3.53	21Gy/1f
#3	peripheral region	14.65	15Gy/1f
#4	peripheral region	4.13	18Gy/1f
#5	peripheral region	8.34	18Gy/1f
#6	deep central region	11.04	15Gy/1f
#7	deep central region	20.76	24Gy/3f
#8	peripheral region	24.70	15Gy/1f
#9	deep central	28.65	21Gy/3f

complication probability according to the dose curve. For the uniform dose D, we used the generalized equivalent uniform dose (gEUD), as shown in:

$$\text{gEUD} = \left(\sum_{i=1}^{N} V_i D_i^a\right)^{\frac{1}{a}} \quad (3)$$

where Di is the dose for each bin in a differential dose–volume histogram (DVH), vi is the volume in a specific dose bin i, and N is the unequal fractional sub-volume. The 'a' value is a parameter equal to 1/n, in which n represents the volume dependence of the complication probability. We adopted the following parameters to evaluate the radiation-induced brain necrosis as an endpoint: TD50 = 60, m = 0.15, a = 4. In radiosurgery, the dose is delivered in a single fraction. The single-fraction doses were converted to equivalent 2 Gy per fraction total doses using the biologically effective dose (BED) formalism of the linear-quadratic model assuming an α/β ratio of 2 Gy for normal tissue and 10 Gy for tumor tissue [36]. The formula used to calculate EQD2 was:

$$\text{EQD2} = N \times d \times \frac{\text{d} + \alpha/\beta}{2 + \alpha/\beta} \quad (4)$$

with N = number of fractions, d = dose, α = linear coefficient reflecting cellular radiosensitivity, and β = quadratic coefficient reflecting cell repair mechanisms.

Tumor Control Probability and Dose De-Escalation Study

To explore the TCP and NTCP relationship in the challenge case (patient #7 and #9) in which single fraction might not be safe due to the risk of RN, a series of dose de-escalation plans were performed using VMAT and IMPT. The corresponding TCP was accessed based on the logistic model as following:

$$TCP(\{D_i\}) = \prod_{i=1}^{N}\left[\frac{1}{1+\left(\frac{D50}{D_i}\right)^{4*\gamma 50}}\right]^{\frac{1}{N}} \quad (5)$$

N is the total number of voxel in tumor, each voxel receiving a uniform dose. D50 denotes the dose to control 50% of tumors, and γ_{50} is the relative slope of the TCP curve at D50, which are 27.04 Gy and 0.75, respectively (36, 37).

Treatment Beam Delivery Time Calculation

The treatment delivery efficiency of the IMPT and SPArc plans was evaluated based on a proton system with gantry rotation max speed 6 deg/s, 2 ms spot switching time and ELST 0.7s (25). The VMAT plans times were simulated based on the Elekta Versa HD with a dose rate of 600 MU/min and 1,400 MU/min with flattening-filter-free (FFF) beams with 6X photon beams energy and gantry rotation max speed 6 deg/s.

Data and Statistical Analysis

Treatment plan metrics, NTCP, and treatment delivery time among IMPT, VMAT, and SPArc were compared with a paired, two-tailed nonparametric Wilcoxon signed-rank test using SPSS 21.0 software (International Business Machines, Armonk, New York). P values of less than 0.05 were considered statistically significant. All the tests were performed with VMAT as a reference.

Plan Evaluation and Survey Among the Physician Group

To test if the *in silico* model is able to provide useful clinical guidance in the selection of optimal treatment modality, the nine clinical cases from the retrospective study (described in the previous section) were sent to six physicians from different institutions worldwide. To avoid any preference or bias during the plan dosimetric evaluation, the name of each plan was masked as #a, #b, and #c as a blind survey. Only target coverage, CI & R50, mean dose of the brain, and V_{12Gy} along with the 3D dose distribution were presented. Each physician ranked each plan from 1–3 (1: the most preferred choice; 2: the intermediate choice; 3: the least preferred choice) based on their clinical experience. To mitigate other factors that may impact the clinical decision other than dosimetric plan quality, all the physicians were informed that the patients' diagnosis is single brain metastasis from an unknown primary tumor. The patients were in the mid 50s age range and expected to live five years after the treatment. A sample of the survey was included in the supplemental document. Then, the result of the blind plan evaluation survey was unmasked and analyzed.

RESULTS

Brain SRS Dosimetric Comparison and Decision Tree

Figure 2 shows an example of SPArc, VMAT, and IMPT dose distributions for patients with deep central (A) and peripheral

TABLE 2 | Validation of optimal brain sparing modality based on tumor size and location for 9 patients.

Patient	Tumor location	Tumor volume (cc)	CI			R50					V_{12Gy}(brain) (cc)					Mean dose(brain) (cGy)				
			VMAT	IMPT	SPArc	VMAT	Relative to SPArc (model)	IMPT	Relative to SPArc (model)	SPArc	VMAT	Relative to SPArc (model)	IMPT	Relative to SPArc (model)	SPArc	VMAT	Relative to SPArc (model)	IMPT	Relative to SPArc (model)	SPArc
1	deep central	1.66	1.00	0.99	1.00	5.09	8.97	9.15	16.12	5.34	3.55	7.10	7.43	14.87	4.06	77.00	122.97	50.00	79.85	37.00
2	peripheral region	3.53	1.00	0.93	1.00	4.75	5.21	9.07	9.94	5.11	6.21	8.63	13.23	18.38	6.81	81.00	87.62	41.00	44.35	53.00
3	peripheral region	14.65	0.98	0.93	1.00	3.20	3.81	4.05	4.82	2.62	12.62	22.71	16.61	29.89	10.38	148.00	199.87	68.00	91.83	81.00
4	peripheral region	4.13	0.96	0.94	1.00	4.07	4.77	7.17	8.40	4.31	6.57	9.46	12.20	17.57	7.07	79.00	100.58	44.00	56.02	48.00
5	peripheral region	8.34	1.00	1.00	1.00	4.63	4.12	6.84	6.09	4.29	17.42	13.56	32.77	25.51	18.37	161.00	172.33	104.00	111.32	79.00
6	deep central	11.04	0.99	0.98	1.00	3.60	4.00	4.84	5.37	3.17	13.11	14.46	21.17	23.34	12.56	167.00	208.53	102.00	127.37	93.00
7	deep central	20.76	0.97	0.94	1.00	2.93	3.29	3.53	3.96	2.44	21.00	19.75	31.04	29.19	18.60	226.00	289.62	127.00	162.75	120.00
8	peripheral region	24.7	0.99	0.99	1.00	2.71	2.85	3.48	3.66	2.48	15.78	23.96	23.28	35.35	15.05	180.00	227.05	101.00	127.40	110.00
9	deep central	28.65	1.00	0.93	1.00	2.90	3.08	3.03	3.22	2.39	27.99	25.25	37.02	33.40	24.76	343.00	339.78	229.00	226.85	194.00

CI, Conformity Index; (Ratio of the target volume to 100% Prescription isodose volume).

R50, (Ratio of 50% Prescription isodose volume to the target volume).

V_{12}Gy, (Volume of brain tissue minus GTV receiving12 Gy).

Relative to SPArc (model), (Ratio of SPArc plan between the model and case) × (absolute dosimetric metrics).

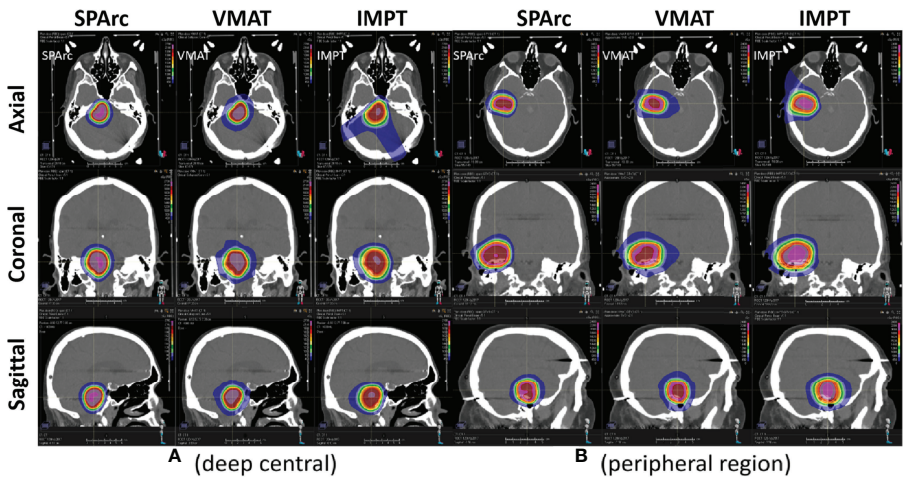

FIGURE 2 | Representative SPArc, VMAT, and IMPT dose distributions for patients with deep central **(A)** and peripheral region **(B)** tumors in transversal, coronal, and sagittal planes. The threshold of 18 Gy was used to display dose distributions (color wash overlay).

region (B). Each dosimetric metric, such as CI, R50, mean dose of the brain, and V_{12Gy} was plotted as a function of the target size in the deep central (**Figure 3**) and peripheral regions (**Figure 4**). Compared to IMPT, VMAT showed its significant advantage in the CI and R50 in any target size less than 30cc in peripheral and deep central locations and V_{12Gy} to the brain. Conversely, SPArc has an equivalent or better CI in any size of peripheral targets and the deep centrally located targets bigger than 9cc compared to VMAT. For the deep centrally located tumor smaller than 9cc, the VMAT plan still offered better dose CI and V_{12Gy}. With the advantage of proton beam characteristics, both SPArc and IMPT significantly reduced brain mean dose by nearly 2-fold compared with VMAT. The SPArc plan would be favored in most cases except deep central located target (< 9 cc) where VMAT shows a slight improvement over SPArc in CI, R50, and V_{12Gy} of the brain (**Figure 5**).

Clinical Validation Tests

The results showed good agreement between the *in silico* model and the clinical cases (GTV range: 1.66 - 28.65 cc). The SPArc

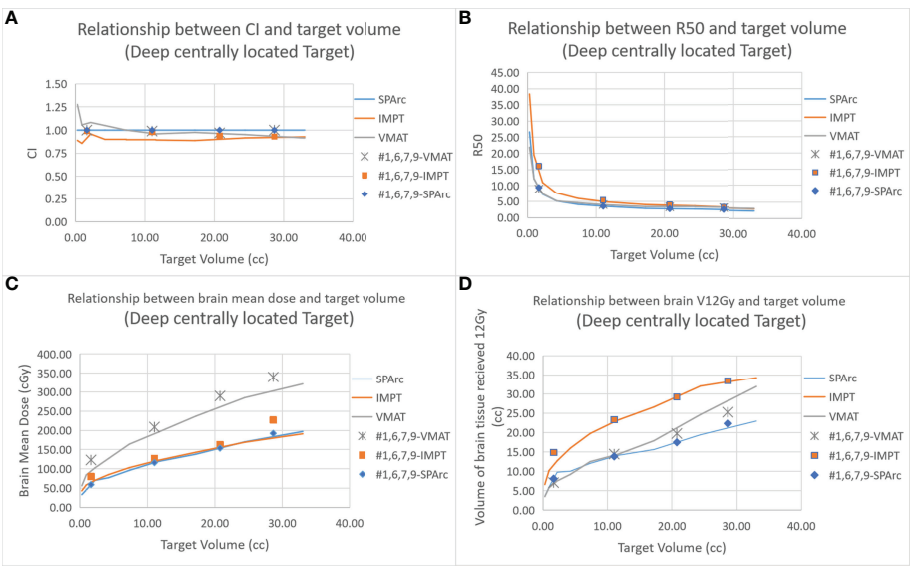

FIGURE 3 | Dosimetric metrics among three planning groups: SPArc, VMAT, and IMPT at deep central **(A–D)** of different target sizes. Dots, squares, and stars are the dosimetric metrics extracted from four clinical validation cases normalized to SPArc plan (**Table 2**).

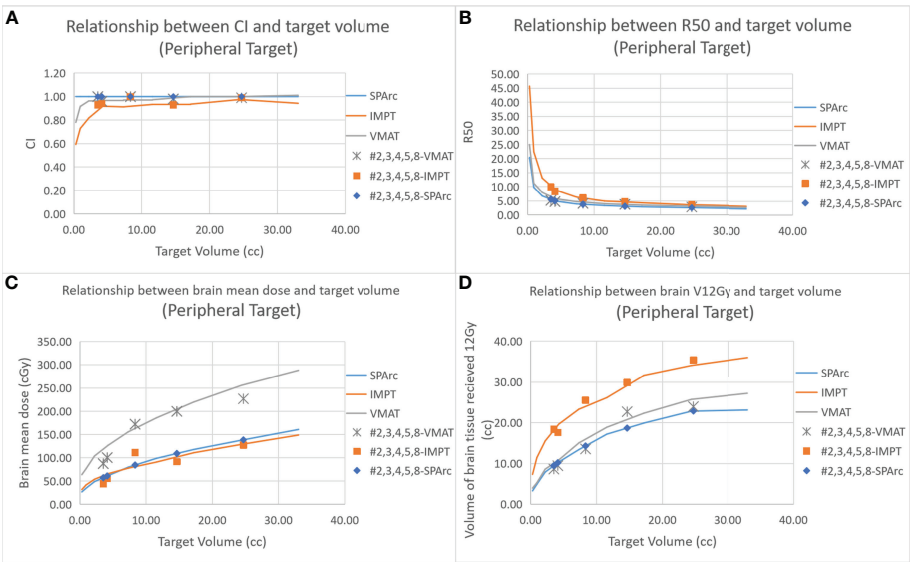

FIGURE 4 | Dosimetric metrics among three planning groups: SPArc, VMAT, and IMPT at peripheral region **(A–D)** of different target sizes. Dots, squares, and stars are the dosimetric metrics extracted from five clinical validation cases normalized to SPArc plan (**Table 2**).

plans spared a significant volume of the normal brain compared to VMAT plans in all five patients with tumors > 9cc at any location (1.83 ± 1.15 cc) (**Figures 3**, **4**, and **Table 2**). Both the SPArc and IMPT planning groups reduced the mean brain dose delivered to all patients by 44.25% ± 5.70% ($p < 0.01$) and 38.44% ± 6.34% ($p < 0.01$) compared to the VMAT planning group. As predicted from the model, the VMAT plan offered slightly better V_{12Gy} (3.55 cc) compared to SPArc (4.06 cc) for patient # 1 with tumor < 9cc at the deep central location. For the three patients with tumor < 9 cc in the peripheral region, the VMAT plan provided a comparable V_{12Gy} compared to SPArc and IMPT. In terms of the delivery time (including irradiation time, gantry rotation, and couch rotation), the VMAT and VMAT (FFF) plans took much longer to deliver than any proton-based radiosurgery plan (**Table 3**). The mean treatment delivery time in the VMAT/VMAT(FFF) plans was 1574.78 ± 213.65 s and 940.89 ± 102.56 s compared with SPArc (260.29 ± 41.74 s) ($p < 0.01$) and IMPT (184.46 ± 59.51 s, $p < 0.01$).

NTCP of brain RN for each patient is listed in **Table 4**. All the NTCP of brain RN is clinically acceptable with 18Gy single fraction prescription doses (< 1%) except patients #7 and #9. More importantly, this study also found that the target location

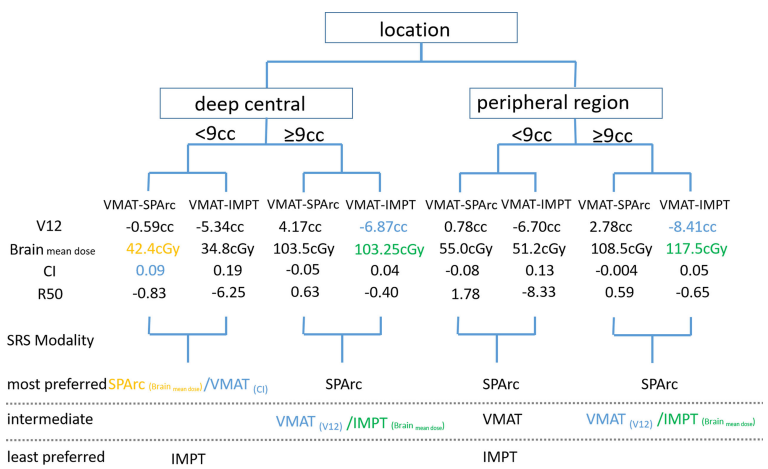

FIGURE 5 | Treatment decision tree and model to predict the optimal treatment modality based on tumor size and location. SPArc would be the optimal choice in most of the target size or location except deep centrally located target. This would be the physician's clinical decision to favor the CI or brain mean dose sparing.

TABLE 3 | Comparison of total delivery time per patient's SRS plan.

Delivery time (Patient#)	VMAT (600 MU/min, s)	VMAT [1-5] (FFF, 1400 MU/min, s)	IMPT (s)	SPArc (s)
1	1635	808	85	207
2	1340	851	128	240
3	1516	972	206	288
4	1369	807	141	217
5	1946	1012	193	251
6	1809	1034	172	238
7	1631	1034	214	259
8	1605	1061	275	313
9	1322	889	244	328
Average	1574.78 ± 213.65	940.89 ± 102.56	184.46 ± 59.51	260.29 ± 41.74
P	–	<0.01*	<0.01*	<0.01*

$P < 0.05$ while comparing the VMAT plan with other two plans.

plays a critical part in the probability of brain RN as the peripheral target has much less EUD than the deep central located target in VMAT planning group. As a result, based on the VMAT technique, the NTCP of brain RN in patient #3 (peripheral target, volume 14.65 cc) and patient #8 (peripheral target, volume 24.70 cc) is 0.03% and 0.13%, respectively in comparison with patient #7 (deep central located target, volume 20.76 cc) 15.62% and patient #9 (deep central located target, volume 28.65 cc) 99.95%, respectively. In contrast, the probability of brain RN of patients #7 and #9 is 0.00% and 0.65% using the SPArc technique, indicating a superior dosimetric plan quality compared to the VMAT. Dose de-escalation for patients #7 and #9 was investigated from 1800cGy to 1000cGy (**Table 5**). The single fraction dose in VMAT had to be reduced to 1500cGy (#7) and 1000cGy (#9), respectively, in order to achieve an probability of RN (<1%).

Lastly, to test if the decision tree would help select the optimal plan from a clinician's point of view, six physicians from different institutions worldwide voluntarily participated in this blind study to evaluate the dosimetric plan quality and preference. The result showed good agreement compared to the decision tree, along with some interesting findings. All the physicians selected the SPArc plan (#c) as the optimal solution for the single lesion brain SRS, even though the VMAT plan of patients #1 and #2 offered a slightly better CI and R50 than SPArc due to the target location and sizes (**Figure S2**). The physicians preferred a better mean dose sparing to the healthy brain tissue when the plans' CI and R50 are comparable but not significantly inferior (**Figure S3**).

DISCUSSION

This study explored the dosimetric features of using the state-of-the-art proton beam therapy technique - IMPT and a new treatment modality - SPArc compared with the reference planning group, VMAT, in single lesion brain SRS. Since the clinical scenarios are very complicated because of the various size of targets and locations, additional time and resources are often needed to generate comparison plans for each patient to justify the benefit of using proton beam therapy. The brain SRS dosimetric model built in this study could assist the clinical decision among IMPT, VMAT, and SPArc techniques. It is also one major step forward since the publication of VMAT for brain SRS model reported by Atkins et al. in 2018 as proton beam therapy becomes more accessible (5). More interestingly, six out of six physicians from different institutions worldwide selected the SPArc plan over the VMAT plan in case #1, where small size targets (1.66 cc) were located in the deep central location, although the VMAT plan offered slightly better V_{12Gy} (3.55 cc) compared SPArc (4.06 cc). In this situation, when the dose conformity is comparable and not significantly different, the physicians considered the mean dose sparing for normal brain as a factor in the selection of the treatment modality, even though the relationship of cognitive function impairment with low radiation dose to the normal brain tissue is still under investigation (38). In the supplemental document, eleven additional patients with single brain metastasis were retrospectively included in the study. The target volumes,

TABLE 4 | Normal tissue complication probabilities (%) calculated using a LKB model based on the Burman et al. Tolerance data.

Patient	Tumor location	Tumor volume (cc)	Normal tissue complication probabilities (%)		
			VMAT	IMPT	SPArc
1	deep central region	1.66	0.00	0.00	0.00
2	peripheral region	3.53	0.00	0.00	0.00
3	peripheral region	14.65	0.03	0.00	0.00
4	peripheral region	4.13	0.00	0.00	0.00
5	peripheral region	8.34	0.26	0.04	0.00
6	deep central region	11.04	0.23	0.01	0.00
7	deep central region	20.76	15.26	0.11	0.00
8	peripheral region	24.70	0.13	0.00	0.00
9	deep central region	28.65	99.95	39.61	0.63
	Average		12.87 ± 33.04	4.42 ± 13.20	0.07 ± 0.21

TABLE 5 | The TCP and NTCP for dose de-escalation in patient #7, and #9.

Patient	Probability	1800cGy/1F			1500cGy/1F		1400cGy/1F		1000cGy/1F	
		VMAT	IMPT	SPArc	VMAT	IMPT	VMAT	IMPT	VMAT	IMPT
#7	TCP(%)	97.45	96.00	97.29	93.96	90.72	91.77	87.50	69.95	59.30
	NTCP(%)	15.26	0.11	0.00	0.85	0.00	0.25	0.00	0.00	0.00
#9	TCP(%)	96.20	96.18	97.08	91.17	91.09	88.09	87.97	60.58	60.20
	NTCP(%)	99.95	39.61	0.63	80.33	2.82	54.42	0.81	0.60	0.00

previous clinical prescribed doses (Gy), dosimetric metrics, and delivery time were summarized in **Tables S2**, **S3**, **S4**, and **Figures S4**, **S5**. The results also showed good agreement between the in silico brain SRS model and clinical cases.

Our study shows that the dosimetric metrics are critical when using the SPArc technique because a sharp dose fall-off and high dose sparing of the healthy brain tissue are clinically desired in brain SRS. In addition to the dosimetric metrics index comparison, the probability of brain RN was estimated based on the NTCP model. The radiation-induced brain necrosis was less than 1% in the majority of patients except patient #7 (15.26% with target volume 20.76 cc (D = 3.4cm)) and #9 (99.95% with target volume 28.65 cc (D =3.8 cm)) in VMAT planning group. The finding was consistent with the inverse relationship between the SRS dose and treatment volume and location with regard to the incidence of brain RN (35, 39, 40). It is worth noting that SPArc could reduce the risk of brain necrosis to less than 1% for all the patients with prescription dose 18 Gy in 1 fraction in these challenging situations, which indicated its potential clinical role in the management of a single brain lesion with large volume.

There are few reports on the brain SRS using the IMPT technique due to the large lateral penumbra. In 2014 and 2015, Hyer at al. and Wang et al. (41–43) discussed the limitation of using IMPT for peripheral single-target brain SRS compared to the VMAT. Thus, they introduced the aperture concept in PBS to sharpen the lateral penumbra. Our findings agreed with theirs, motivating us to investigate SPArc as the new treatment modality for this disease site. The results also indicated that a lower prescription is needed to mitigate such risk using IMPT or VMAT technique for single fractionated brain SRS (40). However, dose de-escalation will compromise the target local control, accessed based on the logistic tumor control probability (TCP) model and the Poission TCP model (36, 44, 45). The results suggest that TCP would have been significantly compromised in order to achieve a similar risk of brain RN as a SPArc plan (**Table 5**). More specifically, for patient #9, the single fraction dose in VMAT and IMPT had to be reduced to 10 Gy and 14 Gy, respectively, in order to achieve less than 1% of brain RN. This prescription dose level represents 60.58% and 87.97% TCP via VMAT and IMPT plan, respectively.

The use of range shifters (RS) in treating superficial targets sometimes complicates the clinical workflow e.g., clearance check with patient body and move in/out the range shifter. Additionally, it also introduces secondary proton scattering from the RS itself, which increases spot size when entering the patient's body resulting in an inferior treatment plan quality due to the larger lateral penumbra. This study demonstrated that SPArc does not need to use RS even for the peripheral target while providing a superior dosimetric plan quality, simplifying the clinical workflow with a practically achievable treatment delivery time compared to the current standard-of-care IMPT.

The results from this study showed that the VMAT/VMAT (FFF) has, in general, the longer treatment delivery time compared to the SPArc treatment technique. Three-field IMPT shows its efficiency in the treatment delivery for single lesion brain SRS at the cost of treatment plan quality compared to SPArc. However, it is important to mention that the estimated treatment delivery time listed in **Table 2** only includes beam-on and gantry rotational times. The beam request time and treatment field loading time from Oncology Information System (OIS), e.g., ARIA or MOSIAQ to the proton delivery system, were not taken into account. In other words, additional time might be needed in the multi-field clinical IMPT workflow. This is one of the motivations why the proton treatment technique is moving towards the arc approach which not only has the potential to improve the plan quality but also simplify the clinical treatment workflow. Furthermore, it has been reported that the ELST could achieve 0.2 s in a cyclotron accelerator energy selection system (46). Such ELST technique and engineering advancements would result in a more efficient SPArc treatment in future clinical implementation.

This study explored the feasibility of utilizing SPArc for single brain metastases treatment. However, please note that such a novel technique is currently in the research and development stage, requiring the upgrades of the existing proton therapy systems, introducing new hardware and software, and incorporating the concept into the commercial treatment planning system. As a result, it may take years of technical and engineering development in order to implement it into routine clinical practice. Besides the SPArc technique, other existing technologies could be an option in brain radiosurgery, such as dynamic collimator system (41) and passive scattering with a unique patient immobilization system (47). Many of these technological limitations are advancing and the manufacturing time for patient devices (apertures and compensators) can be minimized to generate a plan efficiently. Boczkowskiet et al. determined the optimal plan parameters (define the aperture with a tight margin of 0.5mm and use of compensators to better shape distally) on a single metastatic lesion by comparing the proton SRS and photon VMAT SRS treatment plans (48, 49). Righetto et al. investigated the influence of spot spacing, apertures, and the margin from the CTV on the plan quality in treating neuromas and meningiomas (50). Recently,

Atkins et al. reported the retrospective study of 370 patients treated using passive-scattering system. The local control rate and toxicity were found comparable to the conventional photon technique (5). It would be interesting to compare these two merging techniques, SPArc and aperture-based IMPT, to further explore the dosimetric plan quality, especially in the target conformity, low dose sparing, and treatment delivery efficiency. With all of the ongoing developments, it is optimistic that proton beam therapy will become a growing treatment option for brain SRS.

Several points require further discussion. First, we acknowledge that the SPArc for brain tumors is not performed in routine clinical practice; however, our study was designed as a proof-of-principle to determine clinical scenarios in which protons may have the chance to offer superior brain sparing compared to the conventional VMAT. To achieve this, we attempted to equilibrate as many treatment planning variables as possible between the three modalities. Second, the model did not include the brainstem in the consideration, so it may not be suitable for the clinical situation where the target is inside or abutting the brainstem.

In summary, this study validated the brain SRS dosimetric model using nine clinical cases and a blind survey. For the cancer centers equipped with both photon and proton treatment facilities, this model-based decision tree provides a practical tool as *a priori* knowledge in selecting IMPT, VMAT, or SPArc without generating a comparable plan, which has the potential to reduce the planning workload and improve clinical workflow efficiency.

CONCLUSIONS

At the current stage of technological development, VMAT holds the dosimetric advantage in the single brain lesion SRS over IMPT. With the new technology, SPArc showed its potential clinical advantage to offer lower dose to the brain tissue over VMAT with an equivalent or higher CI in the peripheral brain lesion and deep centrally located lesion larger than 9 cc. The brain SRS dosimetric model developed in this study could be used as a future reference tool to assist the clinical decision in selecting the optimal treatment modality for the patient.

DATA AVAILABILITY STATEMENT

The raw data supporting the conclusions of this article will be made available by the authors, without undue reservation.

ETHICS STATEMENT

The study has been approved by Beaumont Health Internal Review Board #2017-455. Written informed consent for participation was not required for this study in accordance with the national legislation and the institutional requirements. Written informed consent was not obtained from the individual(s) for the publication of any potentially identifiable images or data included in this article.

AUTHOR CONTRIBUTIONS

SC and GL contributed to the acquisition, analysis, and interpretation of data and drafted and designed the paper. LZ, WZ, and DY provided technical support. WZ, DY, PChc, XPL, KY, RD, CS, IG and PChi contributed to revising the paper and providing clinical inputs. XQL provided physics and clinical support. XD contributed to the design of the study, revised the draft, and led the research direction. All authors contributed to the article and approved the submitted version.

FUNDING

The study is supported by Ion Beam Application S.A. (IBA, Belgium) and Beaumont health seed grant award. The funders were not involved in the study design, collection, analysis, interpretation of data, the writing of this article, or the decision to submit it for publication.

SUPPLEMENTARY MATERIAL

The Supplementary Material for this article can be found online at: https://www.frontiersin.org/articles/10.3389/fonc.2022.804036/full#supplementary-material

REFERENCES

1. Chin LS, Regine WF eds. *Principles and Practice of Stereotactic Radio Surgery*. New York, NY: Springer (2008).
2. Ma L, Petti P, Wang B, Descovich M, Chuang C, Barani IJ, et al. Apparatus Dependence of Normal Brain Tissue Dose in Stereotactic Radiosurgery for Multiple Brain Metastases. *J Neurosurg* (2011) 114(6):1580–4. doi: 10.3171/2011.1.jns101056
3. Ma L, Nichol A, Hossain S, Wang B, Petti P, Vellani R, et al. Variable Dose Interplay Effects Across Radiosurgical Apparatus in Treating Multiple Brain Metastases. *Int J Comput Assist Radiol Surg* (2014) 9(6):1079–86. doi: 10.1007/s11548-014-1001-4
4. Ma L, Sahgal A, Descovich M, Cho YB, Chuang C, Huang K, et al. Equivalence in Dose Fall-Off for Isocentric and Nonisocentric Intracranial Treatment Modalities and its Impact on Dose Fractionation Schemes. *Int J Radiat Oncol Biol Phys* (2010) 76(3):943–8. doi: 10.1016/j.ijrobp.2009.07.1721
5. Atkins KM, Pashtan IM, Bussière MR, Kang KH, Niemierko A, Daly JE, et al. Proton Stereotactic Radiosurgery for Brain Metastases: A Single-Institution Analysis of 370 Patients. *Int J Radiat Oncol Biol Phys* (2018) 101(4):820–9. doi: 10.1016/j.ijrobp.2018.03.056
6. Paddick I, Lippitz B. A Simple Dose Gradient Measurement Tool to Complement the Conformity Index. *J Neurosurg* (2006) Suppl). 105:194–201. doi: 10.3171/sup.2006.105.7.194
7. Minniti G, Clarke E, Lanzetta G, Osti MF, Trasimeni G, Bozzao A, et al. Stereotactic Radiosurgery for Brain Metastases: Analysis of Outcome and Risk of Brain Radionecrosis. *Radiat Oncol* (2011) 6:48–56. doi: 10.1186/1748-717X-6-48
8. Blonigen BJ, Steinmetz RD, Levin L, Lamba MA, Warnick RE, Breneman JC. Irradiated Volume as a Predictor of Brain Radionecrosis After Linear

Accelerator Stereotactic Radiosurgery. *Int J Radiat Oncol Biol Phys* (2010) 77:996–1001. doi: 10.1016/j.ijrobp.2009.06.006
9. Bohoudi O, Bruynzeel AM, Lagerwaard FJ, Cuijpers JP, Slotman BJ, Palacios MA. Isotoxic Radiosurgery Planning for Brain Metastases. *Radioth Oncol* (2016) 120(2):253–7. doi: 10.1016/j.radonc.2016.05.001
10. Nieder C, Grosu AL, Gaspar LE. Stereotactic Radiosurgery (SRS) for Brain Metastases: A Systematic Review. *Radiat Oncol* (2014) 9:155. doi: 10.1186/1748-717X-9-155
11. Eaton BR, Gebhardt B, Prabhu R, Shu HK, Curran WJJR, Crocker I. Hypofractionated Radiosurgery for Intact or Resected Brain Metastases: Defifining the Optimal Dose and Fractionation. *Radiat Oncol* (2013) 8:135. doi: 10.1186/1748-717X-8-135
12. Vogelbaum MA, Angelov L, Lee SY, Li L, Barnett GH, Suh JH. Local Control of Brain Metastases by Stereotactic Radiosurgery in Relation to Dose to the Tumor Margin. *J Neurosurg* (2006) 104:907–12. doi: 10.3171/jns.2006.104.6.907
13. Han JH, Kim DG, Chung H-T, Paek SH, Park C-K, Jung H-W. Radiosurgery for Large Brain Metastases. *Int J Radiat Oncol Biol Phys* (2012) 83:113–20. doi: 10.1016/j.ijrobp.2011.06.1965
14. Wiggenraad R, Verbeek-de Kanter A, Kal HB, Taphoorn M, Vissers T, Struikmans H. Dose-Effect Relation in Stereotactic Radiotherapy for Brain Metastases. A Systematic Review. *Radioth Oncol* (2011) 98:292–7. doi: 10.1016/j.radonc.2011.01.011
15. Rashid A, Memon MA, Ahmed U, Saleem MA, Bhatti AI, Ahmed N, et al. Multisession Stereotactic Radiosurgery for Large Benign Brain Tumors of >3cm- Early Clinical Outcomes. *J Radiosurg SBRT* (2012) 2(1):29–40.
16. Fatima N, Meola A, Pollom E, Chang SD, Soltys S. Stereotactic Radiosurgery for Large Benign Intracranial Tumors. *World Neurosurg* (2020) 134:e172–80. doi: 10.1016/j.wneu.2019.10.005
17. Geng C, Moteabbed M, Xie Y, Schuemann J, Yock T, Paganetti H. Assessing the Radiation-Induced Second Cancer Risk in Proton Therapy for Pediatric Brain Tumors: The Impact of Employing a Patient-Specific Aperture in Pencil Beam Scanning. *Phys Med Biol* (2016) 61(1):12–22. doi: 10.1088/0031-9155/61/1/12
18. Yoo GS, Yu JI, Cho S, Jung SH, Han Y, Park S, et al. Comparison of Clinical Outcomes Between Passive Scattering Versus Pencil-Beam Scanning Proton Beam Therapy for Hepatocellular Carcinoma. *Radioth Oncol* (2020) 146:187–93. doi: 10.1016/j.radonc.2020.02.019
19. Vogel J, Grewal A, O'Reilly S, Lustig R, Kurtz G, Minturn JE, et al. Risk of Brainstem Necrosis in Pediatric Patients With Central Nervous System Malignancies After Pencil Beam Scanning Proton Therapy. *Acta Oncol* (2019) 58(12):1752–6. doi: 10.1080/0284186X.2019.1659996
20. Verhey LJ, Smith V, Serago CF. Comparison of Radiosurgery Treatment Modalities Based on Physical Dose Distributions. *Int J Radiat Oncol Biol Phys* (1998) 40(2):497–505. doi: 10.1016/s0360-3016(97)00720-7
21. Smith V, Verhey L, Serago CF. Comparison of Radiosurgery Treatment Modalities Based on Complication and Control Probabilities. *Int J Radiat Oncol Biol Phys* (1998) 40(2):507–13. doi: 10.1016/s0360-3016(97)00721-9
22. Moteabbed M, Yock TI, Depauw N, Madden TM, Kooy HM, Paganetti H. Impact of Spot Size and Beam-Shaping Devices on the Treatment Plan Quality for Pencil Beam Scanning Proton Therapy. *Int J Radiat Oncol Biol Phys* (2016) 95(1):190–8. doi: 10.1016/j.ijrobp.2015.12.368
23. Amichetti M, Amelio D, Minniti G. Radiosurgery With Photons or Protons for Benign and Malignant Tumours of the Skull Base: A Review. *Radiat Oncol* (2012) 7:210. doi: 10.1186/1748-717X-7-210
24. Kirkpatrick JP, Laack NN, Halasz LM, Minniti G, Chan MD. Proton Therapy for Brain Metastases: A Question of Value. *Int J Radiat Oncol Biol Phys* (2018) 101(4):830–2. doi: 10.1016/j.ijrobp.2018.05.005
25. Ding X, Li X, Zhang JM, Kabolizadeh P, Stevens C, Yan D. Spot-Scanning Proton Arc (SPArc) Therapy: The First Robust and Delivery-Efficient Spot-Scanning Proton Arc Therapy. *Int J Radiat Oncol Biol Phys* (2016) 96(5):1107–16. doi: 10.1016/j.ijrobp.2016.08.049
26. Pidikiti R, Patel BC, Maynard MR, Dugas JP, Syh J, Sahoo N, et al. Commissioning of the World's First Compact Pencil-Beam Scanning Proton Therapy System. *J Appl Clin Med Phys* (2018) 19(1):94–105. doi: 10.1002/acm2.12225
27. Ding X, Li X, Qin A, Zhou J, Yan D, Stevens C, et al. Have We Reached Proton Beam Therapy Dosimetric Limitations? – a Novel Robust, Delivery-Efficient and Continuous Spot-Scanning Proton Arc (SPArc) Therapy is to Improve the Dosimetric Outcome in Treating Prostate Cancer. *Acta Oncol* (2018) 57(3):435–7. doi: 10.1080/0284186X.2017.1358463
28. Liu G, Li X, Qin A, Zheng W, Yan D, Zhang S, et al. Improve the Dosimetric Outcome in Bilateral Head and Neck Cancer (HNC) Treatment Using Spot-Scanning Proton Arc (SPArc) Therapy: A Feasibility Study. *Radiat Oncol* (2020) 15(1):21. doi: 10.1186/s13014-020-1476-9
29. Li X, Kabolizadeh P, Yan D, Qin A, Zhou J, Hong Y, et al. Improve Dosimetric Outcome in Stage III non-Small-Cell Lung Cancer Treatment Using Spot-Scanning Proton Arc (SPArc) Therapy. *Radiat Oncol* (2018) 13:35. doi: 10.1186/s13014-018-0981-6
30. Ding X, Zhou J, Li X, Blas K, Liu G, Wang Y, et al. Improving Dosimetric Outcome for Hippocampus and Cochlea Sparing Whole Brain Radiotherapy Using Spot-Scanning Proton Arc Therapy. *Acta Oncol* (2019) 58:483–90. doi: 10.1080/0284186X.2018.1555374
31. Chang S, Liu G, Zhao L, Dilworth JT, Zheng W, Jawad S, et al. Feasibility Study: Spot-Scanning Proton Arc Therapy (SPArc) for Left-Sided Whole Breast Radiotherapy. *Radiat Oncol* (2020) 15(1):232. doi: 10.1186/s13014-020-01676-3
32. Liu G, Zhao L, Qin A, Grills I, Deraniyagala R, Stevens C, et al. Lung Stereotactic Body Radiotherapy (SBRT) Using Spot-Scanning Proton Arc (SPArc) Therapy: A Feasibility Study. *Front Oncol* (2021) 11:664455. doi: 10.3389/fonc.2021.664455
33. Liu G, Li X, Qin A, Zhou J, Zheng W, Zhao L, et al. Is Proton Beam Therapy Ready for Single Fraction Spine SBRS? - a Feasibility Study to Use Spot-Scanning Proton Arc (SPArc) Therapy to Improve the Robustness and Dosimetric Plan Quality. *Acta Oncol* (2021) 60(5):653–7. doi: 10.1080/0284186X.2021.1892183
34. Burman C, Kutcher GJ, Emami B, Goitein M. Fitting of Normal Tissue Tolerance Data to an Analytic Function. *Int J Radiat Oncol Biol Phys* (1991) 21:123–35. doi: 10.1016/0360-3016(91)90172-z
35. Fowler JF. The Linear-Quadratic Formula and Progress in Fractionated Radiotherapy. *Br J Radiol* (1989) 62(740):679–94. doi: 10.1259/0007-1285-62-740-679
36. Kim Y, Tomé WA. On the Radiobiological Impact of Metal Artifacts in Head-and-Neck IMRT in Terms of Tumor Control Probability (TCP) and Normal Tissue Complication Probability (NTCP). *Med Bio Eng Comput* (2007) 45:1045–51. doi: 10.1007/s11517-007-0196-8
37. Okunieff P, Morgan D, Niemierko A, Suit HD. Radiation Dose-Response of Human Tumors. *Int J Radiat Oncol Biol Phys* (1995) 32:1227–37. doi: 10.1016/0360-3016(94)00475-z
38. Brown PD, Jaeckle K, Ballman KV, Farace E, Cerhan JH, Anderson SK, et al. Effect of Radiosurgery Alone vs Radiosurgery With Whole Brain Radiation Therapy on Cognitive Function in Patients With 1 to 3 Brain Metastases: A Randomized Clinical Trial. *JAMA.* (2016) 316(4):401–9. doi: 10.1001/jama.2016.9839
39. Kjelberg RN. Isoeffective Dose Parameters for Brain Necrosis in Relation to Proton Radiosurgical Dosimetry. In: *Stereotactic Cerebral Irradiations*. Amsterdam: Elsevier (1979). 157–166 p.
40. Shaw E, Scott C, Souhami L, Dinapoli R, Kline R, Loeffler J, et al. Single Dose Radiosurgical Treatment of Recurrent Previously Irradiated Primary Brain Tumors and Brain Metastases: Final Report of RTOG Protocol 90-05. *Int J Radiat Oncol Biol Phys* (2000) 47(2):291–8. doi: 10.1016/s0360-3016(99)00507-6
41. Hyer DE, Hill PM, Wang D, Smith BR, Flynn RT. A Dynamic Collimation System for Penumbra Reduction in Spot-Scanning Proton Therapy: Proof of Concept. *Med Phys* (2014) 41(9):091701. doi: 10.1118/1.4837155
42. Wang D, Dirksen B, Hyer DE, Buatti JM, Sheybani A, Dinges E, et al. Impact of Spot Size on Plan Quality of Spot Scanning Proton Radiosurgery for Peripheral Brain Lesions. *Med Phys* (2014) 41(12):121705. doi: 10.1118/1.4901260
43. Wang D, Smith BR, Gelover E, Flynn RT, Hyer DE. A Method to Select Aperture Margin in Collimated Spot Scanning Proton Therapy. *Phys Med Biol* (2015) 60(7):N109–19. doi: 10.1088/0031-9155/60/7/N109
44. Lyman JT. Complication Probability as Assessed From Dose-Volume Histograms. *Radiat Res* (1985) Suppl. 8:S13–9.
45. Källman P, Agren A, Brahme A. Tumour and Normal Tissue Responses to Fractionated non-Uniform Dose Delivery. *Int J Radiat Biol* (1992) 62(2):249–62. doi: 10.1080/09553009214552071
46. Koschik A, Bula C, Duppich J, et al. Gantry 3: Further Development of the Psi Proscan Proton Therapy Facility (Accessed Proceedings of IPAC 2015).
47. Giantsoudi D, Seco J, Eaton BR, Simeone FJ, Kooy H, Yock TI. Evaluating Intensity Modulated Proton Therapy Relative to Passive Scattering Proton

Therapy for Increased Vertebral Column Sparing in Craniospinal Irradiation in Growing Pediatric Patients. *Int J Radiat Oncol Biol Phys* (2017) 98(1):37–46. doi: 10.1016/j.ijrobp.2017.01.226
48. Boczkowski A, Kelly P, Meeks SL, Erhart K, Bova FJ, Willoughby TR. Proton vs Hyperarc™ Radiosurgery: A Planning Comparison. *J Appl Clin Med Phys* (2020) 21(12):96–108. doi: 10.1002/acm2.13075
49. Halasz LM, Bussière MR, Dennis ER, Niemierko A, Chapman PH, Loeffler JS, et al. Proton Stereotactic Radiosurgery for the Treatment of Benign Meningiomas. *Int J Radiat Oncol Biol Phys* (2011) 81:1428–35. doi: 10.1016/j.ijrobp.2010.07.1991
50. Righetto R, Fellin F, Scartoni D, Amichetti M, Schwarz M, Amelio D, et al. Is it Beneficial to Use Apertures in Proton Radiosurgery With a Scanning Beam? A Dosimetric Comparison in Neurinoma and Meningioma Patients. *J Appl Clin Med Phys* (2022) 23(2):e13459. doi: 10.1002/acm2.13459

Conflict of Interest: This research was supported by Beaumont Research Seed Grant Award and Ion Beam Application. XD received honorarium from IBA Speaker Bureau outside the work presented in this study.

The remaining authors declare that the research was conducted in the absence of any commercial or financial relationships that could be construed as a potential conflict of interest.

Advantages of publishing in Frontiers

OPEN ACCESS
Articles are free to read for greatest visibility and readership

FAST PUBLICATION
Around 90 days from submission to decision

HIGH QUALITY PEER-REVIEW
Rigorous, collaborative, and constructive peer-review

TRANSPARENT PEER-REVIEW
Editors and reviewers acknowledged by name on published articles

Frontiers
Avenue du Tribunal-Fédéral 34
1005 Lausanne | Switzerland

Visit us: www.frontiersin.org
Contact us: frontiersin.org/about/contact

REPRODUCIBILITY OF RESEARCH
Support open data and methods to enhance research reproducibility

DIGITAL PUBLISHING
Articles designed for optimal readership across devices

FOLLOW US
@frontiersin

IMPACT METRICS
Advanced article metrics track visibility across digital media

EXTENSIVE PROMOTION
Marketing and promotion of impactful research

LOOP RESEARCH NETWORK
Our network increases your article's readership